

In Search of Highly Emissive Fully Organic Compounds for Application in Molecular Electronics

Marta Gulman



A thesis submitted to the University of Dublin for the degree of
Doctor of Philosophy

School of Chemistry
Trinity College Dublin

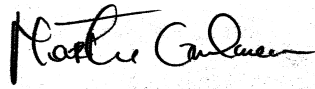
January 2022

Declaration

I declare that this thesis details entirely my own work. Due acknowledgements and references are given to the work of others where appropriate.

I agree to deposit this thesis in the University's open access institutional repository or allow the Library to do so on my behalf, subject to Irish Copyright Legislation and Trinity College Library conditions of use and acknowledgement.

I consent to the examiner retaining a copy of the thesis beyond the examining period, should they so wish.

A handwritten signature in black ink, appearing to read 'Marta Gulman', with a stylized, cursive script.

Marta Gulman

Summary

Chapter One: This Chapter provides a general overview of the field of molecular electronics and its current breakthroughs. The Chapter begins with a brief historical background of the field, and its advantages over conventional electronics. Key molecular devices and circuit components present in the literature are reviewed which are relevant to the research Chapters. Subsequently, relevant photophysical processes such as thermally activated delayed fluorescence and phosphorescence are described.

Chapter Two: This Chapter begins with a general overview about graphene and its bottom-up synthesised fragments coined nanographenes. Literature examples and synthesis of nanographenes, including heteroatom doped nanographenes, are described in-depth. A stepwise and detailed account is given of the synthetic methodological trials which were carried out towards novel nanographene targets, and their outcomes.

Chapter Three: This Chapter focuses on an array of preliminary synthetic explorations and photophysical studies towards novel highly emissive donor-acceptor materials. An alternative approach is taken, utilising Acceptor- π -Donor- π -Acceptor (A- π -D- π -A) architectural backbone for all emitters synthesised. A central phenothiazine donor is utilised in all emitters. Cyano bearing acceptors are used (either benzonitriles or triazines) to study the effect of the cyano positioning on the overall photophysical properties of the material. The understandings of this work shaped the design of Chapter Four.

Chapter Four: This Chapter begins with an overview of three-coordinate boron and its importance in organic light emitting diodes, and proceeds to outlining the current twisted organic materials used for thermally activated delayed fluorescence. Synthesis, characterisation, and photophysical studies of a family of azaborine containing small and twisted organic compounds is described, with its subsequent importance and application in the field of molecular electronics.

Chapter Five: This Chapter outlines summary of findings of the thesis.

Chapter Six: This Chapter describes the complete experimental methods carried out to synthesise and characterise the compounds prepared for this work.

Acknowledgements

I would like to thank Prof. Sylvia Draper for giving me the opportunity to carry out a Ph.D. as part of the group.

A token of gratitude to Dr. John O'Brien for his continued patience and dedication, Dr. Manuel Ruether for continued photophysical help as well as Dr. Gary Hessman for MS analysis. Sincerest thank you to Dr. Brendan Twamley for countless hours spent going over crystallography data.

Extended thanks to all the current and past Draper group members who helped me along the way and worked alongside me throughout the duration of the degree.

To my friends, thank you. Your love supports me like the sea. You are unreal.

Most importantly, I thank my family, who taught me how to work tirelessly and remain determined while always supporting those around me. Without such colossal grounding, I would have never been able to undertake a Ph.D.

Table of Contents

Chapter One	1
Introduction	1
1.0 Introduction	2
1.1 Molecular Electronics	2
1.2 Historical Background	2
1.3 Advantages of Molecular Electronics	5
1.4 Molecular Devices and Circuit Components	6
1.5 Single Molecule Junction.....	6
1.5.1 Fabrication of and Electron Transport through a Single Molecule Junction	7
1.6 Semiconducting Materials	9
1.6.1 Graphene	11
1.7 Molecular Transistor.....	12
1.8 Molecular Diode	14
1.8.2 Organic Light Emitting Diodes (OLEDs)	15
1.9 Aims.....	20
1.9.1 Chapter Two	21
1.9.2 Chapter Three	21
1.9.3 Chapter Four	21
1.10 References.....	22
Chapter Two	26
Synthetic Trials Towards Novel Nanographene Type Compounds.....	26
2.0 Introduction.....	27
2.1 Polycyclic Aromatic Hydrocarbons (PAH's).....	28
2.1.1 Synthesis of PAH	29
2.2 Introduction of Heteroatoms to PAH's.....	31
2.2.1 Introducing Nitrogen	32
2.2.2 Introducing Boron	35
2.3 Developing Synthetic Methodologies Towards Novel Targets.....	38
2.4 Synthesis and Characterisation.....	39
2.4.1 All-carbon PAH	39
2.4.2 Knoevenagel Condensation.....	41
2.4.3 Diels-Alder Cycloaddition	52

2.4.4 Oxidative Cyclohydrogenation	53
2.4.5 Photophysical and Thermal Analysis.....	56
2.4.6 Conclusions and Future Work.....	58
2.5 Nitrogen-doped PAH's	58
2.5.1 Facile Synthesis of Phenazine PAH's.....	59
2.5.2 Conclusions and Future Work.....	61
2.5.3 DDQ/H ⁺ as a Cyclohydrogenation Agent	61
2.5.4 Conclusions and Future Work.....	66
2.6 Boron and Nitrogen Doped PAH.....	67
2.6.1 [4 + 2] Diels-Alder Cycloaddition	68
2.6.2 Suzuki-Miyaura Coupling.....	70
2.6.3 Grignard Reaction	83
2.6.4 Boron Dimerisation.....	86
2.6.5 Conclusions and Future Work.....	90
2.7 Chapter Conclusions and Future Work	91
2.8 References	93
Chapter Three	96
In Search of Highly Emissive Donor-Acceptor Structures for Thermally Activated Delayed Fluorescence Organic Light Emitting Diodes.....	96
3.0 Introduction	97
3.1 Donor-Acceptor Systems	97
3.2 Ideal Donor Candidates	99
3.2.1 Phenothiazine	99
3.3 Acceptor Candidates.....	100
3.3.1 Triazine Acceptors	101
3.4 Design Considerations for the Emitters.....	101
3.5 Results and Discussion	103
3.5.1 Synthesis of D-A Systems.....	104
3.5.2 Synthesis of the Donor Moiety	104
3.5.3 Synthesis of the Acceptor Moiety	105
3.5.4 Sonogashira Coupling	106
3.6 Structural Characterisation	107
3.7 Unsuccessful Synthetic Targets.....	110

3.8 Photophysical Analysis.....	111
3.8.1 Preliminary Studies	111
3.9 Triazines	112
3.9.1 UV-vis Absorption and Emission Solvatochromism	112
3.9.2 Acid Titration Studies of 42 and 43	117
3.9.3 77K Emission Studies of 42 and 43	119
3.9.4 Lifetime Determination of 42 and 43.....	119
3.10 Cyclic Voltammetry.....	120
3.11 Computational Studies.....	122
3.12 Thermal Studies.....	125
3.13 Conclusions.....	126
3.14 Future Work.....	127
3.15 References.....	128
Chapter Four	134
Study of Twisted Azaborine Containing Small Organic Molecules for Thermally Activated Delayed Fluorescence Organic Light Emitting Diodes.....	134
4.0 Introduction.....	135
4.1 Three-Coordinate Boron.....	135
4.1.1 Tri-Coordinate Boron Containing Emitters	137
4.1.2 Azaborine	140
4.2 Carbazole	141
4.3 Design Considerations for the Emitters.....	143
4.5 Results and Discussion	145
4.5.1 C-N Bond Formation Towards Novel Functionalised Tertiary Amines.....	145
4.5.2 Synthesis of Azaborine	151
4.5.3 Suzuki Coupling to Synthesise 54 and 55.....	156
4.5.4 Buchwald–Hartwig Coupling to Synthesise 58 and 60.....	162
4.6 Photophysical Analysis.....	169
4.7 Computational Analysis.....	176
4.8 Thermal Analysis.....	178
4.9 Conclusions.....	179
4.10 Future Work.....	180
4.11 References.....	181
Chapter Five	185

Summary of Findings.....	185
5.1 Summary of Findings	186
Chapter Six	188
Experimental.....	188
Experimental.....	189
4,6,10,12-tetrakis(4-(tert-butyl)phenyl)dicyclopenta[e,l]pyrene-5,11-dione (5).....	191
4,6,10,12-tetrakis(4-(tert-butyl)phenyl)dicyclopenta[e,l]pyrene-5,11-dione (6).....	192
2,7-di-tert-butyl-4,5,9,10-tetrahydropyrene-4,5,9,10-tetrayl)tetrakis((4-(tert-butyl)phenyl)methanone) (7)	193
4,7,11,14-tetrakis(4-(tert-butyl)phenyl)-5,6,12,13-tetraphenyldibenzo[fg,op]tetracene (12)	194
2,9-di-tert-butyl-4,7,11,14-tetrakis(4-(tert-butyl)phenyl)-5,6,12,13-tetraphenyldibenzo[fg,op]tetracene (13)	195
C72 PAH (14).....	196
9b,9b1-dihydrodibenzo[h,j]dibenzo[5',6':7',8']quinoxalino[2',3':9,10]phenanthro[4,5-abc]phenazine (17)	197
11,24-di-tert-butyl-9b,9b1-dihydrodibenzo[h,j]dibenzo[5',6':7',8']quinoxalino[2',3':9,10]phenanthro[4,5- abc]phenazine (18)	198
4,4'-(4,5-dibromo-1,2-phenylene)dipyridine (26)	198
4-(4,5-dibromo-2-iodophenyl)pyridine (28).....	200
5,5'-(4,5-dibromo-1,2-phenylene)dipyrimidine (30)	201
5-(4,5-dibromo-2-iodophenyl)pyrimidine (31)	203
5,5',5''-(5-bromobenzene-1,2,4-triyl)tripyrimidine (32)	204
4,4'-(6-(4-Bromophenyl)-1,3,5-triazine-2,4-diyl)dibenzonitrile (38).....	204
4,4'-((10-Dodecyl-10 <i>H</i> -phenothiazine-3,7-diyl)bis(ethyne-2,1-diyl)dibenzonitrile (39)	205
3,3'-((10-Dodecyl-10 <i>H</i> -phenothiazine-3,7-diyl)bis(ethyne-2,1-diyl)dibenzonitrile (41)	207
3,7-Bis((4-(4,6-diphenyl-1,3,5-triazin-2-yl)phenyl)ethynyl)-10-dodecyl-10 <i>H</i> -phenothiazine (42)	208
4,4',4'',4'''-(((10-Dodecyl-10 <i>H</i> -phenothiazine-3,7-diyl)bis(ethyne-2,1-diyl))bis(4,1-phenylene))bis(1,3,5- triazine-6,2,4-triyl)tetrabenzonitrile (43)	209
2,8-dibromo-5-(4-(tert-butyl)phenyl)-10-(2,4,6-triisopropylphenyl)-5,10- dihydrodibenzo[b,e][1,4]azaborinine (51).....	210
2,8-dibromo-5-methyl-10-(2,4,6-triisopropylphenyl)-5,10-dihydrodibenzo[b,e][1,4]azaborinine (53).....	212
4,4'-(5-(4-(tert-butyl)phenyl)-10-(2,4,6-triisopropylphenyl)-5,10-dihydrodibenzo[b,e][1,4]azaborinine-2,8- diyl)bis(N,N-diphenylaniline) (54).....	213
2,8-bis(4-(9 <i>H</i> -carbazol-9-yl)phenyl)-5-(4-(tert-butyl)phenyl)-10-(2,4,6-triisopropylphenyl)-5,10- dihydrodibenzo[b,e][1,4]azaborinine (55).....	215
5-(4-(tert-butyl)phenyl)-2,8-di(9 <i>H</i> -carbazol-9-yl)-10-(2,4,6-triisopropylphenyl)-5,10- dihydrodibenzo[b,e][1,4]azaborinine (58).....	216
5-(4-(tert-butyl)phenyl)-2,8-bis(3,6-di(thiophen-2-yl)-9 <i>H</i> -carbazol-9-yl)-10-(2,4,6-triisopropylphenyl)- 5,10-dihydrodibenzo[b,e][1,4]azaborinine (60)	218
References	219
Appendix	220

Abbreviations

A Acceptor

A-D-A Acceptor-Donor-Acceptor

APCI Atmospheric-pressure chemical ionisation

BDT benzenedithiol

CRT Cathode ray tubes

CT Charge transfer

CV Cyclic Voltammetry

D donor

D-A Donor-Acceptor

D-A-D Donor-Acceptor-Donor

DFT Density Functional Theory

DMF Dimethylformamide

DMSO Dimethyl sulfoxide

DSC Differential Scanning Calorimetry

DSSC Dye sensitised solar cells

EA electron affinity

Fc⁺/Fc Ferrocenium/Ferrocene

FET field effect transistor

FTIR Fourier-transform infrared spectroscopy

GNR graphene nanoribbon

HBC hexa-*peri*-hexabenzocoronene

HOMO Highest occupied molecular orbital

HMBC Heteronuclear multiple bond correlation

HPLC High pressure liquid chromatography

HSQC Heteronuclear single quantum coherence

IC Internal conversion

IQE Internal Quantum Efficiency

IR Infrared

IRF Instrument response factor

ISC Intersystem crossing

ITO Indium Tin Oxide
IP ionisation potential
LCD Liquid Crystal Displays
LUMO Lowest unoccupied molecular orbital
MALDI TOF Matrix-assisted laser desorption/ionisation
MCBJ mechanically controllable break junction
MeOH Methanol
NBS n-bromosuccinimide
NIR Near-Infrared
NMR Nuclear Magnetic Resonance
OFET organic field-effect transistors
OLED organic light emitting diode
OSC Organic semiconductor
OPV Organic photovoltaic cells
PAH Polycyclic aromatic hydrocarbon
PLQY Photoluminescence quantum yield
PTZ Phenothiazine
rISC Reverse intersystem crossing
Rf Retention factor
RTP Room temperature phosphorescence
RT room temperature
S₁ Singlet excited state
STM Scanning Tunnelling Microscopy
STM-BJ STM controlled break junction
TADF Thermally activated delayed fluorescence
T₁ Triplet excited state
TFA Trifluoroacetic acid
TGA Thermogravimetric analysis
THF Tetrahydrofuran
TLC Thin layer chromatography
TMS Trimethylsilylacetylene

TOCSY Total correlated spectroscopy
TRLI Time-resolved luminescence imaging
TTA Triplet triplet annihilation
UV Ultraviolet
UV/Vis Ultraviolet/Visible

Units

τ Excited state lifetime
 ϵ Molar absorptivity coefficient
 λ Wavelength
 δ ppm
 ν Wavenumber
cm centimetre
eV Electronvolt
g Gram
h Hour
K Kelvin
M Molar
MHz Megahertz
 μ L microlitre
mL millilitre
mm micrometre
mmol micromolar
nm nanometre
ns nanosecond

Chapter One

Introduction

1.0 Introduction

This Chapter aims to broadly introduce the field of molecular electronics, describe relevant molecular devices, and highlight common organic molecules which have been studied for use in molecular devices. Fundamental photochemical processes which take place during device operation will also be described. Each subsequent research Chapter includes a short and specific literature overview.

1.1 Molecular Electronics

Molecular electronics can be broadly defined as a research field which investigates both thermal and photophysical properties of electronic circuits built from individual building blocks.¹ More specifically, it is a field of research which focuses on novel single molecules, small groups of molecules, carbon nanotubes, and metallic semiconducting wires to perform electronic functions.^{2,3} Generally speaking, these specifically designed molecules either conduct electrical current or influence charge transport properties. Therefore, they can be further categorised as active (switching and sensing) or passive (current rectifiers and surface passivants) components within a device.² Molecular devices are designed to mimic traditional components and serve to complement the current silicon based technologies, the development of which is hindered by Moore's Law.⁴

In 1965, Gordon Moore proposed that the number of transistors per cm^2 of silicon will double each year, and will continue to do so for the next ten years. This statement is thus known as 'Moore's Law'.⁵ By 1976, the law was revised to state that chip densities would double every two years.⁶ This reduction in component size is finite and will eventually reach molecular and atomic level, at which point the current fabrication methods for circuits would have been surpassed.⁷ In order for technological advancements to continue, there is a pressing need to develop novel single molecule circuit components to complement the current silicon based technologies.⁸

1.2 Historical Background

A revolution within conventional electronics came about in the 1950's, with the invention of a transistor, followed by the introduction of integrated circuits.¹ The 1970's saw the

emergence of preliminary research in the field of molecular electronics, where the bottom up approach of designing unique single molecule devices and components was seen as the most viable route rather than the continued miniaturisation of existing components.

In 1974, Aviram and Ratner's work on molecular current rectifiers was a pivotal moment in the field, which serves to be the foundation for current work on molecular diodes (defined and further discussed in Section 1.8).⁹ At the time, Aviram was employed by IBM to study charge transfer salts which had been deemed good conductors in their solid form. The collaboration between Aviram and Ratner arose when they jointly started to study the theory of electron transfer through single organic molecules. By combining two units, an electron rich unit and an electron poor unit separated by a σ -bridge, a conducting material which mimics a traditional semiconductor diode could be realised.¹⁰

The design of Aviram and Ratner's molecular rectifying diode is as follows; a donor tetrathiafulvalene π -system, and an acceptor tetracyanoquinodimethane π -system, covalently linked by a σ -bonded methylene bridge (**L1.0**, D- σ -A model).¹¹ The novelty of this idea meant that once this molecule was connected to metallic electrodes at either end, it could in theory support a continuous sequence of electron transfer processes also known as a stationary current (Figure 1.0).¹²

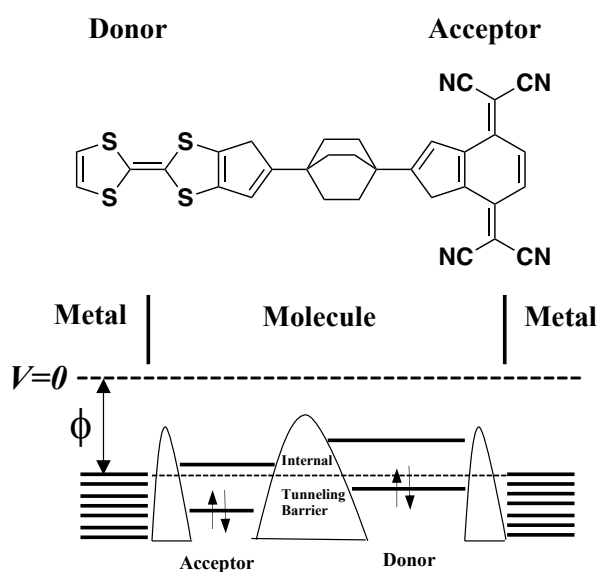


Figure 1.0: Aviram and Ratner's D- σ -A model single molecule rectifier **L1.0**. The transport barrier is annotated with ϕ .¹¹

When fabricating molecular diodes, an electron-donating unit serves as an n-type semiconductor analogue, and an electron-accepting unit serves as a p-type semiconductor analogue. The electron-donating unit should have high electron density, and conversely the electron-accepting unit should have low electron density.⁹ The energy gap between the highest occupied molecular orbital (HOMO, localised to the donor) and the lowest occupied molecular orbital (LUMO, localised to the acceptor) is known as a HOMO/LUMO gap.⁷ Bridging two metallic electrodes by a single molecule causes these discrete energy states to merge into continuous states, and allows for current to flow in one direction only.¹³

Aviram and Ratner's work combined the donor π -system with an acceptor π -system linked by a tunnelling σ -bridge. The σ -bridge served to spatially separate the HOMO and the LUMO orbitals and ensured an adequate HOMO/LUMO gap. In theory, this design would permit HOMO and LUMO alignment of the molecule to that of the electrodes; which in turn would permit for an electrical current to occur in one direction only, resembling a diode functionality.^{14,15}

This work had come under scrutiny some years later, as it was observed that other molecules which did not have the donor-acceptor design could perform the same functionalities. At the time of this work, there was a complete lack of technology to allow for detailed studies of molecular alignment between electrodes, a visualisation of this process, or characterisation of the functionality it produced.¹⁶ Therefore, progress in the field was slow due to these major setbacks. This example is of particular importance because it set the groundwork upon which all of molecular electronics was built on. Even with this publication undergoing criticism, this donor-acceptor design became increasingly popular and was adapted by many researchers. Due to the vastness of this sub-field of molecular electronics, further detailed discussions on donor-acceptor systems can be located in Chapters Three and Four of this thesis.

1.3 Advantages of Molecular Electronics

Molecular electronics utilises the bottom-up approach to assemble individual molecular devices to produce more complex multi-functioning and commercially viable technologies. Conversely, conventional electronics employ a top-down approach which relies on continued miniaturisation of macroscopic components.¹ There exist key reasonings as to why molecular electronics is superior to conventional inorganic and silicon based technologies. These reasonings are outlined below and illustrated by Figure 1.1.

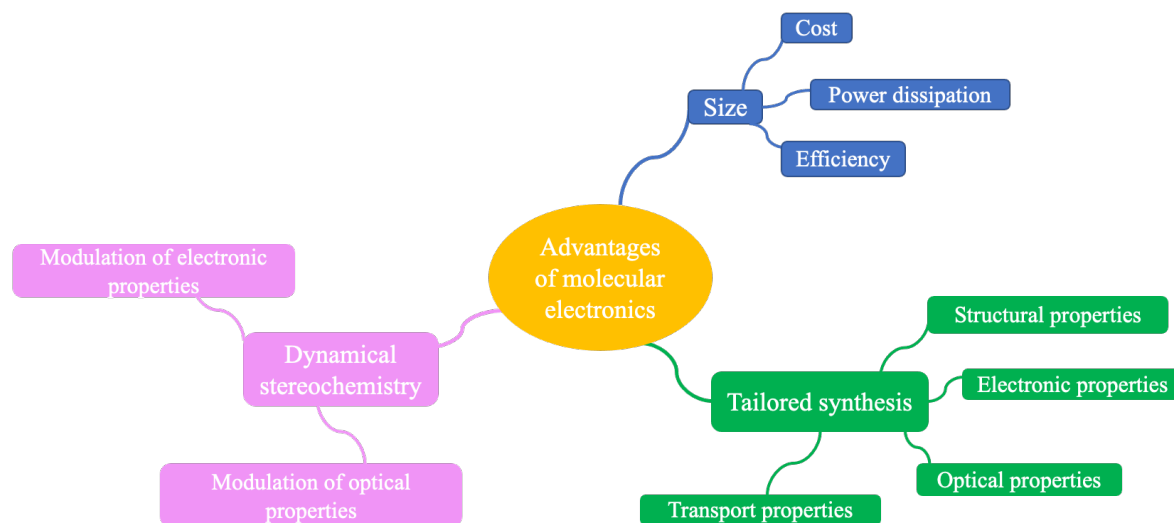


Figure 1.1: Advantages of molecular electronics.¹⁷

The reduction in size of molecular components when compared to silicon based components would allow for higher packing and density of devices, which in turn would increase the operational speed of devices.¹ Utilising organic molecules mimicking a conventional transistor and spanning 1-3 nm, one could potentially fit up to 10^{14} molecules in 1 cm^2 of a computer chip.¹⁸ Molecular circuits built by wiring of single molecules could raise device density by a factor of up to $\sim 10^4$ compared to current silicon-based devices.¹⁹ The reduction in size has an added advantage of increased efficiency and a reduction in cost as organic molecules are easily accessible *via* common synthetic methods.¹

Furthermore, a device such as a nanometre-long single molecule has the potential to achieve; increased complexity and functionality, structural flexibility, facile fabrication methods, and allow for synthetic modifications.⁶ To elaborate, molecular devices offer an element of tailorability, where a molecule can be specifically designed and synthesised for its purpose.

In this way, novel functionalities (such as molecular transport, binding, and optical properties) can be introduced into devices, which were not possible with conventional silicon based technologies.²⁰ Molecular interactions could be taken advantage of, for example to form self-assembling monolayers or within films which will in turn behave differently.

With every benefit, there exists a disbenefit. Molecular electronics is still in its infancy due to; chemical and molecular stability challenges, fabrication methods to establish reliable molecular junctions, and control of molecular behaviours at molecular junctions.¹ To progress, further understanding into the relationship between chemical structure of a molecule and its thin film properties is required, as well as consistency of microscopic arrangement of molecules during film formation.²¹ However when evaluating the two arguments, the field of molecular electronics still carries unprecedented potential and possibility, and therefore is worth pursuing.

1.4 Molecular Devices and Circuit Components

Within less than thirty years, molecular electronics' immense potential resulted in a great deal of research and subsequent publications. The literature contains comprehensive works on components such as molecular wires,²² single molecule junctions,²³⁻²⁵ molecular circuits,²⁶⁻²⁸ types of semiconducting materials,²⁹⁻³³ transistors,³⁴⁻³⁸ and organic light emitting diodes.³⁹⁻⁴² Due to the vastness of this field, it is not feasible to review all circuit components and molecular devices present in the literature. Therefore, only the circuit components which are applied within the research Chapters of this thesis and the key processes involved will be discussed herein.

1.5 Single Molecule Junction

A single molecule junction is the most simplistic circuit component which serves to bridge two metal electrodes within a molecular circuit. Molecular orbital hybridization occurs at the metal-molecule-metal interface resulting in charge transfer between the metal electrode and the molecule.⁴³ Even though Aviram and Ratner proposed this theoretically in 1974, experimental research proving its viability only emerged in 1990's with the development of the scanning tunnelling microscopy (STM) technique.¹⁹

Single molecule junctions can be divided into hard, rigid, and linear structures composed of carbon nanotubes,⁴⁴ silicon nanowires,³¹ and organic materials⁴⁵ respectively.⁴⁶ The most published organic materials for linear single molecule junctions are 1,4-benzene dithiol (**L1.1**),⁴⁷ metal phthalocyanines (**L1.2**),⁴⁸ and 4,4-biphenyl dithiol (**L1.3**, Figure 1.2).⁴⁶ The first experimentally fabricated single molecule junction was achieved by Reed *et al.*⁴⁹ in 1997 with a benzenedithiol (BDT) molecule using a mechanically controllable break junction (MCBJ) technique. Graphene, graphitic fragments, and nanographenes are also commonly used as single molecule junctions, which are discussed more in depth in Section 1.6.1 of this Chapter and subsequently applied in Chapter Two.

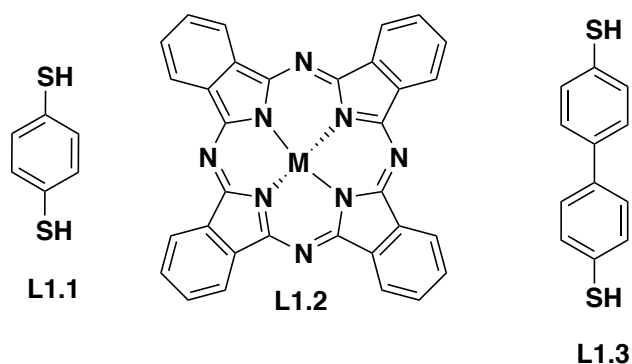


Figure 1.2: Literature examples of organic materials for linear single molecule junctions.^{46–48}

1.5.1 Fabrication of and Electron Transport through a Single Molecule Junction

One of the most vital interfaces in molecular electronics is the single molecule-metal bond, and this interface can be formed using a break junction technique.⁵⁰ In the presence of a suitable molecule, the metal is stretched until the weakest point breaks resulting in the formation of a molecular junction.⁹ Break junction methods are mainly utilised in conductance measurements, with two most prominent methods being STM controlled break junction (STM-BJ) and mechanically controlled break junction (MCBJ) as illustrated by Figure 1.3.⁵¹

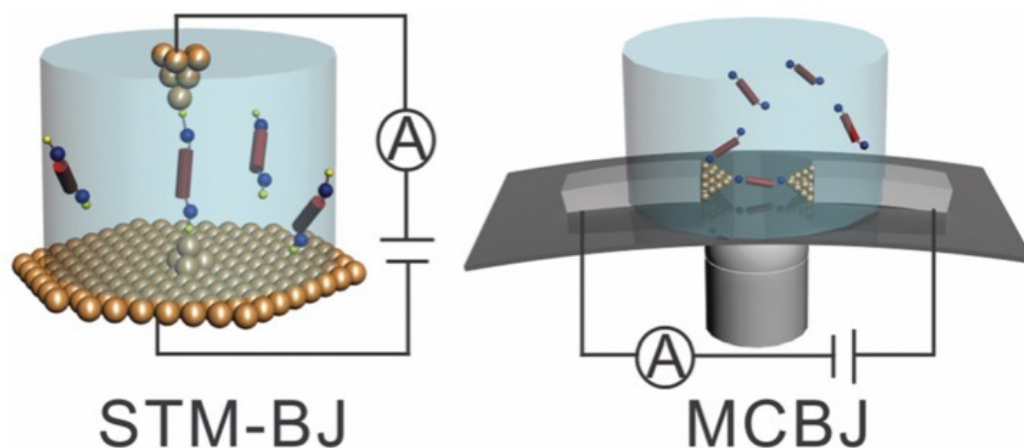


Figure 1.3: STM controlled break junction (STM-BJ), and mechanically controlled break junction (MCBJ).⁵¹

In 1985, Moreland and Eklin successfully measured the electron tunnelling characteristics of superconductors using a thin Nb-Sn filament mounted on a flexible glass beam.⁵² By 1992, Muller *et al.*⁵³ had adapted this methodology and coined it the mechanically controllable break junction. The MCBJ technique utilises a three point bending mechanism.⁵⁴ It relies on the formation and subsequent breakage of molecular junctions between horizontally suspended gold wires.⁵¹ This technique is insensitive to external mechanical vibrations, unlike the room temperature STM-BJ measurements. A major advantage of MCBJ is that it can be used in conjunction with other spectroscopic techniques such as UV-vis and/ or Raman Spectroscopy to gather structural and spectroscopic information about the junction.⁴⁷

Xu *et al.*⁵⁵ developed the STM-BJ technique in 2013. It allowed for thousands of molecular junctions to be formed by repeatedly moving the STM tip in and out of contact with the substrate in the presence of a molecule of interest.⁵⁶ STM-BJ is highly convenient due to its compatibility with commercial STM instruments, allowing for the single molecule target to be imaged prior, during, and after the transport experiment.⁴³ This imaging tool provides invaluable information about structure, and allows for precise positioning of the tip on the target.⁵¹ Performing statistical analysis on the individual measurement curves produced by the STM, the conductance of a single molecule with the most probable contact geometry can

be attained. This approach has been adapted by many researchers in order to get reproducible measurements of single molecule conductance.⁵⁷

In order for molecular devices to become commercially viable, precise control of conductance and understanding of electron transport through molecular junctions is required.⁵⁸ Several conduction mechanisms are possible which can coexist simultaneously within a single molecule junction, such as the Coulomb blockade, hopping, and tunnelling.⁵⁹ It is most common to assume that a single molecule junction is governed by the electron transport mechanism.

For electron transport to occur when a molecule makes contact with a metal electrode, electrons must cross an energy barrier to pass across the junction. This transport can be either dispersive or ballistic. In dispersive transport, electrons collide, and the energy of collision is transferred. Conversely, in ballistic transport, electronic transport is analogous to a linear motion.⁹ The Landauer theory is applied in both dispersive and ballistic transport mechanisms, and operates on the principle that electrons move smoothly from one electrode to the other.⁴⁶ To continue the understanding of electron transport within the single molecule junction, a closer look at the structure of the single molecule is required, also referred to as a semiconductor.

1.6 Semiconducting Materials

A semiconducting material can be broadly defined as a material that has the electrical conductivity between that of a conductor and an insulator. The conductivity difference is due to differences in energetic band structures, namely the conduction band and the valence band of the material.⁶⁰ An insulator can in theory become conducting if a stimulus which is equivalent to the gap between the conduction band and a valence band is applied. The gap between the conduction band and the valence band is known as the forbidden gap. Insulators are known to be large bandgap materials, where the conduction band and the valence band are spaced apart. Conversely, conductors have overlapping conduction and valence bands making them excellent charge transport carriers. Unlike any other material, graphene is a zero bandgap semiconductor, because its conduction and valence bands meet at the Dirac point.⁶¹ A further discussion on graphene can be located in Section 1.6.1 of this Chapter.

Semiconductors have closely spaced conduction and valence bands, with a forbidden gap of $\sim 1\text{-}3\text{ eV}$ which can be crossed with sufficient electrical or photonic stimuli.⁶²

Organic semiconductors (OSCs) can be divided into small molecules, π -conjugated polymers, and composites.⁶³ Their applications range from organic light emitting diodes (OLEDs), infrared applications, hybrid inorganic/ organic solar cells, to printable organic field-effect transistors (OFETs).²¹ In contrast to traditional inorganic semiconductors which have continuous energy bands, organic semiconductors possess discrete energy levels consisting of molecular orbitals. The conduction band is analogous to the LUMO frontier molecular orbitals and the valence band is analogous to the HOMO frontier molecular orbitals of the organic molecule (Figure 1.5).⁶⁰

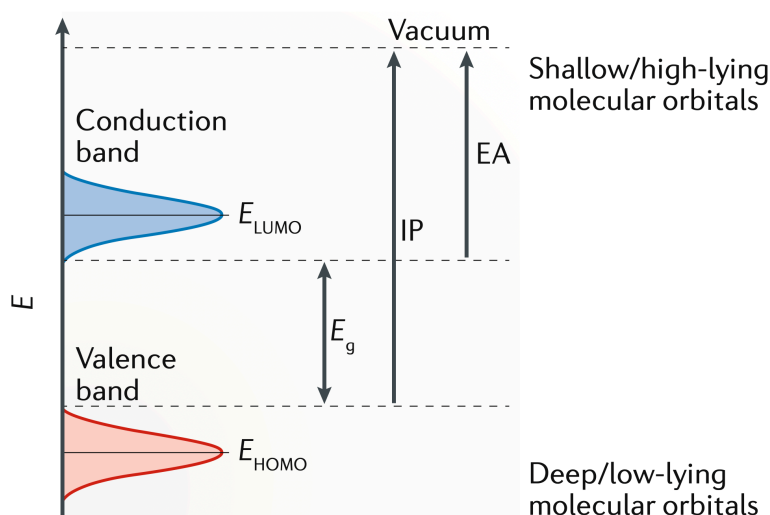


Figure 1.5: Schematic representation of the conduction and valence bands in an organic semiconducting material. The optical bandgap is annotated with E_g . IP is the ionisation potential, the energy required to remove an electron from the molecule and bring it to vacuum level. EA is electron affinity, the energy released when an electron is added to the molecule.⁶⁴

Increased conjugation in a molecule results in more closely spaced HOMO/LUMO orbitals, and thus π -conjugated materials make ideal organic semiconducting candidates. The energy of the HOMO is heavily dependent on the level of delocalisation of the π electrons throughout the molecule. Electron donating substituents such as lone pairs of nitrogen and oxygen will raise the energy of the HOMO. Electron withdrawing substituents lower both

HOMO and LUMO energies. A careful molecular design is necessary in order to obtain an organic semiconductor candidate.

1.6.1 Graphene

Graphene is an atomically thin two-dimensional sheet composed of hexagonal sp^2 -hybridised carbon atoms (Figure 1.6).⁶⁵ It is the building block of many carbon allotropes as it can be wrapped to form 0D fullerenes, rolled to form 1D nanotubes, and stacked to form 3D graphite.⁶⁶ Since its discovery by Geim *et al.*⁶⁷ in 2004, graphene has seen an unprecedented rise in popularity. Long range π -conjugation and extended electron delocalisation of graphene results in unrivalled thermal, mechanical, and electrical properties.⁶⁸ Researchers have utilised graphene as an electrode material in single molecule junctions and incorporated it into single molecule transistor devices.^{35,45}

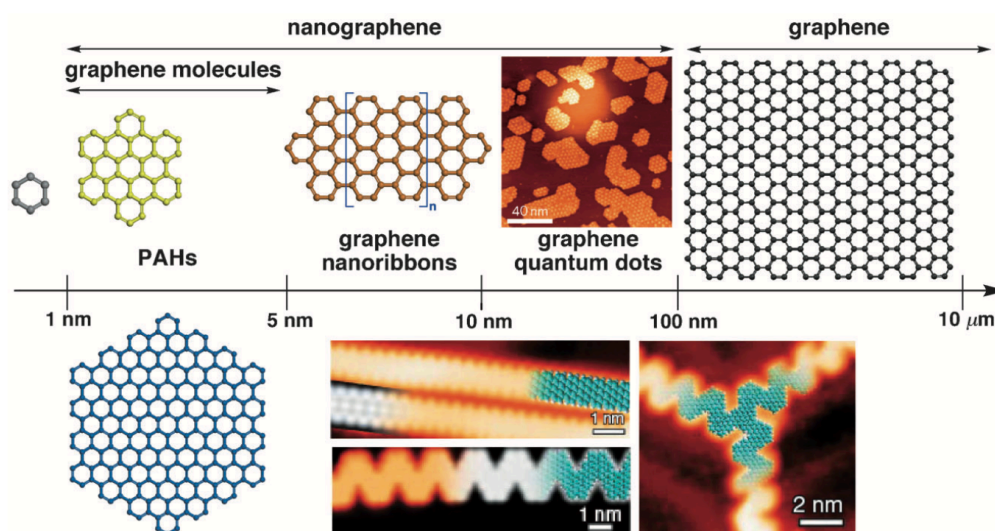


Figure 1.6: A systemic size terminology diagram of graphene and graphene analogues.⁶⁶

The overlapping p_z orbitals from each carbon atom generate a filled band of π orbitals known as the valence band of graphene. The unoccupied π^* orbitals composed of the s , p_z , and p_y atomic orbitals of carbon form three σ bonds with neighbouring carbons are known as the conduction band. Both the valence bands and the conduction bands of graphene are located near the Dirac point, which leads to a gapless energy band making graphene a potent conductor.⁶⁹ However, graphene's use in molecular electronics is facing a challenge due to the absence of bandgap, meaning that conductance cannot be modulated. Additionally,

fragment size is very difficult to control when exfoliating graphene from graphite. Bottom up nanographene synthesis is a viable solution to tackling size disparity of graphene as well as introducing structural functionality and heteroatom doping which will directly affect the bandgap of the material. Nanographene synthesis and application is further discussed in Chapter Two of this thesis.

1.7 Molecular Transistor

A transistor (also known as a field effect transistor, FET) is a vital electronic component which serves to switch electrical current between two electrodes using a gate electrode (Figure 1.6).⁷⁰

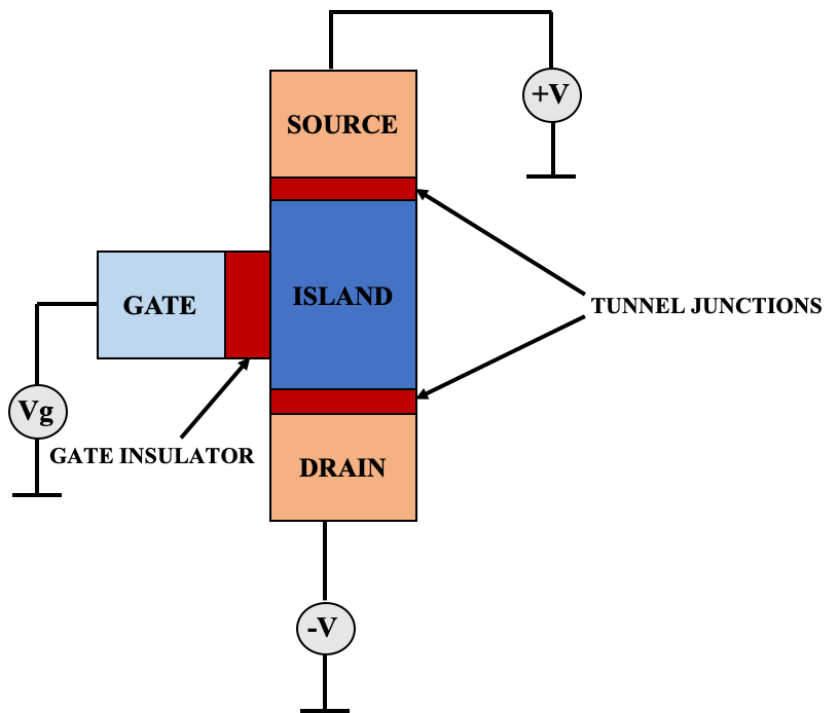


Figure 1.6: Schematic diagram of a transistor. V_g is the gate voltage which controls the current I by controlling the induced charge. $-V$ and $+V$ are negative and positive voltages respectively.⁷¹

A typical transistor has three metallic terminals, two of the terminals act as the source and the drain and the third acts as a gate, a thin insulating layer (dielectric), and a semiconductor.⁹ By applying voltage to one pair of terminals, current can be regulated through the other pair

of terminals. The source and drain are typically low resistance and Ohmic, and the gate electrode and island are isolated by a gate insulator. This all contributes to an efficient charge carrier ability of the transistor.⁷² The voltage output can be higher than the input, thus allowing it to act as an amplifier. Additionally, a transistor can act as a switch, where the voltage between one of the terminals has the ability to regulate the current between the other terminals.⁷³

The first reported single molecule transistor was fabricated by Park *et al.*⁷⁴ in 2000 by depositing C₆₀ molecule (**L1.4**, Figure 1.7) onto a pair of connected gold electrodes, and using the break junction technique to gap the electrodes and the molecule. Following this breakthrough, Yu *et al.*⁷⁵ utilised a rotaxane molecule (**L1.5**, Figure 1.7) as a single molecule transistor. Commonly, publications focus on graphene and graphene nanotubes as candidates for single molecule transistors.⁷⁶ However, the most recent literature has focused extensively on organic field effect transistors (OFETs) rather than single molecule transistors due to their flexibility, light weight structures, low-cost manufacturing, and tailorability.

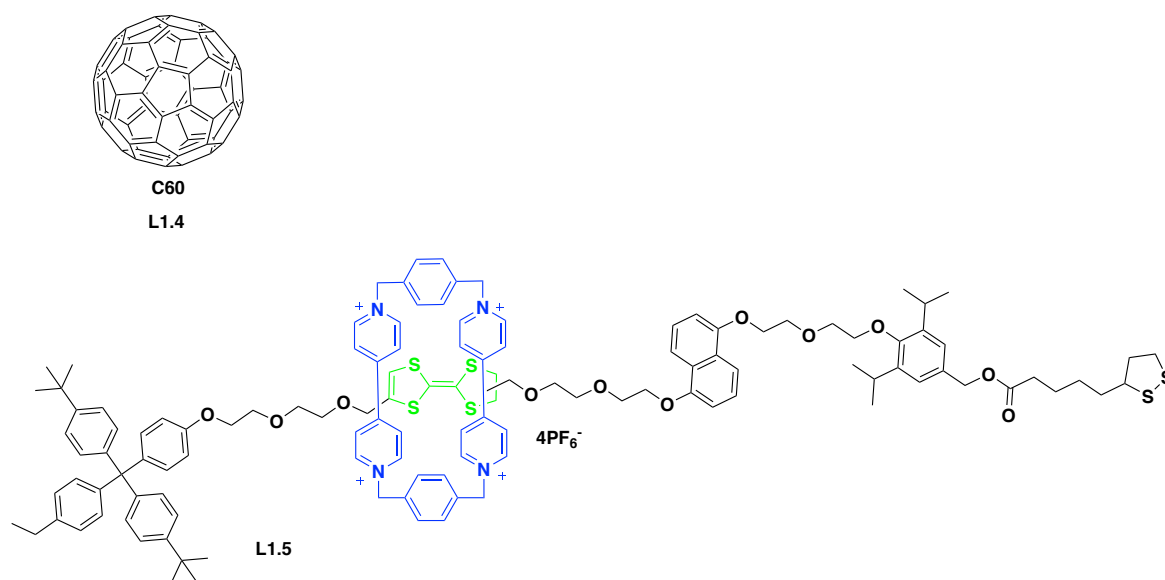


Figure 1.7: Literature examples of single molecule transistors.^{74,75}

The first OFET was fabricated by Tsumura *et al.*⁷⁷ in 1986 using a polythiophene thin film semiconductor. Since then, OFETs have been extensively used with OSCs as well as incorporated into other charge transport devices such as organic solar cells and biological

and environmental sensors.^{78–80} The semiconducting layer of the OFET is often a π -conjugated small molecule or polymer, commonly containing perylene or thiophene derived functionalities (**L1.5-L1.7**, Figure 1.8).^{81–83} Boron containing π -conjugated small molecules are also used in OFET devices, which are further discussed in Chapter Two of this thesis. These molecules have adequately aligned frontier molecular orbitals which are of similar energies to the electrodes, thus supporting charge transport within the device resulting in a highly efficient OFET.²⁵

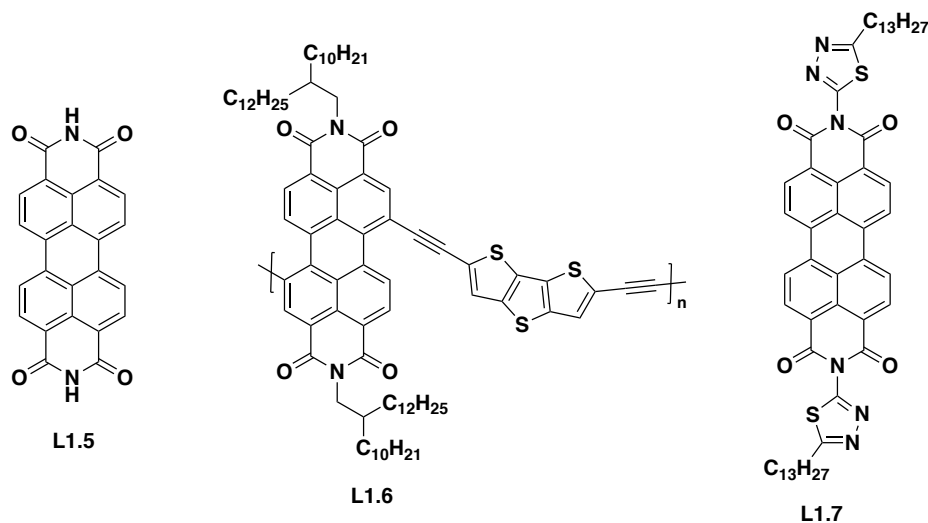


Figure 1.8: Literature examples of the semiconducting organic molecular candidates for OFET devices.^{81–83}

1.8 Molecular Diode

Molecular diodes are one directional conducting circuit components composed of a semiconductor, a p-n junction and two metallic terminals. There exist two fundamental types of diode, a rectifying diode and a resonant tunnelling diode (RTD).⁹ As discussed in depth in Section 1.2 of this Chapter, Aviram and Ratner's pioneering molecular diode was a rectifying diode, and these are more prevalent over RTDs. Rectifiers are components which can convert an alternating current into a direct current. For a molecule to act as a rectifier, it should possess a highly asymmetrical structure, such as a donor-acceptor model. This allows a variation to be introduced into the forward and reverse bias.⁸⁴ Specific attention is given to organic light emitting diodes (OLEDs), which will be discussed in depth below, and applied in Chapters Three and Four of this thesis.

1.8.2 Organic Light Emitting Diodes (OLEDs)

Electroluminescence is the emission of light from a material when subjected to an electric field. This phenomenon was first observed from single crystals of anthracene in 1964.⁸⁵ OLEDs are diodes containing lightweight, flexible sheets of highly electroluminescent organic materials for use in visual displays. These materials vary from purely organic to polymeric, to heavy metal phosphorescent complexes. The principal requirements for OLEDs are high luminescence quantum yield, n- or p-type carrier mobility, film formation ability, high thermal and oxidative stability, and high colour purity. Early materials included cathode ray tubes (CRT) and liquid crystal displays (LCD), which suffered from poor electrical contact quality and required high working voltages due to their high crystal thickness.⁸⁶ They also tend to be inflexible, as all LCD and inorganic crystalline materials had to be deposited on a rigid glass surface. Polymeric electroluminescent structures were designed to combat this issue, and can be deposited on flexible films. However, batch-to-batch polymer discrepancy led to unpredictable device performance.⁸⁷

OLEDs are composed of a thin film emissive organic material sandwiched between two electrodes (Figure 1.9). Standard organic emissive layers are composed of highly conjugated molecules, which behave as insulators in their ground state. Commonly, the anode is made from indium tin oxide (ITO) due to its high work function and transparency. The cathode is a highly reflective material and is made with metals such as Mg/Ag alloys of aluminium due to their low work function.⁸⁶ Once a voltage is applied, charge recombination of holes and electrons occurs at the electrode surface and the emissive layer respectively, which results in photonic emission. In order for the recombination to be efficient, the emissive layer must be very thin, between 100 and 150 nm.⁸⁶ The HOMO/LUMO band gap directly influences the energy of the released photons, and thus their colour.⁸⁸ The size of the band gap can be easily controlled by alterations to the structure and degree of conjugation of the emissive molecules. The anode and the cathode both require a low energetic barrier, with the HOMO level of the organic material typically 5-6 eV, and the LUMO level typically 2-3 eV.⁸⁶

In recent years, there has been an upsurge in the research, development, and fabrication of these active emitting materials, resulting in three sequential generations of OLED materials. The first generation of OLEDs were fluorescent low-voltage organic p-n heterostructural devices composed of thin film organic materials. Tang and VanSlyke from Kodak first

reported these in 1987.⁴⁰ Upon electrical excitation, 25% of excitons populate the singlet-excited state, and 75% populate the triplet-excited state. Due to this phenomenon, the first generation of fluorescent OLED materials suffered a maximum internal quantum efficiency (IQE) of 25%.

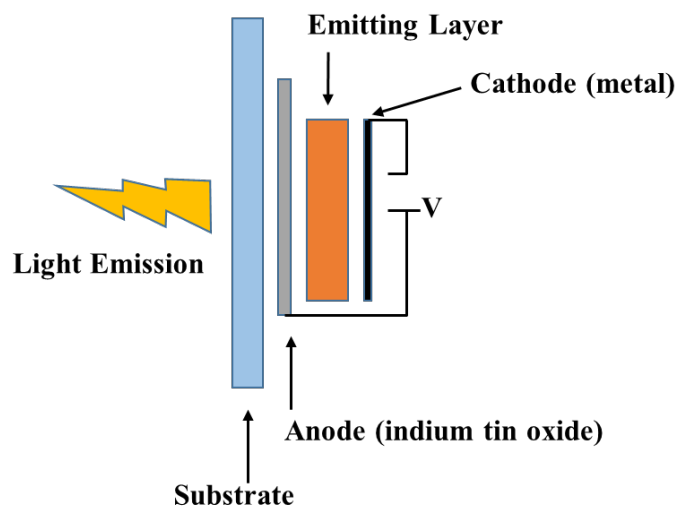


Figure 1.9: Simplified structure of an OLED.⁸⁶

To combat this issue, second generation OLEDs used heavy metal iridium and platinum phosphorescent complexes. The presence of the heavy metal increases spin-orbit coupling and intersystem crossing, thus favouring triplet harvesting. The first red phosphorescent dye, 2,3,7,8,12,13,17,18-octaethyl-21*H*,23*H*-porphine platinum(II) (**L1.8**, second generation OLED candidate, Figure 1.10) was reported by Baldo and co-workers in 1998.⁸⁹ The IQE of 75% was achieved, by conversion of triplet excitons to emissive triplet excited states. However, heavy metals such as iridium and platinum introduced a much higher cost of device fabrication, which was not industrially feasible.

A monumental breakthrough came in 2012, when Adachi *et al.*⁹⁰⁻⁹⁴ pioneered the third generation OLED materials by utilising the photophysical phenomenon of thermally activated delayed fluorescence (TADF, further discussed in Section 1.8.2.1), resulting in a theoretically achievable IQE of up to 100%. By adopting a twisted donor-acceptor-donor framework of an electron accepting triazine building block covalently bonded to dicarbazole donors (**L1.9**, Figure 1.10), an IQE of 84% was achieved.⁹⁰ Following the initial breakthrough, a myriad of donor and acceptor structures were explored towards finding the

most efficient design and resulting OLED candidate. Examples of common donor structures include phenoxazine (**L1.10**), phenylacridine (**L1.12**), and diphenylamine (**L1.13**). A further specific discussion on relevant donor and acceptor structures and their resulting photophysical properties can be located in Chapters Three and Four of this thesis.

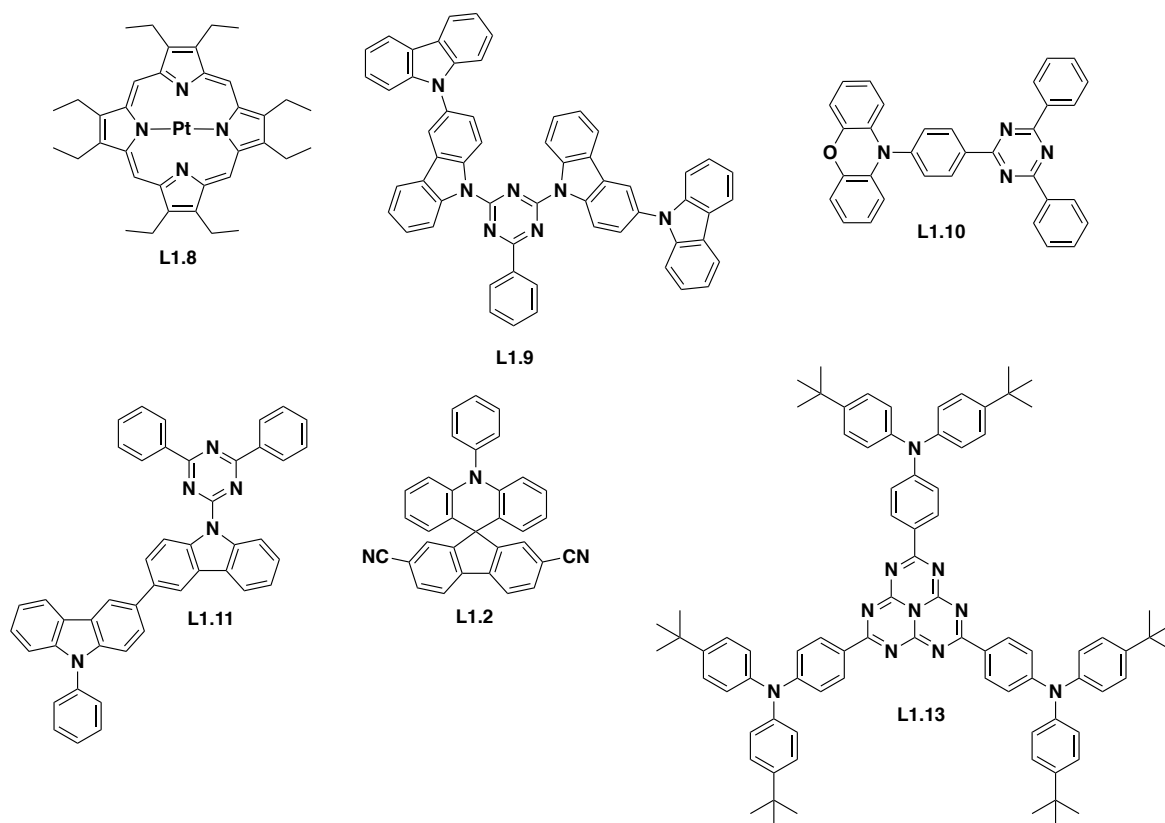


Figure 1.10: Literature examples of second generation OLED candidate (**L1.8**), and third generation OLED candidates (**L1.9-L1.13**).^{89–94}

1.8.2.1 Thermally Activated Delayed Fluorescence

Thermally activated delayed fluorescence (TADF) is a photophysical phenomenon, whereby the energetic gap between the singlet excited state and the triplet excited state of a molecule (ΔE_{S-T}) is small enough that thermal energy from the environment is sufficient to upconvert an electron from the triplet to the singlet state and allow decay from the singlet excited state (Figure 1.11).⁹⁵

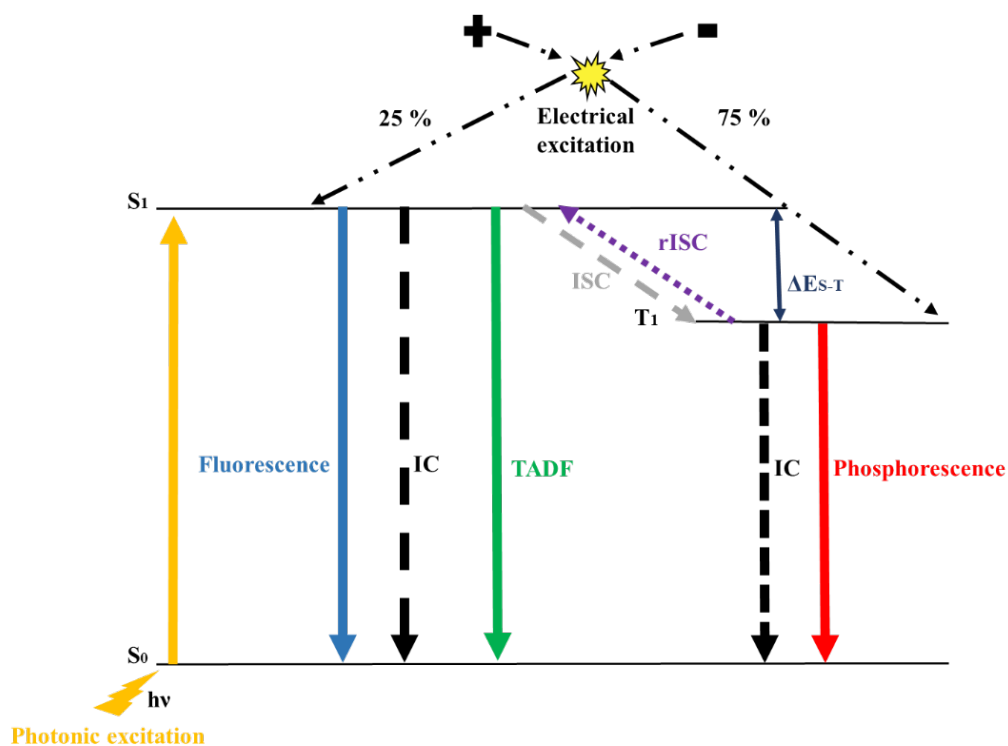


Figure 1.11: A simplified Jablonski diagram of TADF processes in an OLED. Intersystem crossing (ISC) allows singlet excited state electrons to decay to the triplet excited state non-radiatively. With thermal energy from the environment, reverse intersystem crossing (rISC) occurs if the ΔE_{S-T} gap is below 0.6 eV. Non-radiative internal conversion (IC), a direct competing process to photonic emission can occur, quenching emission.⁹⁵

There are two means of excitation: electrical and photonic. In electrical excitation, due to spin statistics, the population of triplet states occurs first. In photonic excitation only singlet states are produced, which then decay to the lower energy triplet excited state *via* intersystem crossing (ISC). The primary feature of TADF molecules is their small (ΔE_{S-T}) gap, requiring minimum thermal energy to repopulate the singlet-excited state.

Since decay from S_1 - S_0 happens twice, firstly *via* fluorescence and secondly *via* TADF, the lifetimes differ significantly. The first wave of fluorescence, prompt fluorescence, has a short lifetime of 1 – 100 ns. The second wave, termed delayed fluorescence due to the spin forbidden nature of the T_1 - S_1 , commonly displays lifetimes of 1 – 100 μ s.⁹⁵ The photophysical process of TADF is further studied and applied in Chapters Three and Four of this thesis.

1.8.2.2 Differences Between Delayed Fluorescence and Phosphorescence

Both phosphorescence and TADF involve the harvesting of the triplet-excited state, but it is possible to optically distinguish the two processes. TADF originates from S_1 (Figure 1.11) and possesses intramolecular charge transfer (ICT) character, the emission of which appears as a broad structureless Gaussian band. Excited states arising from ICT have a large permanent dipole moment, and consequently their emission bands are strongly affected by solvent polarity. Solvent rearrangement is faster than the decay from the excited state to the ground state.⁹⁶ Thus, with increasing solvent polarity the solvent can stabilise the excited state, shifting its emission to lower energies and reducing the intensity of emission. Phosphorescence is due to the direct emission from T_1 , which is a local excited state with near zero dipole moment. Due to this, its emission appears as a sharp structured band, which is unaffected by solvent polarity.⁸⁸ The phosphorescence emission profile will contain elements of both its donor and acceptor moieties, and can be clearly assigned. Conversely, a ICT emission profile cannot be structurally assigned.

TADF involves the harvesting of the excited electrons from the triplet-excited state to the singlet-excited state *via* reverse intersystem crossing (rISC). This occurs by using thermal energy from the environment. Reducing the temperature during measurements will see a direct reduction of TADF emission.⁹⁷ Conversely, the reduction of temperature sees a direct increase of phosphorescence emission due to the formation of aggregates and the quenching of non-radiative vibronic effects, a direct competitive process to phosphorescence.⁹⁸

The excited state lifetimes of both phosphorescence and TADF follow the triplet-excited state. However, TADF depends on the efficiency of interconversion between T_1 and S_1 *via* rISC. Therefore, its lifetime is directly dependent on the rate of rISC, k_{rISC} .⁸⁸ There are many deactivation pathways, with non-radiative internal conversion (IC) being one of the primary deactivation pathways for rISC. According to Kasha's rule, suppression of non-radiative pathways such as IC is difficult, as electrons tend to occupy the lowest energy states first.⁹⁹ Direct phosphorescence is the result of decay of T_1 - S_0 , a spin forbidden process, causing phosphorescence lifetimes to range from microseconds to milliseconds.⁹⁷

Due to the fundamental similarity of these two processes, both delayed fluorescence and room temperature phosphorescence (RTP) can occur within the same molecule. Commonly, the probability of $k_{\text{ISC}}^{\text{S}^1\text{-T}^1}$ is a slow process for purely organic materials, and cannot compete with prompt fluorescence. Suppression of any non-radiative decay pathways from $\text{T}_1\text{-S}_0$ will increase both TADF and RTP probability. If the $\Delta E_{\text{S-T}}$ gap is very small ($\Delta E_{\text{S-T}} > 0.1$ eV), TADF will dominate. However, if $\Delta E_{\text{S-T}}$ is large ($\Delta E_{\text{S-T}} \sim 0.4$ eV) some rISC will occur but k_{ISC} is low, and the emission will be phosphorescent in origin.⁹⁵ Careful structural design and considerations can control which process will dominate.

1.8.2.3 Design Considerations of TADF Systems

In order to attain TADF properties within small organic molecules, certain design considerations must be taken into account. Firstly, a small energetic gap between the singlet-excited state and the triplet-excited state ($\Delta E_{\text{S-T}}$) must be obtained for efficient rISC. This can be achieved by spatially separating the frontier molecular orbitals HOMO and LUMO. The energetic gap ($\Delta E_{\text{S-T}}$) is directly related to the electron exchange energy J (see eq. 1).^{100,101} The more spatially separated the frontier molecular orbitals, the smaller the electron exchange and thus smaller the energetic gap between S_1 and T_1 .

$$\Delta E_{\text{S-T}} = E_{\text{S}_1} - E_{\text{T}_1} = 2J \quad (1)$$

Orbital separation also reduces the spin exchange energy within the molecule, a competitive process to ICT.⁹⁵ The reduction in $\Delta E_{\text{S-T}}$ increases the rate of reverse intersystem crossing k_{rISC} . In order to successfully separate the frontier molecular orbitals, donor-acceptor architectures are used. A more in-depth discussion on donor-acceptor architectures can be found in Chapters Three and Four of this work.

1.9 Aims

The aim of this work can be split into two separate undertakings, with a global aim to design, synthesise, and study novel organic materials for application in molecular electronics. The first undertaking (Chapter Two) requires detailed synthetic methodological studies to develop novel pathways towards PAH-type molecules. The second undertaking (Chapters Three and Four) focuses on designing and synthesising small donor-acceptor systems for application in the OLED devices.

1.9.1 Chapter Two

The aim of this Chapter is to develop novel and sound synthetic methodologies towards an array of PAH-type compounds, from all carbon, to nitrogen doped, to boron doped nanographenes.

1.9.2 Chapter Three

The aim of this Chapter is to carry out preliminary synthetic trials and photophysical studies towards novel donor-acceptor semiconducting materials for application in the OLED devices. The lessons learned from this study are incorporated into designing target compounds for Chapter Four.

1.9.3 Chapter Four

The aim of this work is to develop a deeper understanding into twisted donor-acceptor molecules, studying their design, synthesis, and photophysical properties. Specifically, the aim of this Chapter is to understand the effects of the sterically induced structural twists between donor and acceptor moieties on their resulting photophysical properties.

1.10 References

- 1 S. Elke and C. J. Carlos, *Molecular electronics: an introduction to theory and experiment*, World Scientific, 2017, vol. 15.
- 2 J. R. Heath, *Adv. Rev. Mater. Res.*, 2009, 1–23.
- 3 R. L. Carroll and C. B. Gorman, *Angew. Chemie - Int. Ed.*, 2002, **41**, 4378–4400.
- 4 A. Harzheim, *Mater. Sci. Technol.*, 2018, **34**, 1275–1286.
- 5 G. E. Moore, *Electronics*, 1965, **38**, 114–117.
- 6 K. Wan and B. Xu, in *Molecular-Scale Electronics*, Springer, 2019, pp. 1–43.
- 7 G.-P. Zhang, Z. Xie, Y. Song, G.-C. Hu and C.-K. Wang, in *Molecular-Scale Electronics*, Springer, 2019, pp. 137–172.
- 8 P. Tyagi, *J. Mater. Chem.*, 2011, **21**, 4733–4742.
- 9 P. T. Mathew and F. Fang, *Engineering*, 2018, **4**, 760–771.
- 10 L. Wang, L. Wang, L. Zhang and D. Xiang, in *Molecular-Scale Electronics*, Springer, 2019, pp. 45–86.
- 11 A. Aviram and M. A. Ratner, *Chem. Phys. Lett.*, 1974, **29**, 277–283.
- 12 M. Elbing, R. Ochs, M. Koentopp, M. Fischer, C. von Hanisch, F. Weigend, F. Evers, H. B. Weber and M. Mayor, *Proc. Natl. Acad. Sci.*, 2005, **102**, 8815–8820.
- 13 M. Taniguchi, *Phys. Chem. Chem. Phys.*, 2019, **21**, 9641–9650.
- 14 M. Bendikov, F. Wudl and D. F. Perepichka, *Tetrathiafulvalenes, oligoacenes, and their buckminsterfullerene derivatives: The brick and mortar of organic electronics*, 2004, vol. 104.
- 15 Y. Tanaka, M. Kiguchi and M. Akita, *Chem. - A Eur. J.*, 2017, **23**, 4740.
- 16 D. Vuillaume, *Chempluschem*, 2019, **84**, 1215–1221.
- 17 C. Ngô and M. Van de Voorde, *Nanotechnol. a Nutshell*, 2014, 165–178.
- 18 J. M. Tour, *Acc. Chem. Res.*, 2000, **33**, 791–804.
- 19 R. L. McCreery, H. Yan and A. J. Bergren, *Phys. Chem. Chem. Phys.*, 2013, **15**, 1065–1081.
- 20 Y. Kim and H. Song, *J. Nanosci. Nanotechnol.*, 2015, **15**, 921–938.
- 21 P. Friederich, A. Fediai, S. Kaiser, M. Konrad, N. Jung and W. Wenzel, *Adv. Mater.*
- 22 L. Lafferentz, F. Ample, H. Yu, S. Hecht, C. Joachim and L. Grill, *Science (80-.)*, 2009, **323**, 1193–1197.
- 23 T. Kim, P. Darancet, J. R. Widawsky, M. Kotiuga, S. Y. Quek, J. B. Neaton and L. Venkataraman, *Nano Lett.*, 2014, **14**, 794–798.
- 24 S. V. Aradhya, J. S. Meisner, M. Krikorian, S. Ahn, R. Parameswaran, M. L. Steigerwald, C. Nuckolls and L. Venkataraman, *Nano Lett.*, 2012, **12**, 1643–1647.
- 25 M. Natali, M. Prosa, A. Longo, M. Brucalè, F. Mercuri, M. Buonomo, N. Lago, E. Benvenuti, F. Prescimone and C. Bettini, *ACS Appl. Mater. Interfaces*, 2020, **12**, 30616–30626.
- 26 Y. Chen, G. Y. Jung, D. A. A. Ohlberg, X. Li, D. R. Stewart, J. O. Jeppesen, K. A. Nielsen, J. F. Stoddart and R. S. Williams, *Nanotechnology*, 2003, **14**, 462–468.
- 27 L. Venkataraman, J. E. Klare, I. W. Tam, C. Nuckolls, M. S. Hybertsen and M. L. Steigerwald, *Nano Lett.*, 2006, **6**, 458–462.
- 28 Y. Luo, C. P. Collier, J. O. Jeppesen, K. A. Nielsen, E. DeIonno, G. Ho, J. Perkins, H. R. Tseng, T. Yamamoto, J. F. Stoddart and J. R. Heath, *ChemPhysChem*, 2002, **3**, 519–525.
- 29 J. E. Anthony, *Chem. Rev.*, 2006, **106**, 5028–5048.
- 30 C. Joachim, J. K. Gimzewski and A. Aviram, *Nature*, 2000, **408**, 541–548.
- 31 R. S. Klausen, J. R. Widawsky, M. L. Steigerwald, L. Venkataraman and C. Nuckolls, *J. Am. Chem. Soc.*, 2012, **134**, 4541–4544.
- 32 L. Zhang, Y. Cao, N. S. Colella, Y. Liang, J. L. Brédas, K. N. Houk and A. L. Briseno, *Acc. Chem. Res.*, 2015, **48**, 500–509.

- 33 M. Ball, B. Zhang, Y. Zhong, B. Fowler, S. Xiao, F. Ng, M. Steigerwald and C. Nuckolls, *Acc. Chem. Res.*, 2019, **52**, 1068–1078.
- 34 A. Nasri, A. Boubaker, B. Hafsi, W. Khaldi and A. Kalboussi, *Org. Electron. physics, Mater. Appl.*, 2017, **48**, 7–11.
- 35 P. Gehring, J. K. Sowa, J. Cremers, Q. Wu, H. Sadeghi, Y. Sheng, J. H. Warner, C. J. Lambert, G. A. D. Briggs and J. A. Mol, *ACS Nano*, 2017, **11**, 5325–5331.
- 36 A. Candini, L. Martini, Z. Chen, N. Mishra, D. Convertino, C. Coletti, A. Narita, X. Feng, K. Müllen and M. Affronte, *J. Phys. Chem. C*, 2017, **121**, 10620–10625.
- 37 S. Tans, A. Verschueren and C. Dekker, *Nature*, 1998, **672**, 669–672.
- 38 J. Park, A. N. Pasupathy, J. I. Goldsmith, C. Chang, Y. Yalsh, J. R. Petta, M. Rinkoski, J. P. Sethna, H. D. Abruña, P. L. McEuen and D. C. Ralph, *Nature*, 2002, **417**, 722–725.
- 39 A. Endo, M. Ogasawara, A. Takahashi, D. Yokoyama, Y. Kato and C. Adachi, *Adv. Mater.*, 2009, **21**, 4802–4806.
- 40 C. W. Tang and S. A. Vanslyke, *Appl. Phys. Lett.*, 1987, **51**, 913–915.
- 41 A. Nasri, A. Boubaker, B. Hafsi, W. Khaldi and A. Kalboussi, *Org. Electron.*, 2017, **48**, 7–11.
- 42 Y. Komoto, S. Fujii, M. Iwane and M. Kiguchi, *J. Mater. Chem. C*, 2016, **4**, 8842–8858.
- 43 Y. Komoto, S. Fujii, M. Iwane and M. Kiguchi, *J. Mater. Chem. C*, 2016, **4**, 8842–8858.
- 44 J. C. Reis-Silva, D. F. S. Ferreira, J. F. P. Leal, F. A. Pinheiro and J. Del Nero, *Solid State Commun.*, 2017, **252**, 46–50.
- 45 S. Leitherer, P. B. Coto, K. Ullmann, H. B. Weber and M. Thoss, *Nanoscale*, 2017, **9**, 7217–7226.
- 46 A. Nitzan and M. A. Ratner, *Science (80-.)*, 2003, **300**, 1384–1389.
- 47 S. Kaneko, D. Murai, S. Fujii and M. Kiguchi, *Int. J. Mod. Phys. B*, 2016, **30**, 1642010.
- 48 Z. Li, B. Li, J. Yang and J. G. Hou, *Acc. Chem. Res.*, 2010, **43**, 954–962.
- 49 M. A. Reed, C. Zhou, C. J. Muller, T. P. Burgin and J. M. Tour, *Science (80-.)*, 1997, **278**, 252–254.
- 50 B. Capozzi, Q. Chen, P. Darancet, M. Kotiuga, M. Buzzeo, J. B. Neaton, C. Nuckolls and L. Venkataraman, *Nano Lett.*, 2014, **14**, 1400–1404.
- 51 V. Kaliginedi, A. V. Rudnev, P. Moreno-García, M. Baghernejad, C. Huang, W. Hong and T. Wandlowski, *Phys. Chem. Chem. Phys.*, 2014, **16**, 23529–23539.
- 52 J. Moreland and J. W. Ekin, *J. Appl. Phys.*, 1985, **58**, 3888–3895.
- 53 C. J. Muller, J. M. Van Ruitenbeek and L. J. De Jongh, *Phys. C Supercond.*, 1992, **191**, 485–504.
- 54 L. Wang, L. Wang, L. Zhang and D. Xiang, *Top. Curr. Chem.*, 2017, **375**, 1–42.
- 55 B. Xu and N. J. Tao, *Science (80-.)*, 2003, **301**, 1221–1223.
- 56 M. Kiguchi, T. Takahashi, M. Kanehara, T. Teranishi and K. Murakoshi, *J. Phys. Chem. C*, 2009, **113**, 9014–9017.
- 57 J. L. Xia, I. Diez-Perez and N. J. Tao, *Nano Lett.*, 2008, **8**, 1960–1964.
- 58 B. Xu, *Small*, 2007, **3**, 2061–2065.
- 59 A. Vilan, D. Aswal and D. Cahen, *Chem. Rev.*, 2017, **117**, 4248–4286.
- 60 C. Wang, H. Dong, L. Jiang and W. Hu, *Chem. Soc. Rev.*, 2018, **47**, 422–500.
- 61 S. Fujii and T. Enoki, *Acc. Chem. Res.*, 2013, **46**, 2202–2210.
- 62 V. Coropceanu, J. Cornil, D. A. da Silva Filho, Y. Olivier, R. Silbey and J. L. Brédas, *Chem. Rev.*, 2007, **107**, 926–952.
- 63 S. E. Root, S. Savagatrup, A. D. Printz, D. Rodriguez and D. J. Lipomi, *Chem. Rev.*, 2017, **117**, 6467–6499.

- 64 H. Bronstein, C. B. Nielsen, B. C. Schroeder and I. McCulloch, *Nat. Rev. Chem.*, 2020, **4**, 66–77.
- 65 F. Banhart, J. Kotakoski and A. V Krasheninnikov, *ACS Nano*, 2011, **5**, 26–41.
- 66 L. Chen, Y. Hernandez, X. Feng and K. Müllen, *Angew. Chemie - Int. Ed.*, 2012, **51**, 7640–7654.
- 67 K. S. Novoselov, A. K. Geim, S. V Morozov, D. Jiang, Y. Zhang, S. V Dubonos, I. V Grigorieva and A. A. Firsov, *Science (80-.)*, 2004, **306**, 666–669.
- 68 M. J. Allen, V. C. Tung and R. B. Kaner, 2010, 132–145.
- 69 P. Tian, L. Tang, K. S. Teng, J. Xiang and S. P. Lau, *Adv. Mater. Technol.*, 2019, **4**, 1–30.
- 70 B. Xu, X. Xiao, X. Yang, L. Zang and N. Tao, *J. Am. Chem. Soc.*, 2005, **127**, 2386–2387.
- 71 A. Srivastava, B. Santhibhushan, V. Sharma, K. Kaur, M. Shahzad Khan, M. Marathe, A. De Sarkar and M. Shahid Khan, *J. Electron. Mater.*, 2016, **45**, 2233–2241.
- 72 A. W. Ghosh, T. Rakshit and S. Datta, *Nano Lett.*, 2004, **4**, 565–568.
- 73 M. L. Perrin, E. Burzurí and H. S. J. Van Der Zant, *Chem. Soc. Rev.*, 2015, **44**, 902–919.
- 74 H. Park, J. Park, A. K. L. Lim, E. H. Anderson, A. P. Alivisatos and P. L. McEuen, *Nature*, 2000, **407**, 57–60.
- 75 H. Yu, Y. Luo, K. Beverly, J. F. Stoddart, H. R. Tseng and J. R. Heath, *Angew. Chemie - Int. Ed.*, 2003, **42**, 5706–5711.
- 76 C. Dekker, *Nat. Electron.*, 2018, **1**, 518.
- 77 A. Tsumura, H. Koezuka and T. Ando, *Appl. Phys. Lett.*, 1986, **49**, 1210–1212.
- 78 H. Sirringhaus, *Adv. Mater.*, 2014, **26**, 1319–1335.
- 79 S. G. Surya, H. N. Raval, R. Ahmad, P. Sonar, K. N. Salama and V. R. Rao, *TrAC - Trends Anal. Chem.*, 2019, **111**, 27–36.
- 80 D. Wang, V. Noël and B. Piro, *Electronics*, 2016, **5**, 9.
- 81 F. Lüttich, D. Lehmann, M. Friedrich, Z. Chen, A. Facchetti, C. Von Borczyskowski, D. R. T. Zahn and H. Graaf, *Phys. Status Solidi Appl. Mater. Sci.*, 2012, **209**, 585–593.
- 82 C. T. Hsieh, C. Y. Chen, H. Y. Lin, C. J. Yang, T. J. Chen, K. Y. Wu and C. L. Wang, *J. Phys. Chem. C*, 2018, **122**, 16242–16248.
- 83 R. Centore, L. Ricciotti, A. Carella, A. Roviello, M. Causà, M. Barra, F. Ciccullo and A. Cassinese, *Org. Electron.*, 2012, **13**, 2083–2093.
- 84 R. Liu, S.-H. Ke, W. Yang and H. U. Baranger, *J. Chem. Phys.*, 2006, **124**, 24718.
- 85 Helfrich W and Schneider, *Phys. Rev. Lett.*, 1965, **14**, 229.
- 86 B. Geffroy, P. le Roy and C. Prat, *Polym. Int.*, 2006, **55**, 572–582.
- 87 C. Maglione, A. Carella, R. Centore, P. Chávez, P. Lévêque, S. Fall and N. Leclerc, *Dye. Pigment.*, 2017, **141**, 169–178.
- 88 T. J. Penfold, F. B. Dias and A. P. Monkman, *Chem. Commun.*, 2018, **54**, 3926–3935.
- 89 M. A. Baldo, D. F. O’Brien, Y. You, A. Shoustikov, S. Sibley, M. E. Thompson and S. R. Forrest, *Nature*, 1998, **395**, 151–154.
- 90 S. Youn Lee, T. Yasuda, H. Nomura and C. Adachi, *Appl. Phys. Lett.*, 2012, **101**, 1–5.
- 91 H. Tanaka, K. Shizu, H. Miyazaki and C. Adachi, *Chem. Commun.*, 2012, **48**, 11392–11394.
- 92 C. H. Chang, M. C. Kuo, W. C. Lin, Y. T. Chen, K. T. Wong, S. H. Chou, E. Mondal, R. C. Kwong, S. Xia, T. Nakagawa and C. Adachi, *J. Mater. Chem.*, 2012, **22**, 3832–3838.

- 93 J. Li, T. Nakagawa, J. Macdonald, Q. Zhang, H. Nomura, H. Miyazaki and C. Adachi, *Adv. Mater.*, 2013, **25**, 3319–3323.
- 94 H. Tanaka, K. Shizu, H. Nakanotani and C. Adachi, *Chem. Mater.*, 2013, **25**, 3766–3771.
- 95 P. Pander, A. Swist, R. Motyka, J. Soloducho, F. B. Dias and P. Data, *J. Mater. Chem. C*, 2018, **6**, 5434–5443.
- 96 N. Mataga, Y. Kaifu and M. Koizumi, *Bull. Chem. Soc. Jpn.*, 1956, **29**, 465–470.
- 97 R. Huang, J. Avó, T. Northey, E. Channing-Pearce, P. L. Dos Santos, J. S. Ward, P. Data, M. K. Etherington, M. A. Fox, T. J. Penfold, M. N. Berberan-Santos, J. C. Lima, M. R. Bryce and F. B. Dias, *J. Mater. Chem. C*, 2017, **5**, 6269–6280.
- 98 H. Noda, H. Nakanotani and C. Adachi, *Sci. Adv.*, 2018, **4**, 1–8.
- 99 Y. Tao, K. Yuan, T. Chen, P. Xu, H. Li, R. Chen, C. Zheng, L. Zhang and W. Huang, *Adv. Mater.*, 2014, **26**, 7931–7958.
- 100 T. Chen, L. Zheng, J. Yuan, Z. An, R. Chen, Y. Tao, H. Li, X. Xie and W. Huang, *Sci. Rep.*, 2015, **5**, 1–11.
- 101 L. Xue, B. Cui, S. Xie and S. Yin, *J. Phys. Chem. Lett*, 2019, **10**, 308.

Chapter Two
Synthetic Trials Towards Novel Nanographene Type
Compounds

2.0 Introduction

Graphene has garnered significant interest since its discovery in 2004. As a material, it has huge potential in optoelectronics,¹⁰² gas sensing and detecting,¹⁰³ and in hydrogen storage.¹⁰⁴ However due to its planar hexagonal aromatic structure, its use faces several obstacles; it is prone to aggregation and cannot be solubilised in common organic solvents or water, making it difficult to functionalize and analyse in solution. Top-down synthetic approaches to graphene yield fragments of various sizes and shapes, thus adding to the inconsistency of the material sample.

Bottom-up syntheses of graphene materials (termed nano-sized graphene or nanographene) allow strict control of the size (typically 1–100 nm in size) and functionalisation of the material from the start.¹⁰⁵ There has been a huge demand for the development of elegant synthetic routes towards nanographenes with defined size and shape, heteroatom doping as well as high quality and quantity. The ability to control the size, shape, and edge topography of nanographenes and introduction of various heteroatoms allows one to control its optoelectronic and physical properties.¹⁰⁶ Nanographene properties lie between that of bulk graphene and a large polycyclic aromatic hydrocarbon (PAH) molecule, but with more control of size, and ability to introduce side chains will further control and change its properties.¹⁰⁵

Despite there being a growing interest in the research of bottom-up nanographene synthesis, the literature is still lacking in well-developed synthetic methodologies. The examples that are present in the literature focus primarily on successful syntheses of a select few compounds. All of these compounds require specific multistep syntheses, with a high risk of failure at any of the reaction steps. This chapter aims to delve deeper into the development of various synthetic pathways towards novel PAH's, and specifically characterise both the successes and the failures towards each target compound. The importance of this chapter lies in the progress made through failure, rather than just showcasing successful synthetic pathways. Ahead of the methodological discussion, a short overview of the relevant literature examples of PAH's and their syntheses is outlined.

2.1 Polycyclic Aromatic Hydrocarbons (PAH's)

Polycyclic aromatic hydrocarbon (PAH) is a common name given to aromatic hydrocarbons which contain more than two unsubstituted fused benzene rings, and are the most studied of π -conjugated systems in the literature.^{107–111} They were first isolated from coal and tar in the nineteenth century, and their presence has been identified in as far as interstellar space.¹¹² The first synthetically attained PAH molecules were achieved by R. Scholl and E. Clar at the start of the 20th century.^{113–116}

PAH's are a series of six membered rings composed of sp^2 hybridised carbon atoms. For PAH's composed of numerous fused rings, the peripheral ring arrangement plays a key role in the molecules stability which correlates to resonance stabilisation. Arm-chair periphery achieves the highest stabilisation resulting in highly stable molecules, with a zig-zag edge known to be chemically unstable and molecules with a zig-zag periphery can often only be handled under inert conditions (Figure 2.0).¹¹⁷

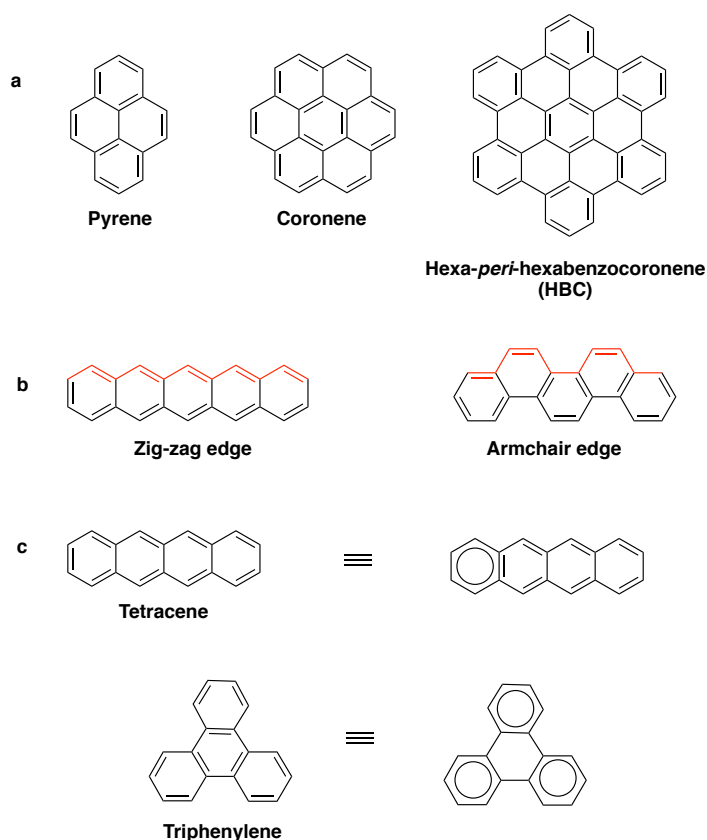


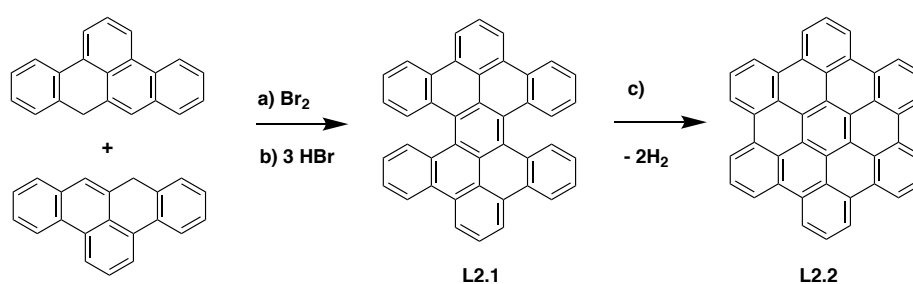
Figure 2.0: **a)** Examples of common polycyclic aromatic hydrocarbons (PAH). **b)** An illustration of armchair and zig-zag edge topology of PAH's. **c)** Electronic structures of tetracene and triphenylene highlighting the structure of Clar's π -sextets; the rings with the

*circles indicate the sextet, and the electrons not in a sextet remain annotated by a double bond, also known as Kekule style.*¹¹⁷

According to Clar's aromatic sextet rule, benzene rings within the fused PAH system which have six π -electrons and are fully aromatic are annotated with a circle, and not-fully benzoid rings are symbolised in Kekule style (Scheme 2.0 above). The stability of these systems increases with the increasing number of π -sextets, resulting in high thermal and chemical stability.¹¹⁸ This can be better explained by example of tetracene and triphenylene, two isomers with the same number of six-membered carbon rings. When the rings are bonded in a linear arrangement as in tetracene, this results in a zig-zag periphery, and only one sextet, making this the less stable isomer. Triphenylene has an armchair periphery, and all 18 π -electrons can be grouped into sextets, resulting in a highly stable isomer.

2.1.1 Synthesis of PAH

Scholl and Clar pioneered early synthetic attempts towards PAHs through a two-step synthesis of hexa-*peri*-hexabenzocoronene (HBC), which involved elevated temperatures and strongly oxidising reaction melts, furnishing HBC in low yields (Scheme 2.0).¹¹⁹

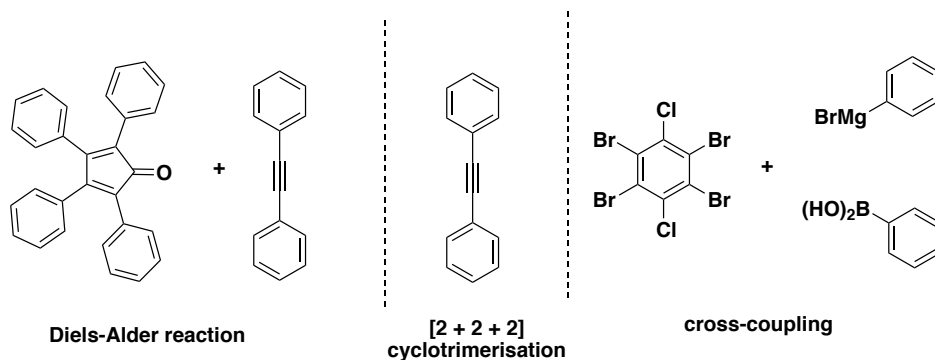


Scheme 2.0: Early synthetic pathway towards HBC: a) bromine and C_6H_6 ; b) 153°C and c) 481°C .¹¹⁹

Since then Mullen and co-workers have spearheaded the development of milder synthetic pathways towards PAH's, allowing the field to progress significantly since its humble beginnings.¹¹⁸ The synthesis can be split into two key steps, formation of the required precursors, and the cyclohydrogenation step as visualised in Figure 2.1 below. Using

synthesis of HBC (**L2.2**) as an example, precursor synthesis revolves around synthesis of the required polyphenylene, in this case hexaphenylbenzene **L2.3**. This can be achieved *via* a pericyclic [2 + 4] Diels-Alder reaction between diphenylacetylene and tetraphenylcyclopentadienone, a cobalt mediated [2 + 2 + 2] cyclotrimerisation of diphenylacetylene, or cross-coupling reactions such as a Grignard reaction or palladium-mediated cross-coupling reactions. The polyphenylene synthesis can be adapted and functionalised to include moieties such as aliphatic side chains, halogens, and heteroatoms, to yield highly functionalised PAH molecules; thus, making this synthetic approach highly adaptable and versatile. The cyclohydrogenation reaction is performed in the presence of a Lewis acid and/ or an oxidant and **L2.3**, to yield a fully planarized HBC.¹²⁰ The cyclohydrogenation conditions can vary significantly and depend on the polyphenylene in question. Commonly, Lewis acids such as FeCl₃ or oxidant/ Lewis acid combinations such as AlCl₃/Cu(OTf)₂ and AlCl₃/CuCl₂ furnish HBC in high yields. More advanced cyclohydrogenation reactions utilise 2,3-dichloro-5,6-dicyano-1,4-benzoquinone (DDQ) in the presence of an acid to yield HBC in equally high or often increased yields. Choice of oxidant for the cyclohydrogenation step will be discussed more in-depth in the results section of this work.

a) Precursor Synthesis



b) Cyclohydrogenation or Graphitisation

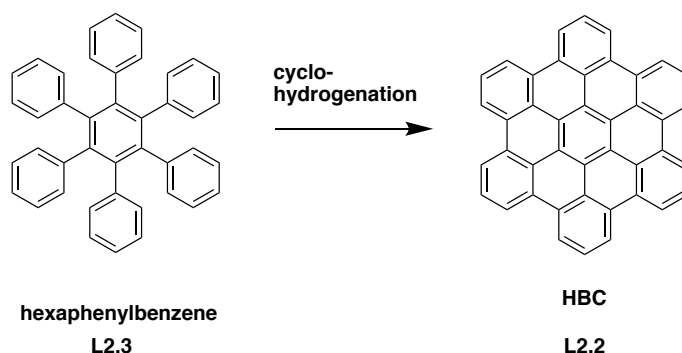


Figure 2.1: Commonly utilised stepwise syntheses of HBC applied to known PAH's. **a)** Synthetic route towards hexaphenylbenzene via a [2 + 4] Diels-Alder reaction, [2 + 2 + 2] cyclotrimerization, and cross-coupling syntheses. **b)** Cyclohydrogenation to furnish HBC.¹²⁰

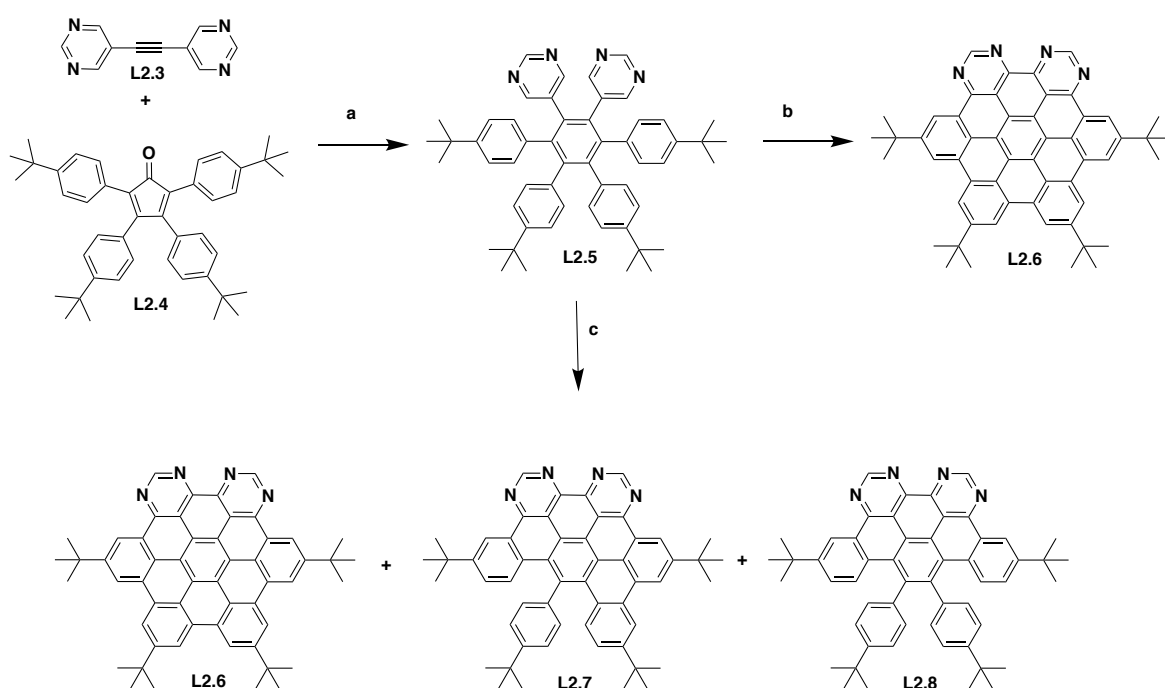
2.2 Introduction of Heteroatoms to PAH's

As previously mentioned, inclusion of heteroatoms (such as nitrogen,¹²¹ boron,¹²² sulfur,¹²³ phosphorus,¹²⁴ and oxygen¹²⁵) into PAH's *via* replacement of one or more of the sp^2 carbon atoms results in modified electronic and optical properties. This is an important tool available to an organic chemist to develop materials with tailor-made and specific properties. It also allows for complete control over the placement of heteroatoms within the π -conjugated system, be it on the periphery, or in the centre. The specific placement of the heteroatoms directly dictates the resulting electronic and optical properties.¹²⁶ However, introducing heteroatoms poses a great synthetic challenge, and careful tailoring of reaction conditions is required at each synthetic step. This means that heteroatom-doped PAH's are

much more sparse in the literature compared to their all-carbon analogues. For this work, specific focus is given to nitrogen containing and boron containing PAH's.

2.2.1 Introducing Nitrogen

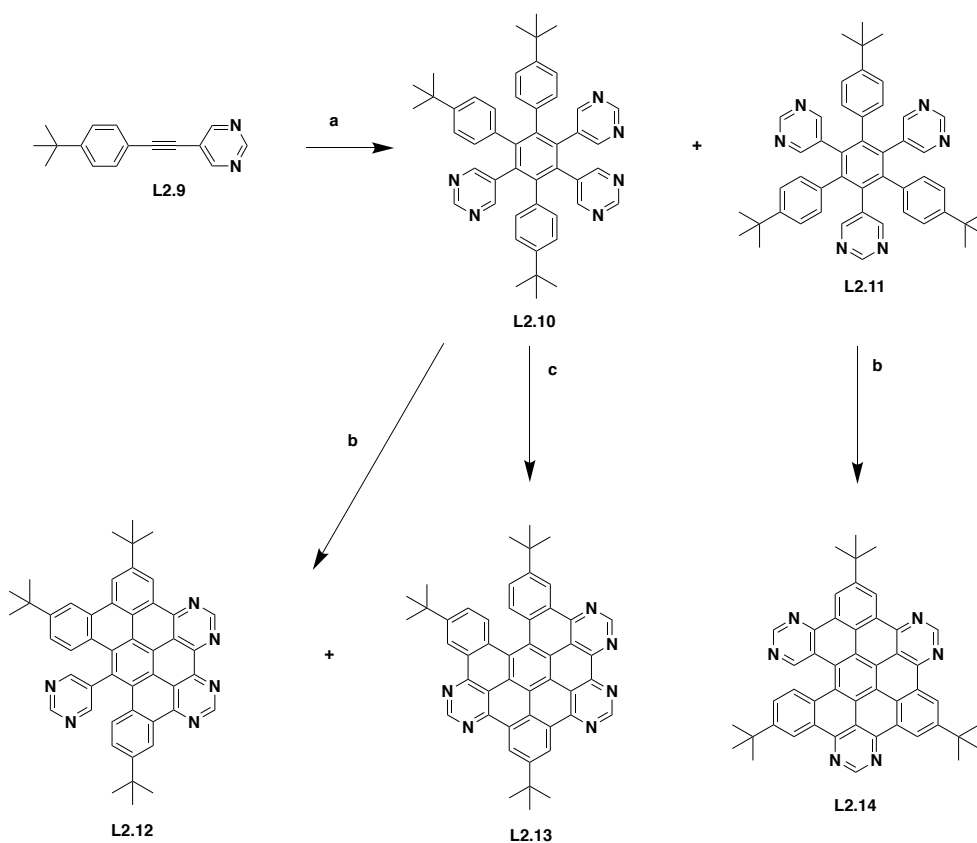
Nitrogen is the most common heteroatom to be incorporated into PAH, and this is due to an abundance of synthetic protocols as well as higher stability when compared to the aforementioned heteroatoms. Draper *et al.*^{121,127} published a report in 2002 and a subsequent one in 2005, outlining a facile route towards nitrogen functionalised heterosuperbenzenes; opening up opportunity towards greater functionalisation, metal coordination and therefore electron accepting properties, and greater solubility. The nitrogen functionalised heterosuperbenzenes (N-HSB) have four nitrogen atoms incorporated on the periphery of the structure as shown in Scheme 2.1 below. **L2.5**, the N-substituted polyphenylene precursor was synthesised through a [2 + 4] Diels-Alder cycloaddition of 1,2-di(pyrimidin-5-yl)ethylene (**L2.3**) to 2,3,4,5-tetrakis(4-(tert-butyl)phenyl)cyclopenta-2,4-dien-1-one (**L2.4**) in a benzophenone melt. Oxidative cyclohydrogenation of **L2.5** with AlCl₃/CuCl₂ in CS₂ furnished the N-HSB (**L2.6**) in a 49% yield. Altering the conditions to trial a milder oxidative agent FeCl₃ resulted in three separate products: fully fused N-HSB (**L2.6**), two-thirds fused product 2/3-N-HSB (**L2.7**), and a half-cyclised product 1/2-N-HSB (**L2.8**).



Scheme 2.1: Synthesis of nitrogen doped heterosuperbenzenes as reported by Draper et al.^{121,127} **a)** Ph₂CO, melt, 1 h, 81% **b)** AlCl₃/CuCl₂ in CS₂, RT, 72 h, 49% **c)** FeCl₃ in MeNO₂, CH₂Cl₂, RT, 30 mn, yielding **L2.7** in 45%, **L2.8** in 23%, and **L2.9** in 20%.

N-HSB compounds exhibited high solubility in organic solvents, a property which is not common in all carbon PAH. Additionally, the distribution of N atoms within the structure meant that the N-HSB compounds possessed N[^]N ligand functionality. The authors successfully synthesised Pd(II) and Ru(II) complexes with **L2.6**, resulting in emissive properties which were not possible in an analogous all carbon PAH system.¹²⁷ Pd(II) complex with N-HSB resulted in complete quenching of emission, whereas complexation with Ru(II) resulted in absorption in the visible region characteristic of a ‘black absorber’, and emission in the near-infrared (NIR) region. These strikingly different optical properties highlight the facile modifications of N-HSB, when compared to PAH, further showcasing the benefit of heteroatom doping of PAH type compounds.

Following the initial reports, the authors published a methodology towards 6N-doped nanographenes, coined hexaazasuperbenzenes (HASB) *via* an elegant one-step cobalt mediated [2 + 2 + 2] cyclotrimerisation of specially prepared acetylenes.¹²⁸ N-substituted polyphenylene precursors **L2.10** and **L2.11** were synthesised by subjecting 5-((4-(*tert*-butyl)phenyl)ethynyl)pyrimidine (**L2.9**) to standard dicobalt octacarbonyl-catalysed cyclotrimerisation conditions (Scheme 2.2 below).



Scheme 2.2: Synthesis of 6N-doped HASB as reported by Draper et al.¹²⁸ **a)** $\text{Co}_2(\text{CO})_8$, dioxane, 115 °C, 24 h, yielding **L2.10** in 68% and **L2.11** in 27%. **b)** FeCl_3 , CH_3NO_2 , CH_2Cl_2 , RT, 72 h, yielding **L2.12** in 10%, **L2.13** in 20% and **L2.14** in 23%. **c)** DDQ, MeSO_3H or $\text{CF}_3\text{SO}_3\text{H}$, CH_2Cl_2 , 60%.

Oxidative cyclohydrogenation of **L2.10** was trialled with $\text{AlCl}_3/\text{CuCl}_2/\text{CS}_2$, FeCl_3 , and DDQ/H^+ . The $\text{AlCl}_3/\text{CuCl}_2/\text{CS}_2$ route resulted in an array of products with challenging purification and isolation. The milder FeCl_3 route resulted in **L2.12** and **L2.13** as the major products. Interestingly, the more novel ring closure route *via* DDQ/H^+ oxidation has been the most yielding, furnishing **L2.13** in a 60% yield. This method has been increasingly utilised in the literature as a metal-free alternative oxidant for cyclohydrogenation reactions, and is particularly appealing as it avoids any potential chlorinated side products which are common with AlCl_3 or FeCl_3 .¹²⁹ In the same report, the authors note that incorporating electron-donating methoxy groups on the periphery of the polyphenylene precursors results in promotion of the cyclohydrogenation process, and complete bond closure.

2.2.2 Introducing Boron

Tri-coordinate boron is widely sought after as it possesses a vacant p_z orbital, and when incorporated into structures, results in highly luminescent properties. The vacant p_z orbital results in facilitation of electronic communication between the adjacent aryl substituents, and boron containing PAH's (B-PAH's) are known to be excellent electron acceptors. The electron accepting ability and facile intramolecular communication results in a HOMO-LUMO transition in an ideal range for visible light emission. Incorporation of boron into a PAH is a relatively young field, but has quickly gained prominence due to the aforementioned promising properties of B-PAH, and their potential use in optoelectronics.¹³⁰

Synthesis of B-PAH is immensely challenging, with many precursors being both air and moisture sensitive, or incompatible with the reaction conditions for the required transformation. Boron atoms located on the periphery of PAH must be protected by bulky functionalities to shield the boron centre from potential nucleophilic attack resulting in decomposition of the molecule. This has a direct knock-on effect on the resulting charge carrier properties of the bulk material if utilised in an optoelectronic device as the protecting groups hinder π -stacking of the molecules in the solid state.¹¹⁷ B-PAH's with centrally located boron atoms are more stable but are significantly more challenging to prepare.

Figure 2.2 below outlines the common synthetic approaches to arylboranes. Transmetalation reactions involving reaction of aryllithium (ArLi), aryl Grignard (ArMgBr), arylsilanes (ArSiR₃), and arylstannanes (ArSnR₃) with haloboranes (XBR₂) or alkoxyboranes (ROBR₂) are the most present in the literature. Specifically, arylsilanes and arylstannanes are useful when preparing aryldihaloboranes through electrophilic Si/B or Sn/B exchange reactions with BX₃ (X = Cl, Br). Arenes can undergo electrophilic borylation reactions related to a Friedel-Crafts transformation, *via* a highly reactive borenium cation intermediate [L-BX₂]⁺ generated from BX₃, an amine ligand L, and AlX₃. The amine ligand role is crucial to stabilise the cationic borenium ion.^{131,132} Transition metal catalysis has also found use in arylboranes synthesis: in palladium-mediated C-Br and Ir-catalysed C-H activation/ borylation reactions, although they are less common in the literature. For this work, the focus will lie with transmetalation reactions towards B-PAH's.

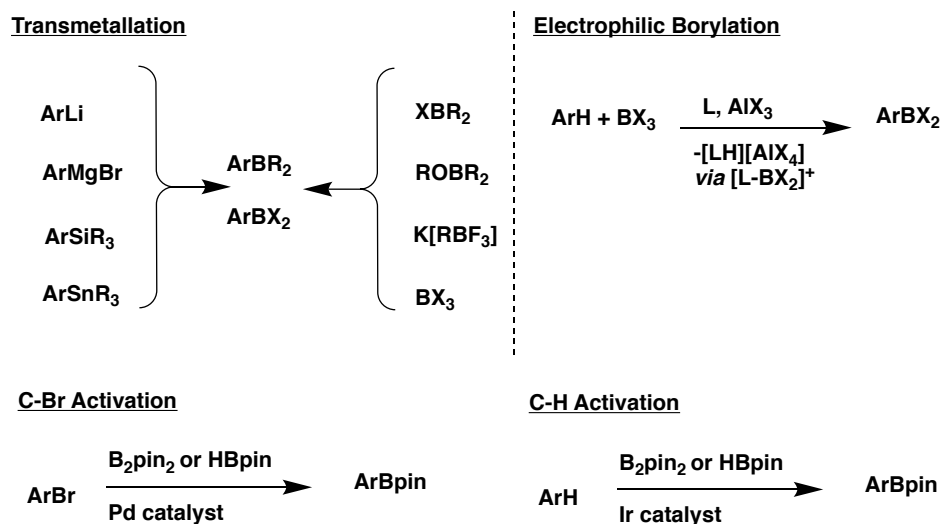
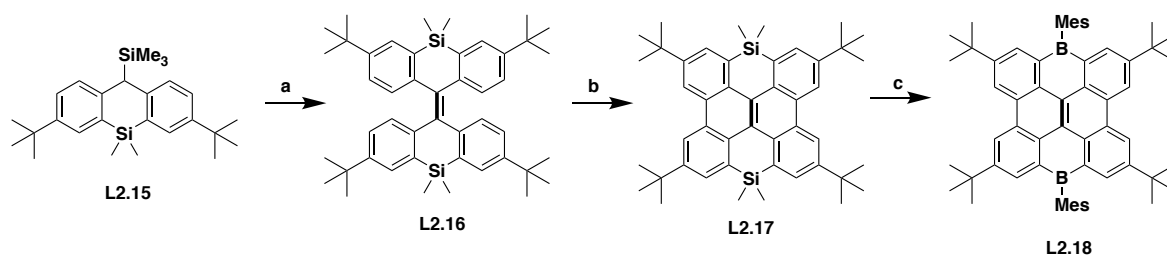


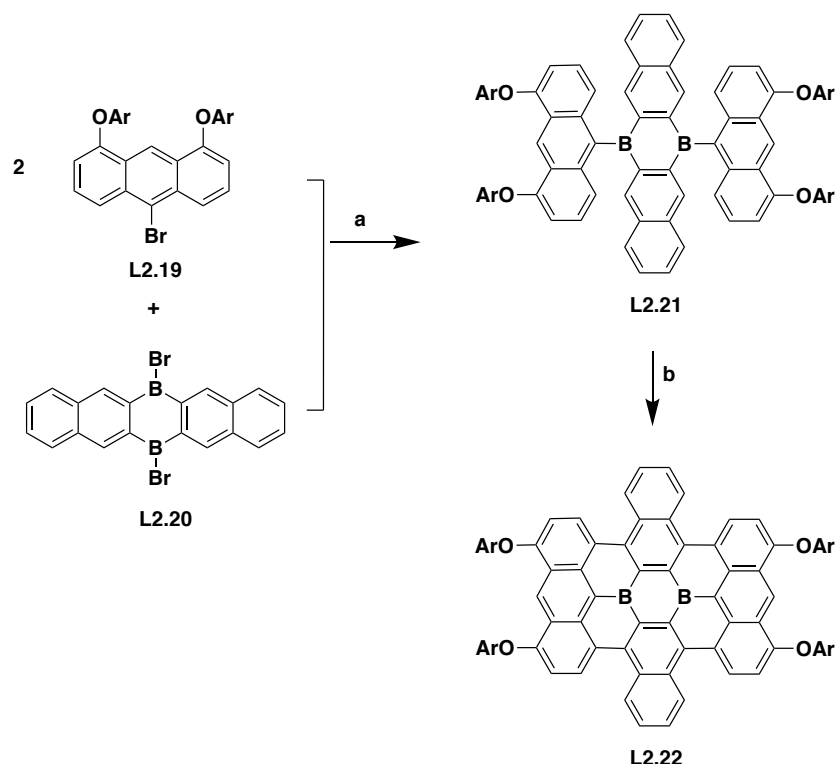
Figure 2.2: Common synthetic strategies towards the preparation of arylboranes.¹³⁰

Over the last decade, Wagner and Yamaguchi have both contributed heavily towards the development of novel methodologies for B-PAH's. Wagner *et al.*¹³³ designed an adaptable synthetic methodology towards a boron containing bisanthene compound **L2.18**, with the boron atoms located on the periphery of the structure and protected by bulky mesityl groups (Scheme 2.3). **L2.18** was synthesised by a three-step synthetic method. A Peterson olefination of **L2.15** furnished the olefin **L2.16**, followed by a dehydrogenative C-C coupling to form **L2.17** by UV irradiation, which is compatible with acid-sensitive, silicon-containing species. The double Si/B exchange was the most challenging step due to the rigidity of precursor **L2.17** and required stringent conditions of an excess of neat BBr₃, elevated temperature of 200 °C, and an extended reaction duration of four days to form **L2.18** in a reduced yield of 11%. This synthetic pathway highlights the difficulty with which B-PAH's are to synthesise. **L2.18** was air and moisture stable, and a highly efficient blue emitter ($\lambda_{\text{em}} = 449 \text{ nm}$, $\Phi_F = 0.78$).



Scheme 2.3: Synthesis of **L2.18** reported by Wagner et al.¹³³ **a)** 1.1 equiv. *n*BuLi. THF, -78 °C to RT, 54% yield. **b)** UV irradiation (Hg medium-pressure lamp; I2, propylene oxide), toluene, RT, 38% yield. **c)** Excess neat BBr₃, 200 °C, 4 days; 2.3 equiv MesMgBr, toluene/THF, 0 °C, yield 11%.

Yamaguchi and co-workers designed a radically different path towards B-PAH's to that of Wagner: reporting the first B-doped PAH where the boron atoms are localised in the centre of the structure, with the synthesis more akin to that of an all-carbon PAH (Scheme 2.4).¹²² The replacement of one sp² carbon by a boron atom results in a one-electron oxidation of the polycyclic skeleton, forming an unstable open-shell compound. For this reason, if doping PAH with boron atoms in the centre, two boron atoms are required to be introduced simultaneously to form a stable closed-shell structure.¹³⁴



Scheme 2.4: Synthesis of **L2.22** reported by Yamaguchi et al.¹²² **a)** *n*BuLi, Et₂O, 0 °C to 25 °C; followed by **L2.20** in toluene, 0 °C to 25 °C, 54% yield. **b)** FeCl₃, CH₂NO₂ in CH₂Cl₂, RT, yield 51%.

L2.22 was synthesised *via* a two-step synthesis: formation of the precursor **L2.21**, followed by oxidative cyclodehydrogenation. Lithiation of 9-bromobis(mesityloxy)anthracene (**L2.19**) with *n*-BuLi, and further addition of dibromodiborapentacene (**L2.20**) furnished **L2.21** in a

54% yield. Mesityloxy substituents (*para*-directing substituents) at the 4,5-positions of **L2.19** serve a dual role of promoting cyclohydrogenation at the 1,8-positions of **L2.22** and hindering aggregation of **L2.22**. Cyclohydrogenation of **L2.21** with FeCl₃ formed the desired B-doped PAH **L2.22** in a 51% yield, which was both air and moisture stable. Photophysical studies showed **L2.22** to emit in the visible/ near IR region albeit with a reduced PLQY ($\lambda_{em} = 679 \text{ nm}$, $\Phi_F = 0.04$). Despite its reduced PLQY, **L2.22** boasts rich redox abilities with reversible oxidation and reduction waves and a wide HOMO/LUMO gap; important properties for use in OFET's. An analogue of **L2.22** was prepared using on-surface cyclohydrogenation to form a boron-doped graphene nanoribbon (GNR).¹³⁵

Another way to overcome the requirement for bulky substituents to protect the boron atom is to introduce a nitrogen atom into the polycyclic skeleton to form B-N subunits; thus forming a new class of heteroatom doped PAHs (BN-doped PAH's).¹³⁶ The lone pair of the nitrogen atom interacts with the vacant p_z orbital which improves the stability and results in novel control over the redox properties but inadvertently leads to a reduction of Lewis acidity and electron accepting properties.¹²² Piers *et al.*¹³⁷ pioneered the way towards BN-doped PAH's, reporting BN-substituted triphenylene synthesised *via* chelation of pyridazine derivatives with various 2,2'-diborabiphenyl precursors. However, BN-doped PAH's are by far the least reported in the literature. The latter part of this work will focus exclusively on developing synthetic methodologies towards a number of novel boron and nitrogen doped PAH's (both on the periphery and centrally doped) molecules in order to expand the current library of compounds and expand synthetic pathways.

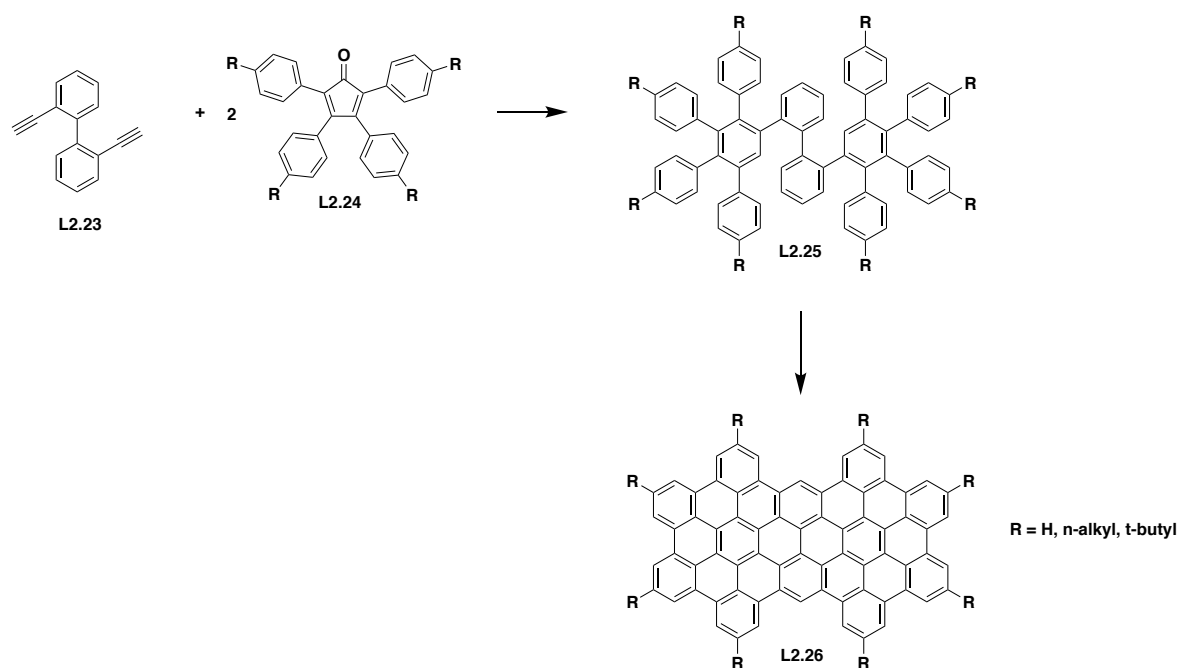
2.3 Developing Synthetic Methodologies Towards Novel Targets

A previously mentioned, the search for novel PAH type compounds is ever more pressing, due to their promising optoelectronic and luminescent properties. Every PAH compound has a unique stepwise synthesis, and careful tailoring of conditions and mechanistic understanding is required for each target. This work aims to expand the current mechanistic understandings, as well as contribute to building upon an existing family of known PAH compounds. The focus of this research can be divided into three separate undertakings: synthesis of novel all-carbon PAH compounds, synthesis of novel nitrogen doped PAH compounds, and synthesis of boron and nitrogen containing PAH compounds.

2.4 Synthesis and Characterisation

2.4.1 All-carbon PAH

All-carbon PAH compounds are the most prevalent in the literature. C_{72} PAH (**L2.26**) which is the focus herein has been previously synthesised by Mullen and co-workers, utilising harsh conditions, hazardous chemicals, and elevated temperatures (Scheme 2.5).¹³⁸ The authors reacted 2,2'-bisethynylbiphenyl (**L2.23**) with 1,2,3,4-tetraphenylcyclopenta-1,3-dien-5-ones (**L2.24**) in an intermolecular [4 + 2] cycloaddition, resulting in a quantitative conversion to **L2.54**, which was further reacted with a series of cyclohydrogenation conditions to furnish C_{72} PAH (**L2.26**) in a 90% yield.

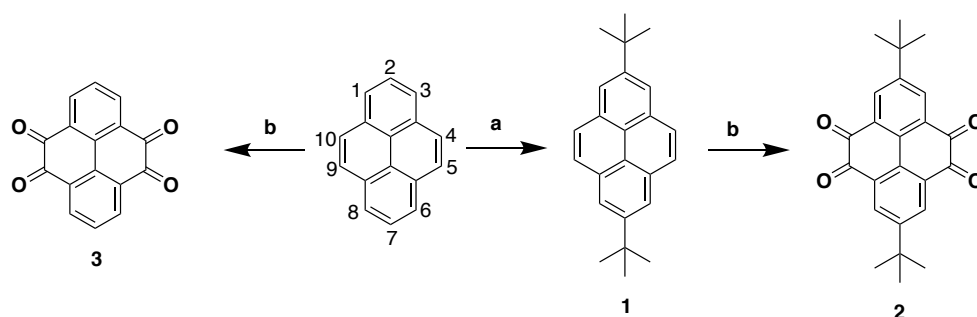


Scheme 2.5: Published synthetic route towards C_{72} PAH. **a)** Diphenylether at 230 °C, quantitative yield. **b)** Copper dichloride/aluminium trichloride in 1,1,2,2-tetrachloroethane at 145 °C; *t*-butyl lithium in hexanes at 50 °C, 90% yield.¹³⁸

The approach taken to synthesise C_{72} in this work is milder and more permissible towards functionalisation than that of Mullen and uses pyrene as the starting material for all chemical transformations rather than 2,2'-bisethynylbiphenyl. Pyrene, a commercially available white solid was used without further purification in a Friedel-Crafts alkylation in the presence of

AlCl₃ and *tert*-butylchloride to introduce *tert*-butyl groups at the 2,7 positions of the aromatic unit (Scheme 2.6). This transformation furnished **1** in a 75% yield, and was the only product formed. The 2,7 positions of pyrene are the only nucleophilic sites of the aromatic unit, which in the presence of a strong electrophile react in an electrophilic aromatic substitution process. The product was fully structurally characterised and was in good agreement with the literature.¹³⁹ The *tert*-butyl groups were introduced to increase solubility of the synthetic precursors and the final C₇₂ PAH, as well as probe cyclohydrogenation *ortho*- to the *tert*-butyl groups. The literature does not report C₇₂ which is substituted at those positions.

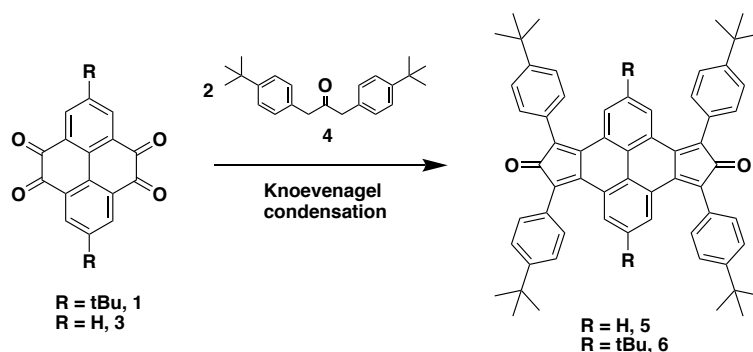
According to Clar, the 4,5 and the 9,10 positions of pyrene are the most electrophilic sites of the aromatic unit, such that oxidation can be performed at these positions, resulting in a tetra-ketone functionality.¹⁴⁰ In order to oxidise the pyrene unit, an active RuO₄ catalytic species was formed *in situ* from RuCl₃.nH₂O and NaIO₄. The active catalyst reacted with the double bonds of pyrene (at the 4,5 and 9,10 positions) to form a cyclic ruthenium (VI) diester species, which were converted to carbonyl functionalities *via* oxidative cleavage of the carbon-carbon double bonds. The RuO₄ catalytic species can be inactivated with carboxylic acids forming a low valent ruthenium carboxylate species. This complexation and subsequent inactivation is prevented by acetonitrile in a biphasic system, to ensure full conversion to the carbonyl functionality. The reaction furnished **2** in 23% yield and **3** in a reduced yield of 20%, and were both needle-like orange crystals, with structural characterisation in good agreement with the literature.¹⁴¹ Products **2** and **3** were utilised in a Knoevenagel condensation discussed in depth in 2.4.2.



Scheme 2.6: **a)** AlCl₃, *tert*-butyl chloride, RT, 2h, 75%. **b)** RuCl₃, NaIO₄, CH₂Cl₂, MeCN, H₂O, 35 °C, 48 h, **2** yield of 23%, **3** yield of 20%.

2.4.2 Knoevenagel Condensation

The Knoevenagel condensation is a versatile organic transformation used to convert an aldehyde or a ketone and an activated methylene to a substituted olefin, which is commonly catalysed by an amine base. This reaction requires a ketone/aldehyde, a methylene CH₂ (α -proton), and a catalytic to equimolar quantity of base, commonly cyclic amine bases such as piperidine or DBU. The reaction begins by the protonation of the activated methylene CH₂ by the base to form a resonance stabilised enolate. The amine base reacts with the ketone/aldehyde to form an iminium ion intermediate, which upon formation gets nucleophilically attacked by the enolate in solution. The newly formed intermediate gets deprotonated in a proton transfer step with the amine base, followed by a rearrangement forming an olefin in a cyclisation step which regenerates the catalyst. To optimise the reaction conditions, a series of amine bases and solvents were trialled to determine the optimal conditions for the required precursors shown below (Scheme 2.7).



Scheme 2.7: Knoevenagel condensation to synthesise precursors 5 and 6.

Substituted 1,3-diaryl-1,2-propanone **4** was synthesised according to a known literature method, using commercially available 4-*tert*-butylbenzylbromide and catalytic quantities of Fe(CO)₅ in a liquid-liquid phase transfer system with CH₂Cl₂/H₂O, Ca(OH)₂ and Bu₄N⁺HSO₄, to furnish **4** as a white crystalline powder in a 71% yield, which was in good agreement with the literature.¹⁴² To probe Knoevenagel condensation reactivity, **3** was chosen to react with **4**, using different bases and solvents (Table 2.0). Past Draper group members utilised equimolar quantities of KOH as a base in an ethanol reflux for 20 minutes to form the required cyclopentadienone precursor. When these conditions were trialled on a pyrene core, they did not seem to yield the required product. A dropwise addition of KOH to a solution of **3** and **4** in ethanol under an argon atmosphere resulted in a colour change from orange to black, with evident precipitate formation. Allowing the solution to stir at

reflux for 20 minutes and cooling down to RT resulted in a black solution, and addition of water resulted in a black precipitate forming. Extraction with CH₂Cl₂ and water proved challenging as the black precipitate was not soluble in CH₂Cl₂. Further attempts to solubilise the precipitate with ultrasound sonication, and reducing the organic washings *in vacuo* proved fruitless, and therefore structural characterisation of the black precipitate was not possible. Based on these synthetic observations, the method used by the group to successfully synthesise cyclopentadienones with KOH in the past could not be used in this case on a pyrene core. This could be due to a more aromatic precursor which hindered solubility in common organic solvents and subsequent reactivity.

Table 2.0: Knoevenagel condensation trials.^{a,b}

Trial	Base	Solvent	Outcome
1	KOH	Ethanol ^a	No product
2	Piperidine	Methanol ^b	No product
3	DBU	Ethanol ^a	Product formed

^a All reactions were carried out at reflux of ethanol (which was pre-dried on molecular sieves) for a period of 20 min to 1 h under an inert atmosphere. ^b Reaction in methanol was carried out at reflux of methanol overnight.

Piperidine, a cyclic amine has been previously reported in Knoevenagel condensation reactions and was the next choice of base. Methanol was chosen as solvent as it serves a role of a co-catalyst alongside of the piperidine base, and care was taken to not deviate from the reported successful procedures.^{143,144} The base was added dropwise to a suspension of **3** and **4** in methanol under an argon atmosphere. Piperidine is a weak base and a poor nucleophile and was added in excess to further force the equilibrium towards product formation. Upon addition of the base, the suspension turned from orange to black, suggesting reactivity, and was refluxed overnight. The extended reaction time was given due to the reduced solubility of the starting materials **3** and **4** in methanol. After 12 h, an evident black precipitate was formed, which was filtered off, and attempted to be solubilised in an array of common organic solvents (acetone, hexane, CH₂Cl₂) with little success. The product that could be solubilised in CH₂Cl₂ was washed with 2M HCl to neutralise any residual base. The organic washings were dried over MgSO₄ and reduced *in vacuo* to yield a black precipitate. Flash column chromatography was attempted on the isolated black precipitate (SiO₂, CH₂Cl₂),

which resulted in co-elution of an array of products as observed by thin layer chromatography (TLC), with no trace of starting materials observed. One fraction was isolated which contained a singly eluting product, suspected to be the desired product, but when reduced *in vacuo*, produced an oily substance. All crystallisation attempts failed to produce a solid. NMR and HRMS were carried out on the isolated fraction, which were inconclusive of product formation. It is evident that piperidine was too weak a base and was not suitable for this transformation, combined with the reduced solubility of the starting materials in methanol. The side products that were formed were not the desired final product, and due to the hindered solubility of the product and the complexity of purification this route was not pursued further.

A report published in 2016 by Mastalerz *et al.*¹⁴⁵ used equimolar quantities of DBU base in ethanol to perform the Knoevenagel condensation. These conditions were applied to this work, in a final attempt to overcome this synthetic hurdle. DBU was syringed dropwise to a solution of **3** and **4** in dried ethanol under argon at 78 °C. Care was taken to not allow the flask to heat above 80 °C, since DBU is a low boiling point liquid (BP 80-83 °C), and heating beyond 80 °C would result in the loss of the base from the reaction vessel. Addition of the base caused the solution to turn from orange to black, and the reaction was allowed to stir for 1 h, after which the reaction vessel was cooled to RT and allowed to settle. Upon cooling, a black precipitate was observed, which was filtered off and washed with cold ethanol, and dried to furnish **5** in 23% yield. No further purification was required as any residual starting materials and the base were washed down into the ethanol filtrate, producing a pure product. The product was sparingly soluble in CH₂Cl₂ and deuterated chloroform, such that structural elucidation could be gathered using NMR. The successful synthesis of **5** was applied in synthesising **6**, which furnished **6** as a black solid in an increased yield of 78%. The increased yield is due to an increased solubility of **1** in ethanol.

To date, compound **5** has not been previously reported, and as part of this work has been structurally characterised using ¹H NMR, ¹³C{¹H} NMR, HRMS, and IR. Figure 2.3a presents the ¹H NMR spectrum of **5**, which clearly shows four aromatic multiplets between δ 8.6 and δ 7.3 ppm, and one singlet in the aliphatic region at 1.3 ppm corresponding to the *tert*-butyl groups. Both the splitting patterns and peak integration allow facile peak assignment of the aromatic multiplets. A doublet which appears most upfield at δ 8.06-8.05

ppm and integrates to four protons, corresponds to **H2** of the central pyrene unit. A triplet at δ 7.88-7.86 integrates to two protons, and is assigned to **H1**, its peak split by the two neighbouring **H2** protons. Phenyl protons **H3** and **H4** are the most downfield of the aromatic multiplets and appear as two distinct doublets at δ 7.80-7.79 ppm and δ 7.39-7.38 ppm respectively, both integrating to eight protons each. Figure 2.3b shows the $^{13}\text{C}\{^1\text{H}\}$ NMR spectrum of **5**. A distinct feature of the $^{13}\text{C}\{^1\text{H}\}$ NMR spectrum: a peak at δ 197.37 ppm is characteristic of a carbonyl carbon (C=O), proving the presence of the carbonyls in the structure. Phenyl **C3** and **C4** were assigned using a 2D HSQC spectrum, with **C3** at δ 127.03 ppm and **C4** at 125.62 ppm. Similarly, pyrene **C2** and **C1** were assigned at δ 125.57 ppm and 124.19 ppm respectively.

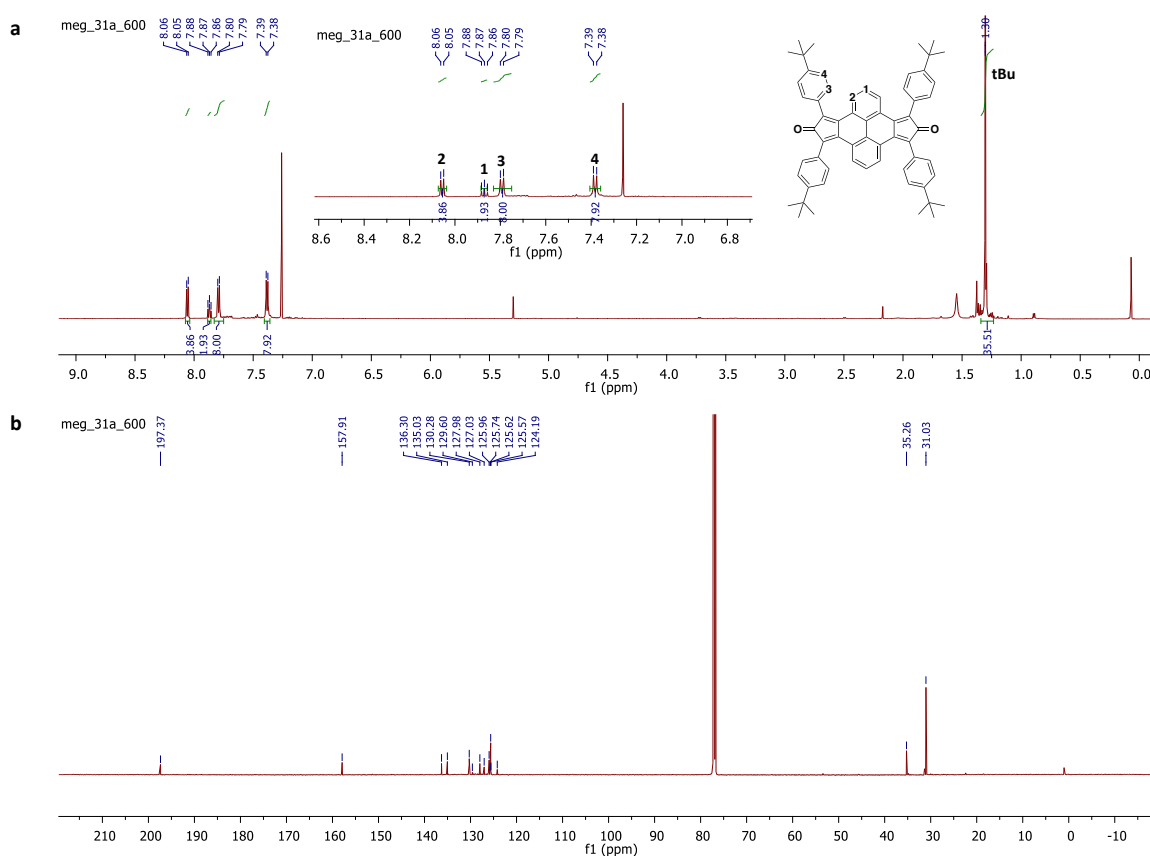


Figure 2.3: NMR spectra of **5**. **a)** ^1H NMR spectrum of **5** (600 MHz, CDCl_3 , RT). **b)** $^{13}\text{C}\{^1\text{H}\}$ NMR spectrum of **5** (151 MHz, CDCl_3 , RT).

Since commencement of this work, an independent report has been published structurally characterising **6** and so its structural characterisation discussion will not be included herein, however the spectra (^1H NMR, $^{13}\text{C}\{^1\text{H}\}$ NMR) can be located in Appendix 1.0b of this thesis. As noted above, both **5** and **6** are black solids, and when solubilised in CDCl_3 form a

black solution. An NMR sample of **6** was prepared and analysed to confirm the structure and purity, however the sample was not immediately disposed of. After leaving the sample in the lab overnight, the sample turned from deep black to clear yellow. The newly coloured sample was analysed again using ^1H NMR to produce a shift in peak positions, which appeared more upfield (Figure 2.4). Running a HRMS MALDI TOF experiment yielded a peak corresponding to the ring opened product **7** ($\text{C}_{68}\text{H}_{74}\text{O}_4$, calc. 954.5587, found 954.5589). This observation was a recurrent event over the course of a few months and leaving a solution of **5** in air overnight also resulted in a colour change from black to clear yellow. A thorough literature search produced other examples of aromatic systems with a pentatone functionality, which in the presence of air, and light, undergo a [4 + 2] Diels Alder reaction with $^3\text{O}_2$ to form a ring opened product. Mastalerz *et al.* do not report this property of **6** as being air-sensitive in their 2016 report, however a subsequent report published in 2017 discusses in-depth the decomposition of these systems when exposed to air.¹⁴⁶

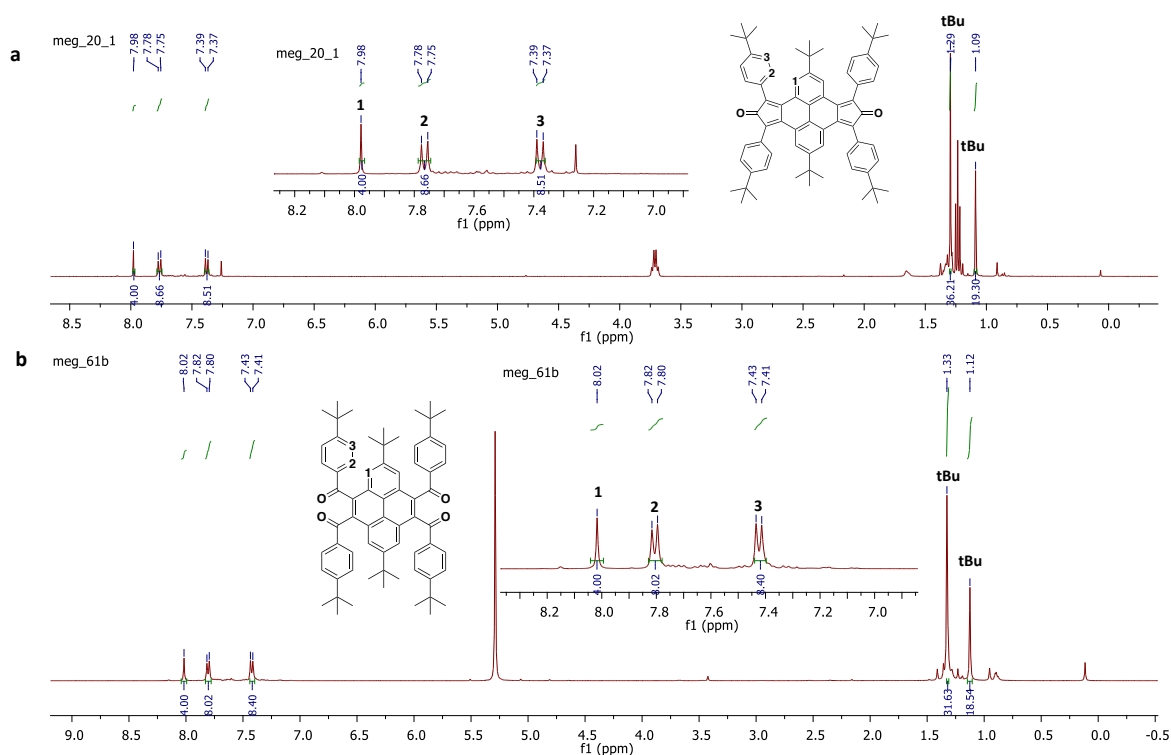
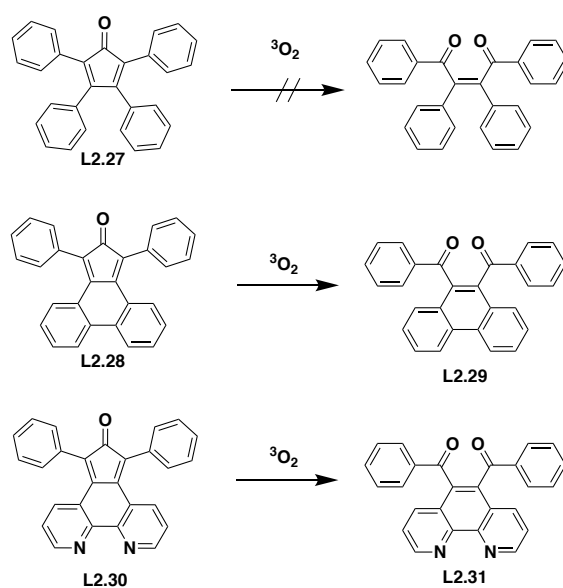


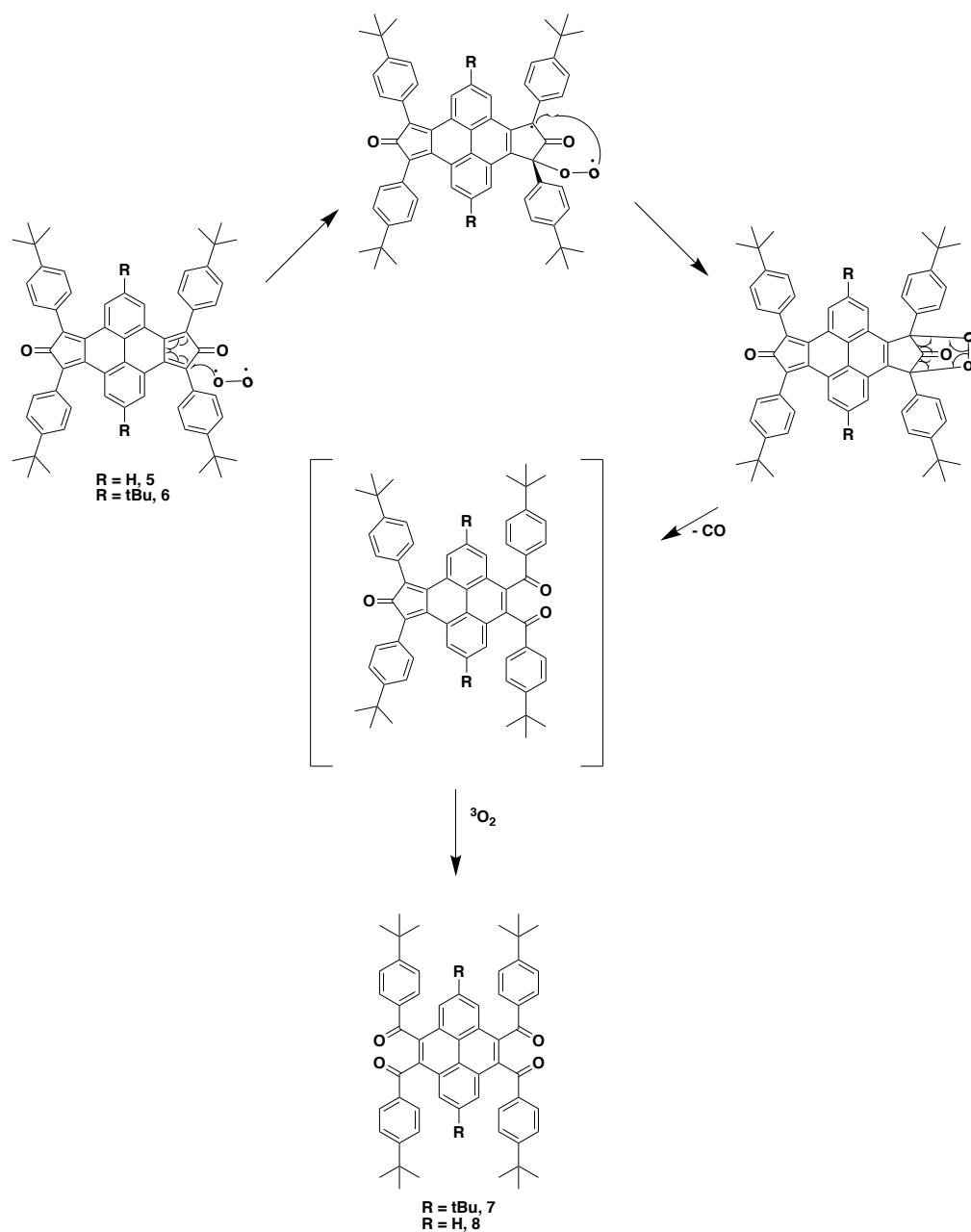
Figure 2.4: NMR spectra of **6** and **7**. **a)** ^1H NMR spectrum of **6** (400 MHz, CDCl_3 , RT). **b)** ^1H NMR spectrum of **7** (400 MHz, CDCl_3 , RT).

The report mentions that depending on the substitution pattern at the cyclone, the products may be prone to decomposition, however the report does not delve deeper into the mechanistic explanation. A paper written in 1938 by Dilthey, Henkels, and Leonhard¹⁴⁷ investigated the reaction of various cyclones with atmospheric oxygen, concluding that *ortho*-dibenzoyls are formed from reactions of oxygen with phencyclone or acecylone, however tetracyclone is not oxidised by atmospheric oxygen. This is in lieu of previous findings within the group, where cyclopentadienones (2,3,4,5-tetraphenylcyclopenta-2,4-dien-1-one, **L2.27**) were found to be air and moisture stable and used as precursors for PAH synthesis. However, Dr. Robert Conway-Kenny observed that within his increasingly aromatic systems, phenanthroline or phenanthrene based cyclones (1,3-diphenyl-2*H*-cyclopenta[*l*]phenanthrene-2-one **L2.28** and 5,7-diphenyl-6*H*-cyclopenta[*f*][1,10]phenanthroline-6-one, **L2.30**) were prone to decomposition in the presence of oxygen (Scheme 2.8).¹⁴⁸ Literature reports state that elevated temperatures are required, such as refluxing the cyclones in xylenes in the presence of oxygen, to achieve the ring opening. When considering the extended aromatic nature of **5** and **6**, with a dual reactive site, it is logical that the ring opening can occur at room temperature and within a short time frame of 24 h, making these systems highly reactive and not bench stable. For that reason, compounds **5** and **6** were synthesised only when required, used imminently, and in the interim stored at -20 °C and under an inert atmosphere to avoid any decomposition.



Scheme 2.8: Examples of cyclones which are prone to decomposition in atmospheric oxygen.

Scheme 2.9 illustrates the postulated ring-opening mechanism, which has been adapted for this work from Watson *et al.*¹⁴⁹ Products **5** and **6** undergo a $^3\text{O}_2$ mediated concerted Diels-Alder [4 + 2] cycloaddition, resulting in a ring opening and expulsion of CO.¹⁵⁰ It is known that employment of $^3\text{O}_2$ is a spin forbidden process, and for this reason, the authors proposed a step-wise mechanism, *via* an endoperoxide intermediate formation.¹⁵¹ The cyclone undergoes an attack by the $^3\text{O}_2$ species, resulting in the formation of the diradical species. This species undergoes a rapid spin-inversion ring closure to form the highly reactive endoperoxide intermediate, which in turn undergoes a thermal cycloreversion which is spin-allowed. This results in the expulsion of CO, an entropically favoured process, further forcing the ring opening mechanism to form the stable compounds **7** and **8**. A competing reaction with $^1\text{O}_2$ is plausible, which the authors disproved by carrying out experiments in the dark, where photoactivation $^3\text{O}_2$ to $^1\text{O}_2$ was not a feasible process. This theory was tested on both samples **5** and **6**, which were left in the dark, and both observed the full conversion from the ring closed to the ring opened products, further showcasing the sensitive nature of these highly aromatic compounds.



Scheme 2.9: Postulated mechanism of the $^3\text{O}_2$ mediated concerted [4 + 2] Diels-Alder reaction, forming the ring opened products **7** and **8**. The mechanism has been adapted from Watson et al.¹⁴⁹

The formation of **7** and **8** has been further confirmed by X-ray crystallography which was carried out by Dr. Brendan Twamley at Trinity College Dublin. A crystal sample of **7** suitable for X-ray crystallography measurements was grown from a reaction mixture containing benzophenone. A specimen of $\text{C}_{94}\text{H}_{94}\text{O}_6$, approximate dimensions 0.120 mm x 0.180 mm x 0.500 mm, was used for the X-ray crystallographic analysis. The structure was solved with the XT structure solution program using Intrinsic Phasing and refined with the

XL refinement package using Least Squares minimisation with Olex2, using the space group $P\bar{1}$, with $Z = 1$ for the formula unit, $C_{94}H_{94}O_6$. The final anisotropic full-matrix least-squares refinement on F^2 with 693 variables converged at $R1 = 4.82\%$, for the observed data and $wR2 = 13.80\%$ for all data. The goodness-of-fit was 1.023 (refer to Appendix 1.1a for the full crystallographic tables).

Crystals of **8** suitable for single crystal X-ray diffraction measurements were successfully obtained *via* slow evaporation of a $CDCl_3$ solution of the pure compound. A specimen of $C_{64}H_{64}N_2O_4$, approximate dimensions 0.013 mm x 0.090 mm x 0.370 mm, was used for the X-ray crystallographic analysis. The structure was solved with the XT structure solution program using Intrinsic Phasing and refined with the XL refinement package using Least Squares minimisation with Olex2, using the space group $C2/c$, with $Z = 4$ for the formula unit, $C_{64}H_{64}N_2O_4$. The final anisotropic full-matrix least-squares refinement on F^2 with 323 variables converged at $R1 = 10.27\%$, for the observed data and $wR2 = 27.16\%$ for all data. The goodness-of-fit was 1.003 (refer to Appendix 1.1a for the full crystallographic tables). Figure 2.5 below shows the asymmetric units of both **7** and **8**.

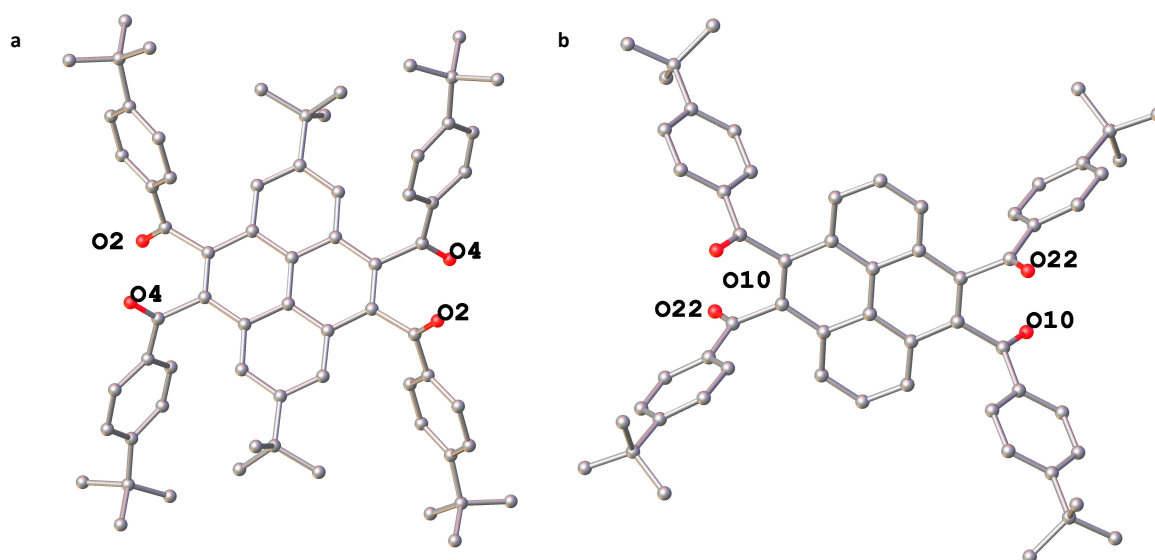


Figure 2.5: *a)* Asymmetric unit of **7**, with hydrogen atoms omitted for clarity (ball and stick shown at 50% probability). The majority occupancy disordered model is shown (disorder in the tert-butyl moiety at 50% occupancy). *b)* Asymmetric unit of **8**, with hydrogen atoms omitted for clarity (thermal ellipsoids shown at 50% probability).

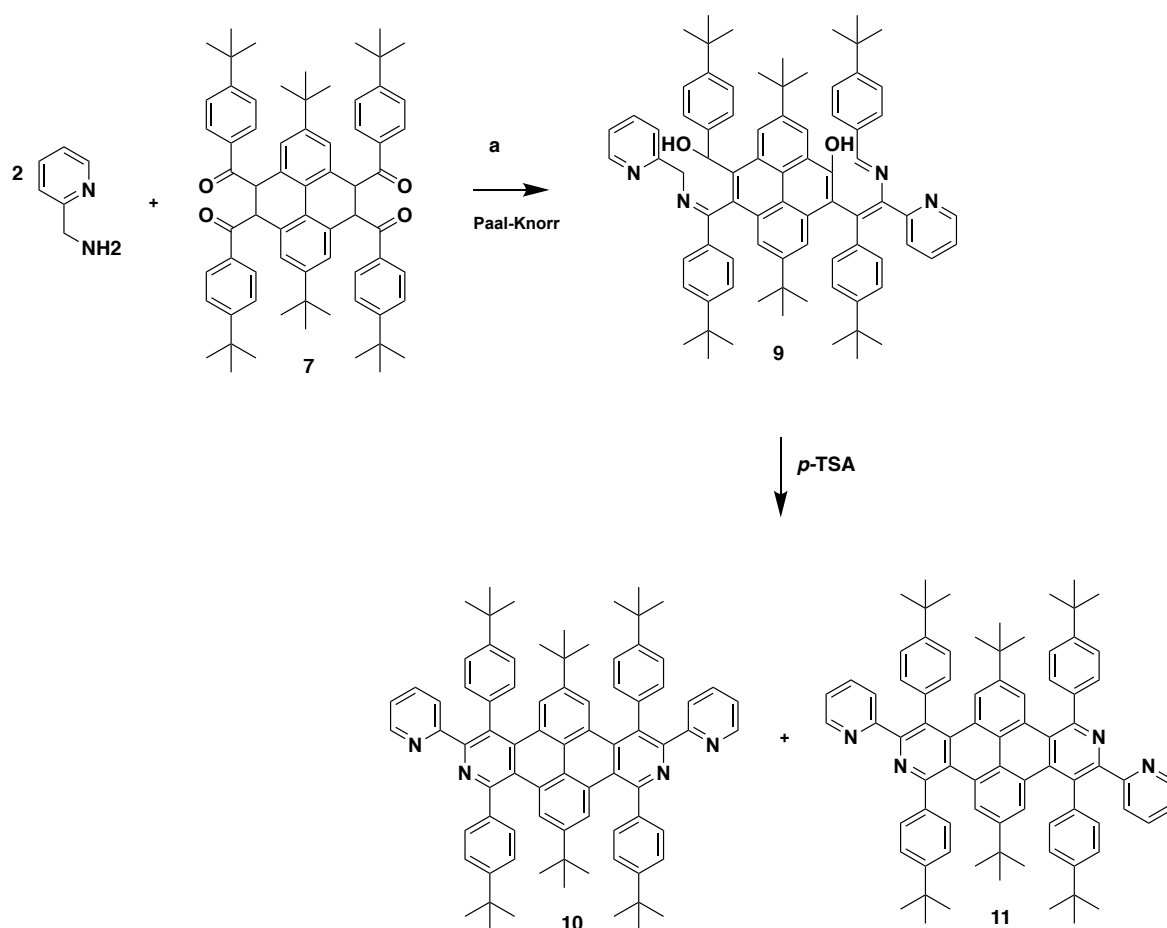
Compound **7** was highly disordered at *tert*-butyl and benzophenone moieties (full disordered images can be located in Appendix 1.1b). The structures bear resemblance in their bonding which is unexceptional (C-C, C-H, and C=O bonding), with C=O bond lengths typically reported as 1.210 Å, in lieu with the experimental values calculated (1.2163(18) Å for **7** and 1.236(7) Å for **8**).⁵¹ Both structures have highly twisted conformations at the phenyl rings. However, packing arrangements differ greatly due to drastically different co-crystallisations with the solvent, and the presence of the two *tert*-butyl groups at the 2 and 7 positions of **7**. An examination of the packing arrangements did not show any significant intermolecular interactions as a result of the highly twisted nature of both **7** and **8** (packing diagrams can be located in Appendix 1.1c - 1.1g of this thesis).

2.4.2.1 Potential Synthetic Pathways with **7** and **8**

Deviating from the synthetic discussion towards the target C₇₂ PAH, the serendipitous formation of **7** and **8** resulted in alternative routes towards novel targets *via* **7** and **8** as synthetic intermediates which were not part of the original synthetic planning. The positioning of the diketone functionality on such a highly aromatic pre-fused scaffold as pyrene presented itself with other opportunities: an array of ring closing reactions, possibility to introduce heteroatoms into the structure, and ligand functionality for transition metal coordination.

To test this, **7** was formed by dissolving **6** in minimal amounts of chloroform and allowing the solution to sit in daylight for 24 h, resulting in a full conversion of **6** to **7**. Following that, the Paal-Knorr ring closure was trialled, by refluxing the commercially bought 2-(aminomethyl)pyridine with **7** and KOH in ethanol for one h, in the presence of air (Scheme 2.10).¹⁵³ The reaction mixture was analysed after 1 h using MALDI TOF HRMS, which confirmed the presence of the partially ring closed product **9** with a hydroxy functionality (MALDI TOF C₈₀H₈₈N₄O₂ calc 1136.69, found 1137.6218, Appendix 1.0f). To further force the reaction towards product formation, *p*-TSA was added, and the reaction refluxed overnight to dehydrate the -OH groups and promote the ring closure towards products **10** and **11**. The crude reaction mixture was further analysed to confirm the disappearance of **9** and formation of **10** and **11**. However, attempts at isolating **10** and **11** from the crude reaction

mixture proved a significant challenge. Thin layer chromatography (SiO₂, CH₂Cl₂/MeOH 100:1, v/v) identified the solvent system as the only solvent mixture to be able to separate **10** and **11**, albeit on a sluggish purification system. When carrying out the flash column chromatography, the column failed to produce pure eluents of the products. These synthetic challenges were a significant hurdle and deviated from the target research, and so this route remains a part of the future work. If ring closing syntheses are successful as part of future work, cyclohydrogenation attempts of any subsequent ring closed products will also yield novel planarized heteroatom doped PAH's.



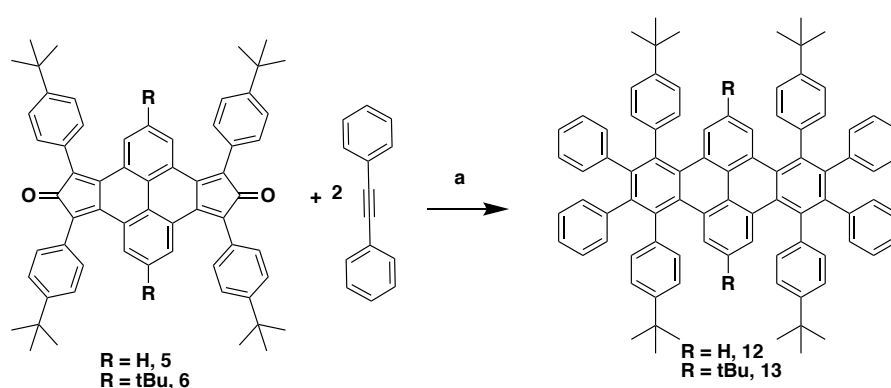
Scheme 2.10: Paal-Knorr synthetic trial.¹⁵³

Even with the substantial synthetic and purification hurdles, this is still an immensely promising deviation, and 2-(aminomethyl)pyridine was chosen initially as it would furnish the products with a double N^N ligand functionality. Analogous bidentate aromatic ligands

have been utilised with transition metal complexes (metals such as Ru, Pt, and Pd) being applied in water splitting and hydrogen generation.^{154,155}

2.4.3 Diels-Alder Cycloaddition

Diels-Alder reactions are a versatile tool to synthesise benzene rings, by employing a conjugated diene and a dienophile in a pericyclic cycloaddition mechanism. The driving force of the reaction is the formation of two novel carbon-carbon bonds as well as the expulsion of CO.^{156–160} To synthesise the required precursors for the final oxidative cyclohydrogenation step towards C₇₂ PAH, Knoevenagel products **5** and **6** (behaving as dienes) were reacted with a commercially attained diphenylacetylene (behaving as a dienophile) in a double [4 + 2] Diels-Alder cycloaddition (Scheme 2.11).



Scheme 2.11: Diels-Alder [4 + 2] cycloaddition. **a)** Benzophenone melt, 300 °C, 5 h, furnishing **12** in a 84% yield and **13** in a reduced yield of 20%.

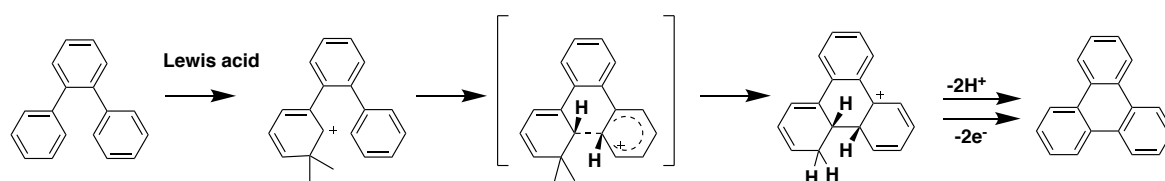
This reaction was carried out in a sand burner at 300 °C under argon and using benzophenone as solvent for 5 h. The resulting maroon reaction mixture of **12** was allowed to cool, dissolved in a minimal quantity of CH₂Cl₂, and upon slow addition of methanol, resulted in an evident red precipitate formation. The product was allowed to crystallise from CH₂Cl₂/MeOH at -20 °C overnight under an argon atmosphere. Filtration and further washings with cold MeOH furnished **12** as a dark red solid in an 84% yield, which was confirmed with HRMS (MALDI TOF C₈₈H₇₈ Calc. 1134.6104 Found 1134.6080). However, **12** was very sparingly soluble in CDCl₃, such that ¹H NMR studies resulted in broadened and poorly resolved peaks due to π-π stacking, and the sample was too dilute for ¹³C{¹H} NMR, culminating in lack of full structural characterisation. Further purification attempts

using flash column chromatography were futile also, as the product seemed to be air sensitive, decomposing within hours into two separate products as observed by TLC (green and red fluorescent bands). Product **12** was thus treated as a reactive intermediate and was used imminently and without further purification or characterisation in the subsequent cyclohydrogenation step.

Polyphenylene precursor **13** was synthesised in an analogous reaction with **12**, furnishing **13** as a pale brown solid in a reduced yield of 20%, a result of a more sterically hindered diene **6**. Similarly, to **12**, **13** appeared to be air sensitive, and was only prepared when required for further synthetic reactions. Full structural characterisation of **13** was not feasible for the same reasons as **12**, however HRMS (MALDI TOF $C_{96}H_{94}$ Calc. 1246.7356 Found 1246.7312) identified the presence of the product.

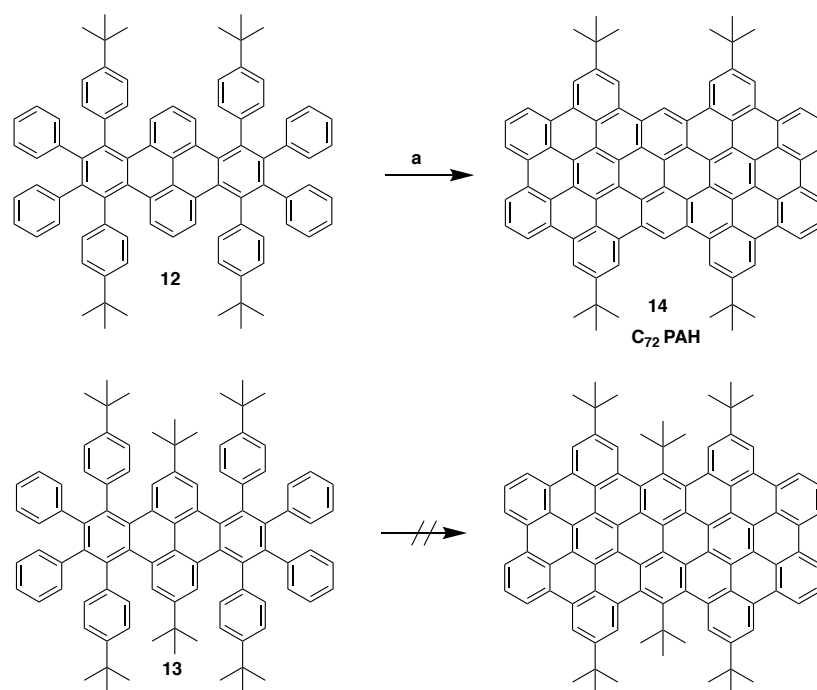
2.4.4 Oxidative Cyclohydrogenation

To synthesise PAH type molecules, oxidative cyclohydrogenation of the appropriate polyphenylene is carried out by promoting C-C bond closure. More specifically, oxidative cyclohydrogenation is otherwise termed oxidative aromatic coupling if the reaction occurs with electron rich polyphenylenes, at room temperature, and is mediated by oxidants, as is the case for synthesis of C_{72} .¹⁶¹ The mechanism of the reaction depends solely on the cyclohydrogenation agent of choice, and it is known that the arenium cation mechanism (illustrated by Scheme 2.12) prevails in larger PAHs such as C_{72} .¹⁶² The mechanism favours the formation of an arenium cation intermediate *via* the formation of an electrophilic σ -complex between the proton/ Lewis acid, and the polyphenylene. The electrophilic σ -complex is nucleophilically attacked by the neighbouring aromatic ring, resulting in C-C bond formation, which is preceded by hydrogen elimination which is an entropically favoured process.



Scheme 2.12: Arenium cation mechanism as described by King *et al.*¹⁶² utilising *o*-terphenyl as an example.

Extreme air and moisture free conditions are required to synthesise **14** (Scheme 2.13). Polyphenylene **12** was dissolved in minimal amounts of CH₂Cl₂ and stirred under a constant flow of argon and at RT. A solution of FeCl₃ in nitromethane was added dropwise, which resulted in an instant colour change from red to black, and the reaction was allowed to stir for 24 h. FeCl₃ serves a dual role as the oxidising agent and the Lewis acid in the reaction. Following that, the reaction mixture was quenched in methanol, resulting in the formation of a red solid, which was further purified using flash column chromatography (SiO₂, MeOH/CH₂Cl₂, 1:9, v/v) to afford **14** a single eluent and a resulting as an air and moisture stable red solid in 94% yield. The purity of the eluent was further confirmed by TLC, with **14** being the sole product collected. When analogous conditions were trialled with polyphenylene **13**, the resulting cyclohydrogenated product was not formed. It is postulated that the presence of the *tert*-butyl groups at the 2- and 7-positions has hindered complete C-C bond closure. For this reason, future focus was given exclusively to **14**. As part of initial planning, peripheral substitution of C₇₂ along the outer edges with solubilising *tert*-butyl groups (by use of an adequately substituted diphenylacetylene) was disregarded, as it was envisioned that this C₇₂ would serve as a single molecule junction, and so excessive *tert*-butyl substitution would hinder any potential contact between the molecule and its electrode in the device. However, as a result of this requirement, the final PAH suffered solubility challenges, with solution-based characterisation (such as NMR), and further testing of properties (such as solution UV-vis absorption and emission measurements) becoming immensely challenging.



Scheme 2.13: Oxidative cyclodehydrogenation of **12** a) FeCl₃/CH₃NO₂ in CH₂Cl₂, 24 h, furnishing **14** in 94%.

Structural characterisation of **14** was greatly hindered due to its extended planar structure. ¹H NMR spectrum of **14** in 1,1,2,2-tetrachloroethane/TFA was obtained with great difficulty, however clearly illustrating six distinct aromatic regions of the molecule (Figure 2.6).

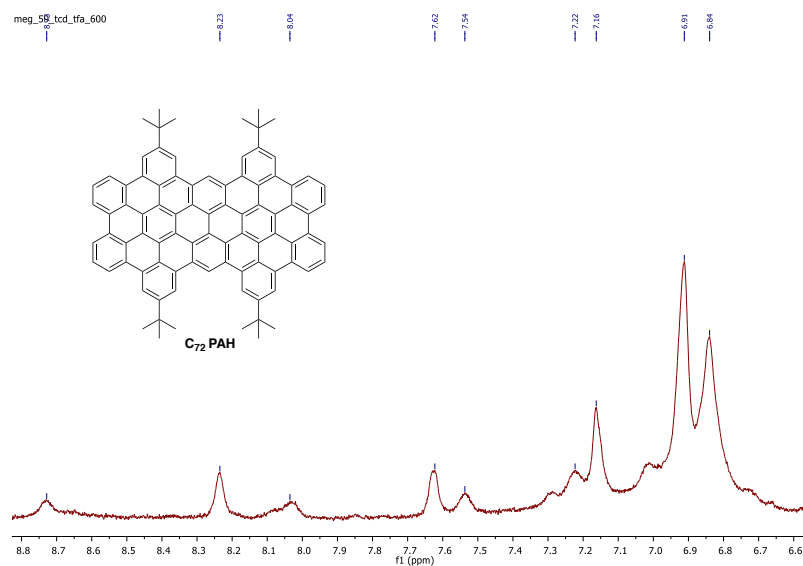


Figure 2.6: Aromatic region of the ^1H NMR spectrum of **14** (1,1,2,2-tetrachloroethane/ TFA, 600 MHz). Due to solubility and stacking, the spectrum cannot be structurally assigned, however the spectrum illustrates the presence of an aromatic compound.

Full assignment (integration ratios or peak multiplicity) of the spectrum is not possible, due to presence of both π - π stacked aggregates and free molecules in solution. However, fully assigned and well resolved spectra of large PAH's are absent from the literature also. Commonly, large PAH's are characterized using solid state NMR, and/ or MALDI TOF HRMS and isotropic ratio matching, which was done for **14** (Figure 2.7). Experimental and calculated isotopic distributions of **14** show peak value matching, confirming the presence of **14**.

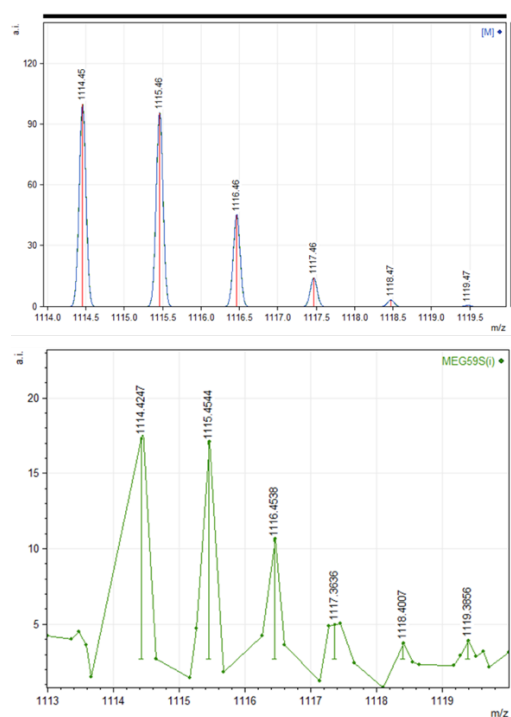


Figure 2.7: Calculated versus experimental isotopic distribution of **14**; MALDI TOF $\text{C}_{88}\text{H}_{58}$ Calc. 114.4539 Found 114.4541, HRMS measurement run on both CHCA and DHB matrices, confirming the presence of **14**.

2.4.5 Photophysical and Thermal Analysis

The successful synthesis and purification of **14** called for further studies to be carried out on its potential properties, such as photophysical and thermal properties. Compound **14** observed red fluorescence when irradiated with UV light, which is common of PAH's and

is expected due to its highly conjugated nature. All attempts to make accurate concentration solutions of **14** in CH₂Cl₂ for absorption and emission measurements failed, with evident precipitate formation, even after sonication. A UV-vis spectrum of **14** (Figure 2.8) was collected to gain an insight into the absorption bands which could be present, however it is not of accurate concentration ($\sim 1 \times 10^{-4}$ M). The absorbance spectrum shows three distinct bands (217, 356, and 488 nm), with PAH absorption is common between 300 and past 500 nm, indicating that the absorption values are in the correct spectrum range.¹⁶³

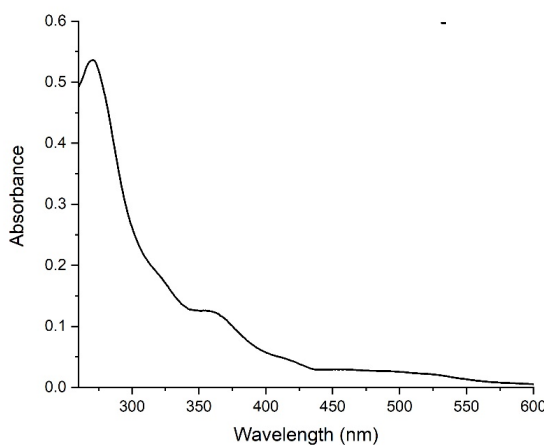


Figure 2.8: UV-vis absorption spectra of **14** ($\sim 1 \times 10^{-4}$ M) in CH₂Cl₂.

Thermogravimetric analysis of **14** was carried out as follows; the compound was weighted into a clean ceramic crucible prior to placing the crucible into the furnace. The furnace program was as follows: heating to 120 °C and holding the sample at this temperature (isothermal step) for 30 minutes to evaporate any trapped solvent molecules, followed by continuous heating to 700 °C at a rate of 10 °C per minute. All measurements were carried out under N₂ gas, to eliminate any potential side reactions with oxygen. Figure 2.9 shows a ~21 % weight loss corresponding to the two tert-butyl substituents, with no further weight loss past 750 °C observed, showcasing extreme thermal stability. TGA measurements prove the validity of **14** as a material for organic electronics and device incorporation, as a potential semiconducting layer in an OFET device or as a conductive single molecule junction.

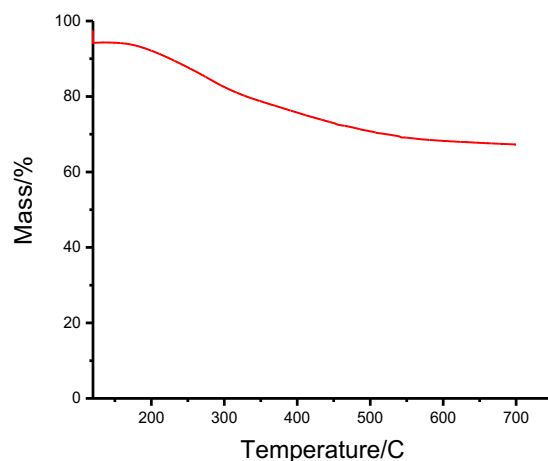


Figure 2.9: Thermogravimetric analysis (TGA) of **14** carried out under an N_2 atmosphere.2.4.5

2.4.6 Conclusions and Future Work

This work describes an in-depth synthetic study of alternative and milder pathways towards C_{72} , different peripheral functionalisation as well as its structural, photophysical, and thermal analyses which are absent from the literature. This work suffered an array of synthetic blocks, with the final product exhibiting very poor solubility in common organic solvents, resulting in limited structural and photophysical characterisation. As part of future work, single molecular junctions are proposed with C_{72} , to probe conductive properties of this extended PAH. Additionally, novel organometallic compounds are envisioned with C_{72} as a ligand, which are due to be synthesised in collaboration with Prof. Andrew Weller at the University of York, UK.

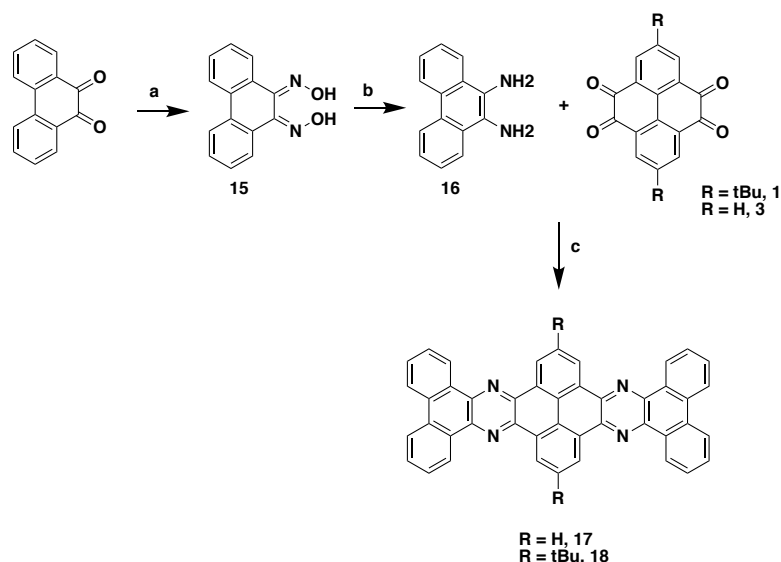
2.5 Nitrogen-doped PAH's

Nitrogen-doped PAH's are widely sought after as they provide opportunity for alteration of the electronic properties of PAH's, by inclusion of nitrogen atoms both centrally and on the periphery. When studying nitrogen doped PAH's as part of this work, two independent main aims were pursued: synthesis of longitudinally extended nitrogen PAH's for application as single molecule junctions, and a study of DDQ/ H^+ as a cyclohydrogenation agent towards peripherally doped nitrogen PAH's.

2.5.1 Facile Synthesis of Phenazine PAH's

Phenazine ring systems are found in the literature in an array of compounds, and are fully aromatic ring systems.¹⁶⁴⁻¹⁶⁶ Inclusion of phenazine as a central moiety of a longitudinally extended aromatic structure would result in unprecedented electronic and conductive properties, with these compounds potentially useful as single molecule junctions and semiconductors.¹⁶⁷ Novel longitudinally extended nitrogen doped PAH's were envisioned, reenlisting previously synthesised **1** and **3** as key synthetic building blocks.

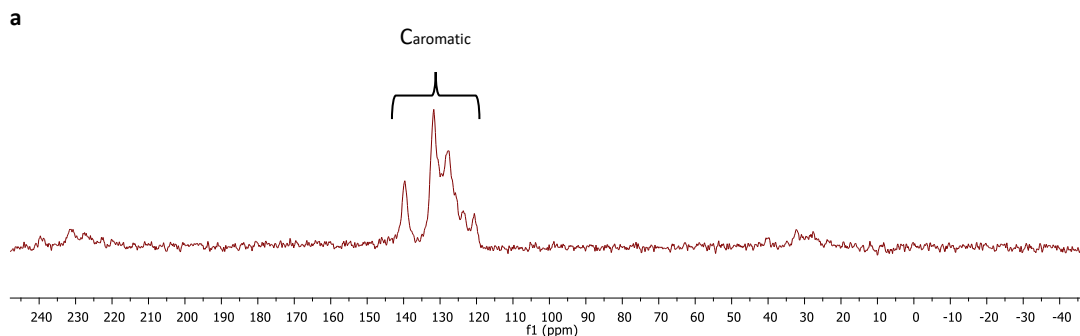
Product **16** was prepared in a two-step synthesis, which was then reacted with the appropriate pyrene derivative in a Schiff base condensation to furnish the desired nitrogen doped PAH's (Scheme 2.14). (9Z,10Z)-phenanthrene-9,10-dione dioxime (**15**) was prepared using an amended literature protocol. Commercially bought phenanthrene-9,10-dione was refluxed with hydroxyamine hydrochloride and potassium acetate in ethanol for 20 h under argon, after which 0.1M HCl was added to quench the reaction and allowed to stir for a another 2 h. The white precipitate was filtered and washed with ethyl acetate and ethanol to furnish **15** as a mustard yellow solid in 96% yield, which was in good agreement with the literature.¹⁶⁸ Product **15** was further reduced to the diamine product **16** by refluxing with sodium dithionite in ethanol for 2 h under argon, which resulted in a green precipitate formation. The precipitate was filtered, washed with 3% ammonia solution, and THF, and dried to furnish **16** as an air sensitive green solid in a 62% yield, which was in good agreement with the literature.¹⁶⁹ The final products **17** and **18** were prepared by employing **16** and the appropriate pyrene (**1** or **3**) in a Schiff base condensation. The reactants were fully dissolved in ethanol, to which 10% *p*-TSA was added, and the solution was refluxed under argon for 24 h, resulting in a pale brown precipitate forming. The precipitate was filtered, washed with cold ethanol, and dried to produce **17** in a 96% yield and **18** in a 97% yield. The unprecedentedly high yields of this condensation illustrate how synthetically attainable these systems are, and showing promise for potential industrial scalability, and further functionalisation.



Scheme 2.14: Synthesis of **17** and **18** **a)** hydroxyamine hydrochloride, potassium acetate, reflux of ethanol, 20 h, argon; 0.1M HCl, 2 h, to furnish **15** in 96% yield. **b)** sodium dithionite, reflux of ethanol, 2 h, argon, to furnish **16** in a 62% yield. **c)** Schiff base condensation, 10% *p*-TSA, reflux of ethanol, argon, 24 h, to furnish **17** in 96%, and **18** in 97%.

As expected, the final products exhibited immensely limited solubility in common organic solvents, such that structural characterisation was not possible using conventional NMR. Solid state $^{13}\text{C}\{^1\text{H}\}$ NMR measurements, IR, and HRMS were thus chosen to structurally characterise **16** and **17** (Figure 2.10). Solid state NMR spectra is less sensitive when compared to solution NMR, however a degree of peak assignment can be carried out. In both spectra, there is a clear broad set of peaks at δ 145-115 ppm which correspond to aromatic carbon atoms. Figure 2.10b displays an extra broad peak at δ 38-30 ppm corresponding to the aliphatic carbon atoms of **18**. HRMS measurements were run to confirm the presence of the products, with difficulty locating product **17**. This was due to extreme aggregation and solubility issues, and thus difficult to identify using MALDI. However, isotopic distribution patterns showed presence of product in the spectra (Appendix 1.0k and 1.0l). HRMS confirmed presence of **18** (MALDI TOF $\text{C}_{52}\text{H}_{40}\text{N}_4$ Calc.720.3253 Found 720.3239). Upon closer examination of the products, and their solid $^{13}\text{C}\{^1\text{H}\}$ NMR spectra, **17** and **18** exhibit extreme correlations, given the almost identical structure, and as part of future work, more thorough HRMS studies are required to fully characterise **17**.

meg_29
Standard CP experiment
60kHz carbon, 70kHz proton, 6ms contact time, 25C, 10kHz spin rate, 50kHz proton decoupling



meg_30
Standard CP TOSS experiment
60kHz carbon, 70kHz proton, 6ms contact time, 25C, 7.5kHz spin rate, 50kHz proton decoupling

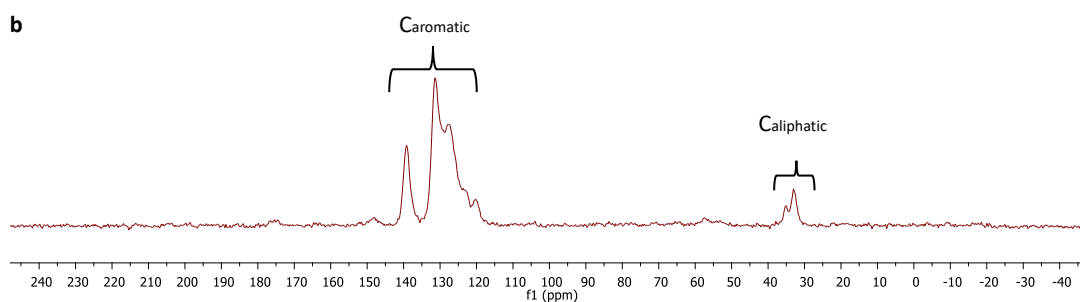


Figure 2.10: Solid state $^{13}\text{C}\{^1\text{H}\}$ NMR spectra of **a) 17** and **b) 18**.

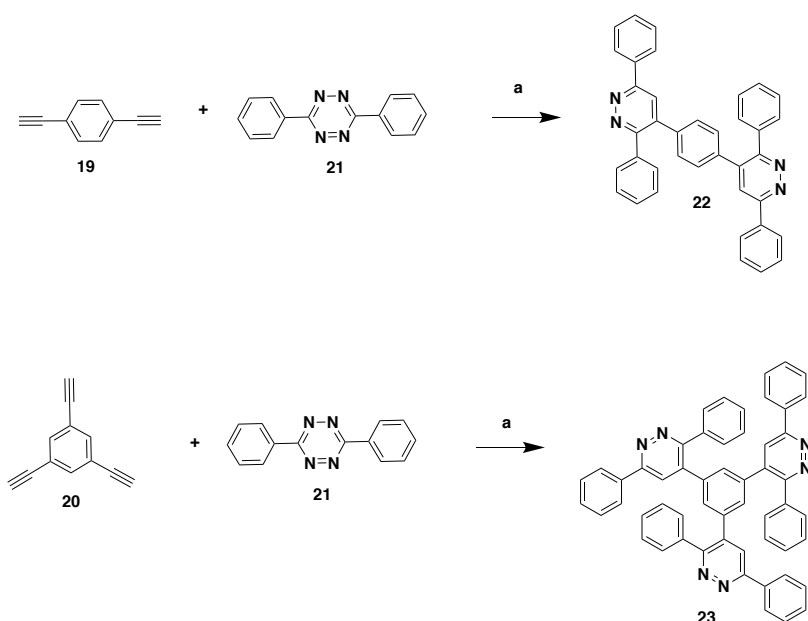
2.5.2 Conclusions and Future Work

The above brief synthetic discussions of **17** and **18** highlight that synthesis of extended nitrogen containing PAH's is not always a cumbersome multi-step process. Large PAH's can indeed be synthetically accessible by employing adequately functionalised pre-fused precursors in a final 'click' reaction to furnish PAH's in almost quantitative yields. However, as with other known PAH's, solubility challenges hinder full structural characterisation of the materials, which will in turn hinder potential application. Compound **18** was sparingly soluble in THF, a solvent often used in fabrication of electronic devices. As part of future work, conductivity measurements are envisioned, to probe the potential of these materials as semiconductors for future electronics devices.

2.5.3 DDQ/H⁺ as a Cyclohydrogenation Agent

The aim of this work was to probe DDQ/H⁺ as a cyclohydrogenation agent on previously synthesised pyrazidine containing polyphenylenes made by Dr. Gearóid Ó Máille.¹⁷⁰ Compounds **19** and **20** were resynthesised for this work using standard palladium catalysed

conditions for Sonogoshira cross-coupling of commercially bought brominated benzenes and trimethylsilylacetylene, and further deprotection steps furnished both products as white crystalline powders (**19** in 35% yield, and **20** in 93% yield). Both acetylenes were structurally characterised and in good agreement with the literature.¹⁷¹ Compound **21** was prepared by Dr. Gearóid Ó Máille, and used without further purification.¹⁷⁰ Polyphenylenes **22** and **23** were also prepared according to Dr. Gearóid Ó Máille's methods, in a [4 + 2] Diels-Alder cycloaddition of the appropriate acetylene and **21** (Scheme 2.15).



Scheme 2.15: [4 + 2] Diels-Alder cycloaddition to synthesise **22** and **23** a) toluene, pressure tube, 150 °C, 7 days, furnishing **22** in a 21% yield and **23** in a 60% yield.

The precursors were dissolved in minimal amounts of dried and degassed toluene and heated under pressure at 150 °C for 7 days. Following that, the reaction mixtures were reduced *in vacuo*, and purified using flash column chromatography (SiO₂, CH₂Cl₂/MeOH 100:5 – 100:15, *v/v*) and product containing eluents further recrystallised from slow addition of hexanes to a concentrated solution of the product, furnishing **22** as an off white/ orange solid in a 21% yield, and **23** as an off white/ peach solid in a 60% yield. Both products were fully structurally characterised and were in good agreement with the literature.¹⁷⁰

Crystals of **23** suitable for single crystal X-ray diffraction measurements were successfully obtained *via* slow evaporation of a CH₂Cl₂ solution of the pure compound. A specimen of

$C_{55}H_{38}Cl_2N_6$, approximate dimensions 0.040 mm x 0.110 mm x 0.130 mm, was used for the X-ray crystallographic analysis. The structure was solved with the XT structure solution program using Intrinsic Phasing and refined with the XL refinement package using Least Squares minimisation with Olex2, using the space group $P\bar{1}$, with $Z = 2$ for the formula unit, $C_{55}H_{38}Cl_2N_6$. The final anisotropic full-matrix least-squares refinement on F^2 with 568 variables converged at $R1 = 9.02\%$, for the observed data and $wR2 = 20.22\%$ for all data. The goodness-of-fit was 0.981 (refer to Appendix 1.2a for the full crystallographic tables). Figure 2.11 displays the asymmetric unit of **23**, showing a highly twisted structure with no significant intermolecular interactions (packing diagram can be located in Appendix 1.2c). The bonding within the structure, mainly C-N (typically reported as 1.336 Å) and N-N bonding lengths (typically reported as 1.366 Å) are in lieu with standard values (1.344(8)Å and 1.322(7)Å respectively).⁵¹

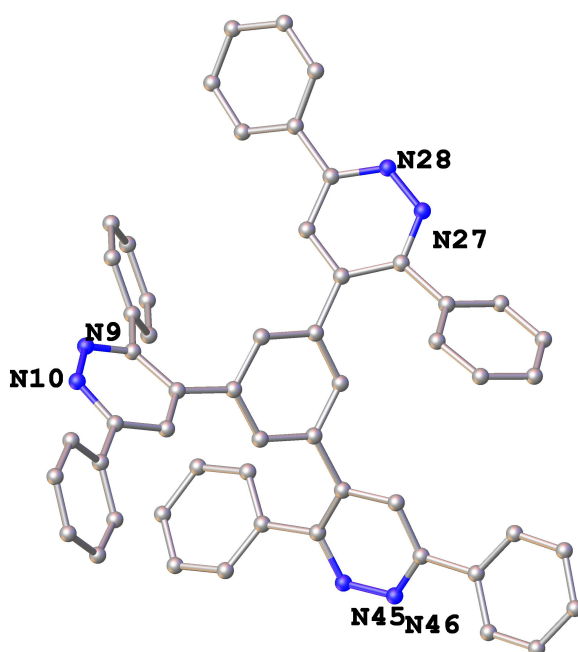
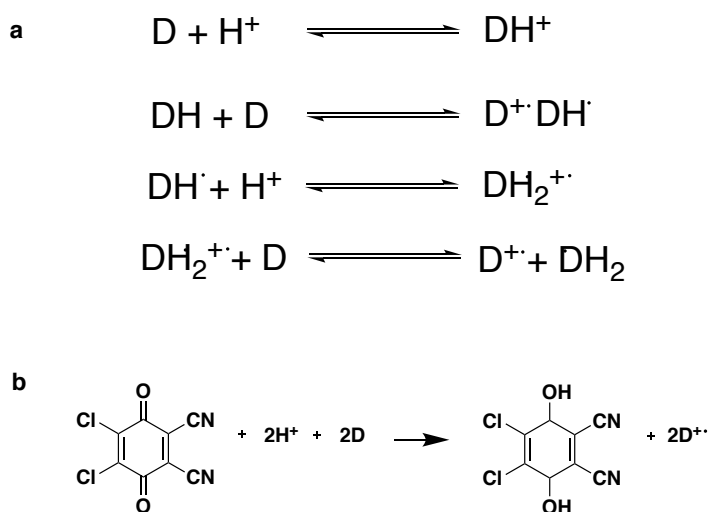


Figure 2.11: Asymmetric unit of **23**, with hydrogen atoms omitted for clarity (ball and stick shown at 50% probability). The majority occupancy disordered model is shown (disorder in the tert-butyl moiety at 50% occupancy).

Cyclohydrogenation of **22** and **23** was attempted by Dr. Gearóid Ó Máille, using $FeCl_3$ as the cyclohydrogenation agent, however neither partially nor fully cyclohydrogenated products were observed. Dr. Gearóid Ó Máille altered the structure to promote cyclisation by including methoxy (-OMe) at the *para*- positions to cyclohydrogenation sites, resulting

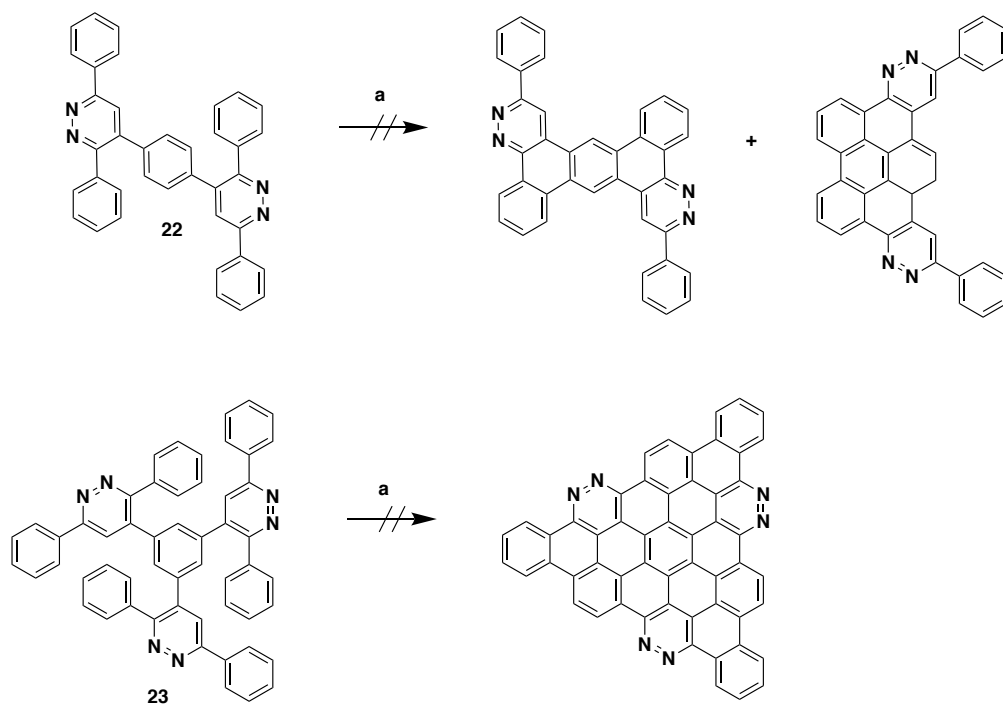
in mixed success producing a mixture of partially cyclised products albeit in negligible yields. At the time, DDQ/H⁺ was not probed as a cyclohydrogenation agent, which has been known to successfully perform Scholl oxidation on substrates which were inert to FeCl₃.

Additionally, due to the past success that Draper *et al.*¹²⁸ observed when successfully preparing **L2.12** – **L2.14** *via* oxidative cyclohydrogenation of the pyrimidine containing polyphenylene precursor **L2.10** with DDQ/H⁺ (Section 2.1.2, Scheme 2.2), this method was trialled on the pyrazidine containing polyphenylenes also. The authors also used AlCl₃/CuCl₂/CS₂ and FeCl₃, with mixed successes, with DDQ/H⁺ proving to be the highest yielding cyclohydrogenation agent. 2,3-Dichloro-5,6-dicyano-1,4-benzoquinone (DDQ) is a known oxidant used for dehydration of alcohols, phenols, and ketones, and as a reagent for removal of hydrogen atoms from organic molecules. Radical cations can be generated from organic donors in solution in the presence of a strong acid (Scheme 2.16a), however generation of radical cations is increased to almost quantitative yields in the presence of an oxidant, such as DDQ (Scheme 2.16b). The resulting hydroquinone is poorly soluble in common organic solvents, and facilitates a facile workup of successful syntheses.



Scheme 2.16: **a)** Postulated interconversion from cation to radical cation in the presence of acid, with *D* indicating an aromatic donor.¹⁷² **b)** Generation of an organic radical cation with DDQ as oxidant in the presence of acid.

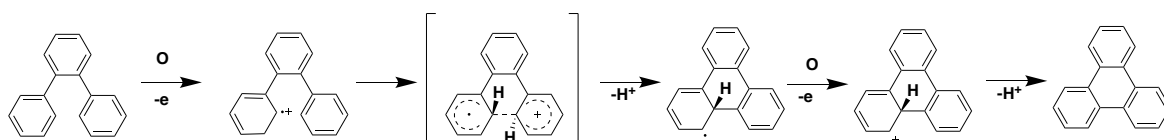
The polyphenylene precursors (**22** or **23**) and ten equivalents of DDQ were dissolved in minimal amounts of dried and degassed CH_2Cl_2 , to which $\text{CF}_3\text{SO}_3\text{H}$ was syringed in. Upon the addition of acid, the solution went from clear to green to black, and was allowed to stir for 2-4 h, with reaction progress being monitored by TLC. After 4 h, the solution turned clear brown. The crude residues of the reaction mixtures were analysed by NMR and HRMS for traces of partially or fully fused products, however only starting materials were observed in both instances (Scheme 2.17).



Scheme 2.17: Cyclohydrogenation conditions: DDQ, $\text{CF}_3\text{SO}_3\text{H}$, CH_2Cl_2 , RT.

The colour changes observed indicated DDQ/ H^+ reactivity, and in an attempt to track the progress, the reactions were repeated in deuterated chloroform (CDCl_3), and for an extended reaction time of 24 h. However, identical observations were gathered, even with the extended reaction times. Only starting materials were observed in ^1H NMR and HRMS spectra, with no trace of partially or fully fused products. The pyridazine ring systems are analogous to the pyrimidine ring systems: both contain two nitrogens within a six membered aromatic ring. In both cases, the heterocycles are known to be electron deficient aromatic units, and it was postulated that if pyrimidine containing polyphenylenes facilitate cyclohydrogenation, pyridazine containing polyphenylenes would also. However, this was not observed experimentally, and **22** and **23** appear inert to cyclohydrogenation.

Taking a deeper look into the mechanistic understandings of the reaction, DDQ/H⁺ supports the radical cation mechanism (Scheme 2.18). This mechanism is backed up by experimental work and operates on the formation of a radical cation by one electron oxidation, which is the reaction's rate determining step.¹⁷³ The new C-C bond is generated *via* electrophilic attack of the second aromatic ring. The elimination of the first hydrogen results in aromatisation of one ring, followed by further oxidation and aromatisation of the second ring through second hydrogen elimination, to form the fused product. Incorporation of heteroatoms into the structure alters its electron density and distribution, however, it does not, in theory, inhibit or promote cyclisation. This is however a broad statement, which requires to be tested on a case-by-case basis. All carbon analogues of the above cyclised targets have been prepared, however, in this case, the presence of pyrazidine rings induces a complete inertness towards various modes of cyclodehydrogenation. The radical cation mechanism is known to be immensely sensitive towards electron density distribution within a molecule and occurs at sites where electron density is maximised (typically at *ortho*- or *para*- positions of the ring). Precursors **22** and **23** have reactive cyclohydrogenation sites at *ortho*- or *para*- positions, which are structurally and electronically uninhibited. Therefore, radical cation mechanism should have been permissible in the above structures. Due to the elusiveness and complexity of cyclohydrogenation mechanisms, further computational work is required to specifically understand the electronic density distribution within **22** and **23**.



Scheme 2.18: Radical cation mechanism as described by Negri *et al.*¹⁷⁴ using *o*-terphenyl as example. *O* refers to oxidant of choice.

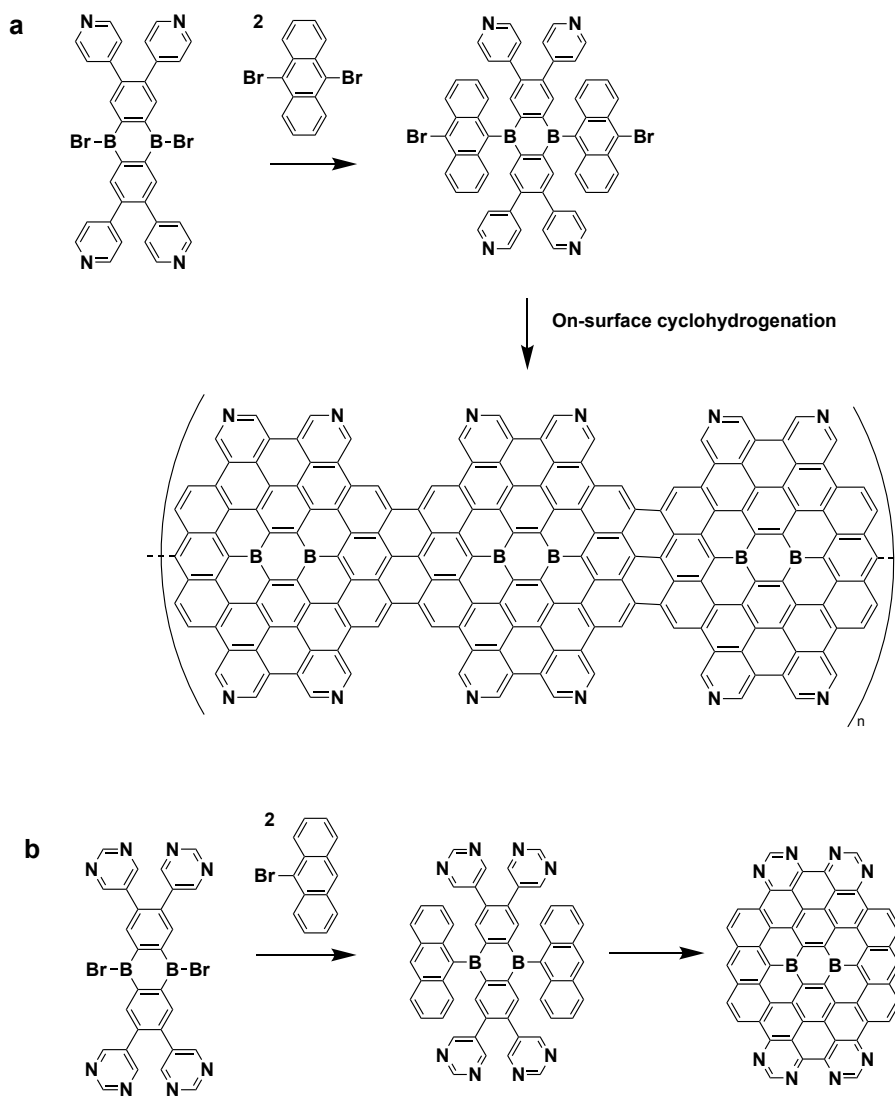
2.5.4 Conclusions and Future Work

Pyrazidine containing polyphenylenes were prepared to test potential use of DDQ/H⁺ on these systems. Dr. Gearóid Ó Máille had thoroughly tested FeCl₃ as a cyclohydrogenation agent and observed no reactivity. All attempts to cyclohydrogenate the pyrazidine precursors with DDQ/H⁺ failed, highlighting particular inertness of these systems towards cyclohydrogenation in solution. As part of future work, through mechanistic studies will be

carried out as well as on-surface cyclohydrogenation trials are envisioned to probe reactivity of the precursors on Au(111).

2.6 Boron and Nitrogen Doped PAH

As outlined in section 2.2.2, boron and nitrogen doped PAH molecules are immensely rare in the literature, due to their often complex and air/moisture-sensitive syntheses. Those that are present in the literature contain a B-N bonding motif, whereby the boron and nitrogen atoms are directly bonded to each other within the fused aromatic system, resulting in reduced Lewis acidity, and less promising optoelectronic properties. Methodologies of boron and nitrogen containing systems where the atoms are not bonded to each other is even rarer or altogether absent from the literature.¹⁷⁵ As part of this work, extensive synthetic trials were carried out in search of a methodology towards boron and nitrogen containing precursors, with centrally boron doped and peripherally nitrogen doped compounds proposed. The final precursors would be subjected to different fates: on-surface cyclohydrogenation to synthesise heteroatom doped graphene nanoribbons (GNR's), and solution cyclohydrogenation trials to synthesise novel PAH molecules. Given the extensive solubility issues of the previously synthesised PAH's as part of this work, priority is given to pyridine containing precursor synthesis for on-surface cyclohydrogenation (Scheme 2.19a). Subsequently, precursors for solution cyclohydrogenation containing pyrimidine motifs are also proposed (Scheme 2.19b).

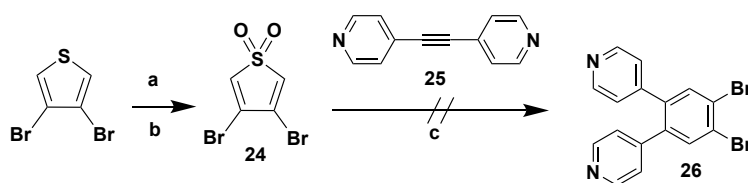


Scheme 2.19: Proposed nitrogen and boron containing precursor targets.

2.6.1 [4 + 2] Diels-Alder Cycloaddition

To attain the required precursors shown in Scheme 2.19a, pyridine needed to be synthetically introduced onto the benzene ring at the 1- and 2- positions. To do that, an adapted [4 + 2] Diels-Alder reaction between a sulfone and dipyridine acetylene was trialled (Scheme 2.20). 3,4-Dibromothiophene (a commercially attained colourless liquid) was oxidised with *m*-CPBA in CH₂Cl₂ at RT for 60 h. The reaction mixture was washed with aqueous NaHSO₃ and NaHCO₃ and extracted with chloroform. The organic layer was reduced *in vacuo*, and purified using PTLC (SiO₂, Hex/CH₂Cl₂, 2:3, v/v), which contained three bands, 3,4-dibromothiophene, 3,4-dibromothiophene 1-oxide, and the product **24**. Due to the extended reaction duration and the low yielding reaction, this method was not pursued further. A subsequent route involved mixing 30% H₂O₂ and trifluoroacetic acid anhydride at 0 °C over

a period of 30 minutes and followed by the addition 3,4-dibromothiophene in minimal CH_2Cl_2 . The reaction mixture turned from clear to milky white, with evident bubbling observed, and was allowed to stir at RT for 3 h. The pH of the reaction mixture was slowly brought up to pH 9 using a concentrated aqueous solution of NaHCO_3 , and the product extracted with CH_2Cl_2 . The organic layer was reduced *in vacuo*, and the product precipitated by slow addition of hexanes to furnish **24** as yellow needles in 40% yield. The product was structurally characterised and was in good agreement with the literature.¹⁷⁶ Sulfone **24** was stored at $-20\text{ }^\circ\text{C}$ to prevent any potential decomposition.



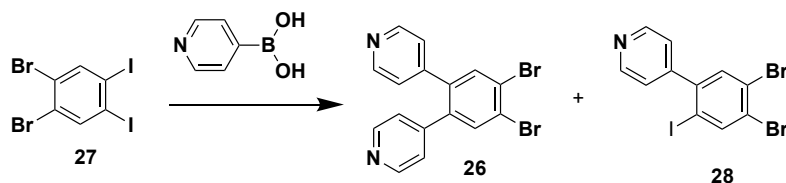
Scheme 2.20: Proposed [4 + 2] Diels-Alder reaction between a sulfone and acetylene. a) *m*-CPBA, CH_2Cl_2 , 60 h, RT. b) Trifluoroacetic acid anhydride, 30 % H_2O_2 , CH_2Cl_2 , 3 h, 40%. c) *m*-CPBA, $-20\text{--}0\text{ }^\circ\text{C}$, $\text{BF}_3\cdot\text{Et}_2\text{O}$, argon, 3 h, no product obtained.

Dipyridineacetylene **25** was prepared according to a known literature method.¹⁷⁷ Sonogoshira cross-coupling of 4-iodopyridine and trimethylsilylacetylene, subsequent deprotection, and a second Sonogoshira cross-coupling of the air sensitive deprotected product and 4-iodopyridine furnished **25** as an off-white solid in a 94% yield, which was in good agreement with the literature. The Diels-Alder conditions for the coupling of **24** and **25** differ greatly from any prior cycloadditions described as part of this work. Products **24** and **25** were dissolved in CH_2Cl_2 at $-20\text{ }^\circ\text{C}$ under argon, to which $\text{BF}_3\cdot\text{Et}_2\text{O}$ was added *via* syringe, and allowed to stir for 20 minutes. A solution of *m*-CPBA in CH_2Cl_2 was added dropwise to the reaction mixture which resulted in a colour change from yellow to brown, with evident precipitate formation. The reaction was allowed to stir for 3 h, then returned to RT, and poured over a concentrated aqueous solution of NaHCO_3 to neutralise the Lewis acid. The reaction mixture was worked up with CH_2Cl_2 , and the organic layer was reduced *in vacuo*. Attempted purification was carried out using flash column chromatography (SiO_2 , $\text{CH}_2\text{Cl}_2/\text{MeOH}$, 95:5, *v/v*) to isolate potential products, with no success. NMR and HRMS data of eluents were inconclusive. This transformation is present in the literature, with an analogous di-bromo thiophene diene and cyano-substituted dienophile, and therefore this reaction was a promising route towards **26**.¹⁷⁸ To confirm substrate inertness towards these

reaction conditions, the above-described syntheses were repeated on thiophene: to trial if the di-bromo functionality is hindering any diene reactivity, with no Diels-Alder reactivity observed. It is suspected that in these reaction conditions, the pyridinic nitrogens are responsible for deactivating the acetylene bridge, weakening the dienophile **25**, and thus hindering the cycloaddition. For that reason, this synthetic route was not pursued further.

2.6.2 Suzuki-Miyaura Coupling

Suzuki-Miyaura coupling was the next choice of synthetic pathway, requiring a palladium source, a base, and typically higher boiling solvents to couple an aryl halide and a boronic acid. Structural requirements dictate that the bromine substitution is required to be at 1- and 2-positions for the future boron dimerisation reaction to be possible. Therefore, a di-halide substituted benzene ring is required, with two iodo- atoms and two bromo- atoms to facilitate both the Suzuki coupling, and the future boron dimerisation. The dihalide system required careful tailoring of synthetic conditions, with only the iodo- substituents activated towards the Suzuki coupling, and not the bromo- substituents (Scheme 2.21, Table 2.1).



Scheme 2.21: Suzuki-Miyaura coupling.

Compound **27** was prepared according to the literature method, by reacting 1,2-dibromobenzene with iodine, NaIO₃, in H₂SO₄ (90% v/v) at 0 °C for 4 h.¹⁷⁹ Upon the addition of 1,2-bromobenzene, the solution turned from deep purple to light pink, with evident precipitate formation. Following the reaction duration, the reaction mixture was poured onto ice, the precipitate filtered off, redissolved in chloroform, and washed with an aqueous solution of NaHSO₃ (10% v/v) to remove any residual iodine. The organic layer was reduced *in vacuo*, and the product was precipitated from a concentrated solution of CHCl₃/Hex, to furnish the product as a white crystalline solid in quantitative yields.

Suzuki-Miyaura couplings on a di-halogenated substrate are not common in the literature, especially when combined with a heterocyclic boronic acid as in Scheme 2.21. Therefore, a

careful synthetic methodology was carried out to determine the optimal reaction conditions for this transformation (Table 2.1).

Table 2.1: Suzuki-Miyaura coupling trials.^a

Reaction duration	Base	Solvent mixture	°C	Catalyst loading (% mmol) ^b	Yield	Outcome/ characterisation
12 h	Ba(OH) ₂ (s)	1,2-Dioxane/H ₂ O	100	18	n/a	26 and 28 HRMS (APCI ⁺)
12 h	Na ₂ CO ₃ (s)	EtOH/CH ₃ -Ph	80	15	n/a	n/a
24 h	K ₃ PO ₄ (2M soln.)	EtOH/CH ₃ -Ph	95	15	22%	26 and 28 NMR, HRMS (APCI ⁺)
24 h	K ₂ CO ₃ (2M soln.)	EtOH/CH ₃ -Ph	82	8	n/a	n/a
24 h	K ₂ CO ₃ (2M soln.)	EtOH/CH ₃ -Ph	95	8	23%	28 NMR, MS
48 h	K ₂ CO ₃ (2M soln.)	EtOH/CH ₃ -Ph	95	8	40%	26 and 28 NMR, HRMS, X-ray
48 h	K ₂ CO ₃ (2M soln.)	EtOH/CH ₃ -Ph	110	8	40%	26 and 28 NMR, HRMS, X-ray
60 h	K ₂ CO ₃ (2M soln.)	EtOH/CH ₃ -Ph	100	8	n/a	n/a

^a All solvents were thoroughly degassed prior to reactant addition, and the reactions carried out under an inert atmosphere. ^b Catalyst of choice was Pd(PPh₃)₄.

Structurally, the proposed product **26** is simplistic, however the synthesis proved a significant challenge. The first trials with Ba(OH)₂ as the base of choice and 1,2-dioxane/H₂O solvent mix for the duration of 12 h resulted in product formation (proven by HRMS), but in negligent yields, such that the product could not be isolated from the reaction mixture. The successful conditions involved dissolving **27** and the commercially bought pyridin-4-ylboronic acid in thoroughly degassed ethanol/toluene 1:1, to which degassed 2M K₂CO₃ was added. Once the reactants were fully solubilised, 8% mmol Pd(PPh₃)₄ was added in one portion, and the reaction brought up to 110 °C for 48 h. Following the reaction duration, the reaction was cooled to RT, reduced *in vacuo*, redissolved in CH₂Cl₂, and washed with brine. The organic layer was dried over MgSO₄, and further reduced *in vacuo*. The products **26** and **28** were precipitated from the crude residues with cold Et₂O, and further

purified using flash column chromatography (SiO₂, CH₂Cl₂/MeOH, 100:1, v/v) to furnish the products as white crystalline solids (**26** in 24% yield, and **28** in 25% yield). The reduced yields are due to the low reactivity of pyridin-4-ylboronic acid in the double Suzuki coupling. Product **28** was further reacted with another equivalent of pyridin-4-ylboronic acid in an analogous reaction to furnish **26** in a 24% yield.

The products are not reported in the literature and were fully structurally characterised using NMR, HRMS, and X-ray crystallography herein. Figure 2.12a illustrates the ¹H NMR spectrum of **28**, containing four proton signals in the aromatic region. Pyridinic protons are easily assignable as two doublets at δ 8.70-8.69 ppm corresponding to H4, and δ 7.25-7.24 ppm corresponding to H3, both integrating to two protons each. Benzylic protons appear as two singlets both integrating to one proton each, with H2 most upfield at δ 8.20 ppm due to the iodo- and bromo- substituents. H1 appears at δ 7.50 ppm. ¹³C{¹H} NMR spectra shown in Figure 2.12b, shows nine carbon peaks in the aromatic region, corresponding to the structure of **28**: with the pyridinic C4 and C3 appearing at δ 149.94 ppm and δ 123.76 ppm respectively, and C2 and C1 at δ 144.41 ppm and δ 133.69 ppm respectively.

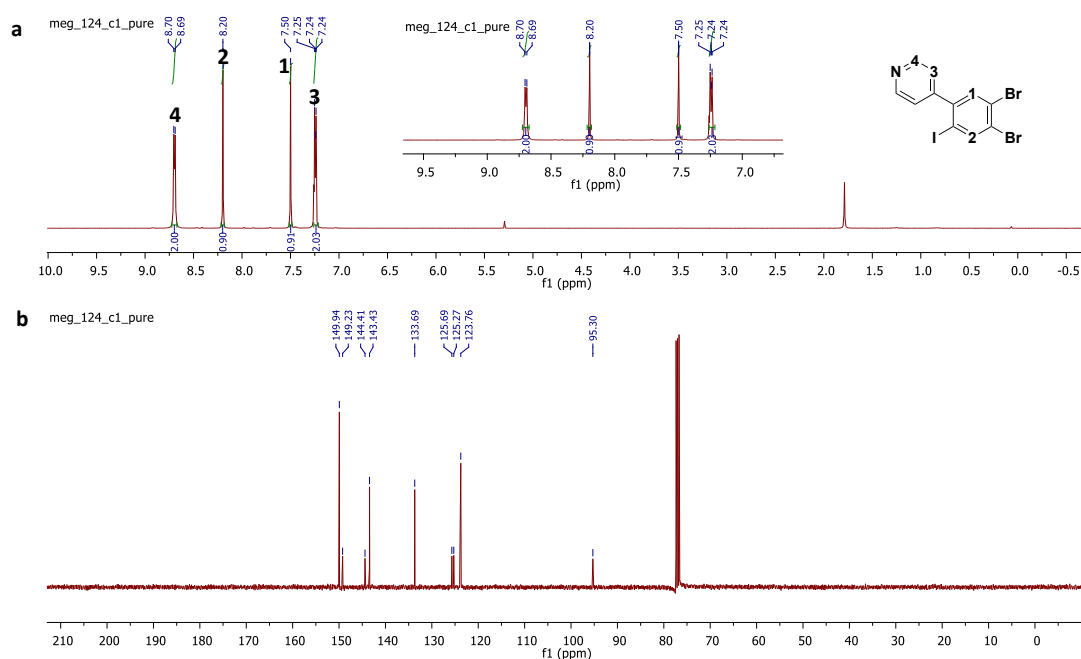


Figure 2.12: NMR spectra of **28**. **a)** ¹H NMR spectrum of **5** (600 MHz, CDCl₃, RT). **b)** ¹³C{¹H} NMR spectrum of **5** (151 MHz, CDCl₃, RT).

Figure 2.13 illustrates ^1H NMR and $^{13}\text{C}\{^1\text{H}\}$ NMR of **26**. Due to the symmetric nature of **26**, the ^1H NMR spectrum contains one less signal than that of **28**, with two pyridinic proton signals, and one benzylic signal. The pyridinic protons H3 and H2 appear as doublets at δ 8.50-8.49 ppm and δ 7.01-6.99 ppm respectively, both integrating to four protons each. The benzylic proton H1 appears as a singlet at δ 7.69 ppm, integrating to one proton. Similarly, the $^{13}\text{C}\{^1\text{H}\}$ NMR spectra contains fewer peaks due to the symmetric nature of **26**, with six peaks in the aromatic region of the spectrum corresponding well to the structure, assigned in lieu of **28** using 2D HSQC spectrum. Pyridinic C3 and C2 appear at δ 150.01 ppm and δ 124.09 ppm respectively, and the benzylic C1 appears at δ 135.12 ppm.

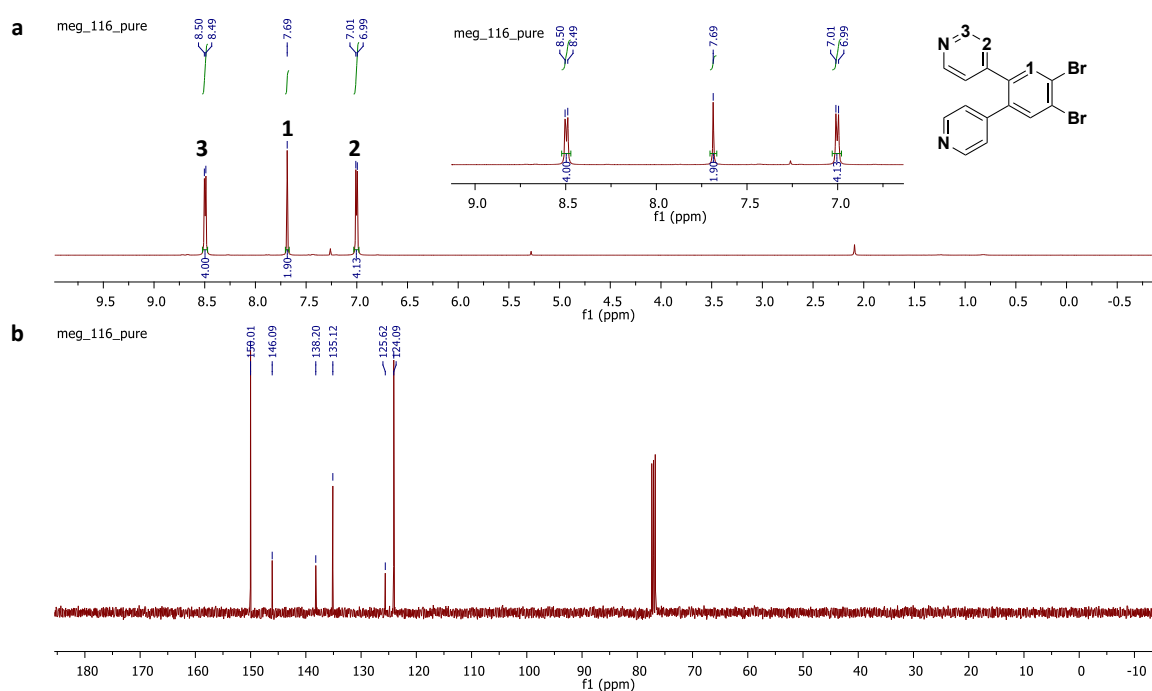


Figure 2.13: NMR spectra of **26**. **a)** ^1H NMR spectrum of **5** (600 MHz, CDCl_3 , RT). **b)** $^{13}\text{C}\{^1\text{H}\}$ NMR spectrum of **5** (151 MHz, CDCl_3 , RT).

Crystals of **28** suitable for single crystal X-ray diffraction measurements were successfully obtained *via* slow diffusion of hexanes into a solution of the pure compound in CH_2Cl_2 . A specimen of $\text{C}_{11}\text{H}_6\text{Br}_2\text{IN}$, approximate dimensions 0.020 mm x 0.040 mm x 0.260 mm, was used for the X-ray crystallographic analysis. The structure was solved with the XT structure solution program using Intrinsic Phasing and refined with the XL refinement package using

Least Squares minimisation with Olex2, using the space group $P2_1/n$, with $Z = 4$ for the formula unit, $C_{11}H_6Br_2IN$. The final anisotropic full-matrix least-squares refinement on F^2 with 136 variables converged at $R1 = 5.30\%$, for the observed data and $wR2 = 12.07\%$ for all data. The goodness-of-fit was 1.018 (refer to Appendix 1.3a for the full crystallographic tables).

Crystals of **26** suitable for single crystal X-ray diffraction measurements were successfully obtained *via* slow diffusion of hexanes into a solution of the pure compound in CH_2Cl_2 . A specimen of $C_{16}H_{10}Br_2N_2$, approximate dimensions 0.019 mm x 0.310 mm x 0.340 mm, was used for the X-ray crystallographic analysis. The structure was solved with the XT structure solution program using Intrinsic Phasing and refined with the XL refinement package using Least Squares minimisation with Olex2, using the space group $C2/c$, with $Z = 4$ for the formula unit, $C_{16}H_{10}Br_2N_2$. The final anisotropic full-matrix least-squares refinement on F^2 with 92 variables converged at $R1 = 1.62\%$, for the observed data and $wR2 = 4.03\%$ for all data. The goodness-of-fit was 1.081 (refer to Appendix 1.3a for the full crystallographic tables).

Figure 2.14a displays the asymmetric unit of **28** showing a highly twisted structure, which displays weak hydrogen bonding interactions in the extended structure (packing diagram can be located in Appendix 1.3b). For **28**, bonding appeared unexceptional (for C-N, C-C, C-H, and C-X), noting C-Br reported at 1.966 Å (measured at 1.902(10) Å) and C-I reported at 2.095 Å (measured at 2.109(10) Å).⁵¹

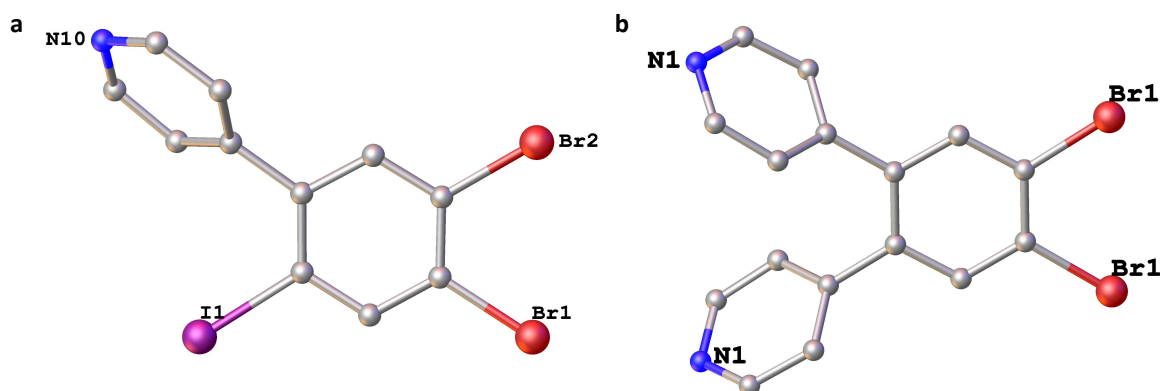


Figure 2.14: **a)** Asymmetric unit of **28**, with hydrogen atoms omitted for clarity (thermal ellipsoids shown at 50% probability). **b)** Asymmetric unit of **26**, with hydrogen atoms omitted for clarity (thermal ellipsoids shown at 50% probability).

Figure 2.14b displays the asymmetric unit of **26**, which due to its highly symmetric structure observed weak non-traditional CH...N bonding interactions (3.1583(11) Å, in lieu with reported 3.12 Å),⁷⁹ shown in Figure 2.15. In **26**, bonding bears close resemblance to **28** (C-C, C-N, C-H, and C-Br), with no exceptional bonding lengths to note.

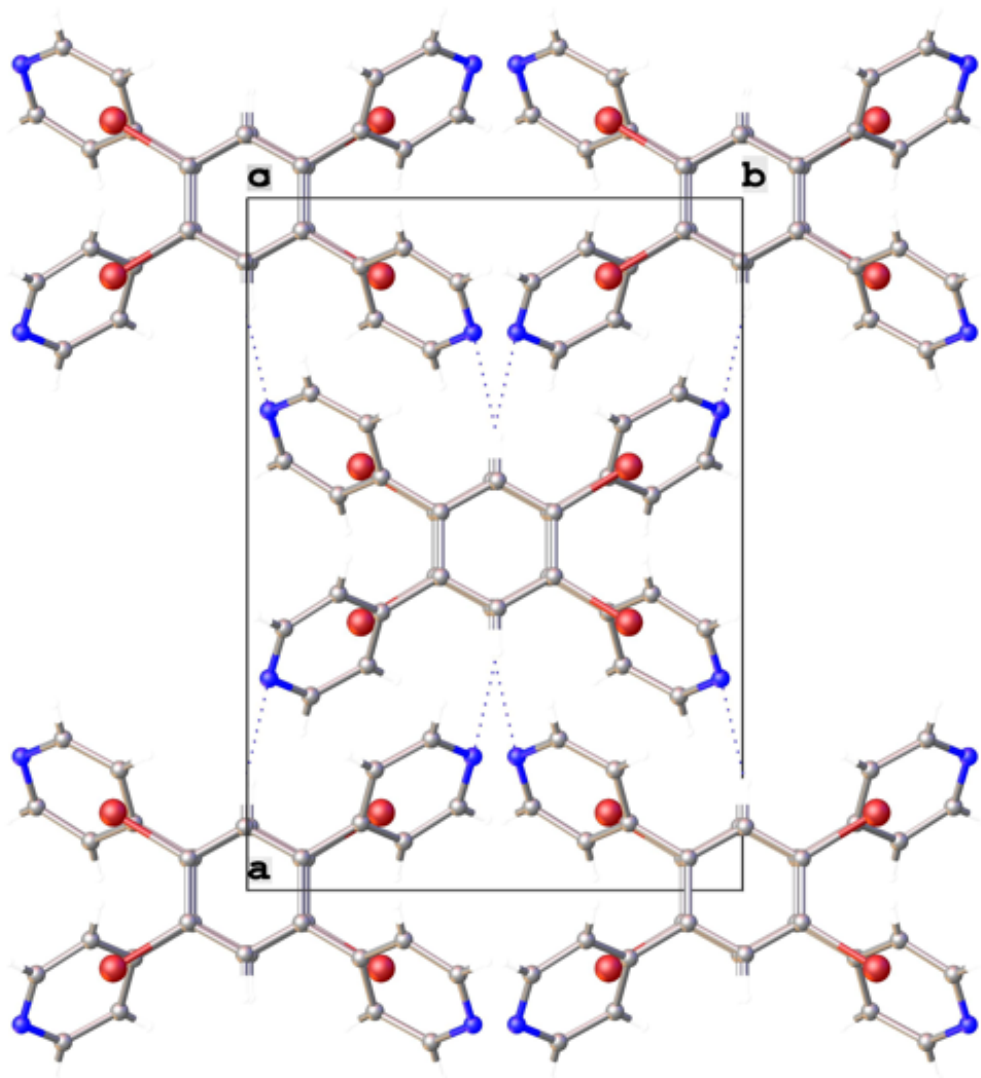


Figure 2.15: Schematic packing diagram of **26**, viewed along the *c*-axis. Atomic displacement shown at 50% probability. Weak non-traditional CH...N hydrogen interactions are annotated with blue dotted lines, 3.1583(11) Å.

Interestingly, during the synthesis of **26** and **28**, the Et₂O filtrate was left on the bench overnight, producing a crystal suitable for single crystal X-ray diffraction measurements. A specimen of C_{50.60}H_{45.68}Br₂I_{1.08}N_{0.92}OP₂Pd, approximate dimensions 0.140 mm x 0.220 mm x 0.300 mm, was used for the X-ray crystallographic analysis. The structure was solved with the XT structure solution program using Intrinsic Phasing and refined with the XL refinement package using Least Squares minimisation with Olex2, using the space group $P\bar{1}$, with $Z = 2$ for the formula unit, C_{50.60}H_{45.68}Br₂I_{1.08}N_{0.92}OP₂Pd. The final anisotropic full-matrix least-squares refinement on F^2 with 625 variables converged at $R1 = 3.50\%$, for the observed data and $wR2 = 9.20\%$ for all data. The goodness-of-fit was 1.054 (refer to Appendix 1.3 for the full crystallographic tables, disorder and packing diagrams). The Pd-I bond length was measured to be 2.6878(3) Å, which corresponds to reported literature value of 2.624 Å.⁵¹ The Pd-P bond length was measured to be 2.3255(7) Å, which is shorter when compared to the reported value of 2.452 Å.⁵¹ Interestingly, the Pd-C bond was measured to be 2.021(3) Å, which is shorter when compared to the reported literature values (2.148 Å).⁵¹ The stronger bonding of the Palladium centre (namely Pd-C and Pd-P) allude to the heightened stability of the metal complex, and its ultimate crystallisation from the Et₂O filtrate. Other bonding within the structure (C-C, C-N, C-H, C-Br and C-I) have no exceptional bonding lengths to note.

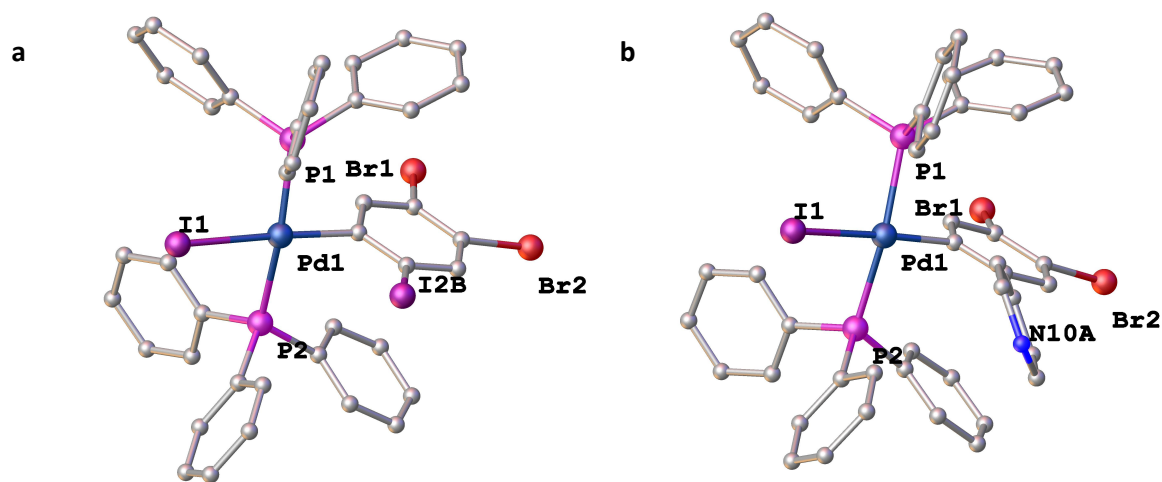
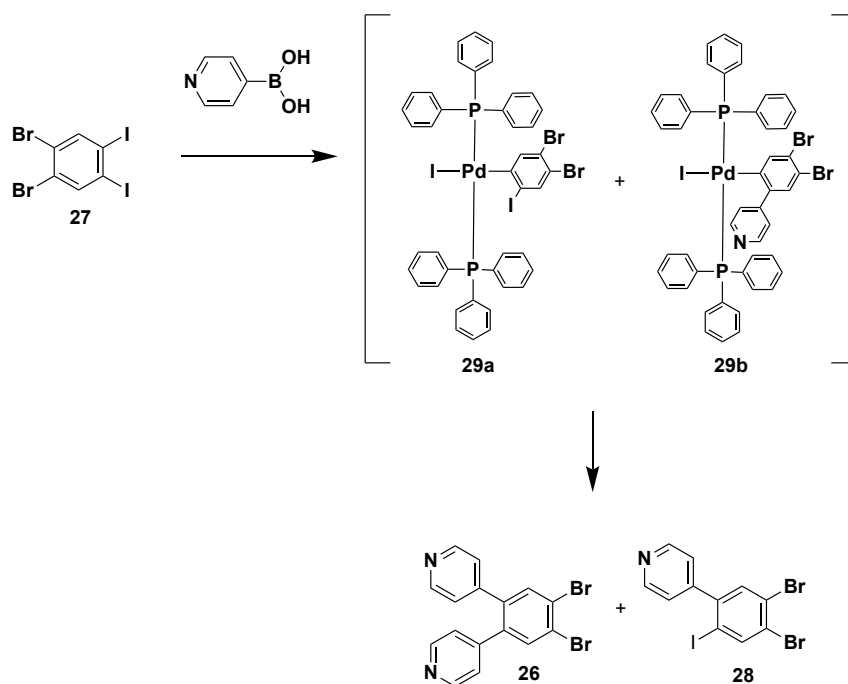


Figure 2.16: Asymmetric unit of **29** showing (a) **29a**, minority occupied disordered moiety with 8% occupancy (b) **29b**, majority occupied disordered moiety with 92% occupancy. Ball and stick diagram with atomic displacement shown at 50% probability, heteroatoms labelled only and hydrogen atoms omitted for clarity.

When further analysed, the crystal structure was the oxidative addition intermediate **29** of the Suzuki reaction: clearly showing the palladium metal centre bonded to one iodo-moiety, and the aryl substrate (Scheme 2.22).



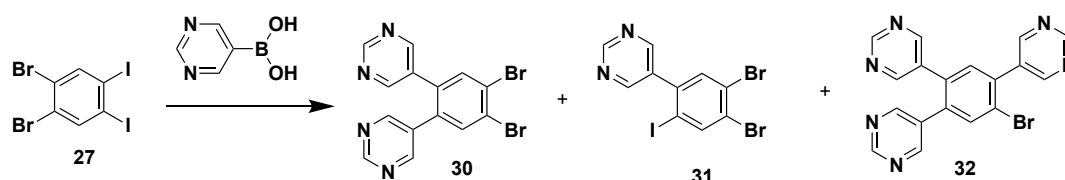
Scheme 2.22: Oxidative addition of the Suzuki-Miyaura reaction, illustrating the air and moisture stable intermediates **29a** and **29b**.

The X-ray data has marked a pivotal point in the Suzuki synthetic study, clearly showing the reluctance of the reaction to progress to completion, as the oxidative addition intermediate is stable beyond 110 °C (of the reaction temperature), and is moisture, air, and light stable. This further highlights why these systems are mainly absent from the literature, and explains the reduced yields of the reaction. In an attempt to characterise the metal complexes, the filtrate was reduced, and its residues analysed with ^1H NMR and HRMS. NMR spectra of **29** suggested complex presence, however, the data was too weak for full structural characterisation to be carried out. HRMS was not successful either in characterising the oxidative addition intermediates.

2.6.2.1 Suzuki-Miyaura Coupling of the Pyrimidine

As for the pyridine analogues, reaction conditions were also tested to find the optimal conditions for pyrimidin-5-ylboronic acid (Scheme 2.23, Table 2.3). Pyrimidin-5-ylboronic

acid observed higher solubility in the reaction solvent mixture than the pyridin-4-ylboronic acid, and for that reason observed higher yielding reactions. Flash column chromatography of the crude residues (SiO₂, CH₂Cl₂/MeOH, 100:2, v/v) furnished the products as white crystalline solids (yielding **30** in a 33% yield and **31** in a 50% yield). A subsequent reaction of **31** with another equivalent of pyrimidin-5-ylboronic acid using analogous conditions furnished **30** in a 25% yield. It was postulated that raising the temperature and the catalyst loading would result in the activation of the bromine substituents towards a Suzuki coupling. Raising the temperature to 115 °C, and the catalyst loading to 15% mmol resulted in the formation of **32** as a minor product in 15% yield and **30** as the major product in 73% yield.



Scheme 2.23: Suzuki-Miyaura coupling.

Table 2.3: Suzuki-Miyaura coupling trials.^a

Reaction duration	Base	Solvent mixture	°C	Catalyst loading (% mmol) ^b	Yield	Outcome/ characterisation
12 h	Ba(OH) ₂ (s)	1,2-Dioxane/H ₂ O	100	18	n/a	n/a
24 h	K ₂ CO ₃ (2M soln.)	EtOH/CH ₃ -Ph	95	8	40%	30 and 31 NMR, MS
24 h	K ₂ CO ₃ (2M soln.)	EtOH/CH ₃ -Ph	115	15	88%	30 and 32 NMR, MS
48 h	K ₂ CO ₃ (2M soln.)	EtOH/CH ₃ -Ph	95	8	72%	30 and 31 NMR, HRMS, X-ray
48 h	K ₂ CO ₃ (2M soln.)	EtOH/CH ₃ -Ph	110	8	82%	30 and 31 NMR, HRMS

^a All solvents were thoroughly degassed prior to reactant addition, and the reactions carried out under an inert atmosphere. ^b Catalyst of choice was Pd(PPh₃)₄.

Products **30**, **31**, and **32** were fully structurally characterised using NMR, HRMS, and IR. The ¹H NMR spectra were easily assignable as all aromatic peaks appear as singlets. The asymmetric structure of **31** results in four singlets in the aromatic region between δ 9.28 ppm

and δ 6.99 ppm (Figure 2.17a). The pyrimidinic hydrogen H4 appears most upfield at δ 9.28 ppm, integrating to one proton, followed by H3 at δ 8.76 ppm. Benzylic protons are similar to that of **28**, with two singlets corresponding to H2 and H1 at δ 8.24 ppm and δ 7.55 ppm respectively. $^{13}\text{C}\{^1\text{H}\}$ NMR spectra was assigned using a 2D HSQC spectrum, with the pyrimidine C4 and C3 at δ 158.14 ppm and δ 156.49 ppm respectively, and the benzylic carbons C2 and C1 at δ 143.56 ppm and δ 134.68 ppm respectively.

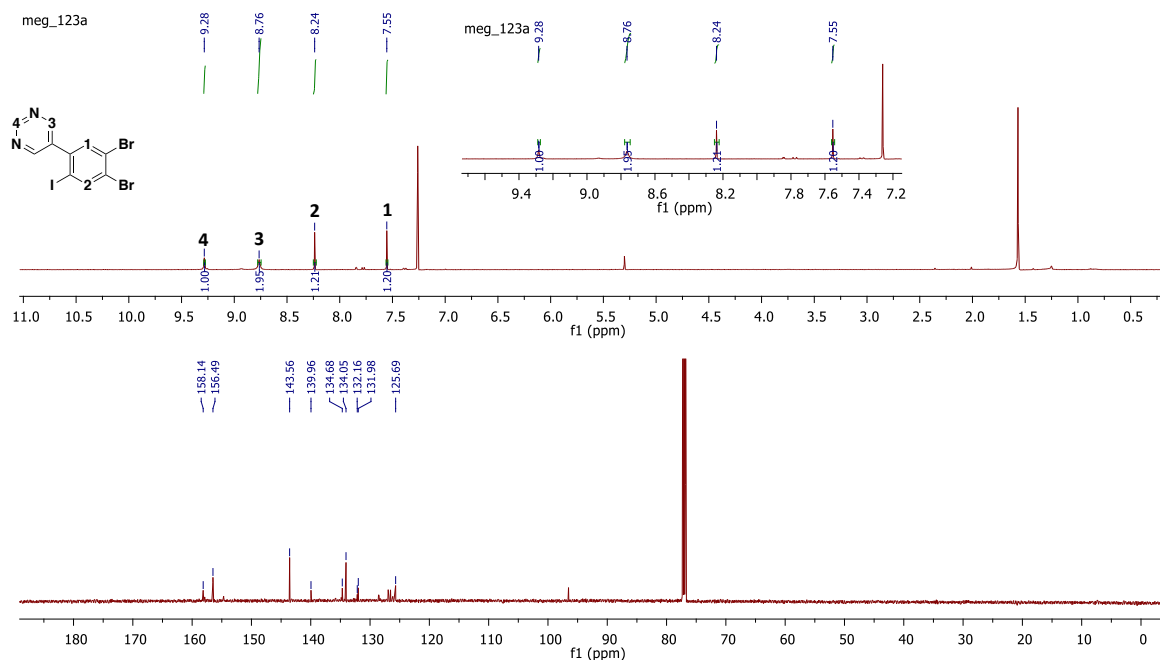


Figure 2.17: NMR spectra of **31**. **a)** ^1H NMR spectrum of **5** (600 MHz, CDCl_3 , RT). **b)** $^{13}\text{C}\{^1\text{H}\}$ NMR spectrum of **31** (151 MHz, CDCl_3 , RT).

Figure 2.18 shows the ^1H NMR and $^{13}\text{C}\{^1\text{H}\}$ NMR spectra of **30**. ^1H NMR spectrum of **30** contains one less peak than that of **31**, due to the increased symmetry. The pyrimidine proton H3 appeared most upfield at δ 9.16 ppm followed by H2 at δ 8.51 ppm, both integrating to two protons each. The benzylic proton H1 appeared at δ 7.76 ppm, integrating to two protons. The $^{13}\text{C}\{^1\text{H}\}$ NMR spectrum was fully structurally assigned using HSQC and HMBC 2D spectral analysis, with six aromatic carbon peaks between δ 158.02 ppm and δ 126.71 ppm. Similarly to the ^1H NMR spectra, C3 appears most upfield at δ 158.02 ppm, C2 at δ 156.79 ppm, and C1 at δ 135.53 ppm. The quaternary carbons are accountable for the more downfield aromatic peaks. (between δ 134.05 ppm and δ 126.71 ppm).

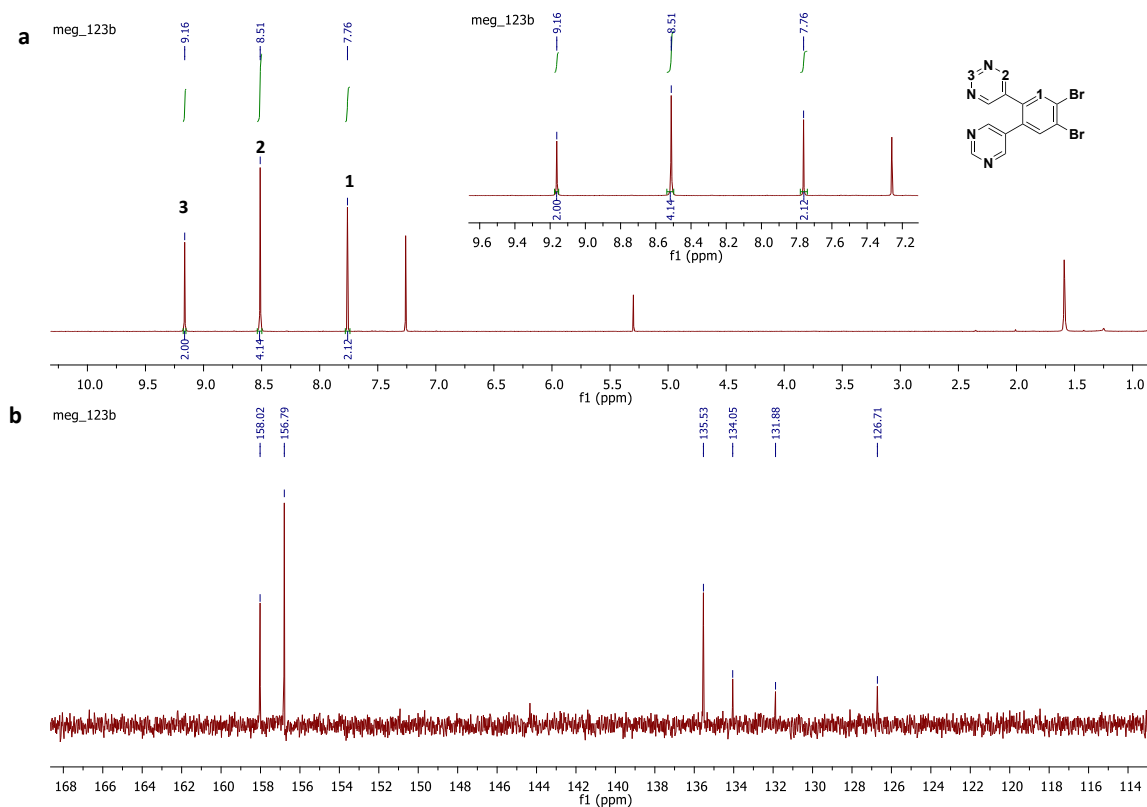


Figure 2.18: NMR spectra of **30**. **a)** ^1H NMR spectrum of **5** (600 MHz, CDCl_3 , RT). **b)** $^{13}\text{C}\{^1\text{H}\}$ NMR spectrum of **5** (151 MHz, CDCl_3 , RT).

The tri-substituted product **32** produced the most complicated spectrum of the series, with 8 aromatic singlets between δ 9.31 ppm and δ 7.46 ppm (Figure 2.19). The ^1H NMR spectrum was assigned analogously to **31** and **30**, with the pyrimidine protons the most deshielded, and thus appearing most upfield (δ 9.31 ppm, δ 9.18 ppm, δ 9.16 ppm corresponding to H6, H8, and H4 respectively), and integrating to one proton each. In the same manner, pyrimidinyl protons H5, H3, and H7 followed at δ 8.92 ppm, δ 8.58 ppm, and δ 8.56 ppm respectively, integrating to two protons each. The benzylic protons H2 appeared δ 7.90 ppm, and H1 at δ 7.46 ppm, integrating to one proton each. $^{13}\text{C}\{^1\text{H}\}$ NMR spectrum shows fifteen signals between δ 158.40 ppm and δ 124.33 ppm and was assigned in an analogous manner to **31** and **30**, utilising 2D HSQC spectrum for CH carbon peak assignment and HMBC spectrum for quaternary carbon assignment.

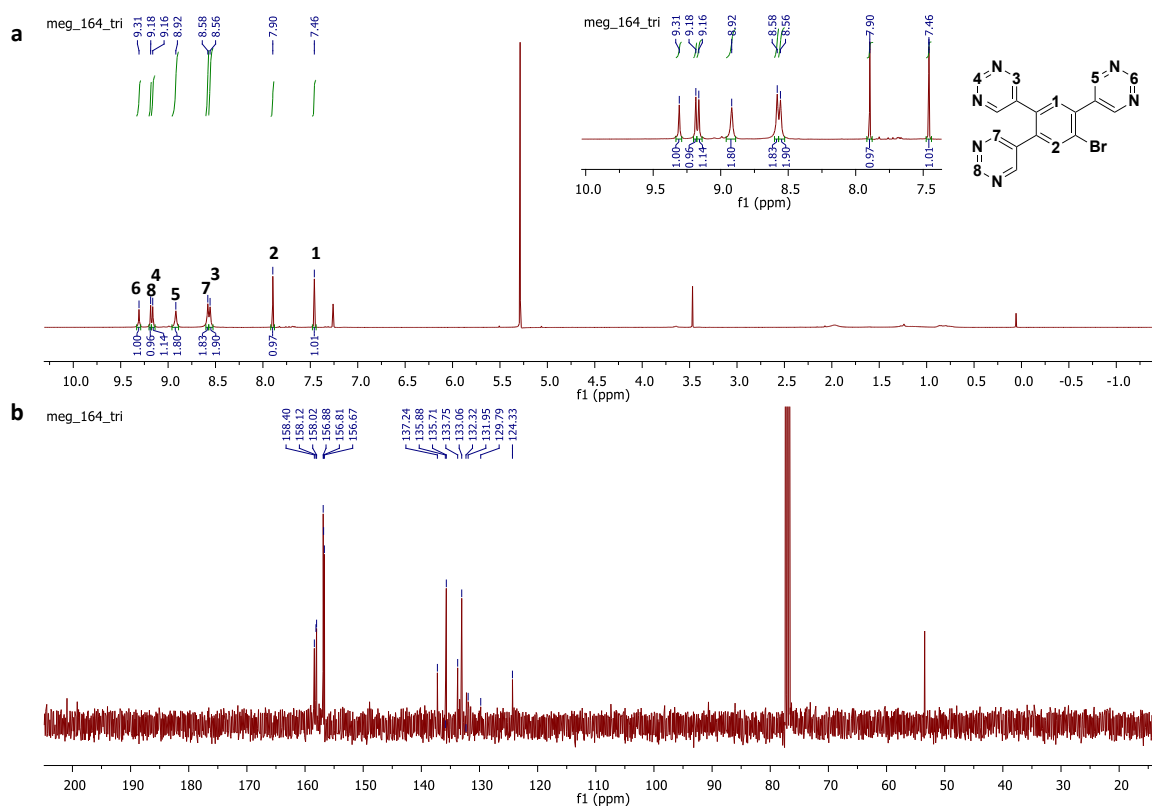


Figure 2.19: NMR spectra of **32**. **a)** ^1H NMR spectrum of **5** (600 MHz, CDCl_3 , RT). **b)** $^{13}\text{C}\{^1\text{H}\}$ NMR spectrum of **5** (151 MHz, CDCl_3 , RT).

Crystals of **30** suitable for single crystal X-ray diffraction measurements were successfully obtained *via* slow diffusion of hexanes into a solution of the pure compound in CH_2Cl_2 . A specimen of $\text{C}_{13.92}\text{H}_{7.94}\text{Br}_2\text{I}_{0.02}\text{N}_{3.96}$, approximate dimensions 0.090 mm x 0.190 mm x 0.240 mm, was used for the X-ray crystallographic analysis. The structure was solved with the XT structure solution program using Intrinsic Phasing and refined with the XL refinement package using Least Squares minimisation with Olex2, using the space group $\text{C2}/c$, with $Z = 4$ for the formula unit, $\text{C}_{13.92}\text{H}_{7.94}\text{Br}_2\text{I}_{0.02}\text{N}_{3.96}$. The final anisotropic full-matrix least-squares refinement on F^2 with 100 variables converged at $R1 = 1.89\%$, for the observed data and $wR2 = 4.17\%$ for all data. The goodness-of-fit was 1.100 (refer to Appendix 5.4a for the full crystallographic tables). Figure 2.20 illustrates the asymmetric unit of **30**, the majority occupied disordered moiety (for full disorder refer to Appendix 1.4b). In **30**, bonding bears close resemblance to **26** (C-C, C-N, C-H, and C-Br), with no exceptional bonding lengths to note. Figure 5.21 shows the schematic packing of **30**, with intermolecular π - π interactions calculated at 3.984 Å, which is larger than typically reported values, signifying weak π - π bonding. Typically π - π interactions are reported between 3.4 Å and 3.6 Å.⁸⁰ The pyrimidinic

nitrogens are weakly hydrogen bonded to the adjacent hydrogens of the neighbouring ring systems (annotated with blue dotted lines).

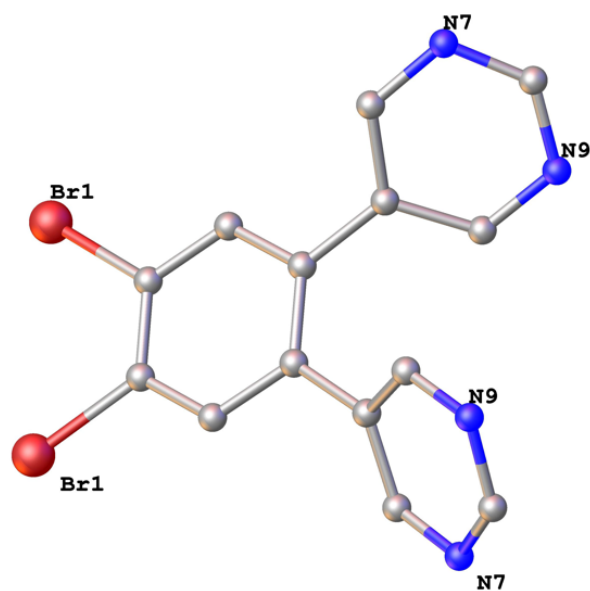


Figure 2.20: Asymmetric unit of 30, with hydrogen atoms omitted for clarity (thermal ellipsoids shown at 50% probability).

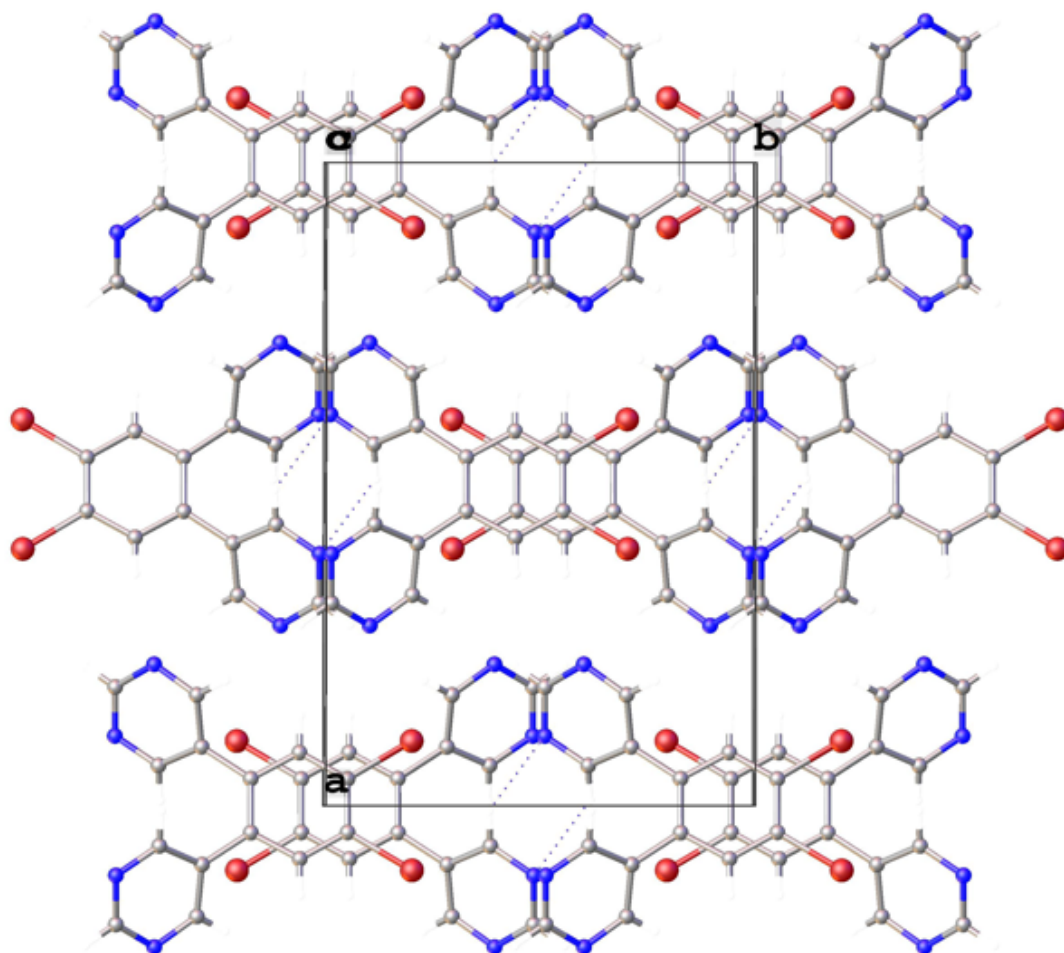
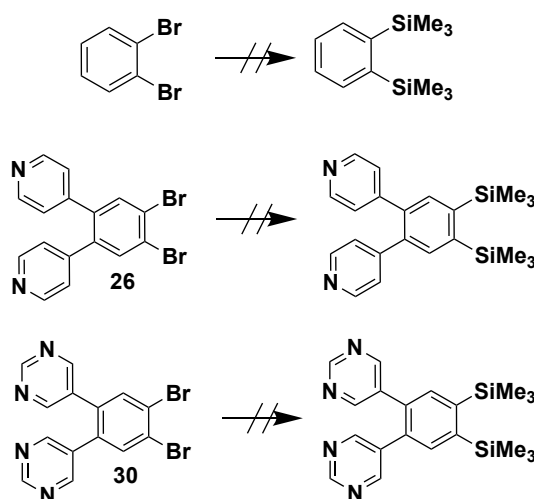


Figure 2.21: Schematic packing diagram of **30** (full disorder), viewed along 1-x, 1-y, -z. Atomic displacement shown at 50% probability. Weak non-traditional CH...N hydrogen interactions are annotated with blue dotted lines. Intermolecular π - π interactions calculated at 3.984 Å.

2.6.3 Grignard Reaction

The Suzuki products **26** and **30** were carried forward to the subsequent Grignard trials to form the doubly silylated product, which would serve as a starting material for the boron dimerisation. Several non-traditional and traditional Grignard conditions were trialed on three substrates: 1,2-dibromobenzene, **26**, and **30** (Scheme 2.24, Table 2.4). The commercially available 1,2-dibromobenzene was used as a basic substrate to test the reaction conditions and eliminate the chance of reaction failure being due to nitrogen containing **26** and **30** substrates. Oyamada *et al.*¹⁸² reported a facile and mild approach towards a double silylation of 1,2-dibromobenzenes using a Mg/LiCl/DMI system and TMS-Cl as the silylation source. DMI (1,3-Dimethyl-2-imidazolidinone), a cyclic urea, is a high boiling aprotic solvent is excellent at solubilising both organic and inorganic compounds and was specifically used here to solubilise the reactants and the resulting charged species formed during the reaction. The clever use of LiCl provides the reaction with Li⁺ and Cl⁻ ions which forms MgCl₂ and ⁺SiMe₃ in solution which subsequently reacts with the bromoarene forming the desired product and LiBr. The salt formation is entropically favoured, and pushes the reaction towards product formation.



Scheme 2.24: Grignard trials on bromoarene substrates.

When these reaction conditions were replicated on the bromoarenes as part of this work: by slow addition of TMS-Cl to a solution of the 1,2-bromobenzene, magnesium powder, LiCl in DMI, the solution changed from deep black to red, with intense blue fluorescence observed. Identical conditions with **26** resulted in a colour change to yellow, and with **30** to bright green. These drastic and bright colour changes are a sign that the organometallic Grignard complex has been successfully formed, and that the reaction is progressing. The brightly coloured solutions turned to cloudy grey towards the end of the reaction duration, suggesting that product formation is complete, and that the organometallic Grignard complex has been consumed. The reactions were stirred at 40 °C for 4 h, following which they were quenched with an aqueous saturated solution of NaHCO₃ and worked up with hexanes. During the work up, the majority of DMI solvent was trapped in the aqueous layer, however extreme vigilance was observed due to the highly toxic nature of DMI, that residues were not left in the organic layer. The organic layer was reduced *in vacuo* and analysed using ¹H NMR which did not find product formation.

The reactions were repeated for the duration of 24 h to test if an elongated reaction time is required for this transformation, with no success. It was postulated that TMS-Cl carried residual water which could be responsible for the quenching of the Grignard. For this reason, the reactions were replicated with TMS-OTf as the silylation course, which resulted in deep blue fluorescence formation, a direct suggestion of product formation, since silylated compounds are typically deeply blue fluorescent. Crude residues of the reactions were analysed for product presence, with ¹H NMR showing TMS peak presence, but in negligent yields with residual DMI also present despite the efforts to remove it from organic layer. Purification was attempted using an array of flash column chromatography conditions, trialling both SiO₂ and AlO₃ as the stationary phase, and petroleum ether/CH₂Cl₂ as the mobile phase, with no products isolated. Due to the difficulty in removing the DMI solvent from any crude residues, a different Grignard route was trialled.

Table 2.4: Grignard trials.^a

Trial	Bromoarene	Reaction conditions	Silylation source	Outcome
-------	------------	---------------------	-------------------	---------

x3	1,2 dibromobenzene, 26 30	LiCl ^b Mg powder DMI	TMS-Cl	n/a
x1	1,2 dibromobenzene, 26 30	Mg turnings ^c 1,2- dibromoethane/iodine THF	TMS-Cl	n/a
x1	1,2 dibromobenzene, 26 30	Mg turnings ^c 1,2-dibromoethane THF	TMS-Cl	n/a
x2	1,2 dibromobenzene, 26 30	LiCl ^b Mg powder DMI	TMS-OTf	Product – intense blue fluorescence Not isolated Crude NMR shows TMS peak
x2	1,2 dibromobenzene, 30	Mg turnings ^c 1,2-dibromoethane THF	TMS-OTf	Product – intense blue fluorescence Not isolated Crude NMR shows TMS peak

^a All solvents were thoroughly degassed prior to reactant addition, and the reactions carried out under an inert atmosphere. ^b Reaction stirred at 40°C for 4 – 24 h. ^c Mg turnings were activated *via* sonication of the reaction vessel (sonicated until bubbling was observed, typically 5-10 minutes) prior to reaction commencement. Reaction stirred at reflux for 24 h.

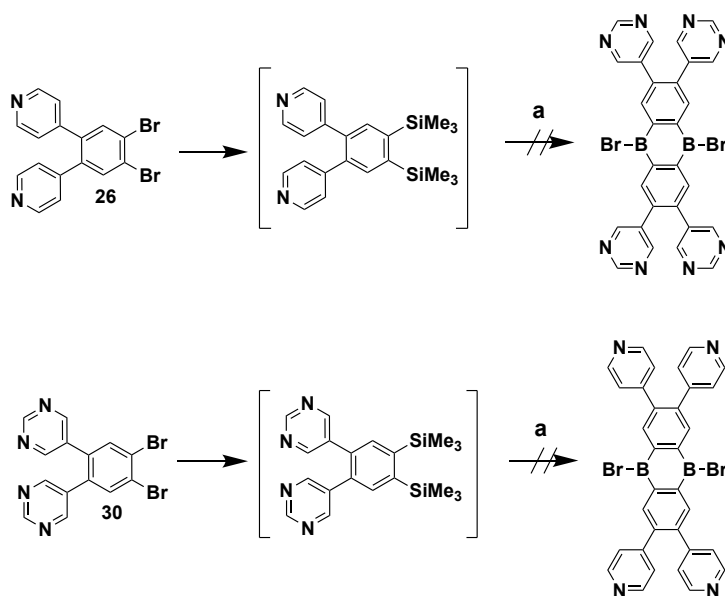
Traditional Grignard conditions were trialled, by using magnesium turnings (activated by either 1,2-dibromoethane or a crystal of iodine) in THF, with the bromoarene and TMS-Cl as the silylation source.¹⁸³ These conditions resulted in identical colour changes and blue fluorescence formation as the above Mg/LiCl/DMI system, a sign that the organometallic Grignard was forming in both instances. The reaction was refluxed in THF for 24 h, following which the reaction vessel was returned to RT, and opened to air to oxidise activated magnesium. The reaction was dissolved in hexanes and filtered through Celite to trap any metal residues. All volatiles were removed *in vacuo*, and flash column chromatography was attempted (SiO₂, CH₂Cl₂/MeOH, 100:1, v/v). The column contained a bright blue fluorescent band, however, no eluents appeared to contain the desired product. The conditions were replicated with TMS-OTf as the silylation source and omitting the use

of iodine, which at elevated temperatures can form Grignard homocoupled side-products. These conditions resulted in the same observations as the prior trials.

The literature reports silylated products to be bench stable (air and moisture) and stable to flash column chromatography conditions, and this assumption was carried forward to these systems also. However, literature examples do not contain heterocyclic starting materials. It was suspected that the desired products are not moisture stable, and do not survive aqueous work-ups, or flash column chromatography conditions. Any product residues which were exposed to air and moisture gradually observed a disappearance of the blue fluorescence, a suspected hydrolysis of the products, and an appearance of hydroxy- peaks in ^1H NMR spectra. In all cases, no silylated products were successfully isolated.

2.6.4 Boron Dimerisation

Given that the boron dimerisation reaction is known to be the pivotal point of B-PAH synthesis; with highly sensitive reaction conditions, and high risk of failure, the unstable nature of the silylated precursor proved to be a grave synthetic block. It is suspected that the silylated product formation occurs, however the products are not stable in air or moisture. *In situ* reactions were considered, however BBr_3 which is the boron source is not compatible to traditional Grignard conditions, as it reacts violently with water and other protic solvents, and reacts with THF. BBr_3 is compatible with the aforementioned $\text{Mg}/\text{LiCl}/\text{DMI}$ system. Scheme 2.25 illustrates the synthetic trial towards the boron dimerisation.

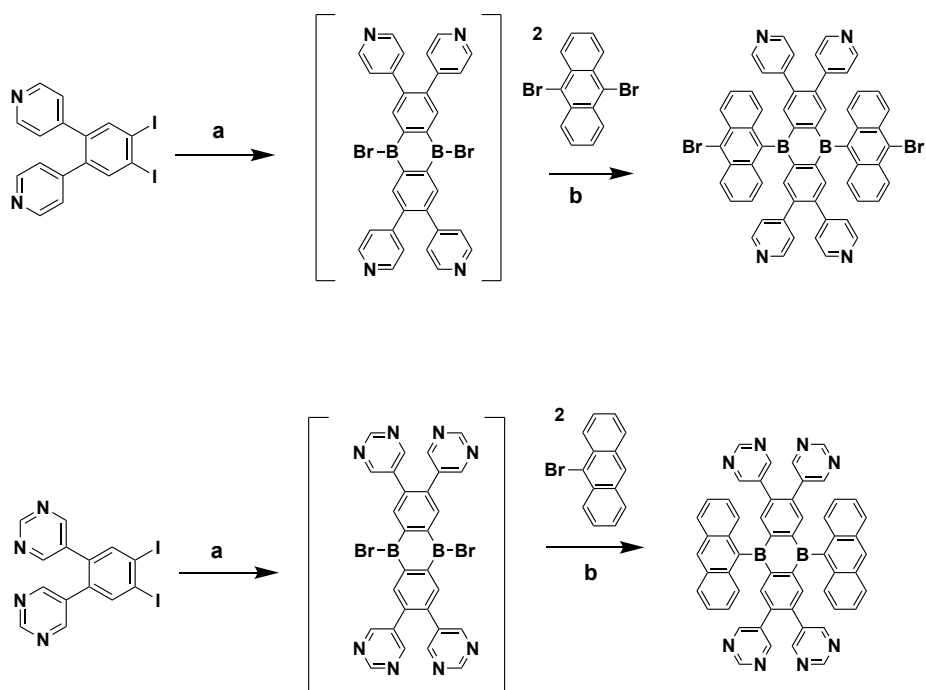


Scheme 2.25: Attempted *in-situ* synthesis via the silylated products a) 1M BBr₃ in CH₂Cl₂, toluene, reflux, 24 h.

A final attempt towards the dimerised product was carried out *via* the silylated substrate prepared using the Mg/LiCl/DMI system, without isolating the silylated product. The silylation reaction solvent was cannulated into a clean and dry flask containing degassed toluene at 0 °C, to which 3 equivalents of BBr₃ was added (commercially bought 1M solution in CH₂Cl₂). This addition resulted in a colour change from clear to orange, and a complete quenching of fluorescence. The reaction was then heated to reflux of toluene for 24 h. Upon reaction completion, the crude residues were reduced *in vacuo* and analysed using ¹H NMR, which showed DMI as the overpowering signal, with difficulty determining if product formation was successful. ¹¹B NMR only showed presence of BBr₃ (~ 15 ppm), and no aryl-boron signals (expected ~ 60 – 85 ppm). The brominated boron dimerisation products are also known to be highly air and moisture sensitive, often do not survive standard purification protocols are usually treated as reactive intermediates. Due to the extensive synthetic challenges with both the silylation step and the subsequent dimerisation step, a different route was proposed *via* an iodination, which bypasses the requirement for the silylated products.

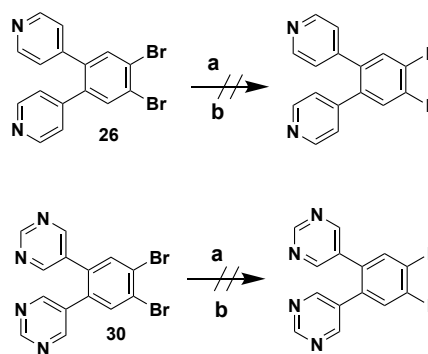
2.6.4.1 Iodination

To bypass the silylation step, a Br/I halogen exchange was proposed, which would then be used in a tandem one step synthesis of the required precursors. Hatakeyama *et al.*¹⁸⁴ successfully synthesised boron containing PAH compounds *via* an iodo precursor, without isolating the reactive brominated boron intermediate, using a lithiation source and cyclohydrogenation conditions to furnish a final bench stable PAH. The authors however do not have any other heteroatoms within their structure. Scheme 2.26 illustrates the proposed synthetic pathway towards the required precursors. Since both synthetic steps require the same reagents, the precursors could be prepared *in situ* and carried forward to the final lithiation, in an elegant synthetic pathway. For this reason, pure and bench stable iodinated products are required.



Scheme 2.26: Proposed synthesis towards the boron and nitrogen doped precursors **a**) $n\text{BuLi}$, BBr_3 , toluene, reflux, 24 h **b**) $n\text{BuLi}$, Et_2O , $0\text{ }^\circ\text{C}$ to $25\text{ }^\circ\text{C}$; followed by the reactive precursor in toluene, $0\text{ }^\circ\text{C}$ to $25\text{ }^\circ\text{C}$.

Gingras *et al.*¹⁸⁵ report a successful highly yielding double Br/I exchange by refluxing the brominated materials with CuI and KI in DMF for 45 h. This synthesis was trialed on **26** and **30** (Scheme 2.27), by dissolving the brominated starting materials in dry and degassed DMF, with 20 equivalents and CuI and 22 equivalents of KI . The translucent yellow solution formed a white precipitate upon heating, which disappeared after 45 h. HRMS of the crude residues did not locate product formation. Flash column chromatography (SiO_2 , $\text{CH}_2\text{Cl}_2/\text{MeOH}$, 100:2, v/v) did not yield the desired products. Lukas Hallen of the Draper group trialed this synthetic pathway on analogous aryl bromides, with no product formation. For this reason, this pathway was not pursued further. Additionally, the use of such a high quantity of CuI poses toxicity risks and a high environmental threat.



Scheme 2.27: Br/I exchange reaction **a)** CuI, KI, DMF, reflux, 45 h. **b)** Cu₂O/L-Proline, KI, EtOH, pressure tube, 110 °C, 30-48 h.

Bao *et al.*¹⁸⁶ report aryl and heteroaryl bromide iodide conversion which is catalysed by copper oxide and L-Proline. This method was trialled by reacting the brominated starting material (**26** and **30**) with Cu₂O (10% mmol), L-Proline (20% mmol), and six equivalents of KI in dried and degassed ethanol in a pressure tube at 110 °C for 30-48 h. The reaction turned from deep red to green after 2 h suggesting activation of the copper catalyst, with evident white precipitate formation after 12 h. The success of this reaction relies on higher solubility of KI versus KBr in EtOH, and for that reason minimal EtOH must be used. As the reaction progresses, the formation of KBr, and subsequent precipitation of KBr pushes the reaction towards product formation. After 24 h, the solution turned dark green/ black, with white precipitate observed. The reaction was cooled to RT, dissolved in CH₂Cl₂, passed through Celite to trap copper residues, and washed with water. The organic layer was reduced *in vacuo* and analysed using ¹H NMR and HRMS. ¹H NMR shows trace of product formation, however in negligible yields, and HRMS failed to locate product presence.

The reaction observations suggest that the reaction is progressing, and in a final effort an array of commercially available bromoarenes were trialled with identical reaction conditions (Table 2.5). Compounds **26** and **30** were not reactive towards these reaction conditions. 1,4-dibromobenzene observed product formation, showing that the iodination reaction is possible with these reaction conditions, and is successful if the bromine atoms are *para*-substituted, with this success mirrored with 2,5-dibromopyridine. However, on larger aromatic skeletons such as 2,7-dibromo-9*H*-fluorene, only a mono-iodinated product was

achieved after 48 h. No other bromoarenes showered reactivity towards the Cu₂O/L-Proline/KI system, further highlighting the difficulty of this transformation.

Table 2.5: Iodination trials.^a

Bromoarene	Outcome
26	n/a, starting material only
30	n/a, starting material only
1,2-dibromobenzene	n/a, starting material only
1,4-dibromobenzene	Main product formation by NMR, singlet at δ 7.43 ppm
1,6-dibromopyrene	n/a, starting material only
2,5-dibromopyridine	Mixture of products, main product formation, conformed by HRMS (ESI ^{+/-} and APCI ^{+/-})
2,7-dibromo-9 <i>H</i> -fluorene	Mono-iodinated product only conformed by HRMS (ESI ^{+/-} and APCI ^{+/-})
9,10-dibromoanthracene	n/a, starting material only
2,6-dibromopyridine	n/a, starting material only
3,6-dibromo-9 <i>H</i> -carbazole	n/a, starting material only
3,4-dibromothiophene	n/a, starting material only

^a 1-2 mL of EtOH used, which was thoroughly degassed prior to reactant addition, and the reactions carried out under an inert atmosphere. All reactants were newly purchased, pure, and contained no traces of moisture.

2.6.5 Conclusions and Future Work

Due to time constraints, further synthetic studies towards boron and nitrogen doped PAH molecules were not possible. However, this synthetic discussion carries a great deal of importance, carefully characterising all efforts which were undertaken to develop synthetic methodologies towards these highly desired systems. This discussion carries both the failures and the successes which were made during this study, highlighting that synthetic blocks can occur at any of the reaction steps, and often quite early on in the synthetic path. This discussion also shows that small and often simplistic transformations towards organic compounds can pose a great synthetic challenge. As part of future work, a radical redesign

of the synthetic path is envisioned, to further study syntheses towards boron and nitrogen doped PAH's.

2.7 Chapter Conclusions and Future Work

PAH synthesis is often a cumbersome and multi-step process, with careful tailoring of conditions necessary for successful syntheses to occur. C_{72} was successfully synthesised using a novel route *via* a Knoevenagel condensation, however the products proved to be highly air sensitive. The mechanism of the ring opening was proposed, as well as future synthetic pathways which are possible with this deviation. C_{72} was insoluble in common organic solvents, hindering ^1H NMR data collection and UV-vis studies. Future work envisions C_{72} applied as a single molecule junction and utilised as an organometallic ligand.

Longitudinally extended phenazine PAH's were successfully synthesised in a facile one step Schiff base condensation, showcasing that synthetic routes towards PAH's are possible, if the correct pre-fused aromatic units are synthesised. The final products were highly insoluble in common organic solvents; however, they were successfully characterised using solid state $^{13}\text{C}\{^1\text{H}\}$ NMR spectrometry. Unprecedented electronic and conductive properties of these compounds are predicted, with these compounds potentially useful as single molecule junctions and semiconductors. As part of future work, conductance measurements are envisioned, to probe the materials validity for application in organic electronics.

DDQ/ H^+ as a cyclohydrogenation agent was trialled on previously synthesised pyrazidine containing polyphenylenes made by Dr. Gearóid Ó Máille. However, after repeated trials, the polyphenylene precursors appeared to be inert to these cyclohydrogenation conditions. Further computational studies are required to further understand the electronic distribution of the polyphenylenes, to probe if any potential functionalisation could promote cyclohydrogenation.

A myriad of synthetic methodologies were trialled towards centrally boron doped and peripherally nitrogen doped PAH compounds. However, after repeated trials, and a mixture of successes and failures, the desired final compounds were not attained. Future work

envisions a radical rethinking of the synthetic pathway, to further attempt the synthesis of boron and nitrogen doped PAH's.

2.8 References

- 1 F. Bonaccorso, Z. Sun, T. Hasan and A. C. Ferrari, 2010, **4**, 611–622.
- 2 F. Schedin, A. K. Geim, S. V Morozov, E. W. Hill, P. Blake, M. I. Katsnelson and K. S. Novoselov, 2007, **6**, 6–9.
- 3 V. Tozzini and V. Pellegrini, *Phys. Chem. Chem. Phys.*, 2013, **15**, 80–89.
- 4 Y. Dai, Y. Liu, K. Ding and J. Yang, *Mol. Phys.*, 2018, **0**, 1–16.
- 5 L. Zhi and K. Müllen, *J. Mater. Chem.*, 2008, **18**, 1472–1484.
- 6 R. G. Harvey, *Polycyclic aromatic hydrocarbons: chemistry and carcinogenicity*, CUP Archive, 1991.
- 7 J. Xiao, B. Yang, J. I. Wong, Y. Liu, F. Wei, K. J. Tan, X. Teng, Y. Wu, L. Huang, C. Kloc, F. Boey and J. Ma, 2011, 11–14.
- 8 Z. Wang, P. Gu, G. Liu, H. Yao, Y. Wu, Y. Li, G. Rakesh, J. Zhu, H. Fu and Q. Zhang, *Chem. Commun.*, 2017, **53**, 7772–7775.
- 9 P. Y. Gu, Z. Wang, G. Liu, H. Yao, Z. Wang, Y. Li, J. Zhu, S. Li and Q. Zhang, *Chem. Mater.*, 2017, **29**, 4172–4175.
- 10 F. Tian, T. Wang, W. Dang, J. Xiao and X. Zhao, *Dye. Pigment.*, 2020, **177**, 108298.
- 11 M. M. Haley and R. R. Tykwinski, *Carbon-rich compounds: from molecules to materials*, John Wiley & Sons, 2006.
- 12 E. Clar and R. Schoental, *Polycyclic hydrocarbons*, Springer, 1964, vol. 2.
- 13 R. Scholl, C. Seer and R. Weitzenböck, *Berichte der Dtsch. Chem. Gesellschaft*, 1910, **43**, 2202–2209.
- 14 E. Clar and D. G. Stewart, *J. Am. Chem. Soc.*, 1953, **75**, 2667–2672.
- 15 E. Clar, *Tetrahedron*, 1979, **35**, 2673–2680.
- 16 R. Rieger and K. Müllen, *J. Phys. Org. Chem.*, 2010, **23**, 315–325.
- 17 J. Wu, W. Pisula and K. Müllen, *Chem. Rev.*, 2007, **107**, 718–747.
- 18 E. Clar, C. T. Ironside and M. Zander, *J. Chem. Soc.*, 1959, 142–147.
- 19 H. Ito, K. Ozaki and K. Itami, *Angew. Chemie - Int. Ed.*, 2017, **56**, 11144–11164.
- 20 S. M. Draper, D. J. Gregg and R. Madathil, *J. Am. Chem. Soc.*, 2002, **124**, 3486–3487.
- 21 C. Dou, S. Saito, K. Matsuo, I. Hisaki and S. Yamaguchi, *Angew. Chemie - Int. Ed.*, 2012, **51**, 12206–12210.
- 22 C. J. Martin, B. Gil, S. D. Perera and S. M. Draper, *Chem. Commun.*, 2011, **47**, 3616.
- 23 R. Szűcs, P. A. Bouit, L. Nyulászi and M. Hissler, *ChemPhysChem*, 2017, **18**, 2618–2630.
- 24 L. Đorđević, C. Valentini, N. Demitri, C. Mézière, M. Allain, M. Sallé, A. Folli, D. Murphy, S. Mañas-Valero, E. Coronado and D. Bonifazi, *Angew. Chemie*, 2020, **132**, 4135–4143.
- 25 M. Hirai, N. Tanaka, M. Sakai and S. Yamaguchi, *Chem. Rev.*, 2019, **119**, 8291–8331.
- 26 D. J. Gregg, E. Bothe, P. Höfer, P. Passaniti and S. M. Draper, *Inorg. Chem.*, 2005, **44**, 5654–5660.
- 27 L. P. Wijesinghe, S. D. Perera, E. Larkin, G. M. Ó Máille, R. Conway-Kenny, B. S. Lankage, L. Wang and S. M. Draper, *RSC Adv.*, 2017, **7**, 24163–24167.
- 28 M. Grzybowski, K. Skonieczny, H. Butenschön and D. T. Gryko, *Angew. Chemie - Int. Ed.*, 2013, **52**, 9900–9930.
- 29 E. von Grotthuss, A. John, T. Kaese and M. Wagner, *Asian J. Org. Chem.*, 2018, **7**, 37–53.
- 30 T. S. De Vries, A. Prokofjevs and E. Vedejs, *Chem. Rev.*, 2012, **112**, 4246–4282.

- 31 M. J. Ingleson, *Synlett*, 2012, **23**, 1411–1415.
- 32 V. M. Hertz, M. Bolte, H. W. Lerner and M. Wagner, *Angew. Chemie - Int. Ed.*, 2015, **54**, 8800–8804.
- 33 S.-S. Yu and W.-T. Zheng, *Nanoscale*, 2010, **2**, 1069–1082.
- 34 S. Kawai, S. Saito, S. Osumi, S. Yamaguchi, A. S. Foster, P. Spijker and E. Meyer, *Nat. Commun.*, 2015, **6**, 6–11.
- 35 X. Y. Wang, J. Y. Wang and J. Pei, *Chem. - A Eur. J.*, 2015, **21**, 3528–3539.
- 36 D. J. H. Emslie, W. E. Piers and M. Parvez, *Angew. Chemie*, 2003, **115**, 1290–1293.
- 37 M. Müller, C. Kübel, F. Morgenroth, V. S. Iyer and K. Müllen, *Carbon N. Y.*, 1998, **36**, 827–831.
- 38 N. Kulisic, S. More and A. Mateo-Alonso, *Chem. Commun.*, 2011, **47**, 514–516.
- 39 Y. Liu, T. Shan, L. Yao, Q. Bai, Y. Guo, J. Li, X. Han, W. Li, Z. Wang, B. Yang, P. Lu and Y. Ma, *Org. Lett.*, 2015, **17**, 6138–6141.
- 40 J. Hu, D. Zhang and F. W. Harris, *J. Org. Chem.*, 2005, **70**, 707–708.
- 41 S. Varughese and S. M. Draper, *Cryst. Growth Des.*, 2010, **10**, 2298–2305.
- 42 E. V Dalessandro, H. P. Collin, L. G. L. Guimarães, M. S. Valle and J. R. Pliego Jr, *J. Phys. Chem. B*, 2017, **121**, 5300–5307.
- 43 C. Pigot, G. Noirbent, S. Peralta, S. Duval, M. Nechab, D. Gigmes and F. Dumur, *Helv. Chim. Acta*, 2019, **102**, e1900229.
- 44 K. Baumgärtner, A. L. Meza Chinchá, A. Dreuw, F. Rominger and M. Mastalerz, *Angew. Chemie - Int. Ed.*, 2016, **55**, 15594–15598.
- 45 K. Baumgärtner, T. Kirschbaum, F. Krutzek, A. Dreuw, F. Rominger and M. Mastalerz, *Chem. - A Eur. J.*, 2017, **23**, 17817–17822.
- 46 W. Dilthey, S. Henkels and M. Leonhard, *J. für Prakt. Chemie*, 1938, **151**, 97–126.
- 47 R. Conway-Kenny, Trinity College Dublin, 2018.
- 48 V. Singh, A. Srikrishna, A. P. Marchand, G. Srinivas, W. H. Watson, S. Raina, B. A. B. Prasad and V. K. Singh, .
- 49 C. S. Foote, J. Valentine, A. Greenberg and J. F. Liebman, *Active oxygen in chemistry*, Springer Science & Business Media, 1995, vol. 2.
- 50 M. Seip and H. D. Brauer, *J. Am. Chem. Soc.*, 1992, **114**, 4486–4490.
- 51 A. G. Orpen, L. Brammer, F. H. Allen, O. Kennard, D. G. Watson and R. Taylor, in *Structure correlation*, Verlag Chemie, Weinheim, 1994, pp. 751–858.
- 52 P. Y. Boamah, N. Haider and G. Heinisch, *J. Heterocycl. Chem.*, 1989, **26**, 933–939.
- 53 Y. Halpin, M. T. Pryce, S. Rau, D. Dini and J. G. Vos, *Dalt. Trans.*, 2013, **42**, 16243.
- 54 M. G. Pfeffer, B. Schäfer, G. Smolentsev, J. Uhlig, E. Nazarenko, J. Guthmüller, C. Kuhnt, M. Wächter, B. Dietzek, V. Sundström and S. Rau, *Angew. Chemie - Int. Ed.*, 2015, **54**, 5044–5048.
- 55 J. Sauer, *Angew. Chemie Int. Ed. English*, 1966, **5**, 211–230.
- 56 J. Sauer, *Angew. Chemie Int. Ed.*, 1967, **6**, 16–33.
- 57 J. G. Martin and R. K. Hill, *Chem. Rev.*, 1961, **61**, 537–562.
- 58 F. Fringuelli and A. Taticchi, *The Diels–Alder Reaction*, 2001.
- 59 G. Brieger and J. N. Bennett, *Chem. Rev.*, 1980, **80**, 63–97.
- 60 M. Grzybowski, K. Skonieczny, H. Butenschön and D. T. Gryko, *Angew. Chemie - Int. Ed.*, 2013, **52**, 9900–9930.
- 61 P. Rempala, J. Kroulík and B. T. King, *J. Org. Chem.*, 2006, **71**, 5067–5081.
- 62 G. Rouillé, M. Steglich, F. Huisken, T. Henning and K. Müllen, *J. Chem. Phys.*, 2009, **131**, 204311.
- 63 K. Nagaraj, K. Senthil Murugan, P. Thangamuniyandi and S. Sakthinathan, *J. Fluoresc.*, 2014, **24**, 1701–1714.
- 64 E. Ishow, A. Gourdon, J.-P. Launay, C. Chiorboli and F. Scandola, *Inorg. Chem.*,

- 1999, **38**, 1504–1510.
- 65 S. Rau, D. Walther and J. G. Vos, *J. Chem. Soc. Dalton Trans.*, 2007, 915–919.
- 66 S. Wohlthat, F. Pauly and J. R. Reimers, *J. Phys. Condens. Matter*, 2008, **20**, 295208.
- 67 C. Abeywickrama and A. D. Baker, *J. Org. Chem.*, 2004, **69**, 7741–7744.
- 68 P. Comba, R. Krämer, A. Mokhir, K. Naing and E. Schatz, *Eur. J. Inorg. Chem.*, 2006, 4442–4448.
- 69 G. M. Ó Máille, Trinity College Dublin, 2012.
- 70 Y. Yuan, H. Huang, L. Chen and Y. Chen, *Macromolecules*, 2017, **50**, 4993–5003.
- 71 R. Rathore and J. K. Kochi, *Acta Chem. Scand.*, 1998, **52**, 114–130.
- 72 O. Hammerich and V. D. Parker, *Adv. Phys. Org. Chem.*, 1984, **20**, 55–189.
- 73 M. Di Stefano, F. Negri, P. Carbone and K. Müllen, *Chem. Phys.*, 2005, **314**, 85–99.
- 74 V. M. Hertz, J. G. Massoth, M. Bolte, H. W. Lerner and M. Wagner, *Chem. - A Eur. J.*, 2016, **22**, 13181–13188.
- 75 D. Xia, X. Guo, L. Chen, M. Baumgarten, A. Keerthi and K. Müllen, *Angew. Chemie - Int. Ed.*, 2016, **55**, 941–944.
- 76 B. J. Fallon, J. B. Garsi, E. Derat, M. Amatore, C. Aubert and M. Petit, *ACS Catal.*, 2015, **5**, 7493–7497.
- 77 Y. Li, T. Thiemann, K. Mimura, T. Sawada, S. Mataka and M. Tashiro, *Engineering*, 1998, 10–12.
- 78 M. Juríček, P. H. J. Kouwer, J. Reháč, J. Sly and A. E. Rowan, *J. Org. Chem.*, 2009, **74**, 21–25.
- 79 A. L. Webber, J. R. Yates, M. Zilka, S. Sturniolo, A.-C. Uldry, E. K. Corlett, C. J. Pickard, M. Pérez-Torrallba, M. Angeles Garcia and D. Santa Maria, *J. Phys. Chem. A*, 2019, **124**, 560–572.
- 80 C. A. Hunter and J. K. M. Sanders, *J. Am. Chem. Soc.*, 1990, **112**, 5525–5534.
- 81 T. Kitamura, R. Yamada, K. Gondo, N. Eguchi and J. Oyamada, *Synthesis (Stuttg.)*, 2017, **49**, 2495–2500.
- 82 A. John, S. Kirschner, M. K. Fengel, M. Bolte, H. W. Lerner and M. Wagner, *Dalt. Trans.*, 2019, **48**, 1871–1877.
- 83 F. Miyamoto, S. Nakatsuka, K. Yamada, K. I. Nakayama and T. Hatakeyama, *Org. Lett.*, 2015, **17**, 6158–6161.
- 84 S. Goretta, C. Tasciotti, S. Mathieu, M. Smet, W. Maes, Y. M. Chabre, W. Dehaen, R. Giasson, J. M. Raimundo, C. R. Henry, C. Barth and M. Gingras, *Org. Lett.*, 2009, **11**, 3846–3849.
- 85 X. Feng, L. Li, X. Yu, Y. Yamamoto and M. Bao, *Catal. Today*, 2016, **274**, 129–132.

Chapter Three

In Search of Highly Emissive Donor-Acceptor Structures for Thermally Activated Delayed Fluorescence Organic Light Emitting Diodes

3.0 Introduction

The focus of chapter to is to carry out preliminary synthetic explorations, as well as photophysical studies, in search of novel highly emissive donor-acceptor materials. Commonly, the literature boasts Donor-Acceptor-Donor structures (D-A-D), Donor- π -Acceptor- π -Donor (D- π -A- π -D), and polymeric or asymmetric Donor-Acceptor (D-A) structures. As part of this work, an alternative Acceptor- π -Donor- π -Acceptor (A- π -D- π -A) approach is taken. This approach allows for an in-depth study to be carried out on the effects that multiple acceptors covalently bonded to a central donor unit will have on the resulting photophysical properties of the materials.

The central donor utilised for this work is Phenothiazine (PTZ), and the acceptor utilised is Triazine (TRZ). Novel synthetic methodologies are explored, as well as a lesser known approach to separate HOMO/LUMO molecular orbitals by incorporation of a π -conjugated acetylene linker in order to induce intermolecular charge transfer (ICT). The purpose of this Chapter is to gain a further understanding into ICT materials, effects of extended conjugation and planarity on PLQY, as well as the effect of varying the positioning of electron withdrawing groups on its emission properties. The materials future application as an n-type semiconductor in a commercially available OLED, as well as processes such as TADF are explored. The lessons learned whilst carrying out this work are collectively applied to Chapter Four and in order to successfully synthesise future families of novel highly emissive compounds for applications in the OLED industry.

3.1 Donor–Acceptor Systems

There exist many different types of D-A systems, which differ by the number of donors and acceptors, and whether the donor and acceptor moieties are separated by a π -conjugated linker. Molecules which have a difference between the ground state and the excited state dipoles are defined as ICT materials.^{95,187} Donor-acceptor (D-A) structures are the most facile method to construct ICT materials. The HOMO is located on the donor moiety, and the LUMO on the acceptor. A desirable property of these moieties is that the HOMO orbitals are extended throughout the molecule or at least partially extended to aid ICT, and the LUMO orbitals are highly localised.¹⁸⁸ This ensures that the dipole moment of the molecule is different in the ground state to that of the excited state.

There are two methods by which to separate the frontier molecular orbitals; *via* extended conjugation such as an acetylene linker, or by introducing a large dihedral angle through sterically bulky functional groups.⁹⁹ The former method relies on extended π -conjugation, which also introduces planarity and rigidity to the structure. If a π -conjugated linker is incorporated into the structure, the requirement for an induced twist within the molecule is not as stringent, since there now exists an adequate spacer in order to induce ICT. Below Figure 3.0 illustrates a D- π -A structure (the phenyl ring is one of the π spacers commonly utilised within these systems) with a large dihedral angle θ and a D- π -A with a small dihedral angle θ . As part of this work, an acetylene linker is incorporated into all target structures, thus the latter approach was taken when designing all target molecules.

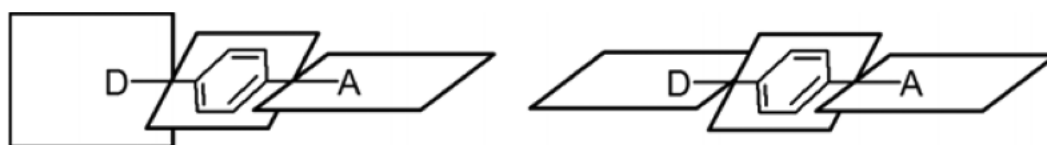


Figure 3.0: A D- π -A structure with a large dihedral angle θ and a D- π -A with a small dihedral angle θ .¹⁸⁹

The number of donors and acceptors within the system will determine if it is an n- or a p-type OLED.¹⁹⁰ There are also two distinct classes of D-A systems: intramolecular D-A systems and intermolecular D-A systems. Intramolecular D-A systems are those which contain both the donor and the acceptor moieties within the same structure, connected by a suitable bridge such as a single bond or π -conjugated linker. These structures are responsible for single molecule exciton emission.⁹⁵ Intermolecular D-A systems are formed *via* charge transfer from separate electron donors (D) and electron acceptors (A) in a polymeric film blend. This results in exciplex emission, exhibiting faster recombination at the electrode surface, and has been utilised to tune OLED emission and deliver white light.⁹⁹ Despite that, it is often red shifted compared to exciton emission, and both blend purity and polydispersity index are difficult to control.⁸⁷ Long, linear, and planar structures (herein specifically referring to small molecules, not polymers) exhibit higher degrees of horizontal alignment, increased efficiency, and higher colour purity.¹⁹¹ Randomly oriented molecules suffer a decreased output of $\sim 20\%$, and thus horizontal planar structures are desirable. Planarity coincides with π - π stacking and aggregate formation which promotes intersystem crossing

(IC), having a negative impact on the internal quantum efficiency (IQE) of the OLED. Increased conjugation also inevitably results in a bathochromic shift of the emission wavelength. The latter method relies on a large dihedral angle which produces a twisted structure. Twisted molecules are accessible by use of bulky substituents which restrict bond rotations within the structure.¹⁹² Reduced conjugation length produces blue emitting materials. However twisted structures can suffer from closely positioned donor and acceptor moieties within the structure, which does not give enough spatial separation of the frontier molecular orbitals - such overlap does not generate sufficient ICT character.

3.2 Ideal Donor Candidates

By definition a donor is an electron rich moiety, and in order to efficiently participate in charge transfer with an acceptor it must possess a high lying HOMO. There are many different examples of donors in the literature, but those that dominate are heterocyclic aromatic structures.^{193–195} Heterocycles are readily accessible *via* many common synthetic routes, are easy to functionalise, and are thermally stable entities.

3.2.1 Phenothiazine

Phenothiazine (PTZ) possesses the strongest donor ability of all known amine heterocycles, outperforming triphenylamine, tetrahydroquinoline, and carbazole.^{33,35–42} The presence of nitrogen and sulfur atoms allows this heterocycle to be incredibly electron rich, as well as strongly bonded to avoid low decomposition temperatures of PTZ containing materials. It contains a small torsional angle related to the nitrogen and sulfur atoms, allowing π -delocalisation to be extended over the entire structure, increasing molar absorptivity. PTZ functionalised with π -extensions have been widely studied, with varied acceptor moieties possessing a broad and structure-less UV-vis profile stretching from 300 – 600 nm. Its wide and strong absorption profile in the visible region, fully reversible oxidation and reduction potentials, as well as a high lying HOMO has resulted in its use in organic photovoltaic cells (OPV), OLEDs, and dye sensitised solar cells (DSSCs).^{43–52} In its ground state configuration, it is non-planar and displays a butterfly-shape which hinders aggregate formation. Non-radiative IC is favoured in aggregates, which reduces photovoltaic performance.²¹⁷

The most interesting example of PTZ as a donor moiety was reported by Adachi and co-workers in 2018.²¹⁴ As illustrated in Figure 3.1, **L2.0** has a central triazine acceptor unit, with three PTZ donor appendages. Triazines are the most widely used acceptor moieties in the literature, which will be further discussed in Subsection 2.4.1. The compound has four conformers, which display dual emission of green/ yellow light. The ΔE_{S-T} gap of E1 ($\Delta E_{S-T} = 0.0079$ eV) is exceptionally small, allowing for very efficient k_{rISC} , and the display of TADF behaviour. Yellow emitters are of particular interest,^{218,219} as they are a straightforward way to achieve white light *via* combination with blue emitters.²¹⁴

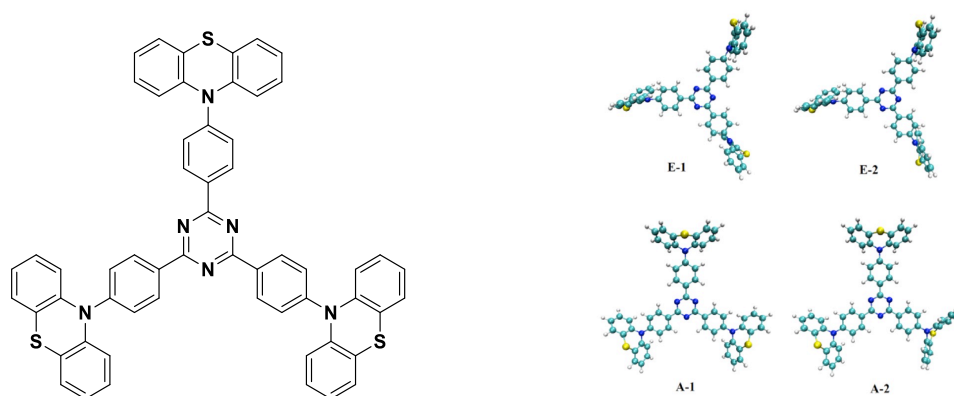


Figure 3.1: An example of PTZ D-A structure (**L2.0**) utilised for TADF, and its four respective equatorial and axial conformers. Optimised by B3LYp/6-31G*.²¹⁴

3.3 Acceptor Candidates

The vast majority of D-A literature focuses on functionalisation of donor systems to increase donor capabilities, and less so on the acceptor moiety. The primary requirement of the acceptor is an electron deficient environment, with a low lying LUMO. Literature examples of acceptors include small, conjugated systems with electron withdrawing functionalities such as diphenyl amine,²²⁰ triazine,^{100,221–233} and diphenyl sulfoxide.²³⁴ The UV profile of D-A structures is heavily dependent on the acceptor, and a bathochromic shift is observed with increasing strength of the acceptor.¹⁹⁰ The cyano functional group has been liberally integrated into acceptor systems to enhance electron accepting ability. It has shown to reduce aggregation tendency, and increase thermal and morphological stabilities.⁹⁹ In the next section, focus will be centred on triazine systems, with methods to control their acceptor abilities in order to tune their luminescent properties.

3.3.1 Triazine Acceptors

Triazine structures are the most common acceptors in the literature. They can be synthesised *via* many different synthetic routes, proving versatility and facile chemical modification. Structurally, triazines are incredibly robust and stable beyond 400 °C allowing them to be used in OLED materials.^{72–81} Generally, triazines are used as core accepting materials with donor appendages (Figure 3.1), designed for mainly blue, green, and (less so) yellow emitting TADF materials. The three reactive sites on the 1,3,5-triazine core allow for both symmetric and asymmetric substitution to take place.

In order to tune luminescent properties, the effect of substitution on the triazine core must be thoroughly understood. Chen *et al.*¹⁰⁰ have carried out a comprehensive theoretical-experimental study to understand the effect of substitution on triazines' acceptor ability. The ΔE_{S-T} gap that governs the efficiency of k_{ISC} , as well as the excited state energy levels can be controlled by the degree of substitution on the central triazine ring. If the triazine core structure is asymmetrically substituted, the ΔE_{S-T} gap varies from 0.001 – 0.46 eV, with large localisation of the HOMO and the LUMO orbitals, and minimal spatial overlap. However symmetrically substituted triazines have high orbital overlap, and a ΔE_{S-T} gap of up to 1.47 eV. Compounds which have a large ΔE_{S-T} gap typically exhibit triplet-triplet annihilation (TTA). In this way, by only controlling the degree of substitution on the triazine ring, the photo-luminescent properties can be controlled.

3.4 Design Considerations for the Emitters

Literature examples of small molecule candidates as emissive materials have very similar design approaches; the vast majority are twisted donor-acceptor systems with large dihedral angles and symmetric D-A-D systems in order to induce ICT. Extensive literature searches were carried out during the design stage of this work in search of novel approaches and design architectures, in this way paving the way towards previously unexplored emissive material designs. Usta *et al.*²⁵⁰ designed a radically different small solution-processable fluorescent molecule with A- π -D- π -A architecture as observed in Figure 3.2.

L2.1 is a rod shaped oligo(*p*-phenyleneethynylene) with a central donor phenyl ring functionalised with two solubilizing alkyl chains, connected to the electron deficient benzonitriles *via* acetylene bridges acting as π -spacers. These types of molecules are not

common in the literature, and to observe an oligo(*p*-phenyleneethynylene) behave as a deep-blue emitter is even more scarce due to its extended conjugated backbone. Commonly, deep-blue emitters are twisted with reduced conjugation length. Designing a small molecule with high colour purity, high device performance, and solution processability continues to be a great challenge.

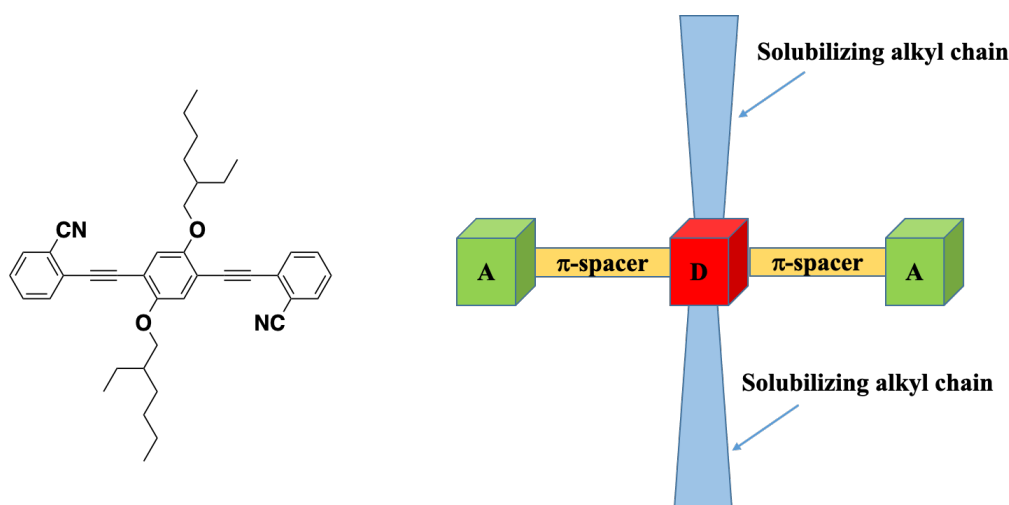


Figure 3.2: 1,4-bis((2-cyanophenyl)ethynyl)-2,5-bis(2ethylhexyloxy)benzene (**L2.1**) as a literature example of a blue emitting A- π -D- π -A OLED.²⁵⁰

However, Usta *et al.* successfully designed **L2.1** as a deep-blue emitter with a wide band gap (2.98 eV), high fluorescence quantum yield (0.9 in-solution, and 0.5 in the solid state), and boasting an impressive device performance EQE_{max} of 7.06%. This EQE_{max} is among the highest achieved to date for a deep-blue OLED based on a solution-processed fluorescent molecule.²⁵⁰ TDDFT calculations proved that **L2.1** exhibits a high radiative exciton yield which originates from reverse intersystem crossing (RISC) between high-lying triplet states and the first singlet excited state ($T_2/T_3 - S_1$), with hybridized local and charge transfer (HLCT) excited state characteristics. This type of emission is coined the hot exciton mechanism: upon excitation, higher triplet levels are populated (energetically close to the S_1 excited state), which non-radiatively decay to S_1 , and emission occurs from the S_1 state in the form of HLCT fluorescence.²⁵¹ Taking inspiration from this novel and unorthodox approach towards small molecule based emissive material design, di-acceptor systems are proposed herein (Figure 3.3).

Utilising PTZ as the central core, one or two triazine appendages are linked *via* an acetylene bridge. Increased aliphatic chain length incorporated within organic emitting systems has

been shown to increase the efficiency of recombination at a semiconducting surface, as well as hinder excimer formation *via* π - π stacking.¹⁸⁸ The PTZ amine moiety is substituted with a long aliphatic chain, which serves to reduce π - π stacking and protect the amine from any further undesired reactions both during synthesis and in an OLED device. The acetylene linker has been incorporated to spatially separate the HOMO and LUMO orbitals in order to induce ICT, as well as retain planarity to limit non-radiative decay pathways.¹⁰¹ All triazines are asymmetric appendages to the donor PTZ core, to ensure a small ΔE_{S-T} gap and efficient k_{HSC} .¹⁰⁰ The effect of the positioning of the cyano functionality on the materials photophysical properties is studied. Furthermore, cyano functionality has been incorporated to enhance the accepting capabilities of the target triazine emitters. The cyano functionality enhances an n-type OLED response.²⁵² It is envisioned that the proposed structures will serve as highly emissive and efficient OLED materials.

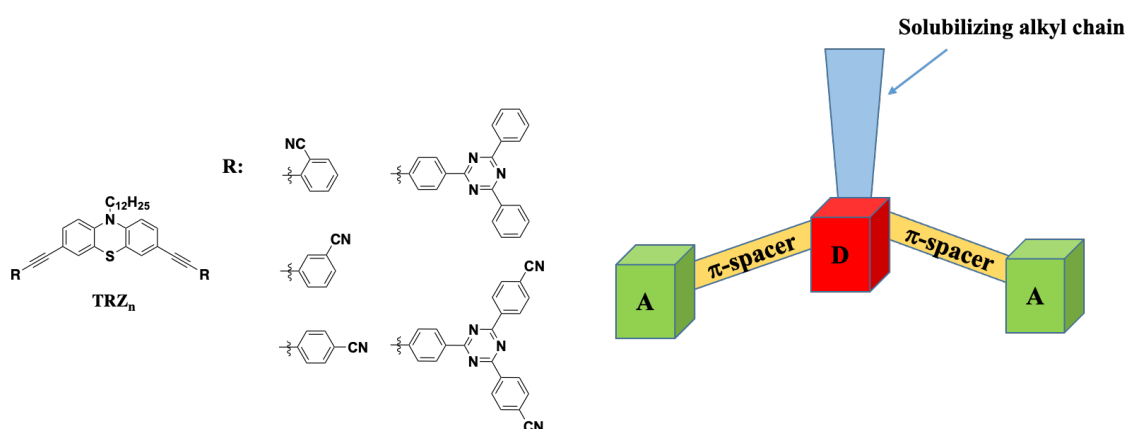


Figure 3.3: Proposed A- π -D- π -A structures for OLED materials.

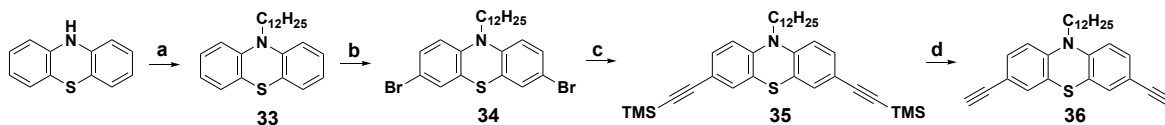
3.5 Results and Discussion

The results and discussion section of this Chapter contains a thorough synthetic discussion of the emitters. Following that, the emitter properties are studied using a myriad of photophysical, thermal, electrochemical, and computational techniques to elucidate their validity as OLED candidates.

3.5.1 Synthesis of D-A Systems

3.5.2 Synthesis of the Donor Moiety

The synthesis of **36** proceeded *via* four synthetic steps (Scheme 3.0 below).



Scheme 3.0: Complete synthesis of **36** **a)** 1-bromododecane, sodium hydroxide, DMSO, 24 h, RT, 89% **b)** *n*-bromosuccinimide, DMF, 4 h, 0 °C, 94% **c)** Trimethylsilylacetylene, Pd(PPh₃)₂Cl₂, CuI, Et₃N, 24 h, 80 °C, 92% **d)** sodium hydroxide, CH₂Cl₂:MeOH 1:1, 1 h, RT, 72%.

PTZ, a commercially available white solid was used without further purification. The aliphatic chain was introduced on the amine of PTZ *via* an S_N2 reaction with 1-bromododecane to form **33**. Dimethyl sulfoxide (DMSO), the polar aprotic solvent of choice favours the S_N2 pathway and does not engage in hydrogen bonding with the nucleophile, thus not engaging in side reactions.²⁵³ Flash column chromatography (SiO₂, hexanes:ethyl acetate, 18:1, v/v) furnished **33** as a colourless oil in 89% yield, which was in good agreement with the literature.²⁵⁴ The aliphatic chain serves an important role in hindering any reactions at the amine site, as well as hindering π-π stacking.

Clar's π sextet rule can be applied in order to qualitatively predict the reactivity of polycyclic aromatic hydrocarbons (PAHs).²⁵⁵ In PTZ, C-2 and C-3 of the outer benzenoid rings retain a stronger localised double bond character with respect to the rest of the structure. For this reason, using stoichiometric quantities of *n*-bromosuccinimide (NBS) as the brominating agent, the C-3 positions were selectively brominated to form **34**. The reaction proceeded *via* electrophilic addition, with a nucleophilic attack of the double bond to the bromine atom of NBS. This formed a three membered ring intermediate, which collapsed to form the brominated species **34**.^{256,257} Subsequent work-up and purification with flash column chromatography (SiO₂, hexane:ethyl acetate, 20:1, v/v) afforded **34** as a yellow oil in 94% yield, which was in good agreement with the literature.²⁵⁴ The brominated product **34** served as the starting material for the Sonogoshira cross coupling reaction with trimethylsilylacetylene (TMS-acetylene).

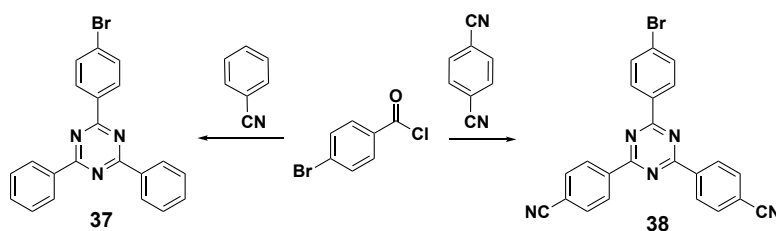
Palladium catalysed Sonogoshira carbon-carbon cross coupling reactions are an incredibly versatile tool to introduce a myriad of structural functionalities.^{258–260} In order to introduce an acetylene linker, this type of coupling was utilised. Previously synthesised bis(triphenylphosphine)palladium(II) dichloride,²⁶¹ was chosen as the catalyst. The copper iodide co-catalyst was used in minimal amounts (> 1%) in order to reduce the probability of homo-coupling.²⁵⁹ Triethylamine served a dual role, both as the solvent of the reaction and as the base. The reaction proceeded at 80 °C, for 24 h. Subsequent washing with water, extraction with CH₂Cl₂, and purification with flash column chromatography (SiO₂, hexanes) furnished **35** as a yellow oil in 92% yield. The product was in good agreement with the literature.²⁶² In order to carry out further reactions on **35**, TMS deprotection was carried out. By stirring **35** with sodium hydroxide in CH₂Cl₂:MeOH 1:1 at room temperature for one hour, the TMS functionality was deprotected to form the terminal acetylene **36**. This deprotection is favoured due to the high affinity silicon atoms possess towards electronegative atoms such as oxygen.²⁶³ Sodium hydroxide and methanol form an equilibrium in solution, allowing the hydroxy to nucleophilically attack the electropositive silicon atom of TMS. Methanol being a protic solvent, readily donates free H⁺ ions in solution, thus forcing the equilibrium towards product formation. A facile workup with water, and removal of CH₂Cl₂ *in vacuo* afforded **36** as a deep red oil in 72% yield. The product gave characterisation data in good agreement a literature report,²⁶² and was carried forward without further purification.

3.5.3 Synthesis of the Acceptor Moiety

In order to form the triazine ring, 4-bromobenzoyl chloride was reacted with two equivalents of benzonitrile, and one equivalent of ammonia (Scheme 3.1). The carbonyl of 4-bromobenzoyl chloride is a hard electrophilic site, and thus requires a hard nucleophile. Hard nucleophile/electrophile reactions are predominantly charge controlled.²⁶³ Thus to favour selective nucleophilic attack at the carbonyl site, a Lewis acid was used. The Lewis acid of choice was antimony pentachloride, which coordinates to the oxygen and chlorine atoms of 4-bromobenzonitrile, increasing the δ^+ charge on the sp² carbonyl carbon. The formation of this coordination complex was observed by the vivid colour changes of the reaction mixtures of both **35** and **36**, going from white to bright orange upon the addition of antimony pentachloride. The vivid colour can be attained to the highly energetic nature of this reaction intermediate.²⁶³ The cyano group can act as either a hard or a soft nucleophile, depending on

whether the nucleophilic attack originates from the nitrogen or the carbon of the cyano functionality respectively.²⁶³

In this instance, the cyano functionality acts as a hard nucleophile to attack the δ^+ sp^2 carbonyl carbon. A further attack occurs by a second equivalent of benzonitrile on the δ^+ sp^2 N-bonded carbon, and a thermodynamically favoured ring closure is forced by the addition of one equivalent of ammonia. The crude product was refluxed in DMF to remove impurities and afford a white solid. Triazine **37** was furnished in a higher yield of 70%, which showed good agreement with the literature.²⁶⁴ Triazine **38** was insoluble in all common organic solvents, which hindered collection of well resolved NMR data, with only broad peaks observable. It also suffered a lowered yield of 46%.

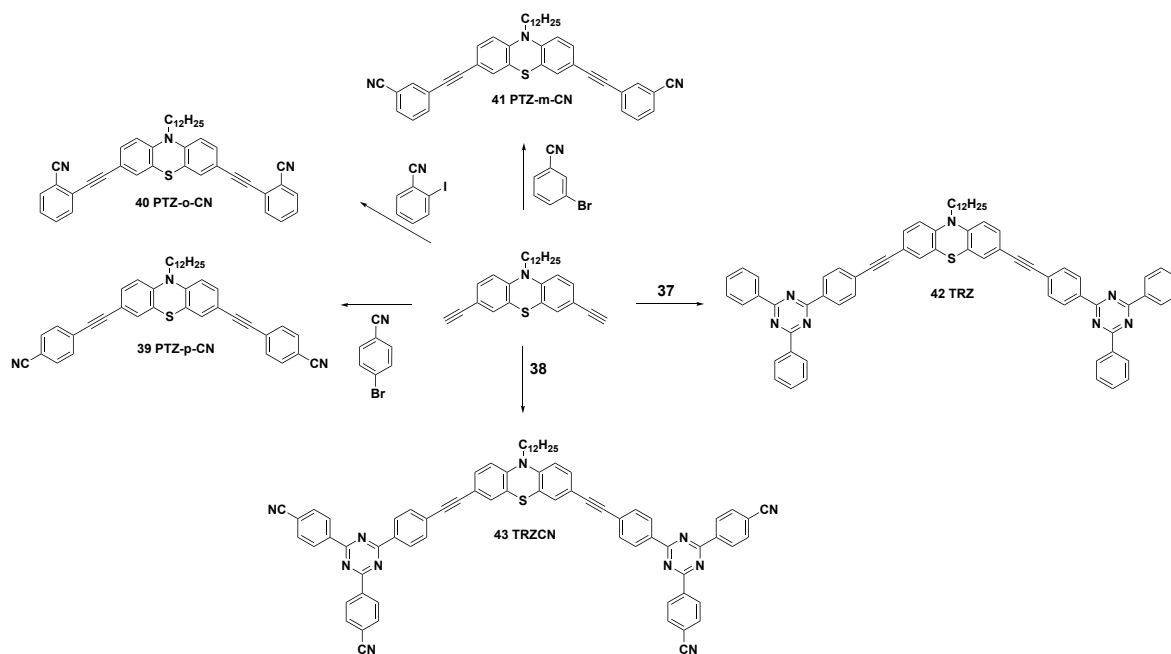


Scheme 3.1: Synthesis of **37** and **38** using antimony pentachloride, CH_2Cl_2 , 12 h, 40 °C, followed by 35% aq. ammonia at RT, yielding 70% and 46% respectively.

3.5.4 Sonogashira Coupling

By altering the aryl halide, five novel A-D-A type systems were successfully synthesised (Scheme 3.2). All compounds displayed in Scheme 3.2 were subjected to identical reaction conditions, including duration, temperature, and catalyst loadings. These systems proved to be synthetically accessible, and were obtained in moderate yields. Prior to designing more sophisticated systems, structurally primitive cyano-bearing compounds **39**, **40**, and **41** were synthesised. These compounds were synthesised in order to test the optimal position of the cyano group on the acceptor-moiety. These compounds were all highly luminescent oils, which proved a significant challenge to purify. Flash column chromatography (SiO_2 , ethyl acetate:hexanes, 1:5, v/v) afforded **39** as an orange oil in a reduced yield of 11%, **40** as an orange oil in a yield of 42%, and **41** as a yellow oil in a yield of 48%. The reduced yields are attributed to the difficulty in obtaining singly eluting fractions. The benzonitrile-derived compounds **39**, **40**, and **41** were fully structurally characterised with 1H NMR, $^{13}C\{^1H\}$ NMR and HRMS (see Appendix 2.0-2.2).

Triazine compounds **42** and **43** were obtained as orange and red solids respectively. Due to its higher solubility, the purification of **42** was more straightforward. Flash column chromatography (SiO₂, CH₂Cl₂:petroleum ether, 3:7, v/v) afforded **42** as a bright orange solid in 50% yield. The successful purification of **43** proved highly challenging, and required numerous flash column chromatography trials (SiO₂, CH₂Cl₂:MeOH, 100:0.3, v/v), recrystallisation with CH₂Cl₂/diethyl ether, followed by preparative thin layer chromatography (PTLC) to furnish **43** as a dark red solid in 59% yield. Both triazine compounds **42** and **43** were fully structurally characterised (see Appendix 2.3-2.4).



Scheme 3.2: Sonogashira coupling to synthesise **39**, **40**, **41**, **42**, and **43** using 4% mmol Pd(PPh₃)₂Cl₂, CuI, THF:Et₃N 5:1, 12 h, 67 °C yielding 11%, 42%, 48%, 50%, and 59% respectively.

3.6 Structural Characterisation

All compounds were spectroscopically characterised using ¹H NMR, ¹³C {¹H} NMR, HSQC, HMBC, and selective spin TOCSY experiments. As an example of the mode of assignment, ¹H NMR data of **43** is presented in Figure 3.4a. The aromatic protons H1, H2, and H3, as well as the aliphatic chain protons were assigned according to a literature report.²⁶² H1, H2 and H3 appear most upfield of all the aromatic protons between 6.8 and 7.5 ppm, due to the electron rich nature of phenothiazine. Triazine protons H4, H5, H6, and H7 appear much

more downfield, and were easily distinguishable due to their 1:2 integration ratio, providing a clear distinction between the two spin systems of the triazine.

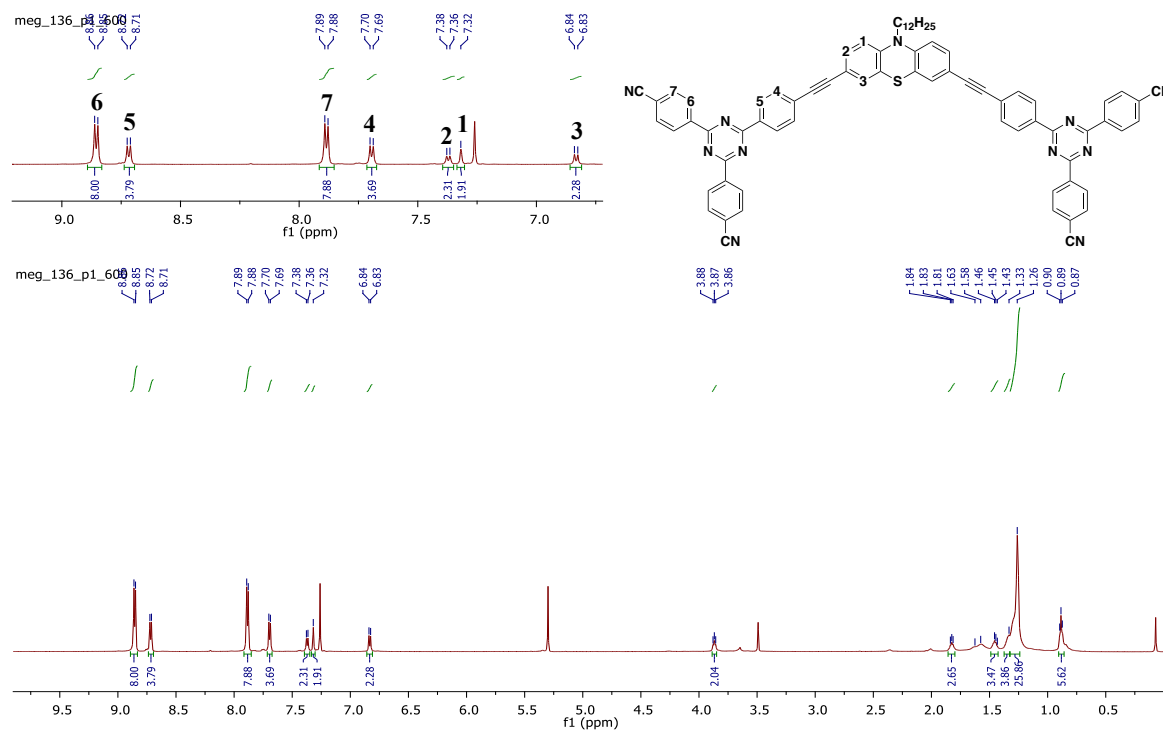


Figure 3.4a: ^1H NMR spectrum of **43**.

Spin selective TOCSY experiments supported this. In order to assign the $^{13}\text{C}\{^1\text{H}\}$ spectra (Fig. 3.4b below), 2D HSQC and HMBC experiments were utilised. The HSQC spectrum (Fig. 3.4c) allowed assignment of all of the C-H aromatic carbons, with the HMBC spectrum (Fig. 3.4d) aiding assignment of quaternary carbons and the cyano moieties.

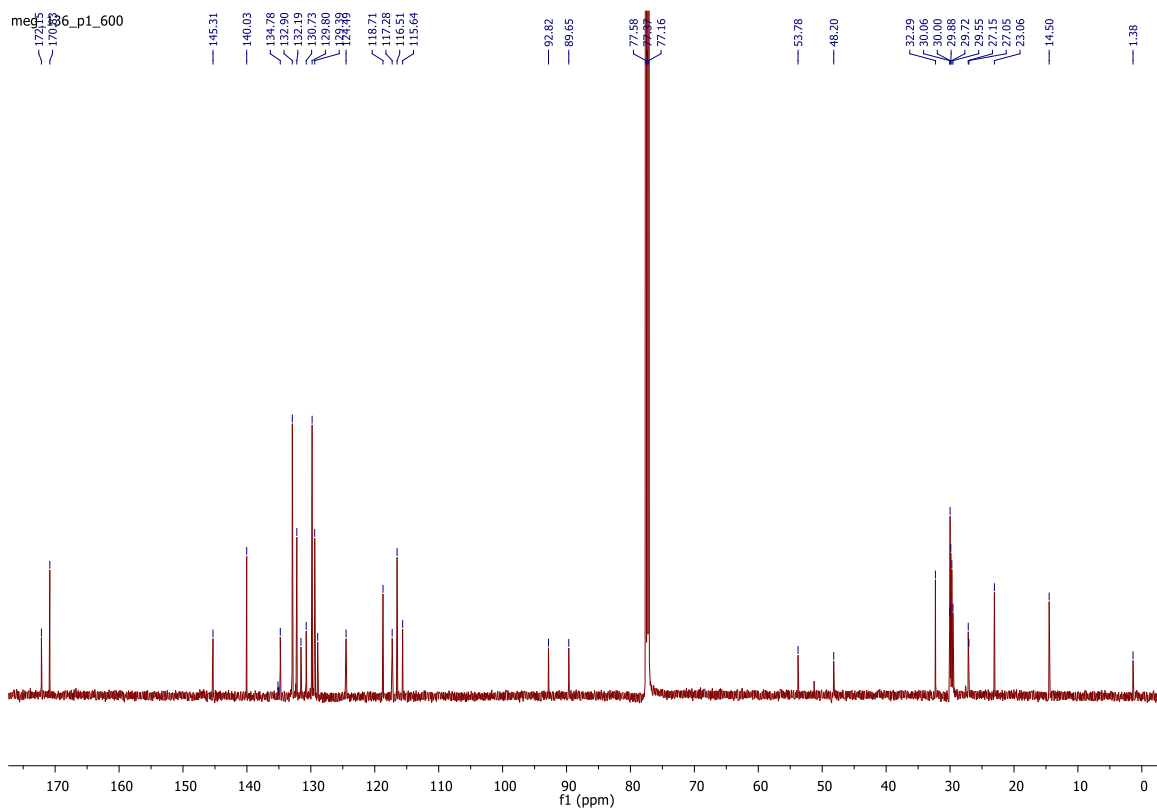


Figure 3.4b: $^{13}\text{C}\{^1\text{H}\}$ NMR spectrum of **43**.

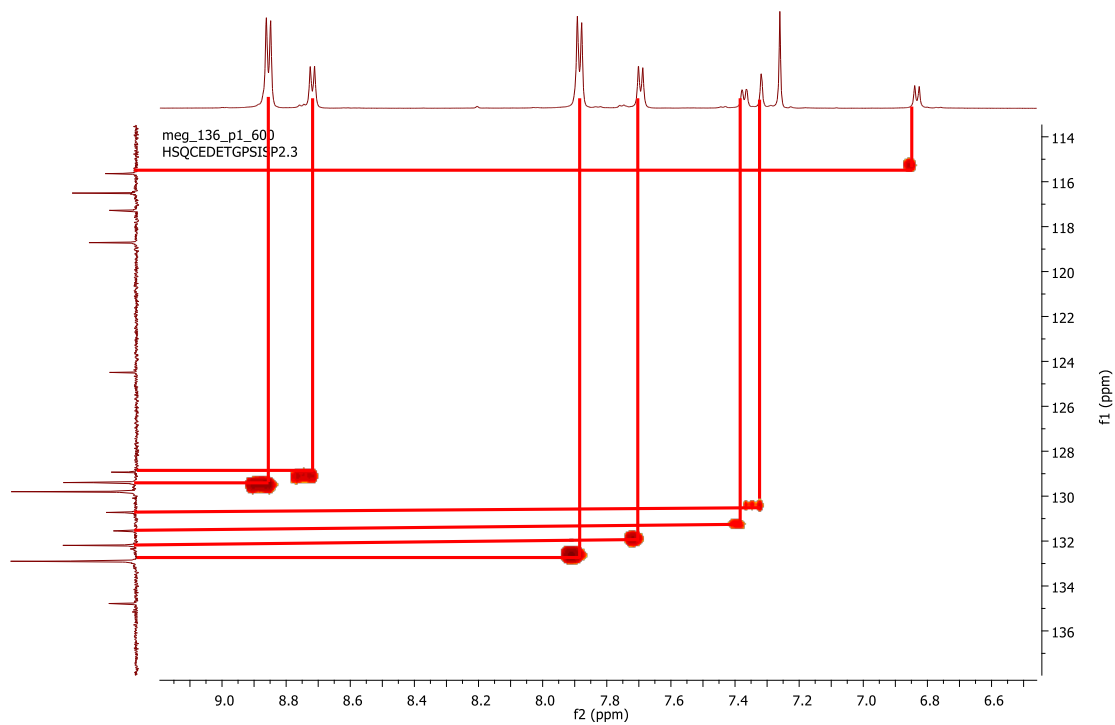


Figure 3.4c: HSQC spectrum of **43**.

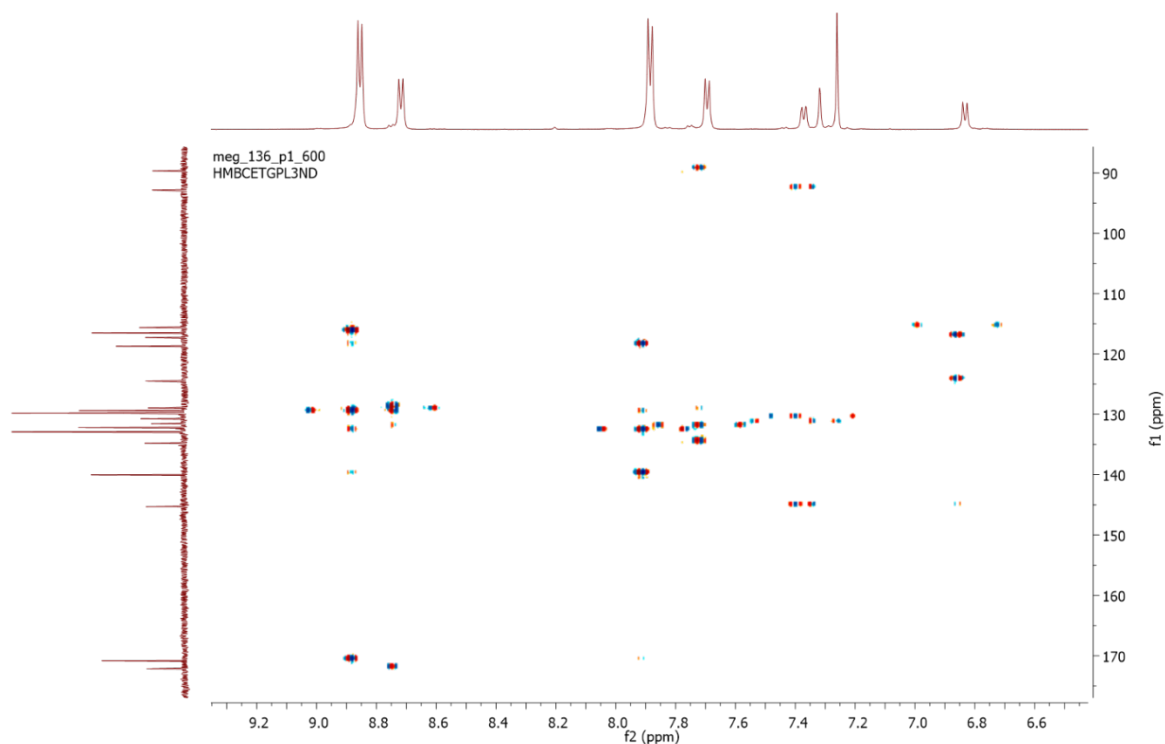
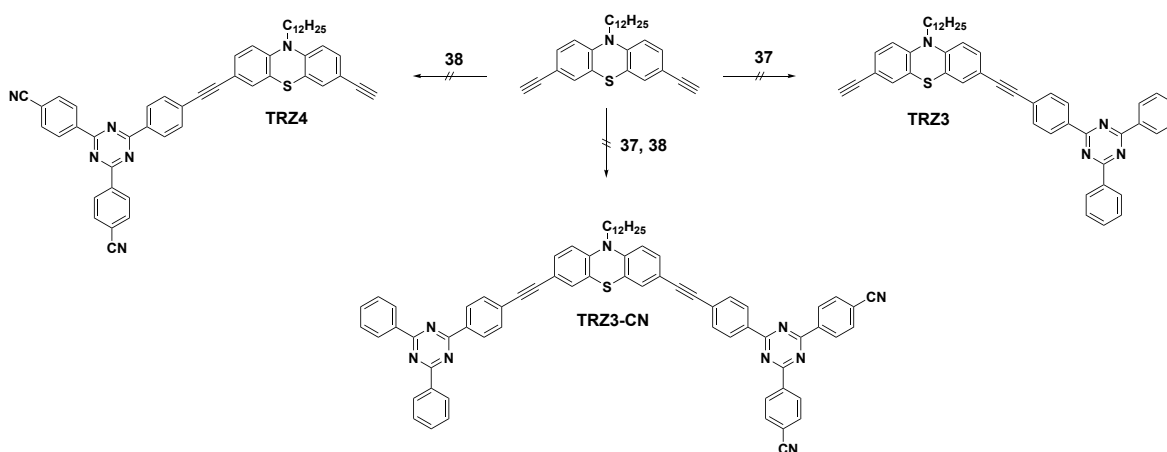


Figure 3.4d: HMBC spectrum of **43**.

3.7 Unsuccessful Synthetic Targets

Upon commencement of this project, it was envisaged that asymmetric compounds could be easily attainable using the same reaction conditions as mentioned above. However, after numerous attempts the reactivity of the terminal acetylene could not be controlled. In all cases, only disubstituted compounds were formed. Thus, compounds presented below in Scheme 3.4 were not synthesised. As part of future work, a novel methodology must be devised to successfully synthesise asymmetric systems.



Scheme 3.4: Unsuccessful synthesis of asymmetric D- π -A and A- π -D- π -A systems.

3.8 Photophysical Analysis

3.8.1 Preliminary Studies

UV-vis absorption and emission spectra of **36**, **39**, **40**, and **41** were collected (Figure 3.5). In order to test the effect of the position of the cyano functionality, all spectra were compared to the basic donor structure **36**. The UV-vis spectra of the four compounds show great similarity, with two prominent bands observed around 300 and 400 nm. The λ_{max} between $\lambda = 276$ and 298 nm is assigned as the π - π^* transition of PTZ, and the band at $\lambda = 400$ nm assigned as ICT.²⁶⁵ Thus, the absorption profiles are primarily attributed to the PTZ donor.

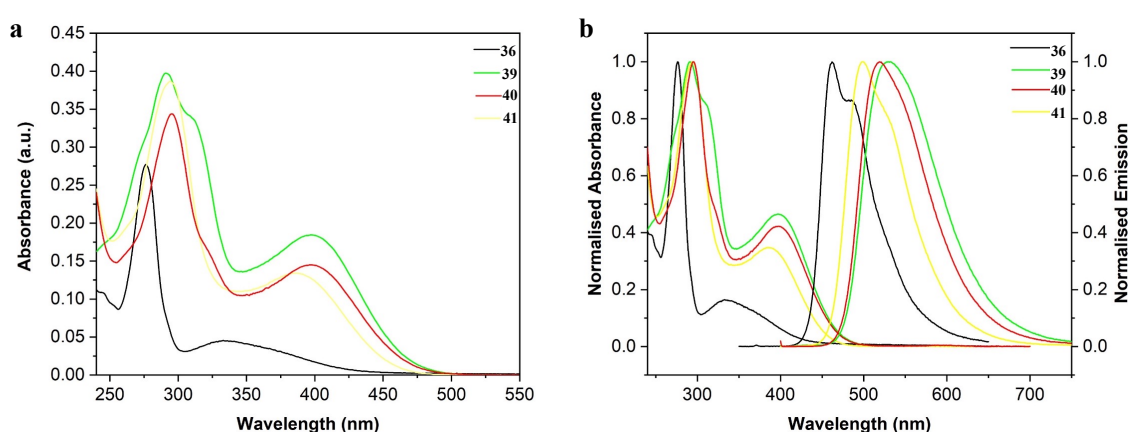


Figure 3.5: **a)** UV-vis absorption spectra of **39**, **40**, and **41** compared to **36** (1×10^{-5} M) in CH_2Cl_2 at $\lambda_{\text{exc}} = 380$ nm in air at RT. **b)** Normalised UV-Vis absorption and emission spectra of **39**, **40**, and **41** compared to **36** (1×10^{-5} M) in CH_2Cl_2 at $\lambda_{\text{exc}} = 380$ nm under N_2 at RT.

The emission spectra (λ_{exc} given in Table 3.0) appear broad and structureless for **39**, **40**, and **41**: the profiles contain local excited states (LE) and intramolecular charge transfer (ICT) arising from hybridized local charge transfer (HLCT). For ease, HLCT will be referred to as ICT in this text. A Stokes shift of > 100 nm is observed, with **7** attaining the most positively bathochromic shift (Table 3.0).

Table 3.0: UV-vis absorption and emission data of **36**, **39**, **40**, and **41**.^a

	$\lambda_{\text{abs}} / \text{nm}$	ε ^[b]	$\lambda_{\text{em}} / \text{nm}$	Φ_F ^[c]	Stokes Shift ^[d]
36	276, 333	0.045	462 ^{λ_{max}} , 488 (333)	Not observed	129
39	291, 397	0.184	532 (397)	0.77	135
40	296, 322, 398	0.145	519 (398)	0.88	116
41	294, 383	0.134	499 ^{λ_{max}} , 530 (383)	0.84	121

^a UV-vis absorption and emission data of 4-9 (1×10^{-5} M) in CH_2Cl_2 at $\lambda_{\text{ex}} > 400$ nm under N_2 at RT. ^b Molar extinction coefficient at the absorption maxima. ε : $10^5 \text{ M}^{-1} \text{ cm}^{-1}$. ^c PLQY were calculated with all samples under N_2 , with quinine sulfate as reference ($\Phi_F = 0.55$, 0.5 M H_2SO_4).²⁶⁶ ^d The Stokes shifts were determined by conversion of λ_{abs} and λ_{em} to wavenumbers prior to subtraction (nm).

Broad and structureless emission profiles are attributed to ICT,⁸⁸ indicating that ICT is occurring in the above A- π -D- π -A systems. Photoluminescence quantum yields (PLQY) were determined for all compounds, with the *ortho*- position exhibiting the highest PLQYs of the series ($\Phi_F = 0.88$). However, even though the *ortho*- and the *meta*- positions exhibit higher PLQY, compound **39** has the highest molar absorptivity coefficient ($\varepsilon = 0.184 \text{ M}^{-1} \text{ cm}^{-1}$) and boasts the largest bathochromic shift. Thus, the cyano functionality has the strongest effect on the acceptor in the *para*- position. Noting this, the triazine **43** was functionalised with the cyano group in the *para*- position (Scheme 3.2).

3.9 Triazines

3.9.1 UV-vis Absorption and Emission Solvatochromism

As discussed in Section 1.8.2.2, the ICT excited state possesses a dipole moment, and thus is quenched in polar solvents. For this reason, all photophysical studies on **42** and **43** were carried out in three solvents ranging from non-polar to highly polar: cyclohexane, methylene chloride, and ethanol to serve as a comparison. An emission concentration study from 1×10^{-5} M to 1×10^{-9} M in methylene chloride was carried out on both **42** and **43** to ensure the spectral features were not due to excimer/aggregate formation (Figure 3.6 below).

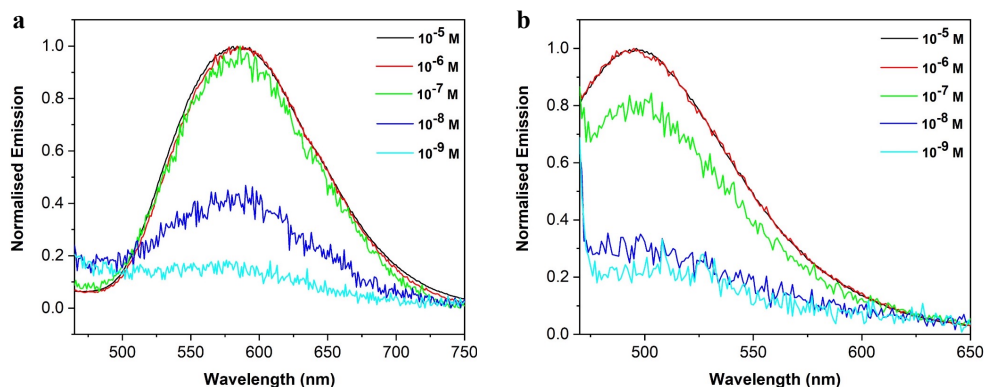


Figure 3.6: Emission spectra of **a)** **42** ($\lambda_{exc} > 404$ nm) and **b)** **43** ($\lambda_{exc} > 410$ nm), 1×10^{-5} M in CH_2Cl_2 in air at RT. No shift in λ_{em} with changing concentration signifies emission at all concentrations was due to single molecule emission and not aggregate emission.

If the emission was due to excimer formation, a gradual blue shift would be observed with reduction in concentration. No such shift was observed for **42** or **43**. Below, Figure 3.7 shows the UV-vis absorption and emission profiles at 1×10^{-5} M. The absorption profile of **42** does not shift in wavelength with changing solvent polarity, which is contrary to that of **43** where a bathochromic shift is observed in ethanol.

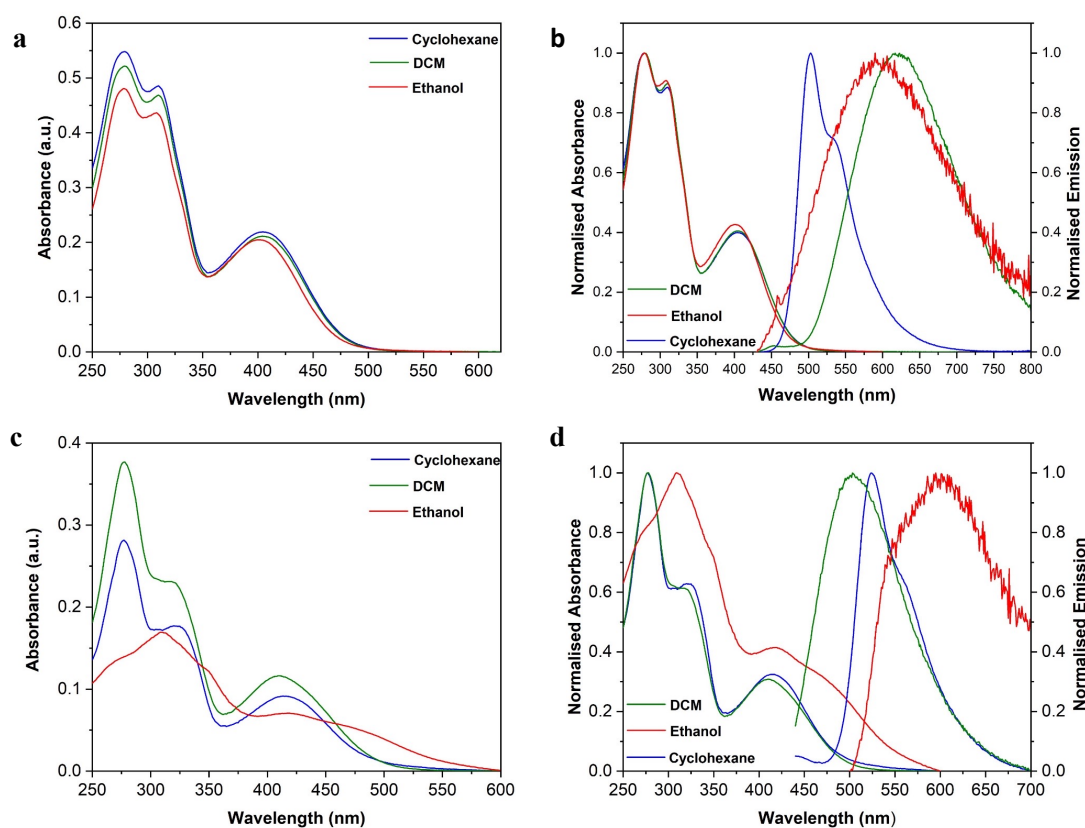


Figure 3.7: **a)** UV-vis absorption spectra of **42** (1×10^{-5} M) in cyclohexane, CH_2Cl_2 , and Ethanol. **b)** Normalised UV-vis absorption and emission spectra of **42** (1×10^{-5} M) in cyclohexane, CH_2Cl_2 , and Ethanol at $\lambda_{\text{exc}} = 404$ nm under N_2 at RT. **c)** UV-vis absorption spectra of **43** (1×10^{-5} M) in cyclohexane, CH_2Cl_2 , and Ethanol. **d)** Normalised UV/Vis absorption and emission spectra of **43** (1×10^{-5} M) in cyclohexane, CH_2Cl_2 , and Ethanol at $\lambda_{\text{exc}} = 404$ nm under N_2 at RT.

Both **42** and **43** display three prominent absorption bands around $\lambda = 280$, 300, and 400 nm. The λ_{max} around 280 nm can be attributed to the PTZ $\pi\text{-}\pi^*$ transition (refer to Section 3.3.1), 300 nm is attributed to the $\pi\text{-}\pi^*$ transition of the triazine,²⁶⁷ and the band around 400 nm is due to a ICT transition.⁸⁸ Preliminary studies proved that the addition of the cyano groups increased the molar absorptivity coefficient ϵ and red-shifted both the absorption and emission profiles. However, the emission profile of **43** is blue shifted with respect to **42**, with a difference of 126 nm (Figure 3.7, Table 3.1). Thus, the addition of the cyano groups did not shift the emission to higher wavelengths in **43** as predicted, but actually shifted it to higher wavelengths.

The molar absorptivity coefficient ϵ is twofold higher for **42** than **43**, and **43** exhibits a lowered PLQY (Table 3.1). The compound **43** permits more non-radiative paths of decay, thus its absorption and emission intensities are reduced. This is visually observable under UV irradiation ($\lambda = 365$ nm, Appendix 2.8). However, even with reduced emission when compared to **42**, both **42** and **43** boast higher PLQY and lifetimes (τ_1) (refer to Section 3.10.4) when directly compared to the reported D-A carbazole-triazine TADF systems (PLQY = 0.05, $\tau_1 = 0.88$ ns).⁹⁷

Table 3.1 Photophysical parameters of **42** and **43**.^a

	$\lambda_{\text{abs}} / \text{nm}$	ϵ [b]	$\lambda_{\text{em}} / \text{nm}$	Φ_F [c]	Stokes Shift [d]	τ / ns [e]
42 Cyclohex	279, 310, 404	0.548	$504^{\lambda_{\text{max}}}$, 539 (404)	0.44	100	3.45
42 CH_2Cl_2	279, 310, 404	0.521	626 (404)	0.14	222	1.93
42 Ethanol	279, 309, 402	0.480	600 (404)	0.02	141	2.8

43 Cyclohex	277, 325, 416	0.282	524 ^{λ_{max}} , 554 (410)	0.41	108	2.39
43 CH ₂ Cl ₂	277, 317, 410	0.377	503 (410)	0.08	93	1.53
43 Ethanol	309, 350, 419	0.193	599 (410)	Not observed	180	2.33

^a UV-vis absorption and emission data of 10 and 11 (1×10^{-5} M) in cyclohexane, CH₂Cl₂, and ethanol at $\lambda_{\text{exc}} > 400$ nm under N₂ at RT. ^b Molar extinction coefficient at the absorption maxima. ϵ : $10^5 \text{ M}^{-1} \text{ cm}^{-1}$. ^c PLQY were calculated with all samples under N₂, with quinine sulfate as reference ($\Phi_{\text{F}} = 0.55$, 0.5 M H₂SO₄).²⁶⁶ ^d The Stokes shifts were determined by conversion of λ_{abs} and λ_{em} to wavenumbers prior to subtraction (nm). ^e Excited state lifetime determination of 10 and 11 (1×10^{-5} M) in cyclohexane, CH₂Cl₂, and ethanol at $\lambda_{\text{exc}} > 400$ nm. NanoLED with $\lambda_{\text{exc}} = 458$ nm was used to irradiate the samples. All data was fit with mono-exponential decays, with $\chi^2 = 1$. All lifetimes were corrected with an instrument response factor (IRF), which was a non-scattering solution of silica particles.

In order to determine if the emission profiles had a triplet excited state component in **42** and **43**, emission measurements were run under N₂ (Figure 3.8). The triplet excited state is quenched by triplet oxygen (³O₂),²⁶⁸ and thus if the triplet excited state was being accessed, the emission intensity should increase under nitrogen when compared to aerated samples. Figure 3.8a shows no change in the emission intensity of **42**, signifying that triplet character is not being accessed, and ICT emission originates from the singlet excited state. However, Figure 3.8b shows a 16% increase in emission intensity in cyclohexane, 1% increase in CH₂Cl₂, and no change in ethanol. This proves that triplet character is being accessed in **43**, and it is most prominent in non-polar cyclohexane, which cannot quench the excited state.

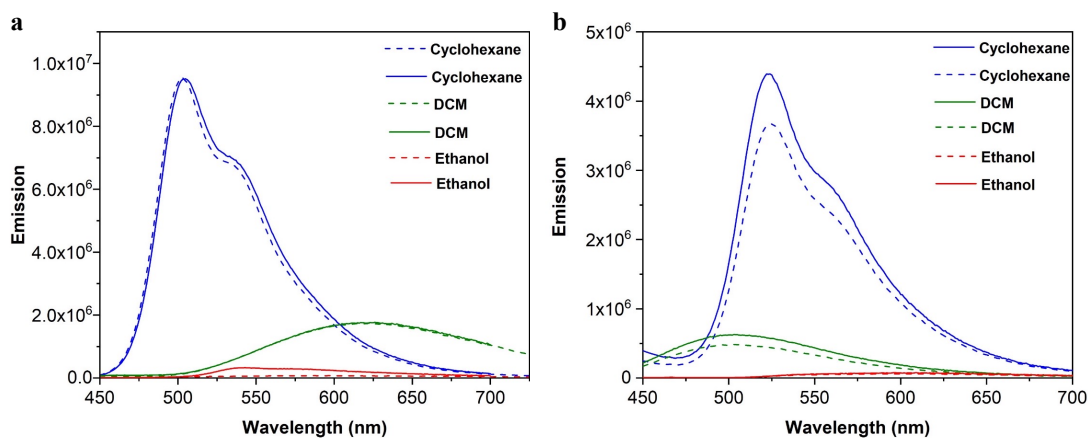


Figure 3.8: Emission spectra of **a) 42** ($\lambda_{\text{exc}} = 404$ nm) and **b) 43** ($\lambda_{\text{exc}} = 410$ nm), (1×10^{-5} M) in cyclohexane, CH₂Cl₂, and ethanol under N₂ at RT (solid line) and in air (dashed line).

Alongside the above measurements, an extended UV-vis absorption and emission solvatochromic study was carried out on **42** and **43** in order to probe the effect solvent polarity has on the absorption and emission spectra (Figure 3.9). For **42** (Figure 3.9a and 3.9b), UV-vis absorption is lowered with increased polarity of solvent, however the effect is minor. An observable quenching and bathochromic shift occurs in the emission profile with increased polarity of solvent. The emission intensity is almost completely quenched in ethanol, and $\lambda_{em} = 600$ nm. The emission profile in toluene exhibits the highest intensity spectrum with $\lambda_{em} = 550$ nm, which is attributed to ICT emission from the triazine moiety of **42**. The UV-vis absorption spectrum in toluene is omitted from the graph due to its lower solvent cut-off of 284 nm, which interferes with the absorption bands of **42** and **43**.

The relationship described above between solvent polarity and UV-vis absorption and emission profiles is not strictly upheld in **43** (Figure 3.9c and 3.9d). UV-vis absorption in tetrahydrofuran and methylene chloride is much more intense than that of cyclohexane, and methanol and ethanol have red shifted profiles with respect to the above solvents. The emission profiles of toluene and cyclohexane are more red shifted than polar solvents tetrahydrofuran, methylene chloride, methanol, and ethanol. The spectral differences for methanol and ethanol (when directly compared to other polar solvents such as tetrahydrofuran) are due to the protic nature of these solvents, which readily donate H^+ . This effect is minor for **42**, but is greatly enhanced in **43** due to the extra cyano functionalities present in the structure.

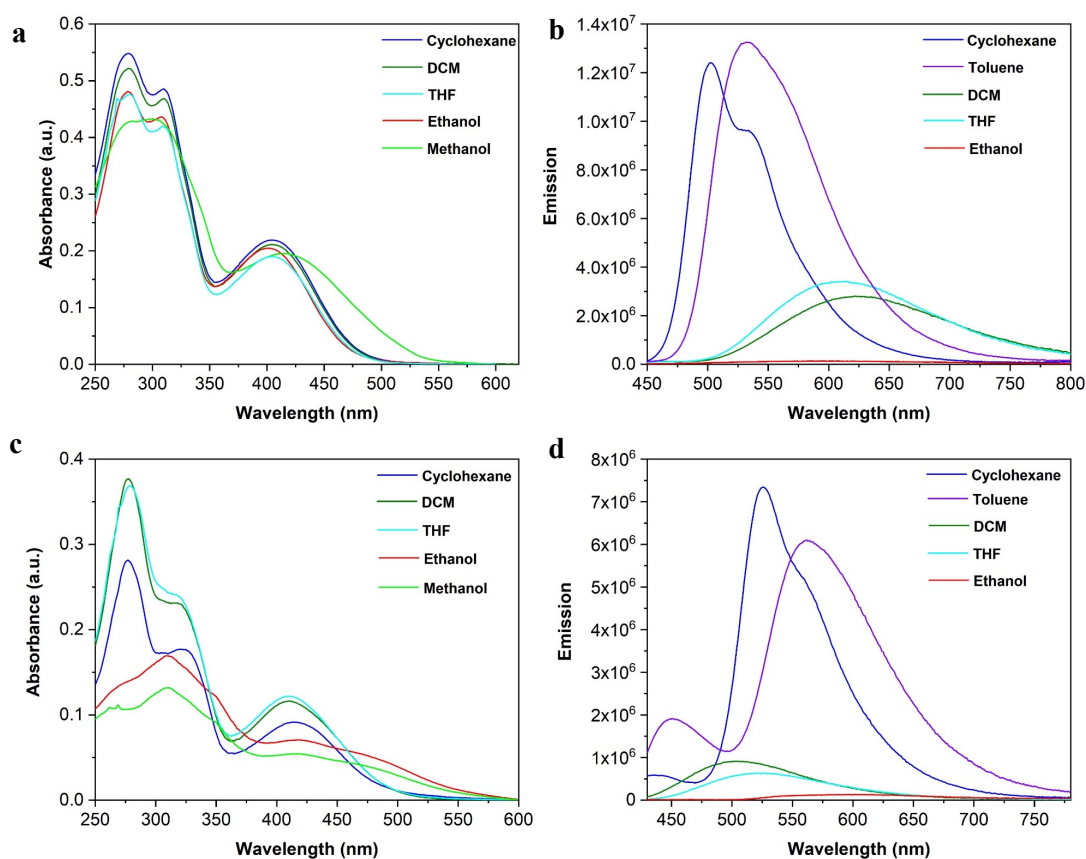


Figure 3.9: *a)* UV-vis absorption and *b)* emission spectra of **42** (1×10^{-5} M) $\lambda_{exc} = 404$ nm in a range of solvents. *c)* UV-vis absorption and *d)* emission spectra of **43** (1×10^{-5} M) $\lambda_{exc} = 410$ nm in a range of solvents. All spectra were run in air and RT.

3.9.2 Acid Titration Studies of **42** and **43**

Trifluoroacetic acid (TFA) UV-vis absorption and emission titration measurements were carried out on **42** and **43** in order to investigate the effect of increasing acid concentration on the absorption and emission spectra (Figure 3.10). The triazine nitrogen atoms possess a lone pair which is positioned perpendicular to the π aromatic cloud of the ring.^{269–271} Thus, the triazine nitrogens could be protonated by the sequential addition of acid. Likewise, the sulfur atom of PTZ could also be protonated.²⁷² Figure 3.10a shows the gradual decrease in absorption of **42** with increasing acid concentration. This trend is mirrored by Figure 3.10b, where gradual emission quenching of $\lambda_{em} = 600$ nm and gradual increase of $\lambda_{em} = 450$ nm with increasing acid concentration is observed. The emission at 600 nm is due to the triazine ICT excited state decay, thus it is quenched with increasing acid concentration, as the triazine rings are protonated. On the contrary, with increasing acid concentration, an increase in

emission intensity at 450 nm is observed, which is attributed to the PTZ LE emission. At 1000 μL 0.1 M TFA, almost complete quenching of emission is observed.

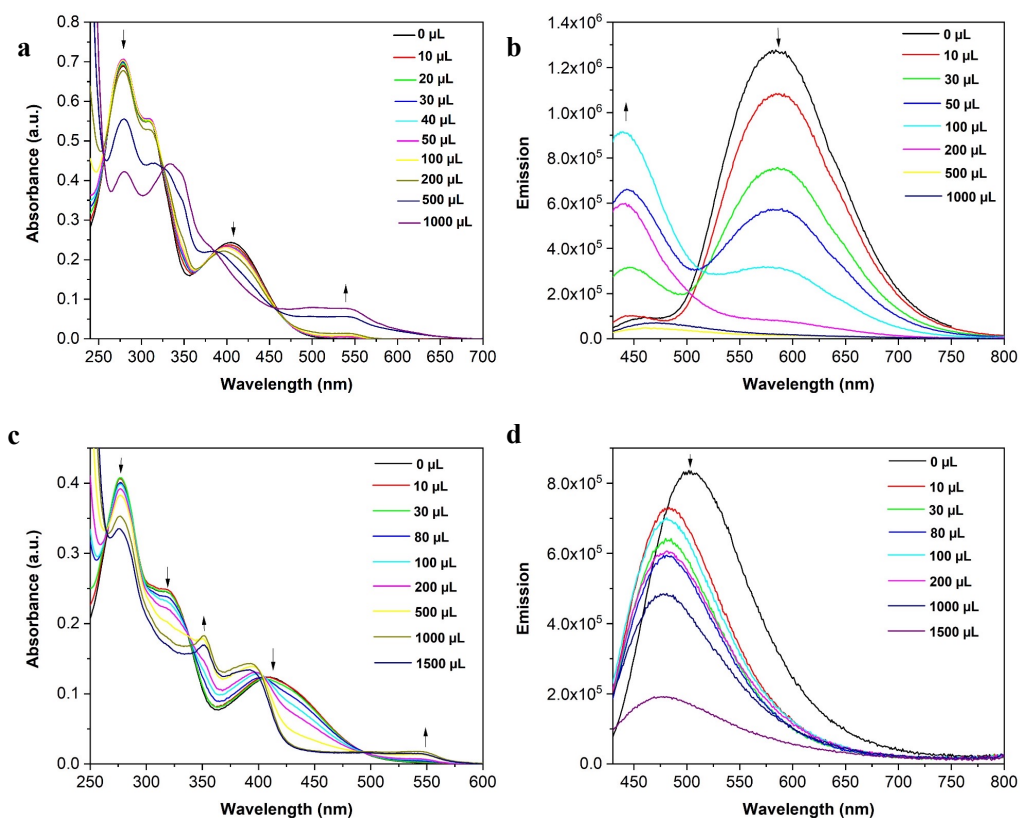


Figure 3.10: **a)** UV-vis absorption and **b)** emission spectral changes of **42** in CH_2Cl_2 (1×10^{-5} M) upon sequential addition of 0.1 M TFA in CH_2Cl_2 , $\lambda_{\text{exc}} = 404$ nm. **c)** UV-vis absorption and **d)** emission spectra of **43** in CH_2Cl_2 (1×10^{-5} M) upon sequential addition of 0.1 M trifluoroacetic acid in CH_2Cl_2 , $\lambda_{\text{exc}} = 410$ nm. All spectra were run in air and at RT.

Figure 3.10c and 3.10d illustrate the effect of increasing acid concentration on **43**. Due to the increased electron withdrawing character of the cyano-functionalised triazine moieties, higher concentrations of TFA were required in order to observe spectral changes, when compared to **42**. The UV-vis absorption spectra of **43** shows less immediate decrease in absorption at 500 μL and 1000 μL . Figure 3.10d presents only one emission band at 500 nm, due to the ICT transition of the triazine. No emission from PTZ LE is observed. The emission bands show a decrease in intensity and a hypsochromic shift with increasing acid concentrations, which was not observed for **42**.

TFA titration studies demonstrated that the most prominent emission band was from the triazine moieties of both **42** and **43**, and could be quenched by protonation. Thus, ICT is occurring within **42** and **43**.

3.9.3 77K Emission Studies of **42** and **43**

Solvatochromic studies and acid titration studies proved that ICT was occurring within **42** and **43**. In order to further prove this, 77K emission studies were carried out in toluene (Figure 3.11). Toluene was chosen in order to be able to directly compare to reported spectra. If charge transfer processes are occurring, the 77K emission spectra should be blue shifted when compared to RT emission measurements.²⁷² This blue shift is observed for both **42** and **43**, proving that the emission profile has ICT character. The reduction in temperature also sees a direct reduction in emission intensity, alluding to temperature's effect on emission profiles. If TADF is occurring within these systems, a reduction in temperature would have an effect on the rate at which RISC can occur (k_{RISC}). The 77K emission studies support the findings of Sections 3.10.1 and 3.10.2 in that ICT is occurring within both **42** and **43**.

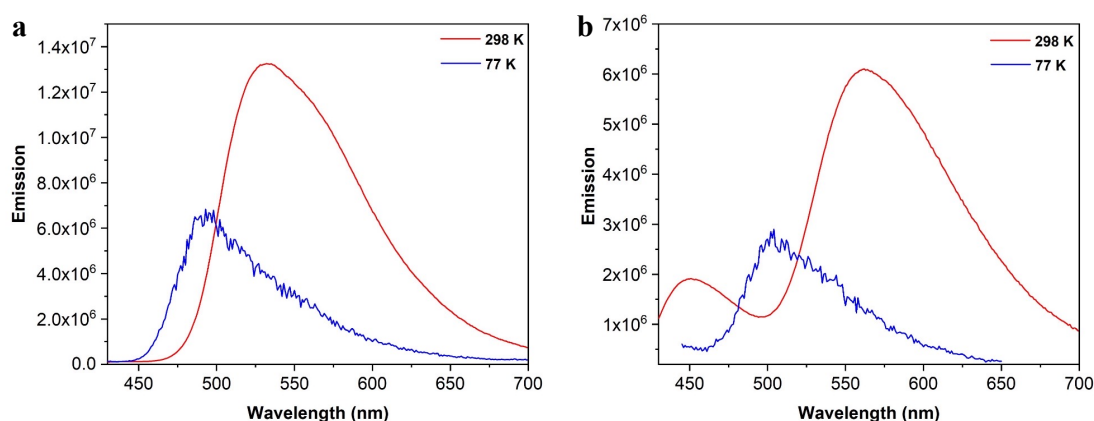


Figure 3.11: Emission spectra of **a) 42** ($\lambda_{\text{exc}} = 404 \text{ nm}$) and **b) 43** ($\lambda_{\text{exc}} = 410 \text{ nm}$), $1.0 \times 10^{-5} \text{ M}$ in toluene at 77K and 298 K. Reduction in temperature sees a direct decrease in emission intensity. The blue graph is due to phosphorescent emission, and the red graph is due to charge transfer induced fluorescence.²⁷³

3.9.4 Lifetime Determination of **42** and **43**

Excited state lifetime measurements were determined for **42** and **43** in cyclohexane, CH_2Cl_2 , and ethanol solutions under nitrogen (Table 3.2, Appendix 2.9-2.10). All lifetimes ranged

from $\tau_1 = 1.5$ to 3.5 ns, which correspond to fluorescence.⁹⁵ No delayed fluorescence was observed following multiple trials. To further explore this, Dr. Xiaoneng Cui carried transient absorption studies in Dalian University of Technology in China in order to study the excited state of **42** and **43** in greater detail. For TADF and RTP and to conclusively prove delayed fluorescence or phosphorescence is occurring, lifetimes of $\tau_1 > 100$ ns are expected.⁸⁸ However, no such lifetimes were observed, proving that a delayed fluorescence component is not present within these systems. Therefore, TADF is not occurring within **42** or **43** *via* RISC. These results are in lieu with the reported **L2.1**, where no delayed fluorescence lifetimes were observed.

The fluorescence lifetimes in the ns range are nevertheless promising: these systems can be utilised as purely fluorescent OLED candidates, as observed for **L2.1**. Usta *et al.* report that **L2.1** emits via the hot exciton mechanism (Sections 1.8.2.4 and 3.5). The hot exciton mechanism was determined by studying natural transition orbitals (NTO's) calculated by TDDFT. Preliminary TDDFT was calculated for this work (Section 3.12 below), however as part of future work NTO calculations are required in order to determine the emission mechanism of **42** and **43**.

Table 3.2: Excited state lifetime determination of **42** and **43**.^a

	Cyclohexane ($\tau_1 = \text{ns}$)	CH ₂ Cl ₂ ($\tau_1 = \text{ns}$)	Ethanol ($\tau_1 = \text{ns}$)
42	3.45	1.93	2.8
43	2.39	1.53	2.33

^a (1×10^{-5} M) in cyclohexane, CH₂Cl₂, and ethanol at $\lambda_{\text{exc}} > 400$ nm. NanoLED with $\lambda_{\text{exc}} = 458$ nm was used to irradiate the samples. All data was fit with mono-exponential decays, with $\chi^2 = 1$. All lifetimes were corrected with an instrument response factor (IRF), which was a non-scattering solution of silica particles.

3.10 Cyclic Voltammetry

In order to be a suitable candidate for use in organic materials, a low reversible oxidation potential is required.²⁷⁴ Cyclic voltammetry measurements were obtained to determine the

oxidation and reduction potentials for **39**, **40**, **41**, **42**, and **43** quoted versus ferrocene/ferrocenium couple (Figure 3.12, Table 3.3). This technique is a facile method to experimentally determine the HOMO (oxidation potential) and LUMO (reduction potential) energies.²⁷⁵ Figure 3.12a illustrates that all compounds possess single electron fully reversible low-lying oxidation potentials, where the phenothiazine moiety is being oxidized.²⁷⁶ A more detailed study of the oxidation potentials reveals a reduction in the HOMO energies in the following trend: **41** > **39** > **40** > **42** > **43**. Thus, by gradual extension of the conjugation and strength of the acceptor moieties the HOMO energy level can be controlled.

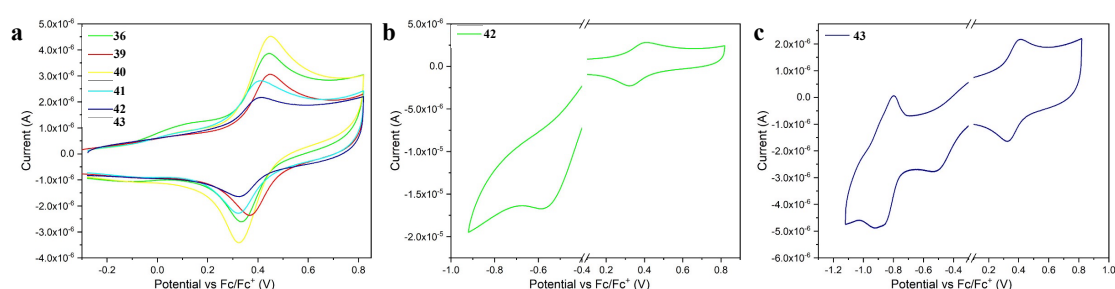


Figure 3.12: Cyclic voltammograms 1×10^{-4} M solutions in CH_2Cl_2 , 0.1 M TBAPF6 as supporting electrolyte. Potential values quoted vs Fc/Fc^+ . **a)** Reversible oxidation potentials of **39**, **40**, **41**, **42**, and **43**. **b)** Reversible oxidation and reduction potentials for **42**. **c)** Reversible oxidation and reduction potentials for **43**.

Compounds **39**, **40**, and **41** have reduction potentials which lie outside of the solvent window, and the voltammograms could not be recorded.

Table 3.3. Cyclic voltammogram data.^a

	$E_{1/2}^{\text{ox}} [b]$	$E_{1/2}^{\text{red}} [b]$	$E_g [b]$	HOMO [b]	LUMO [b]	Bandgap [b]
36	0.555	-	2.446	-5.244	-2.890	2.354
39	0.594	-	2.546	-5.250	-2.996	2.254
40	0.549	-	2.446	-5.248	-2.894	2.354
41	0.524	-0.659	2.446	-5.206	-2.852	2.354
42	0.530	-0.663	2.417	-5.210	-2.827	2.383

43	0.555	-	2.446	-5.244	-2.890	2.354
-----------	-------	---	-------	--------	--------	-------

^a Cyclic voltammogram data of 39, 40, 41, 42, and 43 (1×10⁻⁴ M) in CH₂Cl₂, with 0.1 M TBAPF₆ as supporting electrolyte. Potential values shown vs Fc/Fc⁺. Eg values were calculated using UV-vis absorption onset values. HOMO (eV) = [- (Ep₂^{ox} + 4.8)]. LUMO (eV) = [(HOMO - Eg) + 4.8]. ^bThe values are given in eV.

However, **42** and **43** have reduction potentials within the solvent window (Figure 3.12b and 3.12c, Table 3.3). Compound **42** has an irreversible reduction potential (Figure 3.12b), and compound **43** has a fully reversible reduction potential (Figure 3.12c). In both cases, the reduction occurs at the triazine moiety. This signifies that for **42** and **43**, the LUMO energies are much lower, and thus the HOMO/LUMO bandgap is closer for the triazine-based compounds than that of the benzonitrile-derived compounds. As the HOMO/LUMO gap is analogous with the S₀-S₁ gap, the triazine systems possess a much lower lying singlet excited state than the benzonitriles.

The optical bandgap Eg was calculated with the onset values from the absorption spectra. The HOMO/LUMO bandgap was calculated from E₂^{ox} oxidation and reduction potentials, with E_{1/2}^{ox} and E_{1/2}^{red} potentials quoted in Table 3.3 above.

To experimentally determine the HOMO and LUMO levels, the following formulas (2) and (3) were applied.²⁷⁷ HOMO/LUMO energies were also computationally calculated using DFT calculations (B3LYP|6-31G*). This will be discussed in more detail in Section 3.11.

$$\text{HOMO (eV)} = [- (\text{Ep}_2^{\text{ox}} + 4.8)] \quad (2)$$

$$\text{LUMO (eV)} = [(\text{HOMO} - \text{Eg}) + 4.8] \quad (3)$$

3.11 Computational Studies

TDDFT calculations using B3LYP|6-31G* were carried out by Dr. Xiaoneng Cui, in order to computationally determine the HOMO/LUMO separation and energy levels and to give further insight into this work. In order to design an efficient ICT system, Wang *et al.* proved that the HOMO orbital must be spatially extended to the bridging linkers, whereas the LUMO must be highly spatially localised.¹⁸⁸ As observed in Figure 3.13, the HOMO is spatially extended over the PTZ donor core as well as the acetylene linkers for all of the emitters. However, the LUMO of the benzonitrile emitters **39**, **40**, and **41** is also spatially distributed over the whole molecule. Significant HOMO/LUMO overlap energetically

separates S_1 and T_1 excited states and promotes triplet-triplet annihilation (TTA).¹⁰⁰ A large $\Delta E_{S_1-T_1}$ gap of ~ 0.5 eV is observed for **39**, **40**, and **41**. This gap is too large for rISC to occur, as k_{rISC} is too slow, and cannot compete with prompt fluorescence and non-radiative decay.²⁷⁸

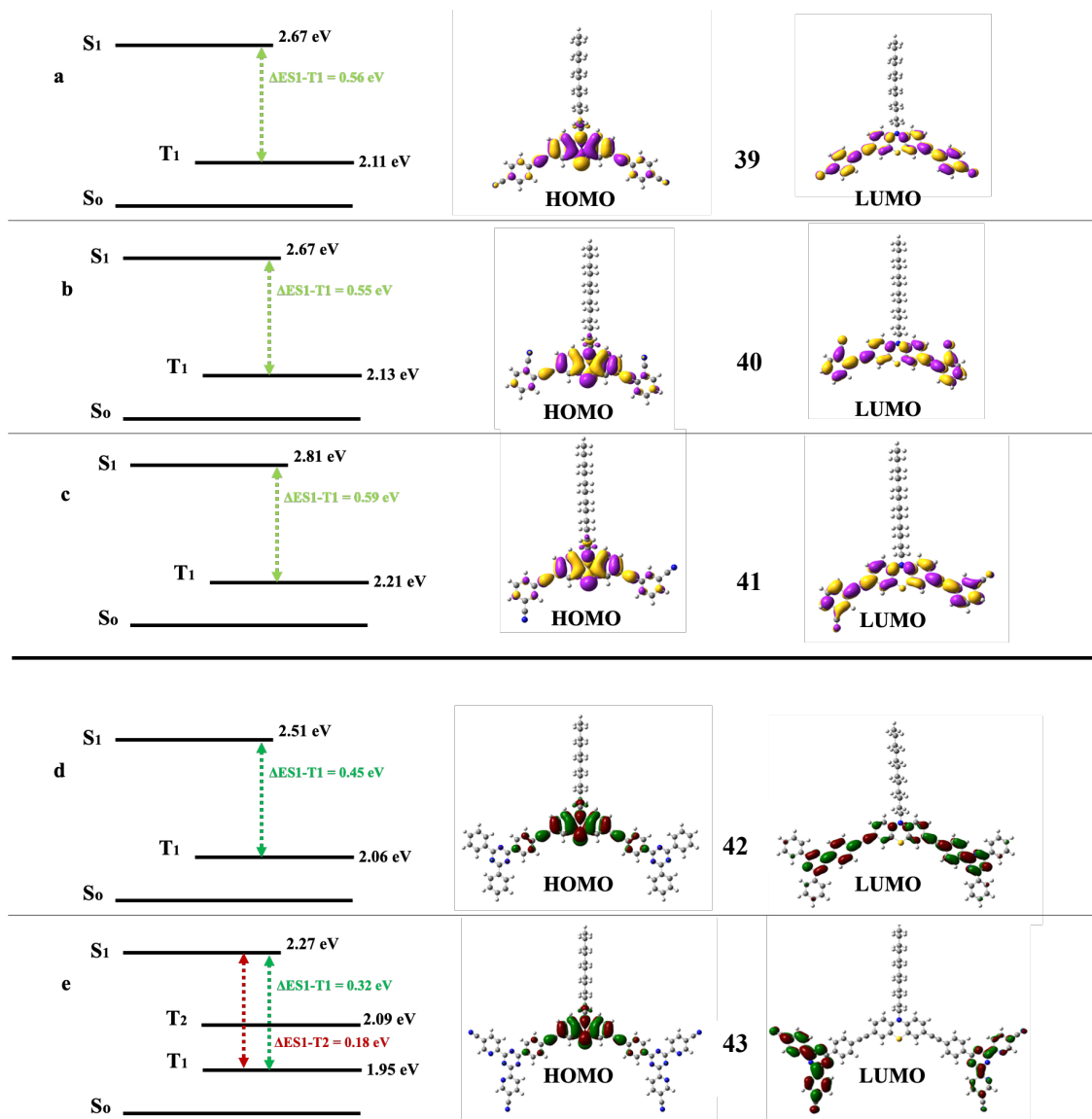


Figure 3.13: Computationally calculated HOMO/LUMO energy levels using B3LYP|6-31G*.

Figure 3.13d demonstrates that for **42**, the HOMO lies on the PTZ core, with some overlap over the acetylene linker, with the LUMO extended over the triazines. The effect of the energy gap law also dictates that non-radiative constant will increase with a red shift in emission spectra,¹⁸⁸ with the emission spectra of **42** significantly red shifted to $\lambda_{em} = 626$ nm.

Even though the HOMO/LUMO overlap is greatly reduced for **42** when compared to the benzonitriles **39-41**, it is still too large for efficient TADF to occur.

Figure 3.13e illustrates that even though the HOMO of **43** is similarly extended over the acetylene linkers as in **42**, a very spatially localized LUMO is observed. Compound **43** is the only one of the series which has a localized LUMO orbital. The HOMO/LUMO band gap is smaller for **43** when directly compared to **39-42**, and the smallest in the series (Table 3.4). Likewise, the $\Delta E_{S_1-T_1}$ gap of 0.32 eV is theoretically small enough to permit rISC, albeit with a reduced k_{rISC} .²⁷⁹ Since no delayed lifetimes were observed using transient absorption measurements, emission *via* the TADF mechanism can be ruled out.

Table 3.4. Complete computationally calculated HOMO and LUMO energy levels for **39-43** using B3LYP|6-31G*.

	HOMO (eV) ^[a]	LUMO (eV) ^[a]	Bandgap (eV) ^[a]
36	-5.2836 (-5.244)	-2.1989 (-2.891)	3.0847 (2.354)
39	-5.0707 (-5.250)	-1.9643 (-2.996)	3.1064 (2.254)
40	-5.2084 (-5.248)	-1.9347 (-2.894)	3.2737 (2.354)
41	-4.9867 (-5.206)	-2.5201 (-2.852)	2.4650 (2.354)
42	-5.2708 (-5.210)	-2.7336 (-2.827)	2.5372 (2.383)
43	-5.2836 (-5.244)	-2.1989 (-2.891)	3.0847 (2.354)

^a Experimentally calculated CV values are given in parentheses.

The role of the higher triplet excited states (T_n) must be must not be excluded from the mechanistic argument for **43**. For all emitters the higher triplet excited states are closer in energy than the lowest triplet excited state, but compounds **39-42** have some degree of HOMO/LUMO overlap which serves to further energetically separate the excited state levels. Compound **43** is the only emitter with a localised LUMO and spatially separate HOMO and LUMO orbitals. The hot exciton mechanism of emission is one whereby upconversion of electrical excited triplet excitons can occur between higher energy levels (T_n) and S_1 resulting in short delayed lifetimes in nanosecond range.²⁸⁰ This mechanism does not strictly obey Kasha's Rule, nevertheless it has been observed in a myriad of organic systems.²⁸¹⁻²⁸³ For this reason, the TDDFT calculations presented herein serve as exploratory

work, and further studies such as NTO determination are necessary to study the role of the higher triplet excited states on the emission properties of **43**.

When considering the photophysical measurements alongside the above preliminary TDDFT calculations, it is clear that ICT is occurring within **39-43**, with triplet character only accessed in emitter **43**. Furthermore, the incorporation of cyano functionality in the *para*-position of the triazine acceptor in **43** has resulted in a highly localised LUMO orbital. These findings will form the basis of further research Chapter Four, and when designing other novel families of highly luminescent emitters as OLED candidates.

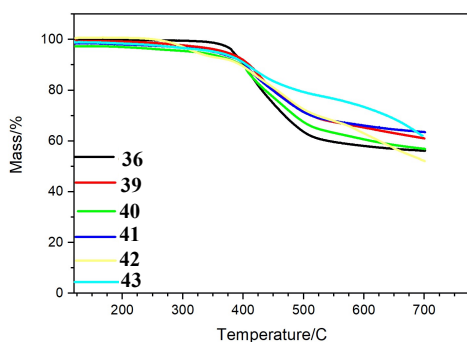
3.12 Thermal Studies

In order to test the compounds' validity as OLED candidates, their thermal properties were studied. Device fabrication methods such as vacuum thermal deposition require organic compounds to be stable beyond 200 °C.²⁸⁴ Thermogravimetric analysis was utilised to determine decomposition temperatures of the emitters (Figure 3.14 below).

Table 3.5: Thermogravimetric analysis (TGA) data for **36**, and **39-43** under an N₂ atmosphere.

Compound	Temperature °C
36	375
39	380
40	380
41	380
42	265, 380, 550
43	377, 604

Figure 3.14: Thermogravimetric analysis (TGA) of **36**, and **39-43** under an N₂ atmosphere.



An identical TGA method was utilised for all the emitters (as described in Chapter 2, Section 2.4.5). Table 3.5 provides a summary of all decomposition temperatures recorded. All emitters observe the first decomposition step ~ 380 °C resulting in $\sim 40\%$ loss in mass, which is commonly observed in phenothiazine containing systems.^{201,233,285} The triazine compounds observe a second decomposition step between 550-600 °C resulting in a further $\sim 10\%$ loss in mass, which could be due to the triazine ring systems collapsing. Therefore, all emitters are stable beyond 200 °C which would make them applicable for OLED device fabrication.

3.13 Conclusions

Five novel A- π -D- π -A systems were successfully synthesized, with a PTZ donor centre and varying acceptor appendages. An acetylene linker was incorporated into all structures to ensure planarity, full conjugation extension, and HOMO/LUMO orbital separation. All compounds synthesised possess ICT emissive character and are green to orange emitters. The benzonitrile emitters **39-41** were found to be highly luminescent ($\Phi_F=0.77$ for **39**, $\Phi_F=0.88$ for **40**, and $\Phi_F=0.84$ for **41**) but possessed no triplet excited state character and were purely fluorescent. Exploration into the most effective positioning of the electron-withdrawing cyano moiety proved that the *para*- positioning has the largest effect on the emissive properties of the materials. The compounds also exhibited highly overlapping HOMO/LUMO orbitals, resulting in a wide bandgap.

Following that, two triazine containing A- π -D- π -A systems were synthesized, with a cyano-functionalized triazine in the *para*- position. The emission of triazine **42** possesses ICT character and is an orange emitter with $\lambda_{em}=626$ nm, but it did not show TADF behavior due to its HOMO/LUMO overlap, no triplet excited state character, and an increased $\Delta E_{S_1-T_1}$. Successful ICT is also observed for **43**, due a localized LUMO, evident triplet excited state character, and a small $\Delta E_{S_1-T_1}$ gap. However, both **42** and **43** suffer a sufficiently reduced PLQY (0.45 for **42**, and 0.41 for **43**), due to their extended conjugation resulting in more non-radiative decay pathways.

It can be understood from this body of work, that utilizing an acetylene linker as a means to separate donor and acceptor structures is an effective method to induce ICT, but not an effective method in fully separating HOMO and LUMO frontier molecular orbitals. Further

extending the structure by incorporation of stronger accepting structures such as the use of the triazine moiety resulted in compounds which were too conjugated, which then suffered reduced PLQY values. Incorporation of the cyano moiety in the *para*- position resulted in highly localised LUMO orbitals, as observed from TDDFT. Learning from these preliminary findings, more efficient systems were designed for Chapter Four in search of highly luminescent novel organic materials as OLED candidates.

3.14 Future Work

All of the photophysical measurements were carried out in solution, and thus film formation is envisaged in order to study the photoluminescent properties in the solid state. Further computational studies and NTO analysis is required for **43** to study the role of the higher triplet excited states on the emission mechanism and in the resulting emission profiles.

In order to progress the ideas explored in this work, novel acceptor and donor structures are theorised within Chapter Four. Novel methodologies are required to synthesise more twisted symmetric and asymmetric systems with varied donor and acceptor structures. This variation and asymmetry is hoped to increase the PLQY and the excited state lifetimes (τ), and the twisted nature will serve to ensure full spatial separation of the HOMO/LUMO orbitals.

Further afield and outside the scope of this work, compounds **39-43** could be further applied as semiconducting materials and molecular diodes due to their extended conjugated structures.^{9,30}

3.15 References

- 1 R. Pashazadeh, P. Pander, A. Bucinskas, P. J. Skabara, F. B. Dias and J. V. Grazulevicius, *Chem. Commun.*, 2018, 13857–13860.
- 2 P. Pander, A. Swist, R. Motyka, J. Soloducho, F. B. Dias and P. Data, *J. Mater. Chem. C*, 2018, **6**, 5434–5443.
- 3 Y.-K. Wang, C.-C. Huang, S. Kumar, S.-F. Wu, Y. Yuan, A. K. Aziz Khan, Z.-Q. Jiang, M.-K. Fung and L.-S. Liao, *Mater. Chem. Front.*, 2019, **3**, 161–167.
- 4 Y. Tao, K. Yuan, T. Chen, P. Xu, H. Li, R. Chen, C. Zheng, L. Zhang and W. Huang, *Adv. Mater.*, 2014, **26**, 7931–7958.
- 5 Q. Zhang, H. Kuwabara, W. J. Potscavage Jr, S. Huang, Y. Hatae, T. Shibata and C. Adachi, *J. Am. Chem. Soc.*, 2014, **136**, 18070–18081.
- 6 S. Ghosh, R. Raveendran, A. Saeki, S. Seki, M. Namboothiry and A. Ajayaghosh, *ACS Appl. Mater. Interfaces*, 2018, **11**, 1088–1095.
- 7 C. Maglione, A. Carella, R. Centore, P. Chávez, P. Lévêque, S. Fall and N. Leclerc, *Dye. Pigment.*, 2017, **141**, 169–178.
- 8 Y.-T. Lee, P.-C. Tseng, T. Komino, M. Mamada, R. J. Ortiz, M. Leung, T.-L. Chiu, C.-F. Lin, J.-H. Lee and C. Adachi, *ACS Appl. Mater. Interfaces*, 2018, **10**, 43842–43849.
- 9 Y.-T. Lee, P.-C. Tseng, T. Komino, M. Mamada, R. J. Ortiz, M. Leung, T.-L. Chiu, C.-F. Lin, J.-H. Lee, C. Adachi, C.-T. Chen and C.-T. Chen, *ACS Appl. Mater. Interfaces*.
- 10 Z. Cai, M. Zhou, B. Li, Y. Chen, F. Jin and J. Huang, *New J. Chem.*, 2014, **38**, 3042–3049.
- 11 P. Ganesan, R. Ranganathan, Y. Chi, X. K. Liu, C. S. Lee, S. H. Liu, G. H. Lee, T. C. Lin, Y. T. Chen and P. T. Chou, *Chem. - A Eur. J.*, 2017, **23**, 2858–2866.
- 12 Y. Geng, A. D'Aleo, K. Inada, L. S. Cui, J. U. Kim, H. Nakanotani and C. Adachi, *Angew. Chemie - Int. Ed.*, 2017, **56**, 16536–16540.
- 13 J. Li, W. Wu, J. Yang, J. Tang, Y. Long and J. Hua, *Sci. China Chem.*, 2011, **54**, 699–706.
- 14 E. A. Onoabedje, S. A. Egu, M. A. Ezeokonkwo and U. C. Okoro, *J. Mol. Struct.*, 2019, **1175**, 956–962.
- 15 G. Bagdžiunas, G. Grybauskaite, N. Kostiv, K. Ivaniuk, D. Volyniuk and A. Lazauskas, *RSC Adv.*, 2016, **6**, 61544–61554.
- 16 M. Fingerle, M. Hemgesberg, Y. Schmitt, S. Lach, M. Gerhards, W. R. Thiel and C. Ziegler, *ChemPhysChem*, 2015, **16**, 1996–2005.
- 17 R. L. Mitchell, H. R. Costantino, A. Sileno, T. Duffy, G. Brandt and S. C. Quay, *Drug Dev. Res.*, 2008, **69**, 143–152.
- 18 K. Jongseong, K. Shanmugasundaram, R. K. Chitumalla, J. Jang and Y. Choe, *J. Lumin.*, 2018, **197**, 383–388.
- 19 Z. Yang, D. Shao, J. Li, L. Tang and C. Shao, *Spectrochim. Acta - Part A Mol.*

- Biomol. Spectrosc.*, 2018, **196**, 385–391.
- 20 N. Aizawa, C. J. Tsou, I. S. Park and T. Yasuda, *Polym. J.*, 2017, **49**, 197–202.
- 21 H. Cao, Z. Chen, Y. Liu, B. Qu, S. Xu, S. Cao, Z. Lan, Z. Wang and Q. Gong, *Synth. Met.*, 2007, **157**, 427–431.
- 22 S. S. Deshpande, H. S. Kumbhar and G. S. Shankarling, *Spectrochim. Acta - Part A Mol. Biomol. Spectrosc.*, 2017, **174**, 154–163.
- 23 C. Poriel, J. Rault-Berthelot, S. Thiery, C. Quinton, O. Jeannin, U. Biapo, D. Tondelier and B. Geffroy, *Chem. - A Eur. J.*, 2016, **22**, 17930–17935.
- 24 D. B. Shinde, J. K. Salunke, N. R. Candeias, F. Tinti, M. Gazzano, P. P. Wadgaonkar, A. Priimagi, N. Camaioni and P. Vivo, *Sci. Rep.*, 2017, **7**, 1–10.
- 25 Y. C. Chen, Y. T. Kuo and C. J. Liang, *RSC Adv.*, 2018, **8**, 9783–9789.
- 26 J. K. Salunke, F. L. Wong, K. Feron, S. Manzhos, M. F. Lo, D. Shinde, A. Patil, C. S. Lee, V. A. L. Roy, P. Sonar and P. P. Wadgaonkar, *J. Mater. Chem. C*, 2016, **4**, 1009–1018.
- 27 J. Daub, R. Engl, J. Kurzawa, S. E. Miller, S. Schneider, A. Stockmann and M. R. Wasielewski, *J. Phys. Chem. A*, 2001, **105**, 5655–5665.
- 28 I. H. Lee and J. Y. Lee, *RSC Adv.*, 2015, **5**, 97903–97909.
- 29 K. Gunasekar, W. Cho, D. X. Long, S. S. Reddy, M. Song, Y. Y. Noh and S. H. Jin, *Adv. Electron. Mater.*, 2016, **2**, 1–8.
- 30 J. S. Ward, R. S. Nobuyasu, A. S. Batsanov, P. Data, A. P. Monkman, F. B. Dias and M. R. Bryce, *Chem. Commun.*, 2016, **52**, 2612–2615.
- 31 I. Marghad, D. H. Kim, X. Tian, F. Mathevet, C. Gosmini, J. C. Ribierre and C. Adachi, *ACS Omega*, 2018, **3**, 2254–2260.
- 32 T. Personality, R. Steinmayr, A. F. Weidinger and A. Wigfield, , DOI:10.1016/j.dt.2018.04.004.
- 33 D.-H. Yun, H.-S. Yoo, S.-W. Heo, H.-J. Song, D.-K. Moon, J.-W. Woo and Y.-S. Park, *J. Ind. Eng. Chem.*, 2013, **19**, 421–426.
- 34 B. Nagarajan, S. Kushwaha, R. Elumalai, S. Mandal, K. Ramanujam and D. Raghavachari, *J. Mater. Chem. A*, 2017, **5**, 10289–10300.
- 35 H. Tanaka, K. Shizu, H. Nakanotani and C. Adachi, *Chem. Mater.*, 2013, **25**, 3766–3771.
- 36 H. Tanaka, K. Shizu, H. Nakanotani and C. Adachi, *J. Phys. Chem. C*, 2014, **118**, 15985–15994.
- 37 F. B. Dias, K. N. Bourdakos, V. Jankus, K. C. Moss, K. T. Kamtekar, V. Bhalla, J. Santos, M. R. Bryce and A. P. Monkman, *Adv. Mater.*, 2013, **25**, 3707–3714.
- 38 T. Chen, L. Zheng, J. Yuan, Z. An, R. Chen, Y. Tao, H. Li, X. Xie and W. Huang, *Sci. Rep.*, 2015, **5**, 1–11.
- 39 J. Hu, C. Zhao, T. Zhang, X. Zhang, X. Cao, Q. Wu, Y. Chen, D. Zhang, Y. Tao and W. Huang, *Adv. Opt. Mater.*, 2017, **5**, 1–7.

- 40 S. Gu, J. Guo, Q. Huang, J. He, Y. Fu, G. Kuang, C. Pan and G. Yu, *Macromolecules*, 2017, **50**, 8512–8520.
- 41 Y. Xiang, S. Gong, Y. Zhao, X. Yin, J. Luo, K. Wu, Z. H. Lu and C. Yang, *J. Mater. Chem. C*, 2016, **4**, 9998–10004.
- 42 T. Wang, H. Sun, T. Lu, F. Li, D. Liu, W. Li, X. Zhou, L. Wang, T. Wang, H. Sun, T. Lu, F. Li, W. Hu, W. Li, X. Zhou, L. Wang, C. N. Bridgmohan, L. Wang, D. Liu, W. Li, X. Zhou and W. Hu, *Dye. Pigment.*, 2017, **139**, 264–273.
- 43 L. Zhang, L. Zou, J. Xiao, P. Zhou, C. Zhong, X. Chen, J. Qin, I. F. A. Mariz and E. Maçôas, *J. Mater. Chem.*, 2012, **22**, 16781–16790.
- 44 C. H. Chang, M. C. Kuo, W. C. Lin, Y. T. Chen, K. T. Wong, S. H. Chou, E. Mondal, R. C. Kwong, S. Xia, T. Nakagawa and C. Adachi, *J. Mater. Chem.*, 2012, **22**, 3832–3838.
- 45 F. Pop, F. Riobé, S. Seifert, T. Cauchy, J. Ding, N. Dupont, A. Hauser, M. Koch and N. Avarvari, *Inorg. Chem.*, 2013, **52**, 5023–5034.
- 46 Z. Bin Cai, L. F. Liu, M. Zhou, B. Li and Y. Chen, *Dye. Pigment.*, 2014, **102**, 88–93.
- 47 R. Braveenth, D. H. Ahn, J. H. Han, J. S. Moon, S. W. Kim, H. Lee, W. Qiong, J. H. Kwon and K. Y. Chai, *Dye. Pigment.*, 2018, **157**, 377–384.
- 48 X. K. Liu, C. J. Zheng, M. F. Lo, J. Xiao, Z. Chen, C. L. Liu, C. S. Lee, M. K. Fung and X. H. Zhang, *Chem. Mater.*, 2013, **25**, 4454–4459.
- 49 K. Matsuoka, K. Albrecht, A. Nakayama, K. Yamamoto and K. Fujita, *ACS Appl. Mater. Interfaces*, 2018, **10**, 33343–33352.
- 50 T. Lin, Q. Song, Z. Liu, B. Chu, W. Li, Y. Luo, C. S. Lee, Z. Su and Y. Li, *Synth. Met.*, 2017, **234**, 95–99.
- 51 Y. Wang, W. Liu, J. Deng, G. Xie, Y. Liao, Z. Qu, H. Tan, Y. Liu and W. Zhu, *Chem. - An Asian J.*, 2016, **11**, 2555–2563.
- 52 B. Huang, Q. Qi, W. Jiang, J. Tang, Y. Liu, W. Fan, Z. Yin, F. Shi, X. Ban, H. Xu and Y. Sun, *Dye. Pigment.*, 2014, **111**, 135–144.
- 53 T. Lu, H. Sun, N. D. Colley, C. N. Bridgmohan, D. Liu, W. Li, W. Hu, X. Zhou, T. Wang and L. Wang, *Dye. Pigment.*, 2017, **136**, 404–415.
- 54 S. Narayanan, A. Abbas, C. P. Anjali, S. Xavier, C. S. Kartha, K. S. Devaky, K. Sreekumar and R. Joseph, *J. Lumin.*, 2018, **198**, 449–456.
- 55 G. V. Baryshnikov, S. V. Bondarchuk, V. A. Minaeva, H. Ågren and B. F. Minaev, *J. Mol. Model.*, 2017, **23**, 1–8.
- 56 J. Luo, J. Lu and J. Zhang, *J. Mater. Chem. A*, 2018, **6**, 15154–15161.
- 57 V. M. Vidya, A. Tripathi and C. Prabhakar, *J. Mol. Struct.*, 2019, **1176**, 855–864.
- 58 D. Branowska, E. Olender, W. Wysocki, Z. Karczmarzyk, I. Bancercz, P. Ledwon, M. Lapkowski, B. Mirosław, Z. Urbańczyk-Lipkowska and P. Kalicki, *Electrochim. Acta*, 2016, **214**, 19–30.
- 59 H. Tanaka, K. Shizu, H. Miyazaki and C. Adachi, *Chem. Commun.*, 2012, **48**,

11392–11394.

- 60 C. J. Shih, C. C. Lee, T. H. Yeh, S. Biring, K. K. Kesavan, N. R. Al Amin, M. H. Chen, W. C. Tang, S. W. Liu and K. T. Wong, *ACS Appl. Mater. Interfaces*, 2018, **10**, 24090–24098.
- 61 Y. Duan, X. Xu, H. Yan, W. Wu, Z. Li and Q. Peng, *Adv. Mater.*, 2017, **29**, 1605115.
- 62 X. K. Chen, Y. Tsuchiya, Y. Ishikawa, C. Zhong, C. Adachi and J. L. Brédas, *Adv. Mater.*, 2017, **29**, 1–8.
- 63 T. Wang, H. Sun, L. Zhang, N. D. Colley, C. N. Bridgmohan, D. Liu, W. Hu, W. Li, X. Zhou and L. Wang, *Dye. Pigment.*, 2017, **139**, 601–610.
- 64 J. I. Nishide, H. Nakanotani, Y. Hiraga and C. Adachi, *Appl. Phys. Lett.*, 2014, **104**, 1–6.
- 65 L. Stagi, D. Chiriu, M. Scholz, C. M. Carbonaro, R. Corpino, A. Porcheddu, S. Rajamaki, G. Cappellini, R. Cardia and P. C. Ricci, *Spectrochim. Acta Part A Mol. Biomol. Spectrosc.*, 2017, **183**, 348–355.
- 66 X. Hu, Y. Guo, D. Wang, X. Pu and Q. Chen, .
- 67 J.-R. Cha, M.-S. Gong, T. J. Lee, T. H. Ha and C. W. Lee, *J. Korean Phys. Soc.*, 2018, **72**, 873–879.
- 68 H. Usta, D. Alimli, R. Ozdemir, S. Dabak, Y. Zorlu, F. Alkan, E. Tekin and A. Can, *ACS Appl. Mater. Interfaces*, 2019, **11**, 44474–44486.
- 69 H. Usta, D. Alimli, R. Ozdemir, E. Tekin, F. Alkan, R. Kacar, A. G. Altas, S. Dabak, A. G. Gürek, E. Mutlugun, A. F. Yazici and A. Can, *J. Mater. Chem. C*, 2020, **8**, 8047–8060.
- 70 L. Xue, B. Cui, S. Xie and S. Yin, *J. Phys. Chem. Lett*, 2019, **10**, 308.
- 71 S. Ghosh, R. Raveendran, A. Saeki, S. Seki, M. Namboothiry and A. Ajayaghosh, *ACS Appl. Mater. Interfaces*.
- 72 A. Streitwieser, *Chem. Rev.*, 1956, **56**, 571–752.
- 73 D. H. Yun, H. S. Yoo, S. W. Heo, H. J. Song, D. K. Moon, J. W. Woo and Y. S. Park, *J. Ind. Eng. Chem.*, 2013, **19**, 421–426.
- 74 M. Solà, *Front. Chem.*, 2013, **1**, 4–11.
- 75 C. C. Wamser and L. T. Scott, *J. Chem. Educ.*, 1985, **62**, 650.
- 76 J. H. Incremona and J. C. Martin, *J. Am. Chem. Soc.*, 1970, **92**, 627–634.
- 77 S. Thorand and N. Krause, *J. Org. Chem.*, 1998, **63**, 8551–8553.
- 78 A. Elangovan, Y. H. Wang and T. I. Ho, *Org. Lett.*, 2003, **5**, 1841–1844.
- 79 K. Sonogashira, *J. Organomet. Chem.*, 2002, **653**, 46–49.
- 80 A. S. N. Miyaura, *Org. Synth.*, 1990, **68**, 130.
- 81 J. Liao, Y. Xu, H. Zhao, Q. Zong and Y. Fang, *Org. Electron. physics, Mater. Appl.*, 2017, **49**, 321–333.

- 82 Linus Pauling, *Am. Mineral.*, 1980, **65**, 321–323.
- 83 D. G. Chen, T. C. Lin, Y. A. Chen, Y. H. Chen, T. C. Lin, Y. T. Chen and P. T. Chou, *J. Phys. Chem. C*, 2018, **122**, 12215–12221.
- 84 B. Nagarajan, S. Kushwaha, R. Elumalai, S. Mandal, K. Ramanujam and D. Raghavachari, *J. Mater. Chem. A*, 2017, **5**, 10289–10300.
- 85 W. H. Melhuish, *J. Phys. Chem.*, 1961, **65**, 229–235.
- 86 T. J. Penfold, F. B. Dias and A. P. Monkman, *Chem. Commun.*, 2018, **54**, 3926–3935.
- 87 G. P. Sheeja Mol, D. D. Arul Dhas, I. Hubert Joe and S. Balachandran, *Chem. Phys. Lett.*, 2016, **654**, 125–134.
- 88 R. Huang, J. Avó, T. Northey, E. Channing-Pearce, P. L. Dos Santos, J. S. Ward, P. Data, M. K. Etherington, M. A. Fox, T. J. Penfold, M. N. Berberan-Santos, J. C. Lima, M. R. Bryce and F. B. Dias, *J. Mater. Chem. C*, 2017, **5**, 6269–6280.
- 89 F. B. Dias, J. Santos, D. R. Graves, P. Data, R. S. Nobuyasu, M. A. Fox, A. S. Batsanov, T. Palmeira, M. N. Berberan-Santos, M. R. Bryce and A. P. Monkman, *Adv. Sci.*, 2016, **3**, 1–10.
- 90 T. J. Mooibroek and P. Gamez, *Inorganica Chim. Acta*, 2007, **360**, 381–404.
- 91 J. S. Costa, A. G. Castro, R. Pievo, O. Roubeau, B. Modéc, B. Kozlevčar, S. J. Teat, P. Gamez and J. Reedijk, *CrystEngComm*, 2010, **12**, 3057–3064.
- 92 V. Maheshwari, P. A. Marzilli and L. G. Marzilli, *Inorg. Chem.*, 2008, **47**, 9303–9313.
- 93 B. Li, Y. Ge, Y. Wu, J. Chen, H. H. K. Xu, M. Yang, M. Li, B. Ren, M. Feng and M. D. Weir, *Molecules*, 2017, **22**, 2013.
- 94 M. Y. Wong, S. Krotkus, G. Copley, W. Li, C. Murawski, D. Hall, G. J. Hedley, M. Jaricot, D. B. Cordes, A. M. Z. Slawin, Y. Olivier, D. Beljonne, L. Muccioli, M. Moral, J. C. Sancho-Garcia, M. C. Gather, I. D. W. Samuel and E. Zysman-Colman, *ACS Appl. Mater. Interfaces*, 2018, **10**, 33360–33372.
- 95 M. Poddar, P. Gautam, Y. Rout and R. Misra, *Dye. Pigment.*, 2017, **146**, 368–373.
- 96 F. Marken, A. Neudeck and A. M. Bond, *Electroanal. Methods Guid. to Exp. Appl.*, 2010, 57–106.
- 97 A. Shafiee, M. M. Salleh and M. Yahaya, *Sains Malaysiana*, 2011, **40**, 173–176.
- 98 Y. Hua, S. Chang, D. Huang, X. Zhou, X. Zhu, J. Zhao, T. Chen, W. Y. Wong and W. K. Wong, *Chem. Mater.*, 2013, **25**, 2146–2153.
- 99 J. M. Mewes, *Phys. Chem. Chem. Phys.*, 2018, **20**, 12454–12469.
- 100 L. S. Cui, H. Nomura, Y. Geng, J. U. k. Kim, H. Nakanotani and C. Adachi, *Angew. Chemie - Int. Ed.*, 2017, **56**, 1571–1575.
- 101 C. Fu, S. Luo, Z. Li, X. Ai, Z. Pang, C. Li, K. Chen, L. Zhou, F. Li and Y. Huang, *Chem. Commun.*, 2019, **55**, 6317–6320.
- 102 J. Jayabharathi, S. Panimozhi and V. Thanikachalam, *RSC Adv.*, 2018, **8**, 37324–

37338.

- 103 J. Jayabharathi, S. Panimozhi and V. Thanikachalam, *Sci. Rep.*, 2020, **10**, 1–11.
- 104 C. Zhou, S. Xiao, M. Wang, W. Jiang, H. Liu, S. Zhang and B. Yang, *Front. Chem.*, 2019, **7**, 1–10.
- 105 B. Geffroy, P. Le Roy and C. Prat, *Polym. Int.*, 2006, **55**, 572–582.
- 106 M. Okazaki, Y. Takeda, P. Data, P. Pander, H. Higginbotham, A. P. Monkman and S. Minakata, *Chem. Sci.*, 2017, **8**, 2677–2686.
- 107 C. Joachim, J. K. Gimzewski and A. Aviram, *Nature*, 2000, **408**, 541–548.
- 108 P. T. Mathew and F. Fang, *Engineering*, 2018, **4**, 760–771.

Chapter Four

Study of Twisted Azaborine Containing Small Organic Molecules for Thermally Activated Delayed Fluorescence Organic Light Emitting Diodes

4.0 Introduction

The purpose of this chapter is to gain an understanding into twisted small organic compounds: to study their design, synthesis, and their resulting photophysical properties. An induced steric twist within a donor-acceptor structure is a known effective method of separating HOMO/LUMO frontier molecular orbitals and inducing intramolecular charge transfer (ICT). In contrast to Chapter Three, the vision for this work is to understand the effects of the sterically induced structural twists between the donor and acceptor moieties on the resulting photophysical properties of the compounds.

A different route of utilising a central accepting core (rather than a central donor core as in Chapter Three) is adopted, with *N*-heterocyclic donors connected to the central azaborine acceptor core either *via* a single σ -bond or a phenyl π -bridge. The azaborine heterocycle has been sparingly reported in the literature, both as a known structure and its subsequent use as an acceptor within donor-acceptor compounds for organic light emitting diode (OLED) applications. The reason for the limited use and application of azaborines is due to synthetic challenges, both in synthesis of the heterocycle itself and further structural modifications. These synthetic challenges are addressed herein, in an attempt to expand the current azaborine family of compounds and develop novel synthetic methodologies. Furthermore, the use of a single σ -bond when compared to a phenyl π -bridge as a means to covalently connect donor and acceptor moieties is studied. The donors of choice for this work can be separated into three categories: amine donors with a conjugated linker, amine donors without a conjugated linker, and PAH-type donors, with ranging steric bulk and donor abilities. It is envisaged that the materials designed for this work will make excellent candidates as thermally activated delayed fluorescence (TADF) blue emitting OLED materials.

4.1 Three-Coordinate Boron

Boron contains one valence electron less than carbon which results in an empty p_z orbital. A boron atom can participate in either three-coordinate or four-coordinate bonding, with an ability to swap between both bonding forms.²⁸⁶ Four-coordinate boron has a limited use in OLED applications due to its reduced electron accepting ability, however recently some reports have been published.²⁸⁷ For the purpose of this chapter, the focus will be exclusively on three-coordinate boron, and its incorporation into novel donor-acceptor structures.

Three-coordinate boron has a trigonal planar geometry analogous with a carbonium ion; incorporation of which results in strong Lewis acidic properties and resulting electron accepting structures being highly sought after in target OLED materials.²⁸⁸ Trivalent boron has the ability to simultaneously act as a π -electron acceptor and a σ -electron donor, with boron containing heterocycles behaving as anti-aromatic species.²⁸⁹ However, structures containing boron are open to nucleophilic attack, which compromises structural integrity of the material. One way to overcome this challenge is to introduce large bulky substituents on the boron atom or rigidify the structure in order to protect it from undesired side reactions and avoid decomposition (Figure 4.0). A useful outcome of the reactivity with nucleophiles resulted in application of three-coordinate boron in sensing. Bulky substitution or rigidification does not protect the boron atom from nucleophiles such as F^- and CN^- , resulting in boron-containing materials acting as selective F^- and CN^- chemosensors.²⁹⁰

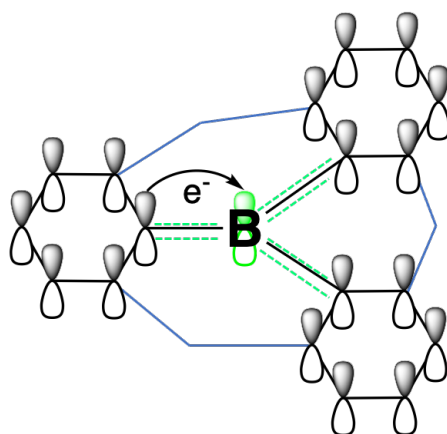


Figure 4.0: A three-coordinate boron centre. Blue lines indicate additional structural constraints which can be introduced to protect the boron centre from undesired side reactions. The empty p_z orbital on the central boron atom is annotated in green, with green dashed lines signifying π -conjugation with the adjacent carbon atoms.²⁹¹

Three-coordinate boron has found uses in an array of applications including OLEDs,²⁸⁸ boron-containing polycyclic aromatic hydrocarbons,²⁹² anion sensing,²⁹³ and bioimaging.²⁹⁴ The π^* - p_z electron transfer process results in a lowered LUMO of the material, resulting in an increased electron affinity and subsequently an increased electron accepting ability.²⁹⁵ This property of boron containing heterocycles proves them ideally suited for use in OLED material design further expanded upon in Section 4.1.1.

4.1.1 Tri-Coordinate Boron Containing Emitters

The use of three-coordinate boron as an acceptor in the form of triarylboranes within TADF emitting structures is a relatively new field. However, these emitters possess external quantum efficiency (EQE) and device stability which outperforms conventional reported OLED devices.²⁹⁶ This highlights the need for further boron containing emitters to expand the current literature. Adachi *et al.*²⁹⁷ reported the first boron-containing TADF emitters in 2015 comprising of a twisted donor-acceptor (D-A) architecture: 10*H*-phenoxaborin acceptor covalently bonded to *N*-heterocyclic donors (Figure 4.1, **L4.0** and **L4.1**). Both 10*H*-phenoxaborin acceptor and the *N*-heterocyclic donors were chosen specifically due to their wide HOMO/LUMO gap and high T₁ energies producing blue emitting materials. It is standard in the literature for boron containing TADF materials to observe blue emission. **L4.0** and **L4.1** were among the first reported emitters to display doping-concentration-independent emission ($\lambda_{em} < 475$ nm, $\Phi_F = 1$ for **L4.0** and $\Phi_F = 0.56$ for **L4.1**) and when incorporated into a device exhibited an EQE of 20%.

An important requirement for OLED performance is a reduction in device efficiency roll-off, also defined as a drop-off in device performance at high brightness.²⁹⁸ Cheng *et al.*²⁹⁹ addressed this problem by designing flat symmetrical diboraanthracene molecules with functionalised carbazole donors covalently bonded to the central acceptor (**L4.2** and **L4.3**). This type of geometry resulted in an alignment of the compounds molecular axes with those of the device substrate surface during vacuum deposition, yielding emitter thin films with horizontally oriented dipoles.³⁰⁰ This is important as it directly affects the light output coupling factor and therefore the EQE of the device.³⁰¹ **L4.2** and **L4.3** exhibit narrowband green emission ($\lambda_{em} < 550$ nm, $\Phi_F = 1$ for **L4.2** and $\Phi_F = 0.86$ for **L4.3**). Narrowband emission profiles contribute to better colour purity and are therefore a desired property of TADF emitters.³⁰² Devices fabricated with **L4.2** and **L4.3** exhibited record-high EQEs of 37.8% and 32.4% respectively, showcasing this design as a viable route towards efficient boron containing TADF materials.

More recently, Wang *et al.*³⁰³ published a linear donor-acceptor-acceptor (D-A-A) structure containing a phenoxazine donor bonded to a triazine and a terminal acyclic triarylborane (**L4.4**). This tandem-acceptor architecture resulted in a LUMO orbital spatially localised to the acceptor moiety due to the unique π^* -p_z ability of the terminal triarylborane. The HOMO orbital was spatially localised to the donor, thus yielding emitters with very small singlet-triplet splitting energies ($\Delta E_{S1-T1} < 0.04$ eV). **L4.4** exhibited green emission ($\lambda_{em} < 546$ nm),

however suffered a reduced PLQY of $\Phi_F = 0.44$. The device fabrication measurements observed EQE values of 24.8%, proving the validity of **L4.4** as a TADF material, albeit with a reduced PLQY. Lastly, Choi *et al.*³⁰⁴ published a styrene co-polymer acting as a host material in OLED devices with alternating diphenylacridine donor and 5,9-dioxa-13b-boranaphtho[3,2,1-*de*]anthracene acceptor monomers (Figure 4.1, **L4.5**). Polymers are known to have superior device properties: one can control film homogeneity as well as uniform structural distribution of donors.⁸⁷ **L4.5** exhibited a blue emission profile ($\lambda_{em} < 400$ nm) and an EQE $< 22\%$.

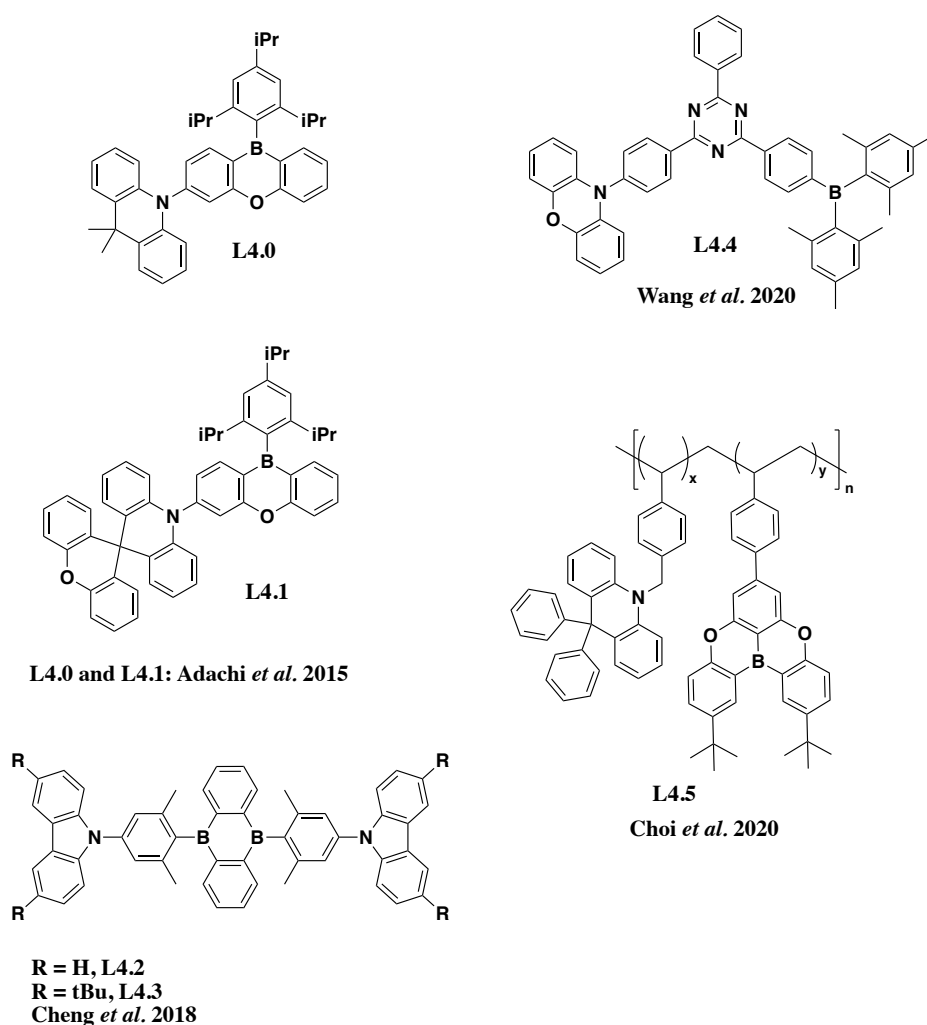


Figure 4.1: Literature examples of boron-containing TADF emitters.

In order to achieve spatially separate HOMO and LUMO orbitals, the donor and acceptor moieties must be structurally separated either *via* a conjugated bridge or by restricting rotation. However, a novel concept termed ‘multiresonance HOMO/LUMO separation’ has been developed by Hatakeyama and co-workers which achieves HOMO/LUMO separation

through resonance.³⁰⁵ This concept utilises the fact that boron and nitrogen impart opposing resonance effects when embedded in a fused π -system.³⁰⁶ The multiresonance approach realises HOMO and LUMO separation based on the π -orbital contribution of each carbon atom within the polycyclic aromatic hydrocarbon (PAH), therefore removing the requirement for either a steric twist or a conjugated bridge within the structure for TADF to still be viable. Figure 4.2 shows **L4.6** reported as a blue emitter with a narrowband emission ($\lambda_{em} = 462$ nm, $\Phi_F = 0.89$), an EQE < 20%, and exhibiting multiresonance induced TADF (MR-TADF). However, devices with **L4.6** and analogues suffered from low brightness and significant roll-off.³⁰⁵ To address this issue Huang *et al.*³⁰⁷ reported **L4.7**, which possesses a functionalised carbazole donor *para*- to the boron atom. Incorporation of the carbazole donor resulted in a redshifted and broadened emission profile ($\lambda_{em} = 470$ nm, $\Phi_F = 0.97$) but observed an improved EQE of 32.1%.

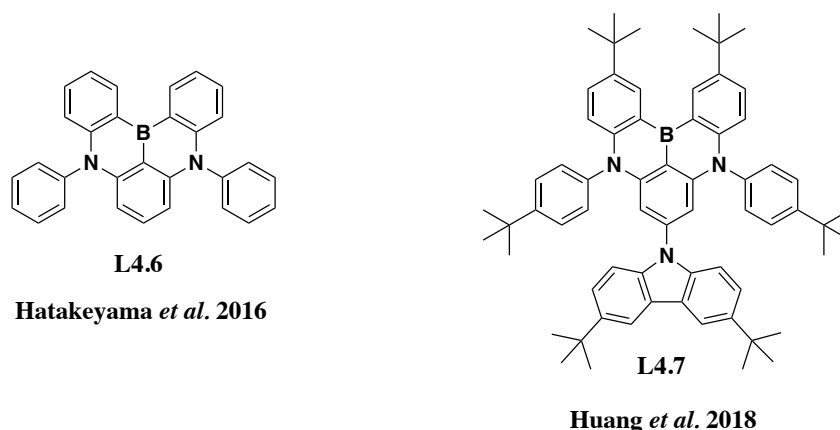


Figure 4.2: Literature examples of multiresonance TADF emitters.

The aforementioned literature examples highlight tri-coordinate boron's potent effect on the photophysical properties of the emitters and OLED device performance. However the literature examples are not extensive, and further research is required to both expand the synthetic methodologies towards the target compounds and expand on the current library of tri-coordinate boron containing emitters. A particular focus is given to azaborines: the synthesis, published literature examples, and their photophysical properties are all discussed in Section 4.1.2.

4.1.2 Azaborine

Azaborines are heterocyclic compounds containing boron and nitrogen atoms within a fused aromatic system (Figure 4.3). Heteroatom substitution directly affects the aromaticity of the ring system such that 1,2-azaborines are the most aromatic and 1,4-azaborines are the least aromatic in the family.³⁰⁸ For the purpose of this Chapter, particular focus will be given to 1,4-azaborines, from here on exclusively referred to as azaborines. Historically, azaborines have been difficult to synthesise requiring moisture and air free reaction conditions, hazardous reagents, elevated temperatures, extended reaction times, and often as a result suffered reduced yields.^{309–316} The reaction intermediates are typically accessed through amination reactions *via* the palladium catalysed Buchwald-Hartwig mechanism or the copper catalysed Ullmann-Goldberg coupling to form C-N bonds. In both instances, high catalytic loadings and elevated temperatures are required. Boron ring closure *via* the Friedel-Crafts C-H borylation, transmetalation, or lithiation mechanisms yield the desired azaborine.³¹⁶ C-H borylation reactions are known to be highly air and moisture sensitive, and require hazardous sources of boron (typically BBr₃) at elevated temperatures to succeed. Similarly for the lithiation route, excess equivalents of *tert*-butyllithium or *n*-butyllithium are required to access the final azaborine.³⁰⁹ Given the stringent reaction conditions, structural functionalisation is often not accessible, resulting in a reduced number of published synthetic methodologies for these systems.

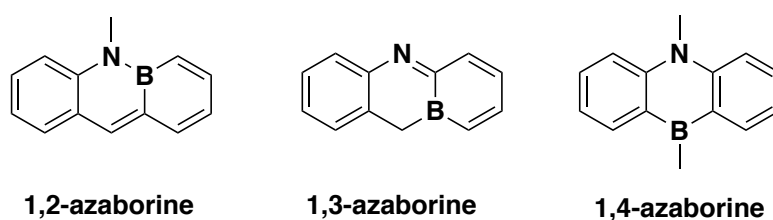


Figure 4.3: Azaborine nomenclature.³⁰⁸

Azaborine is a known phosphorescent emitter due to the presence of boron which induces a heavy atom effect.¹³⁶ Literature reports have been published utilising azaborine as an acceptor in both donor-acceptor (D-A) and donor-acceptor-donor (D-A-D) systems. Cheng *et al.*³¹⁷ studied the role of the *N*-heterocyclic donor on inducing TADF within azaborine containing emitters (Figure 4.4). The report clearly highlights the importance of a large dihedral angle to spatially separate HOMO/LUMO orbitals and induce TADF behaviour. *N*-heterocyclic donors tetramethylcarbazole, dimethylacridine, and phenoxazine resulted in a

sterically induced twist of $>85^\circ$, resulting in TADF in those compounds. Interestingly, for **L4.8** and **L4.9** no TADF was observed as the steric twist was less than for the aforementioned donors. However, both **L4.8** and **L4.9** observed PLQY of 0.99 and 0.98 respectively. Particular attention is drawn to **L4.8** and **L4.9** because the substitution pattern of carbazole clearly plays a role on the resulting donating abilities and TADF behaviour of the compounds. Can this be predicted and studied further, enabling a turn on function of TADF in carbazole containing compounds? This particular turn on/off element is of great interest which has not been extensively studied in the literature. Within this chapter, this effect will be explored through varied substitution patterns of carbazole, and incorporation of a phenyl linker to separate the donor and acceptor moieties and thereby separate the HOMO/LUMO orbitals (Section 4.3).

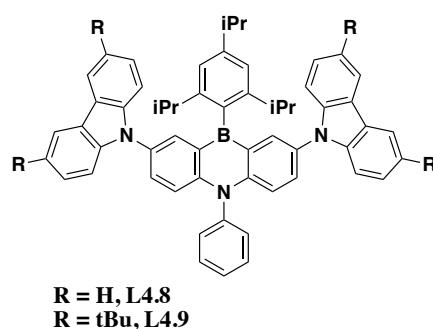


Figure 4.4: Literature examples of 1,4-azaborine utilised as an acceptor structure in OLED devices.³¹⁷

4.2 Carbazole

The most prevalent donor structure in TADF literature is carbazole. It has a high lying HOMO, which paired with a low lying LUMO of an acceptor forms an ideal candidate for blue TADF emitting materials.^{318–320} Only a decade ago, blue emitting TADF materials were rare as they require a wider HOMO/LUMO gap.³²¹ The challenge arose in obtaining a donor material with a highly energetic HOMO, and an acceptor with a matching and spatially localised LUMO in order to achieve blue emission generated by charge transfer. Carbazole containing TADF structures exhibit longer lifetimes and overall higher device photostability when compared to phenoxazine or acridine donors.³²¹

However, even though blue emitting TADF compounds are the most widely present in the literature, key research is yet to be carried out on blue emitting TADF compounds. All blue emitting compounds suffer drawbacks due to their highly energetic nature - for example

degradation, and annihilation between excitons and polarons. This occurs as high energy triplet states can form energetically hot states (~ 6 eV) which cause bond dissociation, as well as photo- and electro-oxidation processes which all unite to decompose high energy triplet states.³²² Therefore, all blue emitting TADF compounds must be structurally rigid and composed of strong bonds, to ensure that minimal bond dissociation occurs within an OLED device.

Many prominent literature examples display carbazole donors within donor-acceptor-donor (D- π -A- π -D) type architectures (Figure 4.5). Serevičius and co-workers designed a system whereby simply altering the side group functionality on the pyrimidine core could tune the properties from TADF to RTP.³²³

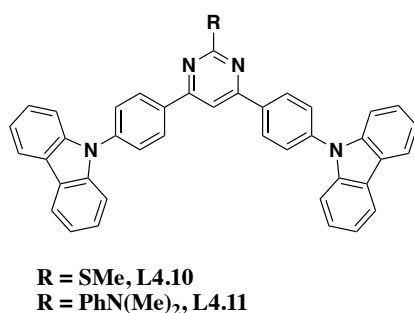


Figure 4.5: Examples of a carbazole containing TADF/RTP system; D- π -A- π -D blue emitting TADF system, with a central pyrimidine functionalised acceptor core, and two carbazole donors.³²³

As previously outlined in Section 1.8.2.2., TADF and RTP are fundamentally similar processes, which both require at least two closely spaced triplet excited states which are lower in energy than the first excited singlet state.^{97,187} Depending on the electronic structure, the presence of heavier atoms (such as sulfur) and the amount of other heteroatoms present will determine the emission process. When the pyrimidine core was functionalised with a thioether **L4.10**, the ΔE_{S-T} gap was calculated to be 0.54 eV, and the observed emission was RTP. The presence of the heavy sulfur atom increased k_{ISC} , the S_1-T_1 energetic gap, and the spin-orbit coupling. However, when the core was functionalised with dimethyl aniline **L4.11**, ΔE_{S-T} gap was calculated to be 0.25 eV, allowing increased efficiency of k_{ISC} , and resulting in TADF emission. By enhancing charge transfer character, RTP could be transformed to TADF in this D- π -A- π -D system, highlighting how structural

functionalisation can play such a vital role on the resulting photophysical processes within the molecule.

4.3 Design Considerations for the Emitters

The main goal of this work is to design novel tri-coordinate boron emitters, thereby expanding the current literature of boron-containing OLED candidates. All proposed emitters are donor- π -acceptor- π -donor (D- π -A- π -D) or donor-acceptor-donor (D-A-D) compounds, with a central azaborine acceptor covalently bonded to a family of chosen donors (Figure 4.6). Symmetry plays a key role on the resulting ICT and the excited state dynamics: utilising two donors rather than one leads to faster photonic relaxation when compared to a single donor molecule and reduces highly energetic non-photonic decay pathways.³²⁴

Novel synthetic routes to structurally functionalise azaborine are explored in order to modulate the accepting ability of the azaborine core. The modulation through the nitrogen atom is the most synthetically achievable, and a range of functional groups are chosen with varying electron donating or withdrawing abilities (Figure 4.6, R1). Of particular interest is the incorporation of the pentafluorosulfanyl group, and therefore increasing the electron accepting ability of the azaborine. The pentafluorosulfanyl functional group is highly polar, lipophilic, electronegative, small in size, and thermally and hydrolytically stable.³²⁵ Incorporation of the SF₅ group into OLED candidates has immense potential to aid modulation of electron accepting ability, but has not yet been explored in the literature. The effect of varying the electron accepting ability of the azaborine on the resulting photophysical properties of the compounds is studied in-depth.

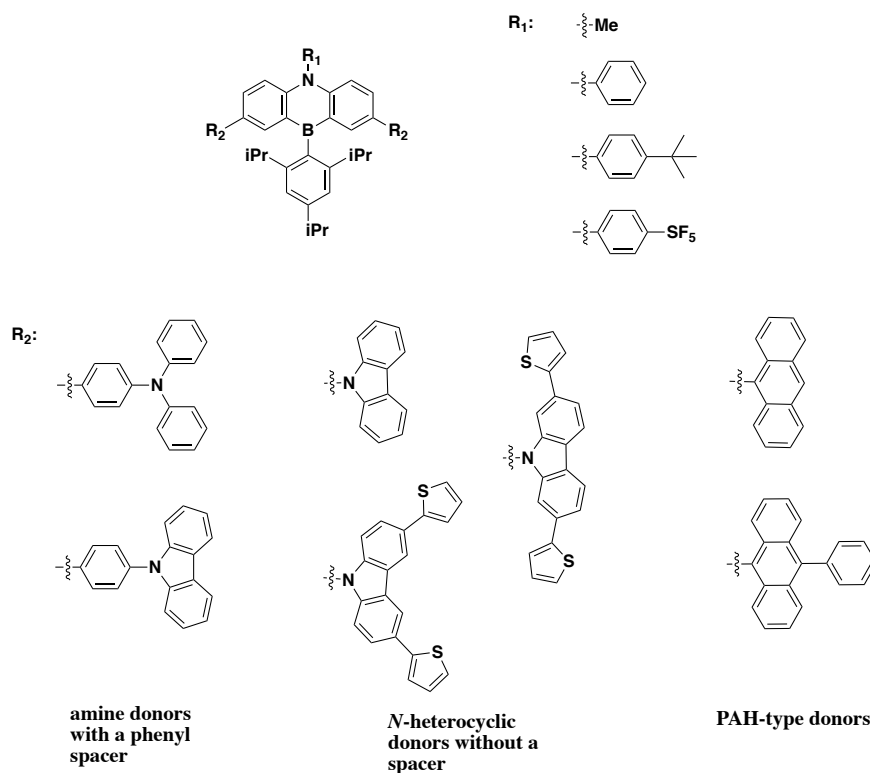


Figure 4.6: *D-π-A-π-D* and *D-A-D* target structures with proposed functionalisation to the central accepting core and varied donors.

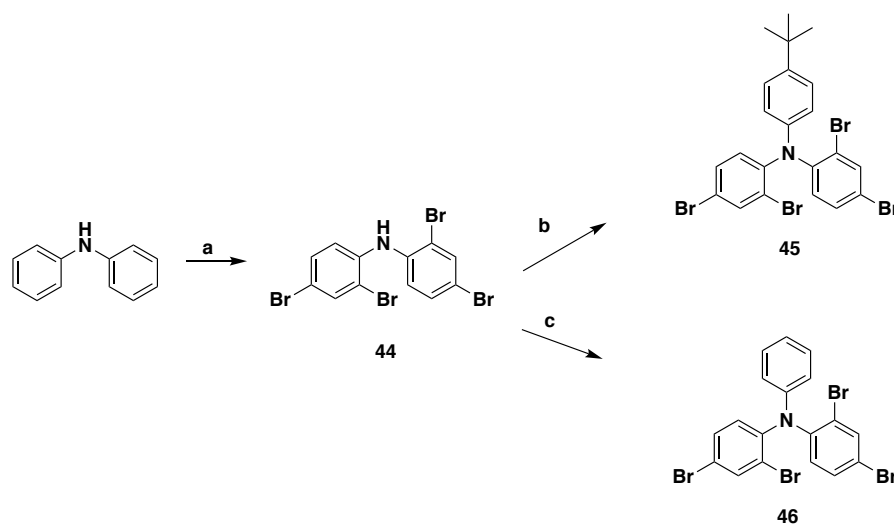
The donors of choice for this work can be separated into three categories (Figure 4.6, R₂): amine donors with a conjugated linker, amine donors without a conjugated linker, and PAH-type donors. The relationship between chromophore rigidity and TADF are well researched, with highly rigidified structures being the best candidates for blue emitting OLED materials.³²⁶ This relationship is further studied herein, by directly comparing the acyclic triphenylamine and the rigid phenyl carbazole which has fewer rotational degrees of freedom. The role of the conjugated linker to separate the donor and acceptor moieties is further studied in this work, and directly compared to the *D-A-D* emitters without an incorporated conjugated linker. Furthermore, by adapting the key findings of Cheng *et al.*³²⁷ analogues of **L4.8** and **L4.9** are proposed. It is postulated that TADF can be switched on by functionalising the carbazole donor with the electron rich and conjugated terminal thiophene rings.³²⁸ This functionalisation is proposed at the 3,6 positions and 2,7 positions which will result in a highly rotationally restricted compound with a large dihedral angle between the acceptor and donors. Finally, donors which are PAH analogues and do not contain any heteroatoms are also considered for this work. Anthracene can behave as both a donor and an acceptor depending on the structure.^{329,330} By studying the all-carbon anthracene

compounds, the heteroatom role on the donating ability of the structure can be further understood. In order to gain further understanding into structural requirements for TADF: modulation of the acceptor strength, utilisation of a conjugated linker, structural rigidification, restricted rotation, and heteroatom effect on the donor ability are all studied herein.

4.5 Results and Discussion

4.5.1 C-N Bond Formation Towards Novel Functionalised Tertiary Amines

The synthesis of **45** and **46** proceeded *via* two analogous synthetic steps (Scheme 4.0). Diphenylamine, a commercially available white solid was used without further purification. The brominating agent of choice, *n*-bromosuccinimide (NBS) was added portion wise at 0 °C and allowed to stir for 15 minutes. Following that, water was added to quench the reaction and the newly formed white solid was filtered off. The solid was washed with an acetone/water mix (50/50 v/v), and further recrystallized by refluxing in toluene under a flow of N₂ gas. The recrystallisation afforded **44** as an off-white needle like crystalline solid in a 77% yield, which was in good agreement with the literature.³³¹



Scheme 4.0: Complete synthesis of **45** and **46** **a)** NBS, acetone, 0 °C, 15 mn, 77%. **b)** CuI, 1-tertbutyl,4-iodobenzene, K₂CO₃, 3-4 days pressure tube, 185-190 °C, 76%. **c)** CuI, iodobenzene, K₂CO₃, 3-4 days pressure tube, 185-190 °C, 99%.

Synthetic steps **b)** and **c)** of Scheme 4.0 underwent rigorous synthetic trials, resulting in the copper catalysed Ullmann-Goldberg path as the only viable route towards **45** and **46**. The

successful syntheses of **45** and **46** are further discussed in Section 3.5.1.3 below. However, prior to this, other synthetic pathways were explored. Tertiary amines can be synthetically attained via palladium catalysed Buchwald-Hartwig coupling reactions or copper catalysed Ullmann-Goldberg coupling reactions between a secondary amine and an aryl halide. Ullmann-Goldberg couplings are comparable to Buchwald-Hartwig but often require high temperatures, prolonged reaction times, and stoichiometric amounts of copper.³³² This heightens both the environmental hazard and exposure to large quantities of copper. In an effort to improve and expand the synthetic methodology towards novel functionalised acyclic tertiary amines, a series of Buchwald-Hartwig conditions were trialled.

4.5.1.1 Buchwald-Hartwig Methodology Studies

Palladium catalysed Buchwald-Hartwig amination reactions generally proceed *via* five steps: generation of Pd(0) species, oxidative addition of the aryl halide, addition of the amine to the palladium oxidative addition complex, deprotonation of the amine by the base, and reductive elimination and subsequent regeneration of the Pd(0) species. The literature boasts an array of palladium sources, solvents, bases, and ligands, leading to a need for careful tailoring of reaction conditions for each precursor. Amines act as nucleophiles in the catalytic cycle, and thus the more electron rich amines such as secondary amines and specifically cyclic amines are the most reactive.³³³ Aryl halides range in reactivity and this reactivity is directly correlated to the palladium source and ligand choice. For monodentate ligand systems aryl bromides are most reactive, with aryl iodides secondary, and aryl chlorides the least reactive. For bidentate chelating ligand systems, the amine undergoes a deprotonation prior to amine insertion into the active palladium complex. Aryl iodides are most reactive in bidentate ligand systems, with both electron rich aryl iodides and electron poor aryl iodides reported to work successfully.³³⁴

Yasuda *et al.*³³⁵ reported a successful palladium catalysed amination on multi-halogenated system in 2018. The coupling product 2,5-dibromo-*N*-(2-bromophenyl)aniline was attained in a 91% yield by refluxing 2,5-dibromoaniline and 1-bromo-2-iodobenzene with Pd₂(dba)₃, dppf, and sodium tert-butoxide in toluene under an inert atmosphere. Mirroring the success of this protocol, a facile coupling of **44** and various aryl iodides was envisioned. In order to trial this, precursor **44** and the commercially sourced 1-tertbutyl,4-iodobenzene were exposed to a series of Buchwald-Hartwig conditions (Table 4.0). However, each trial proved fruitless and no reaction was observed. In each case, only the starting materials were

observed in ^1H NMR spectra and HRMS of the crude reaction mixtures. It is postulated that **44** was not a strong enough nucleophile and is unreactive towards a Buchwald-Hartwig type C-N coupling.

Table 4.0: Buchwald-Hartwig Synthetic Methodology.^a

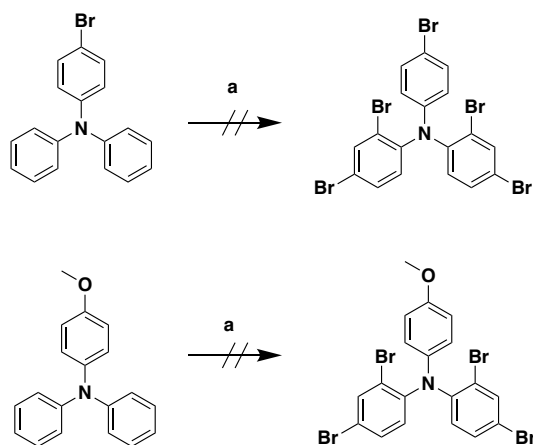
Trial	Catalyst (1% mmol)	Ligand (2% mmol)	Solvent	Base (2.5 equiv.)	Outcome
1	$\text{Pd}_2(\text{dba})_3$	Tris- <i>o</i> -tolylphosphine	1,4-dioxane	potassium tert-butoxide	No reaction
2	$\text{Pd}_2(\text{dba})_3$	dppf	toluene	Potassium tert-butoxide	No reaction
3	$\text{Pd}_2(\text{dba})_3$	Tris- <i>o</i> -tolylphosphine	1,4-dioxane	sodium tert-butoxide	No reaction
4	$\text{Pd}_2(\text{dba})_3$	dppf	toluene	sodium tert-butoxide	No reaction
5	$[\text{Pd}(\text{OAc})_2]_n$	Tris- <i>o</i> -tolylphosphine	1,4-dioxane	sodium tert-butoxide	No reaction
6	$[\text{Pd}(\text{OAc})_2]_n$	Tris- <i>o</i> -tolylphosphine	toluene	sodium tert-butoxide	No reaction
7	$[\text{Pd}(\text{OAc})_2]_n$	BINAP	1,4-dioxane	sodium tert-butoxide	No reaction
8	$\text{Pd}_2(\text{dba})_3$	BINAP	1,4-dioxane	sodium tert-butoxide	No reaction
9	$\text{Pd}(\text{tBuP})_2$	-	toluene	sodium tert-butoxide	No reaction
10	$\text{Pd}(\text{tBuP})_2$	-	1,4-dioxane	sodium tert-butoxide	No reaction

^a All reactions were carried out at reflux of solvent for a period of 24 h under an inert atmosphere.

4.5.1.2 Unsuccessful Bromination of Tertiary Amines

With C-N bond formation proving a significant challenge and a roadblock in this project, bromination of tertiary amines was attempted instead. The four bromine functionalities on **44** are essential for the subsequent ring closure and introduction of the boron atom to synthesise the azaborine accepting core. If the presence of the four bromine functionalities on **44** were hindering the compounds reactivity towards palladium catalysed couplings, introduction of the required bromine functionalities could be added in a latter synthetic step. To test this, commercially available electron poor 4-bromo-*N,N*-diphenylaniline and an electron rich 4-methoxy-*N,N*-diphenylaniline were chosen. Both of the tertiary amines were subjected to the same reaction conditions as diphenylamine (Scheme 4.1). When NBS was added to a solution of 4-bromo-*N,N*-diphenylaniline in acetone at 0 °C, the reaction turned from clear to green. ^1H NMR and HRMS analyses showed that the reaction had failed, and

the presence of product formation was not observed. Similarly, the addition of NBS to a solution of 4-methoxy-*N,N*-diphenylaniline in acetone at 0 °C resulted in a colour change from clear to black. ¹H NMR and HRMS analyses were inconclusive and showed no presence of product formation. No further trials were attempted, and this synthetic path was abandoned.



Scheme 4.1: Unsuccessful bromination trials **a)** NBS, acetone, 0 °C, 15 mn.

4.5.1.3 Successful Ullmann-Goldberg C-N Coupling

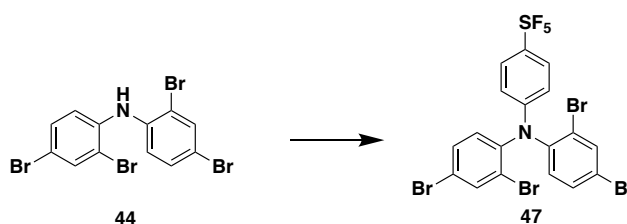
Tertiary amines **45** and **46** were successfully synthesised using the Ullmann-Goldberg C-N coupling reaction between a secondary amine **44** and either 1-tertbutyl,4-iodobenzene or iodobenzene (Scheme 4.0).

Stoichiometric amounts of copper iodide, potassium carbonate and **44** were dissolved in the aryl halide of choice. The aryl halide is used as both the reactant and the solvent in this reaction. The reactants were thoroughly degassed, sealed in a pressure tube, and stirred at 185-190 °C for 4 days. The suspension was yellow/ orange in colour throughout the reaction duration. After four days, the crude reaction mixture was cooled, dissolved in methylene chloride, passed through celite to trap copper, extracted with ammonium chloride and brine, and dried over magnesium sulfate. Flash column chromatography (SiO₂, petroleum ether, petroleum ether:ethyl acetate, 100:1, v/v) afforded **45** as a white crystalline solid in a 76% yield, and **46** as a white crystalline solid in a 99% yield. For both **45** and **46**, flash column chromatography in petroleum ether resulted in full elution of the aryl halide as the first fraction. Subsequent addition of 1% ethyl acetate allowed the pure elution of the tertiary amines. Both **45** and **46** were attained in sufficient quantities to proceed to the subsequent

ring closing reaction to synthesise azaborine and were in good agreement with the literature (Section 4.5.2 below).³³⁶

4.5.1.4 Unsuccessful Ullmann-Goldberg C-N Coupling

When designing the target compounds for this project, varying functionalisation of the acceptor core was envisaged, with both electron donating and withdrawing substituents being introduced onto the azaborine core. As discussed in Section 4.3, the pentafluorosulfonyl group would increase the electron accepting ability of the azaborine core. The exact synthetic conditions used to synthesise **45** and **46** were applied (Scheme 4.2).



Scheme 4.2: Unsuccessful synthesis of **47**: CuI, pentafluoro(4-iodophenyl)- λ^6 -sulfane, K_2CO_3 , 4 days pressure tube, 185-190 °C. Solvents trialed were toluene and xylenes.

The aryl halide pentafluoro(4-iodophenyl)- λ^6 -sulfane is a commercially available light sensitive white solid which was used without further purification. The reactants were dissolved in either dried toluene or xylenes (to trial the success of both solvents) and thoroughly degassed with argon gas. The pressure tubes were heated to 185-190 °C for four days in the dark to ensure that the aryl halide does not suffer decomposition prior to reacting. Both reaction mixtures were dissolved in methylene chloride, passed through celite, extracted with ammonium chloride and brine, and the solvent reduced *in vacuo*. ^{19}F NMR studies of the toluene reaction mixture identified the presence of two types of fluorinated compounds, albeit in a quantity too small for flash column chromatography.

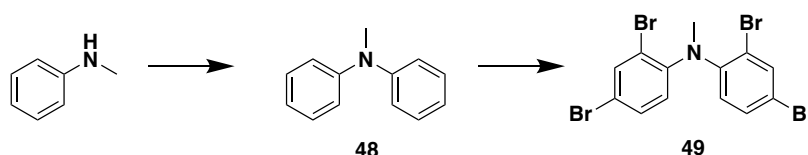
^{19}F NMR spectrum of the xylenes reaction mixture showed one quintet and one doublet signal, which suggested the presence of product. The xylenes crude reaction mixture was further recrystallized from toluene to selectively crystallize out **44**, and the green filtrate containing **47** was purified with flash column chromatography (SiO_2 , petroleum

ether:methylene chloride, 8:2, v/v). The purification system contained a series of co-eluting side products, with **47** present in a small quantity. It was postulated that four days were insufficient due to the low reactivity of the aryl halide, and a longer reaction time was required in order to attain **47** in a higher yield. In an attempt to force further reactivity, the reaction in xylenes was repeated and allowed to heat for 7 days. However after 7 days no product formation was observed, with NMR and HRMS only identifying the starting materials. Pentafluoro(4-iodophenyl)- λ^6 -sulfane seemed to be unreactive towards Ullmann-Goldberg type conditions, and thus this synthetic pathway was abandoned.

4.5.1.5 Synthesis of 2,4-dibromo-N-(2,4-dibromophenyl)-N-methylaniline

In order to introduce the methyl functionality onto the azaborine, the tertiary amine must be synthesised first followed by the bromination step. The purpose of the methyl group is to gain understanding into the substitution on the heterocyclic nitrogen of the azaborine: its significance on the overall photophysical properties of the resulting OLED candidates.

The synthesis of **49** proceeded in two synthetic steps (Scheme 4.3 below). N-methylaniline, a commercially available liquid was used without further purification in a Buchwald-Hartwig coupling reaction with bromobenzene to synthesise **48**. The reactants were dissolved in dried toluene and thoroughly degassed before 0.1% Pd(PtBu₃)₂ was added. The reaction mixture was refluxed for 20 hours, following which the solvent was reduced *in vacuo*. The crude residues were dissolved in methylene chloride, washed with brine, and purified using flash column chromatography (SiO₂, petroleum ether:ethyl acetate, 9.8:0.2, v/v) to afford **48** as a yellow oil in a 85% yield.



Scheme 4.3: Successful synthesis of **49** **a)** N-methylaniline, bromobenzene, sodium tert butoxide, 0.1% mmol Pd(PtBu₃)₂, dry toluene, reflux, 20 h, 85%. **b)** **48**, NBS, acetone, RT, 1 h, 97%.

Purified tertiary amine **48** was dissolved in cold acetone prior to addition of NBS at 0 °C. During the addition of NBS, the reaction mixture went from yellow to green to black, and

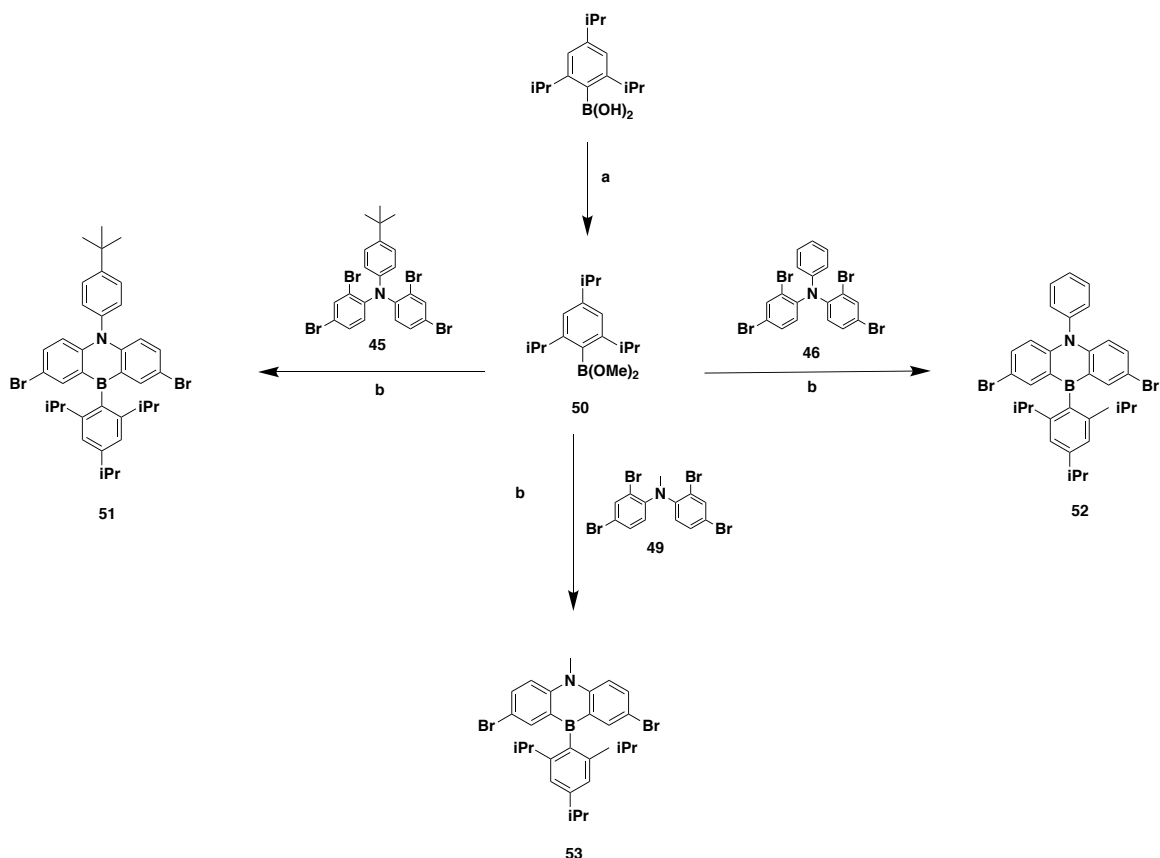
after five minutes had elapsed the solution turned yellow again with evident white precipitate forming. The reaction was allowed to come up to room temperature and stir for 1 h, following which the formed precipitate was filtered off and dried. The white precipitate was identified as the product **49** attained in a 97% yield which was used without further purification in the subsequent ring closing reaction to form azaborine (Section 4.5.2).

4.5.2 Synthesis of Azaborine

Synthesising the required specifically substituted tertiary amines was the biggest synthetic roadblock of this project. Once **45**, **46**, and **49** were synthesised, azaborine ring closing reactions could be attempted. First, (2,4,6-triisopropylphenyl)boronic acid needed to be converted to its boronic ester equivalent in order to be compatible with the ring-closing *n*-butyl lithium reaction conditions (Scheme 4.4). Commercially available trimethyl orthoformate, 2,4,6-(triisopropylphenyl)boronic acid, and TFA were stirred vigorously overnight at room temperature which resulted in a full esterification reaction of the boronic acid. After the 12 h had elapsed, the white residue reaction mixture had been fully converted to a yellow oil. ¹H studies and ¹¹B NMR studies confirmed full conversion from the boronic acid to **50** and was in good agreement with the literature.³³⁷ The boronic ester **50** is air and moisture sensitive and thus was stored under Argon gas at -20 °C until required for further syntheses.

Successful synthesis of the azaborine acceptor required pristine air and moisture free conditions. *N*-butyllithium was added to a solution of tertiary amine in thoroughly degassed dry diethyl ether at -78 °C, which resulted in a yellow suspension, identified as the lithiated amine. After the amine was successfully lithiated, a solution of **50** in diethyl ether was syringed into the reaction vessel resulting in a colour change from yellow to red, and the reaction was allowed to come up to room temperature and stir overnight. After 12 h, the solvent was removed *in vacuo*, the product was extracted with methylene chloride and ammonium chloride, the organic layer was dried over magnesium sulfate and purified using flash column chromatography or crystallisation. The azaborine **51** was crystallised from the crude mixture (DCM/MeOH, freezer) to afford a pale pink solid in a 63% yield. The crude residues of **52** and **53** were purified by flash column chromatography (SiO₂, methylene chloride/petroleum ether 1:10, v/v) to afford **52** as a yellow solid in a reduced yield of 11 % and **53** as a yellow solid in a reduced yield of 6.2%. Although the purification systems for both **52** and **53** were successful, they provided yields too low for further couplings. Only **51**

could be recovered in sufficient quantities to proceed to the Suzuki and Buchwald-Hartwig couplings. Due to the difficulty in obtaining sufficient amounts of **52** and **53**, target compounds with phenyl and methyl azaborines could not be realised.



Scheme 4.4: Successful synthesis of azaborine **a**) (2,4,6-triisopropylphenyl)boronic acid, trimethyl orthoformate, TFA, RT, 12 h, 100%. **b**) *n*BuLi, -78 °C – RT, diethyl ether, 12 h, yielding **51** in 63%, **52** in 11%, and **53** in 6.2%.

3.5.2.1 X-ray Crystallography of **51**

Crystals of **51** suitable for single crystal X-ray diffraction measurements were successfully obtained *via* slow evaporation of a CDCl_3 solution of the pure compound. X-ray measurements, data collection, and refinement of the structure was carried out by Dr. Brendan Twamley. A specimen of $\text{C}_{37}\text{H}_{42}\text{BBr}_2\text{N}$, approximate dimensions 0.040 mm x 0.170 mm x 0.460 mm, was used for the X-ray crystallographic analysis. The structure was solved using a highly symmetric space group Aba_2 , with $Z = 12$ for the formula unit, $\text{C}_{37}\text{H}_{42}\text{BBr}_2\text{N}$. The final anisotropic full-matrix least-squares refinement on F^2 with 681 variables converged at $R1 = 5.28\%$, for the observed data and $wR2 = 13.14\%$ for all data, and the goodness-of-fit was 1.035. (Appendix 3.3a for full crystallographic table). Figure 4.7 below

illustrates the symmetry generated asymmetric unit of **51**. Both the phenyl and the Tip rings lie orthogonal to the central azaborine moiety, with angles of $91.825(4)^\circ$ and $100.745(3)^\circ$ respectively. The large twist between the azaborine and the Tip ring are of particular importance because it provides effective steric protection of the boron centre. This twist has been observed in analogous structures reported in the literature.³⁴ Bonding within the structure (C-C, C-N, C-H, and C-Br), has no exceptional bonding lengths to note. Azaborine C-B bond was measured to be $1.503(13)$ Å, which is shorter when compared to reported literature value of 1.606 Å of C_{ar} -B structures.⁵⁷

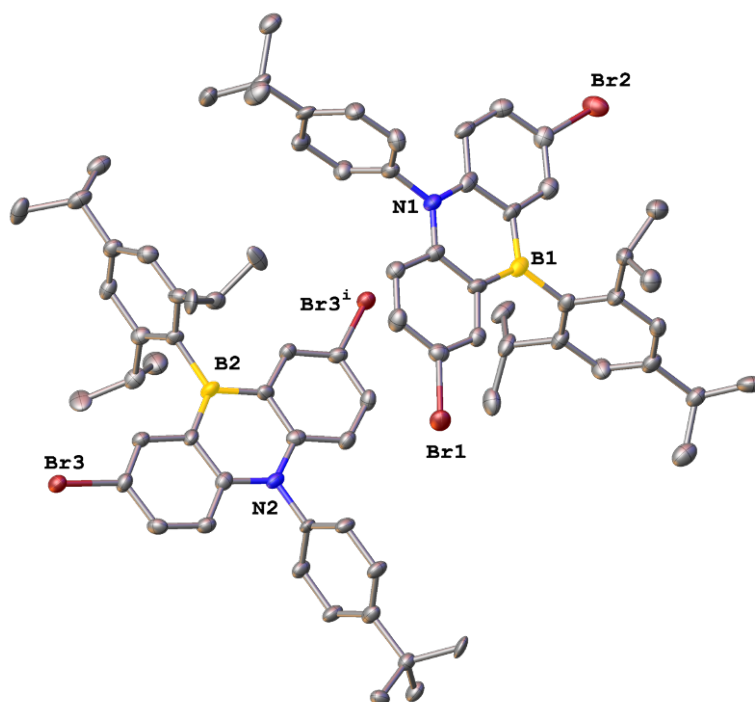


Figure 4.7: Symmetry generated molecular structure of **51**, showing the single symmetry unique molecule and the unique half molecule completed using the symmetry transformation $i = 2-x, 1-y, +z$. This is along the twofold axis. Symmetry generated atoms are annotated with i . Hydrogen atoms omitted for clarity and atomic displacement shown at 50% probability. Tip substituent disordered 50% and *t*Bu disordered in 4 positions. Only one disordered moiety is shown.

Figure 4.8 shows the packing structure of **51**, viewed normal to the *a*-axis. The packing diagram directly illustrates the symmetric nature of the Aba_2 space group. Due to the highly

twisted nature of **51**, the packing diagram observed no significant intermolecular interactions.

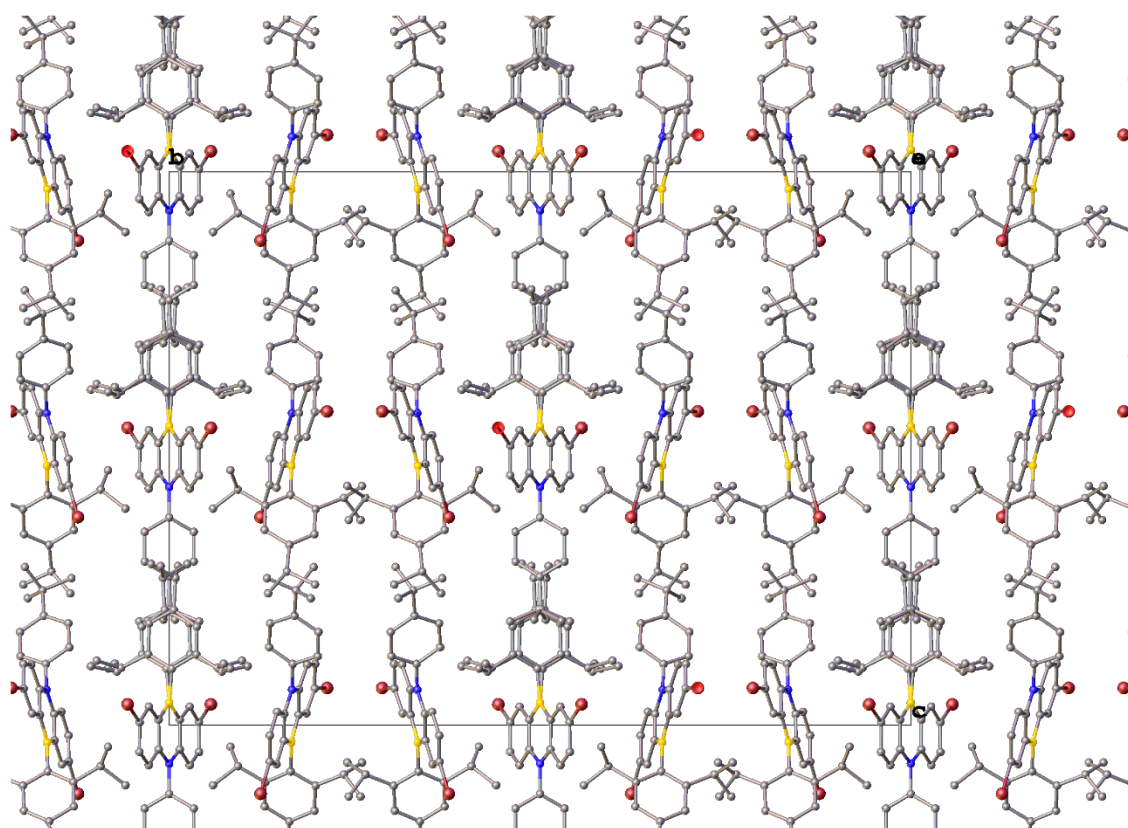


Figure 4.8: Schematic crystal packing diagram of **51**, viewed normal to the *a*-axis, showing the unit cell outline. Hydrogen atoms have been omitted for clarity. All disordered moieties shown.

4.5.2.2 X-ray Crystallography of **53**

Crystals of **53** suitable for single crystal X-ray diffraction measurements were successfully obtained *via* slow evaporation of a CDCl_3 solution of the pure compound. X-ray measurements, data collection, and refinement of the structure was carried out by Dr. Brendan Twamley. A specimen of $\text{C}_{28}\text{H}_{32}\text{BBr}_2\text{N}$, approximate dimensions 0.130 mm x 0.140 mm x 0.180 mm, was used for the X-ray crystallographic analysis. The structure was solved using the space group $\text{P}2_1/\text{n}$, with $Z = 4$ for the formula unit, $\text{C}_{28}\text{H}_{32}\text{BBr}_2\text{N}$. The final anisotropic full-matrix least-squares refinement on F^2 with 326 variables converged at $R1 = 3.28\%$, for the observed data and $wR2 = 9.04\%$ for all data. The goodness-of-fit was 1.093

(Appendix 3.3a for full crystallographic table). Figure 4.9 below illustrates the asymmetric unit of **53**, (Appendix 3.3d, individual disorder representations). The structure bears resemblance to **51**, with the Tip ring perpendicular to the central azaborine heterocycle at an angle of $89.1055(18)^\circ$. Unlike **51**, the nitrogen atom of **53** lies out of plane, resulting in a curved structure. This has been reported in other analogous literature.³⁴ Bonding within the structure bears resemblance to **51** (C-C, C-N, C-H, and C-Br), and has no exceptional bond lengths to note. Azaborine C-B bond was measured to be $1.528(3)$ Å, which is longer when compared to **51**, but shorter when compared to reported literature value of 1.606 Å of C_{ar} -B structures.⁵⁷

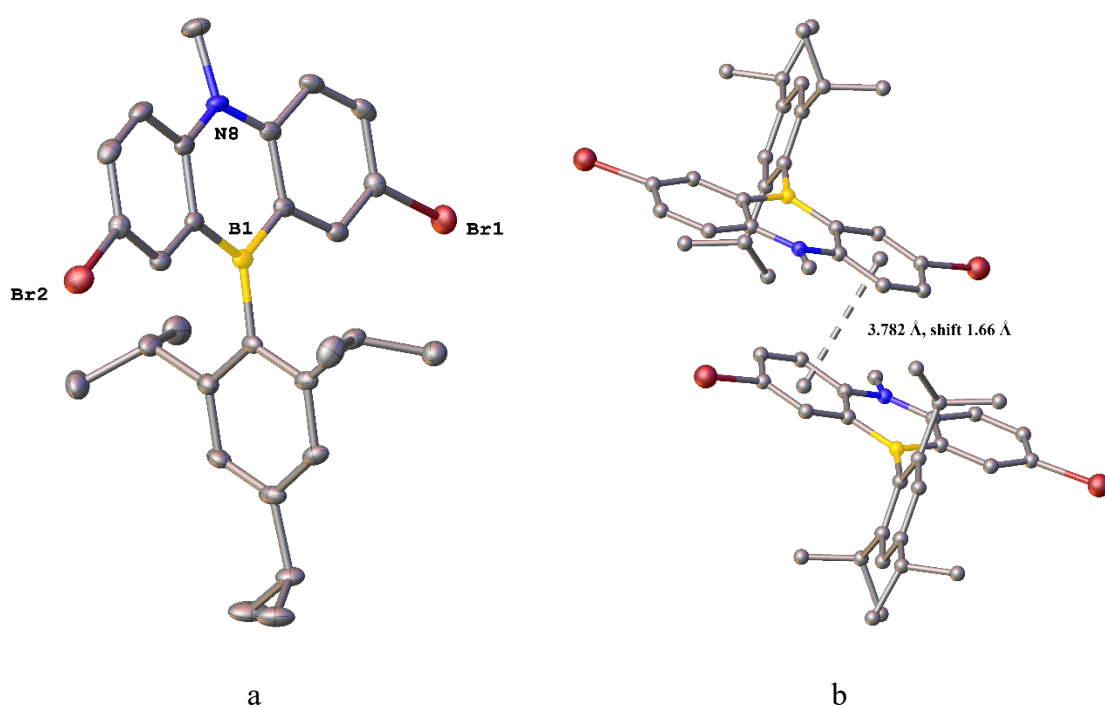


Figure 4.9 (a) Asymmetric unit of **53**, with hydrogen atoms omitted for clarity (thermal ellipsoids shown at 50% probability). The majority occupancy disordered model is shown (disorder in the para isopropyl group of 69:31 % occupancy). **(b)** π - π interaction of the C2-C7 ring of 3.782 Å dotted line joined to centroids, with centroid shift 1.66 Å.

Figure 4.10 shows the crystal packing structure of **53**, viewed normal to the a-axis. Replacing the phenyl group with a methyl group results in a very different packing arrangement. However, even with a less bulky substitution on the nitrogen atom allows the azaborine rings

to interact and there is a π - π interaction between two molecules of 3.782 Å (which is weaker when compared to reported π - π interactions of 3.4-3.6 Å) with a shift between centroids of 1.66 Å.⁵⁸

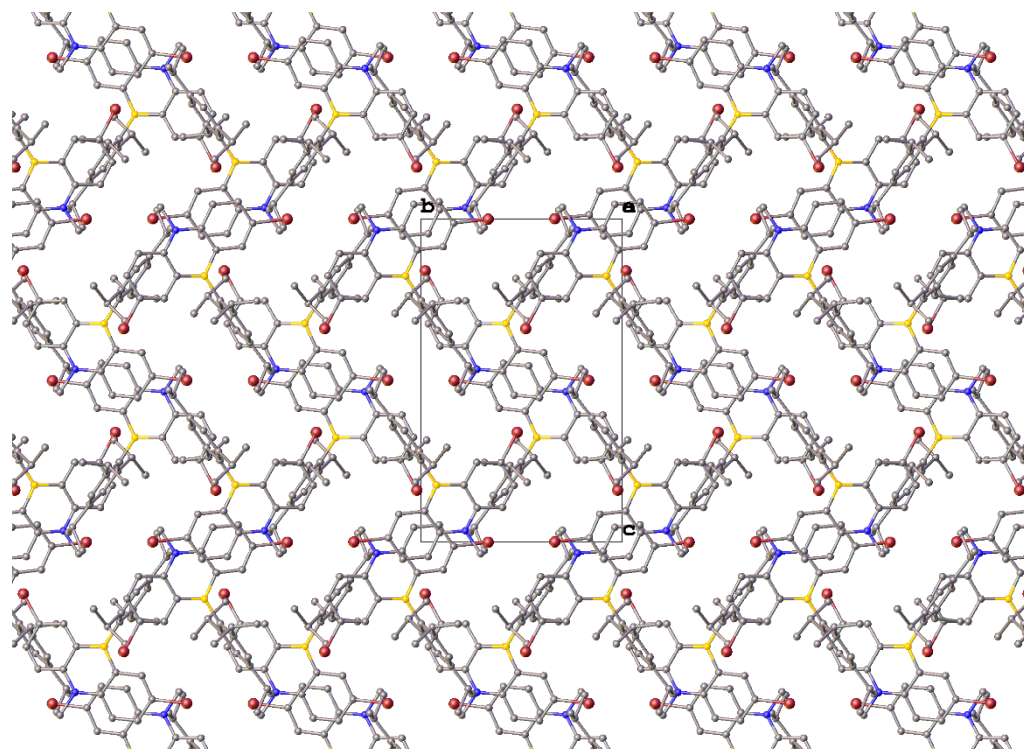
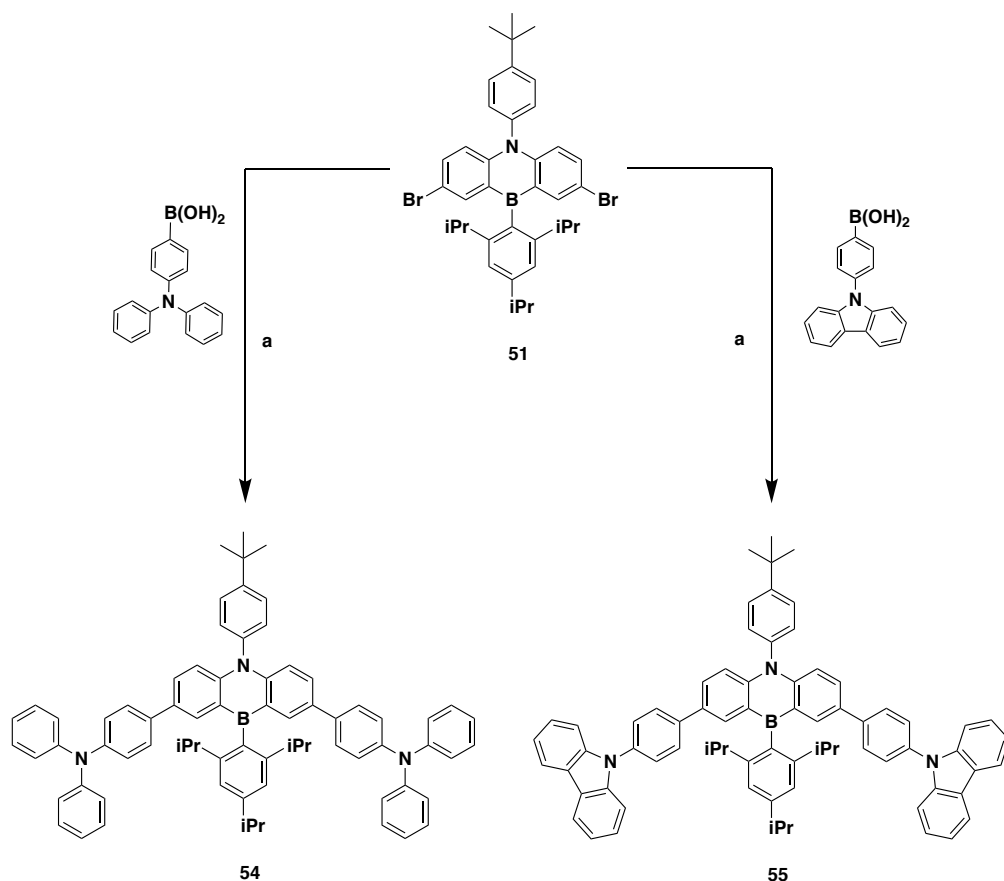


Figure 4.10: Crystal packing arrangement of **53**, viewed along the *a*-axis.

4.5.3 Suzuki Coupling to Synthesise **54** and **55**

The palladium catalysed Suzuki cross coupling reaction was utilised to synthesise the final target compounds **54** and **55** (Scheme 4.5). Azaborine precursor **51** was used without further purification. The boronic acid of choice and **51** were dissolved in 1:1 toluene:ethanol, thoroughly degassed, and 2M K_2CO_3 base was syringed in. The base is vital to ensure full deprotonation of the boronic acid. A catalyst loading of 8% $Pd(PPh_3)_4$ was added to the reaction vessel, and heated to 110 °C overnight. After 12 h, all volatiles were removed *in vacuo*, redissolved in methylene chloride, extracted with brine, and the organic layer dried over magnesium sulfate. The crude residues were purified using flash column chromatography (for **54**, SiO_2 , methylene chloride/petroleum ether 20:80 v/v; for **55**, SiO_2 , methylene chloride/petroleum ether 40:60, v/v) to afford **54** as a yellow solid in a reduced yield of 27% and **55** as an off white solid in a 58% yield.



Scheme 4.5: Successful synthesis of **54** and **55** a) 2M K_2CO_3 , 8% $Pd(PPh_3)_4$, 1:1 toluene:ethanol, 110 °C, 12 h, yielding **54** in a 27 % yield and **55** in a 58% yield.

4.5.3.1 Structural Characterisation of **54** and **55**

54 and **55** were spectroscopically characterised using 1H NMR, $^{13}C\{^1H\}$ NMR, HSQC, HMBC, and selective spin TOCSY experiments. 1H NMR for **54** is presented below in Figure 4.11. The aromatic protons of the azaborine core H1, H2, H3, and H4 were assigned according to the literature report.³³⁶ Azaborine protons appear more downfield due to the electron poor nature of the heterocycle, and observe an AMX splitting pattern which could be clearly identified using selective spin TOCSY experiments. Triphenylamine aromatic protons H7 and H8 were clearly distinguishable from H9, H10, and H11 as they are in two different spin systems, clearly identifiable using selective spin TOCSY experiments and distinguishable due to their 1:2 integration ratio. Spin selective TOCSY experiments were invaluable to assign all the protons of **44** due to the overlap of all the signals in the aromatic region.

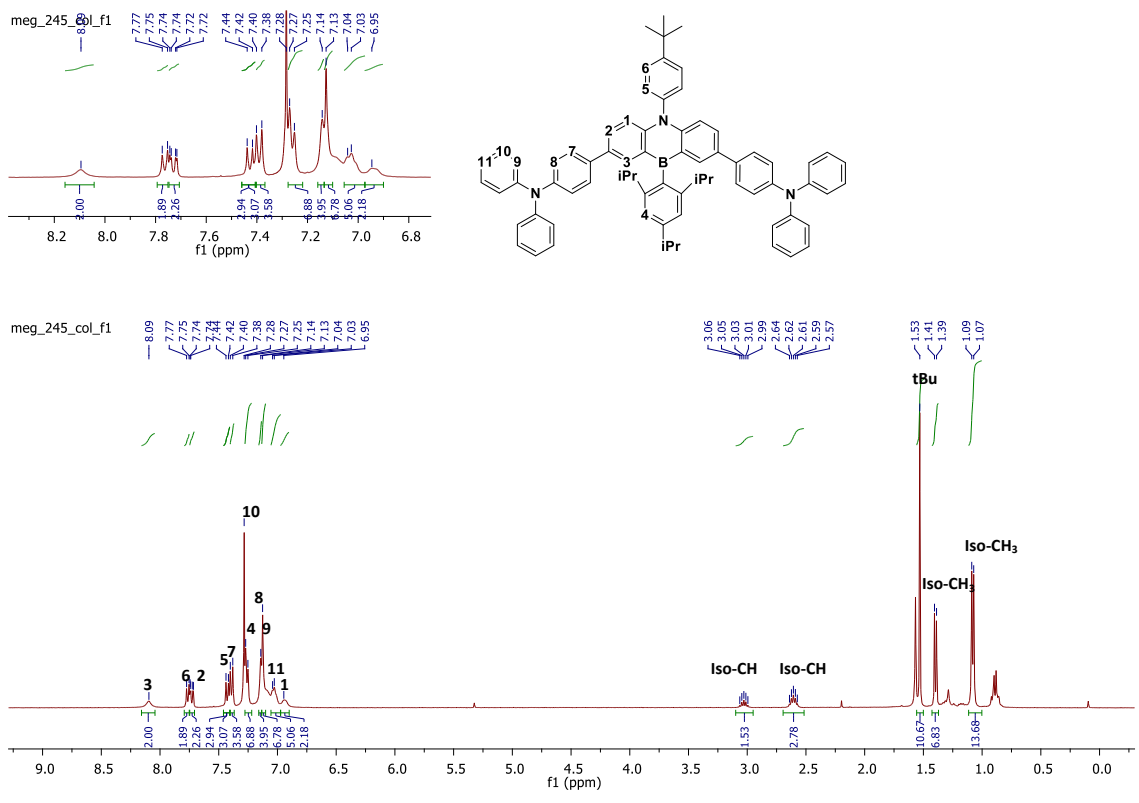


Figure 4.11: ^1H NMR spectrum of 54.

In order to assign the $^{13}\text{C}\{^1\text{H}\}$ NMR spectrum, HSQC (to assign the C-H aromatic carbons) and HMBC (to assign the quaternary carbons) experiments were utilised (Figure 4.12).

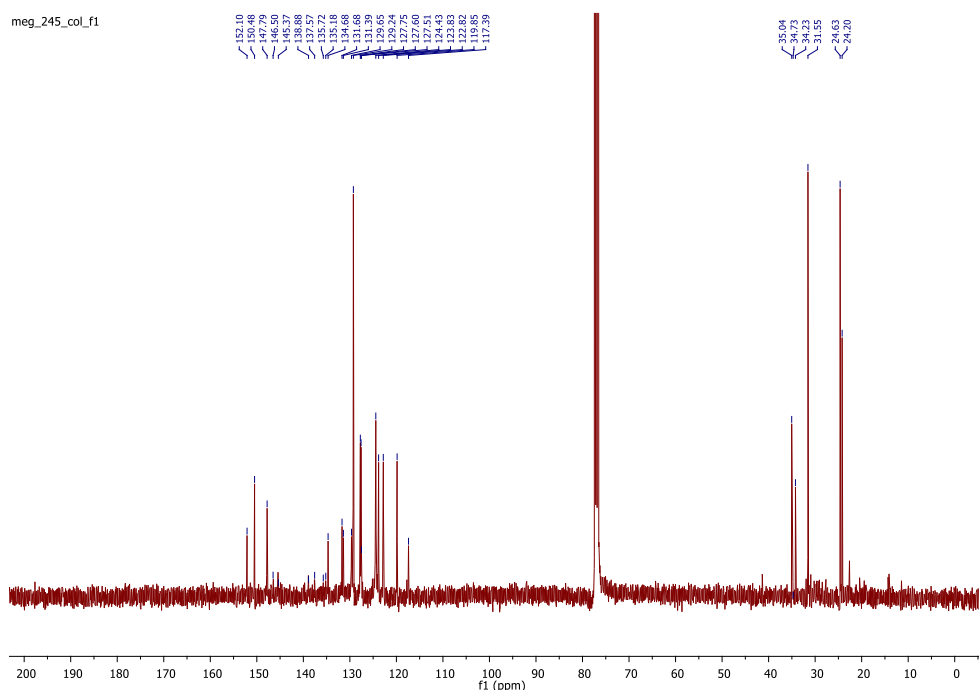


Figure 4.12: $^{13}\text{C}\{^1\text{H}\}$ NMR spectrum of 54.

A similar structural assignment approach was taken for **55**. However, the ^1H spectrum of **55** is much more spectroscopically resolved when compared to **54** with all aromatic protons very clearly distinguishable (Figure 4.13). Similarly to **54**, the azaborine core protons H1, H2, and H3 of **55** are clearly identifiable with an AMX splitting pattern. H3 appears the most downfield, as it is closest to the electron-poor boron atom. Phenylcarbazole contains two spin systems, H7 and H8, and H9-H12, which are both clearly identifiable in the ^1H NMR spectrum due to their 1:2 integration ratio and correlate well with a published literature report.³³⁹

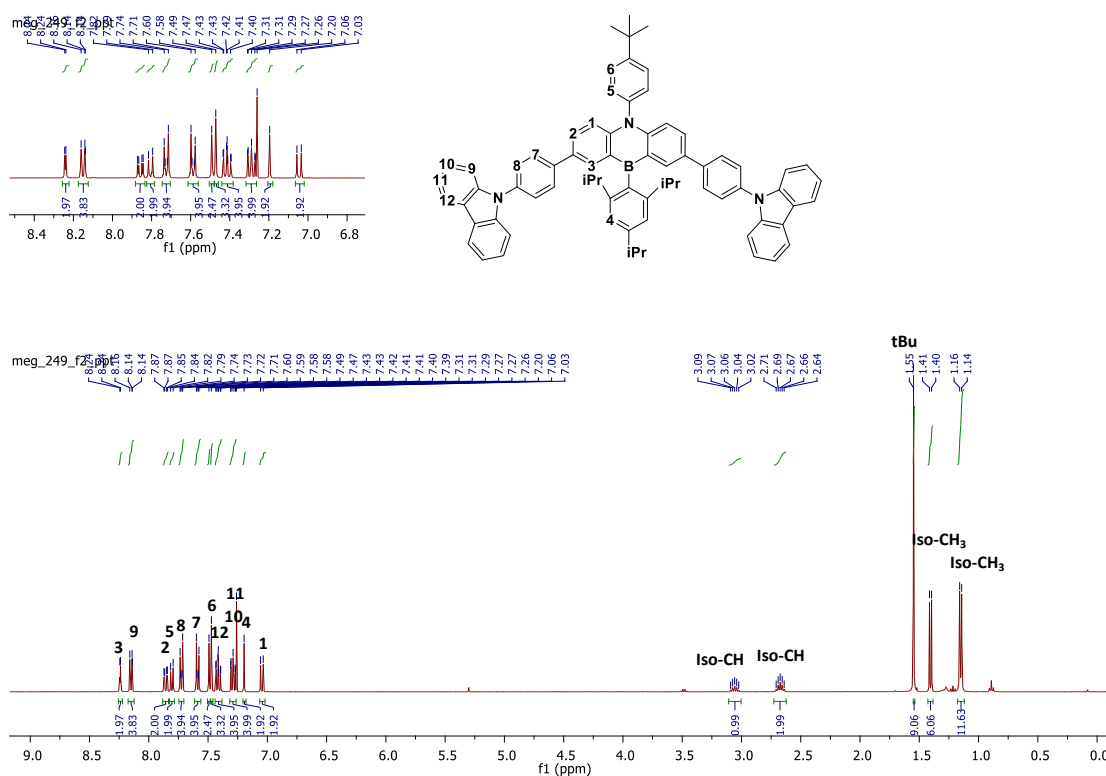


Figure 4.13: ^1H NMR spectrum of **55**.

2D selective spin TOCSY experiment aided in facile aromatic proton assignment by clearly showing which protons were in the same spin systems through correlation signals as observed in Figure 4.14.

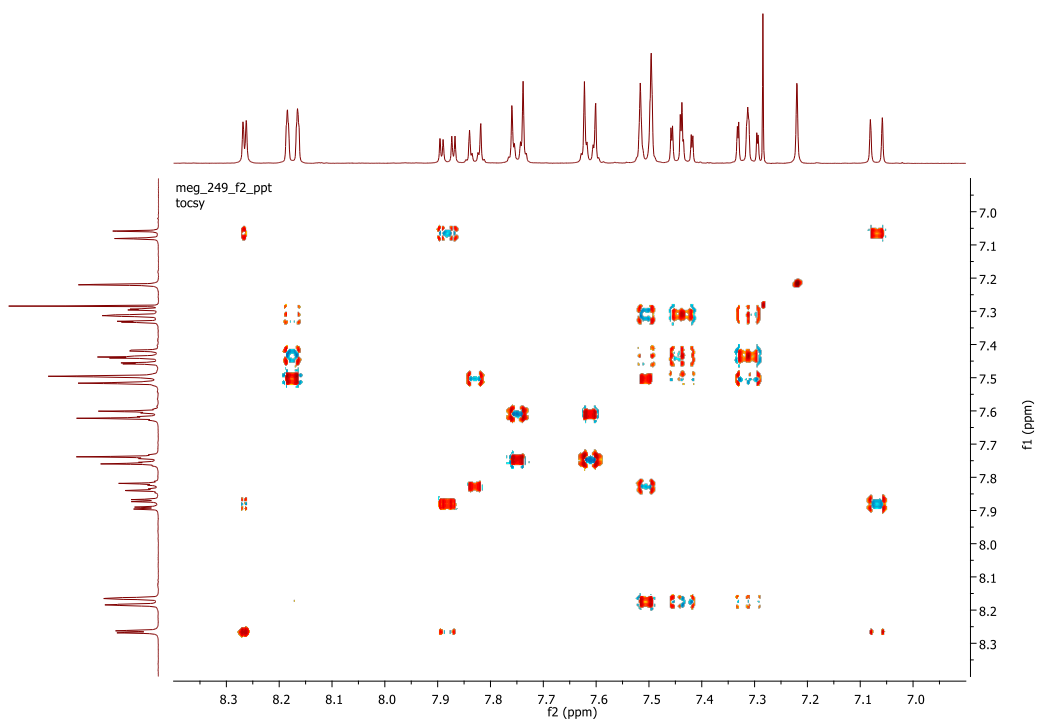


Figure 4.14: 2D Spin selective TOCSY spectrum of **55**.

$^{13}\text{C}\{^1\text{H}\}$ NMR spectrum assignment of **55** was facilitated by HSQC and HMBC spectra (Figure 4.15).

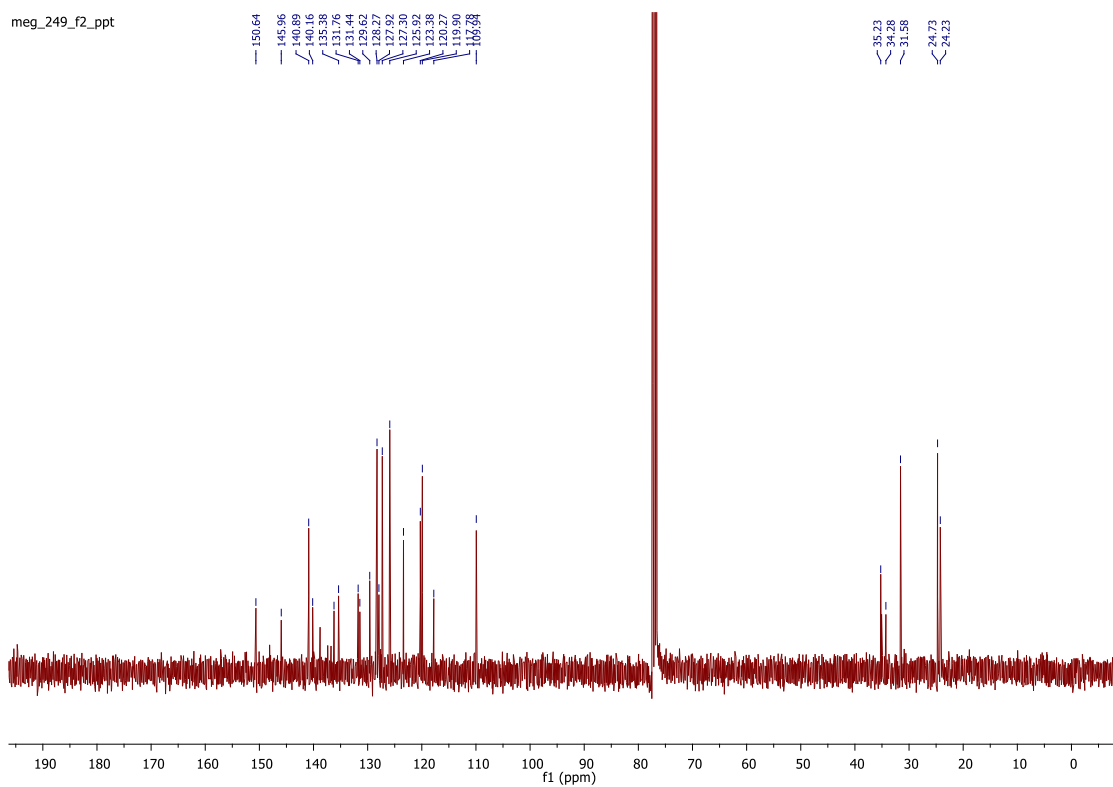
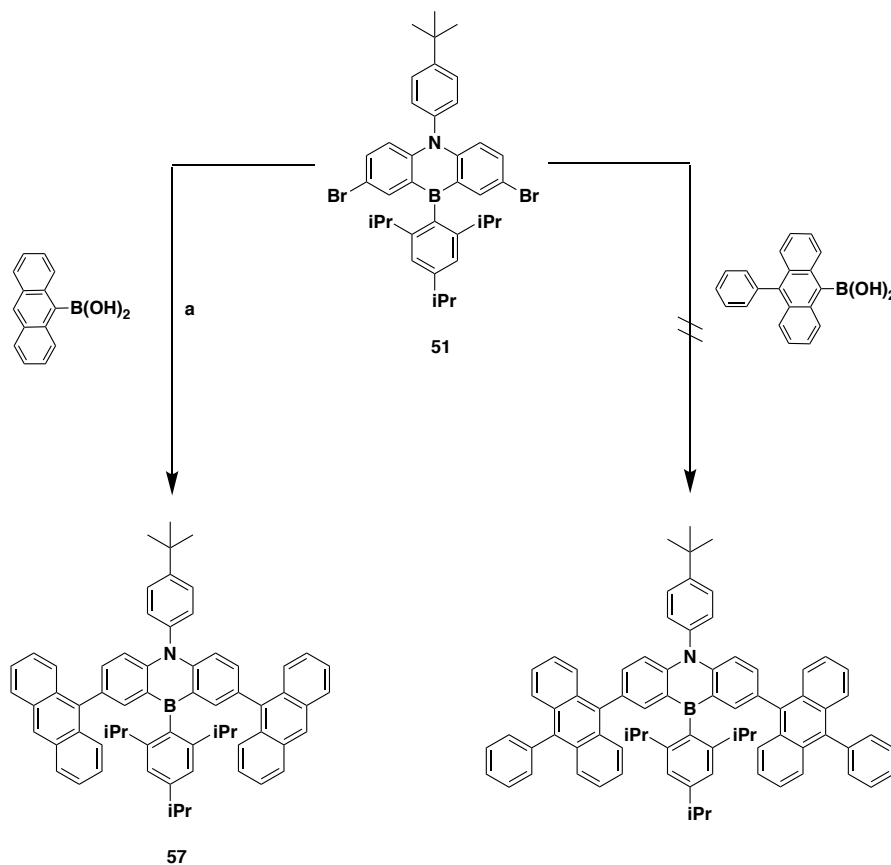


Figure 4.15: $^{13}\text{C}\{^1\text{H}\}$ NMR spectrum of **55**.

4.5.3.2 Unsuccessful Suzuki Coupling

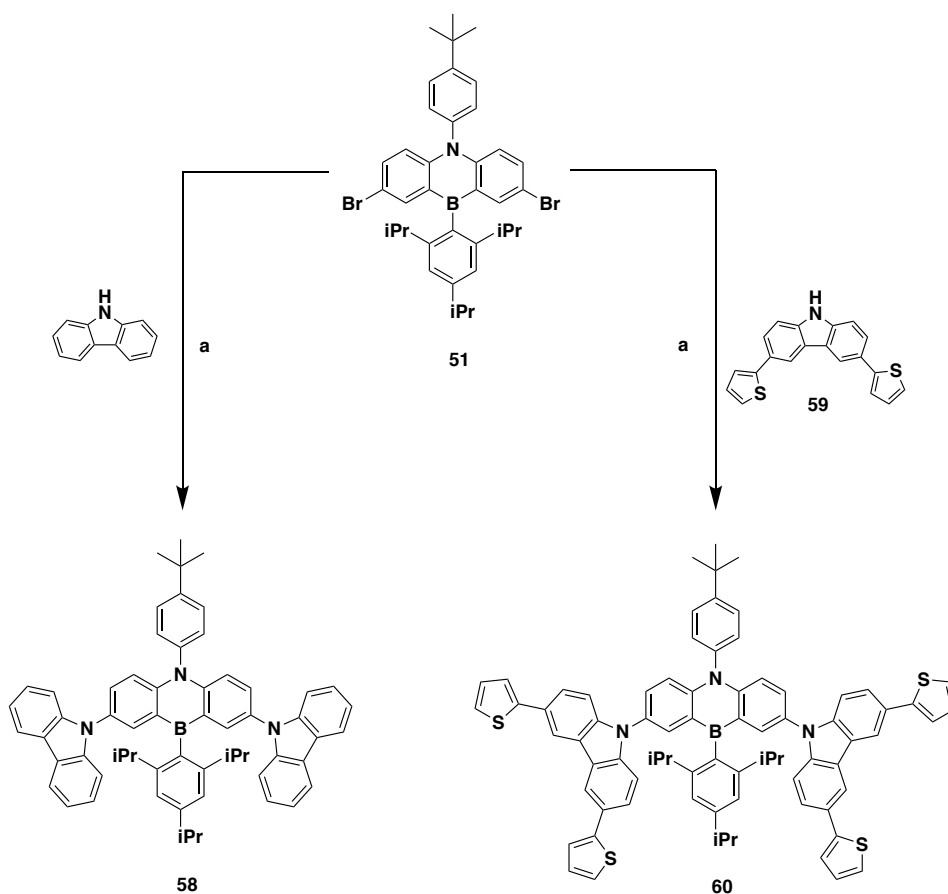
Anthracene based PAH-type donors were envisioned for this work to serve as comparison to the various heterocyclic donors (Scheme 4.6 below). Anthracen-9-ylboronic acid, a commercially sourced white solid was used without further purification in a Suzuki coupling with **51**, in a synthetic prep analogous to **54** and **55**. The product **56**, a grey solid was crystallised from the crude residues using methylene chloride and diethyl ether at $-20\text{ }^{\circ}\text{C}$. However, the product seemed to decompose over time as well as contain trace amounts of the boronic acid starting material. Further purification trials (PTLC, methylene chloride/petroleum ether 80:20, v/v) proved fruitless, with residual impurities clearly identifiable in the ^1H NMR spectra. It was thought that the highly planar anthracene structure contributed to π - π stacking between the boronic acid molecules and the product. In an attempt to reduce π - π stacking, (10-phenylanthracen-9-yl)boronic acid was used in an identical Suzuki coupling with **51**. However, the crystallisation (methylene chloride/diethyl ether, $-20\text{ }^{\circ}\text{C}$) of the crude residues failed, as did flash chromatography trial (SiO_2 , methylene chloride/petroleum ether 30:70 v/v). HRMS of the crude residues was not successful in finding the product, concluding in a failed synthetic attempt.



Scheme 4.6: Unsuccessful Suzuki couplings: **a)** 2M K₂CO₃, 8% Pd(PPh₃)₄, 1:1 toluene:ethanol, 110 °C, 12 h, **57** synthesised but not purified successfully.

4.5.4 Buchwald–Hartwig Coupling to Synthesise **58** and **60**

Buchwald-Hartwig couplings were carried out to introduce carbazole donors to the final target compounds **58** and **60**. The synthesis required pristine air and moisture free conditions in order to work, due to the sensitivity of the catalyst. Bis(tri-*tert*-butylphosphine)palladium(0) is highly moisture and air sensitive and for that reason was only handled under a nitrogen atmosphere in a specialised glove bag in order to avoid decomposition. The reaction Scheme 4.7 below illustrates the synthetic pathway. Carbazole, a commercially sourced yellow solid was used without further purification. Thiopene functionalised carbazole donor **59**, an off-white solid was synthesised using a known literature procedure.³⁴⁰ For the Buchwald-Hartwig coupling, the carbazole of choice, **51**, and sodium *tert*-butoxide were dissolved in dry toluene and thoroughly degassed. Separately, the catalyst was handled in a glove bag, dissolved in minimal amounts of dry and degassed toluene, and syringed into the reaction mixture, which was subsequently brought up to reflux and stirred overnight. Following that, all volatiles were removed *in vacuo*, and the crude residues dissolved in methylene chloride, washed with water. The organic layer was dried over magnesium sulfate and purified using flash column chromatography (SiO₂, methylene chloride/petroleum ether 30:70 v/v) to afford **58** as a pale-yellow solid in 56% yield and **60** as a bright yellow solid in a 37% yield.



Scheme 4.6: Successful synthesis of **58** and **60** a) sodium tert-butoxide, 0.1% mmol $\text{Pd}(\text{PtBu}_3)_2$, toluene, N_2 , 12 h reflux, yielding **58** in a 56% and **60** in a 37%.

4.5.4.1 Structural Characterisation of **58** and **60**

58 and **60** were spectroscopically characterised using ^1H NMR, $^{13}\text{C}\{^1\text{H}\}$ NMR, HSQC, HMBC, and selective spin TOCSY experiments. The ^1H and $^{13}\text{C}\{^1\text{H}\}$ spectra bear similarity to **54** and **55**, and the azaborine core is assigned accordingly (Figures 4.16-4.17 below). For **58**, the aromatic carbazole protons H7-H10 were assigned using a literature report, and are also easily distinguished from the azaborine aromatic protons due to the 1:2 integration ratio (Figure 4.16). The $^{13}\text{C}\{^1\text{H}\}$ NMR spectra of **58** was assigned with aid of HSQC and HMBC 2D spectra, and literature reports.³⁴¹

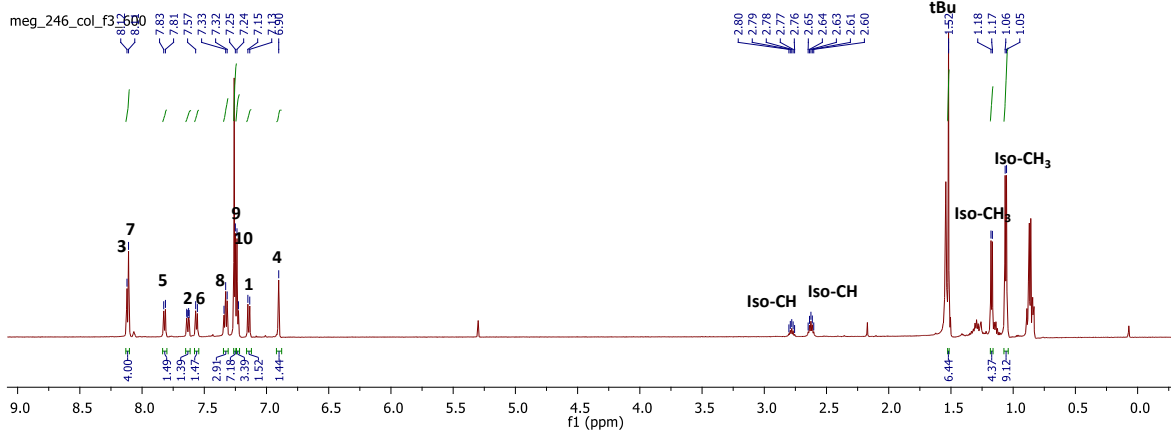
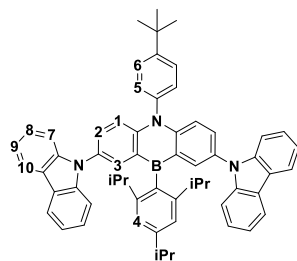
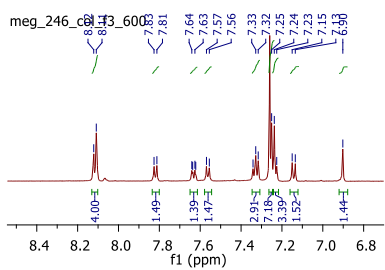


Fig 4.16: ^1H NMR spectrum of 58.

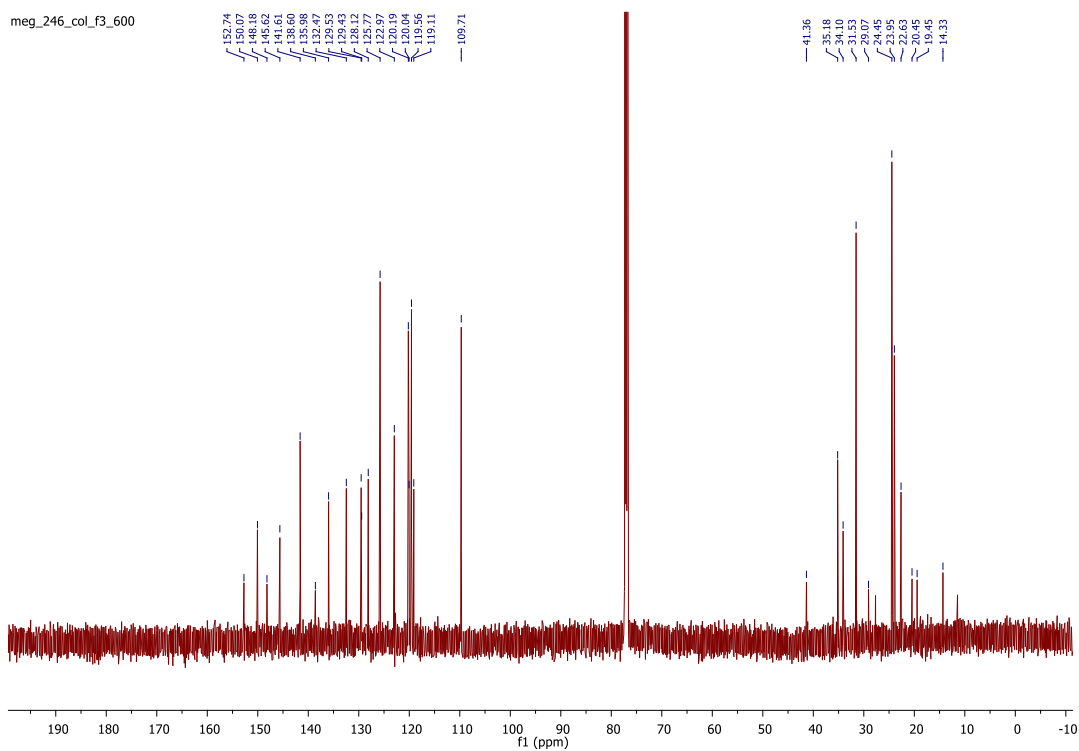


Figure 4.17: $^{13}\text{C}\{^1\text{H}\}$ NMR spectrum of 58.

Similarly for **60**, the ^1H spectrum was assigned using previous compounds as reference (Figure 4.18). The carbazole aromatic protons H7-H9 observe an AMX splitting pattern due to the position of the thiophene rings at the 3 and 6 position of the ring system, and are easily identifiable by their 1:2 integration ratio to the azaborine protons. Thiophene aromatic protons H10-H12 were assigned using a literature report.³⁴² Figure 4.19 illustrates $^{13}\text{C}\{^1\text{H}\}$ spectra, which was assigned in lieu of the previous family of compounds.

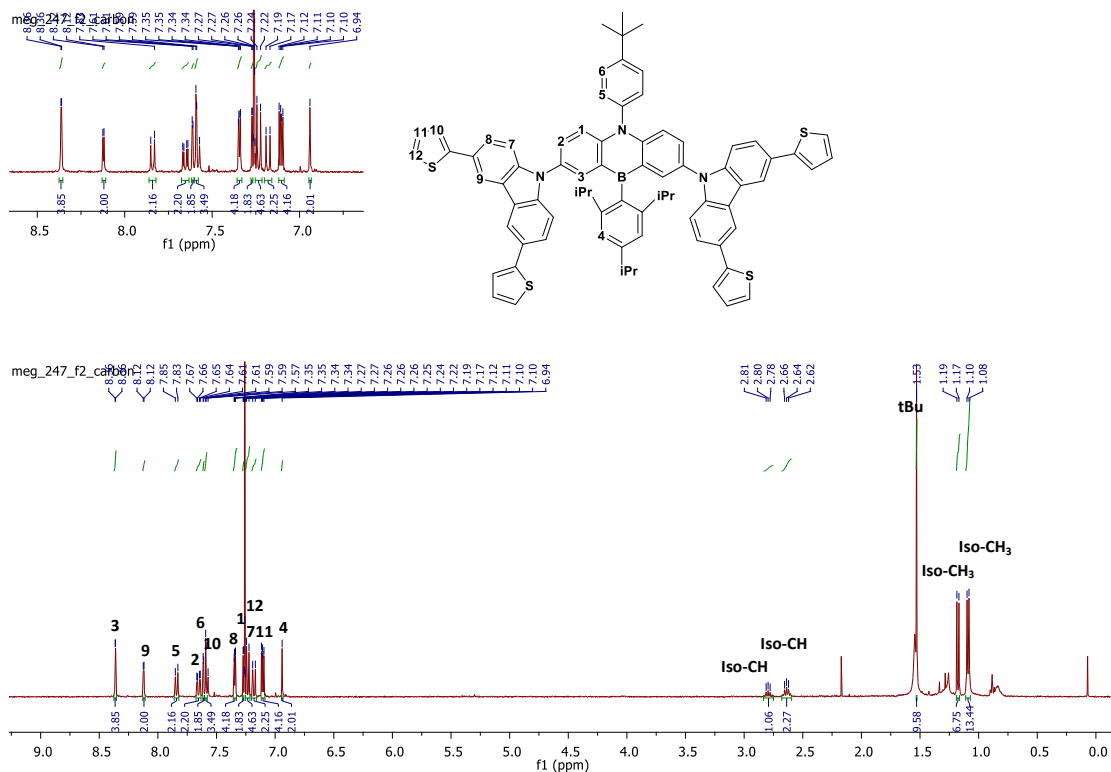


Figure 4.18: ^1H NMR spectrum of **60**.

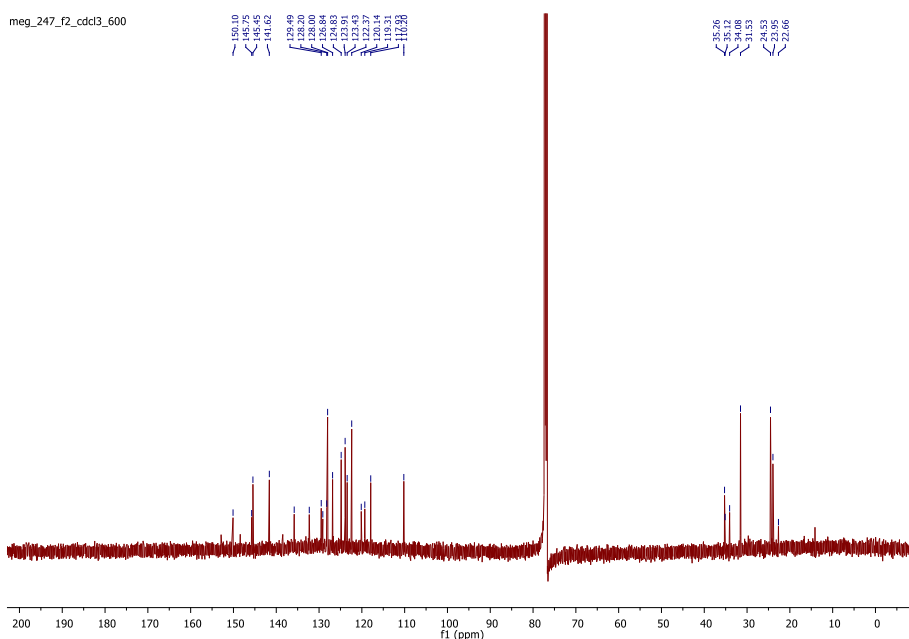


Figure 4.19: $^{13}\text{C}\{^1\text{H}\}$ NMR spectrum of **60**.

4.5.4.2 X-ray Crystallography of **58**

Crystals of **58** suitable for crystal X-ray diffraction measurements were successfully obtained via slow evaporation of a CDCl_3 solution of the compound. X-ray measurements, data collection, and refinement of the structure was carried out by Dr. Brendan Twamley. A specimen of $\text{C}_{37}\text{H}_{42}\text{BBr}_2\text{N}$, approximate dimensions 0.040 mm x 0.170 mm x 0.460 mm, was used for the X-ray crystallographic analysis. The structure was solved using the space group Aba_2 , with $Z = 12$ for the formula unit, $\text{C}_{37}\text{H}_{42}\text{BBr}_2\text{N}$. The final anisotropic full-matrix least-squares refinement on F^2 with 681 variables converged at $R1 = 5.28\%$, for the observed data and $wR2 = 13.14\%$ for all data. The goodness-of-fit was 1.035 (Appendix 3.3a for full crystallographic table).

Figure 4.20 below illustrates the asymmetric unit of **58**, with hydrogen atoms omitted for clarity. SQUEEZE was performed to remove the ethanol solvent molecules from the final structure. The structure has three disordered moieties each modelled in two locations, a part of the azaborine ring with one carbazole 74:26%, the TIP ring 80:20% and the tBuphenyl ring, 74:26% occupied. These individual disordered representations are illustrated in Appendix 3.3e. The central azaborine heterocycle and its pendant phenyl and tip rings are analogous to **51**, with both rings perpendicular to the azaborine centre. The dihedral angle of two intersecting planes, azaborine one plane and carbazole the other, was calculated to be 88.46° , directly demonstrating the large induced steric twist between the donor and the

acceptor moiety. Bonding within the structure bears resemblance to **51** and **53** (C-C, C-N, C-H, and C-Br), and has no exceptional bond lengths to note. Azaborine C-B bond was measured to be 1.531(4) Å, which is longer when compared to **51** and **53**, but shorter when compared to reported literature value of 1.606 Å of analogous C_{ar}-B structures.⁵⁷

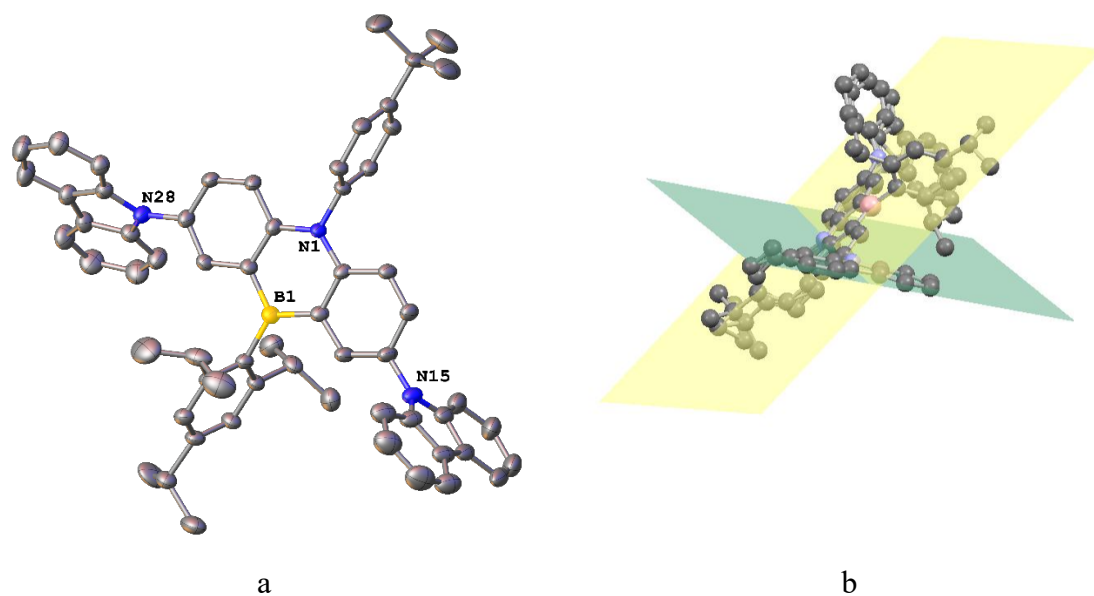


Figure 4.20: **a)** Asymmetric unit of **58**, showing only the majority occupied disordered moiety with hydrogen atoms omitted for clarity and atomic displacement shown at 50% probability. **b)** Asymmetric unit of **58** showing two intersecting planes at a dihedral angle of 88.46°.

Figure 4.21 shows the crystal packing structure of majority disorder **58**, viewed along the a-axis (refer to Appendix 3.3f and 3.3g for the individual major and minor disorder packing diagrams). Due to the highly twisted structure, no significant intermolecular interactions were found. This is an important indicator that these types of twisted compounds will not produce excimer emission in the solid state, and in the OLED device.

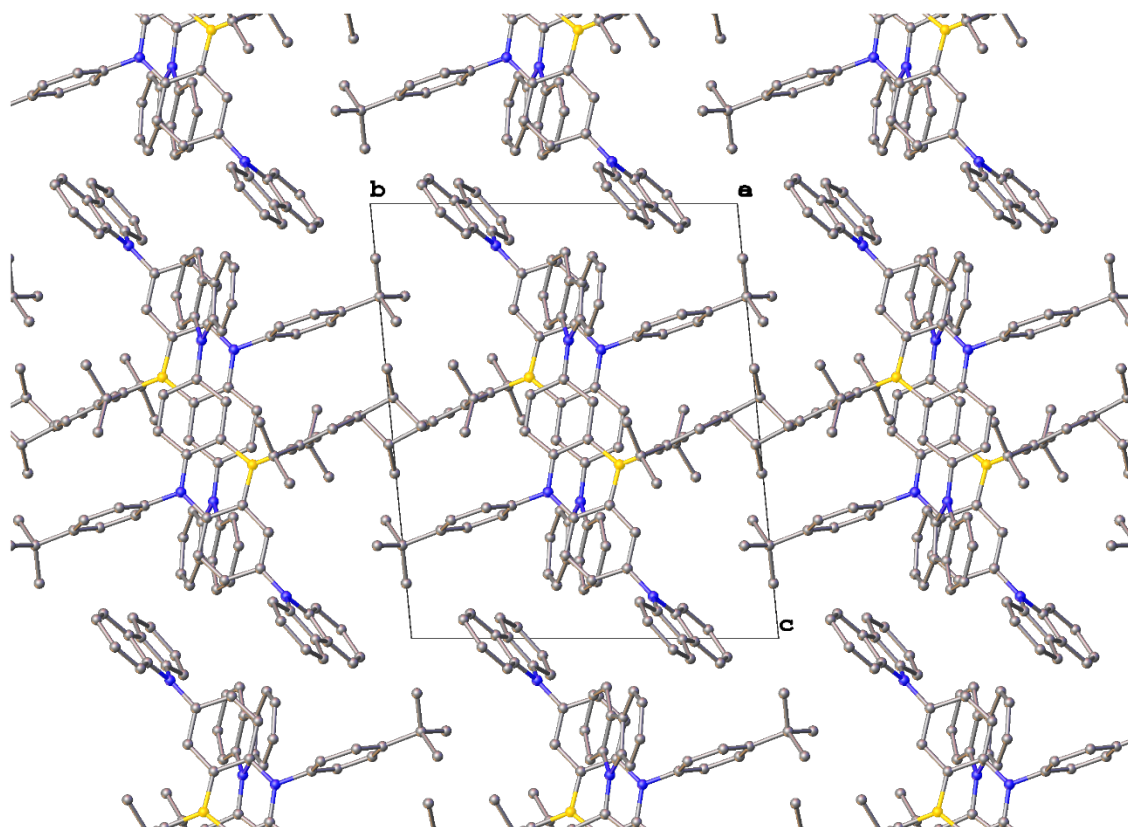
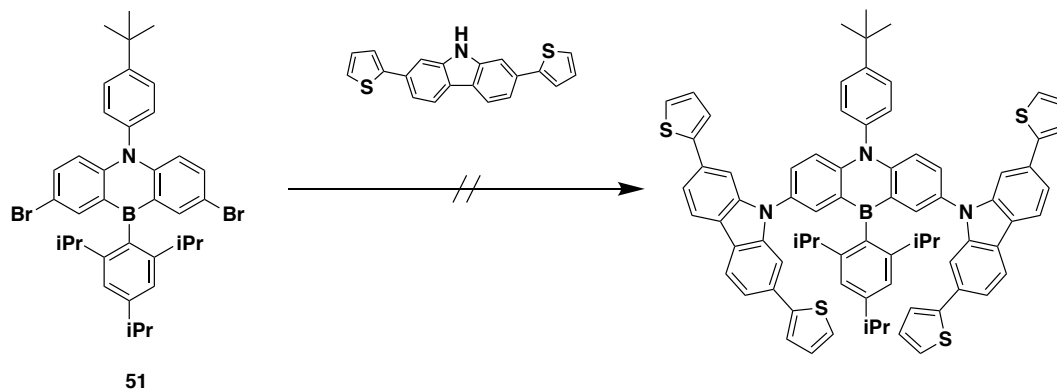


Figure 4.21: Packing diagram of the majority occupied moiety of **58**, viewed normal to the *a*-axis. Hydrogen atoms are omitted for clarity.

4.5.4.3 Unsuccessful Buchwald-Hartwig Coupling

As discussed in Section 4.3 of this chapter and illustrated by Figure 4.6, a highly rotationally restricted target compound was envisaged by introducing the thiophene rings at the 2,7 positions of the carbazole ring system, herein referred to as **AZB-2,7-TPN**. However, during synthesis of 2,7-di(thiophen-2-yl)-9*H*-carbazole, the product proved to be highly insoluble, with structural characterisation not accessible due to solubility challenges. The Buchwald-Hartwig trial was attempted with 2,7-di(thiophen-2-yl)-9*H*-carbazole, with hopes that the final product would be more soluble and thus easier to purify. A luminescent blue yellow powder was isolated from the reaction mixture, which was postulated to be the product. The yellow solid was highly insoluble, and did not appear to be air and moisture stable, decomposing into numerous side products after being exposed to light. This hindered the collection of well resolved NMR spectra. A pure product could not be attained, after numerous flash column chromatography and crystallisation trials. The product was not found

using HRMS. Due to the difficulty in purifying and characterising the residues, this target compound was not attained.



Scheme 4.7: Unsuccessful Buchwald-Hartwig coupling towards AZB-2,7-TPN.

4.6 Photophysical Analysis

In order to gain understanding into the types of photophysical processes occurring within the target molecules, solution UV-vis absorption and emission spectra of the target compounds were collected in toluene (Figure 4.22). The dominant absorption bands between 320-380 nm are assigned as the π - π^* transition, and the broad shoulder around 400 nm is due to the intramolecular charge transfer (ICT) from the amine-type donors to the central azaborine acceptor. **60** exhibits the highest molar extinction coefficient ϵ of the series due to the presence of four thiophene rings ($\epsilon = 1.067 \cdot 10^5 \text{ M}^{-1} \text{ cm}^{-1}$). Thus, from the series of compounds studied, **60** absorbs the most strongly in the visible region of the spectrum.

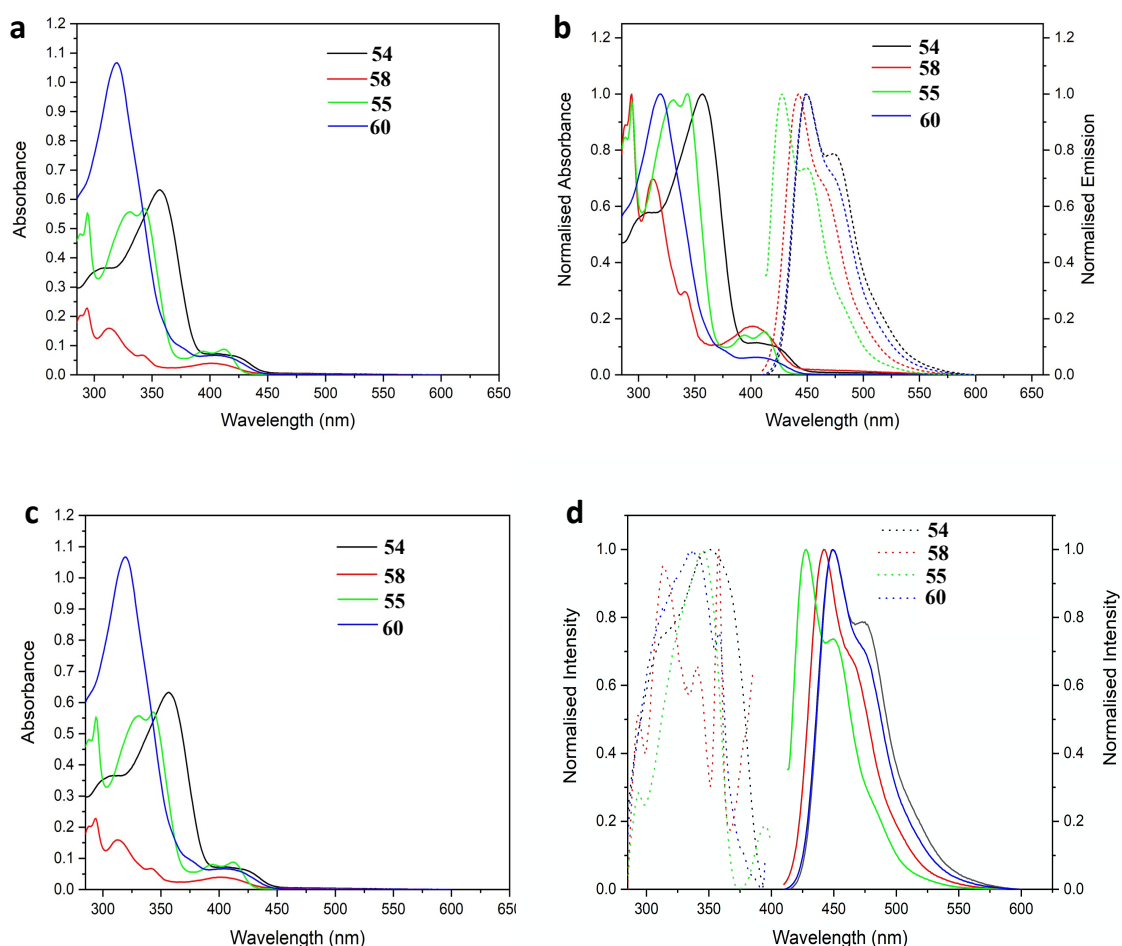


Figure 4.22: **a)** UV-vis absorption spectra (1×10^{-5} M) in toluene. **b)** Normalised UV-vis absorption and emission spectra (1×10^{-5} M) in toluene at RT **c)** UV-vis absorption spectra (1×10^{-5} M) in toluene, serves as a direct comparison to the excitation spectra of **d.)** Normalised excitation and emission spectra (1×10^{-5} M) in toluene at RT.

Steady state solution photoluminescence spectra were collected to study the compounds luminescence properties. It is common for blue emitting charge transfer compounds to observe a small Stokes shift.³⁴³ The non-bonding HOMO and LUMO orbitals of the molecule play a role in minimising the vibronic coupling between S_0 and S_1 excited states and the vibrational relaxation at the S_1 excited state, resulting in a small Stokes shift.³⁴⁴ A small Stokes shift is observed for all compounds in the family with the smallest Stokes shift of 15 nm observed for **58**. This results in an observable spectral overlap of the absorption and emission spectra for all compounds in the series (Figure 4.22b). The photoluminescence spectra exhibit dual emission (Table 4.1), ascribed to the donor emission (or local excited

state emission, LE), and ICT emission arising from hybridized local charge transfer (HLCT). All compounds exhibited narrow FWHM with the following trend: **58** < **55** < **60** < **54**, which are comparable to published reports of blue TADF-based OLEDs.^{335,343,345,346} Emitters which have narrowband emission of less than 60 nm have reduced exciton annihilation and quenching processes which all negatively affect the overall device performance; therefore narrowband emission is a desirable property of the OLED candidates.³⁴⁴

Table 4.1. Photophysical parameters.^a

	$\lambda_{\text{abs}} / \text{nm}$	ε ^[b]	$\lambda_{\text{em}} / \text{nm}$	Φ_{F} ^[c]	O ₂ response ^[d]	Stokes Shift ^[e]	FWHM / nm ^[f]
54	310, 357, 405	0.632	450 λ_{max} , 474 (405)	0.4244	28%	45	58
58	288, 294, 315, 341, 401	0.228	442 λ_{max} , 468 (401)	0.7314	n/a	41	48
55	288, 294, 331, 343, 394, 412	0.569	427 λ_{max} , 449 (412)	0.5458	15%	15	49
60	319, 403	1.067	449 λ_{max} , 470 (403)	0.6066	19%	46	54

^a UV-vis absorption and emission data (1×10^{-5} M) in toluene at $\lambda_{\text{ex}} > 400$ nm under Argon at RT. ^b Molar extinction coefficient at the absorption maxima. ε : $10^5 \text{ M}^{-1} \text{ cm}^{-1}$. ^c PLQY were calculated with all samples under Argon, with quinine sulfate as reference ($\Phi_{\text{F}} = 0.55$, 0.5 M H₂SO₄). ^d The Stokes shifts were determined by conversion of λ_{abs} and λ_{em} to wavenumbers prior to subtraction. ^e FWHM (full width at half maximum) values are given in nm. ^f

Photoluminescence quantum yields (PLQY) were determined for all compounds, with an observable trend as follows: **58** > **60** > **55** > **54**. By studying the trend closely, it is clear that the donor bond connectivity to the acceptor plays a role on the resulting PLQY. For **58** and **60**, the carbazole donors are bonded *via* the nitrogen (C-N bond, no phenyl spacer) atom of the carbazole ring system, improving charge transfer properties between the donor and acceptor moieties, and resulting in an observable positive effect on the luminescence properties. When the donor moieties were connected via C-C bond (containing a phenyl spacer) to the central acceptor, this resulted in an impairment of the charge transfer process,

which directly correlated to the reduction of the PLQY. **54** showed the lowest PLQY of the series. The reduced PLQY is attributed to triphenylamine donor chromophore flexibility, resulting in more non-radiative decay pathways. Chromophore rigidity plays a direct role on PLQY, and higher structural rigidification correlates with higher PLQY.³²⁶

For an organic donor-acceptor structure to exhibit TADF behaviour, the S_1 - T_1 excited state levels must be close in energy for RISC to be viable, and the triplet excited state must be energetically accessible (Chapter One, 1.8.2.1). Atmospheric oxygen can quench the triplet excited state (Chapter Two, 3.9.1). To probe for the triplet excited state character, photoluminescence measurements were collected: aerated samples, under an atmosphere of argon, and reaerated. The purpose of the reaerated spectra is to eliminate the possibility of concentration changes being the responsible for emission intensity changes between the aerated and the argon samples. Figure 4.23 below illustrates the collected spectra.

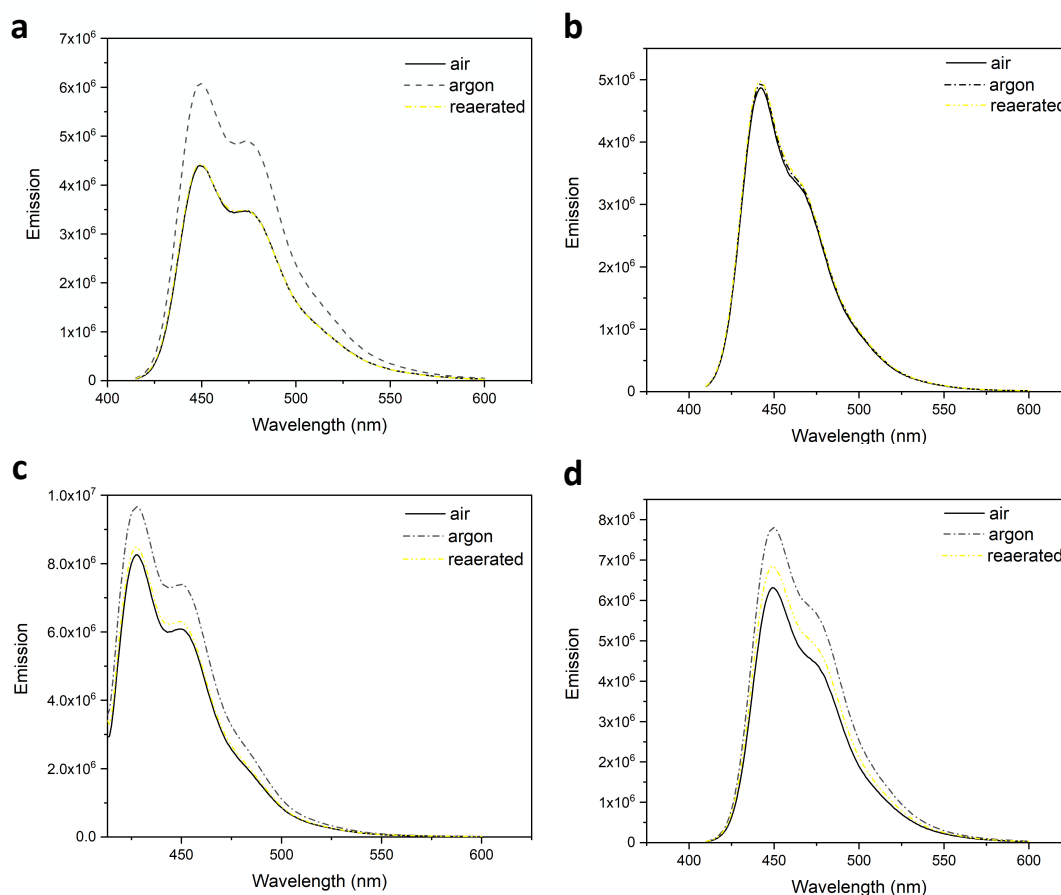


Figure 4.23: **a)** Emission spectra of **54** (1×10^{-5} M) in toluene at RT. **b)** Emission spectra of **55** (1×10^{-5} M) in toluene at RT. **c)** Emission spectra of **58** (1×10^{-5} M) in toluene at RT. **d)** Emission spectra of **60** (1×10^{-5} M) in toluene at RT.

54 exhibits the highest oxygen response with a 28% increase in emission intensity under argon, followed by **60** with 19% emission intensity increase and **55** at 15% emission intensity increase; proving triplet excited state is being accessed in these compounds. However, **58** showed no oxygen response, and the emission profile is due to the S_1 - S_0 radiative decay. For all compounds, there was no difference in aerated spectra and reaerated spectra, proving that the above observations were not due to concentration changes.

To further support the charge transfer phenomenon and to elucidate the strongest donor of the series, the emission spectra of the compounds were measured in a range of solvents to study the solvatochromic effects (Figure 4.24).

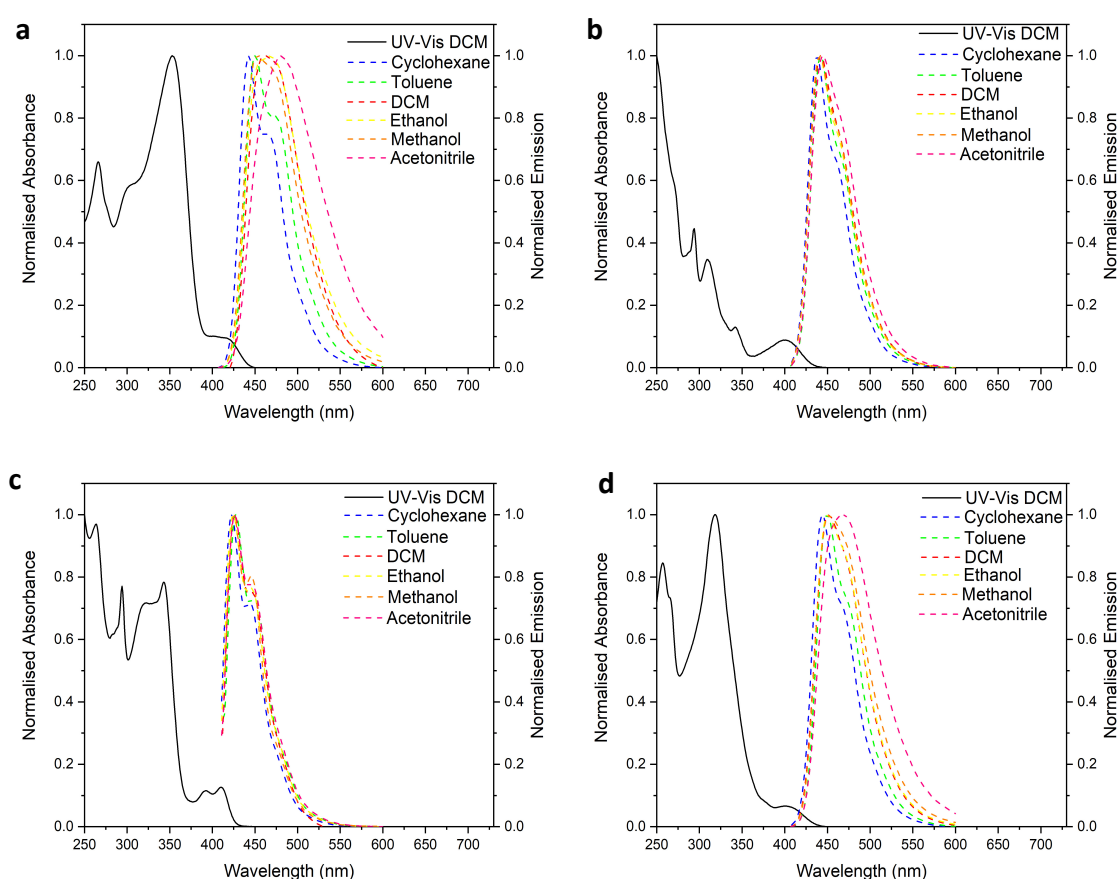


Figure 4.24: **a)** Normalised UV-vis absorption spectra of **54** (1×10^{-5} M) in methylene chloride and emission spectra in various solvents at RT. **b)** Normalised UV-vis absorption spectra of **58** (1×10^{-5} M) in methylene chloride and emission spectra in various solvents at RT. **c)** Normalised UV-vis absorption spectra of **55** (1×10^{-5} M) in methylene chloride and emission spectra in various solvents at RT. **d)** Normalised UV-vis absorption spectra of **60** (1×10^{-5} M) in methylene chloride and emission spectra in various solvents at RT.

The degree of the positive bathochromic shift in high polarity solvents directly correlates to the electron-donating strength of the donor moiety.³⁴⁷ **54** and **60** exhibit the strongest bathochromic shift with increasing solvent polarity. **58** and **55** exhibited negligible solvatochromism, indicating that LE was the dominant emission pathway, and that carbazole and phenyl carbazole donors were the weakest of the series.

To further probe CT phenomenon, 77 K emission measurements were collected in 4:1 ethanol:methanol solvent mixture which formed a transparent glass suitable for 77 K emission measurements (Figure 4.25 below).

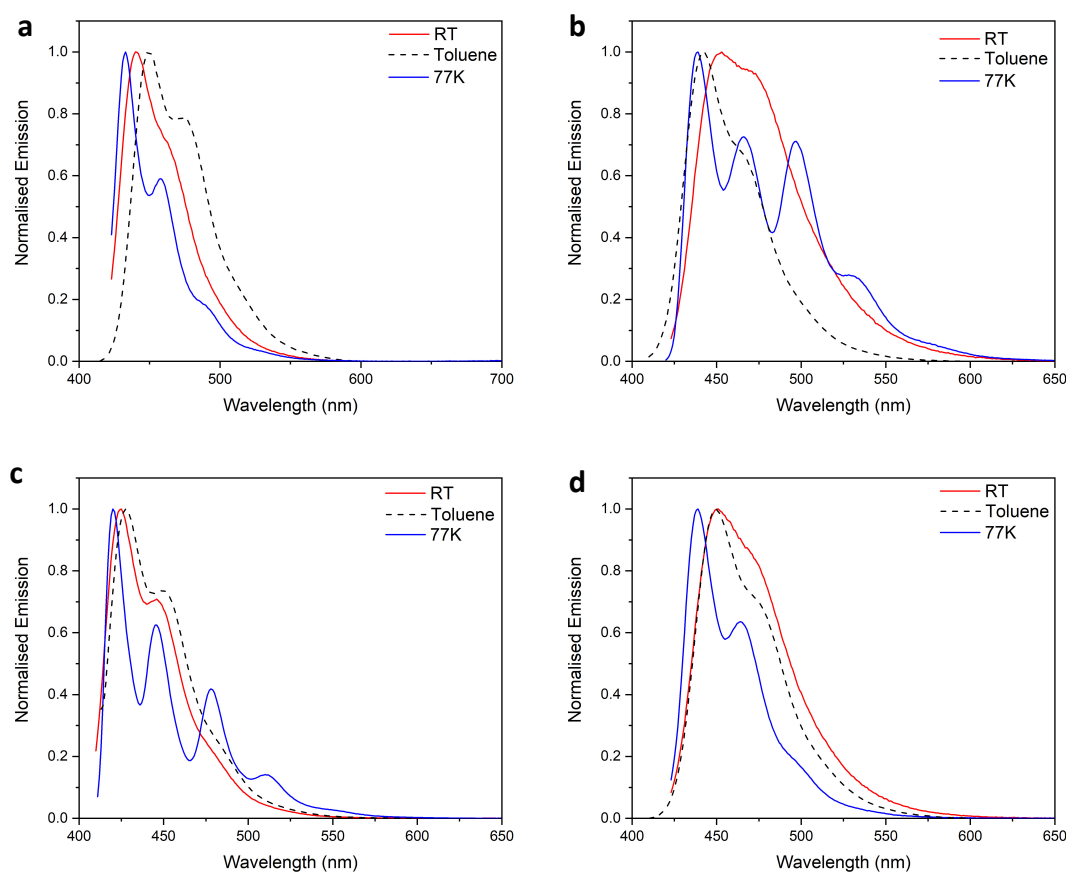


Figure 4.25: **a)** Normalised emission spectra of **54** (1×10^{-5} M) in toluene at RT, and in 4:1 ethanol:methanol mix at RT and at 77 K. **b)** Normalised emission spectra of **58** (1×10^{-5} M) in toluene at RT, and in 4:1 ethanol:methanol mix at RT and at 77 K. **c)** Normalised emission spectra of **55** (1×10^{-5} M) in toluene at RT, and in 4:1 ethanol:methanol mix at RT and at 77 K. **d)** Normalised emission spectra of **60** (1×10^{-5} M) in toluene at RT, and in 4:1 ethanol:methanol mix at RT and at 77 K.

If CT occurs in the molecule, its 77 K spectra will be hypsochromically shifted with respect to the RT spectra, due to emission resulting from LE not CT states.³⁴⁸ The 77 K spectra support the solvatochromic studies (Figure 4.25), and show that **54** and **60** have the biggest hypsochromic shift. **55** and **58** have a negligible hypsochromic shift which also correlates to the observed solvatochromic behaviour.

Upon closer inspection, **55** and **58** have highly structured emission spectra, which could be attributed to fewer rotational degrees of freedom of the chromophores at cooled temperatures. **54** and **60** have more structureless emission spectra, and also have more flexible chromophores. To test this theory, cooling ¹H NMR measurements (-20 °C - 25 °C, CDCl₃) were run to study structural spectral changes with varying temperature (Appendix 3.1). However within the range of study, no spectral changes were observed with varying temperature. As part of future work, this requires further attention, to understand chromophore structural degrees of freedom and its effect on the resulting spectra.

Collectively, solution photophysical analyses provided an understanding of the compounds' emissive properties, and as a result their validity as TADF OLED candidates. **60** surpassed the series of compounds studied: with the highest molar extinction coefficient ϵ , strongest CT character, strongest donor due to the four terminal thiophene rings at the C3 and C6 positions of the carbazole, and the C/N connectivity between the carbazole and azaborine. Additionally, **60** showed moderate structural rigidity, high PLQY, and a high percentage of triplet excited state character in its emission profile. Cheng *et. al* reported no TADF behavior in **L4.9** (Figure 4.4), an analogue of **60** with the same substitution pattern of the carbazole donor: tert-butyl groups at the C3 and C6 positions of the carbazole donor. Introducing four highly emissive thiophene rings in the same positions as **L4.9** resulted in very different photophysical properties, stronger solvatochromism and improved charge transfer behavior. Therefore, the dihedral angle is not the only factor affecting TADF behavior which the authors used as their main argument for TADF, and future OLED candidate design should incorporate the importance of the donor strength, not just restricting rotation.

These properties make **60** the only viable TADF OLED candidate of the series, due to its prevalent CT character and high percentage of triplet excited state character. Although the above findings are promising, they are only preliminary studies. Further transient absorption measurements to elucidate excited state lifetimes, solid state photophysical measurements, and OLED device fabrication are all required to definitively confirm compound **60**'s validity as an OLED candidate.

4.7 Computational Analysis

TDDFT calculations using B3LYP|6-31G* were carried out by Dr. Xiaoneng Cui, in order to computationally determine the HOMO/LUMO separation and energy levels and to give further insight into this work (Figure 4.26 below).

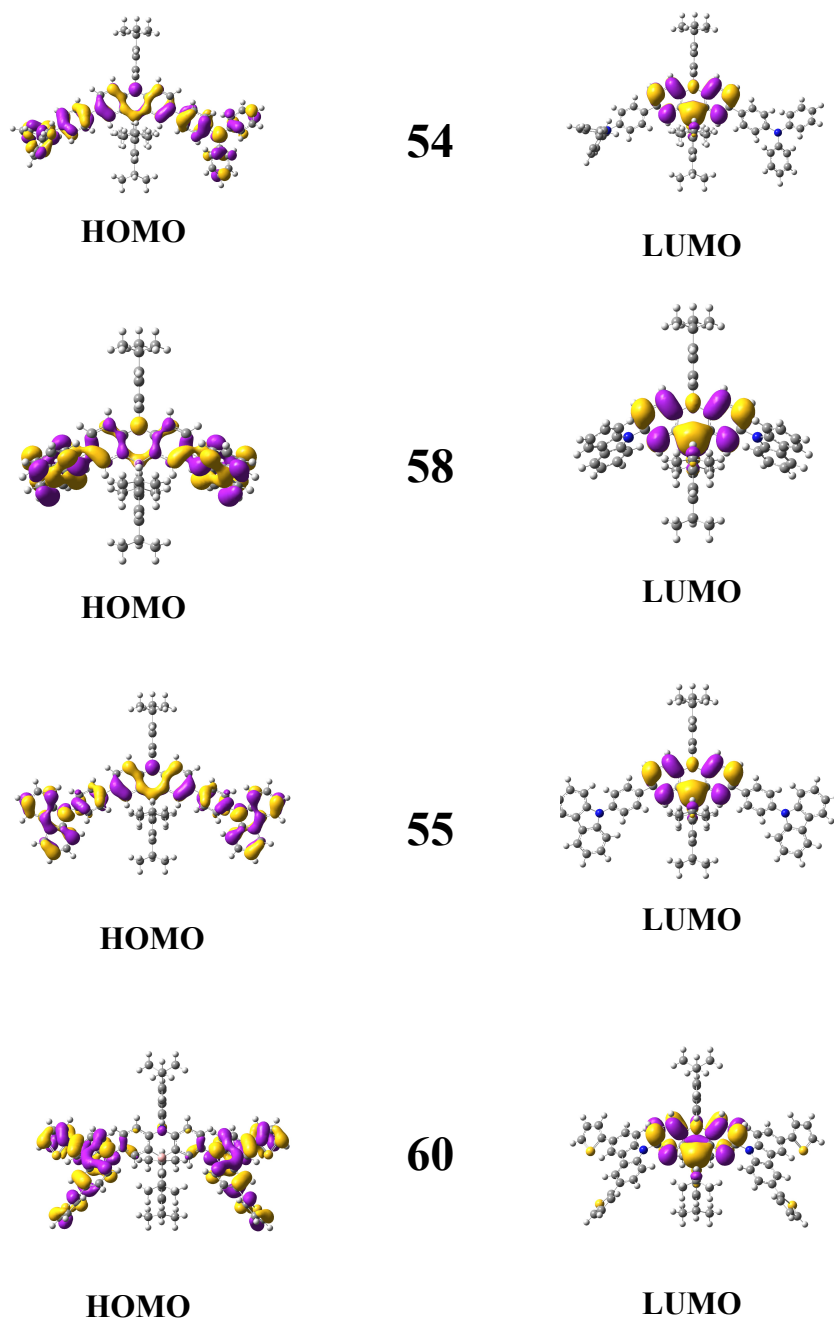


Figure 4.26: Computationally calculated HOMO/LUMO energy levels using B3LYP|6-31G*.

A twisted approach was taken for this body of work to spatially separate the frontier molecular orbitals. A twisted donor-acceptor structure destabilises the T_1 energy level between the HOMO and the LUMO.^{349–352} By varying the dihedral angle between the donor and the acceptor, the HOMO/LUMO gap can be adjusted, restricted overlap resulting in a smaller $\Delta E_{S_1-T_1}$ gap. An important caveat exists whereby according to the Frank-Condon principle, a molecule with a small orbital overlap results in a lower quantum efficiency.³⁴⁷ Therefore, careful consideration must be given when designing the emitters, and a moderate twist is better than a highly rotationally restricted molecule, in order to not negatively affect the quantum efficiency of the emitter.

Figure 4.26 illustrates the frontier molecular orbital distribution on each emitter. **54**, **55**, and **58** all have spatially delocalised HOMO orbitals, extending over both the donor moieties and the central acceptor moiety, which causes a significant overlap with the LUMO orbitals. This overlap is reflected in the elevated $\Delta E_{S_1-T_1}$ gap of the three aforementioned emitters (Table 4.2 below), and explains why CT processes were inhibited as observed in the photophysical measurements. **60** observes highly localised HOMO and LUMO orbitals, and as a result has the smallest $\Delta E_{S_1-T_1}$ gap ($\Delta E_{S_1-T_1} = 0.19$ eV) of the series. Its analogue, **L4.9** has more delocalised HOMO orbital and a much larger $\Delta E_{S_1-T_1}$ gap of 0.3 eV; further illustrating that incorporation of the terminal thiophene rings at the C3 and C6 positions of the carbazole donor had a direct positive effect on the HOMO/LUMO separation. As previously stated in Section 1.8.2.2, a $\Delta E_{S_1-T_1}$ gap of less than 0.3 eV is required for RISC to be efficient enough to permit TADF. Therefore, **60** is the only compound of the series which has a small enough $\Delta E_{S_1-T_1}$ to permit TADF behaviour.

Table 4.2 Complete computationally calculated excited state energies using B3LYP|6-31G*.

	S_1 ^[a]	T_1 ^[a]	$\Delta E_{S_1-T_1}$ ^[a]
54	2.9732	2.5083	0.4649
58	3.0045	2.6497	0.3548
55	3.1963	2.6220	0.5743
60	2.7946	2.5961	0.1985

^a All values stated in eV.

Computational analysis was also performed on **AZB-2,7-TPN**, even though the compound was not realised. The reason for this is to gain further understanding if substituting thiophene rings at the C2 and C7 positions would be superior to C3 and C6 positions of the carbazole donor, and if the additional restricted rotation would contribute to the overall HOMO/LUMO. Interestingly, substituting the carbazole donor at the C2 and C7 positions had a negative effect on the HOMO and LUMO orbital distribution, and resulted in a larger $\Delta E_{S_1-T_1}$ gap (Table 4.3, Figure 4.27). Even though this substitution resulted in a larger dihedral angle and a more twisted molecular structure, it did not manage to separate HOMO and LUMO orbitals, and had a detrimental effect on the $\Delta E_{S_1-T_1}$. Applying these findings to future work, chapter four will utilise 3,6-dithiophene as a donor due to its outstanding donor abilities in **60**, and any further pursuit of 2,7-dithiophene carbazole containing compounds will be abandoned.

Table 4.3 Complete computationally calculated excited state energies using B3LYP|6-31G*.

	S_1 ^[a]	T_1 ^[a]	$\Delta E_{S_1-T_1}$ ^[a]
AZB-2,7-TPN	-2.9853	-2.4459	0.5394

^a All values stated in eV.

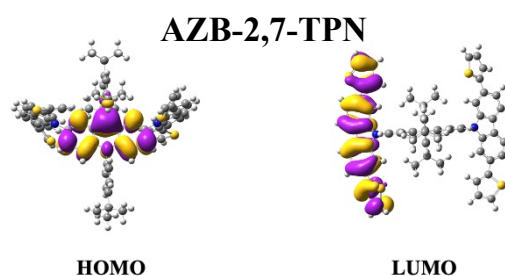


Figure 4.27: Computationally calculated HOMO/LUMO energy levels for **AZB-2,7-TPN**, using B3LYP|6-31G*.

4.8 Thermal Analysis

In order to test the compounds' validity as OLED candidates, their thermal properties were studied. Thermogravimetric analysis was utilised to determine decomposition temperatures of the emitters (Figure 4.27). An identical TGA method was applied as outlined in Chapter Three (Section 3.12). **58** has the lowest first decomposition temperature at 202 °C, resulting in a ~30% loss in mass (Table 4.4). The remaining compounds have much higher thermal stability, stable past 400 °C, making them applicable for OLED device fabrication

Table 4.4: Thermogravimetric analysis (TGA) data of the compounds carried out under an N₂ atmosphere.

Compound	Temperature °C
54	398, 543
58	202, 389
55	421, 535
60	427, 517

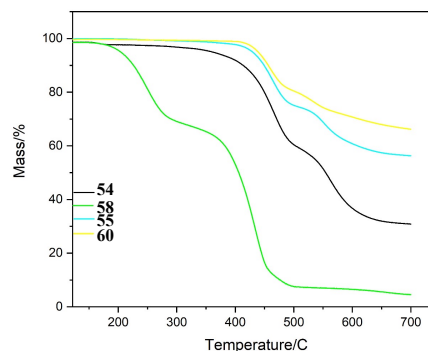


Figure 4.27: Thermogravimetric analysis (TGA) of the compounds carried out under an N₂ atmosphere

4.9 Conclusions

The purpose of this chapter was to design, synthesise, and study highly twisted D- π -A- π -D and D-A-D compounds which would be utilised as blue emitting OLED candidates. During the synthesis stage, to optimise the C-N bond forming reactions, a series of Buchwald-Hartwig reactions were trialled towards novel synthetic pathways to attain acyclic halogenated tertiary amines. However, after numerous trials, it was confirmed that acyclic halogenated secondary amines are not strong enough nucleophiles to participate in palladium catalysed Buchwald-Hartwig coupling reactions.

Four final emitters were attained: **54** (D- π -A- π -D architecture), **58** (D-A-D architecture), **55** (D- π -A- π -D architecture), and **60** (D-A-D architecture). **54** had a highly flexible backbone, which contributed to reduced PLQY of the series. CT behaviour was not observed in **58** or **55**, and both emitters have highly delocalised HOMO orbitals.

Using solution UV-vis absorption and emission studies combined with TDDFT, it was proven that **60** outperformed the series of emitters, and it was the only viable TADF OLED candidate of the series. The C/N bond connectivity between the donors and acceptor contributed to more efficient CT, while introducing thiophene rings at the C3 and C6 positions of the carbazole improved both the donor strength and contributed to greater HOMO localisation. TDDFT studies showed that a large dihedral angle is not the main parameter to consider whilst designing an efficient TADF OLED candidate, as was observed with **AZB-2,7-TPN**. The strength of the donor as well as the acceptor, and a moderate twisted structure is more important than a direct focus on the dihedral angle alone. In all compounds, azaborine was a very efficient electron acceptor, but combined with a strong donor, resulted in very efficient TADF candidate (**60**).

4.10 Future Work

As part of future work, cooling NMR studies of the emitters will be performed to further study the restricted rotation as a function of temperature. Furthermore, transient emission studies are required to study in depth the excited states of the emitters, and the excited state lifetimes. Solid state photophysical measurements and OLED device fabrication are planned in collaboration with St. Andrews University to ascertain the compounds validity as OLED materials.

4.11 References

- 1 R. D. Dewhurst, R. Claessen and H. Braunschweig, *Angew. Chemie Int. Ed.*, 2016, **55**, 4866–4868.
- 2 P. Li, H. Chan, S. L. Lai, M. Ng, M. Y. Chan and V. W. W. Yam, *Angew. Chemie - Int. Ed.*, 2019, **58**, 9088–9094.
- 3 H. Lee, D. Karthik, R. Lampande, J. H. Ryu and J. H. Kwon, *Front. Chem.*, 2020, **8**, 1–16.
- 4 E. von Grotthuss, A. John, T. Kaese and M. Wagner, *Asian J. Org. Chem.*, 2018, **7**, 37–53.
- 5 S. Y. Li, Z. B. Sun and C. H. Zhao, *Inorg. Chem.*, 2017, **56**, 8705–8717.
- 6 S. K. Møllerup and S. Wang, *Trends Chem.*, 2019, **1**, 77–89.
- 7 J. Radtke, K. Schickedanz, M. Bamberg, L. Menduti, D. Schollmeyer, M. Bolte, H. W. Lerner and M. Wagner, *Chem. Sci.*, 2019, **10**, 9017–9027.
- 8 T. W. Hudnall, C.-W. Chiu and F. P. Gabbaï, *Acc. Chem. Res.*, 2009, **42**, 388–397.
- 9 Z. Liu, Q. Fang, D. Wang, G. Xue, W. Yu, Z. Shao and M. Jiang, *Chem. Commun.*, 2002, 2900–2901.
- 10 M. Ito, E. Ito, M. Hirai and S. Yamaguchi, *J. Org. Chem.*, 2018, **83**, 8449–8456.
- 11 L. Ji, S. Griesbeck and T. B. Marder, *Chem. Sci.*, 2017, **8**, 846–863.
- 12 M. Numata, T. Yasuda and C. Adachi, *Chem. Commun.*, 2015, **51**, 9443–9446.
- 13 X. Cai, X. Li, G. Xie, Z. He, K. Gao, K. Liu, D. Chen, Y. Cao and S.-J. Su, *Chem. Sci.*, 2016, **7**, 4264–4275.
- 14 T. L. Wu, M. J. Huang, C. C. Lin, P. Y. Huang, T. Y. Chou, R. W. Chen-Cheng, H. W. Lin, R. S. Liu and C. H. Cheng, *Nat. Photonics*, 2018, **12**, 235–240.
- 15 K.-H. Kim, E. S. Ahn, J.-S. Huh, Y.-H. Kim and J.-J. Kim, *Chem. Mater.*, 2016, **28**, 7505–7510.
- 16 S. Kim, W. Jeong, C. Mayr, Y. Park, K. Kim, J. Lee, C. Moon, W. Brütting and J. Kim, *Adv. Funct. Mater.*, 2013, **23**, 3896–3900.
- 17 J.-M. Teng, Y.-F. Wang and C.-F. Chen, *J. Mater. Chem. C*, 2020, **8**, 11340–11353.
- 18 C. Qu, G. Xia, Y. Xu, Y. Zhu, J. Liang, H. Zhang, J. Wang, Z. Zhang and Y. Wang, *J. Mater. Chem. C*, 2020, **8**, 3846–3854.
- 19 M. Godumala, J. Hwang, H. Kang, J.-E. Jeong, A. K. Harit, M. J. Cho, H. Y. Woo, S. Park and D. H. Choi, *ACS Appl. Mater. Interfaces*, 2020, **12**, 35300–35310.
- 20 C. Maglione, A. Carella, R. Centore, P. Chávez, P. Lévêque, S. Fall and N. Leclerc, *Dye. Pigment.*, 2017, **141**, 169–178.
- 21 T. Hatakeyama, K. Shiren, K. Nakajima, S. Nomura, S. Nakatsuka, K. Kinoshita, J. Ni, Y. Ono and T. Ikuta, *Adv. Mater.*, 2016, **28**, 2777–2781.
- 22 H. Hirai, K. Nakajima, S. Nakatsuka, K. Shiren, J. Ni, S. Nomura, T. Ikuta and T. Hatakeyama, *Angew. Chemie Int. Ed.*, 2015, **54**, 13581–13585.
- 23 X. Liang, Z. Yan, H. Han, Z. Wu, Y. Zheng, H. Meng, J. Zuo and W. Huang, *Angew. Chemie*,

2018, **130**, 11486–11490.

- 24 J. Wu, Y. Kan, Z. Xue, J. Huang, P. Chen, X. Yu, Z. Guo and Z. Su, *J. Mater. Chem. C*, 2017, **5**, 9088–9097.
- 25 S. M. Suresh, E. Duda, D. Hall, Z. Yao, S. Bagnich, A. M. Z. Slawin, H. Bässler, D. Beljonne, M. Buck, Y. Olivier, A. Köhler and E. Zysman-Colman, *J. Am. Chem. Soc.*, 2020, **142**, 6588–6599.
- 26 M. Ando, M. Sakai, N. Ando, M. Hirai and S. Yamaguchi, *Org. Biomol. Chem.*, 2019, **17**, 5500–5504.
- 27 J. Y. Wang and J. Pei, *Chinese Chem. Lett.*, 2016, **27**, 1139–1146.
- 28 C. J. Saint-Louis, L. L. Magill, J. A. Wilson, A. R. Schroeder, S. E. Harrell, N. S. Jackson, J. A. Trindell, S. Kim, A. R. Fisch, L. Munro, V. J. Catalano, C. E. Webster, P. P. Vaughan, K. S. Molek, A. K. Schrock and M. T. Huggins, *J. Org. Chem.*, 2016, **81**, 10955–10963.
- 29 K. Mitsudo, K. Shigemori, H. Mandai, A. Wakamiya and S. Suga, *Org. Lett.*, 2018, **20**, 7336–7340.
- 30 M. Lepeltier, O. Lukoyanova, A. Jacobson, S. Jeeva and D. F. Perepichka, *Chem. Commun.*, 2010, **46**, 7007–7009.
- 31 X. Liu, Y. Zhang, B. Li, L. N. Zakharov, M. Vasiliu, D. A. Dixon and S. Y. Liu, *Angew. Chemie - Int. Ed.*, 2016, **55**, 8333–8337.
- 32 P. G. Campbell, A. J. V. Marwitz and S. Y. Liu, *Angew. Chemie - Int. Ed.*, 2012, **51**, 6074–6092.
- 33 X. Y. Wang, J. Y. Wang and J. Pei, *Chem. - A Eur. J.*, 2015, **21**, 3528–3539.
- 34 T. L. Wu, S. H. Lo, Y. C. Chang, M. J. Huang and C. H. Cheng, *ACS Appl. Mater. Interfaces*, 2019, **11**, 10768–10776.
- 35 S. Krotkus, M. Y. Wong, G. Hedley, M. Jaricot, D. B. Cordes, A. M. Z. Slawin, C. Murawski, M. C. Gather, Y. Olivier, D. Beljonne, E. Zysman-Colman and I. D. W. Samuel, *SID Symp. Dig. Tech. Pap.*, 2018, **49**, 239–242.
- 36 S. W. Li, C. H. Yu, C. L. Ko, T. Chatterjee, W. Y. Hung and K. T. Wong, *ACS Appl. Mater. Interfaces*, 2018, **10**, 12930–12936.
- 37 M. Yokoyama, K. Inada, Y. Tsuchiya, H. Nakanotani and C. Adachi, *Chem. Commun.*, 2018, **54**, 8261–8264.
- 38 M. Y. Wong, S. Krotkus, G. Copley, W. Li, C. Murawski, D. Hall, G. J. Hedley, M. Jaricot, D. B. Cordes, A. M. Z. Slawin, Y. Olivier, D. Beljonne, L. Muccioli, M. Moral, J. C. Sancho-Garcia, M. C. Gather, I. D. W. Samuel and E. Zysman-Colman, *ACS Appl. Mater. Interfaces*, 2018, **10**, 33360–33372.
- 39 R. Wang, Y. Wang, N. Lin, R. Zhang, L. Duan and J. Qiao, *Chem. Mater.*, 2018, **30**, 1–11.
- 40 T. Serevičius, T. Bučiūnas, J. Bucevičius, J. Dodonova, S. Tumkevičius, K. Kazlauskas and S. Juršėnas, *J. Mater. Chem. C*, 2018, **6**, 11128–11136.
- 41 R. Huang, J. Avó, T. Northey, E. Channing-Pearce, P. L. Dos Santos, J. S. Ward, P. Data, M. K. Etherington, M. A. Fox, T. J. Penfold, M. N. Berberan-Santos, J. C. Lima, M. R. Bryce and F. B. Dias, *J. Mater. Chem. C*, 2017, **5**, 6269–6280.

- 42 R. Pashazadeh, P. Pander, A. Bucinskas, P. J. Skabara, F. B. Dias and J. V. Grazulevicius, *Chem. Commun.*, 2018, 13857–13860.
- 43 L. Ji, S. Griesbeck and T. B. Marder, *Chem. Sci.*, 2017, **8**, 846–863.
- 44 J. M. W. Chan, *J. Mater. Chem. C*, 2019, **7**, 12822–12834.
- 45 N. A. Kukhta, A. S. Batsanov, M. R. Bryce and A. P. Monkman, *J. Phys. Chem. C*, 2018, **122**, 28564–28575.
- 46 T. L. Wu, S. H. Lo, Y. C. Chang, M. J. Huang and C. H. Cheng, *ACS Appl. Mater. Interfaces*, 2019, **11**, 10768–10776.
- 47 H. Chen, Y. Deng, X. Zhu, L. Wang, L. Lv, X. Wu, Z. Li, Q. Shi, A. Peng, Q. Peng, Z. Shuai, Z. Zhao, H. Chen and H. Huang, *Chem. Mater.*, 2020, **32**, 4038–4044.
- 48 Y. Yu, L. Ma, Z. Feng, B. Liu, H. Zhou, H. Qin, H. Li, J. Song, G. Zhou and Z. Wu, *J. Mater. Chem. C*, 2019, **7**, 5604–5614.
- 49 C. Zhang, M. Tang, B. Sun, W. Wang, Y. Yi and F. L. Zhang, *Can. J. Chem.*, 2020, **98**, 40–48.
- 50 A. Choi and S. C. Miller, *Org. Lett.*, 2018, **20**, 4482–4485.
- 51 R. A. Altman and S. L. Buchwald, *Nat. Protoc.*, 2007, **2**, 2474–2478.
- 52 T. Wang, D. R. Magnin and L. G. Hamann, *Org. Lett.*, 2003, **5**, 897–900.
- 53 J. P. Wolfe and S. L. Buchwald, *J. Org. Chem.*, 1996, **61**, 1133–1135.
- 54 I. S. Park, K. Matsuo, N. Aizawa and T. Yasuda, *Adv. Funct. Mater.*, 2018, **28**, 1–12.
- 55 T.-L. Wu, S.-H. Lo, Y.-C. Chang, M.-J. Huang and C.-H. Cheng, *ACS Appl. Mater. Interfaces*, 2019, **11**, 10768–10776.
- 56 M. D. Aparece, W. Hu and J. P. Morken, *ACS Catal.*, 2019, **9**, 11381–11385.
- 57 A. G. Orpen, L. Brammer, F. H. Allen, O. Kennard, D. G. Watson and R. Taylor, in *Structure correlation*, Verlag Chemie, Weinheim, 1994, pp. 751–858.
- 58 C. A. Hunter and J. K. M. Sanders, *J. Am. Chem. Soc.*, 1990, **112**, 5525–5534.
- 59 V. Malavade, M. Patil and M. Patil, *European J. Org. Chem.*, 2020, **2020**, 561–569.
- 60 I. A. Jessop, M. Bustos, D. Hidalgo, C. A. Terraza, A. Tundidor-Camba, M. A. Pardo, D. Fuentealba, M. Hssein and J. C. Bernede, *Int. J. Electrochem. Sci.*, 2016, **11**, 9822–9838.
- 61 A. J. Smith, A. Young, S. Rohrbach, E. F. O’Connor, M. Allison, H. Wang, D. L. Poole, T. Tuttle and J. A. Murphy, *Angew. Chemie Int. Ed.*, 2017, **56**, 13747–13751.
- 62 M. Singh, R. Kurchania, J. A. Mikroyannidis, S. S. Sharma and G. D. Sharma, *J. Mater. Chem. A*, 2013, **1**, 2297–2306.
- 63 P. Rajamalli, N. Senthilkumar, P.-Y. Huang, C.-C. Ren-Wu, H.-W. Lin and C.-H. Cheng, *J. Am. Chem. Soc.*, 2017, **139**, 10948–10951.
- 64 Y. Kondo, K. Yoshiura, S. Kitera, H. Nishi, S. Oda, H. Gotoh, Y. Sasada, M. Yanai and T. Hatakeyama, *Nat. Photonics*, 2019, **13**, 678–682.
- 65 G. H. Kim, R. Lampande, J. B. Im, J. M. Lee, J. Y. Lee and J. H. Kwon, *Mater. Horizons*,

2017, **4**, 619–624.

- 66 P. Rajamalli, N. Senthilkumar, P. Gandeepan, P.-Y. Huang, M.-J. Huang, C.-Z. Ren-Wu, C.-Y. Yang, M.-J. Chiu, L.-K. Chu and H.-W. Lin, *J. Am. Chem. Soc.*, 2016, **138**, 628–634.
- 67 T.-L. Wu, S.-H. Lo, Y.-C. Chang, M.-J. Huang and C.-H. Cheng, *ACS Appl. Mater. Interfaces*, 2019, **11**, acsami.8b21568.
- 68 W. Qiu, X. Cai, M. Li, L. Wang, Y. He, W. Xie, Z. Chen, M. Liu and S.-J. Su, *J. Mater. Chem. C*.
- 69 L. Cui, H. Nomura, Y. Geng, J. U. Kim, H. Nakanotani and C. Adachi, *Angew. Chemie Int. Ed.*, 2017, **56**, 1571–1575.
- 70 I. S. Park, H. Komiyama and T. Yasuda, *Chem. Sci.*, 2017, **8**, 953–960.
- 71 Y. Kitamoto, T. Namikawa, D. Ikemizu, Y. Miyata, T. Suzuki, H. Kita, T. Sato and S. Oi, *J. Mater. Chem. C*, 2015, **3**, 9122–9130.
- 72 J. S. Ward, R. S. Nobuyasu, A. S. Batsanov, P. Data, A. P. Monkman, F. B. Dias and M. R. Bryce, *Chem. Commun.*, 2016, **52**, 2612–2615.

Chapter Five
Summary of Findings

5.1 Summary of Findings

The contents of this thesis can be summarised with two separate undertakings, with an overall goal to design, synthesise, and study novel organic materials. The first undertaking (Chapter Two) required detailed synthetic methodological studies to develop novel pathways towards PAH-type molecules (from all carbon to nitrogen doped, to boron doped nanographenes). The second undertaking (Chapters Three and Four) focused on designing and synthesising small donor-acceptor systems for application in the OLED devices.

Chapter Two focused extensively on developing novel synthetic methodologies towards novel PAH-type molecules, with specific focus on all carbon, nitrogen-doped, and boron and nitrogen doped PAH synthesis. All-carbon PAH (referred to in text as C_{72}) was successfully synthesised using a novel route *via* a Knoevenagel condensation, however the products proved to be highly air sensitive. The chapter proposed a mechanism of the ring opening of the Knoevenagel products, as well as future synthetic pathways which are possible with this deviation. Nitrogen doped PAH compounds (longitudinally extended phenazine PAH's) were successfully synthesised in a facile one step Schiff base condensation, showcasing that synthetic routes towards PAH's are possible, if the correct pre-fused aromatic units are synthesised. Unprecedented electronic and conductive properties of these compounds are predicted, with these compounds potentially useful as single molecule junctions and semiconductors. Additionally, a discussion on DDQ/H⁺ as a cyclohydrogenation agent was trialled on previously synthesised pyrazidine containing polyphenylenes in an attempt to synthesise triangular nitrogen-doped PAH targets. However, after repeated trials, the polyphenylene precursors appeared to be inert to these cyclohydrogenation conditions. This chapter finishes with an extensive methodological discussion towards centrally boron doped and peripherally nitrogen doped PAH compounds. After repeated trials, and a mixture of successes and failures, the desired final compounds were not attained. Future work envisions a radical rethinking of the synthetic pathway, to further attempt the synthesis of boron and nitrogen doped PAH's.

Chapter Three summarised the design, synthesis, and photophysical studies of five novel A- π -D- π -A systems, with a PTZ donor centre and varying acceptor appendages. An acetylene linker was incorporated into all structures to ensure planarity, full conjugation extension, and HOMO/LUMO orbital separation. All compounds synthesised possessed ICT emissive character and were green to orange emitters. The benzonitrile emitters **39-41** were found to be highly luminescent but possessed

no triplet excited state character and were purely fluorescent. The chapter detailed an account into the most effective positioning of the electron-withdrawing cyano moiety: proving that the *para*-positioning has the largest effect on the emissive properties of the materials. Following that, two triazine containing A- π -D- π -A systems were synthesized, with a cyano-functionalized triazine in the *para*- position. The emission of triazine **42** possesses ICT character and was determined to be an orange emitter but it did not show TADF behavior due to its HOMO/LUMO overlap, no triplet excited state character, and an increased ΔE_{S1-T1} . Successful ICT is also observed for **43**, due a localized LUMO, evident triplet excited state character, and a small ΔE_{S1-T1} gap. However, both **42** and **43** suffer a sufficiently reduced PLQY due to their extended conjugation resulting in more non-radiative decay pathways. This chapter concluded with an understanding that utilizing an acetylene linker as a means to separate donor and acceptor structures was only effective to induce ICT, but not an effective strategy to separate HOMO and LUMO frontier molecular orbitals. Further extending the structure by incorporation of stronger accepting structures such as the use of the triazine moiety resulted in compounds which were too conjugated, which then suffered reduced PLQY values. Incorporation of the cyano moiety in the *para*- position resulted in highly localised LUMO orbitals, as observed from TDDFT. Learning from these preliminary findings, more efficient systems were designed for Chapter Four.

Chapter Four gives a detailed account of the design, synthesis, and photophysical studies of highly twisted D- π -A- π -D and D-A-D compounds with a central azaborine accepting core and varying donor appendages. This chapter contains a detailed discussion on C-N bond forming reactions, specifically a series of Buchwald-Hartwig amination reactions. Finally, a detailed photophysical study of the four final emitters was outlined: **54** (D- π -A- π -D architecture), **58** (D-A-D architecture), **55** (D- π -A- π -D architecture), and **60** (D-A-D architecture). **54** had a highly flexible backbone, which contributed to reduced PLQY of the series. CT behaviour was not observed in **58** or **55**, and both emitters have highly delocalised HOMO orbitals. Using solution UV-vis absorption and emission studies combined with TDDFT, it was proven that **60** outperformed the series. The strength of the donor as well as the acceptor, and a moderate twisted structure is more important than a direct focus on the dihedral angle alone. In all compounds, azaborine was a very efficient electron acceptor, but combined with a strong donor, resulted in very efficient TADF candidate (**60**).

Overall, this thesis has described a myriad of synthetic and photophysical studies towards novel organic molecules for application in organic electronics. The synthetic targets ranged from planar all carbon PAH molecules to small twisted organic architectures. Where possible, photophysical properties of the synthesised targets were elucidated to gain further understanding in their potential applications in the organic electronics industry.

Chapter Six

Experimental

Experimental

General Information: Unless otherwise specified, all syntheses were carried out under an inert atmosphere of either N₂ or Ar using standard Schlenk techniques. Solvents were used without further drying or purification, with exception of CH₂Cl₂ and THF which were dried over an alumina column. Triethylamine was distilled over sodium and under an N₂ atmosphere. All commercially available starting materials purchased from Merck (formally Sigma Aldrich), VWR, and Fluorochem Ltd. were used without further purification. Flash Chromatography was performed using silica gel (VWR, particle size 40 -63 μM) as the stationary phase. Thin-layer chromatography (TLC) was performed using Merck 60 F254 silica gel (pre-coated, 0.2 mm thick, 20 x 20 cm) and visualised by UV (λ_{\max} = 254 nm).

NMR Spectroscopy: Nuclear magnetic resonance spectra (NMR) were recorded in CDCl₃ on (i) Bruker Avance DPX-400 MHz spectrometer (operating at 400.13 MHz for ¹H, 100.6 MHz for ¹³C{¹H}), (ii) Bruker AV-400 MHz spectrometer (operating at 400.13 MHz for ¹H, 100.6 MHz for ¹³C{¹H}), or (iii) Bruker AV-600 MHz spectrometer (operating at 600.13 MHz for ¹H, 150.6 MHz for ¹³C{¹H}). ¹³C spectra were fully proton decoupled, and reported as ¹³C{¹H}. Chemical shifts (δ) are reported in parts per million (ppm), and coupling constants (J) in Hertz.

Mass Spectrometry: Electrospray mass spectra were recorded on a Micromass-LCT spectrometer. Electron impact mass spectra were measured on a Waters corp. GCT Premier electron impact mass spectrometer. APCI (atmospheric-pressure chemical ionisation) mass spectra were obtained with a Bruker micrOTOF-Q III spectrometer interfaced to a Dionex UltiMate 3000 LC or direct insertion probe. MALDI-TOF mass spectra were recorded on a Waters MALDI-QTOF Premier spectrometer using an α -cyano-4-hydroxy cinnamic acid (CHCA) matrix. Accurate mass spectra were referenced against Leucine enkephalin (555.6 g/mol) or [Glue1]-Fibrinopeptide B (1570.6 g/mol) and reported to within 5 ppm. All samples were dissolved in CH₂Cl₂ unless otherwise stated.

Elemental Analysis: Elemental analyses (CHN) were obtained from the Microanalytical Laboratory, University College Dublin.

Melting Point Analysis: Melting points were determined on a Griffin Melting Point apparatus.

IR: IR analysis was recorded in solid form using a Perkin Elmer Spectrum 100 FTR spectrometer with a Universal ATR accessory.

Photophysical Measurements: All photophysical measurements were carried out with solutions contained in 1 x 1 cm² quartz cuvettes in HPLC grade solvents. UV-vis absorption spectra were recorded on a Shimadzu UV-2450 spectrophotometer. Emission and excitation spectra were obtained with (i) a Horiba Jobin-Yvon Fluorolog FL-3-11 spectrofluorometer with double grating emission and excitation monochromators, or (ii) a Horiba Fluoromax 4-P spectrofluorometer. Emission lifetime measurements were obtained with a Jobin Yvon FluoroHub single photon counting controller fitted with a Jobin-Yvon NanoLED of the appropriate excitation wavelength. The TAC ranges were set to approximately twenty times the average decay time, and the start-stop ratio (α) was maintained below 2%, to prevent pile-up. Data was fit with mono-exponential decays, with χ^2 values as close to 1 as possible, and Durbin-Watson parameters of approximately 2. Short lifetimes (in the nanosecond range) were corrected with an instrument response factor (IRF), which was a non-scattering solution of silica particles (Ludox, Sigma-Aldrich). Luminescence quantum yields of the compounds were measured with Quinine Sulfate as the standard using the relative method ($\Phi_F = 0.546$ in 0.5 M H₂SO₄).²⁶⁶

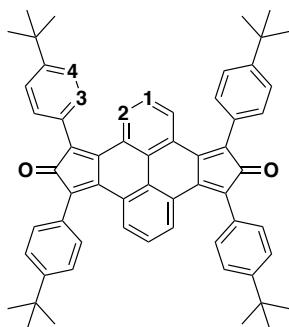
Cyclic Voltammetry: Cyclic voltammetry measurements were carried out using a CH Instruments Electrochemical Analyser Model 600B. All samples were run in CH₂Cl₂ (1 x 10⁻⁴ M) with tetra-*n*-butylammonium hexafluorophosphate (TBAPF₆, 0.1 M) as the supporting electrolyte. A standard three electrode cell was used with a glassy carbon working electrode (of area 0.0707 cm²), a Pt wire counter electrode, and a Ag/AgCl (sat. KCl) reference electrode. Potentials are quoted versus the ferrocene/ferrocenium couple as the internal standard (0.0 V). All samples were degassed with N₂ prior to experiment, and a constant stream of nitrogen gas over the solution was maintained throughout the experiment.

Computational Measurements: Geometry optimizations were calculated by using the B3LYP functional with the 6-31G(g) basis set with density functional theory (DFT).³⁵³ The vertical excitation energy was calculated with the time-dependent DFT (TDDFT) method based on the optimised singlet ground state geometry. The solvents were used in the calculations (CPCM model). All calculations were performed with the Gaussian 09W software (Gaussian Inc.). All computational measurements were carried out by Dr. Xiaoneng Cui in Dalian University, China.

X-ray Crystallography: The single-crystal analysis was performed by Dr. Brendan Twamley in Trinity College Dublin with a Bruker APEX Duo Kappa CCD diffractometer, using graphite

monochromated Mo-K α ($\lambda=0.71073\text{\AA}$) or Cu K α radiation ($\lambda=1.54178\text{\AA}$), with an Oxford Cobra Cryosystem, or on a Bruker D8 Quest ECO using graphite monochromated Mo-K α ($\lambda=0.71073\text{\AA}$) radiation with an Oxford Cryostream Cryosystem, at the temperatures given in tables. Samples were mounted on a MiTeGen microloop and Bruker APEX software was used to collect the raw data. Data reduction was performed using SAINT. Intensities were corrected for Lorentz and polarisation effects and for absorption by SADABS. Space groups were determined from systematic absences and checked for higher symmetry. The structures were solved using Intrinsic Phasing methods with SHELXT and refined on F^2 using all data by full-matrix least-squares procedures with SHELXL. All non-hydrogen atoms were refined with anisotropic displacement parameters. Hydrogen atoms were included in calculated positions with isotropic displacement parameters riding on their carrier atoms. Absolute structure determinations were based on the Flack parameter. In all cases, final Fourier syntheses showed no significant residual electron density in chemically sensible positions. The SQUEEZE/PLATON program was used in the structural refinement in cases where there were a large number of diffuse or unresolvable disordered solvent molecules within the structure.

4,6,10,12-tetrakis(4-(tert-butyl)phenyl)dicyclopenta[e,l]pyrene-5,11-dione (**5**)



Three neck 50 ml round bottom flask was dried overnight to ensure moisture free conditions. **4** (220 mg, 0.68 mmol) and **3** (100 mg, 0.37 mmol) were added, three Ar/vac cycles performed. Dry ethanol (60 ml) was syringed into the reaction and the suspension heated to 78 °C. DBU was syringed (0.12 ml, 0.79 mmol). Upon addition of DBU the suspension turned from orange to black. Reaction allowed to stir under reflux for 1h, at which point it was returned to RT and allowed to settle. Black precipitate observed, which was filtered and washed with cold ethanol to furnish the product as a black solid (70 mg, 23 %).

δ_{H} (600 MHz, CDCl_3): δ 8.06-8.05 (d, $J = 7.9$ Hz, 4H, H2), 7.88-7.86 (t, $J = 7.9$ Hz, 2H, H1), 7.80-7.79 (d, $J = 8.3$ Hz, 8H, H3), 7.39-7.38 (d, $J = 8.6$ Hz, 8H, H4), 1.30 (s, 36H, tBu);

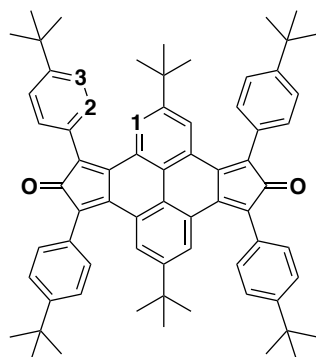
δ_{C} (151.6 MHz, CDCl_3): δ 197.37 (C=O), 157.91 (C_q), 136.30 (C_q), 135.0 (C_q), 130.28 (C_q), 129.60 (C_q), 127.98 (C_q), 127.03 (C3), 125.96 (C_q), 125.74 (C_q), 125.62 (C4), 125.57 (C2), 124.19 (C1), 35.26 (tBu- C_q), 31.03 (tBu- CH_3);

HRMS MALDI TOF $\text{C}_{62}\text{H}_{58}\text{O}_2$ Calc. 834.4437 Found 834.4460;

IR ν_{max} (ATR/ cm^{-1}) 2961.16, 2904.14, 2866.22, 1914.88, 1702.25, 1646.31, 1607.77, 1510.45, 1464.41, 1433.74, 1415.40, 1397.87, 1364.58, 1324.64, 1297.16, 1284.80, 1193.22, 1167.17, 1107.41, 1071.28, 971.27, 920.60, 839.74, 817.44, 778.89, 761.91, 712.74, 633.42, 562.00;

MP 72-74°C.

4,6,10,12-tetrakis(4-(tert-butyl)phenyl)dicyclopenta[e,l]pyrene-5,11-dione (6)



1 (260 mg, 0.69 mmol) and **4** (0.445 g, 1.38 mmol) were added to the flask which was subjected to x3 Ar/vac cycles. Dry ethanol was syringed into the vessel, 20 ml at a time (70 ml total). DBU (0.26 ml, 2.24 mmol) was gently syringed in dropwise. Reaction brought up to 78 °C and left overnight. The flask taken off the heat and allowed to sit so crystallisation could occur. Black solid filtered off and washed with cold ethanol three times to furnish the product as a black solid (0.45 g, 78 %), which was in good agreement with the literature.¹⁴⁵

δ_{H} (400 MHz, CDCl_3): δ 7.98 (s, 4H, H1), 7.78-7.75 (d, $J = 8.4$ Hz, 8H, H2), 7.39-7.37 (d, $J = 8.6$ Hz, 8H, H3), 1.29 (s, 36H, tBu), 1.09 (s, 18H, tBu);

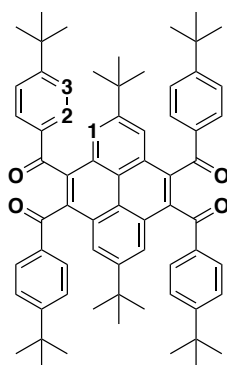
δ_C (101.6 MHz, $CDCl_3$): δ 198.05 (C=O), 165.44 (C_q), 157.55 (C_q), 149.32 (C_q), 136.93 (C_q), 135.71 (C_q), 130.07 (C_q), 127.48 (C2), 125.46 (C3), 123.66 (C1), 122.60 (C_q), 117.65 (C_q), 95.08 (C_q), 58.46 (C_q), 35.21 (tBu- C_q), 31.12 (tBu- C_q), 31.02 (tBu- CH_3), 18.43 (tBu- CH_3);

HRMS MALDI TOF $C_{70}H_{74}O_2$ Calc. 946.5689 Found 946.5708;

IR ν_{max} (ATR/ cm^{-1}) 2953.16, 1697.94;

MP $^{\circ}C$ 350-352 $^{\circ}C$.

2,7-di-tert-butyl-4,5,9,10-tetrahydropyrene-4,5,9,10-tetrayl)tetrakis((4-(tert-butyl)phenyl)methanone) (7)



All samples of **6** were gathered and dissolved in minimal amounts of chloroform. The conical flask was allowed to sit in direct sunlight for 24 h, which resulted in a colour change from black to clear yellow. Flash column chromatography (SiO_2 , CH_2Cl_2) was run to elute the pure sample **7** as the second eluent, which gave a clean NMR and a HRMS spectra.

δ_H (400 MHz, $CDCl_3$): δ 8.02 (s, 4H, H1), 7.82-7.80 (d, $J = 8.2$ Hz, 8H, H2), 7.43-7.41 (d, $J = 8.3$ Hz, 8H, H3), 1.33 (s, 36H, tBu), 1.12 (s, 18H, tBu);

δ_C (151.6 MHz, $CDCl_3$): δ 198.04 (C=O), 157.55 (C_q), 137.62 (C_q), 136.94 (C_q), 135.72 (C_q), 132.43 (C_q), 130.08 (C2), 128.29 (C_q), 127.49 (C_q), 125.47 (C3), 123.67 (C1), 35.21 (tBu- C_q), 31.09 (tBu- CH_3);

HRMS MALDI TOF $C_{68}H_{74}O_4$ Calc. 954.5587 Found 954.5589;

IR ν_{max} (ATR/ cm^{-1}) 377.51, 3662.60, 3682.31, 3302.89, 3055.07, 2958.75, 2905.85, 2868.99, 2162.22, 2029.94, 1718.36, 1659.80, 1602.85, 1566.85, 1459.53, 1406.19;

MP $^{\circ}C$ no decomposition past 360 $^{\circ}C$;

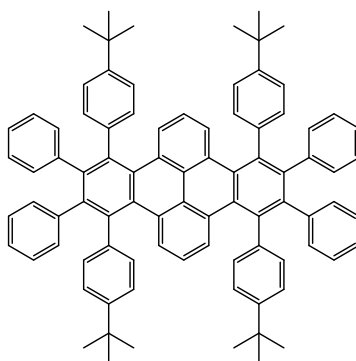
X-ray Crystallography A specimen of C₉₄H₉₄O₆, approximate dimensions 0.120 mm x 0.180 mm x 0.500 mm, was used for the X-ray crystallographic analysis. The X-ray intensity data were measured at 100(2)K on a Bruker D8 Quest ECO with an Oxford Cryosystems low temperature device using a MiTeGen micromount.

A total of 1535 frames were collected. The total exposure time was 16.06 hours. The integration of the data using a triclinic unit cell yielded a total of 36984 reflections to a maximum θ angle of 26.15° (0.81 Å resolution), of which 7455 were independent (average redundancy 4.961, completeness = 99.4%, $R_{\text{int}} = 3.52\%$, $R_{\text{sig}} = 2.88\%$) and 5525 (74.11%) were greater than $2\sigma(F^2)$. The final cell constants of $a = 10.0803(3)$ Å, $b = 11.8326(3)$ Å, $c = 17.7041(5)$ Å, $\alpha = 77.6933(14)^\circ$, $\beta = 82.5030(12)^\circ$, $\gamma = 65.5385(12)^\circ$, volume = 1875.85(9) Å³, are based upon the refinement of the XYZ-centroids of reflections above 20 $\sigma(I)$. Data were corrected for absorption effects using the Multi-Scan method (SADABS). The ratio of minimum to maximum apparent transmission was 0.943. The calculated minimum and maximum transmission coefficients (based on crystal size) are 0.7124 and 0.7453.

The structure was solved with the XT structure solution program using Intrinsic Phasing and refined with the XL refinement package using Least Squares minimisation with Olex2, using the space group $P\bar{1}$, with $Z = 1$ for the formula unit, C₉₄H₉₄O₆. The final anisotropic full-matrix least-squares refinement on F^2 with 693 variables converged at $R1 = 4.82\%$, for the observed data and $wR2 = 13.80\%$ for all data. The goodness-of-fit was 1.023. The largest peak in the final difference electron density synthesis was 0.221 e⁻/Å³ and the largest hole was -0.248 e⁻/Å³ with an RMS deviation of 0.042 e⁻/Å³. On the basis of the final model, the calculated density was 1.168 g/cm³ and $F(000)$, 706 e⁻.

Refinement Note: Benzophenone disordered over two positions (50% occupancy) and modelled with restraints (SIMU, AFIX 66). Two t-Butyl groups on the main molecule are disordered also. C20-C23 was modelled in two positions with 50% occupancy and restraints (DFIX, SIMU, SADI). The other t-Bu group C33-C36 was modelled in 4 positions with occupancies: 39:32:21:8% with restraints (SADI, SIMU).

4,7,11,14-tetrakis(4-(tert-butyl)phenyl)-5,6,12,13-tetraphenyldibenzo[fg,op]tetracene (12)



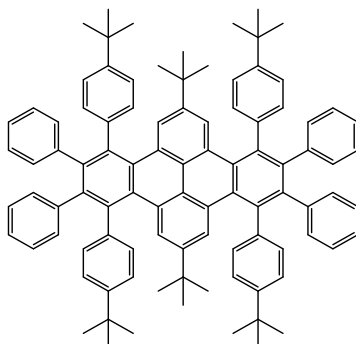
Benzophenone (800 mg, 4.39 mmol) was weighted into a 10 ml round bottom flask. **5** (100 mg, 0.11 mmol) and diphenylacetylene (64 mg, 0.35 mmol) were added to the flask. The sand filled mantle was heated to 300 °C. Whilst observing the temperature rising, it was noted that **5** remained insoluble until ~140 °C, at which point it solubilised forming a dark brown/black homogenous solution. The reaction mixture was stirred gently for 5 h. After 5 h, it was allowed to cool, and dissolved in minimal amount of CH₂Cl₂. This mixture was poured into 3 mL MeOH, and placed on a hot plate to evaporate CH₂Cl₂, and then very slowly cooled down and placed in the freezer. The dark red precipitate formed was filtered and washed with cold MeOH to furnish the product as a dark maroon solid (56.4 mg, 84 %).

δ_{H} (400 MHz, CDCl₃): sample too insoluble in common deuterated organic solvents for full structural characterisation, therefore structural characterisation is incomplete;

δ_{C} (151.6 MHz, CDCl₃): sample too insoluble in common deuterated organic solvents for full structural characterisation, therefore structural characterisation is incomplete;

HRMS MALDI TOF C₈₈H₇₈ Calc. 1134.6104 Found 1134.6080.

2,9-di-tert-butyl-4,7,11,14-tetrakis(4-(tert-butyl)phenyl)-5,6,12,13-tetraphenyldibenzo[fg,op]tetracene (13)

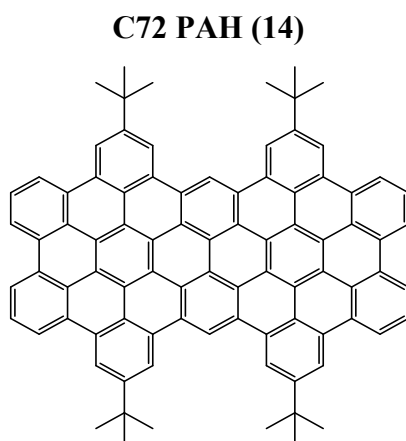


Benzophenone (800 mg, 4.39 mmol) was weighted into a 10 ml round bottom flask. **7** (100 mg, 0.11 mmol) and diphenylacetylene (37.4 mg, 0.21 mmol) were added to the flask. The sand filled mantle was heated to 300 °C. The reaction mixture was stirred gently for 5h. After 5h, it was allowed to cool, and dissolved in minimal amount of CH₂Cl₂. This mixture was poured into 3 mL MeOH, and placed on a hot plate to evaporate CH₂Cl₂, and then very slowly cooled down and placed in the freezer. The mustard yellow precipitate formed was filtered and washed with cold MeOH, furnishing the product as a pale brown solid (24.6 mg, 20%).

δ_{H} (400 MHz, CDCl₃): sample too insoluble in common deuterated organic solvents for full structural characterisation, therefore structural characterisation is incomplete;

δ_{C} (151.6 MHz, CDCl₃): sample too insoluble in common deuterated organic solvents for full structural characterisation, therefore structural characterisation is incomplete;

HRMS MALDI TOF C₉₆H₉₄ Calc. 1246.7356 Found 1246.7312.



12 (50 mg, 0.044 mmol), dissolved in dry CH₂Cl₂ and placed in a three-neck round bottom flask. The flask was subjected to x3 Ar/vac cycles. FeCl₃ (0.32 g, 1.98 mmol) was weighed into a Schlenk tube, and a seal cap placed. The tube was subjected to x3 Ar/vac cycles. To it, 2 mL of NO₂CH₃ was added, in order to solubilise the FeCl₃. This solution was then added dropwise to the round-bottom flask containing the starting material fully dissolved in CH₂Cl₂. The solution turned a deep brown/black upon addition of the FeCl₃/NO₂CH₃ solution. This was left overnight. The following morning, reaction mixture was opened to air, and poured into MeOH to quench the reaction. This over a period of four hours formed a brown precipitate which was filtered in *vacuo* to produce the solid. Column chromatography (SiO₂ MeOH/CH₂Cl₂, 1:9, v/v) afforded a red solid (46 mg, 94 %).

δ_{H} (400 MHz, CDCl_3): sample too insoluble in common deuterated organic solvents for full structural characterisation, therefore structural characterisation is incomplete;

δ_{C} (151.6 MHz, CDCl_3): sample too insoluble in common deuterated organic solvents for full structural characterisation, therefore structural characterisation is incomplete;

HRMS MALDI TOF $\text{C}_{88}\text{H}_{58}$ Calc. 114.4539 Found 114.4541;

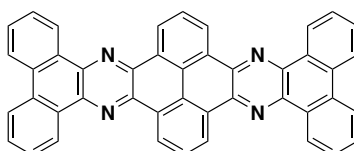
IR ν_{max} (ATR/ cm^{-1}) 2970.03, 2500, 2160.32, 2025.42, 1772.43, 1504.61, 1409.37, 1365.22;

MP $^{\circ}\text{C}$ no decomposition past 360 $^{\circ}\text{C}$;

UV λ_{abs} 271, 356, 488 nm;

TGA (N_2 gas) ~ 21 % weight loss at 210 $^{\circ}\text{C}$ corresponding to the two tert-butyl substituents, with no further weight loss past 750 $^{\circ}\text{C}$ observed.

9b,9b1-dihydrodibenzo[h,j]dibenzo[5',6':7',8']quinoxalino[2',3':9,10]phenanthro[4,5-abc]phenazine (17)



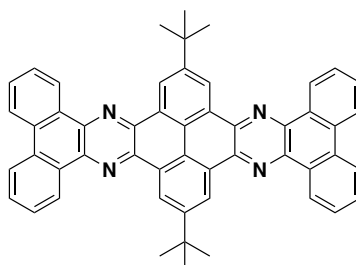
A 50 cm^3 three-necked flask was placed under vacuum and flushed with argon to ensure air-free conditions. **16** was made according to the literature methods¹⁶⁸ (100 mg, 0.48 mmol) was dissolved in dry ethanol (25 cm^3) under Ar. Once full dissolution was observed, **3** (50 mg, 0.189 mmol) and 10 % *p*-TSA (0.5 mg, 0.026 mmol) was added promptly. The solution was stirred under reflux for 24 h to ensure completion. The reaction mixture was left in the freezer over the weekend to promote crystallisation, further filtration and washings with cold ethanol produced a pale brown solid (0.11 g, 95.7 %). The product proved highly insoluble in common organic solvents, resulting in incomplete characterisation.

δ_{C} $^{13}\text{C}\{^1\text{H}\}$ NMR (151 MHz, solid): δ 145-115 ppm ($\text{C}_{\text{aromatic}}$);

IR ν_{\max} (ATR/cm⁻¹) 3064.15, 1996.83, 1676.21, 1304.55, 1373.21, 1221.54, 1121.92, 958.76, 756.19, 718.21, 693.84;

MP °C no decomposition past 360 °C.

**11,24-di-tert-butyl-9b,9b1-
dihydrodibenzo[h,j]dibenzo[5',6':7',8']quinoxalino[2',3':9,10]phenanthro[4,5-abc]phenazine
(18)**



50 cm³ three-necked flask was placed under vacuum and flushed with argon to ensure air-free conditions. **16** was prepared according to literature methods¹⁶⁸ (100 mg, 0.48 mmol) was dissolved in dry ethanol (25 cm³) under argon. Once full dissolution was observed, **1** (50 mg, 0.133 mmol) and 10 % *p*-TSA (0.5 mg, 0.026 mmol) was added promptly. The solution was stirred under reflux for 24 h to ensure completion. The reaction mixture was left in the freezer over the weekend to promote crystallisation, further filtration and washings with cold ethanol produced a pale brown solid (0.93 g, 97 %). The product proved highly insoluble in common organic solvents, resulting in incomplete characterisation.

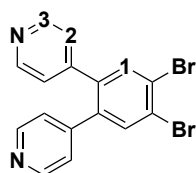
δ_{C} ¹³C{¹H} NMR (151 MHz, solid): δ 145-115 ppm (C_{aromatic}), 38-30 ppm (C_{aliphatic});

IR ν_{\max} (ATR/cm⁻¹) 3062.85, 2967.33, 1674.16, 1603.03, 1419.19, 1373.15, 1282.61, 1223.72, 758.60, 721.87, 694.83;

HRMS MALDI TOF C₅₂H₄₀N₄ Calc.720.3253 Found 720.3239;

MP °C no decomposition past 360 °C.

4,4'-(4,5-dibromo-1,2-phenylene)dipyridine (26)



27 (400 mg, 0.82 mmol) and pyrimidin-5-ylboronic acid (212.93 mg, 1.72 mmol) were dissolved in 20 mL 1:1 ethanol/toluene and 1 mL K_2CO_3 (2 M solution) and thoroughly degassed by bubbling with Ar. Once all reactants were fully solubilised, $Pd(PPh_3)_4$ (165 mg, 0.142 mmol, 8.3%) was added. The solution was heated to 110 °C and stirred overnight. After 48 h, all volatiles were removed *in vacuo*. The residues were dissolved in CH_2Cl_2 , washed with brine, and dried over $MgSO_4$. The organic layer was reduced *in vacuo*, and the product was precipitated with Et_2O , and further purified by column chromatography (SiO_2 , $CH_2Cl_2/MeOH$ 100:2, v/v, $R_f = 0.39$) to afford a white solid (161 mg, 24%).

δ_H (400 MHz, $CDCl_3$): δ 8.50 (d, $J = 5.9$ Hz, 4H, H3), 7.69 (s, 2H, H1), 7.00 (d, $J = 5.9$ Hz, 4H, H2);

δ_C (101.6 MHz, $CDCl_3$): δ 150.01 (C3), 146.09 (C2), 138.20 (C_q), 135.12 (C1), 125.62 (C_q), 124.09 (C_q);

HRMS APCI⁺ $C_{16}H_{11}Br_2N_2$ Calc. 388.9283 Found 388.9276 $[M+H]^+$;

IR ν_{max} (ATR/ cm^{-1}) 3701.81, 3449.24, 3051.99, 2185.74, 1967.84, 1543.89, 1596.06, 1480.91, 1433.42, 1402.64;

MP °C 180-182 °C;

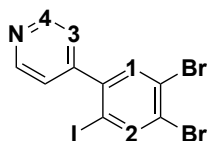
X-ray Crystallography A specimen of $C_{16}H_{10}Br_2N_2$, approximate dimensions 0.019 mm x 0.310 mm x 0.340 mm, was used for the X-ray crystallographic analysis. The X-ray intensity data were measured at 100(2)K on a Bruker D8 Quest ECO with an Oxford Cryostream low temperature device using a MiTeGen micromount. See Table 1 for collection parameters and exposure time. Bruker APEX software was used to correct for Lorentz and polarization effects.

A total of 1020 frames were collected. The total exposure time was 0.28 hours. The integration of the data using a monoclinic unit cell yielded a total of 18327 reflections to a maximum θ angle of 30.66° (0.70 Å resolution), of which 2163 were independent (average redundancy 8.473, completeness = 99.7%, $R_{int} = 2.34\%$, $R_{sig} = 1.38\%$) and 2084 (96.35%) were greater than $2\sigma(F^2)$. The final cell constants of $\underline{a} = 15.4975(7)$ Å, $\underline{b} = 10.5799(4)$ Å, $\underline{c} = 8.9646(4)$ Å, $\beta = 107.3470(10)^\circ$, volume = 1403.00(10) Å³, are based upon the refinement of the XYZ-centroids of reflections above 20 $\sigma(I)$. The

calculated minimum and maximum transmission coefficients (based on crystal size) are 0.2450 and 0.8980.

The structure was solved with the XT structure solution program using Intrinsic Phasing and refined with the XL refinement package using Least Squares minimisation with Olex2, using the space group C2/c, with $Z = 4$ for the formula unit, $C_{16}H_{10}Br_2N_2$. The final anisotropic full-matrix least-squares refinement on F^2 with 92 variables converged at $R1 = 1.62\%$, for the observed data and $wR2 = 4.03\%$ for all data. The goodness-of-fit was 1.081. The largest peak in the final difference electron density synthesis was $0.605 \text{ e}^-/\text{\AA}^3$ and the largest hole was $-0.401 \text{ e}^-/\text{\AA}^3$ with an RMS deviation of $0.081 \text{ e}^-/\text{\AA}^3$. On the basis of the final model, the calculated density was 1.847 g/cm^3 and $F(000)$, 760 e^- .

4-(4,5-dibromo-2-iodophenyl)pyridine (28)



27 (400 mg, 0.82 mmol) and pyridin-4-ylboronic acid (211 mg, 1.72 mmol) were dissolved in 20 mL 1:1 ethanol/toluene and 1 mL K_2CO_3 (2 M solution) and thoroughly degassed by bubbling with Ar. Once all reactants were fully solubilised, $Pd(PPh_3)_4$ (172 mg, 0.142 mmol, 8.3%) was added. The solution was heated to $110 \text{ }^\circ\text{C}$ and stirred overnight. After 48 h, all volatiles were removed *in vacuo*. The residues were dissolved in CH_2Cl_2 , washed with brine, and dried over $MgSO_4$. The organic layer was reduced *in vacuo*, and the product was precipitated with Et_2O , and further purified by column chromatography (SiO_2 , $CH_2Cl_2/MeOH$ 100:2, v/v, $R_f = 0.58$) to afford a white solid (190 mg, 25%).

δ_H (400 MHz, $CDCl_3$): δ 8.70 (d, $J = 5.6 \text{ Hz}$, 2H, H4), 8.20 (s, 1H, H2), 7.50 (s, 1H, H1), 7.24 (d, 2H, H3);

δ_C (101.6 MHz, $CDCl_3$): δ 149.94 (C4), 149.23 (C_q), 144.41 (C2), 143.43 (C_q), 133.69 (C1), 125.69 (C_q), 125.27 (C_q), 123.76 (C3), 95.30 (C_q);

HRMS APCI⁺ $C_{11}H_6Br_2NI$ Calc. 437.7984 Found 437.7987 $[M+H]^+$;

IR ν_{max} (ATR/ cm^{-1}) 3684.53, 3307.78, 3033.48, 2162.28, 1975.33, 1708.81, 1595.54, 1545.01, 1480.69, 1435.01, 1403.62;

MP $^\circ\text{C}$ 150-151 $^\circ\text{C}$;

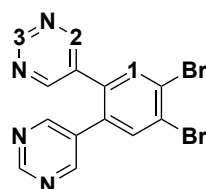
X-ray Crystallography A specimen of C₁₁H₆Br₂IN, approximate dimensions 0.020 mm x 0.040 mm x 0.260 mm, was used for the X-ray crystallographic analysis. The X-ray intensity data were measured at 100(2)K on a Bruker D8 Quest ECO with an Oxford Cryostream low temperature device using a MiTeGen micromount. See Table 1 for collection parameters and exposure time. Bruker APEX software was used to correct for Lorentz and polarization effects.

A total of 567 frames were collected. The total exposure time was 1.57 hours. The integration of the data using a monoclinic unit cell yielded a total of 10722 reflections to a maximum θ angle of 26.46° (0.80 Å resolution), of which 2372 were independent (average redundancy 4.520, completeness = 99.7%, $R_{\text{int}} = 12.23\%$, $R_{\text{sig}} = 9.73\%$) and 1513 (63.79%) were greater than $2\sigma(F^2)$. The final cell constants of $a = 4.1191(4)$ Å, $b = 8.8969(10)$ Å, $c = 31.600(3)$ Å, $\beta = 93.321(5)^\circ$, volume = 1156.1(2) Å³, are based upon the refinement of the XYZ-centroids of reflections above $20\sigma(I)$. The calculated minimum and maximum transmission coefficients (based on crystal size) are 0.1880 and 0.8300.

The structure was solved with the XT structure solution program using Intrinsic Phasing and refined with the XL refinement package using Least Squares minimisation with Olex2, using the space group P2₁/n, with Z = 4 for the formula unit, C₁₁H₆Br₂IN. The final anisotropic full-matrix least-squares refinement on F² with 136 variables converged at R1 = 5.30%, for the observed data and wR2 = 12.07% for all data. The goodness-of-fit was 1.018. The largest peak in the final difference electron density synthesis was 1.474 e⁻/Å³ and the largest hole was -1.212 e⁻/Å³ with an RMS deviation of 0.258 e⁻/Å³. On the basis of the final model, the calculated density was 2.522 g/cm³ and F(000), 808 e⁻.

Refinement Note: All carbon atoms modelled with restraints (SIMU).

5,5'-(4,5-dibromo-1,2-phenylene)dipyrimidine (30)



27 (400 mg, 0.82 mmol) and pyridin-4-ylboronic acid (211 mg, 1.72 mmol) were dissolved in 20 mL 1:1 ethanol/toluene and 1 mL K₂CO₃ (2 M solution) and thoroughly degassed by bubbling with Ar. Once all reactants were fully solubilised, Pd(PPh₃)₄ (172 mg, 0.142 mmol, 8.3%) was added. The solution was heated to 100 °C and stirred overnight. After 48 h, all volatiles were removed *in vacuo*. The residues were dissolved in methylene chloride, washed with brine, and dried over MgSO₄. The

organic layer was reduced *in vacuo*, and the product was precipitated with Et₂O, and further purified by column chromatography (SiO₂, methylene chloride/methanol 100:2, v/v, R_f = 0.58) to afford a white solid (190 mg, 33%).

δ_H (400 MHz, CDCl₃): δ 9.16 (s, 2H, H3), 8.51 (s, 4H, H2), 7.76 (s, 2H, H1);

δ_C (101.6 MHz, CDCl₃): δ 150.01 (C3), 146.09 (C_q), 138.20 (C_q), 135.12 (C1), 125.62 (C_q), 124.09 (C2);

HRMS APCI⁺ C₁₄H₉Br₂N₄ Calc. 390.9188 Found 390.9180 [M+H]⁺;

IR ν_{max} (ATR/cm⁻¹) 3779.52, 3033.65, 2957.68, 2867.37, 2163.13, 2029.36, 1980.80, 1773.93, 1660.16, 1552.83, 1464.15, 1411.12;

MP °C 198-200 °C;

X-ray Crystallography A specimen of C_{13.92}H_{7.94}Br₂I_{0.02}N_{3.96}, approximate dimensions 0.090 mm x 0.190 mm x 0.240 mm, was used for the X-ray crystallographic analysis. The X-ray intensity data were measured at 100(2)K on a Bruker D8 Quest ECO with an Oxford Cryostream low temperature device using a MiTeGen micromount. See Table 1 for collection parameters and exposure time. Bruker APEX software was used to correct for Lorentz and polarization effects.

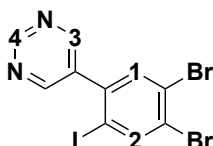
A total of 848 frames were collected. The total exposure time was 2.36 hours. The integration of the data using a monoclinic unit cell yielded a total of 11459 reflections to a maximum θ angle of 30.11° (0.71 Å resolution), of which 1929 were independent (average redundancy 5.940, completeness = 99.9%, R_{int} = 2.51%, R_{sig} = 1.75%) and 1771 (91.81%) were greater than 2σ(F²). The final cell constants of *a* = 16.5297(7) Å, *b* = 10.7656(4) Å, *c* = 7.5398(3) Å, β = 102.670(2)°, volume = 1309.05(9) Å³, are based upon the refinement of the XYZ-centroids of reflections above 20 σ(I). The calculated minimum and maximum transmission coefficients (based on crystal size) are 0.3160 and 0.6040.

The structure was solved with the XT structure solution program using Intrinsic Phasing and refined with the XL refinement package using Least Squares minimisation with Olex2, using the space group C2/c, with Z = 4 for the formula unit, C_{13.92}H_{7.94}Br₂I_{0.02}N_{3.96}. The final anisotropic full-matrix least-squares refinement on F² with 100 variables converged at R1 = 1.89%, for the observed data and wR2 = 4.17% for all data. The goodness-of-fit was 1.100. The largest peak in the final difference electron

density synthesis was $0.422 \text{ e}^-/\text{\AA}^3$ and the largest hole was $-0.479 \text{ e}^-/\text{\AA}^3$ with an RMS deviation of $0.071 \text{ e}^-/\text{\AA}^3$. On the basis of the final model, the calculated density was 1.994 g/cm^3 and $F(000)$, 761 e^- .

Refinement Note: Structure modelled as two compounds 5,5'-(4,5-dibromo-1,2-phenylene)dipyrimidine and 1,2-dibromo-4,5-diiodobenzene in 99:1% occupancy. Restraints used to model the low occupancy Iodine atom (ISOR).

5-(4,5-dibromo-2-iodophenyl)pyrimidine (31)



27 (400 mg, 0.82 mmol) and pyridin-4-ylboronic acid (211 mg, 1.72 mmol) were dissolved in 20 mL 1:1 ethanol/toluene and 1 mL K_2CO_3 (2 M solution) and thoroughly degassed by bubbling with Ar. Once all reactants were fully solubilised, $\text{Pd}(\text{PPh}_3)_4$ (172 mg, 0.142 mmol, 8.3%) was added. The solution was heated to $100 \text{ }^\circ\text{C}$ and stirred overnight. After 48 h, all volatiles were removed *in vacuo*. The residues were dissolved in methylene chloride, washed with brine, and dried over MgSO_4 . The organic layer was reduced *in vacuo*, and the product was precipitated with Et_2O , and further purified by column chromatography (SiO_2 , methylene chloride/methanol 100:2, v/v, $R_f = 0.77$) to afford a white solid (180 mg, 50%).

δ_{H} (400 MHz, CDCl_3): δ 9.28 (s, 1H, H4), 8.76 (s, 2H, H3), 8.24 (s, 1H, H2), 7.55 (s, 1H, H1);

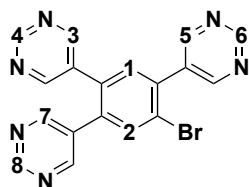
δ_{C} (101.6 MHz, CDCl_3): δ 158.14 (C4), 156.49 (C3), 143.56 (C2), 139.96 (C_q), 134.68 (C1), 134.05 (C_q), 132.16 (C_q), 131.98 (C_q), 126.69 (C_q) ppm;

HRMS APCI⁺ $\text{C}_{10}\text{H}_6\text{Br}_2\text{IN}_2$ Calc. 438.7936 Found 438.7923 $[\text{M}+\text{H}]^+$;

IR ν_{max} (ATR/ cm^{-1}) 37.24.95, 3594.08, 3510.99, 3034.54, 2956.45, 2867.84, 1897.94, 1714.71, 1660.11, 1602.29, 1585.99, 1553.94, 1463.89, 1410.24;

MP $^\circ\text{C}$ 180-181 $^\circ\text{C}$.

5,5',5''-(5-bromobenzene-1,2,4-triyl)tripyrimidine (32)



27 (400 mg, 0.82 mmol) and pyridin-4-ylboronic acid (211 mg, 1.72 mmol) were dissolved in 20 mL 1:1 ethanol/toluene and 1 mL K₂CO₃ (2 M solution) and thoroughly degassed by bubbling with Ar. Once all reactants were fully solubilised, Pd(PPh₃)₄ (172 mg, 0.142 mmol, 8.3%) was added. The solution was heated to 115 °C and stirred overnight. After 24 h, all volatiles were removed *in vacuo*. The residues were dissolved in methylene chloride, washed with brine, and dried over MgSO₄. The organic layer was reduced *in vacuo*, and the product was precipitated with Et₂O, and further purified by column chromatography (SiO₂, methylene chloride/methanol 100:2, v/v, R_f = 0.41) to afford a white solid (66 mg, 15%).

δ_H (400 MHz, CDCl₃): δ 9.31 (s, 1H, H6), 9.18 (s, 1H, H8), 9.16 (s, 1H, H4), 8.92 (s, 2H, H5), 8.58 (s, 2H, H7), 8.56 (s, 2H, H3), 7.90 (s, 1H, H2), 7.46 (s, 1H, H1);

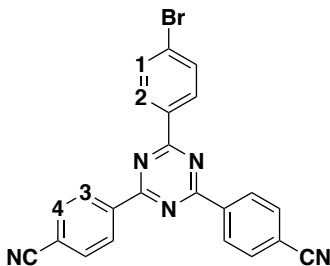
δ_C (101.6 MHz, CDCl₃): δ 158.40 (C6), 158.12 (C8), 158.02 (C4), 156.88 (C5), 156.81 (C7), 156.67 (C3), 137.24 (C_q), 135.88 (C_q), 135.71 (C_q), 135.75 (C2), 133.06 (C1), 132.32 (C_q), 131.95 (C_q), 129.79 (C_q), 124.33 (C_q);

HRMS APCI⁺ C₁₈H₁₁BrN₆ Calc. 391.0229 Found 391.0229 [M+H]⁺;

IR ν_{\max} (ATR/cm⁻¹) 3032.01, 2958.59, 2869.95, 2162.95, 1974.59, 1660.42, 1602.23, 1552.33, 1437.84, 1405.88;

MP °C 219-221 °C.

4,4'-(6-(4-Bromophenyl)-1,3,5-triazine-2,4-diyl)dibenzonitrile (38)



A solution of 4-bromobenzoyl chloride (1.61 g, 7.34 mmol) and 1,4 dicyanobenzene (1.88 g, 14.74 mmol) in CH₂Cl₂ (20 mL) was stirred at 0-5 °C for 30 min under a nitrogen atmosphere. Under a steady flow of nitrogen, antimony pentachloride (2.20 g, 7.36 mmol) was added in a single addition. The reaction mixture was stirred at RT for 2 h, and then heated to reflux for 12 h. The cooled mixture was filtered, and the collected yellow solid was added to a stirred 35% *aq.* ammonia solution (80 mL) at 0 °C. Upon addition, white precipitate formation was observed, which was allowed to stir at room temperature for 3 h. The solid was isolated by filtration and washed with water (3 x 5 mL), and added to DMF (30 mL) which was refluxed for 30 min. The cooled solution was filtered to isolate the solid which was then refluxed with DMF (30 mL) a further three times. Each time, the precipitate was retained and the filtrate discarded. The white precipitate was washed with water (3 x 5 mL) and dried *in vacuo*. The product was carried forward without further purification (1.47 g, 46 %), and was in good agreement with the literature.²⁶⁴

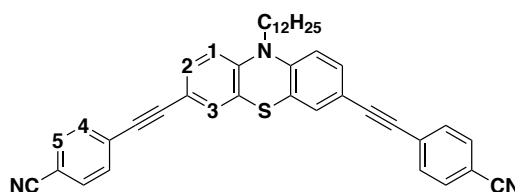
δ_{H} (400 MHz, CDCl₃): 8.81 (s, 4H, H3), 8.57 (s, 2H, H2), 7.83 (s, 4H, H4), 7.69 (s, 2H, H1) ppm. No shift multiplicity observed due to insoluble nature of the compound, only broad peaks observable in ¹H NMR.

δ_{C} (101.6 MHz, CDCl₃): Product too insoluble to obtain a ¹³C{¹H} NMR spectrum.

HRMS APCI⁺ C₂₃H₁₄BrN₅ Calc. 438.0276 Found 438.0227 [M+H]⁺;

IR ν_{max} (ATR/cm⁻¹) 3068, 2976, 2230 (C≡N), 1577, 1408, 1353.

4,4'-((10-Dodecyl-10*H*-phenothiazine-3,7-diyl)bis(ethyne-2,1-diyl)dibenzonitrile (39)



36 (996 mg, 2.4 mmol), 4-bromobenzonitrile (870 mg, 4.8 mmol), Ph(PPh₃)₂Cl₂ (0.13 g, 0.18 mmol) and CuI (6.86 mg, 0.036 mmol) were dissolved in dry THF (30 mL) and Et₃N (7 mL) under nitrogen. The mixture was stirred under reflux for 12 h. After completion of the reaction, solvents were removed under reduced pressure and the crude residue was purified by column chromatography (SiO₂, ethyl acetate/hexane, 1:5, v/v, R_f = 0.25) to yield an orange oil (163 mg, 11%).

δ_{H} (400 MHz, CDCl_3): 7.62 (d, $J = 8.5$ Hz, 2H, H5), 7.56 (d, $J = 8.5$ Hz, 2H, H4), 7.32 (dd, $J = 5.8$, 2.3 Hz, 4H, H2), 7.26 (d, $J = 2.3$ Hz, 4H, H1), 6.81 (d, $J = 9.3$ Hz, 2H, H3), 3.84 (t, $J = 8.9$ Hz, 2H, CH_2), 1.84 – 1.75 (m, 2H, CH_2), 1.48 – 1.39 (m, 2H, CH_2), 1.32 – 1.27 (m, 4H, CH_2), 1.24 (s, 12H, CH_2), 0.87 (t, $J = 6.8$ Hz, 3H, CH_2) ppm;

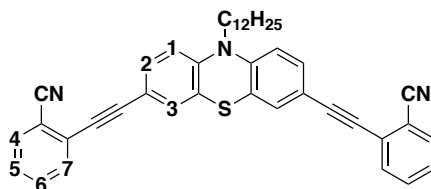
δ_{C} (100.6 MHz, CDCl_3): 145.1 (C_q), 131.9 (C_5), 131.3 (C_3), 131.3 (C_4), 131.2 (C_2), 130.4 (C_1), 129.2 (C_q), 124.1 (C_q), 118.6 (C_q), 115.3 (C_q), 99.9 (C_q), 93.2 (C_q), 47.8 (CH_2), 31.9 (CH_2), 29.5 (CH_2), 29.2 (CH_2), 26.7 (CH_2), 22.7 (CH_2), 14.2 (CH_3) ppm;

HRMS MALDI TOF $\text{C}_{27}\text{H}_{32}\text{N}_3\text{S}$ Calc. 617.2865 Found 617.2876;

IR ν_{max} (ATR/ cm^{-1}) 2921, 2850, 2341 ($\text{C}\equiv\text{N}$), 2360 ($\text{C}\equiv\text{N}$), 2223, 2196, 1603, 1575, 1520, 1500;

UV λ_{abs} 291, 310, 397 nm.

2,2'-((10-Dodecyl-10H-phenothiazine-3,7-diyl)bis(ethyne-2,1-diyl)dibenzonitrile (40)



36 (996 mg, 2.4 mmol), 2-iodobenzonitrile (1.10 g, 4.80 mmol), $\text{Ph}(\text{PPh}_3)_2\text{Cl}_2$ (0.13 g, 0.18 mmol) and CuI (6.86 mg, 0.036 mmol) were dissolved in dry THF (30 mL) and Et_3N (7 mL) under nitrogen. The mixture was stirred under reflux for 12 h. After completion of the reaction, solvents were removed under reduced pressure and the crude residue was purified by column chromatography (SiO_2 , ethyl acetate/hexane, 1:5, v/v, $R_f = 0.2$) to yield an orange oil (620 mg, 42%).

δ_{H} (400 MHz, CDCl_3): 7.63 (d, $J = 7.3$ Hz, 2H, H4), 7.58 – 7.55 (dd, $J = 6.6$, 1.1 Hz, 2H, H5), 7.53 (td, $J = 6.7, 6$, 1.1 Hz, 2H, H6), 7.39 – 7.37 (m, 2H, H7), 7.35 (dd, $J = 5.8$, 1.5 Hz, 2H, H2), 7.28 (d, $J = 1.9$ Hz, 2H, H1), 6.78 (d, $J = 9.7$ Hz, 2H, H3), 3.81 (t, $J = 7.1$ Hz, 2H, CH_2), 1.82 – 1.71 (m, 2H, CH_2), 1.45 – 1.35 (m, 2H, CH_2), 1.34 – 1.26 (m, 4H, CH_2), 1.24 (s, 12H, CH_2), 0.87 (t, $J = 6.8$ Hz, 3H, CH_3) ppm;

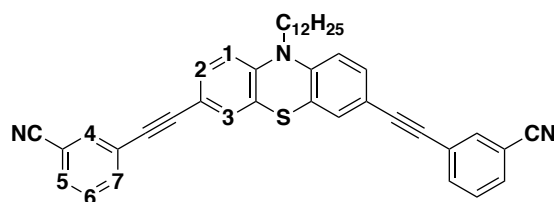
δ_{C} (101.6 MHz, CDCl_3): 145.12 (C_q), 132.6 (C_6), 132.4 (C_4), 131.9 (C_5), 131.6 (C_2), 130.4 (C_1), 128 (C_q), 127.3 (C_7), 124 (C_q), 117.7 (C_q), 116.2 (C_q), 115.3 (C_3), 114.9 (C_q), 95.6 (C_q), 86 (C_q), 53.5 (CH_2), 47.8 (CH_2), 31.9 (CH_2), 29.5 (CH_2), 26.7 (CH_2), 22.7 (CH_2), 14.2 (CH_3) ppm;

HRMS MALDI TOF $\text{C}_{27}\text{H}_{32}\text{N}_3\text{S}$ Calc. 617.2865 Found 617.2876;

IR ν_{max} (ATR/ cm^{-1}) 2921, 2850, 2341 ($\text{C}\equiv\text{N}$), 2360 ($\text{C}\equiv\text{N}$), 2223, 2196, 1603, 1575, 1520, 1500;

UV λ_{abs} 294, 383 nm.

3,3'-((10-Dodecyl-10*H*-phenothiazine-3,7-diyl)bis(ethyne-2,1-diyl)dibenzonitrile (41)



36 (996 mg, 2.40 mmol), 3-bromobenzonitrile (870 mg, 4.80 mmol), $\text{Ph}(\text{PPh}_3)_2\text{Cl}_2$ (0.13 g, 0.18 mmol) and CuI (6.86 mg, 0.036 mmol) were dissolved in dry THF (30 mL) and Et_3N (7 mL) under nitrogen. The mixture was stirred under reflux for 12 h. After completion of the reaction, solvents were removed under reduced pressure and crude residue was purified by column chromatography (SiO_2 , ethyl acetate/hexane, 1:5, v/v, $R_f = 0.35$) to yield a yellow oil (710 mg, 48%).

δ_{H} (400 MHz, CDCl_3): 7.76 (s, 2H, H4), 7.69 (d, $J = 7.5$ Hz, 2H, H5), 7.58 (d, $J = 7.5$ Hz, 2H, H7), 7.45 (t, $J = 7.8$ Hz, 2H, H6), 7.31 (dd, $J = 6.15, 2$ Hz, 2H, H2), 7.26 (s, 2H, H1), 6.81 (d, $J = 8.5$ Hz, 2H, H3), 3.85 (t, $J = 7.3$ Hz, 2H, CH_2), 1.84 – 1.75 (m, 2H, CH_2), 1.47 – 1.39 (m, 2H, CH_2), 1.35 – 1.27 (m, 4H, CH_2), 1.25 (s, 12H), 0.88 (t, $J = 6.8$ Hz, 2H) ppm;

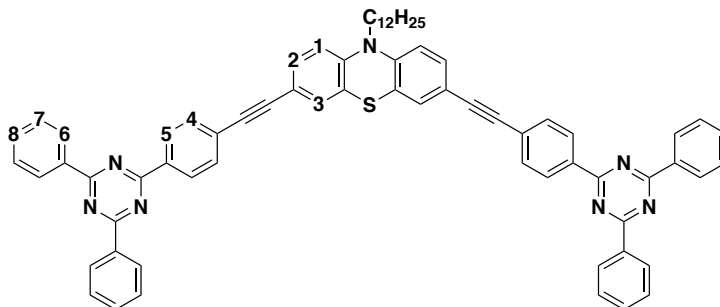
δ_{C} (100.6 MHz, CDCl_3): 145.1 (C_4), 135.5 (C_5), 134.7 (C_q), 131.2 (C_2), 130.3 (C_1), 129.3 (C_7), 125 (C_6), 124.2 (C_q), 118.1 (C_q), 116.5 (C_q), 115.3 (C_3), 112.8 (C_q), 91.2 (C_q), 87.2 (C_q), 47.8 (CH_2), 31.9 (CH_2), 29.4 (CH_2), 26.7 (CH_2), 22.7 (CH_2), 14.1 (CH_3) ppm;

HRMS MALDI TOF $\text{C}_{27}\text{H}_{32}\text{N}_3\text{S}$ Calc. 617.2865 Found 617.2876;

IR ν_{max} (ATR/ cm^{-1}) 2921, 2850, 2341 ($\text{C}\equiv\text{N}$), 2360 ($\text{C}\equiv\text{N}$), 2223, 2196, 1603, 1575, 1520, 1500;

UV λ_{abs} 296, 322, 398 nm.

3,7-Bis((4-(4,6-diphenyl-1,3,5-triazin-2-yl)phenyl)ethynyl)-10-dodecyl-10H-phenothiazine (42)



36 (300 mg, 0.72 mmol) and **5** (560 mg, 1.44 mmol) were dissolved in dry THF (30 mL) and Et₃N (7 mL) and thoroughly degassed. Pd(PPh₃)Cl₂ (50.53 mg, 0.072 mmol) and CuI (2 mg, 0.01 mmol) were added, and the reaction mixture brought up to reflux, and stirred for 12 h. Following that, the solvent was reduced *in vacuo*, and the crude mixture purified by flash chromatography (SiO₂, CH₂Cl₂/Pet Ether, 3/7, v/v, R_f = 0.4) to yield a bright orange solid (370 mg, 50%).

δ_{H} (400 MHz, CDCl₃): 8.79 (d, J = 6.5 Hz, 8H, H6), 8.77 (d, J = 8.54 Hz, 4H, H5) 7.70 (d, J = 8.4 Hz, 4H, H4), 7.63 (t, J = 7.3 Hz, 4H, H8), 7.59 (t, J = 7.3, 8.9 Hz, 8H, H7), 7.37 (d, J = 8.3 Hz, 2H, H2), 7.34 (s, 2H, H1), 6.84 (d, J = 8.3 Hz, 2H, H3), 3.88 (t, J = 7.3 Hz, 2H, CH₂), 1.91 – 1.78 (m, 2H, CH₂), 1.50 – 1.39 (m, 2H, CH₂), 1.39 – 1.28 (m, 4H, CH₂), 1.26 (s, 12H, CH₂), 0.88 (t, J = 6.8 Hz, 2H) ppm;

δ_{C} (100.6 MHz, CDCl₃): 171.79 (C_q), 171.72 (C_q), 144.88 (C_q), 136.06 (C_q), 135.21 (C_q), 132.60 (C8), 131.93 (C4), 131.67 (C1), 130.50 (C2), 130.37 (C5), 128.88 (C6), 128.68 (C7), 127.55 (C_q), 124.19 (C_q), 117.14 (C4), 115.26 (C_q), 91.64 (C_q), 89.51 (C_q), 47.81 (CH₂), 31.93 (CH₂), 29.65 (CH₂), 29.54 (CH₂), 29.37 (CH₂), 29.20 (CH₂), 26.82 (CH₂), 26.72 (CH₂), 22.72 (CH₂), 14.15 (CH₃) ppm;

HRMS MALDI TOF C₇₀H₅₉N₇S Calc. 1029.4553 Found 1029.4542;

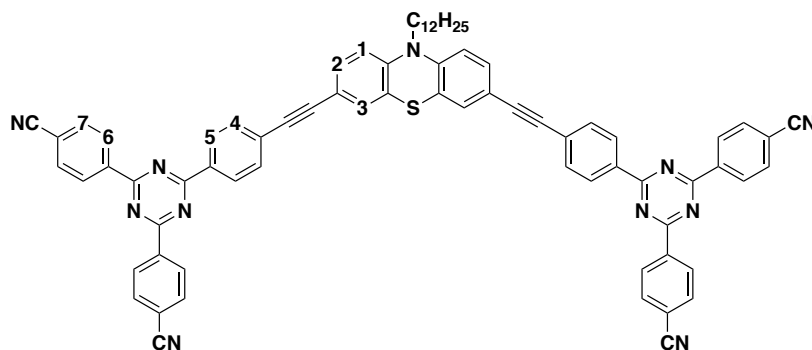
IR ν_{max} (ATR/cm⁻¹) 3057, 2922, 2851, 2340, 2194, 1601, 1587, 1566, 1510, 1473, 1362;

UV λ_{abs} 280, 311, 404 nm;

MP 170-171 °C;

CHN Calc. C₇₀H₅₉N₇S C, 81.60; H, 5.77; N, 9.52; Found C, 81.48; H, 5.81; N, 9.22.

4,4',4'',4'''-(((10-Dodecyl-10H-phenothiazine-3,7-diyl)bis(ethyne-2,1-diyl))bis(4,1-phenylene))bis(1,3,5-triazine-6,2,4-triyl)tetrabenzonitrile (43)



36 (100 mg, 0.24 mmol) and **6** (210 mg, 0.48 mmol) were dissolved in dry THF (20 mL) and Et₃N (5 mL) and thoroughly degassed with bubbling and sparging. Pd(PPh₃)Cl₂ (17 mg, 0.023 mmol) and CuI (0.7 mg, 0.01 mmol) were added, and the reaction mixture brought up to reflux, and stirred for 12 h. Following that, the solvent was reduced *in vacuo*, and the crude mixture purified by flash chromatography (SiO₂, CH₂Cl₂/MeOH, 10:0.1, v/v, R_f = 0.1) to yield a bright orange solid (160 mg, 59%).

δ_H (600 MHz, CDCl₃): δ 8.86 (d, *J* = 7.8 Hz, 8H, H6), 8.72 (d, *J* = 7.81 Hz, 4H, H5), 7.88 (d, *J* = 7.81 Hz, 8H, H7), 7.69 (d, *J* = 7.81 Hz, 4H, H4), 7.37 (d, *J* = 8.1 Hz, 2H, H2), 7.32 (s, 2H, H1), 6.83 (d, *J* = 9.0 Hz, 2H, H3), 3.87 (t, *J* = 6.2 Hz, 2H, CH₂), 1.84 – 1.81 (m, 2H, CH₂), 1.46 – 1.43 (m, 2H, CH₂), 1.33 – 1.29 (m, 2H, CH₂), 1.26 (s, 12H, CH₂), 0.90 – 0.87 (t, *J* = 6.6 Hz, 3H, CH₃) ppm;

δ_C (151.6 MHz, CDCl₃): 172.2 (C_q), 170.8 (C_q), 145.3 (C_q), 140 (C_q), 134.8 (C_q), 132.9 (C7), 132.2 (C4), 131.6 (C2), 130.7 (C6), 129.8 (C5), 129.4 (C1), 128.9 (C_q), 124.5 (C_q), 118.7 (C_q), 117.3 (C3), 116.5 (C_q), 115.6 (C_q), 92.8 (C_q), 89.7 (C_q), 48.2 (CH₂), 32.3 (CH₂), 29.9 (CH₂), 29.7 (CH₂), 29.6 (CH₂), 27.1 (CH₂), 23.1 (CH₂), 14.5 (CH₃) ppm;

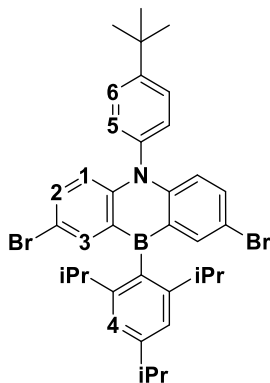
HRMS MALDI TOF C₇₄H₅₅N₁₁S Calc. 1129.4363 Found 1129.4324;

IR *v*_{max} (ATR/cm⁻¹) 3057, 2921, 2850, 2360 (C≡N), 2228, 2192, 1577, 1509, 1471, 1357;

UV *λ*_{abs} 277, 310, 410 nm;

MP 279-281 °C.

2,8-dibromo-5-(4-(tert-butyl)phenyl)-10-(2,4,6-triisopropylphenyl)-5,10-dihydrodibenzo[b,e][1,4]azaborinine (51)



45 (170 mg, 2.8 mmol) was dissolved in diethyl ether (20 mL), and thoroughly degassed by bubbling with Ar gas. The solution was cooled to $-78\text{ }^{\circ}\text{C}$, and n-butyllithium in hexanes (1.6 M, 3.5 mL, 5.61 mmol) was added by syringe and stirred for 30 minutes. Meanwhile, **50** (801 mg, 2.9 mmol) was added to 10 mL of dry diethyl ether, and thoroughly degassed by bubbling with Ar gas. After 30 minutes, with the reaction temperature maintained at $-78\text{ }^{\circ}\text{C}$, the boronate solution was added dropwise to the lithiated reaction mixture. The solution was allowed to warm up to RT gradually, and stirred overnight. After 12 h, all volatiles were removed *in vacuo*. The residues were dissolved in CH_2Cl_2 , washed with saturated ammonium chloride, brine, and dried over MgSO_4 . The organic layer was reduced *in vacuo*, and the product precipitated from the crude mixture ($\text{CH}_2\text{Cl}_2/\text{MeOH}$, freezer) to afford a pale pink solid (117 mg, 63%).

δ_{H} (400 MHz, CDCl_3): δ 7.98 (d, $J = 2.56$ Hz, 2H, H3), 7.72 (d, $J = 8.39$ Hz, 2H, H5), 7.55-7.52 (dd, $J = 6.73, 2.58$ Hz, 2H, H2), 7.31 (d, $J = 8.46$ Hz, 2H, H6), 7.12 (s, 2H, H4), 6.73 (d, $J = 9.15$ Hz, 2H, H1), 3.06-2.98 (m, 1H, iso-CH), 2.41 – 2.32 (m, 2H, iso-CH), 1.49 (s, 9H, tBu), 1.40 (d, $J = 6.8$ Hz, 6H, iso- CH_3), 1.05 (d, $J = 6.8$ Hz, 12H, iso- CH_3);

δ_{C} (101.6 MHz, CDCl_3): δ 152.63 (C_q), 150.54 (C_q), 148.39 (C_q), 144.85 (C_q), 140.08 (C_q), 138.94 (C_3), 138.17 (C_q), 135.59 (C_2), 129.27 (C_6), 128.00 (C_5), 120.18 (C_4), 119.33 (C_1), 113.35 (C_q), 35.20 (tBu- C_q), 35.04 (iso-CH), 34.29 (iso-CH), 31.48 (tBu- CH_3), 24.46 (iso- CH_3), 24.18 (iso- CH_3);

HRMS APCI⁺ $\text{C}_{37}\text{H}_{42}\text{BBr}_2\text{N}$ Calc. 669.1777 Found 669.1793 [$\text{M}+\text{H}$]⁺;

IR ν_{max} (ATR/ cm^{-1}) 3745.94, 3302.31, 2957.97, 2867.74, 2162.56, 1981.04, 1659.78, 1602.35, 1586.72, 1463.69, 1422.82;

MP 267-269 $^{\circ}\text{C}$;

X-ray Crystallography A specimen of $C_{37}H_{42}BBr_2N$, approximate dimensions 0.040 mm x 0.170 mm x 0.460 mm, was used for the X-ray crystallographic analysis. The X-ray intensity data were measured ($\lambda = 0.71073 \text{ \AA}$) at 100(2)K on a Bruker D8 Quest Eco with an Oxford Cryostream low temperature device using a MiTeGen micromount.

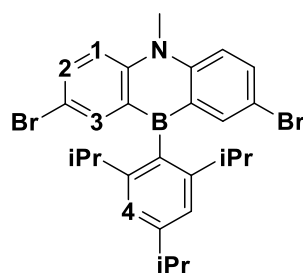
A total of 980 frames were collected. The total exposure time was 8.17 hours. The integration of the data using an orthorhombic unit cell yielded a total of 41492 reflections to a maximum θ angle of 26.85° (0.79 \AA resolution), of which 10434 were independent (average redundancy 3.977, completeness = 99.8%, $R_{int} = 7.80\%$, $R_{sig} = 8.19\%$) and 8176 (78.36%) were greater than $2\sigma(F^2)$. The final cell constants of $a = 10.5518(10) \text{ \AA}$, $b = 35.263(3) \text{ \AA}$, $c = 26.309(2) \text{ \AA}$, volume = $9789.3(16) \text{ \AA}^3$, are based upon the refinement of the XYZ-centroids of 9691 reflections above $20 \sigma(I)$ with $5.414^\circ < 2\theta < 53.33^\circ$. Data were corrected for absorption effects using the Multi-Scan method (SADABS). The ratio of minimum to maximum apparent transmission was 0.600. The calculated minimum and maximum transmission coefficients (based on crystal size) are 0.3910 and 0.9060.

The structure was solved with the XT structure solution program using Intrinsic Phasing and refined with the XL refinement package using Least Squares minimisation with Olex2, using the space group Aba_2 , with $Z = 12$ for the formula unit, $C_{37}H_{42}BBr_2N$. The final anisotropic full-matrix least-squares refinement on F^2 with 681 variables converged at $R_1 = 5.28\%$, for the observed data and $wR_2 = 13.14\%$ for all data. The goodness-of-fit was 1.035. The largest peak in the final difference electron density synthesis was $1.062 \text{ e}^-/\text{\AA}^3$ and the largest hole was $-1.017 \text{ e}^-/\text{\AA}^3$ with an RMS deviation of $0.098 \text{ e}^-/\text{\AA}^3$. On the basis of the final model, the calculated density was 1.367 g/cm^3 and $F(000)$, 4152 e⁻.

Refinement Note: tBu group modelled disordered over the 2 fold with a rigid group and 25 % occupancy (4 positions) and refined with displacement (SIMU, ISOR) restraints. The triisopropylphenyl group was modelled in two positions over the 2 fold, at 50% occupancy for each. A combination of geometric (SADI) and displacement (SIMU, ISOR) restraints were applied.

2,8-dibromo-5-methyl-10-(2,4,6-triisopropylphenyl)-5,10-dihydrodibenzo[b,e][1,4]azaborinine

(53)



49 (349 mg, 0.7 mmol) was dissolved in diethyl ether (10 mL), and thoroughly degassed by bubbling with Ar. The solution was cooled to $-78\text{ }^{\circ}\text{C}$, and *n*-butyllithium in hexanes (1.47 M, 1 mL, 1.47 mmol) was added by syringe and stirred for 30 minutes. Meanwhile, **50** (0.22 mL, excess added) was added to 5 mL of dry diethyl ether, and thoroughly degassed by bubbling with Ar. After 30 minutes, with the reaction temperature maintained at $-78\text{ }^{\circ}\text{C}$, the boronate solution was added dropwise to the lithiated reaction mixture. The solution was allowed to warm up to RT gradually, and stirred overnight. After 12 h, all volatiles were removed *in vacuo*. The residues were dissolved in CH_2Cl_2 , washed with a saturated solutions of ammonium chloride, brine, and dried over MgSO_4 . The organic layer was reduced *in vacuo* and purified by column chromatography (SiO_2 , methylene chloride/petroleum ether 1:10, v/v, $R_f = 0.28$) to afford a (24 mg, 6.2%).

δ_{H} (400 MHz, CDCl_3): δ 7.97 (d, $J = 2.32$ Hz, 2H, H3), 7.82-7.79 (dd, $J = 6.95, 2.03$ Hz, 2H, H2), 7.56 (d, $J = 9.26$ Hz, 2H, H1), 7.08 (s, 2H), 4.06 (s, 3H, Me), 3.04-2.97 (m, 1H, iso-CH), 2.29-2.22 (m, 2H, iso-CH), 1.39 (d, $J = 7.20$ Hz, 6H, iso- CH_3), 0.99 (d, $J = 6.62$ Hz, 12H, iso- CH_3);

δ_{C} (101.6 MHz, CDCl_3): δ 150.43 (C_q), 148.41 (C_q), 144.53 (C_q), 139.60 (C3), 136.22 (C2), 120.18 (C4), 120.14 (C_q), 119.99 (C1), 117.00 (C_q), 113.18 (C_q), 111.84 (C_q), 35.95 (N- CH_3), 35.21 (iso-CH), 34.27 (iso-CH), 24.29 (iso- CH_3), 24.15 (iso- CH_3);

HRMS APCI⁺ $\text{C}_{28}\text{H}_{32}\text{BBr}_2\text{N}$ Calc. 551.0995 Found 551.0979 [M+H]⁺;

IR ν_{max} (ATR/ cm^{-1}) 3850.11, 2957.30, 2922.36, 2864.9, 2568.53, 2162.04, 2035.19, 1886.50, 1728.45, 1602.87, 1587.10, 1554.10, 1532.10, 146.49, 1440.86, 1422.05;

MP 250-251 $^{\circ}\text{C}$;

X-ray Crystallography A specimen of $\text{C}_{28}\text{H}_{32}\text{BBr}_2\text{N}$, approximate dimensions 0.130 mm x 0.140 mm x 0.180 mm, was used for the X-ray crystallographic analysis. The X-ray intensity data were measured

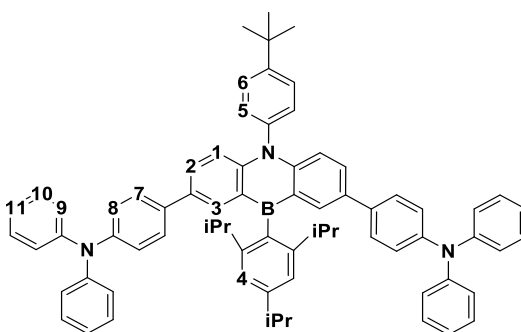
($\lambda = 1.54178 \text{ \AA}$) at 100(2)K on a Bruker Apex Kappa Duo with an Oxford Cobra Cryosystem low temperature device using a MiTeGen micromount.

A total of 3271 frames were collected. The total exposure time was 14.74 hours. The frames were integrated with the Bruker SAINT software package using a wide-frame algorithm. The integration of the data using a monoclinic unit cell yielded a total of 47489 reflections to a maximum θ angle of 70.03° (0.82 \AA resolution), of which 4774 were independent (average redundancy 9.947, completeness = 99.5%, $R_{\text{int}} = 3.67\%$, $R_{\text{sig}} = 1.81\%$) and 4716 (98.79%) were greater than $2\sigma(F^2)$. The final cell constants of $a = 13.6889(6) \text{ \AA}$, $b = 10.7255(5) \text{ \AA}$, $c = 17.8627(8) \text{ \AA}$, $\beta = 105.2586(12)^\circ$, volume = $2530.2(2) \text{ \AA}^3$, are based upon the refinement of the XYZ-centroids of 9816 reflections above $20\sigma(I)$ with $6.693^\circ < 2\theta < 139.4^\circ$. Data were corrected for absorption effects using the Multi-Scan method (SADABS). The ratio of minimum to maximum apparent transmission was 0.806. The calculated minimum and maximum transmission coefficients (based on crystal size) are 0.5210 and 0.6130.

The structure was solved with the XT structure solution program using Intrinsic Phasing and refined with the XL refinement package using Least Squares minimisation with Olex2, using the space group $P2_1/n$, with $Z = 4$ for the formula unit, $C_{28}H_{32}BBr_2N$. The final anisotropic full-matrix least-squares refinement on F^2 with 326 variables converged at $R1 = 3.28\%$, for the observed data and $wR2 = 9.04\%$ for all data. The goodness-of-fit was 1.093. The largest peak in the final difference electron density synthesis was $0.470 e^{-}/\text{\AA}^3$ and the largest hole was $-0.532 e^{-}/\text{\AA}^3$ with an RMS deviation of $0.080 e^{-}/\text{\AA}^3$. On the basis of the final model, the calculated density was 1.452 g/cm^3 and $F(000)$, 1128 e^{-} .

Refinement Note: *iPr* group C27-C29 was disordered and modelled over two positions with geometric restraints (SADI) with the major moiety refined occupancy of 0.685(6).

4,4'-(5-(4-(tert-butyl)phenyl)-10-(2,4,6-triisopropylphenyl)-5,10-dihydrodibenzo[b,e][1,4]azaborinine-2,8-diyl)bis(N,N-diphenylaniline) (54)



51 (100 mg, 0.15 mmol) and (4-(diphenylamino)phenyl)boronic acid (100.84 mg, 0.64 mmol) were dissolved in 20 mL 1:1 ethanol/toluene and 0.1 mL K₂CO₃ (2 M solution) and thoroughly degassed by bubbling with Ar. Once all reactants were fully solubilised, Pd(PPh₃)₄ (31.52 mg, 0.003 mmol, 8%) was added. The solution was heated to 110 °C and stirred overnight. After 12 h, all volatiles were removed *in vacuo*. The residues were dissolved in methylene chloride, washed with brine, and dried over MgSO₄. The organic layer was reduced *in vacuo*, and the product was purified by column chromatography (SiO₂, methylene chloride/petroleum ether 20:80, v/v, R_f = 0.44) to afford a yellow solid (41.5 mg, 27%).

δ_H (400 MHz, CDCl₃): δ 8.09 (s, 2H, H3), 7.76 (d, J = 8.4 Hz, 2H, H6), 7.74-7.72 (dd, J = 6.64, 2.38 Hz, 2H, H2), 7.43 (d, J = 8.32 Hz, 2H, H5), 7.39 (d, J = 8.64 Hz, 4H, H7), 7.27 (d, J = 5 Hz, 8H, H10), 7.25 (s, 2H, H4), 7.14 (s, 4H, H8), 7.13 (s, 8H, H9), 7.04-7.00 (t, J = 6.91, 6.44 Hz, 4H, H11), 6.95 (s, 2H, H1), 3.06-2.99 (m, 1H, iso-CH), 2.61 (m, 2H, iso-CH), 1.53 (s, 9H, tBu), 1.40 (d, J = 6.53 Hz, 6H, iso-CH₃), 1.08 (d, J = 6.53 Hz, 12H, iso-CH₃);

δ_C (101.6 MHz, CDCl₃): δ 152.10 (C_q), 150.48 (C_q), 147.79 (C_q), 146.50 (C_q), 145.37 (C_q), 138.88 (C_q), 137.57 (C_q), 135.72 (C_q), 135.18 (C_q), 134.68 (C3), 131.68 (C2), 131.39 (C_q), 129.65 (C5), 129.24 (C10), 127.75 (C_q), 127.60 (C2), 127.51 (C7), 124.43 (C8), 123.83 (C9), 122.83 (C11), 119.85 (C4), 117.39 (C1), 35.04 (iso-CH), 34.73 (tBu-C_q), 34.23 (iso-CH), 31.55 (tBu-CH₃), 24.63 (iso-CH₃), 24.20 (iso-CH₃);

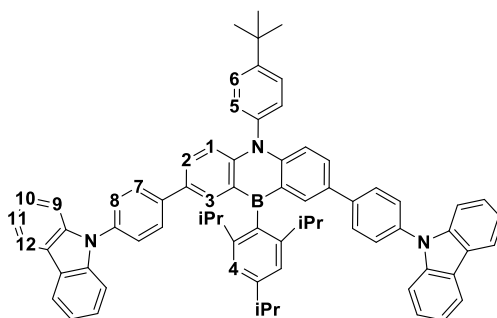
HRMS MALDI TOF C₇₃H₇₀N₃B₁ Calc. 999.5663 Found 999.5671;

IR ν_{max} (ATR/cm⁻¹) 2360.58, 2341.75, 2162.31, 2108.47, 2028, 1742.37, 1591.63, 1487.54, 1451.65, 1361.91, 1329.61, 1275.77, 1229.11;

UV λ_{abs} 310, 357, 405 nm;

MP °C 171-172 °C .

2,8-bis(4-(9H-carbazol-9-yl)phenyl)-5-(4-(tert-butyl)phenyl)-10-(2,4,6-triisopropylphenyl)-5,10-dihydrodibenzo[b,e][1,4]azaborinine (55**)**



51 (200 mg, 0.3 mmol) and (4-(9H-carbazol-9-yl)phenyl)boronic acid (188 mg, 0.3 mmol) were dissolved in 20 mL 1:1 ethanol/toluene and 1 mL K_2CO_3 (2 M solution) and thoroughly degassed by bubbling with Ar. Once all reactants were fully solubilised, $Pd(PPh_3)_4$ (58 mg, 0.05 mmol, 8%) was added. The solution was heated to 110 °C and stirred overnight. After 12 h, all volatiles were removed *in vacuo*. The residues were dissolved in methylene chloride, washed with brine, and dried over $MgSO_4$. The organic layer was reduced *in vacuo*, and the product was purified by column chromatography (SiO_2 , methylene chloride/petroleum ether 40:60, v/v, $R_f = 0.6$) to afford an off white solid (170 mg, 58%).

δ_H (400 MHz, $CDCl_3$): δ 8.24 (d, $J = 2.2$ Hz, 2H, H3), 8.16 – 8.14 (d, $J = 7.55$ Hz, 2H, H9), 7.87 – 7.84 (dd, $J = 6.44, 2.52$ Hz, 2H, H2), 7.81 (d, $J = 8.8$ Hz, 2H, H5), 7.72 (d, $J = 8.49$ Hz, 4H, H8), 7.59 (d, $J = 8.8$ Hz, 4H, H7), 7.49 (d, $J = 9.2$ Hz, 2H, H6), 7.47 (d, $J = 9.2$ Hz, 4H, H12), 7.43 – 7.39 (ddd, $J = 7.07, 5.9, 1.2$ Hz, 2H, H10), 7.311 – 7.26 (ddd, $J = 6.85, 6.81, 1.2$ Hz, 2H, H11), 7.20 (s, 2H, H4), 7.05 (d, $J = 8.97$ Hz, 2H, H1), 3.09 – 3.02 (m, 1H, iso-CH), 2.71 – 2.64 (m, 2H, iso-CH), 1.55 (s, 6H, tBu), 1.41 (d, $J = 6.43$ Hz, 3H, iso- CH_3), 1.15 (d, $J = 6.86$ Hz, 6H, iso- CH_3);

δ_C (101.6 MHz, $CDCl_3$): δ 150.64 (C_q), 150.05 (C_q), 148.19 (C_q), 148.08 (C_q), 145.96 (C_q), 140.89 (C_q), 140.16 (C_q), 138.79 (C_q), 137.37 (C_q), 136.21 (C_q), 135.38 (C3), 131.76 (C_q), 131.44 (C2), 129.62 (C_q), 128.27 (C8), 127.92 (C5), 127.30 (C7), 125.92 (C10), 123.38 (C_q), 120.27 (C9), 119.95 (C4), 119.90 (C11), 117.78 (C1), 109.94 (C12), 35.23 (iso-CH), 35.08 (tBu- C_q), 34.28 (iso-CH), 31.58 (tBu- CH_3), 24.73 (iso- CH_3), 24.23 (iso- CH_3);

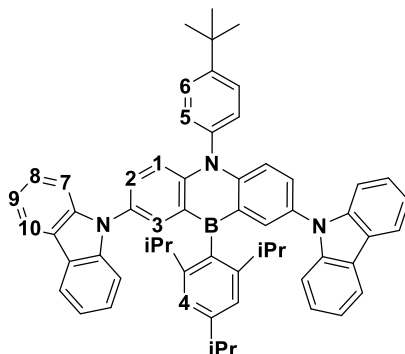
HRMS MALDI TOF $C_{73}H_{66}N_3B_1$ Calc. 995.5350 Found 995.5380;

IR ν_{max} (ATR/ cm^{-1}) 2360.56, 2341.77, 1739.37, 1504.16, 1515.81, 1452.09, 1315.68, 1226.08;

UV λ_{abs} 288, 294, 331, 343, 394, 412 nm;

CHN Calc. C₇₃H₆₆N₃B₁ C, 88.02; H, 6.68; N, 4.22; Found C, 87.27; H, 6.80; N, 4.15.

5-(4-(tert-butyl)phenyl)-2,8-di(9H-carbazol-9-yl)-10-(2,4,6-triisopropylphenyl)-5,10-dihydrodibenzo[b,e][1,4]azaborinine (58)



51 (100 mg, 0.149 mmol), carbazole (50.84 mg, 0.3 mmol), and sodium tert butoxide (35.65 mg, 0.36 mmol) were dissolved in 10 mL pre-dried and degassed toluene. This solution was further degassed. Using a glovebag filled with nitrogen gas, roughly 0.1% mmol Pd(PtBu₃)₂ was added to a 5 mL RBF, and sealed. To it, 5 mL of dry toluene was added and the solution further degassed. Once all reaction flasks were fully degassed, the catalyst was syringed into the reaction mixture, and refluxed for 12 h. After 12 h, all volatiles were removed *in vacuo*, and the residues dissolved in methylene chloride, washed with brine, and the organic layer dried over MgSO₄. The organic layer was reduced *in vacuo* and purified by column chromatography (SiO₂, methylene chloride/petroleum ether 70:30, v/v, R_f = 0.4) to afford a pale yellow solid (70 mg, 56%).

δ_{H} (400 MHz, CDCl₃): δ 8.15 (d, J = 1.18 Hz, 2H, H3) 8.11 (d, J = 6.73 Hz, 4H, H7), 7.82 (d, J = 8.08 Hz, 2H, H5), 7.64-7.62 (dd, J = 6.58, 2.54 Hz, 2H, H2), 7.56 (d, J = 8.35 Hz, 2H, H6), 7.34-7.32 (t, J = 7.24 Hz, 4H, H8), 7.25-7.24 (t, J = 5.35 Hz, 4H, H9), 7.24 (d, J = 8.09 Hz, 4H, H10), 7.14 (d, J = 8.77 Hz, 2H, H1), 6.90 (s, 2H, H4), 2.78 (m, 1H, iso-CH), 2.63 (m, 2H, iso-CH), 1.52 (s, 9H, tBu), 1.17 (d, J = 6.86 Hz, 6H, iso-CH₃), 1.06 (d, J = 6.38 Hz, 12H, iso-CH₃);

δ_{C} (101.6 MHz, CDCl₃): δ 152.74 (C_q), 150.07 (C_q), 148.18 (C_q), 145.62 (C_q), 141.61 (C_q), 138.60 (C_q), 135.98 (C3), 132.47 (C2), 129.53 (C6), 129.43 (C_q), 128.12 (C5), 125.77 (C8), 122.97 (C1), 122.75 (C_q), 120.19 (C7), 120.04 (C4), 119.56 (C9), 119.11 (C10), 114.35 (C_q), 109.71 (C_q), 35.18 (iso-CH), 35.08 (tBu-C_q), 34.02 (iso-CH), 31.53 (tBu-CH₃), 24.36 (iso-CH₃), 23.91 (iso-CH₃);

HRMS MALDI TOF C₆₁H₅₈N₃B₁ Calc. 843.4724 Found 843.4699;

IR ν_{\max} (ATR/cm⁻¹) 2916.72, 2849.12, 2361.40, 2341.45, 1462.41, 1308.37, 1229.99;

UV λ_{abs} 294, 315, 341, 401 nm;

MP °C no decomposition past 360 °C;

X-ray Crystallography A specimen of C₆₁H₅₈BN₃, approximate dimensions 0.160 mm x 0.200 mm x 0.400 mm, was used for the X-ray crystallographic analysis. The X-ray intensity data were measured ($\lambda = 0.71073$ Å) at 100(2)K on a Bruker D8 Quest Eco with an Oxford Cryostream low temperature device using a MiTeGen micromount. Bruker APEX software was used to correct for Lorentz and polarization effects.

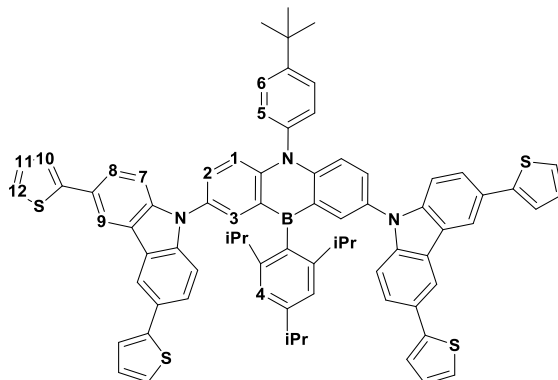
A total of 340 frames were collected. The total exposure time was 3.90 hours. The integration of the data using a triclinic unit cell yielded a total of 19704 reflections to a maximum θ angle of 26.50° (0.80 Å resolution), of which 11648 were independent (average redundancy 1.692, completeness = 98.2%, $R_{\text{int}} = 5.70\%$, $R_{\text{sig}} = 10.92\%$) and 5515 (47.35%) were greater than $2\sigma(F^2)$. The final cell constants of $\underline{a} = 13.343(3)$ Å, $\underline{b} = 13.734(2)$ Å, $\underline{c} = 16.510(3)$ Å, $\alpha = 92.184(5)^\circ$, $\beta = 104.387(5)^\circ$, $\gamma = 101.975(6)^\circ$, volume = 2854.0(9) Å³, are based upon the refinement of the XYZ-centroids of 6265 reflections above $20 \sigma(I)$ with $4.973^\circ < 2\theta < 52.12^\circ$. Data were corrected for absorption effects using the Multi-Scan method (SADABS). The ratio of minimum to maximum apparent transmission was 0.933. The calculated minimum and maximum transmission coefficients (based on crystal size) are 0.6563 and 0.7454.

The structure was solved with the XT structure solution program using Intrinsic Phasing and refined with the XL refinement package using Least Squares minimisation with Olex2, using the space group $P\bar{1}$, with $Z = 2$ for the formula unit, C₆₁H₅₈BN₃. The final anisotropic full-matrix least-squares refinement on F^2 with 852 variables converged at $R1 = 7.38\%$, for the observed data and $wR2 = 23.15\%$ for all data. The goodness-of-fit was 1.016. The largest peak in the final difference electron density synthesis was 0.472 e⁻/Å³ and the largest hole was -0.237 e⁻/Å³ with an RMS deviation of 0.051 e⁻/Å³. On the basis of the final model, the calculated density was 0.982 g/cm³ and $F(000)$, 900 e⁻.

Refinement Note: The central dibenzoazaborinine is partially disordered with N1C2C3C4, C12C13C14, N15-C27 and C56-C65 were modelled in two positions with the majority occupancy refined to 0.736(5). Geometric (SADI) and displacement (SIMU, ISOR) restraints were employed. Geometric and displacement constraints were also used for the carbazole 6 membered rings (AFIX) and C3 (EADP) and C41 (EADP, EXYZ). The triisopropylbenzene group starting at C41 was also disordered in two positions with the majority occupancy refined to 0.804(6). Geometric and

displacement restraints (SADI, SIMU) were used as well as constraints (AFIX) for the six membered rings. Diffuse scattering component of approx. 6.5 EtOH molecules were removed using SQUEEZE (A.L.Spek, Acta Cryst. 2009, D65, 148-155.).

5-(4-(tert-butyl)phenyl)-2,8-bis(3,6-di(thiophen-2-yl)-9H-carbazol-9-yl)-10-(2,4,6-triisopropylphenyl)-5,10-dihydrodibenzo[b,e][1,4]azaborinine (60)



51 (86.8 mg, 0.129 mmol), **59** (90 mg, 0.271 mmol), and sodium tert butoxide (35.65 mg, 0.36 mmol) were dissolved in 15 mL pre-dried and degassed toluene. This solution was further degassed. Using a glovebag filled with nitrogen gas, roughly 0.1% mmol Pd(PtBu₃)₂ was added to a 5 mL RBF, and sealed. To it, 5 mL of dry toluene was added and the solution further degassed. Once all reaction flasks were fully degassed, the catalyst was syringed into the reaction mixture, and refluxed for 12 h. After 12 h, all volatiles were removed *in vacuo*, and the residues dissolved in methylene chloride, washed with brine, and the organic layer dried over MgSO₄. The organic layer was reduced *in vacuo* and purified by column chromatography (SiO₂, methylene chloride/petroleum ether 70:30, v/v, R_f = 0.52) to afford a bright yellow solid (133.3 mg, 37%).

δ_{H} (400 MHz, CDCl₃): δ 8.36 (d, J = 1.18 Hz, 2H, H3), 8.12 (d, J = 2.65 Hz, 4H, H9), 7.84 (d, J = 8.27 Hz, 2H, H5), 7.67-7.64 (dd, J = 6.3, 2.36 Hz, 2H, H2), 7.61 (d, J = 2.36 Hz, 2H, H6), 7.59 (d, J = 1.35 Hz, 4H, H10), 7.35-7.34 (dd, J = 2.39, 1.03 Hz, 4H, H8), 7.27 (d, J = 1.12 Hz, 2H, H1), 7.23 (d, J = 9.84 Hz, 4H, H7), 7.18 (d, J = 9.05 Hz, 4H, H12), 7.11 (dd, J = 3.44, 1.43 Hz, 4H, H11), 6.94 (s, 2H, H4), 2.81 – 2.78 (m, 1H, iso-CH), 2.66 – 2.62 (m, 2H, iso-CH), 1.53 (s, 9H, tBu), 1.18 (d, J = 5.77 Hz, 6H), 1.09 (d, J = 7.21 Hz, 12H);

δ_{C} (101.6 MHz, CDCl₃): δ 152.89 (C_q), 150.10 (C_q), 148.41 (C_q), 145.74 (C_q), 145.45 (C_q), 141.62 (C_q), 138.48 (C_q), 135.97 (C_q), 135.81 (C₉), 132.28 (C₂), 129.49 (C₆), 129.12 (C_q), 128.20 (C₅),

128.00 (C11), 127.03 (C_q), 126.94 (C_q), 124.83 (C2), 123.91 (C1), 123.43 (C_q), 122.37 (C8), 120.14 (C4), 119.31 (C12), 117.93 (C3), 110.19 (C7), 35.22 (iso-CH), 35.08 (tBu-C_q), 34.01 (iso-CH), 31.52 (tBu-CH₃), 24.45 (iso-CH₃), 23.94 (iso-CH₃);

HRMS MALDI TOF C₇₇H₆₆N₃S₄B₁ Calc. 1171.4233 Found 1171.4250;

IR ν_{\max} (ATR/cm⁻¹) 2360.70, 1481.11, 1230.08;

UV λ_{abs} 319, 403 nm;

MP 262-263 °C;

CHN Calc. C₇₇H₆₆N₃S₄B₁ C, 78.88; H, 5.67; N, 3.58; Found C, 78.33; H, 5.64; N, 3.56.

References

- 1 W. H. Melhuish, *J. Phys. Chem.*, 1961, **65**, 229–235.
- 2 A. D. Becke, *Phys. Rev. A*, 1988, **38**, 3098.
- 3 K. Baumgärtner, A. L. Meza Chinchá, A. Dreuw, F. Rominger and M. Mastalerz, *Angew. Chemie - Int. Ed.*, 2016, **55**, 15594–15598.
- 4 C. Abeywickrama and A. D. Baker, *J. Org. Chem.*, 2004, **69**, 7741–7744.
- 5 D. G. Chen, T. C. Lin, Y. A. Chen, Y. H. Chen, T. C. Lin, Y. T. Chen and P. T. Chou, *J. Phys. Chem. C*, 2018, **122**, 12215–12221.

Appendix

Appendix 1: Chapter Two

Elemental Composition Report

Page 1

Single Mass Analysis

Tolerance = 10.0 PPM / DBE: min = -1.5, max = 200.0

Element prediction: Off

Number of isotope peaks used for i-FIT = 5

Monoisotopic Mass, Odd and Even Electron Ions

1 formula(e) evaluated with 1 results within limits (up to 10 best isotopic matches for each mass)

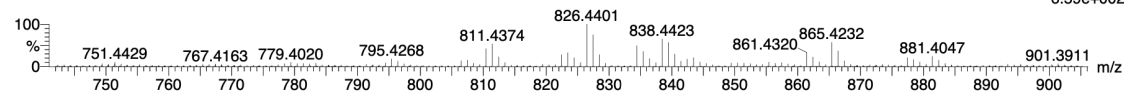
Elements Used:

C: 0-62 H: 0-58 O: 0-2

Marta Gulman (SD), MEG104

Q-TOF20180605MF004 31 (0.574) AM (Cen,6, 80.00, Ht,10000.0,1570.68,0.70); Sm (SG, 2x3.00); Sb (15,10.00); Cm (8:59-34:41)

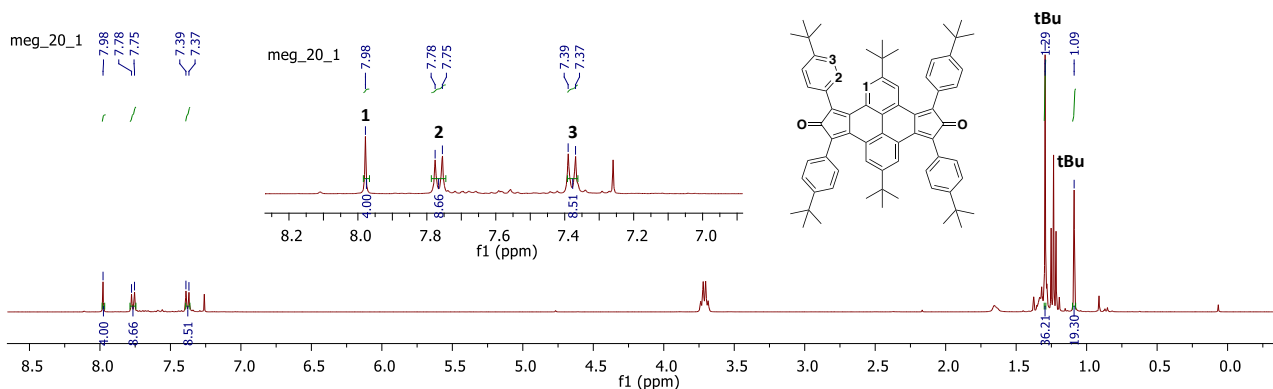
TOF MS LD+
6.59e+002



Minimum: -1.5
Maximum: 200.0

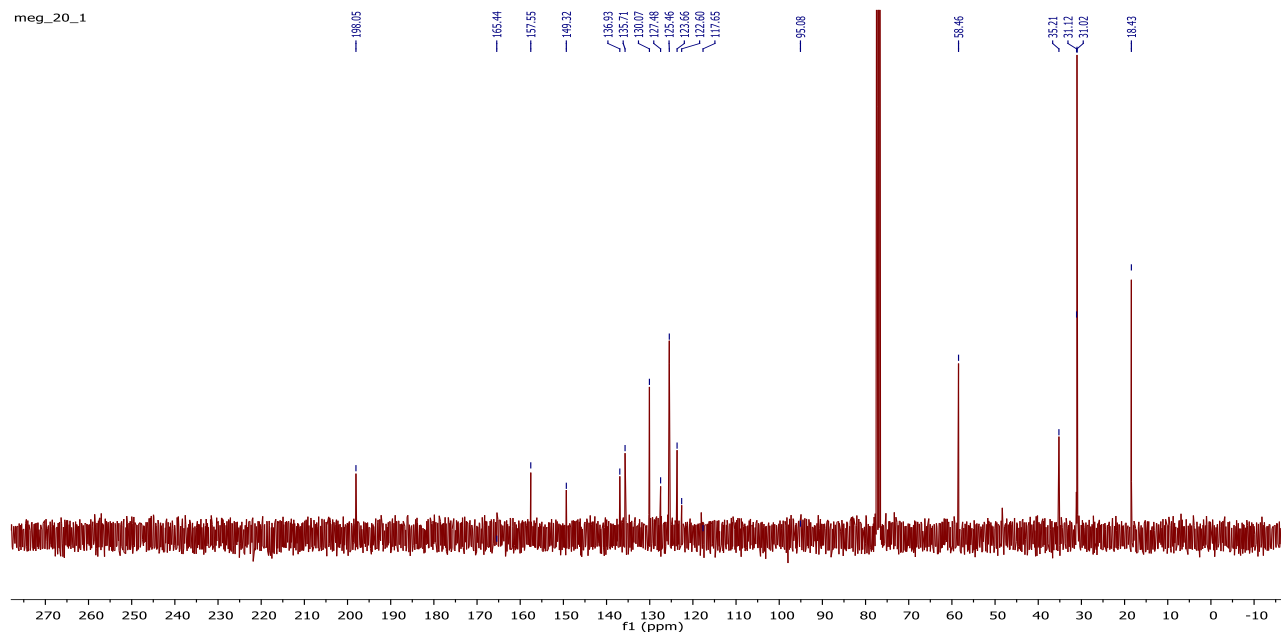
Mass	Calc. Mass	mDa	PPM	DBE	i-FIT	i-FIT (Norm)	Formula
834.4460	834.4437	2.3	2.8	34.0	70.8	0.0	C62 H58 O2

Appendix 1.0a: MALDI TOF data for 5.



Appendix 1.0b: ¹H NMR spectrum of 6 (400 MHz, RT, CDCl₃).

meg_20_1



Appendix 1.0c: $^{13}\text{C}\{^1\text{H}\}$ NMR spectrum of **6** (400 MHz, RT, CDCl_3).

Elemental Composition Report

Page 1

Single Mass Analysis

Tolerance = 10.0 PPM / DBE: min = -1.5, max = 1000.0

Element prediction: Off

Number of isotope peaks used for i-FIT = 3

Monoisotopic Mass, Odd and Even Electron Ions

89 formula(e) evaluated with 1 results within limits (up to 10 closest results for each mass)

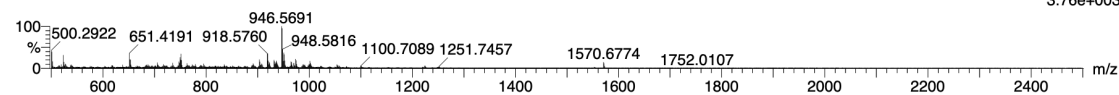
Elements Used:

C: 0-70 H: 0-74 O: 0-5 Ru: 0-2

Martha Gulman (SD), MEG32

Q-TOF20170707MF009 67 (1.236) AM (Cen,4, 80.00, Ht,10000.0,1570.68,0.70); Sm (SG, 2x3.00); Sb (15,10.00); Cm (8:120)

TOF MS LD+
3.76e+003



Minimum: -1.5
Maximum: 5.0 10.0 1000.0

Mass	Calc. Mass	mDa	PPM	DBE	i-FIT	i-FIT (Norm)	Formula
946.5691	946.5689	0.2	0.2	34.0	69.8	0.0	C70 H74 O2

Appendix 1.0d: MALDI TOF data for **6**.

Single Mass Analysis

Tolerance = 20.0 PPM / DBE: min = -1.5, max = 1000.0

Element prediction: Off

Number of isotope peaks used for i-FIT = 5

Monoisotopic Mass, Odd and Even Electron Ions

29 formula(e) evaluated with 1 results within limits (up to 10 closest results for each mass)

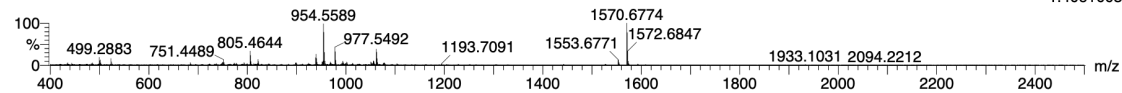
Elements Used:

C: 0-68 H: 0-74 O: 0-4 Pd: 0-1

Martha Gulman (SD), MEG61

Q-TOF20171103MF002 63 (1.167) AM (Cen,4, 80.00, Ht,10000.0,1570.68,0.70); Sm (SG, 2x3.00); Sb (15,10.00); Cm (31:166)

TOF MS LD+
1.40e+003



Minimum: -1.5
Maximum: 1000.0

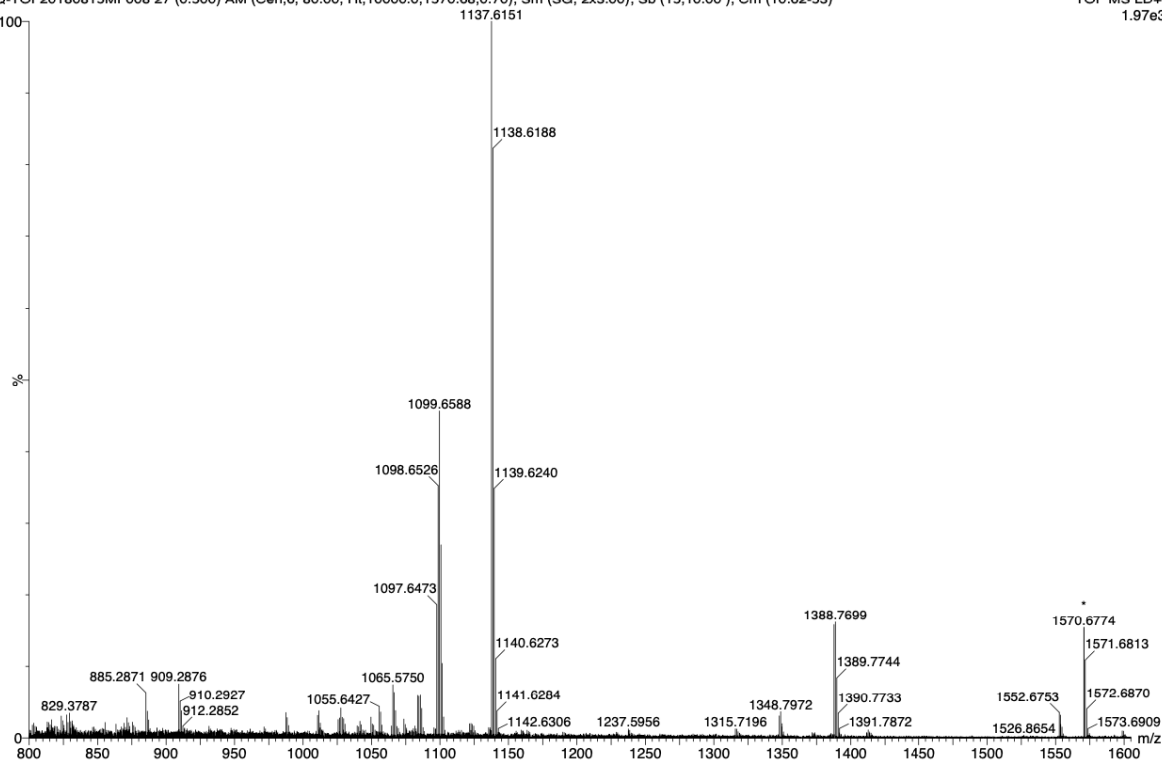
Mass	Calc. Mass	mDa	PPM	DBE	i-FIT	i-FIT (Norm)	Formula
954.5589	954.5587	0.2	0.2	32.0	83.5	0.0	C68 H74 O4

Appendix 1.0e: MALDI TOF data for 7.

Marta Gulman (SD), MEG108

Q-TOF20180815MF008 27 (0.500) AM (Cen,6, 80.00, Ht,10000.0,1570.68,0.70); Sm (SG, 2x3.00); Sb (15,10.00); Cm (10:62-53)

TOF MS LD+
1.97e3



Appendix 1.0f: MALDI TOF spectrum of hydroxy product 9 (MALDI TOF C₈₀H₈₈N₄O₂ calc 1136.69, found 1137.6218).

Single Mass Analysis

Tolerance = 50.0 PPM / DBE: min = -1.5, max = 400.0

Element prediction: Off

Number of isotope peaks used for i-FIT = 5

Monoisotopic Mass, Odd and Even Electron Ions

1 formula(e) evaluated with 1 results within limits (up to 10 best isotopic matches for each mass)

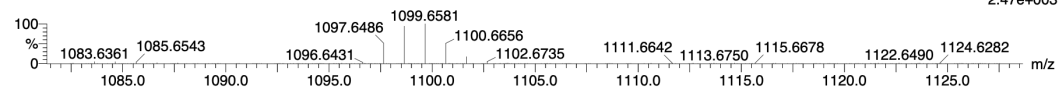
Elements Used:

C: 0-80 H: 0-82 N: 0-4

Martha Gulman (SD), MEG108A

Q-TOF20180820MF002 12 (0.222) AM (Cen,6, 80.00, Ht,10000.0,1570.68,0.70); Sm (SG, 2x3.00); Sb (15,10.00); Cm (12:81)

TOF MS LD+
2.47e+003



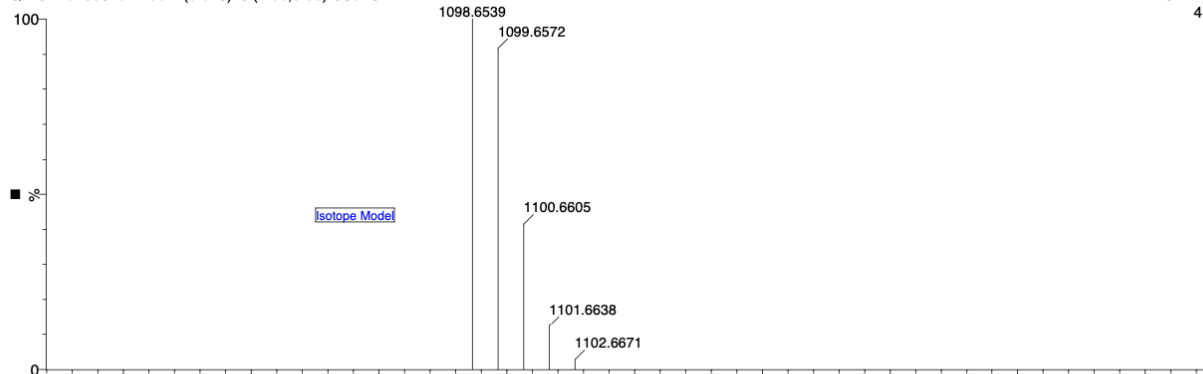
Mass	Calc. Mass	mDa	PPM	DBE	i-FIT	i-FIT (Norm)	Formula
1098.6526	1098.6539	-1.3	-1.2	42.0	104.9	0.0	C80 H82 N4

Appendix 1.0g: MALDI TOF data for isomers 10 and 11.

Martha Gulman (SD), MEG108A

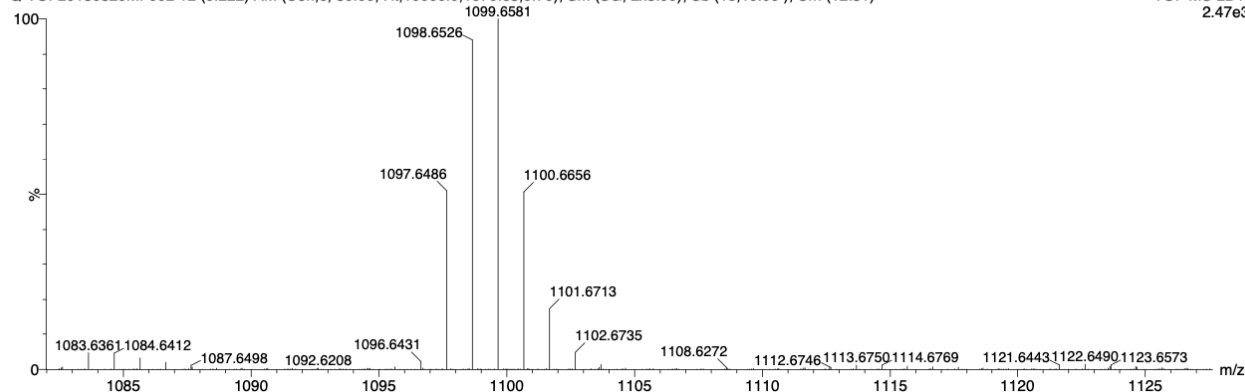
Q-TOF20180820MF002 (0.018) Is (1.00,0.50) C80H82N4

TOF MS LD+
4.02e12



Q-TOF20180820MF002 12 (0.222) AM (Cen,6, 80.00, Ht,10000.0,1570.68,0.70); Sm (SG, 2x3.00); Sb (15,10.00); Cm (12:81)

TOF MS LD+
2.47e3



Appendix 1.0h: MALDI TOF isotopic distribution for isomers 10 and 11.

Elemental Composition Report

Single Mass Analysis

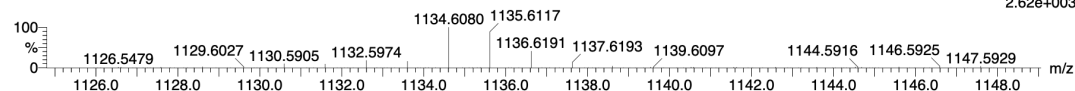
Tolerance = 50.0 PPM / DBE: min = -1.5, max = 1000.0
 Element prediction: Off
 Number of isotope peaks used for i-FIT = 5

Monoisotopic Mass, Odd and Even Electron Ions
 8 formula(e) evaluated with 1 results within limits (up to 10 closest results for each mass)

Elements Used:
 C: 0-96 H: 0-94

Martha Gulman (SD), MEG46
 Q-TOF20170814MF002 67 (1.401) AM (Cen,4, 80.00, Ht,10000.0,1570.68,0.70); Sm (SG, 2x3.00); Sb (15,10.00); Cm (18:75-66:67)

TOF MS LD+
 2.62e+003



Mass	Calc. Mass	mDa	PPM	DBE	i-FIT	i-FIT (Norm)	Formula
1134.6080	1134.6104	-2.4	-2.1	50.0	83.3	0.0	C88 H78

Appendix 1.0i: MALDI TOF data for 12.

Elemental Composition Report

Single Mass Analysis

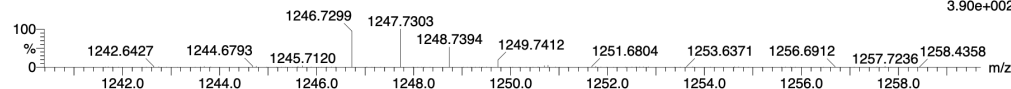
Tolerance = 50.0 PPM / DBE: min = -1.5, max = 1000.0
 Element prediction: Off
 Number of isotope peaks used for i-FIT = 5

Monoisotopic Mass, Odd and Even Electron Ions
 1 formula(e) evaluated with 1 results within limits (up to 10 closest results for each mass)

Elements Used:
 C: 0-96 H: 0-94

Martha Gulman (SD), MEG43
 Q-TOF20170809MF005 52 (1.202) AM (Cen,4, 80.00, Ht,10000.0,1570.68,0.70); Sm (SG, 2x3.00); Sb (15,10.00); Cm (30:60-51:55)

TOF MS LD+
 3.90e+002



Mass	Calc. Mass	mDa	PPM	DBE	i-FIT	i-FIT (Norm)	Formula
1246.7299	1246.7356	-5.7	-4.6	50.0	54.3	0.0	C96 H94

Appendix 1.0j: MALDI TOF data for 13.

Elemental Composition Report

Single Mass Analysis

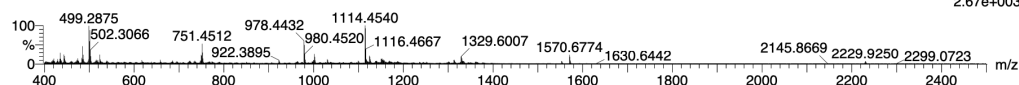
Tolerance = 10.0 PPM / DBE: min = -1.5, max = 1000.0
 Element prediction: Off
 Number of isotope peaks used for i-FIT = 5

Monoisotopic Mass, Odd and Even Electron Ions
 6 formula(e) evaluated with 1 results within limits (up to 10 closest results for each mass)

Elements Used:
 C: 0-88 H: 0-58 Ir: 0-1

Martha Gulman (SD), MEG59RM DCTB
 Q-TOF20171011MF006 66 (1.398) AM (Cen,4, 80.00, Ht,10000.0,1570.68,0.70); Sm (SG, 2x3.00); Sb (15,10.00); Cm (11:97-60:68)

TOF MS LD+
 2.67e+003



Mass	Calc. Mass	mDa	PPM	DBE	i-FIT	i-FIT (Norm)	Formula
1114.4540	1114.4539	0.1	0.1	60.0	87.9	0.0	C88 H58

Appendix 1.0k: MALDI TOF data for 14.

Single Mass Analysis

Tolerance = 5.0 PPM / DBE: min = -1.5, max = 1000.0

Element prediction: Off

Number of isotope peaks used for i-FIT = 3

Monoisotopic Mass, Odd and Even Electron Ions

3182 formula(e) evaluated with 45 results within limits (up to 10 closest results for each mass)

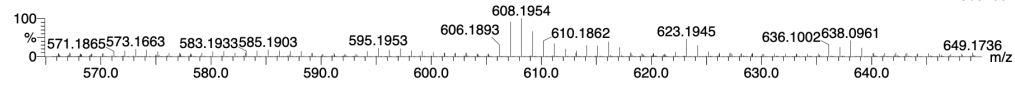
Elements Used:

C: 0-50 H: 0-50 N: 0-50 O: 0-50

Martha Gulman (SD), MEG29 DHB

Q-TOF20170703MF019 60 (1.299) AM (Cen,4, 80.00, Ht,10000.0,1570.68,0.70); Sm (SG, 2x3.00); Sb (15,10.00); Cm (5:100)

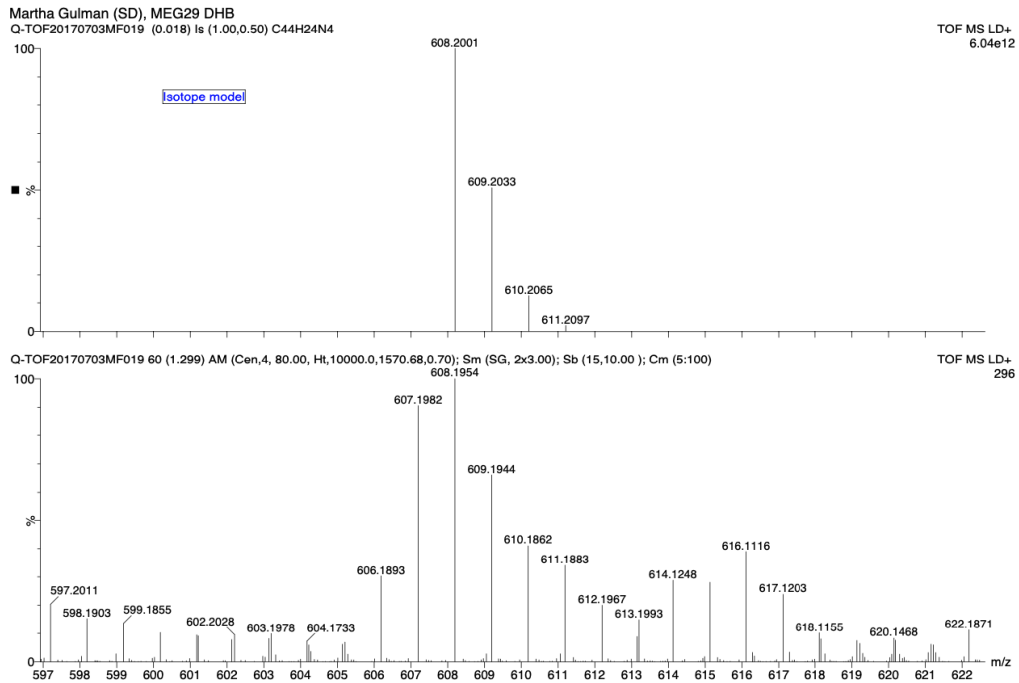
TOF MS LD+
2.96e+002



Minimum: -1.5
Maximum: 1000.0

Mass	Calc. Mass	mDa	PPM	DBE	i-FIT	i-FIT (Norm)	Formula
608.1954	608.1953	0.1	0.2	8.0	52.0	2.8	C25 H36 O17
	608.1952	0.2	0.3	13.5	51.9	2.6	C24 H30 N7 O12
	608.1952	0.2	0.3	19.0	51.7	2.4	C23 H24 N14 O7
	608.1952	0.2	0.3	24.5	51.4	2.1	C22 H18 N21 O2
	608.1957	-0.3	-0.5	6.5	52.3	3.0	C9 H26 N19 O13
	608.1957	-0.3	-0.5	17.5	51.1	1.9	C7 H14 N33 O3
	608.1957	-0.3	-0.5	12.0	51.9	2.6	C8 H20 N26 O8
	608.1958	-0.4	-0.7	1.0	52.5	3.3	C10 H32 N12 O18
	608.1947	0.7	1.2	26.0	51.0	1.7	C38 H28 N2 O6
	608.1961	-0.7	-1.2	31.0	51.2	1.9	C39 H24 N6 O2

Appendix 1.0l: MALDI TOF data 17, with an observable peak at 606.1893 (17, C₄₄H₂₂N₄, exact mass 606.18).



Appendix 1.0m: MALDI TOF isotopic distribution for 17.

Single Mass Analysis

Tolerance = 20.0 PPM / DBE: min = -1.5, max = 1000.0

Element prediction: Off

Number of isotope peaks used for i-FIT = 3

Monoisotopic Mass, Odd and Even Electron Ions

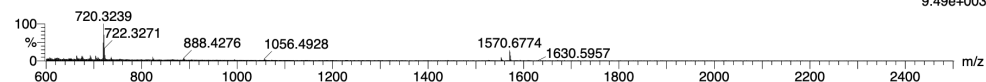
1 formula(e) evaluated with 1 results within limits (up to 10 closest results for each mass)

Elements Used:

C: 0-52 H: 0-41 N: 0-4

Martha Gulman (SD), MEG30

Q-TOF20170707MF013 57 (1.052) AM (Cen,4, 80.00, Ht,10000.0,1570.68,0.70); Sm (SG, 2x3.00); Sb (15,10.00); Cm (19:212)

TOF MS LD+
9.49e+003

Minimum: -1.5
Maximum: 1000.0

Mass	Calc. Mass	mDa	PPM	DBE	i-FIT	i-FIT (Norm)	Formula
720.3239	720.3253	-1.4	-1.9	35.0	97.2	0.0	C52 H40 N4

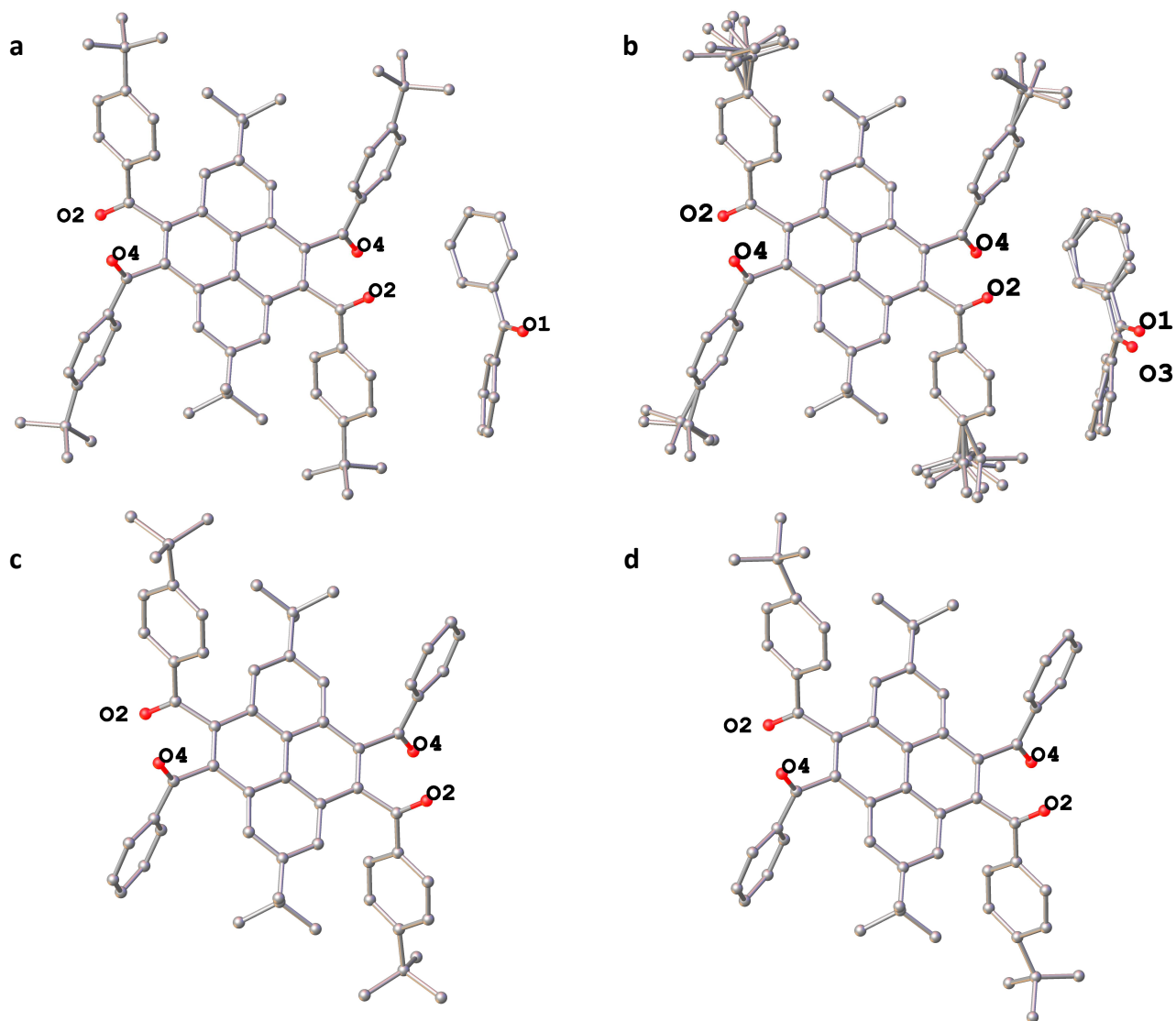
Appendix 1.0n: MALDI TOF data for 18.

Appendix 1.1a: X-ray crystallographic data for 8 and 7.

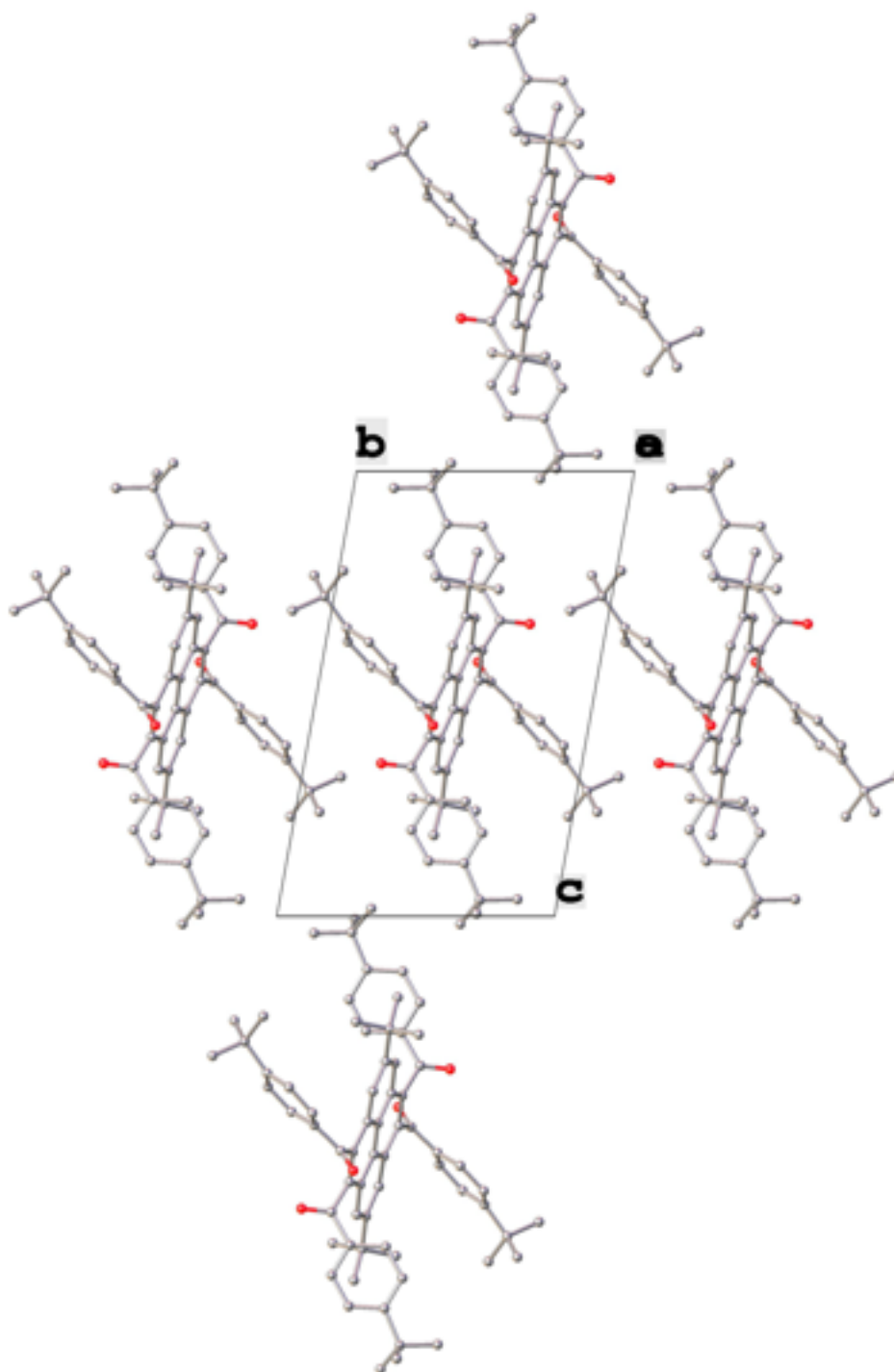
	8	7
Identification code	TCD1141_4	TCD844b
Empirical formula	C ₆₄ H ₆₄ N ₂ O ₄	C ₉₄ H ₉₄ O ₆
Formula weight	925.17	1319.69
Temperature (K)	10.04	100(2)
Wavelength (Å)	0.71073	0.71073
Crystal system	Monoclinic	Triclinic
Space group	C2/c	P $\bar{1}$
	$a = 25.423(6)$	$a = 10.0803(3)$
	$b = 11.283(2)$	$b = 11.8326(3)$
	$c = 21.747(5)$	$c = 17.7041(5)$
Unit cell dimensions (Å, °)	$\alpha = 90$	$\alpha = 77.6933(14)$
	$\beta = 123.700(5)$	$\beta = 82.5030(12)$
	$\gamma = 90$	$\gamma = 65.5385(12)$
Volume (Å ³)	5189.9(19)	1875.85(9)
Z	4	1
Density (calculated) (Mg/m ³)	1.184	1.168
Absorption coefficient (mm ⁻¹)	0.073	0.071
F(000)	1976	706
Crystal size (mm ³)	0.37 x 0.09 x 0.013	0.5 x 0.18 x 0.12

Theta range for data collection (°)	3.044 to 25.439°	2.565 to 26.152
	-30 ≤ h ≤ 30,	-12 ≤ h ≤ 12,
Index ranges	-13 ≤ k ≤ 13,	-14 ≤ k ≤ 14,
	-26 ≤ l ≤ 26	-21 ≤ l ≤ 21
Reflections collected	9293	36984
	4791	7455
Independent reflections	[R(int) = 0.0780]	[R(int) = 0.0367]
Completeness to theta = 25.242° (%)	99.9	99.9%
Absorption correction	Semi-empirical from equivalents	Semi-empirical from equivalents
Max. and min. transmission	0.745211 and 0.661902	0.7453 and 0.7124
Refinement method	Full-matrix least-squares on F^2	Full-matrix least-squares on F^2
Data / restraints / parameters	4791 / 6 / 323	7455 / 584 / 693
Goodness-of-fit on F^2	1.003	1.023
Final R indices [$I > 2\sigma(I)$] ^a	$R1 = 0.1027$	$R1 = 0.0482$
	$wR2 = 0.2090$	$wR2 = 0.1219$
R indices (all data) ^b	$R1 = 0.2343$	$R1 = 0.0717$
	$wR2 = 0.2716$	$wR2 = 0.1380$
Extinction coefficient	0.010(8)	-
Largest diff. peak and hole (e.Å ⁻³)	0.399 and -0.247	0.221 and -0.248

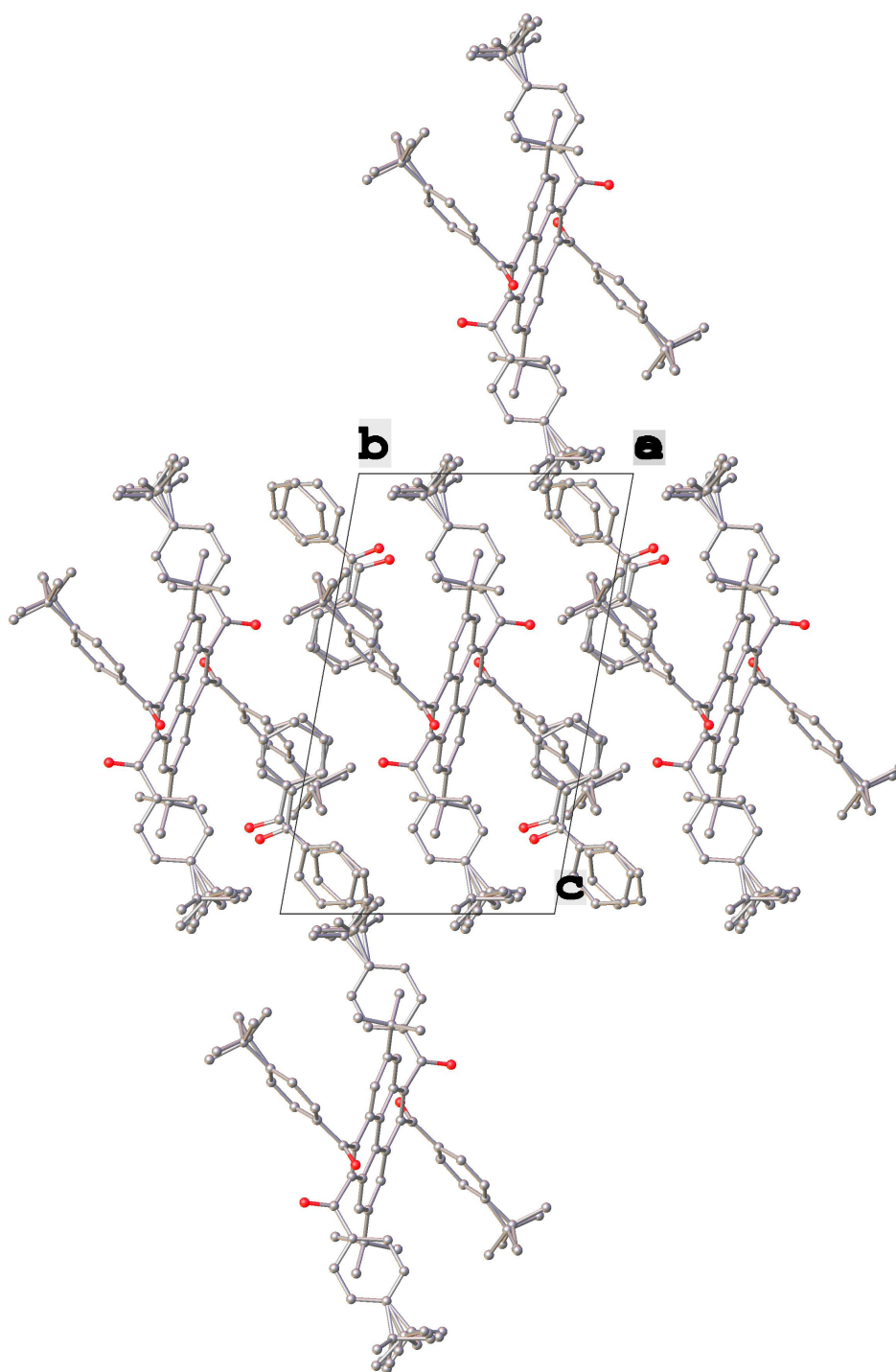
^a $R1 = \sum ||Fo| - |Fc|| / \sum |Fo|$, ^b $wR2 = [\sum \{w(Fo^2 - Fc^2)^2 / \sum w(Fo^2)^2\}]^{1/2}$.



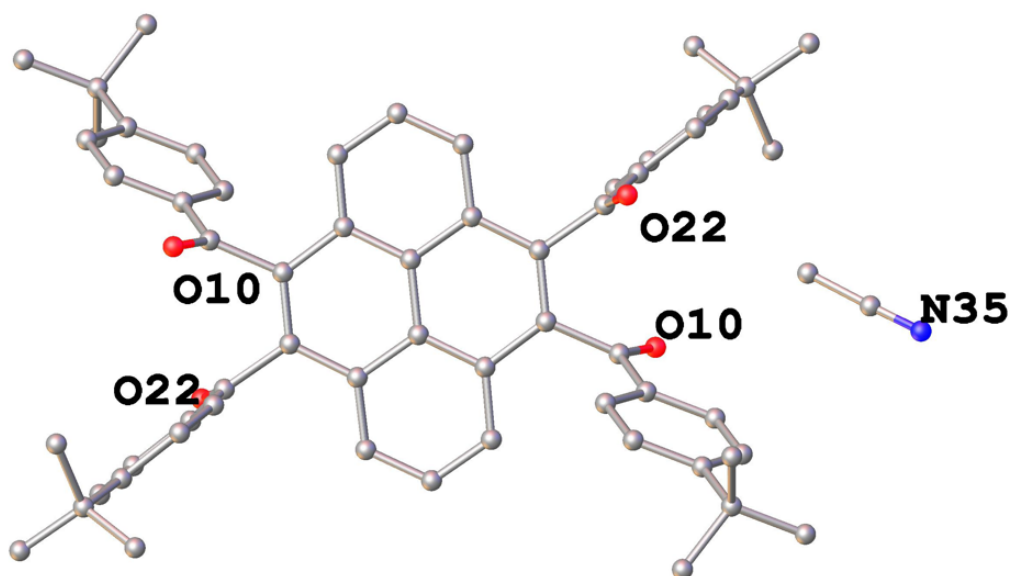
Appendix 1.1b: Compound 7 showing (a) majority occupied disordered moiety with 50% occupancy (b) majority occupied disordered moiety with 32% occupancy, (c) minority disordered moiety has a 32% occupancy (d) majority occupied disordered moiety with 0.08% occupancy. Heteroatoms labelled only and hydrogen atoms omitted for clarity.



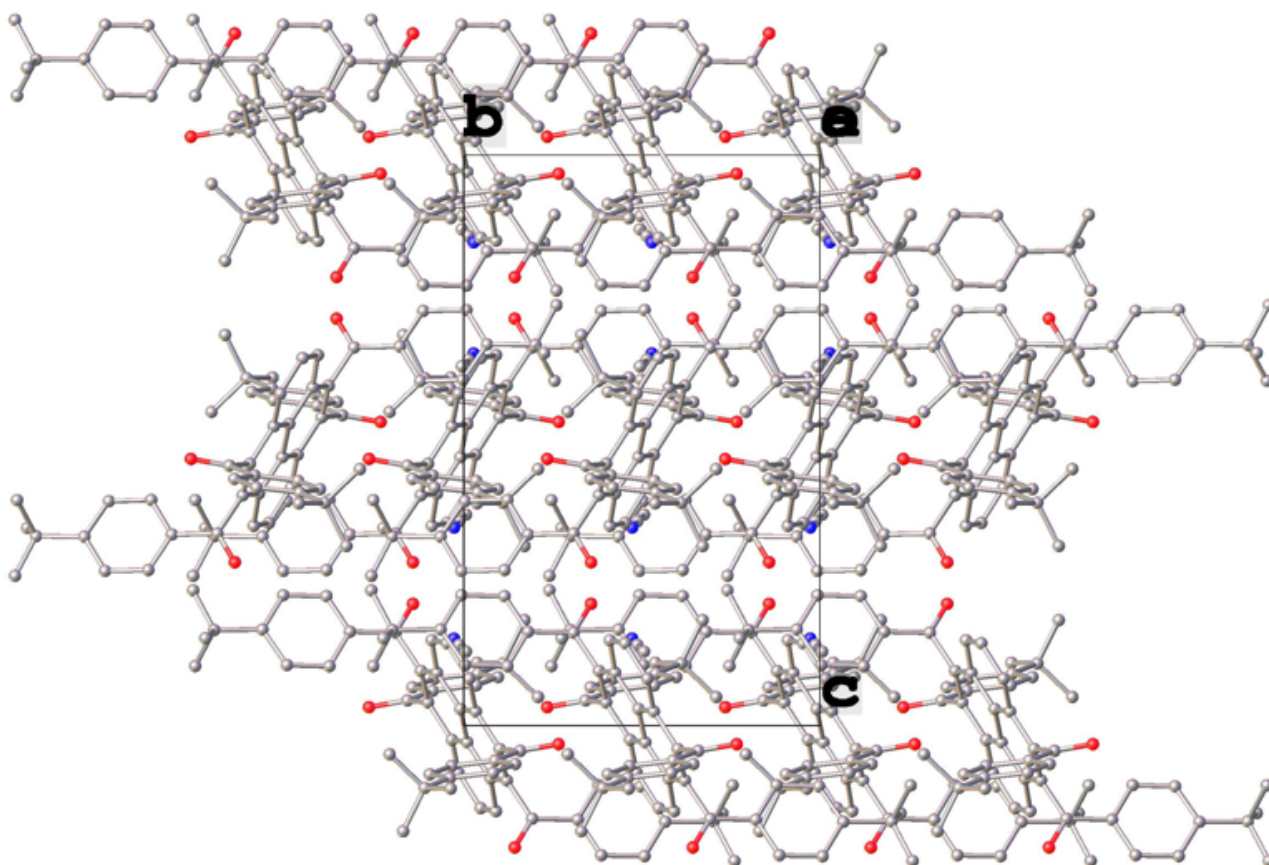
Appendix 1.1c: Schematic packing diagram of the majority disordered component of **7**, viewed normal to the a-axis. Hydrogen atoms are omitted for clarity.



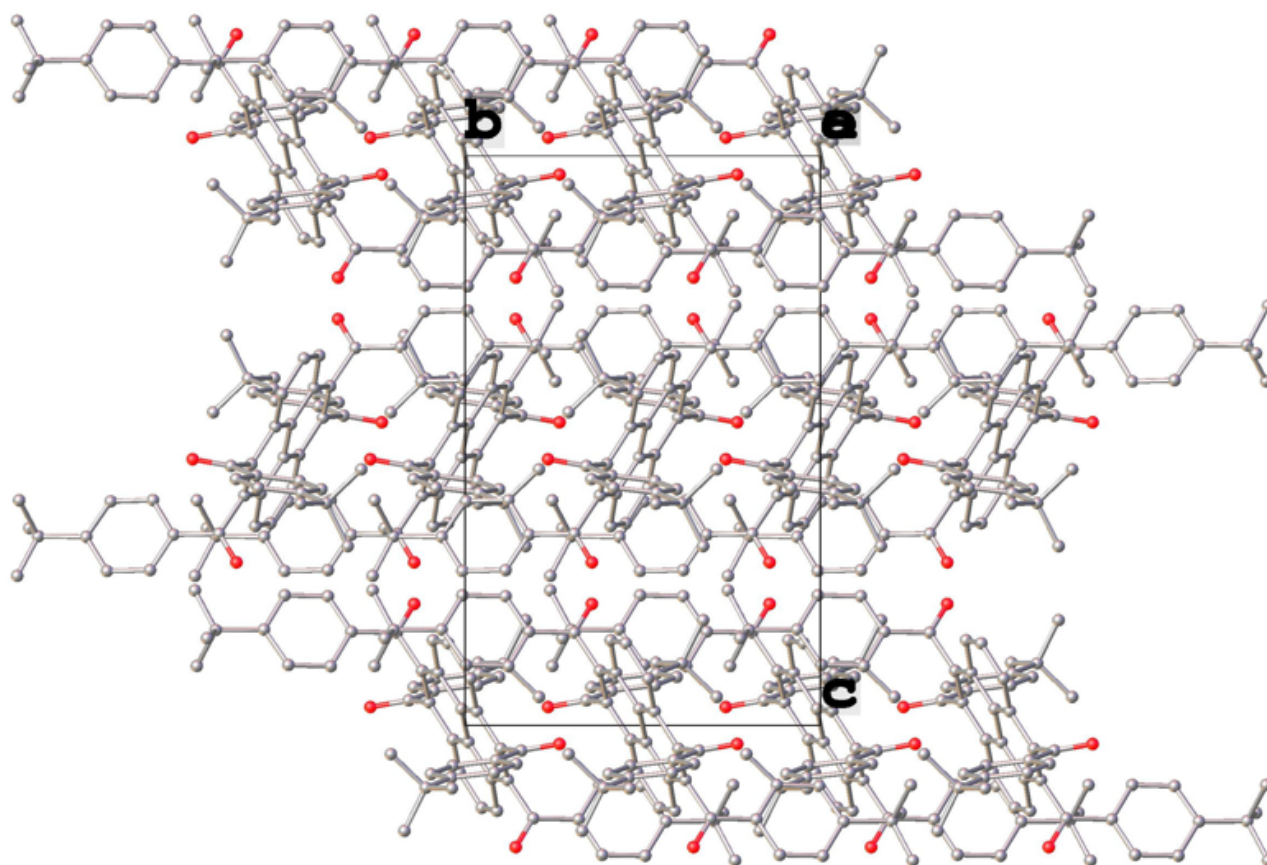
Appendix 1.1d: Schematic packing diagram of **7** including the full disorder, viewed normal to the a-axis. Hydrogen atoms are omitted for clarity.



Appendix 1.1e: Asymmetric unit of compound **8**. Heteroatoms labelled only and hydrogen atoms omitted for clarity.



Appendix 1.1f: Schematic packing diagram of the majority disordered component of **8**, viewed normal to the a-axis. Hydrogen atoms are omitted for clarity.



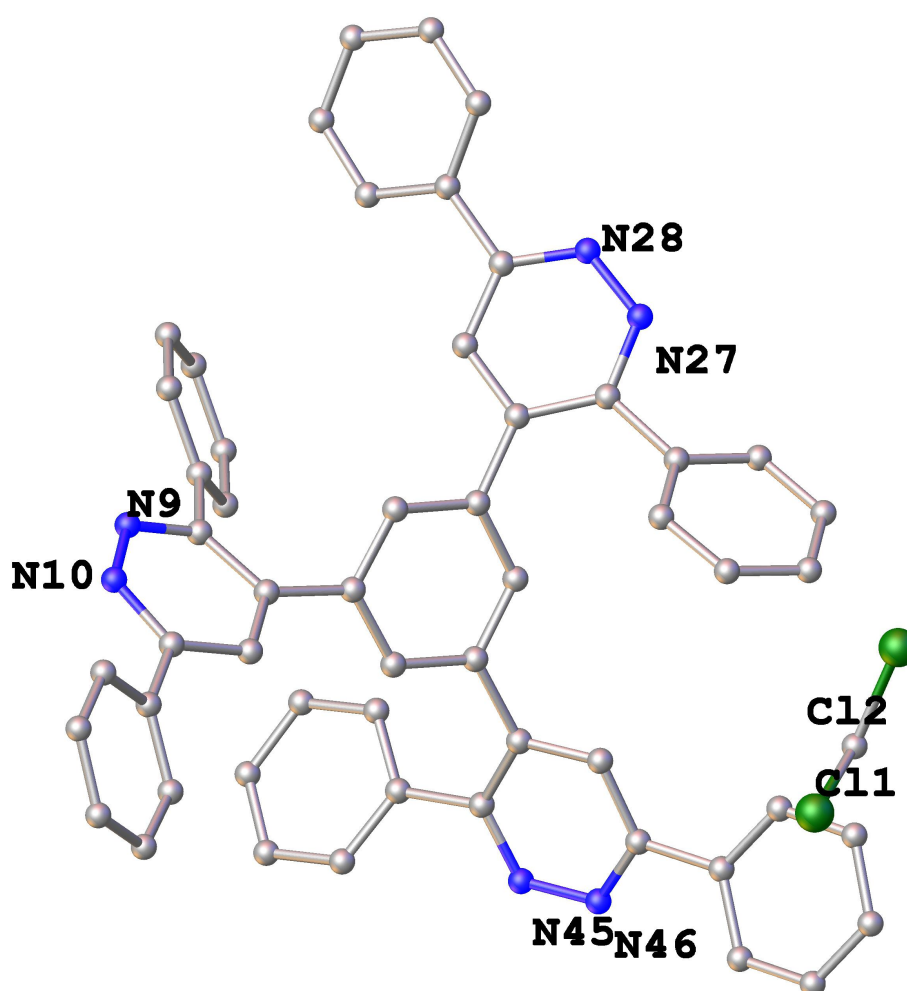
Appendix 1.1g: Schematic packing diagram of **8**, with disorder omitted, viewed normal to the a-axis. Hydrogen atoms are omitted for clarity.

Appendix 1.2a: X-ray crystallographic data for 23.

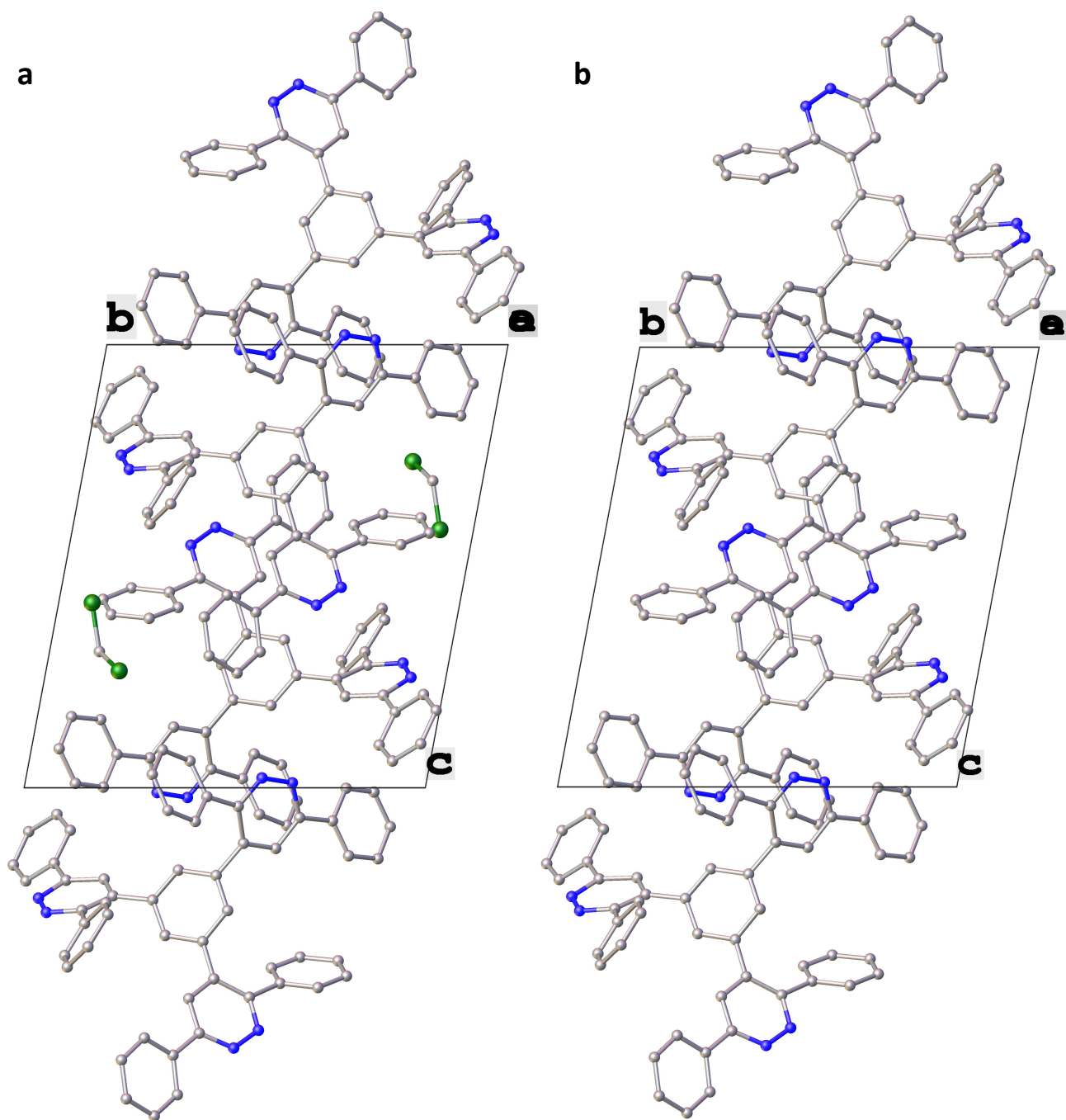
23	
Identification code	TCD1038
Empirical formula	$C_{55}H_{38}Cl_2N_6$
Formula weight	853.81
Temperature (K)	100(2)
Wavelength (Å)	0.71073
Crystal system	Triclinic
Space group	$P\bar{1}$
	$a = 9.7764(12)$
	$b = 14.5624(19)$
	$c = 15.986(2)$
Unit cell dimensions (Å, °)	$\alpha = 77.572(4)$
	$\beta = 81.165(4)$
	$\gamma = 74.882(4)$
Volume (Å ³)	2134.2(5)
Z	2
Density (calculated) (Mg/m ³)	1.329
Absorption coefficient (mm ⁻¹)	0.200
F(000)	888
Crystal size (mm ³)	0.13 x 0.11 x 0.04
Theta range for data collection (°)	2.623 to 25.466°
	$-11 \leq h \leq 11,$
Index ranges	$-17 \leq k \leq 17,$
	$-19 \leq l \leq 19$
Reflections collected	27211
	7848
Independent reflections	[R(int) = 0.3353]
Completeness to theta = 25.242° (%)	99.8
Absorption correction	Semi-empirical from equivalents
Max. and min. transmission	0.7452 and 0.6703
Refinement method	Full-matrix least-squares on F^2
Data / restraints / parameters	7848 / 0 / 568

Goodness-of-fit on F^2	0.981
	$R1 = 0.0902$
Final R indices [$I > 2\sigma(I)$] ^a	$wR2 = 0.1399$
	$R1 = 0.2769$
R indices (all data) ^b	$wR2 = 0.2022$
Largest diff. peak and hole ($e.\text{\AA}^{-3}$)	0.315 and -0.391

^a $R1 = \sum ||F_o| - |F_c|| / \sum |F_o|$, ^b $wR2 = [\sum \{w(F_o^2 - F_c^2)^2 / \sum w(F_o^2)^2\}]^{1/2}$.



Appendix 1.2b: Asymmetric unit of compound **23**. Heteroatoms labelled only and hydrogen atoms omitted for clarity.



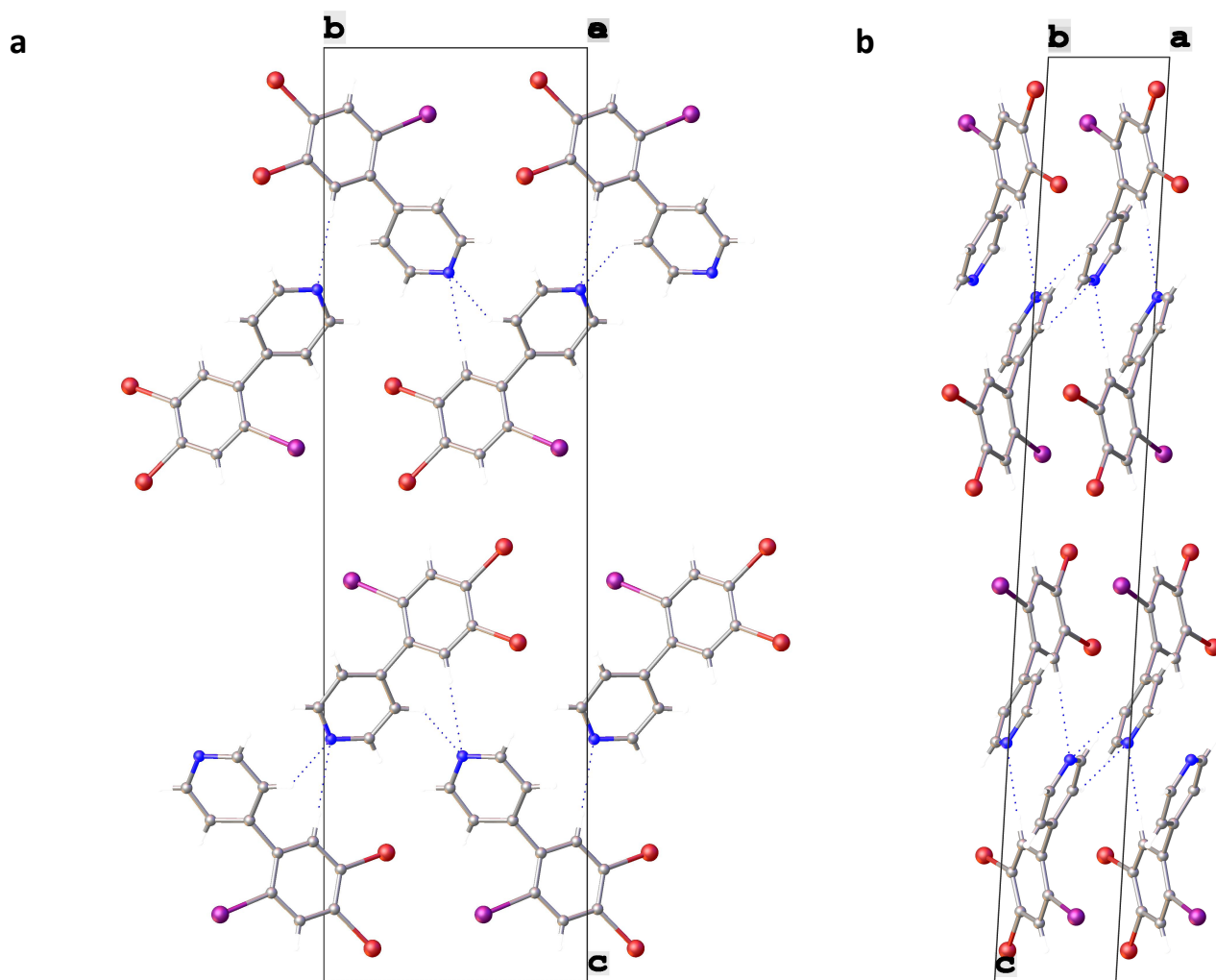
Appendix 1.2c: **a)** Schematic packing diagram of **23**, viewed normal to the *a*-axis. Hydrogen atoms are omitted for clarity. **b)** Schematic packing diagram of **23**, with CH_2Cl_2 molecules omitted, viewed normal to the *a*-axis. Hydrogen atoms are omitted for clarity.

Appendix 1.3a: X-ray crystallographic data for **26**, **28**, and **29**.

	28	26	29
Identification code	TCD1164c	TCD1140	TCD1136b
Empirical formula	C ₁₁ H ₆ Br ₂ I _N	C ₁₆ H ₁₀ Br ₂ N ₂	C _{50.60} H _{45.68} Br ₂ I _{1.08} N _{0.92} OP ₂ Pd
Formula weight	438.89	390.08	1147.85
Temperature (K)	100(2)	100(2)	100(2)
Wavelength (Å)	0.71073	0.71073	0.71073
Crystal system	Monoclinic	Monoclinic	Triclinic
Space group	P2 ₁ /n	C2/c	P $\bar{1}$
	<i>a</i> = 4.1191(4)	<i>a</i> = 15.4975(7)	<i>a</i> = 10.9632(5)
	<i>b</i> = 8.8969(10)	<i>b</i> = 10.5799(4)	<i>b</i> = 11.8715(5)
	<i>c</i> = 31.600(3)	<i>c</i> = 8.9646(4)	<i>c</i> = 18.9432(8)
Unit cell dimensions (Å, °)	α = 90	α = 90	α = 93.8470(10)
	β = 93.321(5)	β = 107.3470(10)	β = 104.1950(10)
	γ = 90	γ = 90	γ = 93.2820(10)
Volume (Å ³)	1156.1(2)	1403.00(10)	2377.85(18)
<i>Z</i>	4	4	2
Density (calculated) (Mg/m ³)	2.522	1.847	1.603
Absorption coefficient (mm ⁻¹)	9.646	5.767	2.876
F(000)	808	760	1134
Crystal size (mm ³)	0.26 x 0.04 x 0.02	0.34 x 0.31 x 0.019	0.3 x 0.22 x 0.14
Theta range for data collection (°)	2.378 to 26.464	3.052 to 30.663	2.450 to 30.100
	-4 ≤ <i>h</i> ≤ 5,	-22 ≤ <i>h</i> ≤ 22,	-15 ≤ <i>h</i> ≤ 15,
Index ranges	-11 ≤ <i>k</i> ≤ 11,	-15 ≤ <i>k</i> ≤ 15,	-16 ≤ <i>k</i> ≤ 16,
	-38 ≤ <i>l</i> ≤ 39	-12 ≤ <i>l</i> ≤ 12	-26 ≤ <i>l</i> ≤ 26
Reflections collected	10722	18327	64080
	2372	2163	13961
Independent reflections	[R(int) = 0.1223]	[R(int) = 0.0234]	[R(int) = 0.0264]
Completeness to theta = 25.242° (%)	99.9	99.8%	99.7
Absorption correction	Semi-empirical from equivalents	Semi-empirical from equivalents	Semi-empirical from equivalents
Max. and min. transmission	0.7454 and 0.5042	0.7461 and 0.5343	0.7460 and 0.6145

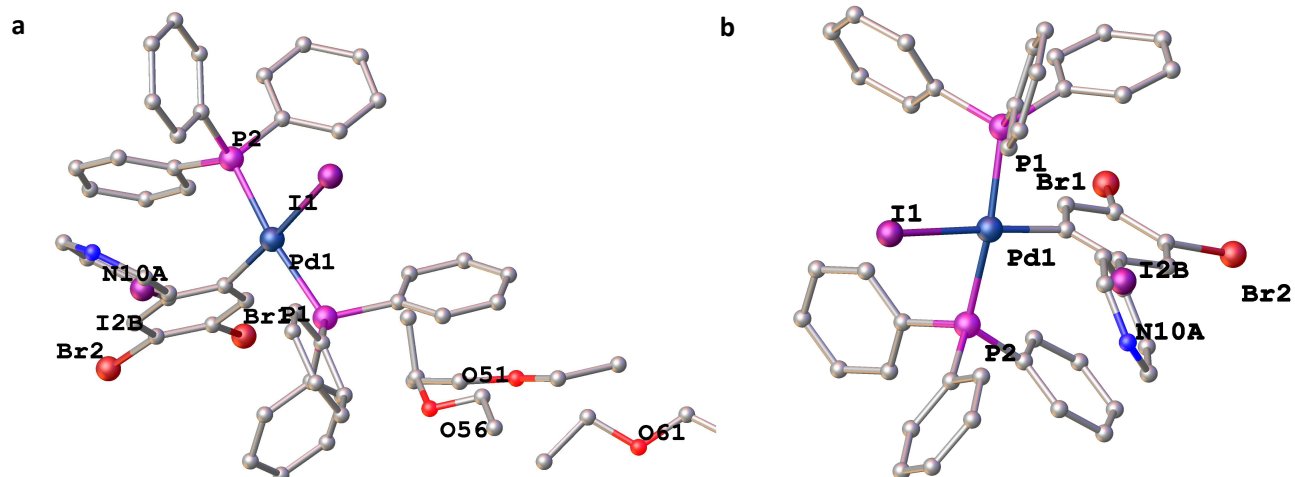
Refinement method	Full-matrix least-squares on F^2	Full-matrix least-squares on F^2	Full-matrix least-squares on F^2
Data / restraints / parameters	2372 / 36 / 136	2163 / 0 / 92	13961 / 191 / 625
Goodness-of-fit on F^2	1.018	1.081	1.054
Final R indices [$I > 2\sigma(I)$] ^a	$R1 = 0.0530$	$R1 = 0.0162$	$R1 = 0.0350$
	$wR2 = 0.1012$	$wR2 = 0.0399$	$wR2 = 0.0895$
R indices (all data) ^b	$R1 = 0.1056$	$R1 = 0.0172$	$R1 = 0.0404$
	$wR2 = 0.1207$	$wR2 = 0.0403$	$wR2 = 0.0920$
Extinction coefficient	-	0.0044(2)	0.00133(17)
Largest diff. peak and hole ($e.\text{\AA}^{-3}$)	1.474 and -1.212	0.605 and -0.401	1.901 and -1.590

^a $R1 = \sum ||F_o| - |F_c|| / \sum |F_o|$, ^b $wR2 = [\sum \{w(F_o^2 - F_c^2)^2 / \sum w(F_o^2)^2\}]^{1/2}$.

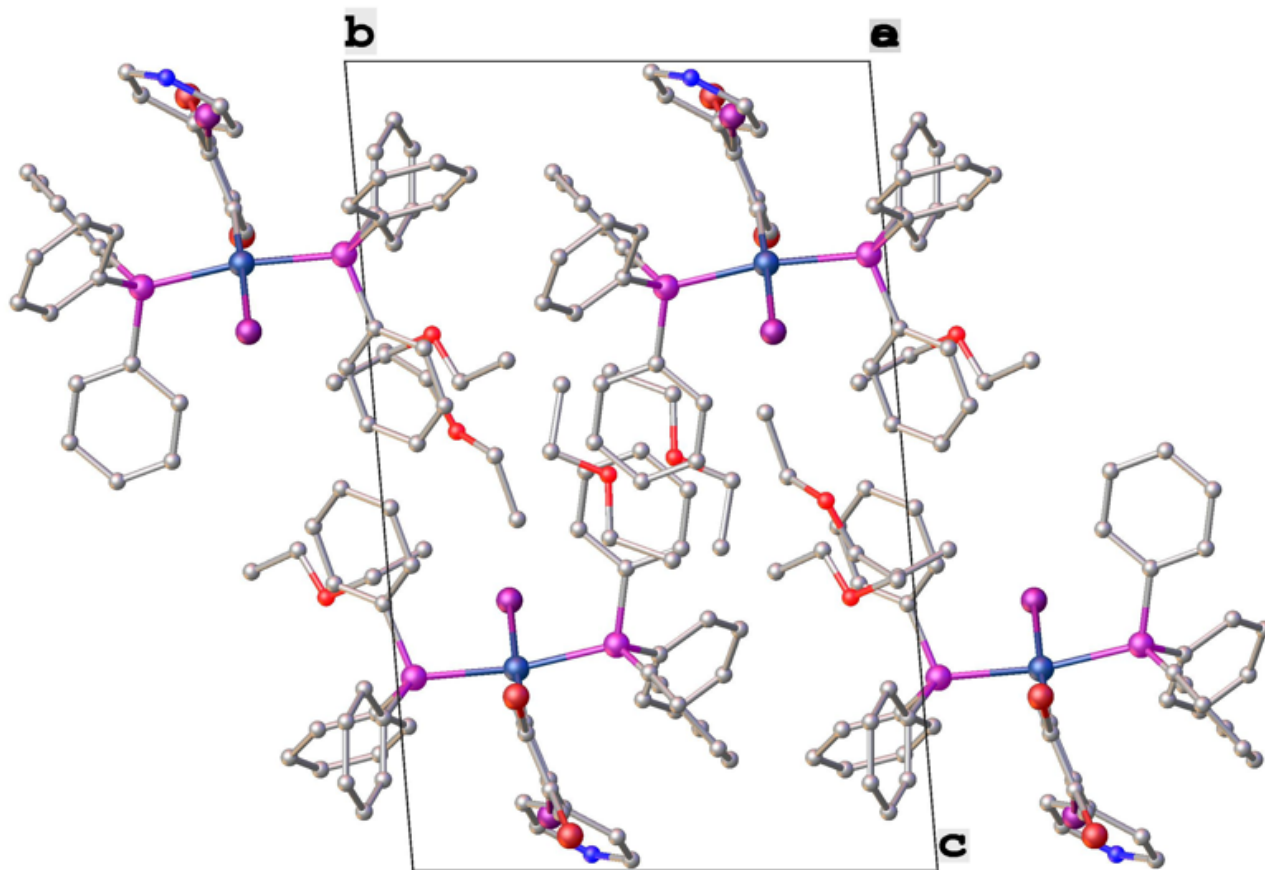


Appendix 1.3b: Schematic packing diagram of 28, a) viewed normal to the a-axis and b) viewed normal to the b axis.

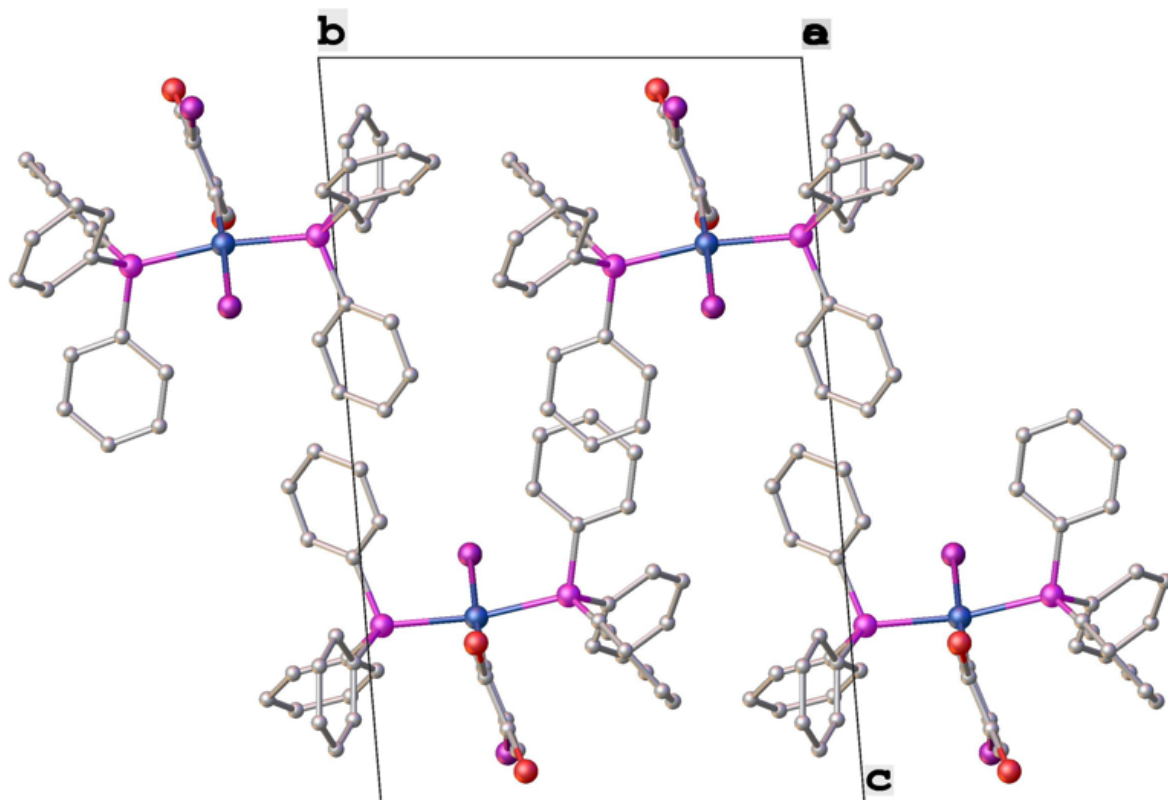
Weak hydrogen interactions are represented with blue dotted lines.



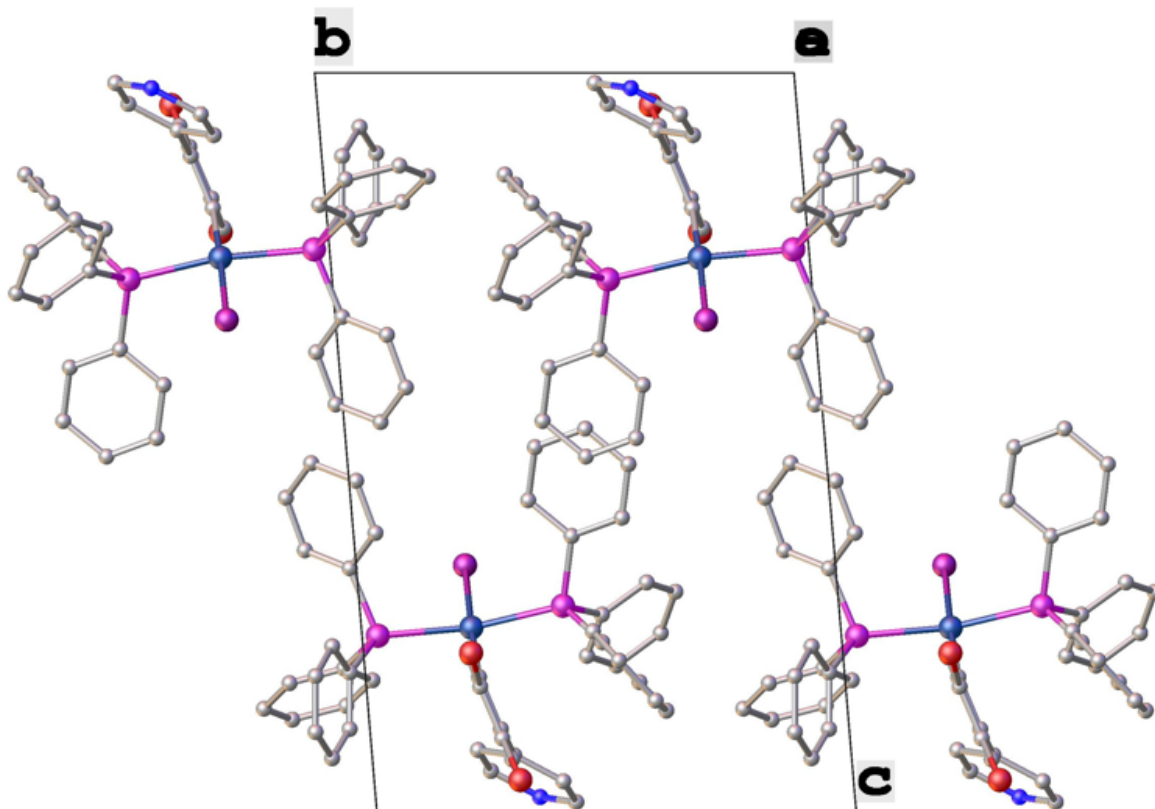
Appendix 1.3c: Compound 29 showing a) full disorder including diethyl ether solvent and b) with diethyl ether omitted. Heteroatoms labelled only and hydrogen atoms omitted for clarity.



Appendix 1.3d: Schematic packing diagram of 29 viewed normal to the a-axis.



Appendix 1.3e: Schematic packing diagram of **29a**, the minority disordered moiety, viewed normal to the a-axis.



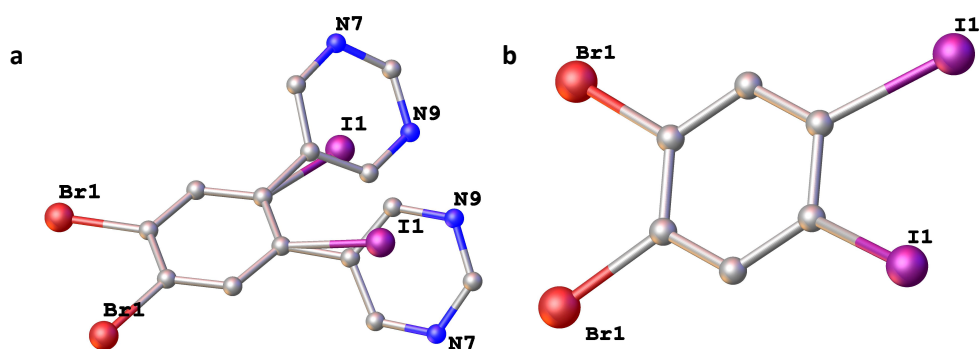
Appendix 1.3f: Schematic packing diagram of **29b**, the majority disordered moiety, viewed normal to the a-axis.

Appendix 1.4a: X-ray crystallographic data for 30.

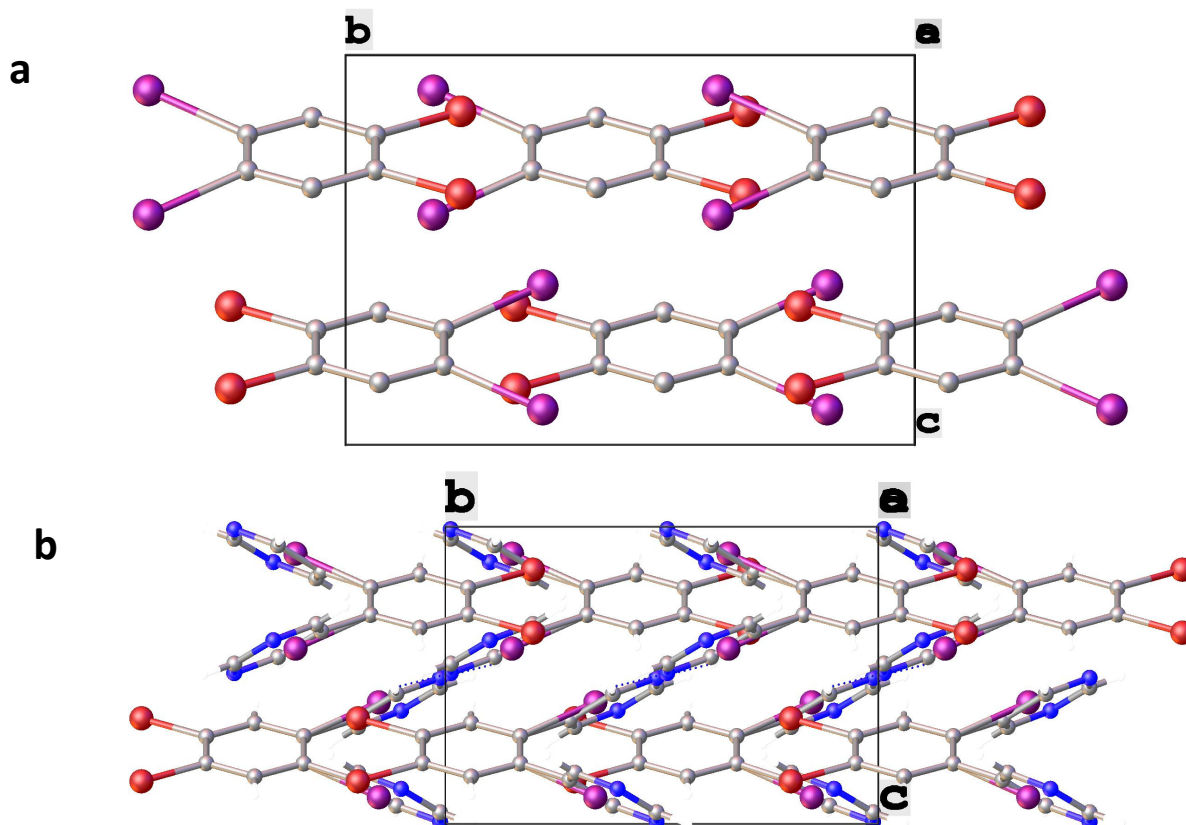
30	
Identification code	TCD1168
Empirical formula	$C_{13.92}H_{7.94}Br_2I_{0.02}N_{3.96}$
Formula weight	393.02
Temperature (K)	100(2)
Wavelength (Å)	0.71073
Crystal system	Monoclinic
Space group	C2/c
	$a = 16.5297(7)$
	$b = 10.7656(4)$
	$c = 7.5398(3)$
Unit cell dimensions (Å, °)	$\alpha = 90$
	$\beta = 102.670(2)$
	$\gamma = 90$
Volume (Å ³)	1309.05(9)
Z	4
Density (calculated) (Mg/m ³)	1.994
Absorption coefficient (mm ⁻¹)	6.233
F(000)	761
Crystal size (mm ³)	0.24 x 0.19 x 0.09
Theta range for data collection (°)	3.363 to 30.113°
	$-23 \leq h \leq 23,$
Index ranges	$-15 \leq k \leq 15,$
	$-10 \leq l \leq 10$
Reflections collected	11459
	1929
Independent reflections	[R(int) = 0.0251]
Completeness to theta = 25.242° (%)	99.8
Absorption correction	Semi-empirical from equivalents
Max. and min. transmission	0.7460 and 0.5710
Refinement method	Full-matrix least-squares on F^2

Data / restraints / parameters	1929 / 6 / 100
Goodness-of-fit on F^2	1.100
Final R indices [$I > 2\sigma(I)$] ^a	R1 = 0.0189 wR2 = 0.0408
R indices (all data) ^b	R1 = 0.0221 wR2 = 0.0417
Largest diff. peak and hole ($e \cdot \text{\AA}^{-3}$)	0.422 and -0.479

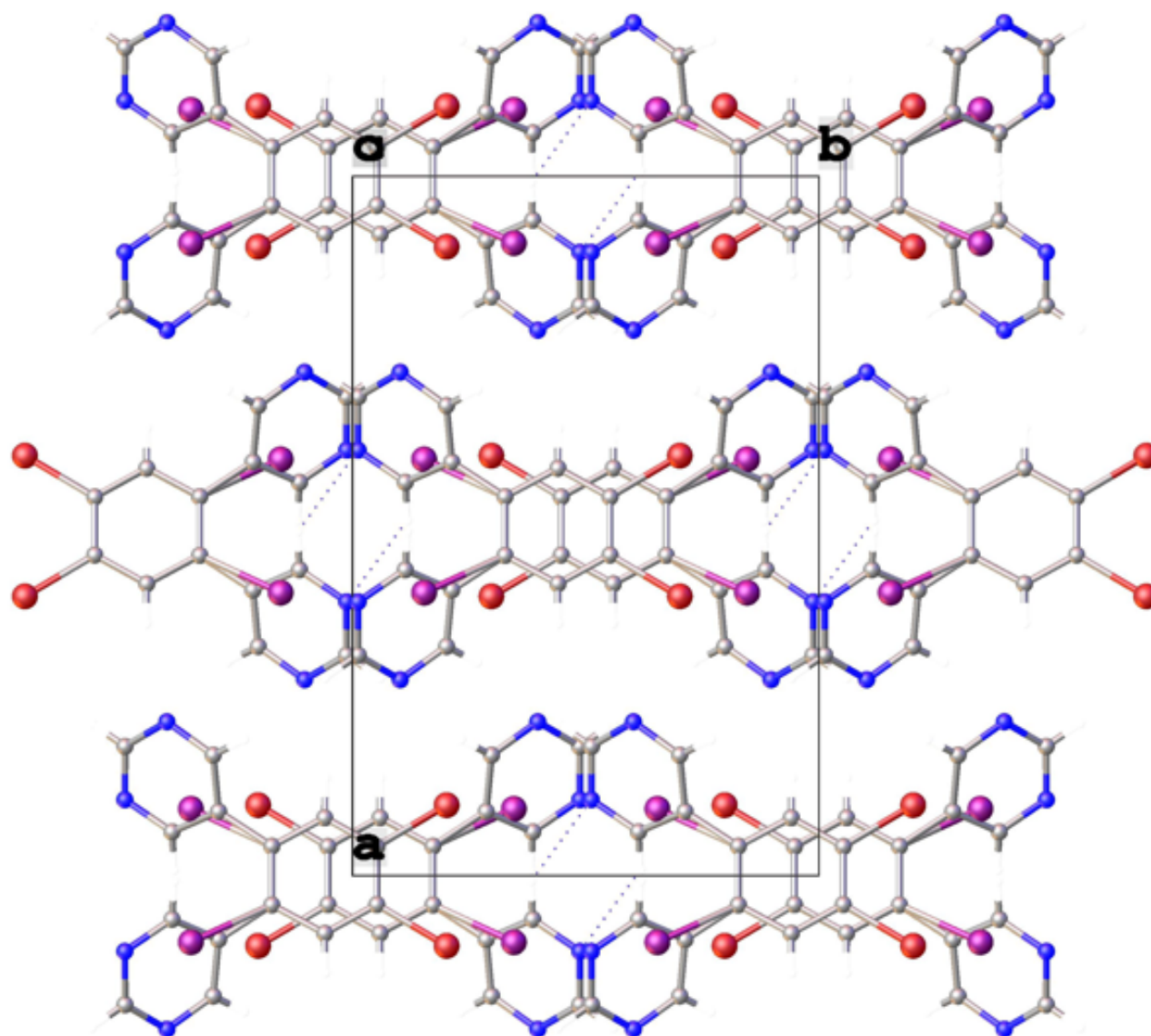
^a $R1 = \frac{\sum ||Fo| - |Fc||}{\sum |Fo|}$, ^b $wR2 = \left[\frac{\sum \{w(Fo^2 - Fc^2)^2\}}{\sum w(Fo^2)^2} \right]^{1/2}$.



Appendix 1.4b: Compound **30** showing a) full disorder and b) minor disordered component at 1% occupancy. Heteroatoms labelled only and hydrogen atoms omitted for clarity.

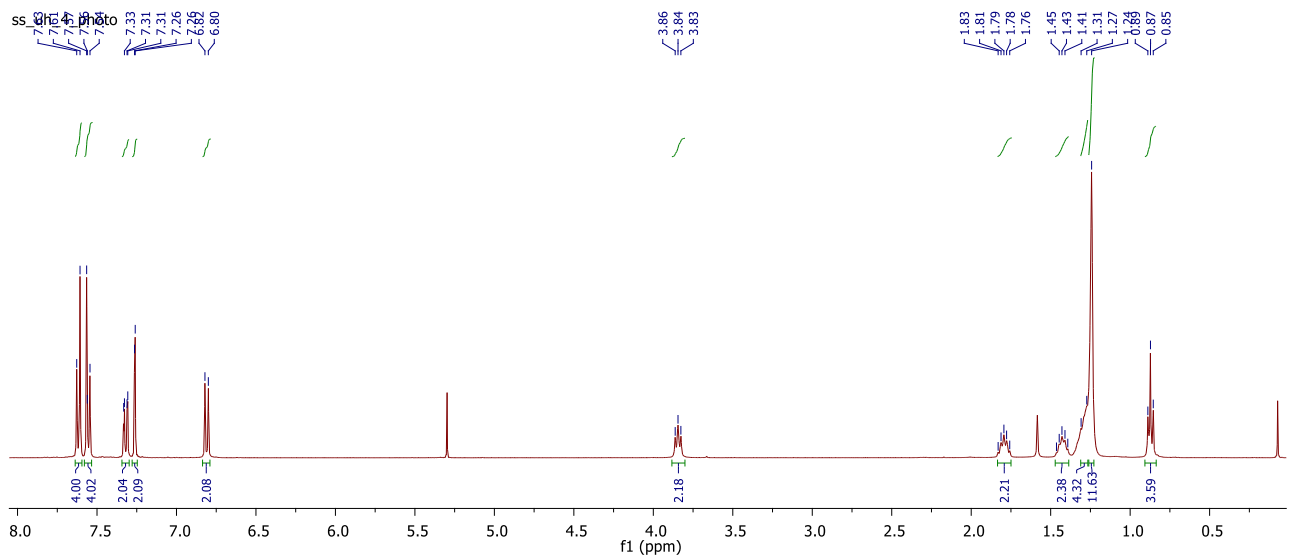
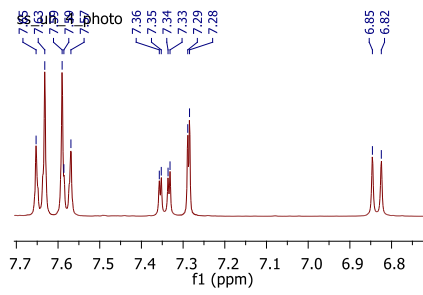


Appendix 1.4c: Schematic packing diagram of **30**, a) minor disorder packing viewed normal to the a-axis and b) full disordered packing viewed normal to the a axis. Weak hydrogen interactions are represented with blue dotted lines.

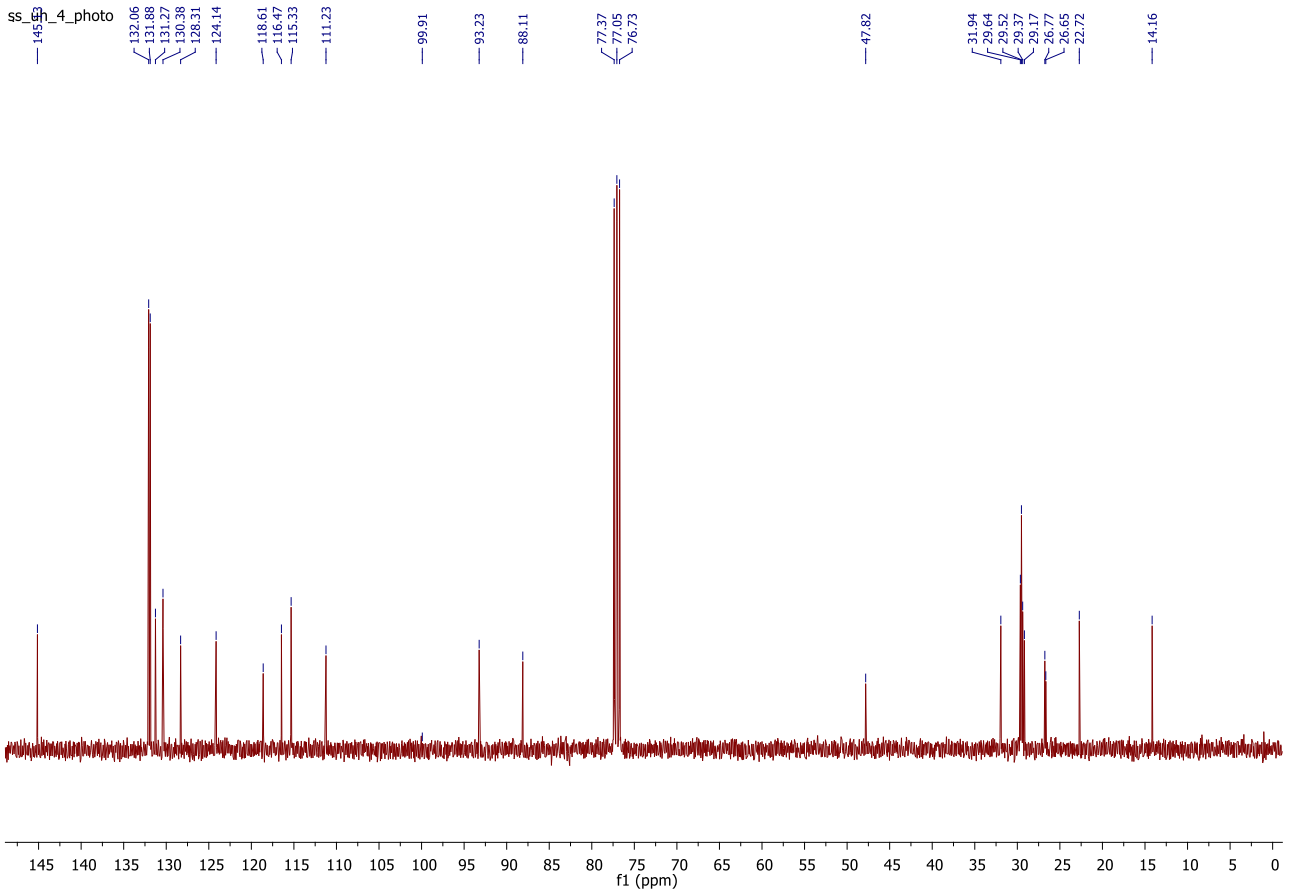


Appendix 1.4d: Schematic packing diagram of **30** (full disorder), viewed along 1-x, 1-y, -z. Atomic displacement shown at 50% probability. Weak non-traditional CH...N hydrogen interactions are annotated with blue dotted lines. Intermolecular π - π interactions calculated at 3.984 Å.

Appendix 2: Chapter Three



Appendix 2.0a: ^1H NMR spectrum of 39.



Appendix 2.0b: $^{13}\text{C}\{^1\text{H}\}$ NMR spectrum of 39.

Elemental Composition Report

Page 1

Single Mass Analysis

Tolerance = 100.0 PPM / DBE: min = -1.5, max = 400.0

Element prediction: Off

Number of isotope peaks used for i-FIT = 5

Monoisotopic Mass, Odd and Even Electron Ions

3 formula(e) evaluated with 1 results within limits (up to 10 closest results for each mass)

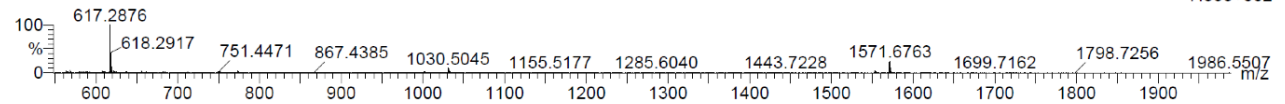
Elements Used:

C: 0-42 H: 0-39 N: 0-3 S: 0-1

Una Harty (SD), SS-UH-4crude

Q-TOF20181019MF003 27 (0.675) AM (Cen,8, 80.00, Ht,10000.0,1570.68,0.70); Sm (SG, 2x3.00); Sb (15,10.00); Cm (3:31)

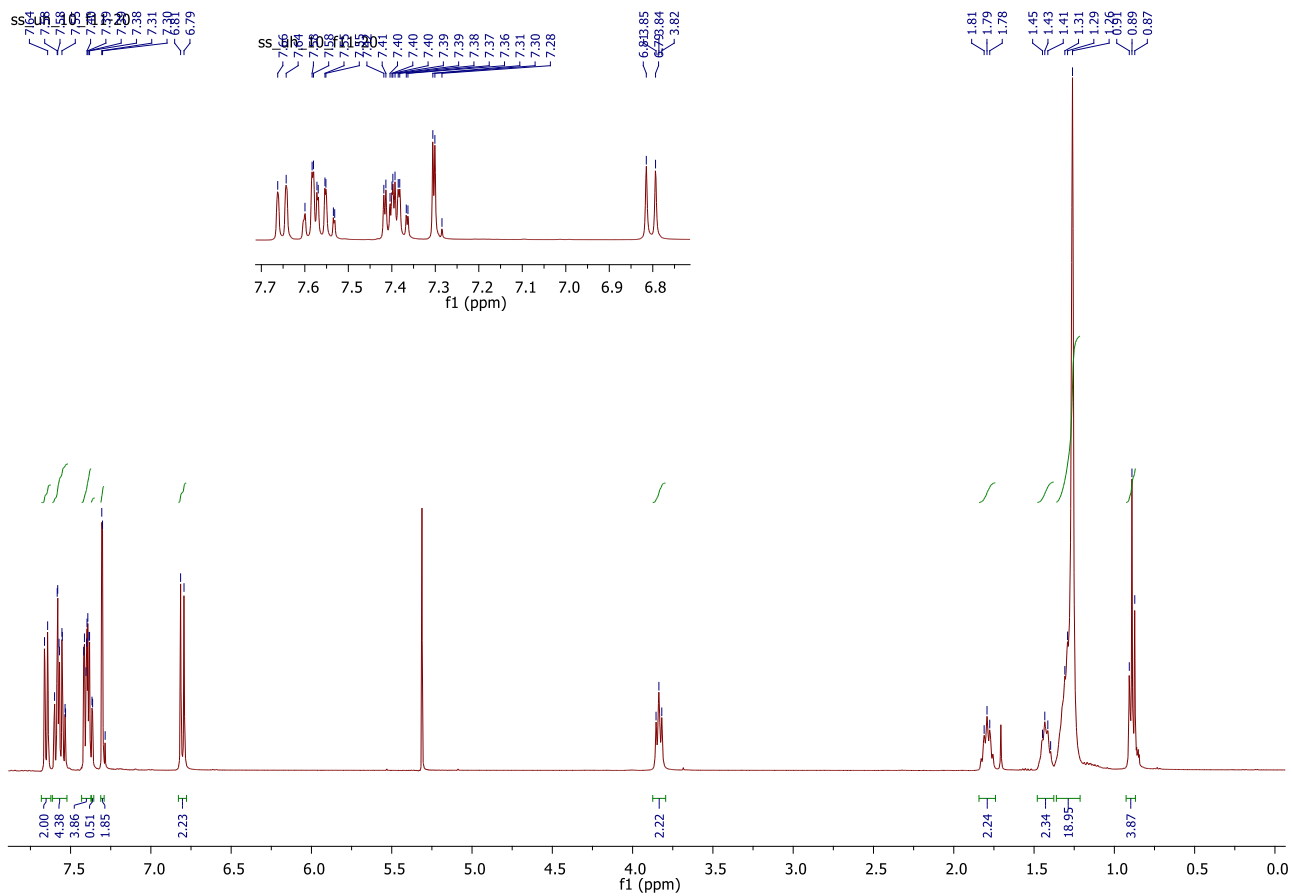
TOF MS LD+
7.85e+002



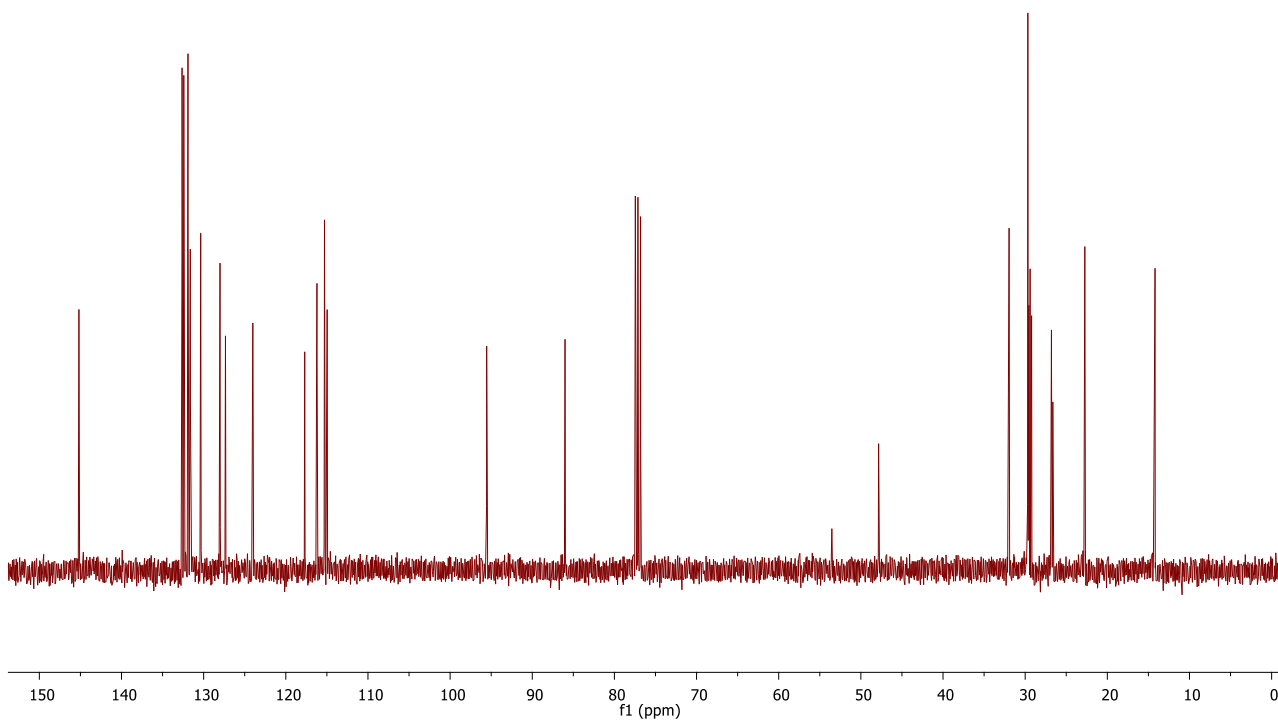
Minimum: -1.5
Maximum: 5.0 100.0 400.0

Mass	Calc. Mass	mDa	PPM	DBE	i-FIT	i-FIT (Norm)	Formula
617.2876	617.2865	1.1	1.8	25.0	57.7	0.0	C42 H39 N3 S

Appendix 2.0c: MALDI TOF data for 39.



Appendix 2.1a: ^1H NMR spectrum of 40.



Appendix 2.1b: $^{13}\text{C}\{^1\text{H}\}$ NMR spectrum of 40.

Elemental Composition Report

Single Mass Analysis

Tolerance = 100.0 PPM / DBE: min = -1.5, max = 400.0

Element prediction: Off

Number of isotope peaks used for i-FIT = 5

Monoisotopic Mass, Odd and Even Electron Ions

3 formula(e) evaluated with 1 results within limits (up to 10 closest results for each mass)

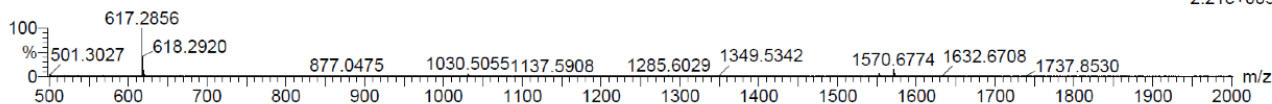
Elements Used:

C: 0-42 H: 0-39 N: 0-3 S: 0-1

Una Harty (SD), SS-UH-9crude

Q-TOF20181101MF003 47 (1.055) AM (Cen,8, 80.00, Ht,10000.0,1570.68,0.70); Sm (SG, 2x3.00); Sb (15,10.00); Cm (12:61)

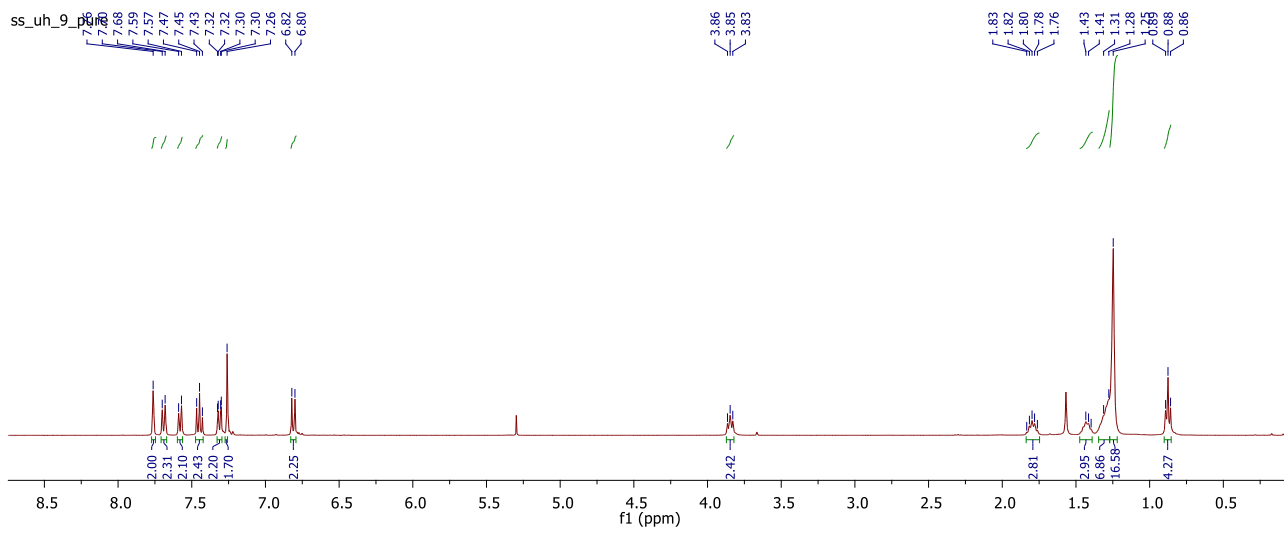
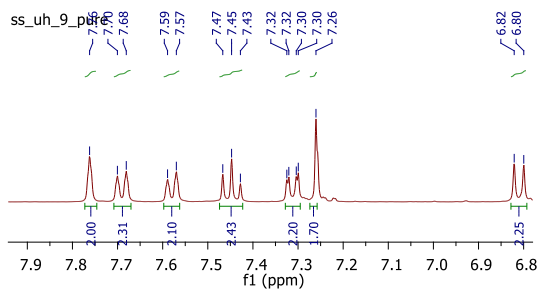
TOF MS LD+
2.21e+003



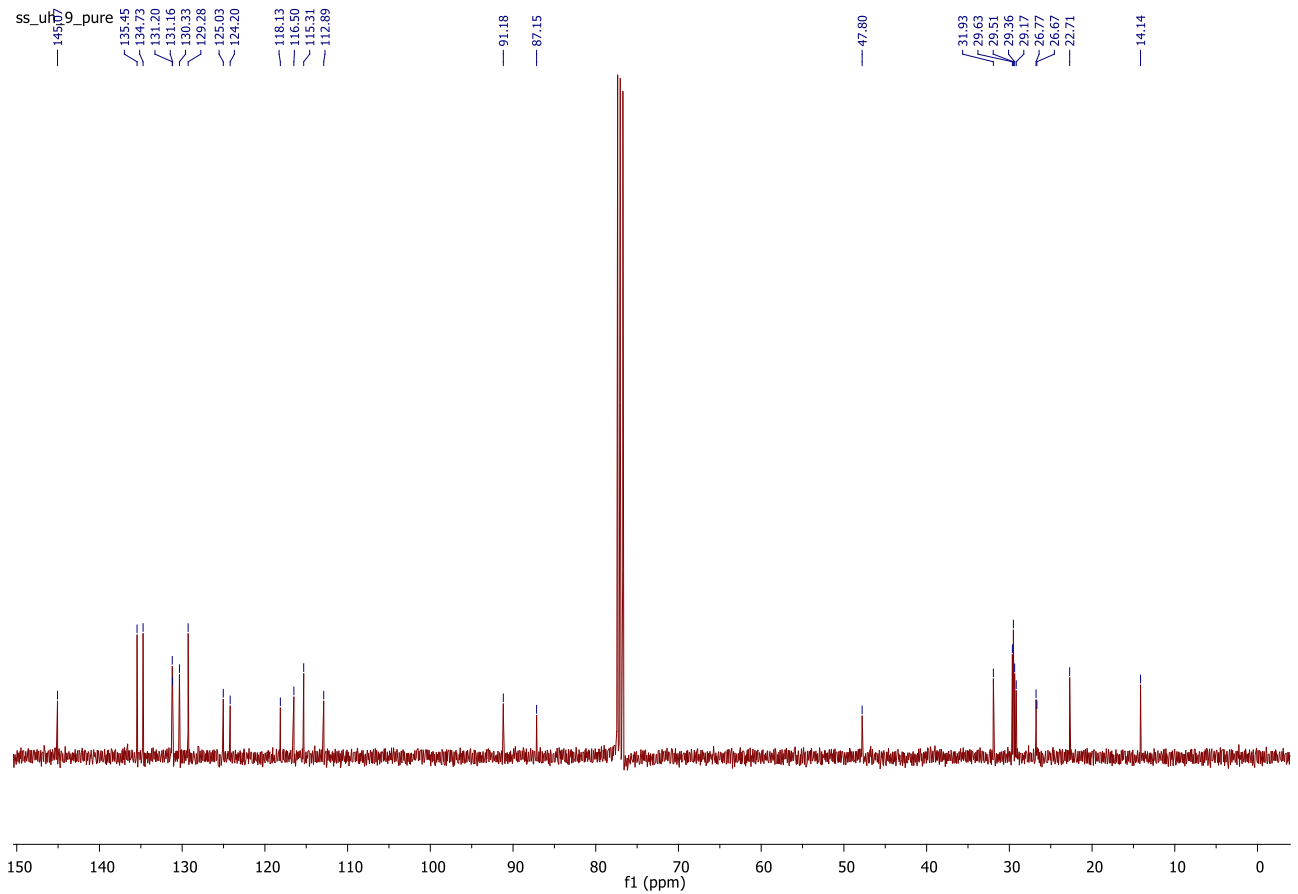
Minimum: -1.5
Maximum: 5.0 100.0 400.0

Mass	Calc. Mass	mDa	PPM	DBE	i-FIT	i-FIT (Norm)	Formula
617.2856	617.2865	-0.9	-1.5	25.0	65.5	0.0	C42 H39 N3 S

Appendix 2.1c: MALDI TOF data for 40.



Appendix 2.2a: ^1H NMR spectrum of **41**.



Appendix 2.2b: $^{13}\text{C}\{^1\text{H}\}$ NMR spectrum of 41.

Elemental Composition Report

Single Mass Analysis

Tolerance = 100.0 PPM / DBE: min = -1.5, max = 400.0

Element prediction: Off

Number of isotope peaks used for i-FIT = 5

Monoisotopic Mass, Odd and Even Electron Ions

3 formula(e) evaluated with 1 results within limits (up to 10 closest results for each mass)

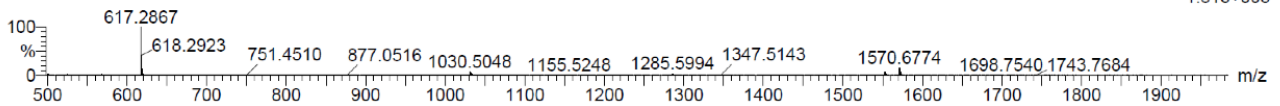
Elements Used:

C: 0-42 H: 0-39 N: 0-3 S: 0-1

Una Harty (SD), SS-UH-10crude

Q-TOF20181101MF002 51 (1.235) AM (Cen,8, 80.00, Ht,10000.0,1570.68,0.70); Sm (SG, 2x3.00); Sb (15,10.00); Cm (8:53)

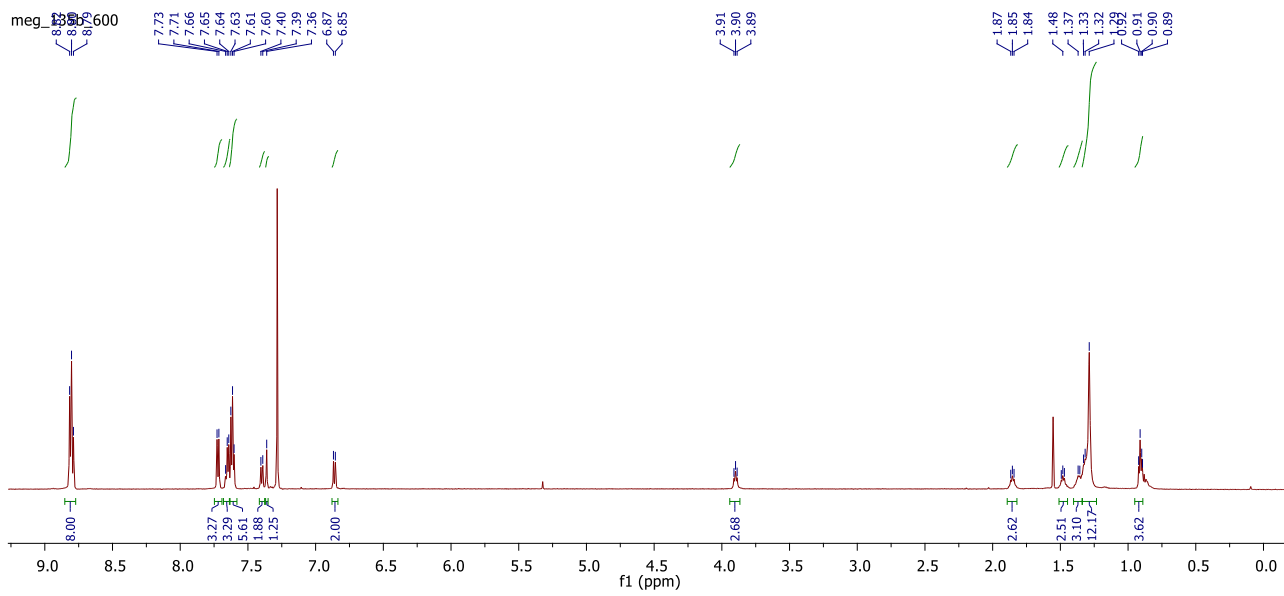
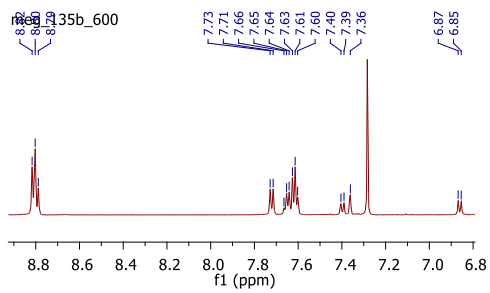
TOF MS LD+
1.81e+003



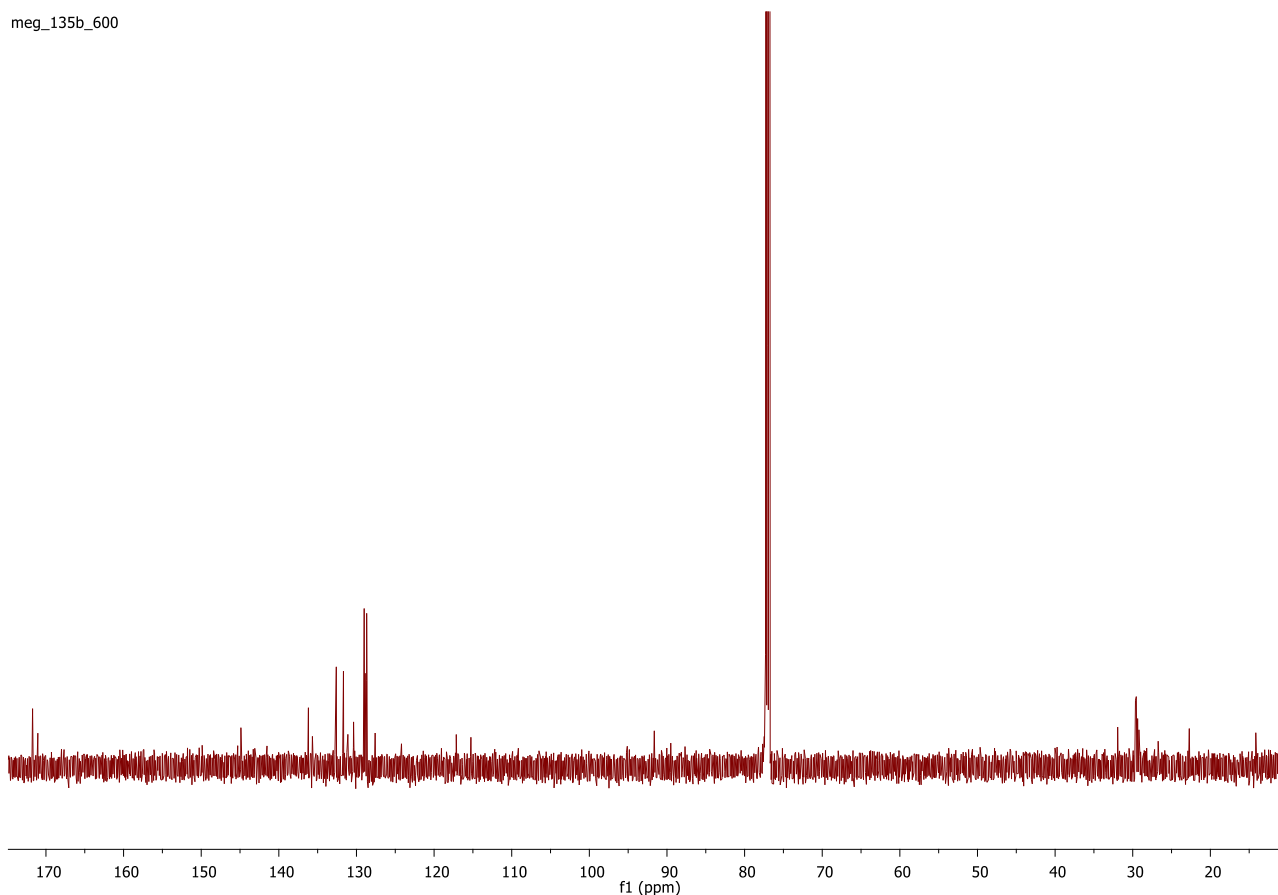
Minimum: -1.5
Maximum: 5.0 100.0 400.0

Mass	Calc. Mass	mDa	PPM	DBE	i-FIT	i-FIT (Norm)	Formula
617.2867	617.2865	0.2	0.3	25.0	43.0	0.0	C42 H39 N3 S

Appendix 2.2c: MALDI TOF data for 41.



Appendix 2.3a: ^1H NMR spectrum of **42**.



Appendix 2.3b: $^{13}\text{C}\{^1\text{H}\}$ NMR spectrum of 42.

Elemental Composition Report

Single Mass Analysis

Tolerance = 100.0 PPM / DBE: min = -1.5, max = 400.0

Element prediction: Off

Number of isotope peaks used for i-FIT = 5

Monoisotopic Mass, Odd and Even Electron Ions

5 formula(e) evaluated with 1 results within limits (up to 10 closest results for each mass)

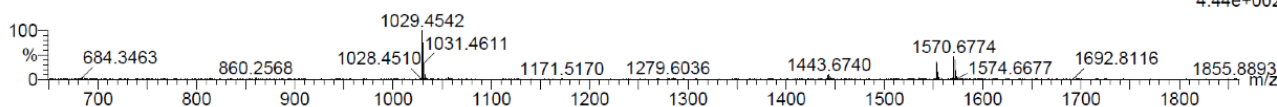
Elements Used:

C: 0-70 H: 0-59 N: 0-7 S: 0-1

Martha Gulman (SD), MEG135A

Q-TOF20181217MF13 52 (0.963) AM (Cen,8, 80.00, Ht,10000.0,1570.68,0.70); Sm (SG, 2x3.00); Sb (15,10.00); Cm (9:79-40:66)

TOF MS LD+
4.44e+002



Minimum:

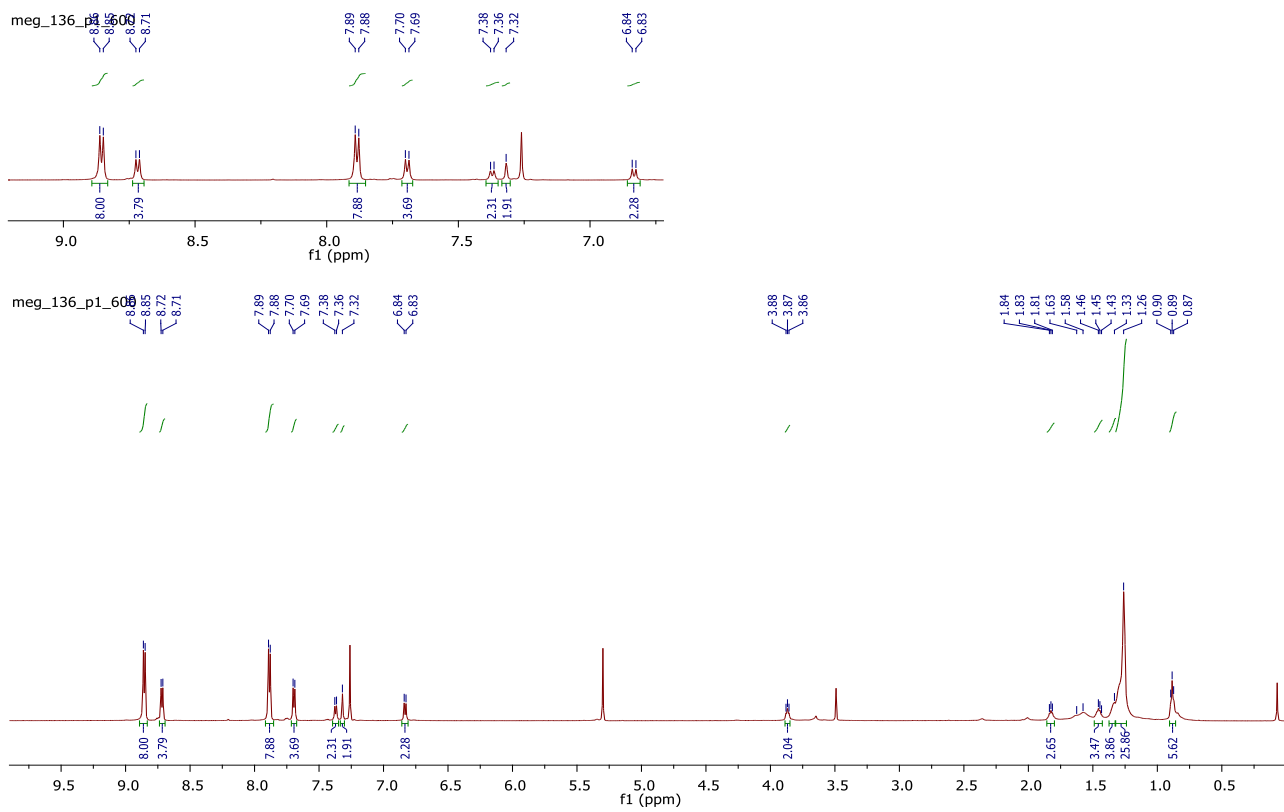
-1.5

Maximum:

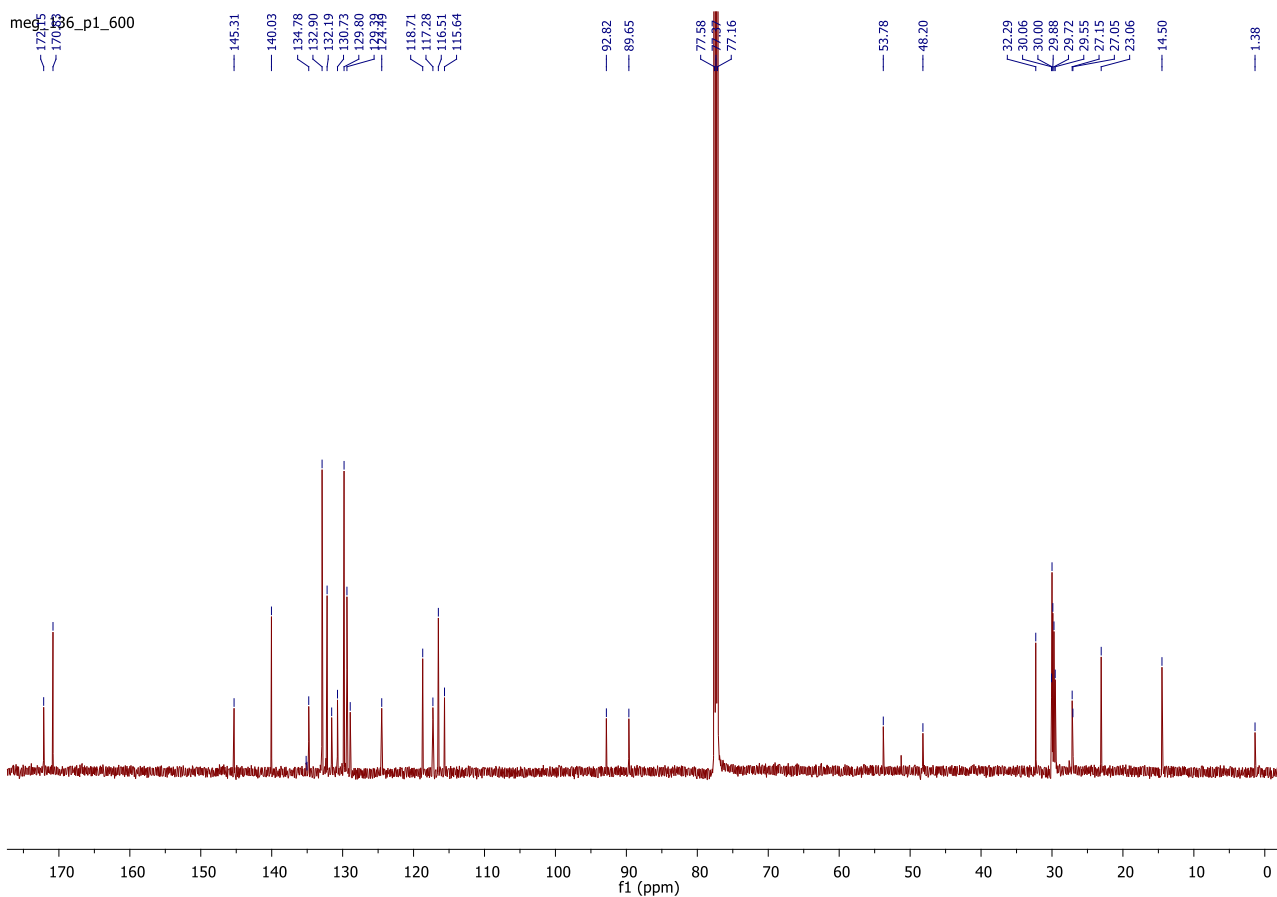
5.0 100.0 400.0

Mass	Calc. Mass	mDa	PPM	DBE	i-FIT	i-FIT (Norm)	Formula
1029.4542	1029.4553	-1.1	-1.1	45.0	22.1	0.0	C70 H59 N7 S

Appendix 2.3c: MALDI TOF data for 42.



Appendix 2.4a: ^1H NMR spectrum of **43**.



Appendix 2.4b: $^{13}\text{C}\{^1\text{H}\}$ NMR spectrum of **43**.

Elemental Composition Report

Single Mass Analysis

Tolerance = 100.0 PPM / DBE: min = -1.5, max = 400.0

Element prediction: Off

Number of isotope peaks used for i-FIT = 5

Monoisotopic Mass, Odd and Even Electron Ions

11 formula(e) evaluated with 1 results within limits (up to 10 closest results for each mass)

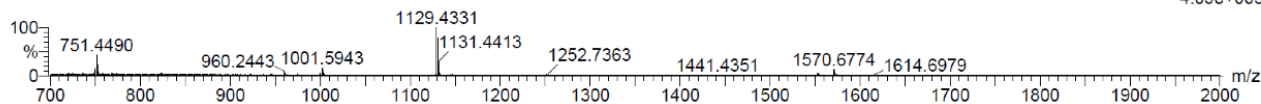
Elements Used:

C: 0-74 H: 0-55 N: 0-11 S: 0-1

Martha Gulman (SD), MEG136p1

Q-TOF2019015MF002 56 (1.036) AM (Cen,8, 80.00, Ht,10000.0,1570.68,0.70); Sm (SG, 2x3.00); Sb (15,10.00); Cm (18.85)

TOF MS LD+
4.09e+003



Minimum: -1.5
Maximum: 5.0 100.0 400.0

Mass	Calc. Mass	mDa	PPM	DBE	i-FIT	i-FIT (Norm)	Formula
1129.4331	1129.4363	-3.2	-2.8	53.0	119.7	0.0	C74 H55 N11 S

Appendix 2.5c: MALDI TOF data for **43**.

Appendix 2.6a. Molar absorptivity of **36**, **39**, **40**, and **41**.^a

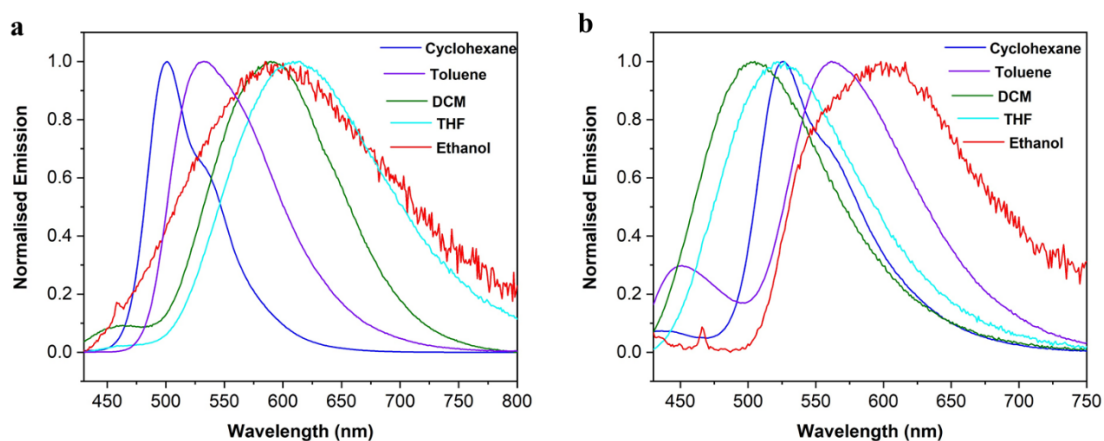
	$\lambda_{\text{abs}} / \text{nm}^{[a]}$	$\epsilon^{[b]}$	$\epsilon^{[b]}$
36	276, 333	2.77 (276)	4.50(333)
39	291, 397	3.97 (291)	1.84 (397)
40	296, 322, 398	3.44 (296)	1.45 (398)
41	294, 383	3.87 (294)	1.34 (383)

^a UV-vis absorption and emission data of **42** and **43** (1×10^{-5} M) in CH_2Cl_2 , at $\lambda_{\text{exc}} > 400$ nm under N_2 at RT. ^b Molar extinction coefficient at the absorption maxima. ϵ : $10^5 \text{ M}^{-1} \text{ cm}^{-1}$.

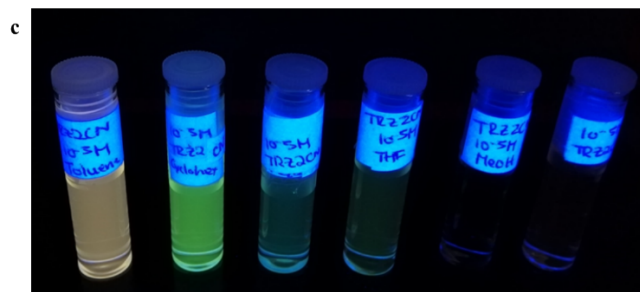
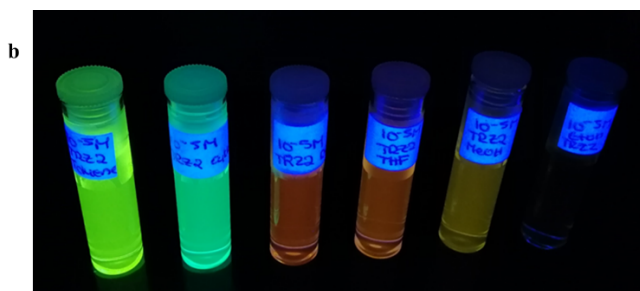
Appendix 2.6b. Molar absorptivity of **42** and **43**.^a

	$\lambda_{\text{abs}} / \text{nm}^{[a]}$	$\epsilon^{[b]}$	$\epsilon^{[b]}$	$\epsilon^{[b]}$
42	280, 311, 404	5.21 (280)	4.67 (311)	2.11 (404)
43	277, 310, 410	3.76 (277)	2.31 (310)	1.16 (410)

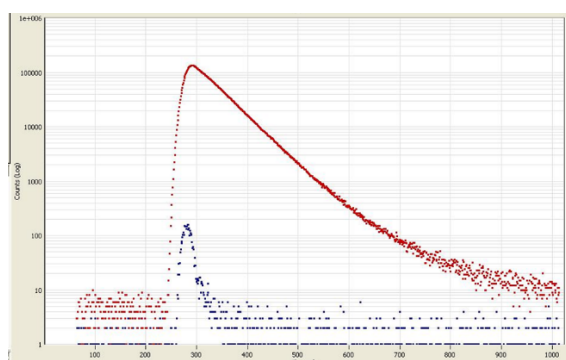
^a UV/Vis absorption and emission data of **42** and **43** (1×10^{-5} M) in CH_2Cl_2 , at $\lambda_{\text{exc}} > 400$ nm under N_2 at RT. ^b Molar extinction coefficient at the absorption maxima. ϵ : $10^5 \text{ M}^{-1} \text{ cm}^{-1}$.



Appendix 2.7: Normalised emission spectra of **a) 42** ($\lambda_{\text{exc}} > 404$ nm) and **b) 43** ($\lambda_{\text{exc}} > 410$ nm), 1×10^{-5} M in a range of solvents in air at RT.

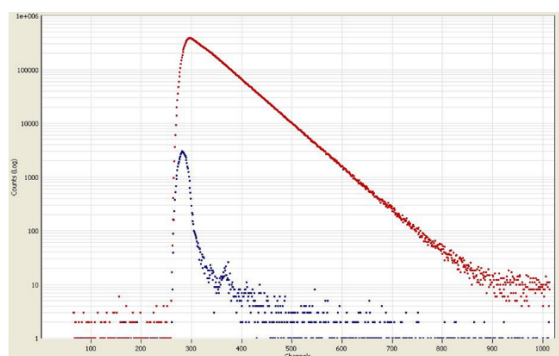


Appendix 2.8: a) (left) **42** and (right) **43** visualised under UV light ($\lambda_{\text{ex}} = 365 \text{ nm}$), $1 \times 10^{-4} \text{ M}$, CH_2Cl_2 b) **42** visualised under UV illumination ($\lambda = 365 \text{ nm}$), $1 \times 10^{-5} \text{ M}$ in a range of solvents: toluene, cyclohexane, CH_2Cl_2 , THF, methanol, and ethanol. c) **43** visualised under UV illumination ($\lambda = 365 \text{ nm}$) $1 \times 10^{-5} \text{ M}$ in a range of solvents: toluene, cyclohexane, CH_2Cl_2 , THF, methanol, and ethanol.



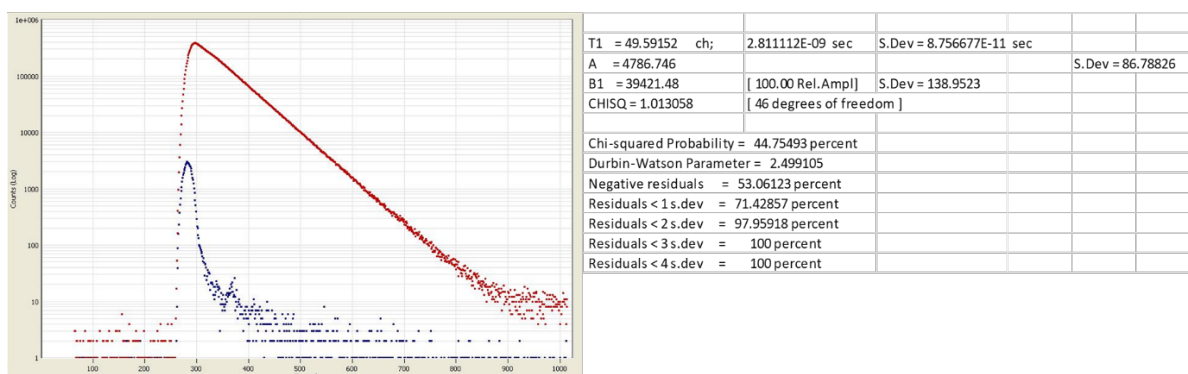
T1 = 60.99682	ch 3.457625E-09 sec	S.Dev = 1.175976E-10 sec	
A = -13303.81			S.Dev = 205.4868
B1 = 89209.41	[100.00 Rel.Ampl]	S.Dev = 280.6107	
CHISQ = 1.016858	[35 degrees of freedom]		
Chi-squared Probability = 44.12808 percent			
Durbin-Watson Parameter = 2.356357			
Negative residuals = 47.36842 percent			
Residuals < 1 s.dev = 68.42105 percent			
Residuals < 2 s.dev = 97.36842 percent			
Residuals < 3 s.dev = 100 percent			
Residuals < 4 s.dev = 100 percent			

Appendix 2.9a: Lifetime determination data, (red) corresponds to **42** $\tau_1 = 3.46 \text{ ns}$ (N_2 , $1 \times 10^{-5} \text{ M}$, cyclohexane); (blue) corresponds to IRF in a non-scattering solution of silica particles.

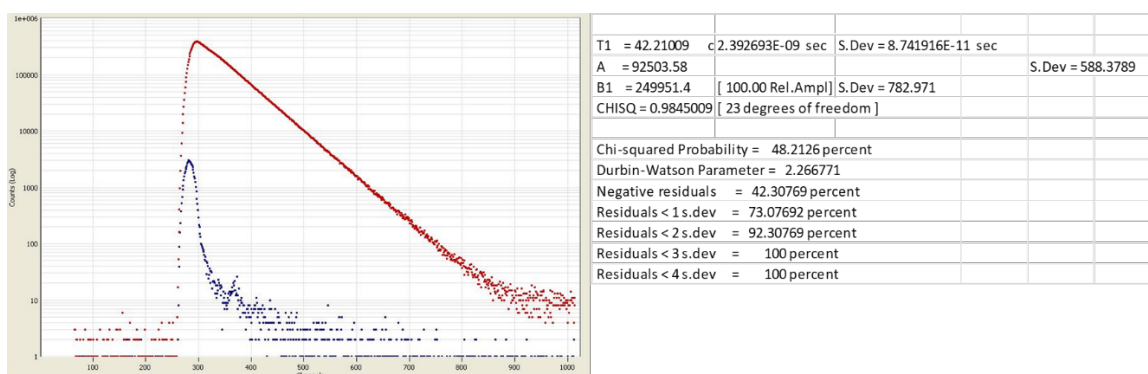


T1 = 34.04186	ch;	1.929674E-09 sec	S.Dev = 8.551758E-11 sec
A = 15903.57			S.Dev = 408.6094
B1 = 207225.4	[100.00 Rel.Ampl]	S.Dev = 570.5245	
CHISQ = 1.078903	[21 degrees of freedom]		
Chi-squared Probability = 36.54639 percent			
Durbin-Watson Parameter = 2.056572			
Negative residuals = 45.83333 percent			
Residuals < 1 s.dev = 70.83334 percent			
Residuals < 2 s.dev = 95.83334 percent			
Residuals < 3 s.dev = 100 percent			
Residuals < 4 s.dev = 100 percent			

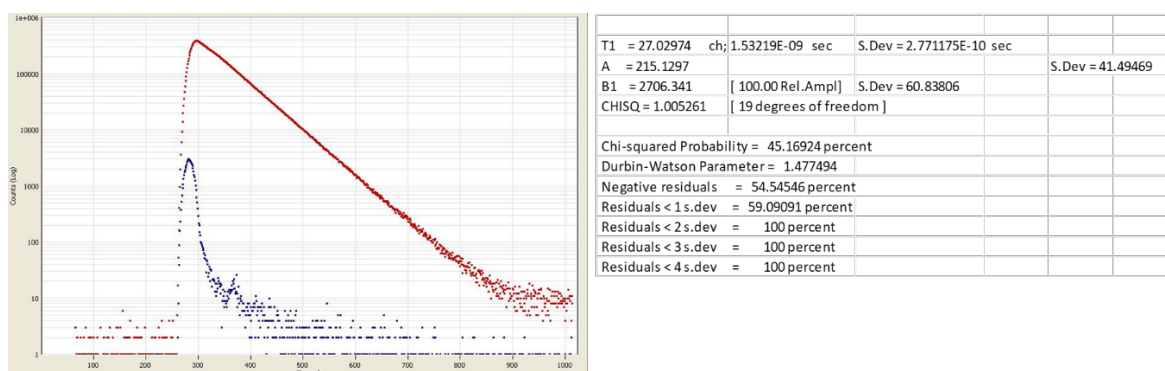
Appendix 2.9b: Lifetime determination data, (red) corresponds to $42 \tau_1 = 1.92 \text{ ns}$ (N_2 , $1 \times 10^{-5} \text{ M}$, CH_2Cl_2); (blue) corresponds to IRF in a non-scattering solution of silica particles.



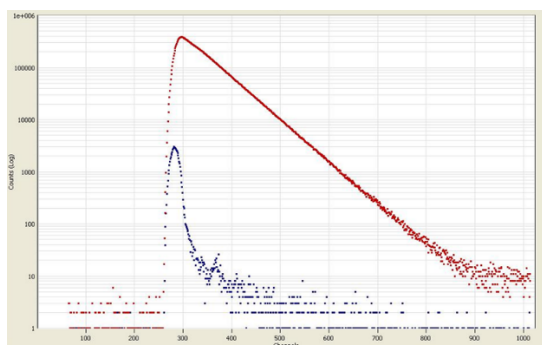
Appendix 2.9c: Lifetime determination data, (red) corresponds to $42 \tau_1 = 2.81 \text{ ns}$ (N_2 , $1 \times 10^{-5} \text{ M}$, ethanol); (blue) corresponds to IRF in a non-scattering solution of silica particles.



Appendix 2.10a: Lifetime determination data, (red) corresponds to $43 \tau_1 = 2.39 \text{ ns}$ (N_2 , $1 \times 10^{-5} \text{ M}$, cyclohexane); (blue) corresponds to IRF in a non-scattering solution of silica particles.



Appendix 2.10b: Lifetime determination data, (red) corresponds to $43 \tau_1 = 153 \text{ ns}$ (N_2 , $1 \times 10^{-5} \text{ M}$, CH_2Cl_2); (blue) corresponds to IRF in a non-scattering solution of silica particles.



T1 = 41.24834	ch 2.338176E-09 sec	S.Dev = 1.582948E-10 sec	
A = 1137.741			S.Dev = 21.23173
B1 = 3857.438	[100.00 Rel.Ampl]	S.Dev = 38.41535	
CHISQ = 1.062768	[51 degrees of freedom]		
Chi-squared Probability = 35.46536 percent			
Durbin-Watson Parameter = 2.085319			
Negative residuals = 46.2963 percent			
Residuals < 1 s.dev = 64.81481 percent			
Residuals < 2 s.dev = 96.2963 percent			
Residuals < 3 s.dev = 100 percent			
Residuals < 4 s.dev = 100 percent			

Appendix 2.10c: Lifetime determination data, (red) corresponds to **43** $\tau_1 = 2.33$ ns (N_2 , 1×10^{-5} M, ethanol); (blue) corresponds to IRF in a non-scattering solution of silica particles.

Appendix 2.11a: B3LYP|6-31G* matrix for **39**.

Charge = 0 Multiplicity = 1

Symbolic Z-Matrix:

C	3.15191	-2.31793	-0.70431
C	2.45602	-1.16588	-1.04746
C	1.04645	-1.16592	-1.15852
C	0.39058	-2.39805	-0.97033
C	0.83696	1.29208	-1.14502
C	2.22632	1.53143	-1.03893
C	2.71743	2.7837	-0.69267
H	3.78943	2.92706	-0.60144
C	1.85316	3.87828	-0.49318
C	0.47391	3.65522	-0.63532
C	-0.01862	2.39163	-0.93897
H	4.23213	-2.27672	-0.60677
H	-0.68565	-2.46301	-1.05287
H	-0.2188	4.47783	-0.49046
H	-1.09076	2.27091	-1.01115
S	3.39525	0.27402	-1.49889
N	0.3334	0.01285	-1.45994
C	2.48605	-3.54521	-0.51599
C	-1.06872	-0.10477	-1.88929
H	-1.28442	0.75986	-2.52486

H	-1.13111	-0.98036	-2.54355
C	-2.12845	-0.20892	-0.77494
H	-1.90575	-1.06023	-0.12163
H	-2.08344	0.67532	-0.12853
C	1.09033	-3.56087	-0.67086
H	0.54782	-4.4912	-0.53787
C	6.65043	-8.01424	0.95585
C	4.57837	-9.28651	0.94974
C	5.94566	-6.86701	0.62157
H	7.72664	-7.97618	1.08998
C	3.87566	-8.13802	0.61559
H	4.05696	-10.22942	1.0792
C	4.54581	-6.90752	0.44564
H	6.46852	-5.92502	0.4928
H	2.79956	-8.17767	0.48213
C	3.82486	-5.73146	0.10554
C	3.20705	-4.72311	-0.18331
C	2.95691	9.89049	0.96708
C	5.21816	8.99979	0.89189
C	2.45417	8.63769	0.64735
H	2.28384	10.72753	1.12211
C	4.71317	7.74783	0.5723
H	6.28854	9.15006	0.98879
C	3.32246	7.54368	0.4441

H	1.38368	8.48909	0.55073
H	5.38755	6.91201	0.41763
C	2.80677	6.26099	0.11648
C	2.36578	5.16174	-0.16463
C	-3.5436	-0.35497	-1.35149
C	-4.63212	-0.42867	-0.27255
H	-3.5916	-1.25673	-1.98014
H	-3.75548	0.49158	-2.02158
C	-6.04754	-0.58651	-0.84312
H	-4.41652	-1.26768	0.4051
H	-4.58897	0.47958	0.34645
C	-7.14091	-0.61052	0.23276
H	-6.24948	0.23613	-1.54514
H	-6.09879	-1.51112	-1.43704
H	-6.93539	-1.42439	0.94384
H	-7.09305	0.32078	0.81659
C	-8.55602	-0.77855	-0.33573
C	-9.65425	-0.74917	0.73497
H	-8.61391	-1.72591	-0.89208
H	-8.74758	0.01667	-1.07163
C	-11.06898	-0.92378	0.16757

H	-9.46071	-1.53734	1.47779
H	-9.59865	0.2032	1.28309
C	-12.17038	-0.85693	1.23306
H	-11.25282	-0.14914	-0.59195
H	-11.13199	-1.88661	-0.36111
H	-11.98667	-1.62757	1.99675
H	-12.1097	0.10859	1.7574
C	-13.58497	-1.03488	0.66655
C	-14.67978	-0.95197	1.73501
H	-13.64914	-2.00368	0.15089
H	-13.76537	-0.26986	-0.10218
H	-15.67636	-1.08493	1.29866
H	-14.546	-1.7256	2.50129
H	-14.66566	0.02053	2.24255
C	5.97306	-9.23534	1.12333
C	6.69926	-10.42051	1.46886
N	7.28875	-11.3839	1.74972
C	4.34436	10.0834	1.09244
C	4.86429	11.37656	1.42232
N	5.2863	12.42754	1.69029

Appendix 2.11b: B3LYP|6-31G* matrix for 40.

Charge = 0 Multiplicity = 1

Symbolic Z-Matrix:

C	3.28816	2.72668	0.51533
C	2.77285	1.49061	0.88439
C	1.38099	1.2911	1.03277
C	0.54905	2.4122	0.84302
C	1.52106	-1.17157	1.05612
C	2.92604	-1.21199	0.90153
C	3.57761	-2.38438	0.54005
H	4.65497	-2.37452	0.40792
C	2.86864	-3.58979	0.37575
C	1.47798	-3.56784	0.57513
C	0.82347	-2.38475	0.89431
H	4.36066	2.83985	0.39218

H	-0.52352	2.3216	0.94639
H	0.9092	-4.48482	0.45962
H	-0.25076	-2.41746	1.01169
S	3.91811	0.20261	1.31972
N	0.8519	0.02867	1.37239
C	2.44697	3.84119	0.33409
C	-0.54051	-0.04372	1.84316
H	-0.61033	-0.91135	2.5071
H	-0.71017	0.83295	2.47613
C	-1.6351	-0.12378	0.76114
H	-1.5422	0.72029	0.06791
H	-1.4952	-1.02203	0.14909
C	1.0657	3.6598	0.51635
H	0.39596	4.5034	0.38417
C	3.27514	9.87388	-1.1548
C	5.56311	9.10787	-1.22387

C	2.85028	8.58303	-0.80861	H	-6.53859	-1.32524	-0.6632
H	2.5359	10.66175	-1.25816	C	-8.09217	-0.34862	0.48194
C	5.15552	7.82287	-0.88088	C	-9.20005	-0.50176	-0.56824
H	6.61838	9.30952	-1.38479	H	-8.23447	0.59751	1.02507
C	3.79542	7.52956	-0.66594	H	-8.19042	-1.14681	1.23272
H	5.88257	7.0245	-0.77381	C	-10.61608	-0.45596	0.02046
C	3.37276	6.22164	-0.31707	H	-9.09574	0.29144	-1.32351
C	2.96815	5.11405	-0.01713	H	-9.06097	-1.45151	-1.10586
C	4.32049	-9.48003	-1.18834	C	-11.72158	-0.61354	-1.03133
C	6.52126	-8.48937	-1.2248	H	-10.72047	-1.2469	0.77814
C	3.76702	-8.24411	-0.82406	H	-10.75637	0.49554	0.55479
H	3.66399	-10.33546	-1.31141	H	-11.61571	0.1755	-1.79097
C	5.98552	-7.25733	-0.86402	H	-11.58342	-1.56641	-1.564
H	7.59243	-8.58225	-1.38009	C	-13.13899	-0.56344	-0.44646
C	4.60156	-7.1044	-0.65587	C	-14.23541	-0.72125	-1.50498
H	6.62884	-6.39268	-0.73763	H	-13.2776	0.38882	0.08519
C	4.04691	-5.85146	-0.29052	H	-13.24581	-1.35227	0.31183
C	3.52688	-4.79606	0.01963	H	-15.23471	-0.68217	-1.0564
C	-3.04109	-0.13389	1.37734	H	-14.17682	0.07468	-2.2577
C	-4.15671	-0.25619	0.33102	H	-14.14348	-1.67971	-2.03074
H	-3.19048	0.78528	1.96324	C	4.62609	10.13682	-1.36211
H	-3.12241	-0.96555	2.09314	H	4.94703	11.13883	-1.62993
C	-5.56699	-0.24033	0.93488	C	5.6923	-9.60378	-1.38844
H	-4.06387	0.5641	-0.3958	H	6.11318	-10.56401	-1.67047
H	-4.0158	-1.18529	-0.24042	C	1.45619	8.32896	-0.59869
C	-6.67842	-0.38291	-0.11302	N	0.32106	8.13534	-0.43087
H	-5.65648	-1.05171	1.67241	C	2.35321	-8.13372	-0.62134
H	-5.71189	0.69585	1.49413	N	1.20345	-8.05703	-0.45903
H	-6.57939	0.42035	-0.85819				

Appendix 2.11c: B3LYP|6-31G* matrix for 41.

Charge = 0 Multiplicity = 1

Symbolic Z-Matrix:

C	-3.69245	-1.60702	0.64397
C	-2.75712	-0.64881	1.01371
C	-1.38749	-0.97285	1.14638
C	-1.02748	-2.31944	0.94523
C	-0.61881	1.371	1.17438

C	-1.91347	1.92276	1.04115
C	-2.09698	3.2549	0.69227
H	-3.10545	3.63927	0.57677
C	-1.00088	4.12226	0.51835
C	0.28662	3.59033	0.69422
C	0.46997	2.24704	1.00073
H	-4.73259	-1.31795	0.53163
H	0.00408	-2.63005	1.03946
H	1.15232	4.23315	0.57237

H	1.48426	1.88581	1.10044
S	-3.34876	0.96487	1.46745
N	-0.43026	0.00712	1.48263
C	-3.32224	-2.95183	0.44749
C	0.89927	-0.43576	1.92916
H	1.29313	0.3435	2.5896
H	0.74869	-1.31631	2.56176
C	1.92768	-0.75491	0.82642
H	1.52814	-1.51778	0.14802
H	2.09643	0.13065	0.2031
C	-1.96973	-3.2878	0.61853
H	-1.65168	-4.31575	0.47792
C	-8.39082	-6.33842	-1.10492
C	-6.67796	-8.04197	-1.11405
C	-5.72562	-7.08961	-0.7608
H	-6.37862	-9.07642	-1.25447
C	-6.09257	-5.74045	-0.57351
H	-4.68754	-7.37612	-0.62572
C	-5.12119	-4.76444	-0.21403
C	-4.29013	-3.93019	0.09186
C	-0.63763	10.20811	-1.102852
C	-3.03197	9.89607	-0.94792
C	-2.84883	8.5589	-0.60557
H	-4.03772	10.29296	-1.04949
C	-1.55107	8.02314	-0.46853
H	-3.70499	7.91282	-0.43994
C	-1.36004	6.65673	-0.11943
C	-1.19638	5.48824	0.17722
C	3.26257	-1.23449	1.41336
C	4.32434	-1.51406	0.3415
H	3.09586	-2.14496	2.00816
H	3.64707	-0.48051	2.1165
C	5.65799	-2.01314	0.91257
H	3.93417	-2.25544	-0.37126
H	4.49865	-0.59729	-0.24069
C	6.72256	-2.26234	-0.16368

H	6.04009	-1.28054	1.63891
H	5.48718	-2.94091	1.4785
H	6.33567	-2.9866	-0.8959
H	6.89609	-1.33079	-0.7226
C	8.05692	-2.77256	0.39585
C	9.12139	-3.00335	-0.68458
H	7.88623	-3.71049	0.945
H	8.43993	-2.05378	1.13548
C	10.45696	-3.51912	-0.13305
H	8.73554	-3.71759	-1.42718
H	9.29298	-2.06342	-1.22999
C	11.5205	-3.74048	-1.21613
H	10.8412	-2.80757	0.61299
H	10.28706	-4.46224	0.40751
H	11.13606	-4.45073	-1.96351
H	11.69122	-2.79689	-1.75578
C	12.8573	-4.25779	-0.66914
C	13.91257	-4.47375	-1.75868
H	12.6875	-5.20153	-0.13129
H	13.24154	-3.54824	0.07753
H	14.85412	-4.84409	-1.33725
H	13.57046	-5.204	-2.50247
H	14.13037	-3.53913	-2.29014
C	-8.01182	-7.67931	-1.2889
H	-8.75856	-8.41654	-1.56425
C	-1.93603	10.72952	-1.16164
H	-2.07235	11.77213	-1.42876
C	-0.4449	8.86426	-0.68426
H	0.55997	8.46951	-0.58371
C	-7.439	-5.37439	-0.74955
H	-7.73959	-4.342	-0.6099
C	0.50016	11.05546	-1.24643
N	1.42094	11.7438	-1.4235
C	-9.76178	-5.95207	-1.28199
N	-10.8737	-5.64267	-1.42636

Appendix 2.11d: B3LYP/6-31G* matrix for 42.

Charge = 0 Multiplicity = 1

Symbolic Z-matrix:

C	2.55856	-0.07275	1.78818
---	---------	----------	---------

C	1.35361	0.55421	2.08077	H	-10.50484	-0.32162	-0.06378
C	1.23386	1.96263	2.05552	C	-7.3858	-2.52551	0.59727
C	2.40459	2.69756	1.78568	H	-8.69208	-4.19389	0.23245
C	-1.23418	1.9628	2.05558	C	-7.2663	-1.12136	0.67057
C	-1.35412	0.55439	2.08081	H	-8.33108	0.74741	0.48262
C	-2.55916	-0.0724	1.78825	H	-6.51111	-3.14112	0.78222
H	-2.60855	-1.15667	1.79421	C	-6.02099	-0.50833	0.97637
C	-3.72413	0.67192	1.51654	C	-4.95856	0.0293	1.23059
C	-3.62059	2.07243	1.53681	C	-11.03896	-2.95796	-0.28495
C	-2.40482	2.69789	1.7858	C	11.0381	-2.95925	-0.28491
H	2.60781	-1.15702	1.79415	N	12.09067	-2.15341	-0.49732
H	2.37986	3.77837	1.76302	N	11.08673	-4.29884	-0.35705
H	-4.5003	2.67558	1.33712	N	13.38754	-4.09804	-0.89697
H	-2.37995	3.7787	1.76316	N	-11.0877	-4.29754	-0.35714
S	-0.00031	-0.45463	2.63758	N	-12.09145	-2.15202	-0.49736
N	-0.00011	2.60055	2.30474	N	-13.38848	-4.09652	-0.89712
C	3.72362	0.67141	1.51642	C	-12.39016	-6.29865	-0.76282
C	0.00001	4.04948	2.5554	C	-13.61465	-6.90191	-1.09044
H	-0.8732	4.27045	3.17723	C	-11.26858	-7.10936	-0.52732
H	0.87329	4.27031	3.17717	C	-13.71373	-8.28803	-1.1804
C	0.00004	4.95768	1.30996	H	-14.47717	-6.27086	-1.27146
H	0.87212	4.73436	0.68484	C	-11.37142	-8.49522	-0.61776
H	-0.87244	4.73495	0.6852	H	-10.32559	-6.63806	-0.27509
C	3.62026	2.07193	1.53666	C	-12.59335	-9.08858	-0.94433
H	4.50005	2.67497	1.33692	H	-14.66606	-8.74534	-1.4349
C	9.74087	-2.3287	0.04763	H	-10.49742	-9.11407	-0.43347
C	9.62622	-0.93037	0.12272	H	-12.67207	-10.17033	-1.01473
C	8.60287	-3.11616	0.29028	C	-14.43905	-1.91917	-1.04315
C	8.41147	-0.33473	0.42809	C	-14.34883	-0.52125	-0.95205
H	10.50421	-0.32286	-0.06387	C	-15.67231	-2.50606	-1.36746
C	7.38497	-2.52644	0.59724	C	-15.47003	0.2722	-1.18146
H	8.69111	-4.19496	0.23252	H	-13.39414	-0.07352	-0.70092
C	7.26559	-1.12228	0.67048	C	-16.79148	-1.7095	-1.59637
H	8.33054	0.74639	0.48246	H	-15.73605	-3.58597	-1.43609
H	6.51023	-3.14197	0.78222	C	-16.69405	-0.31887	-1.50424
C	6.02034	-0.50913	0.97626	H	-15.38973	1.35345	-1.10849
C	4.95796	0.02862	1.23047	H	-17.74159	-2.17351	-1.84701
C	-9.74168	-2.32754	0.04763	H	-17.56833	0.30158	-1.68317
C	-9.62691	-0.92922	0.12279	C	14.43831	-1.92079	-1.04305
C	-8.60375	-3.11511	0.29027	C	14.34821	-0.52286	-0.95199
C	-8.41211	-0.3337	0.4282	C	15.67151	-2.5078	-1.36733

C	15.46948	0.27048	-1.18139
H	13.39355	-0.07503	-0.70089
C	16.79076	-1.71134	-1.59623
H	15.73516	-3.58771	-1.43593
C	16.69346	-0.32071	-1.50414
H	15.38928	1.35174	-1.10846
H	17.74084	-2.17544	-1.84685
H	17.5678	0.29966	-1.68307
C	12.38903	-6.30008	-0.76261
C	13.61348	-6.90346	-1.09016
C	11.26736	-7.11068	-0.52712
C	13.71244	-8.2896	-1.18006
H	14.47606	-6.27249	-1.27117
C	11.37008	-8.49655	-0.61751
H	10.3244	-6.6393	-0.27495
C	12.59197	-9.09003	-0.94401
H	14.66474	-8.747	-1.4345
H	10.49602	-9.11532	-0.43323
H	12.6706	-10.17179	-1.01437
C	-12.28315	-4.8224	-0.66711
C	-13.24547	-2.76564	-0.79994
C	13.24465	-2.76715	-0.79985
C	12.28214	-4.82381	-0.66696
C	0.00062	6.44665	1.6829
C	0.00051	7.36872	0.45628
H	0.87938	6.6698	2.30626
H	-0.8776	6.67034	2.30683

C	0.00133	8.86277	0.8052
H	0.8783	7.14102	-0.16613
H	-0.87801	7.14179	-0.16538
C	0.00115	9.77079	-0.43152
H	-0.87706	9.09271	1.42628
H	0.8805	9.09193	1.42546
H	0.87897	9.53655	-1.05189
H	-0.87759	9.53749	-1.05095
C	0.00214	11.26881	-0.0999
C	0.00191	12.16573	-1.34462
H	0.88126	11.50435	0.51816
H	-0.87603	11.50529	0.51916
C	0.003	13.66639	-1.0251
H	0.87971	11.92635	-1.96315
H	-0.87692	11.92739	-1.96209
C	0.00279	14.55593	-2.27489
H	-0.87507	13.90735	-0.40751
H	0.88211	13.90629	-0.40857
H	0.88065	14.31422	-2.8927
H	-0.87619	14.31538	-2.89157
C	0.00398	16.05813	-1.96302
C	0.00375	16.93521	-3.21936
H	0.88262	16.29962	-1.34798
H	-0.87354	16.30079	-1.34684
H	0.00461	18.00118	-2.96448
H	0.88789	16.73995	-3.83874
H	-0.88143	16.7411	-3.83761

Appendix 2.11e: B3LYP|6-31G* matrix for 43.

Charge = 0 Multiplicity = 1

Symbolic Z-matrix:

C	2.55882	0.3646	1.88921
C	1.35353	0.99424	2.17325
C	1.23371	2.40259	2.13203
C	2.4046	3.1353	1.85572
C	-1.23365	2.4025	2.13209
C	-1.35336	0.99413	2.17331
C	-2.55861	0.36441	1.88932
H	-2.60835	-0.71969	1.9076

C	-3.72356	1.10649	1.61116
C	-3.62055	2.50728	1.61552
C	-2.40461	3.13512	1.85587
H	2.60865	-0.71949	1.9075
H	2.37925	4.21568	1.82071
H	-4.50043	3.10827	1.41034
H	-2.37936	4.21549	1.82089
S	0.00014	-0.00874	2.74086
N	0.00001	3.04332	2.37133
C	3.7237	1.10678	1.61099
C	-0.00003	4.49567	2.60738
H	-0.87305	4.72227	3.22726

H	0.87297	4.72231	3.22728	C	-13.71442	-7.87754	-0.99005
C	-0.00002	5.39068	1.35278	H	-14.47742	-5.86863	-1.08875
H	0.87222	5.16142	0.72997	C	-11.35533	-8.0768	-0.43118
H	-0.87229	5.16146	0.72999	H	-10.31964	-6.21918	-0.10478
C	3.62057	2.50756	1.61532	C	-12.58435	-8.67846	-0.752
H	4.50039	3.10862	1.41008	H	-14.66137	-8.34588	-1.23765
C	9.74204	-1.90934	0.1882	H	-10.48526	-8.69877	-0.24816
C	9.6283	-0.50948	0.25129	C	-14.44287	-1.51391	-0.88376
C	8.6019	-2.6944	0.43352	C	-14.35145	-0.11587	-0.79736
C	8.41346	0.08916	0.54714	C	-15.67619	-2.10356	-1.20201
H	10.50614	0.09761	0.06307	C	-15.46707	0.67977	-1.0241
C	7.38416	-2.10125	0.73124	H	-13.3969	0.33363	-0.55088
H	8.6873	-3.77384	0.3856	C	-16.79725	-1.31581	-1.43069
C	7.26575	-0.69587	0.79218	H	-15.74146	-3.18312	-1.26709
H	8.33313	1.17058	0.59217	C	-16.69918	0.08342	-1.34294
H	6.50838	-2.71434	0.91844	H	-15.3957	1.76041	-0.95706
C	6.02099	-0.07967	1.08826	H	-17.75026	-1.77241	-1.67698
C	4.95821	0.46141	1.3343	C	14.44307	-1.51359	-0.8839
C	-9.74184	-1.90971	0.18834	C	14.35165	-0.11555	-0.79757
C	-9.62811	-0.50986	0.25151	C	15.6764	-2.10326	-1.20209
C	-8.6017	-2.69479	0.4336	C	15.46727	0.68008	-1.02435
C	-8.41327	0.08877	0.54739	H	13.3971	0.33397	-0.55113
H	-10.50596	0.09724	0.06333	C	16.79746	-1.31553	-1.43081
C	-7.38396	-2.10165	0.73135	H	15.74166	-3.18282	-1.26712
H	-8.68709	-3.77422	0.38562	C	16.69939	0.08371	-1.34314
C	-7.26556	-0.69627	0.79237	H	15.3959	1.76073	-0.95737
H	-8.33294	1.17018	0.59248	H	17.75047	-1.77214	-1.67707
H	-6.50817	-2.71475	0.9185	C	12.38769	-5.88764	-0.58712
C	-6.02079	-0.08009	1.08846	C	13.6123	-6.49448	-0.90682
C	-4.95803	0.46102	1.3345	C	11.26255	-6.69293	-0.35065
C	-11.03596	-2.5421	-0.13367	C	13.71464	-7.87724	-0.98977
C	11.03616	-2.54175	-0.13377	H	14.47763	-5.86833	-1.08859
N	12.09547	-1.74143	-0.34771	C	11.35554	-8.07646	-0.43091
N	11.08876	-3.88381	-0.19888	H	10.31985	-6.21882	-0.10466
N	13.39249	-3.68981	-0.73104	C	12.58456	-8.67814	-0.75168
N	-11.08856	-3.88417	-0.19887	H	14.66159	-8.34559	-1.23732
N	-12.09527	-1.74177	-0.34756	H	10.48547	-8.69842	-0.24787
N	-13.39229	-3.69014	-0.73103	C	-12.28275	-4.40897	-0.50045
C	-12.38749	-5.88797	-0.58725	C	-13.24601	-2.35936	-0.64087
C	-13.61209	-6.4948	-0.90701	C	13.2462	-2.35903	-0.64097
C	-11.26234	-6.69327	-0.35082	C	12.28295	-4.40863	-0.50043

C	0.00001	6.88344	1.71073	H	-0.87908	14.32274	-0.44506
C	-0.00012	7.7932	0.47496	H	0.87807	14.32285	-0.44549
H	0.87851	7.11298	2.33205	H	0.87731	14.71254	-2.93256
H	-0.87839	7.11298	2.3322	H	-0.87957	14.71242	-2.93213
C	-0.0001	9.2905	0.80968	C	-0.00103	16.46241	-2.01574
H	0.87801	7.55988	-0.1449	C	-0.00141	17.33058	-3.27822
H	-0.87836	7.55987	-0.14472	H	0.87719	16.70887	-1.40209
C	-0.00032	10.18717	-0.43526	H	-0.87897	16.70875	-1.40164
H	-0.87876	9.52571	1.42836	H	-0.00143	18.39826	-3.0307
H	0.87875	9.52575	1.42809	H	0.88312	17.13175	-3.89588
H	0.8779	9.94802	-1.05319	H	-0.88623	17.13162	-3.89543
H	-0.87872	9.94797	-1.05291	C	-17.85342	0.90113	-1.57803
C	-0.00032	11.68799	-0.11649	N	-18.78946	1.56512	-1.76858
C	-0.00062	12.5747	-1.36847	C	-12.68491	-10.10637	-0.83668
H	0.87842	11.92913	0.49994	N	-12.76648	-11.26479	-0.90548
H	-0.87883	11.92904	0.5003	C	17.85363	0.90141	-1.57826
C	-0.00064	14.07778	-1.06054	N	18.78967	1.56539	-1.76884
H	0.8776	12.33105	-1.98473	C	12.68513	-10.10605	-0.83626
H	-0.87908	12.33096	-1.98436	N	12.76671	-11.26448	-0.904
C	-0.001	14.95802	-2.31686				

Appendix 3 Chapter Four

Elemental Composition Report

Page 1

Single Mass Analysis

Tolerance = 5.0 PPM / DBE: min = -1.5, max = 400.0

Element prediction: Off

Number of isotope peaks used for i-FIT = 5

Monoisotopic Mass, Odd and Even Electron Ions

1 formula(e) evaluated with 1 results within limits (up to 10 closest results for each mass)

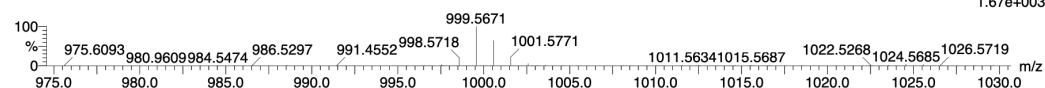
Elements Used:

C: 0-73 H: 0-70 N: 0-3 B: 0-1

Marta Gulman (SD), MEG238p1

Q-TOF20191204MF003 56 (1.278) AM (Cen,8, 80.00, Ht,10000.0,1570.68,0.70); Sm (SG, 2x3.00); Sb (15,10.00); Cm (8:59)

TOF MS LD+
1.67e+003



Minimum:

Maximum: 5.0 5.0 -1.5 400.0

Mass	Calc. Mass	mDa	PPM	DBE	i-FIT	i-FIT (Norm)	Formula
999.5671	999.5663	0.8	0.8	41.0	71.6	0.0	C73 H70 N3 B

Appendix 3.0a: MALDI TOF data for 54.

Elemental Composition Report

Page 1

Single Mass Analysis

Tolerance = 5.0 PPM / DBE: min = -1.5, max = 400.0
 Element prediction: Off
 Number of isotope peaks used for i-FIT = 5

Monoisotopic Mass, Odd and Even Electron Ions
 1 formula(e) evaluated with 1 results within limits (up to 10 closest results for each mass)

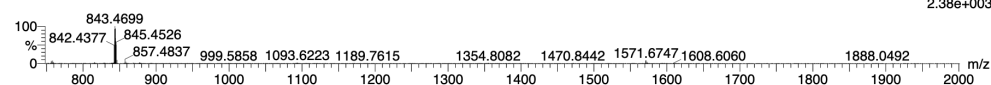
Elements Used:

C: 0-61 H: 0-58 B: 0-1 N: 0-3

Marta Gulman (SD), MEG241

Q-TOF20191204MF005 6 (0.111) AM (Cen,8, 80.00, Ht,10000.0,1570.68,0.70); Sm (SG, 2x3.00); Sb (15,10.00); Cm (5:113)

TOF MS LD+
2.38e+003



Minimum: -1.5
 Maximum: 5.0 5.0 400.0

Mass	Calc. Mass	mDa	PPM	DBE	i-FIT	i-FIT (Norm)	Formula
843.4699	843.4724	-2.5	-3.0	35.0	102.4	0.0	C61 H58 B N3

Appendix 3.0b: MALDI TOF data for 58.

Elemental Composition Report

Page 1

Single Mass Analysis

Tolerance = 50.0 PPM / DBE: min = -1.5, max = 400.0
 Element prediction: Off
 Number of isotope peaks used for i-FIT = 5

Monoisotopic Mass, Odd and Even Electron Ions
 1 formula(e) evaluated with 1 results within limits (up to 10 closest results for each mass)

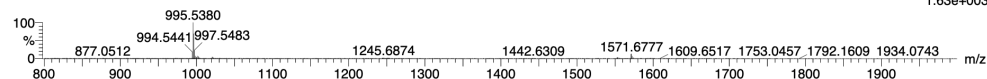
Elements Used:

C: 0-73 H: 0-66 B: 0-1 N: 0-3

Marta Gulman (SD), MEG249F2

Q-TOF20191211MF011 72 (1.528) AM (Cen,8, 80.00, Ht,10000.0,1570.68,0.70); Sm (SG, 2x3.00); Sb (15,10.00); Cm (28:79)

TOF MS LD+
1.63e+003



Minimum: -1.5
 Maximum: 5.0 50.0 400.0

Mass	Calc. Mass	mDa	PPM	DBE	i-FIT	i-FIT (Norm)	Formula
995.5380	995.5350	3.0	3.0	43.0	57.0	0.0	C73 H66 B N3

Appendix 3.0c: MALDI TOF data for 55

Elemental Composition Report

Page 1

Single Mass Analysis

Tolerance = 50.0 PPM / DBE: min = -1.5, max = 400.0
 Element prediction: Off
 Number of isotope peaks used for i-FIT = 5

Monoisotopic Mass, Odd and Even Electron Ions
 19 formula(e) evaluated with 1 results within limits (up to 10 closest results for each mass)

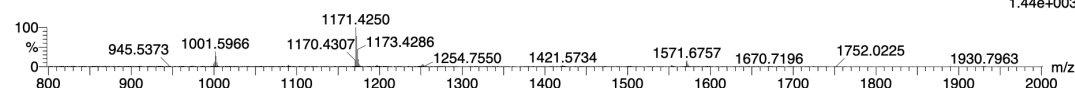
Elements Used:

C: 0-77 H: 0-66 N: 0-3 S: 0-4 B: 0-1

Marta Gulman (SD), MEG247F2

Q-TOF20191211MF009 56 (1.037) AM (Cen,8, 80.00, Ht,10000.0,1570.68,0.70); Sm (SG, 2x3.00); Sb (15,10.00); Cm (12:75-53:60)

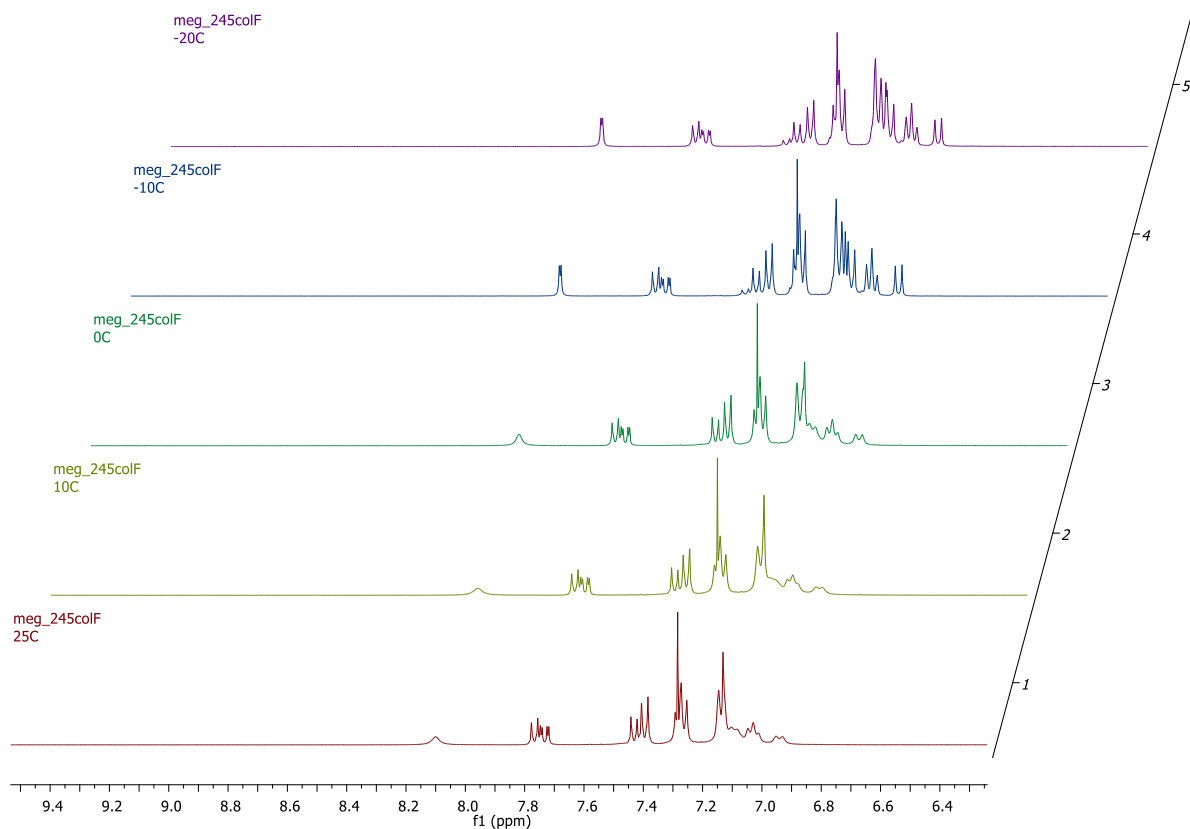
TOF MS LD+
1.44e+003



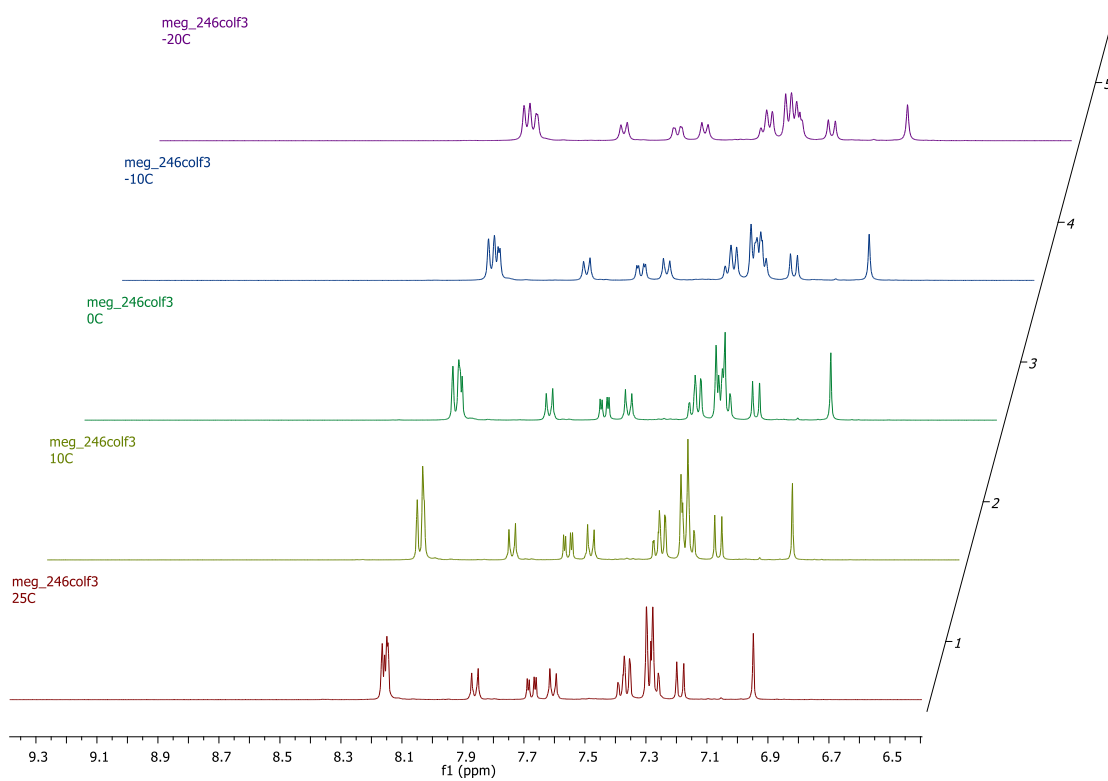
Minimum: -1.5
 Maximum: 5.0 50.0 400.0

Mass	Calc. Mass	mDa	PPM	DBE	i-FIT	i-FIT (Norm)	Formula
1171.4250	1171.4233	1.7	1.5	47.0	83.1	0.0	C77 H66 N3 S4 B

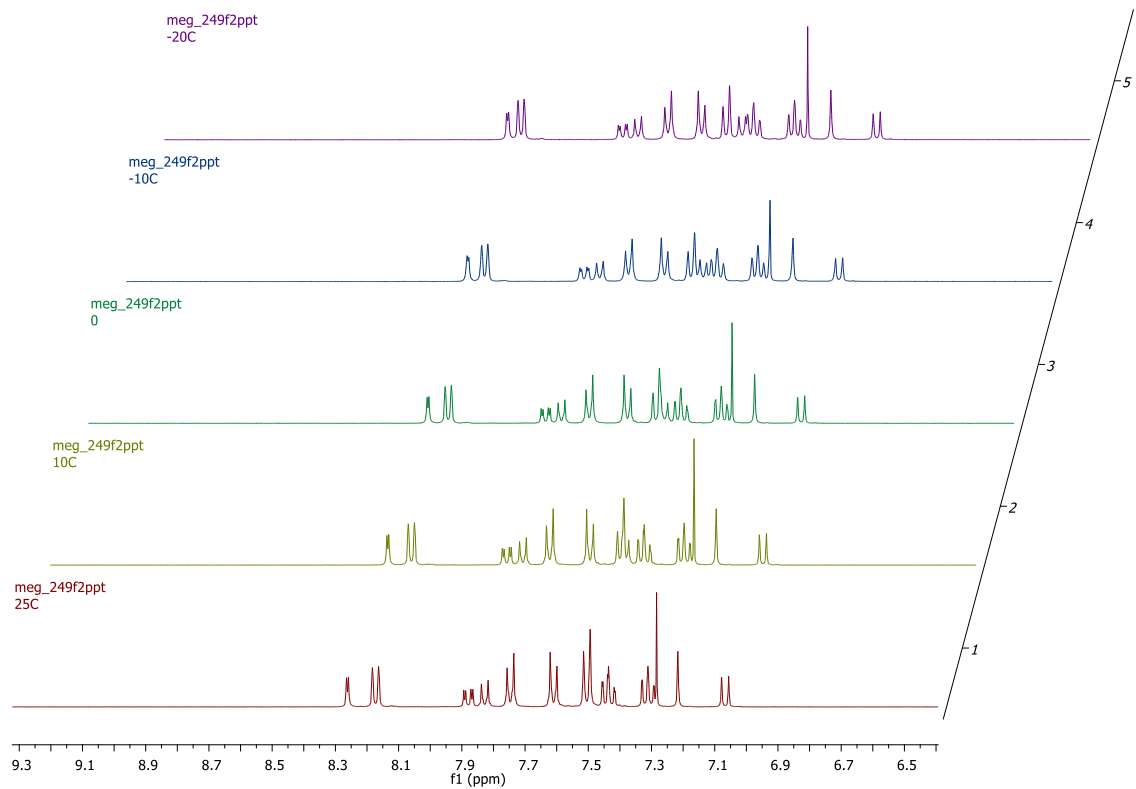
Appendix 3.0d: MALDI TOF data for 60.



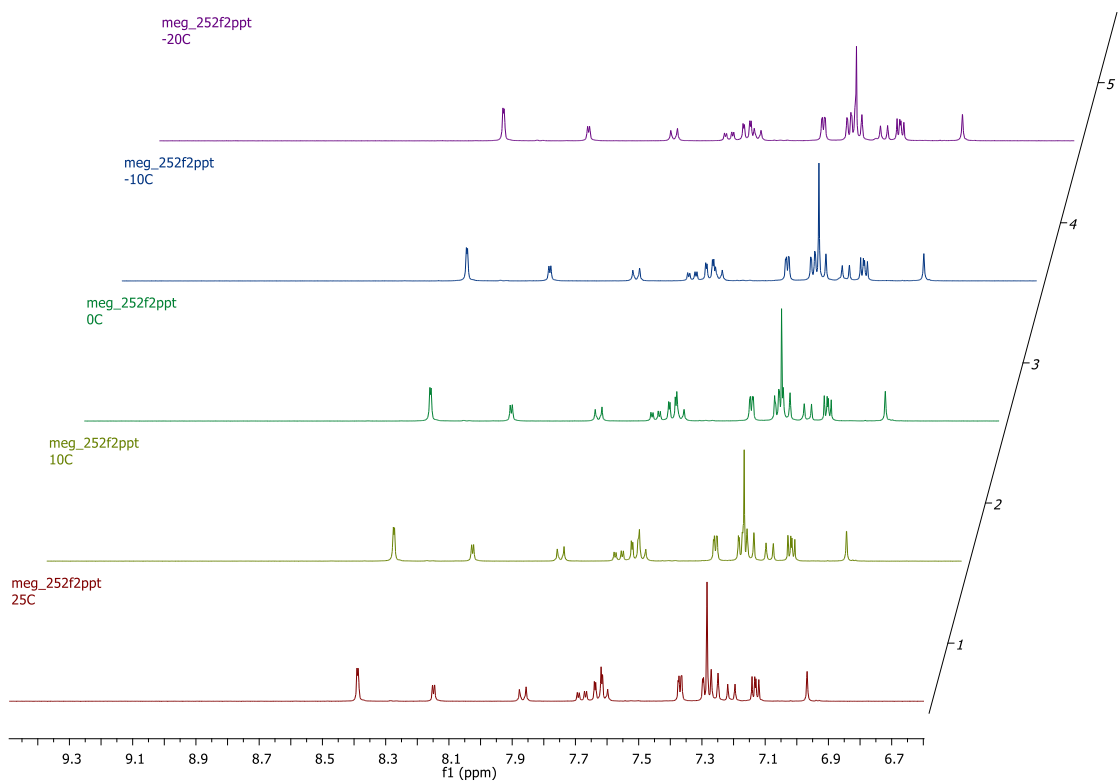
Appendix 3.1a: Stacked ^1H NMR spectra of **54** at varying temperatures in CDCl_3 . Aromatic region of interest shown.



Appendix 3.1b: Stacked ^1H NMR spectra of **58** at varying temperatures in CDCl_3 . Aromatic region of interest shown.



Appendix 3.1c: Stacked ^1H NMR spectra of **55** at varying temperatures in CDCl_3 . Aromatic region of interest shown.



Appendix 3.1d: Stacked ^1H NMR spectra of **60** at varying temperatures in CDCl_3 . Aromatic region of interest shown.

Appendix 3.2a: B3LYP/6-31G* matrix for **54**

Charge = 0 Multiplicity = 1

Symbolic Z-matrix:

C	-2.57199	-0.30092	0.07913
C	-1.29468	0.3066	0.05123
C	-1.23485	1.72744	0.02427
C	-2.43702	2.47276	0.01803
C	-3.66152	1.82735	0.04091
C	1.23247	1.7286	-0.00084
C	1.29392	0.30764	0.00991
C	2.57196	-0.29891	-0.00436
H	2.61465	-1.38493	0.00106
C	3.75888	0.42391	-0.02222
C	3.65901	1.83087	-0.02553
C	2.43374	2.47524	-0.0164
H	-2.61312	-1.38677	0.10246
H	-2.41295	3.55496	-0.00328
H	-4.57135	2.42239	0.03622
H	4.56809	2.42694	-0.03879
H	2.40841	3.5576	-0.02291
N	-0.0016	2.39374	0.00377
B	0.00014	-0.52113	0.04184
C	-0.00242	3.83681	-0.01672
C	-0.00187	4.55849	1.17516
C	-0.00357	4.52355	-1.2334
C	-0.00264	5.95522	1.15008
H	-0.00119	4.02632	2.12202
C	-0.00393	5.91579	-1.24629
H	-0.00374	3.96264	-2.16352
C	-0.00359	6.66734	-0.05748
H	-0.00237	6.48482	2.09589
H	-0.00455	6.42312	-2.20663
C	-0.00377	8.20566	-0.12076
C	-1.2658	8.68863	-0.87466
C	-0.00498	8.84997	1.27859
C	1.25953	8.68856	-0.87261
H	-1.30575	8.29939	-1.89736
H	-2.17816	8.36844	-0.3588
H	-1.27639	9.78351	-0.93496
H	0.883	8.57253	1.85803
H	-0.00557	9.94106	1.17984
H	-0.8933	8.57136	1.85695
H	1.27012	9.78342	-0.93338

H	2.171	8.36869	-0.35497
H	1.30133	8.29873	-1.89502
C	0.00191	-2.10695	0.06241
C	0.05198	-2.81443	1.28534
C	-0.04475	-2.84496	-1.14509
C	0.05547	-4.21502	1.28025
C	-0.04079	-4.24318	-1.11004
C	0.0098	-4.95158	0.09503
H	0.09551	-4.75282	2.22611
H	-0.07769	-4.7954	-2.04688
C	0.10502	-2.074	2.62292
C	1.41812	-2.34765	3.38082
C	-1.11759	-2.38778	3.50609
H	0.07747	-0.9971	2.40917
H	2.2901	-2.06837	2.77956
H	1.45184	-1.77465	4.3158
H	1.51627	-3.40898	3.63787
H	-2.05411	-2.144	2.99269
H	-1.1535	-3.44993	3.77568
H	-1.07893	-1.81046	4.43841
C	-0.10239	-2.13401	-2.49878
C	-1.41603	-2.42811	-3.24801
C	1.11973	-2.4619	-3.37736
H	-0.07837	-1.05267	-2.30872
H	-2.28765	-2.13915	-2.65083
H	-1.45364	-1.87507	-4.19476
H	-1.5112	-3.49495	-3.48245
H	2.05627	-2.20344	-2.87124
H	1.15947	-3.52935	-3.62454
H	1.07705	-1.90475	-4.3217
C	0.01703	-6.47484	0.12416
C	1.26697	-7.0564	-0.5634
C	-1.27042	-7.06894	-0.47799
H	0.05396	-6.77618	1.18027
H	2.18501	-6.66517	-0.11149
H	1.28302	-8.15004	-0.47955
H	1.2875	-6.80395	-1.63029
H	-2.15985	-6.68734	0.03524
H	-1.36589	-6.81726	-1.54102
H	-1.26945	-8.16264	-0.39393
C	-3.7599	0.42062	0.07445
C	5.97879	0.16109	1.12491

C	5.94252	0.14586	-1.23362	C	-5.75213	-0.01864	-2.41142
C	5.74094	0.03629	2.48032	C	-7.18922	0.70868	-0.57852
C	7.17737	0.78019	0.65355	C	-5.6375	-0.0205	2.64765
C	5.66305	0.00372	-2.57935	C	-7.15616	0.7081	0.88225
C	7.15491	0.77074	-0.80739	C	-6.72499	0.45052	-3.30682
C	6.69831	0.52875	3.37991	H	-4.82778	-0.47785	-2.78855
H	4.82268	-0.4381	2.85348	C	-8.14408	1.16904	-1.46968
C	8.11691	1.26349	1.54883	C	-6.56872	0.4482	3.5865
C	6.59209	0.48457	-3.51422	H	-4.697	-0.4799	2.98219
H	4.73381	-0.47519	-2.91794	C	-8.06971	1.16779	1.81605
C	8.06641	1.24228	-1.73729	C	-7.90041	1.03413	-2.84355
C	7.86587	1.13176	2.92168	H	-6.55192	0.35362	-4.38882
H	6.51925	0.43471	4.46119	H	-9.0745	1.63107	-1.11097
H	9.04107	1.74092	1.19411	C	-7.76403	1.03188	3.17738
C	7.77321	1.09296	-3.09995	H	-6.34671	0.35076	4.65948
H	6.37973	0.3769	-4.58818	H	-9.0155	1.62993	1.50025
H	9.00103	1.72394	-1.41741	H	-8.65123	1.39581	-3.56157
H	8.60454	1.51157	3.64294	H	-8.48156	1.39302	3.92892
H	8.48926	1.4633	-3.84843	N	5.13135	-0.27441	-0.03883
C	-5.98259	0.10949	-1.05505	N	-5.11881	-0.30327	0.10495
C	-5.9292	0.10858	1.3032				

Appendix 3.2b: B3LYP|6-31G* matrix for 58.

Charge = 0 Multiplicity = 1

Symbolic Z-matrix:

C	-2.57199	-0.30092	0.07913	H	4.56809	2.42694	-0.03879
C	-1.29468	0.3066	0.05123	H	2.40841	3.5576	-0.02291
C	-1.23485	1.72744	0.02427	N	-0.0016	2.39374	0.00377
C	-2.43702	2.47276	0.01803	B	0.00014	-0.52113	0.04184
C	-3.66152	1.82735	0.04091	C	-0.00242	3.83681	-0.01672
C	1.23247	1.7286	-0.00084	C	-0.00187	4.55849	1.17516
C	1.29392	0.30764	0.00991	C	-0.00357	4.52355	-1.2334
C	2.57196	-0.29891	-0.00436	C	-0.00264	5.95522	1.15008
H	2.61465	-1.38493	0.00106	H	-0.00119	4.02632	2.12202
C	3.75888	0.42391	-0.02222	C	-0.00393	5.91579	-1.24629
C	3.65901	1.83087	-0.02553	H	-0.00374	3.96264	-2.16352
C	2.43374	2.47524	-0.0164	C	-0.00359	6.66734	-0.05748
H	-2.61312	-1.38677	0.10246	H	-0.00237	6.48482	2.09589
H	-2.41295	3.55496	-0.00328	H	-0.00455	6.42312	-2.20663
H	-4.57135	2.42239	0.03622	C	-0.00377	8.20566	-0.12076
				C	-1.2658	8.68863	-0.87466
				C	-0.00498	8.84997	1.27859

C	1.25953	8.68856	-0.87261	H	2.18501	-6.66517	-0.11149
H	-1.30575	8.29939	-1.89736	H	1.28302	-8.15004	-0.47955
H	-2.17816	8.36844	-0.3588	H	1.2875	-6.80395	-1.63029
H	-1.27639	9.78351	-0.93496	H	-2.15985	-6.68734	0.03524
H	0.883	8.57253	1.85803	H	-1.36589	-6.81726	-1.54102
H	-0.00557	9.94106	1.17984	H	-1.26945	-8.16264	-0.39393
H	-0.8933	8.57136	1.85695	C	-3.7599	0.42062	0.07445
H	1.27012	9.78342	-0.93338	C	5.97879	0.16109	1.12491
H	2.171	8.36869	-0.35497	C	5.94252	0.14586	-1.23362
H	1.30133	8.29873	-1.89502	C	5.74094	0.03629	2.48032
C	0.00191	-2.10695	0.06241	C	7.17737	0.78019	0.65355
C	0.05198	-2.81443	1.28534	C	5.66305	0.00372	-2.57935
C	-0.04475	-2.84496	-1.14509	C	7.15491	0.77074	-0.80739
C	0.05547	-4.21502	1.28025	C	6.69831	0.52875	3.37991
C	-0.04079	-4.24318	-1.11004	H	4.82268	-0.4381	2.85348
C	0.0098	-4.95158	0.09503	C	8.11691	1.26349	1.54883
H	0.09551	-4.75282	2.22611	C	6.59209	0.48457	-3.51422
H	-0.07769	-4.7954	-2.04688	H	4.73381	-0.47519	-2.91794
C	0.10502	-2.074	2.62292	C	8.06641	1.24228	-1.73729
C	1.41812	-2.34765	3.38082	C	7.86587	1.13176	2.92168
C	-1.11759	-2.38778	3.50609	H	6.51925	0.43471	4.46119
H	0.07747	-0.9971	2.40917	H	9.04107	1.74092	1.19411
H	2.2901	-2.06837	2.77956	C	7.77321	1.09296	-3.09995
H	1.45184	-1.77465	4.3158	H	6.37973	0.3769	-4.58818
H	1.51627	-3.40898	3.63787	H	9.00103	1.72394	-1.41741
H	-2.05411	-2.144	2.99269	H	8.60454	1.51157	3.64294
H	-1.1535	-3.44993	3.77568	H	8.48926	1.4633	-3.84843
H	-1.07893	-1.81046	4.43841	C	-5.98259	0.10949	-1.05505
C	-0.10239	-2.13401	-2.49878	C	-5.9292	0.10858	1.3032
C	-1.41603	-2.42811	-3.24801	C	-5.75213	-0.01864	-2.41142
C	1.11973	-2.4619	-3.37736	C	-7.18922	0.70868	-0.57852
H	-0.07837	-1.05267	-2.30872	C	-5.6375	-0.0205	2.64765
H	-2.28765	-2.13915	-2.65083	C	-7.15616	0.7081	0.88225
H	-1.45364	-1.87507	-4.19476	C	-6.72499	0.45052	-3.30682
H	-1.5112	-3.49495	-3.48245	H	-4.82778	-0.47785	-2.78855
H	2.05627	-2.20344	-2.87124	C	-8.14408	1.16904	-1.46968
H	1.15947	-3.52935	-3.62454	C	-6.56872	0.4482	3.5865
H	1.07705	-1.90475	-4.3217	H	-4.697	-0.4799	2.98219
C	0.01703	-6.47484	0.12416	C	-8.06971	1.16779	1.81605
C	1.26697	-7.0564	-0.5634	C	-7.90041	1.03413	-2.84355
C	-1.27042	-7.06894	-0.47799	H	-6.55192	0.35362	-4.38882
H	0.05396	-6.77618	1.18027	H	-9.0745	1.63107	-1.11097

C	-7.76403	1.03188	3.17738
H	-6.34671	0.35076	4.65948
H	-9.0155	1.62993	1.50025
H	-8.65123	1.39581	-3.56157

H	-8.48156	1.39302	3.92892
N	5.13135	-0.27441	-0.03883
N	-5.11881	-0.30327	0.10495

Appendix 3.2c: B3LYP|6-31G* matrix for 55.

Charge = 0 Multiplicity = 1

Symbolic Z-Matrix:

C	2.61728	-0.30407	-0.09464
C	1.34037	0.30142	-0.13967
C	1.27883	1.72221	-0.19523
C	2.47779	2.47486	-0.21148
C	3.70471	1.83849	-0.17459
C	-1.18713	1.7222	-0.19522
C	-1.24867	0.30142	-0.13966
C	-2.52558	-0.30408	-0.09461
H	-2.58192	-1.38723	-0.0366
C	-3.61302	1.83848	-0.17456
C	-2.3861	2.47486	-0.21146
H	2.67362	-1.38722	-0.03664
H	2.4477	3.55568	-0.25888
H	4.6188	2.42479	-0.19714
H	-4.52711	2.42478	-0.19715
H	-2.35601	3.55567	-0.25889
N	0.04585	2.38642	-0.22444
B	0.04585	-0.52873	-0.09166
C	0.04584	3.83066	-0.25569
C	0.04586	4.50973	-1.47209
C	0.04582	4.55789	0.9372
C	0.04585	5.90671	-1.49427
H	0.04588	3.94576	-2.4004
C	0.04581	5.94956	0.90232
H	0.04581	4.02932	1.88608
C	0.04583	6.65988	-0.31182
H	0.04587	6.40345	-2.45767
H	0.04579	6.4891	1.84485
C	0.04582	8.19938	-0.30112
C	1.30858	8.70745	0.43498
C	0.04582	8.79539	-1.72169
C	-1.21695	8.70744	0.43497

H	1.34874	8.35462	1.47077
H	2.22064	8.36927	-0.06978
H	1.31949	9.80369	0.45678
H	-0.84238	8.49804	-2.29074
H	0.04581	9.88907	-1.65971
H	0.93404	8.49806	-2.29073
H	-1.22786	9.80369	0.45676
H	-2.12901	8.36925	-0.06978
H	-1.25711	8.35463	1.47077
C	0.04585	-2.10878	0.04088
C	0.04577	-2.94354	-1.09994
C	0.04595	-2.71357	1.32224
C	0.04578	-4.33537	-0.9446
C	0.04596	-4.10734	1.4363
C	0.04587	-4.94124	0.31309
H	0.04572	-4.97114	-1.82802
H	0.04604	-4.55509	2.42776
C	0.04566	-2.35397	-2.51071
C	-1.22145	-2.73897	-3.2979
C	1.3128	-2.73873	-3.29799
H	0.04556	-1.25945	-2.41501
H	-2.13034	-2.45232	-2.75826
H	-1.23305	-2.24527	-4.27759
H	-1.26858	-3.82049	-3.47154
H	2.22166	-2.45186	-2.75843
H	1.36014	-3.82025	-3.47157
H	1.32421	-2.24507	-4.27769
C	0.04607	-1.86326	2.59417
C	1.3167	-2.08487	3.43655
C	-1.22438	-2.08489	3.43681
H	0.04602	-0.80783	2.29065
H	2.22023	-1.87361	2.85444
H	1.31751	-1.42942	4.31617
H	1.38481	-3.11922	3.79349
H	-2.12804	-1.87368	2.85488

H	-1.29239	-3.11923	3.79381	C	10.66705	-1.69303	3.32112
H	-1.22503	-1.4294	4.31641	H	8.71702	-1.02952	2.65509
C	0.04588	-6.45879	0.44633	C	11.95755	-3.07159	1.79005
C	-1.22394	-6.97425	1.14967	C	9.71531	-4.1845	-2.99296
C	1.31579	-6.97423	1.14952	H	7.9563	-3.02977	-2.4849
H	0.04583	-6.87093	-0.57227	C	11.48095	-4.31479	-1.32753
H	-2.12791	-6.64266	0.62725	C	11.82846	-2.42419	3.01577
H	-1.23054	-8.0705	1.18314	H	10.5841	-1.20026	4.28624
H	-1.28343	-6.60969	2.18202	H	12.85432	-3.64117	1.55972
H	2.2197	-6.64264	0.62701	C	10.97858	-4.64582	-2.58279
H	1.37539	-6.60968	2.18187	H	9.34373	-4.44893	-3.97933
H	1.32241	-8.07049	1.18299	H	12.46109	-4.66692	-1.0161
C	-9.40065	-2.93278	-0.96285	H	12.63044	-2.48578	3.74599
C	-9.72752	-2.11544	1.12558	H	11.56766	-5.26383	-3.25449
C	-8.89469	-3.23521	-2.22952	N	-8.83516	-2.15763	0.05204
C	-10.67086	-3.3989	-0.53526	N	8.8602	-2.29691	0.11157
C	-9.59216	-1.47789	2.36161	C	-3.69812	0.43538	-0.11117
C	-10.88014	-2.87635	0.79933	C	-5.05938	-0.28294	-0.06049
C	-9.67541	-4.03144	-3.06488	C	-6.24284	0.46932	-0.07747
H	-7.92984	-2.85822	-2.55284	C	-5.11084	-1.67428	-0.00776
C	-11.43413	-4.19763	-1.39534	C	-7.47611	-0.19719	-0.0394
C	-10.63971	-1.60272	3.27171	C	-6.34119	-2.32996	0.03133
H	-8.70042	-0.90889	2.60523	H	-4.17732	-2.25588	0.00192
C	-11.91711	-2.98549	1.73346	C	-7.52244	-1.58864	0.01609
C	-10.93139	-4.51221	-2.65467	H	-8.41034	0.3842	-0.04569
H	-9.30348	-4.28324	-4.05442	H	-6.37976	-3.428	0.07403
H	-12.40871	-4.56482	-1.08383	H	-6.20527	1.53786	-0.11886
C	-11.79258	-2.34629	2.96396	C	3.78982	0.43539	-0.11121
H	-10.56013	-1.11665	4.24049	C	5.15109	-0.28293	-0.06055
H	-12.8072	-3.56472	1.50125	C	6.33454	0.46934	-0.07754
H	-11.51453	-5.13241	-3.32953	C	5.20228	-1.67341	0.01147
H	-12.59145	-2.42401	3.69603	C	7.56758	-0.19641	-0.02243
C	9.75515	-2.23462	1.18198	C	6.43244	-2.32847	0.06452
C	9.43264	-3.07274	-0.89888	H	4.26868	-2.25473	0.02753
C	9.61528	-1.58896	2.41328	C	7.61372	-1.58726	0.04671
C	10.91649	-2.98325	0.85826	H	8.50199	0.3844	-0.04183
C	8.92688	-3.39174	-2.16156	H	6.47083	-3.42593	0.12022
C	10.71	-3.5191	-0.47148	H	6.29714	1.5373	-0.13191

Appendix 3.2d: B3LYP|6-31G* matrix for 60.

Charge = 0 Multiplicity = 1

Symbolic Z-Matrix:

C -2.57199 -0.30092 0.07913

C	-1.29468	0.3066	0.05123	C	0.05198	-2.81443	1.28534
C	-1.23485	1.72744	0.02427	C	-0.04475	-2.84496	-1.14509
C	-2.43702	2.47276	0.01803	C	0.05547	-4.21502	1.28025
C	-3.66152	1.82735	0.04091	C	-0.04079	-4.24318	-1.11004
C	1.23247	1.7286	-0.00084	C	0.0098	-4.95158	0.09503
C	1.29392	0.30764	0.00991	H	0.09551	-4.75282	2.22611
C	2.57196	-0.29891	-0.00436	H	-0.07769	-4.7954	-2.04688
H	2.61465	-1.38493	0.00106	C	0.10502	-2.074	2.62292
C	3.75888	0.42391	-0.02222	C	1.41812	-2.34765	3.38082
C	3.65901	1.83087	-0.02553	C	-1.11759	-2.38778	3.50609
C	2.43374	2.47524	-0.0164	H	0.07747	-0.9971	2.40917
H	-2.61312	-1.38677	0.10246	H	2.2901	-2.06837	2.77956
H	-2.41295	3.55496	-0.00328	H	1.45184	-1.77465	4.3158
H	-4.57135	2.42239	0.03622	H	1.51627	-3.40898	3.63787
H	4.56809	2.42694	-0.03879	H	-2.05411	-2.144	2.99269
H	2.40841	3.5576	-0.02291	H	-1.1535	-3.44993	3.77568
N	-0.0016	2.39374	0.00377	H	-1.07893	-1.81046	4.43841
B	0.00014	-0.52113	0.04184	C	-0.10239	-2.13401	-2.49878
C	-0.00242	3.83681	-0.01672	C	-1.41603	-2.42811	-3.24801
C	-0.00187	4.55849	1.17516	C	1.11973	-2.4619	-3.37736
C	-0.00357	4.52355	-1.2334	H	-0.07837	-1.05267	-2.30872
C	-0.00264	5.95522	1.15008	H	-2.28765	-2.13915	-2.65083
H	-0.00119	4.02632	2.12202	H	-1.45364	-1.87507	-4.19476
C	-0.00393	5.91579	-1.24629	H	-1.5112	-3.49495	-3.48245
H	-0.00374	3.96264	-2.16352	H	2.05627	-2.20344	-2.87124
C	-0.00359	6.66734	-0.05748	H	1.15947	-3.52935	-3.62454
H	-0.00237	6.48482	2.09589	H	1.07705	-1.90475	-4.3217
H	-0.00455	6.42312	-2.20663	C	0.01703	-6.47484	0.12416
C	-0.00377	8.20566	-0.12076	C	1.26697	-7.0564	-0.5634
C	-1.2658	8.68863	-0.87466	C	-1.27042	-7.06894	-0.47799
C	-0.00498	8.84997	1.27859	H	0.05396	-6.77618	1.18027
C	1.25953	8.68856	-0.87261	H	2.18501	-6.66517	-0.11149
H	-1.30575	8.29939	-1.89736	H	1.28302	-8.15004	-0.47955
H	-2.17816	8.36844	-0.3588	H	1.2875	-6.80395	-1.63029
H	-1.27639	9.78351	-0.93496	H	-2.15985	-6.68734	0.03524
H	0.883	8.57253	1.85803	H	-1.36589	-6.81726	-1.54102
H	-0.00557	9.94106	1.17984	H	-1.26945	-8.16264	-0.39393
H	-0.8933	8.57136	1.85695	C	-3.7599	0.42062	0.07445
H	1.27012	9.78342	-0.93338	C	5.97879	0.16109	1.12491
H	2.171	8.36869	-0.35497	C	5.94252	0.14586	-1.23362
H	1.30133	8.29873	-1.89502	C	5.74094	0.03629	2.48032
C	0.00191	-2.10695	0.06241	C	7.17737	0.78019	0.65355

C	5.66305	0.00372	-2.57935	H	-6.36373	0.35895	4.63288
C	7.15491	0.77074	-0.80739	C	8.77565	1.61141	-4.14778
H	4.82268	-0.4381	2.85348	C	8.62152	1.53382	-5.51415
C	8.11691	1.26349	1.54883	S	10.21554	2.35355	-3.73296
H	4.73381	-0.47519	-2.91794	C	9.73702	2.11095	-6.2023
C	8.06641	1.24228	-1.73729	H	7.76613	1.09308	-6.0293
C	7.86587	1.13176	2.92168	C	10.67861	2.59504	-5.32154
H	9.04107	1.74092	1.19411	H	9.81051	2.15115	-7.29057
C	7.77321	1.09296	-3.09995	H	11.61457	3.0781	-5.59506
H	9.00103	1.72394	-1.41741	C	8.89997	1.66347	3.9314
C	-5.98259	0.10949	-1.05505	C	8.78799	1.60347	5.30276
C	-5.9292	0.10858	1.3032	S	10.32633	2.3998	3.46296
C	-5.75213	-0.01864	-2.41142	C	9.92472	2.18784	5.94877
C	-7.18922	0.70868	-0.57852	H	7.94872	1.17	5.84962
C	-5.6375	-0.0205	2.64765	C	10.8384	2.66089	5.0333
C	-7.15616	0.7081	0.88225	H	10.03231	2.24077	7.03365
H	-4.82778	-0.47785	-2.78855	H	11.7822	3.14731	5.27165
C	-8.14408	1.16904	-1.46968	C	-8.76854	1.53745	4.2295
H	-4.697	-0.4799	2.98219	C	-8.60323	1.47067	5.59513
C	-8.06971	1.16779	1.81605	S	-10.22508	2.24999	3.82095
C	-7.90041	1.03413	-2.84355	C	-9.72446	2.0307	6.28808
H	-9.0745	1.63107	-1.11097	H	-7.73602	1.04907	6.10655
C	-7.76403	1.03188	3.17738	C	-10.68126	2.49191	5.41145
H	-9.0155	1.62993	1.50025	H	-9.79091	2.0758	7.37661
N	5.13135	-0.27441	-0.03883	H	-11.62418	2.95887	5.68902
N	-5.11881	-0.30327	0.10495	C	-8.95152	1.54046	-3.84874
C	6.59209	0.48457	-3.51422	C	-8.84823	1.47465	-5.22051
H	6.39639	0.38557	-4.56151	S	-10.38812	2.25255	-3.37413
C	6.69831	0.52875	3.37991	C	-10.00035	2.03381	-5.86154
H	6.53514	0.44292	4.43391	H	-8.00487	1.05387	-5.77098
C	-6.72499	0.45052	-3.30682	C	-10.91621	2.49488	-4.94216
H	-6.56777	0.36169	-4.36147	H	-10.11666	2.07843	-6.9459
C	-6.56872	0.4482	3.5865	H	-11.87069	2.9621	-5.1764

Appendix 3.2e: B3LYP|6-31G* matrix for 33.

Charge = 0 Multiplicity = 1

Symbolic Z-Matrix:

C	-2.57199	-0.30092	0.07913	C	-3.66152	1.82735	0.04091
C	-1.29468	0.3066	0.05123	C	1.23247	1.7286	-0.00084
C	-1.23485	1.72744	0.02427	C	1.29392	0.30764	0.00991
C	-2.43702	2.47276	0.01803	C	2.57196	-0.29891	-0.00436
				H	2.61465	-1.38493	0.00106
				C	3.75888	0.42391	-0.02222
				C	3.65901	1.83087	-0.02553
				C	2.43374	2.47524	-0.0164

H	-2.61312	-1.38677	0.10246	H	2.2901	-2.06837	2.77956
H	-2.41295	3.55496	-0.00328	H	1.45184	-1.77465	4.3158
H	-4.57135	2.42239	0.03622	H	1.51627	-3.40898	3.63787
H	4.56809	2.42694	-0.03879	H	-2.05411	-2.144	2.99269
H	2.40841	3.5576	-0.02291	H	-1.1535	-3.44993	3.77568
N	-0.0016	2.39374	0.00377	H	-1.07893	-1.81046	4.43841
B	0.00014	-0.52113	0.04184	C	-0.10239	-2.13401	-2.49878
C	-0.00242	3.83681	-0.01672	C	-1.41603	-2.42811	-3.24801
C	-0.00187	4.55849	1.17516	C	1.11973	-2.4619	-3.37736
C	-0.00357	4.52355	-1.2334	H	-0.07837	-1.05267	-2.30872
C	-0.00264	5.95522	1.15008	H	-2.28765	-2.13915	-2.65083
H	-0.00119	4.02632	2.12202	H	-1.45364	-1.87507	-4.19476
C	-0.00393	5.91579	-1.24629	H	-1.5112	-3.49495	-3.48245
H	-0.00374	3.96264	-2.16352	H	2.05627	-2.20344	-2.87124
C	-0.00359	6.66734	-0.05748	H	1.15947	-3.52935	-3.62454
H	-0.00237	6.48482	2.09589	H	1.07705	-1.90475	-4.3217
H	-0.00455	6.42312	-2.20663	C	0.01703	-6.47484	0.12416
C	-0.00377	8.20566	-0.12076	C	1.26697	-7.0564	-0.5634
C	-1.2658	8.68863	-0.87466	C	-1.27042	-7.06894	-0.47799
C	-0.00498	8.84997	1.27859	H	0.05396	-6.77618	1.18027
C	1.25953	8.68856	-0.87261	H	2.18501	-6.66517	-0.11149
H	-1.30575	8.29939	-1.89736	H	1.28302	-8.15004	-0.47955
H	-2.17816	8.36844	-0.3588	H	1.2875	-6.80395	-1.63029
H	-1.27639	9.78351	-0.93496	H	-2.15985	-6.68734	0.03524
H	0.883	8.57253	1.85803	H	-1.36589	-6.81726	-1.54102
H	-0.00557	9.94106	1.17984	H	-1.26945	-8.16264	-0.39393
H	-0.8933	8.57136	1.85695	C	-3.7599	0.42062	0.07445
H	1.27012	9.78342	-0.93338	C	5.97879	0.16109	1.12491
H	2.171	8.36869	-0.35497	C	5.94252	0.14586	-1.23362
H	1.30133	8.29873	-1.89502	C	5.74094	0.03629	2.48032
C	0.00191	-2.10695	0.06241	C	7.17737	0.78019	0.65355
C	0.05198	-2.81443	1.28534	C	5.66305	0.00372	-2.57935
C	-0.04475	-2.84496	-1.14509	C	7.15491	0.77074	-0.80739
C	0.05547	-4.21502	1.28025	C	6.69831	0.52875	3.37991
C	-0.04079	-4.24318	-1.11004	H	4.82268	-0.4381	2.85348
C	0.0098	-4.95158	0.09503	C	8.11691	1.26349	1.54883
H	0.09551	-4.75282	2.22611	C	6.59209	0.48457	-3.51422
H	-0.07769	-4.7954	-2.04688	H	4.73381	-0.47519	-2.91794
C	0.10502	-2.074	2.62292	C	8.06641	1.24228	-1.73729
C	1.41812	-2.34765	3.38082	C	7.86587	1.13176	2.92168
C	-1.11759	-2.38778	3.50609	H	9.04107	1.74092	1.19411
H	0.07747	-0.9971	2.40917	C	7.77321	1.09296	-3.09995

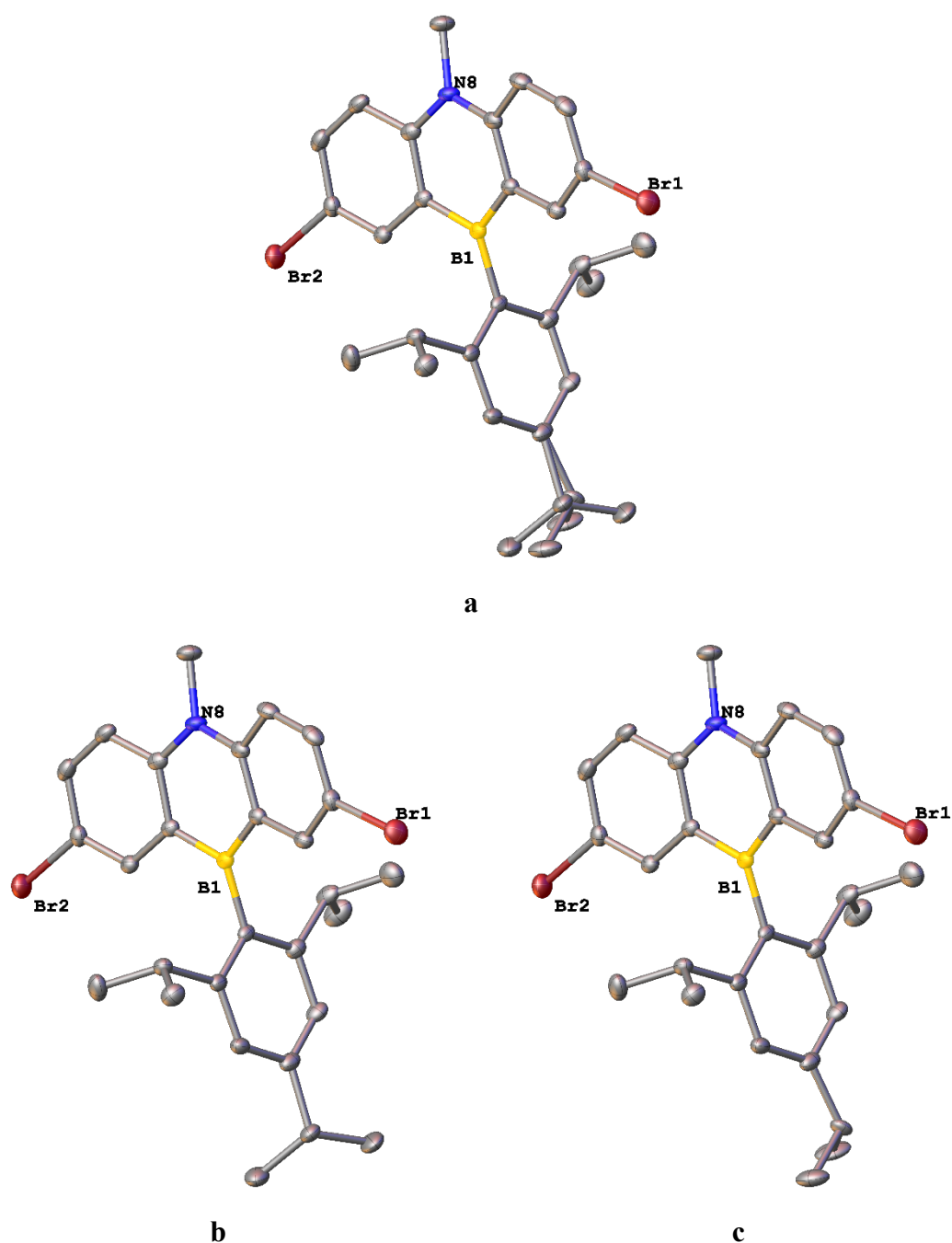
H	9.00103	1.72394	-1.41741	C	6.58422	0.46325	7.33158
H	8.60454	1.51157	3.64294	H	4.64259	-0.53981	7.55889
H	8.48926	1.4633	-3.84843	H	6.87927	0.61389	8.36814
C	-5.98259	0.10949	-1.05505	C	6.2948	0.33384	-5.01772
C	-5.9292	0.10858	1.3032	C	7.11024	0.75626	-6.04405
C	-5.75213	-0.01864	-2.41142	S	4.90028	-0.38459	-5.5968
C	-7.18922	0.70868	-0.57852	C	6.53867	0.4628	-7.32395
C	-5.6375	-0.0205	2.64765	H	8.07408	1.25352	-5.9212
C	-7.15616	0.7081	0.88225	C	5.31959	-0.16595	-7.20077
C	-6.72499	0.45052	-3.30682	H	7.02664	0.71536	-8.26706
H	-4.82778	-0.47785	-2.78855	H	4.68684	-0.49089	-8.02431
C	-8.14408	1.16904	-1.46968	C	-6.4827	0.31486	-4.82158
C	-6.56872	0.4482	3.5865	C	-5.36815	-0.24014	-5.41022
H	-4.697	-0.4799	2.98219	S	-7.58245	0.84374	-5.96481
C	-8.06971	1.16779	1.81605	C	-5.45939	-0.21154	-6.83914
C	-7.90041	1.03413	-2.84355	H	-4.51205	-0.65548	-4.87551
H	-9.0745	1.63107	-1.11097	C	-6.63792	0.36434	-7.25878
C	-7.76403	1.03188	3.17738	H	-4.67942	-0.60335	-7.49449
H	-9.0155	1.62993	1.50025	H	-6.94315	0.50341	-8.294
H	-8.65123	1.39581	-3.56157	C	-6.25792	0.31178	5.08863
H	-8.48156	1.39302	3.92892	C	-7.07382	0.72473	6.11845
N	5.13135	-0.27441	-0.03883	S	-4.84602	-0.37695	5.66163
N	-5.11881	-0.30327	0.10495	C	-6.4877	0.44946	7.39581
C	6.44763	0.3971	4.89366	H	-8.04771	1.20306	5.99978
C	5.33947	-0.17546	5.47752	C	-5.25791	-0.15697	7.26734
S	7.52893	0.95304	6.04164	H	-6.97359	0.69826	8.34099
C	5.4198	-0.13708	6.90687	H	-4.61328	-0.46518	8.08809
H	4.49522	-0.60986	4.93912				

Appendix 3.3a: X-ray crystallographic data for Chapter Four.

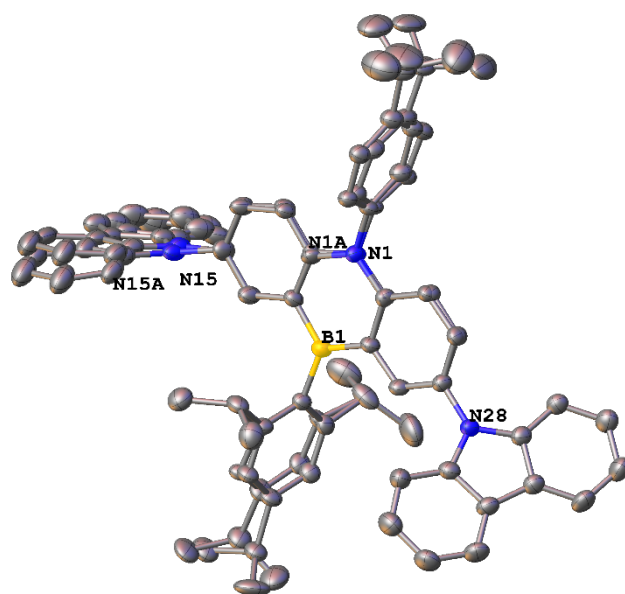
	51	53	58
Identification code	TCD1428	TCD1402	TCD1408
Empirical formula	C ₃₇ H ₄₂ BBr ₂ N	C ₂₈ H ₃₂ BBr ₂ N	C ₆₂ H ₆₀ BCl ₂ N ₃
Formula weight	671.34	553.17	929.02
Temperature (K)	100(2)	100(2)	100(2)
Wavelength (Å)	0.71073	1.54178	0.71073
Crystal system	Orthorhombic	Monoclinic	Triclinic

Space group	Aba2	P2 ₁ /n	P $\bar{1}$
	$a = 10.5518(10)$	$a = 13.6889(6)$	$a = 13.3109(7)$
	$b = 35.263(3)$	$b = 10.7255(5)$	$b = 13.7258(7)$
Unit cell dimensions (Å, °)	$c = 26.309(2)$	$c = 17.8627(8)$	$c = 16.4802(7)$
	$\alpha = 90$	$\alpha = 90$	$\alpha = 92.1727(17)$
	$\beta = 90$	$\beta = 105.2586(12)$	$\beta = 104.2554(18)$
	$\gamma = 90$	$\gamma = 90$	$\gamma = 102.1312(18)$
Volume (Å ³)	9789.4(16)	2530.2(2)	2840.3(2)
Z	12	4	2
Density (calculated) (Mg/m ³)	1.367	1.452	1.086
Absorption coefficient (mm ⁻¹)	2.510	4.166	0.153
F(000)	4152	1128	984
Crystal size (mm ³)	0.46 x 0.17 x 0.04	0.18 x 0.14 x 0.13	0.39 x 0.29 x 0.17
Theta range for data collection (°)	2.707 to 26.852	3.642 to 70.027	2.313 to 26.166
	$-13 \leq h \leq 13,$	$-16 \leq h \leq 16,$	$-16 \leq h \leq 16,$
Index ranges	$-44 \leq k \leq 37,$	$-13 \leq k \leq 13,$	$-15 \leq k \leq 17,$
	$-33 \leq l \leq 33$	$-21 \leq l \leq 21$	$-20 \leq l \leq 20$
Reflections collected	41492	47489	36455
	10434	4774	11281
Independent reflections	[R(int) = 0.0780]	[R(int) = 0.0367]	[R(int) = 0.0694]
Completeness to theta = 25.242° (%)	99.9	100.0	99.8
Absorption correction	Semi-empirical from equivalents	Semi-empirical from equivalents	Semi-empirical from equivalents
Max. and min. transmission	0.7454 and 0.4471	0.7533 and 0.6068	0.7453 and 0.6930
Refinement method	Full-matrix least- squares on F^2	Full-matrix least-squares on F^2	Full-matrix least-squares on F^2
Data / restraints / parameters	10434 / 269 / 681	4774 / 3 / 326	11281 / 1855 / 998
Goodness-of-fit on F^2	1.035	1.093	1.034
	$R1 = 0.0528$	$R1 = 0.0328$	$R1 = 0.0901$
Final R indices [$I > 2\sigma(I)$] ^a	$wR2 = 0.1182$	$wR2 = 0.0901$	$wR2 = 0.2436$
	$R1 = 0.0782$	$R1 = 0.0331$	$R1 = 0.1645$
R indices (all data) ^b	$wR2 = 0.1314$	$wR2 = 0.0904$	$wR2 = 0.2974$
Extinction coefficient	0.010(8)	-	0.015(3)
Largest diff. peak and hole (e.Å ⁻³)	1.062 and -1.017	0.470 and -0.532	0.638 and -0.317

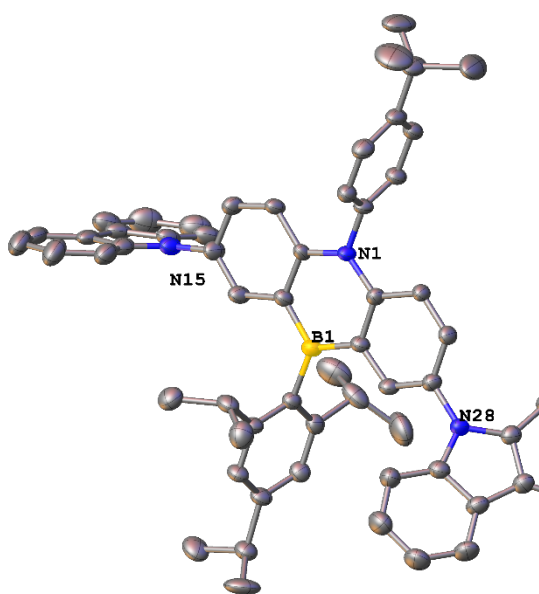
$$^a R1 = \frac{\sum ||Fo| - |Fc||}{\sum |Fo|}, \quad ^b wR2 = \left[\frac{\sum \{w(Fo^2 - Fc^2)^2\}}{\sum w(Fo^2)^2} \right]^{1/2}.$$



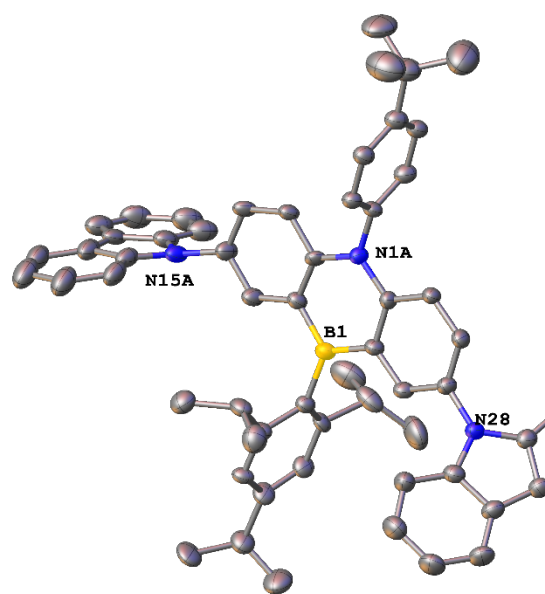
Appendix 3.3d: Compound **51** showing (a) complete molecule with disordered iPr group, and (b) majority occupied disordered moiety with 69% occupancy, and (c) minority disordered moiety has a 31% occupancy. Atomic displacement shown at 50% probability, heteroatoms labelled only and hydrogen atoms omitted for clarity.



a

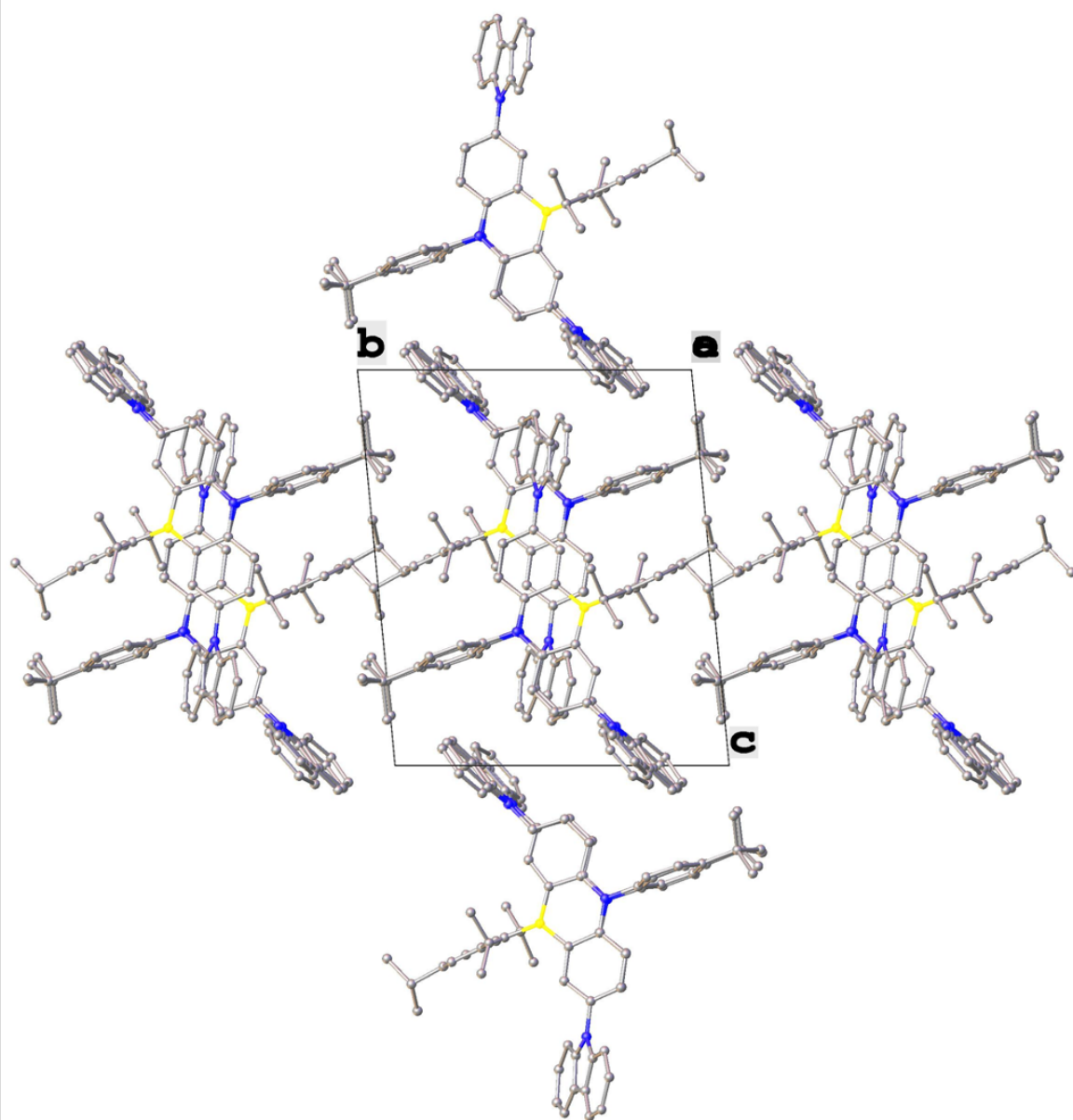


b

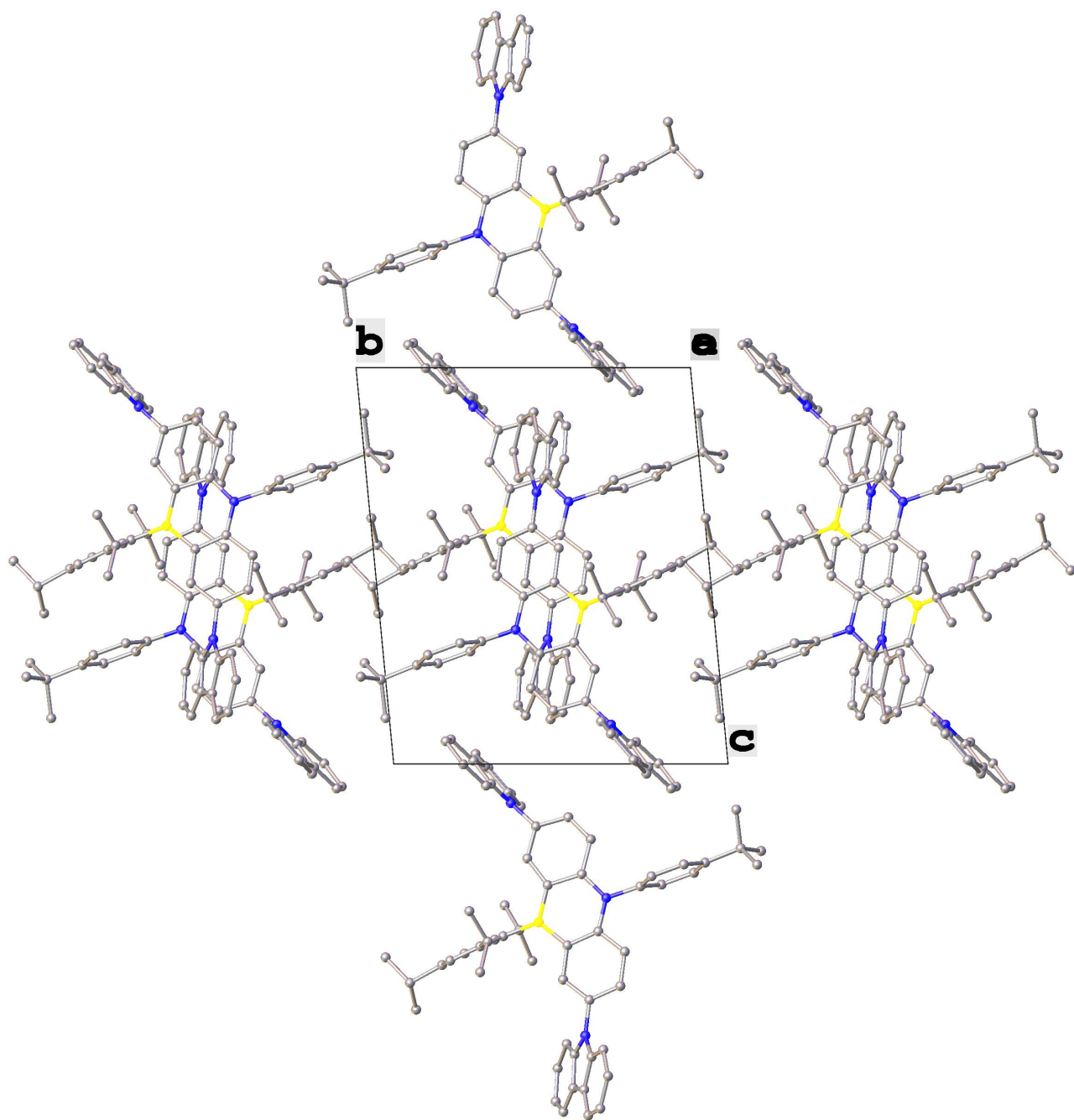


c

Appendix 3.3e: 58 showing (a) complete molecule showing disorder in TIP ring, carbazole and azaborine rings, tBu group, and (b) majority occupied disordered moiety with 70% occupancy, and (c) minority disordered moiety has a 30% occupancy. Atomic displacement shown at 50% probability, heteroatoms labelled only and hydrogen atoms omitted for clarity.



Appendix 3.3f: Schematic packing diagram of **58** including the full disorder, viewed normal to the a-axis. Hydrogen atoms are omitted for clarity.



Appendix 3.3g: Schematic packing diagram of **58** disorder **b**, the minor occupied moiety. (occupancy 30%), viewed normal to the a-axis. Hydrogen atoms are omitted for clarity.